Compaction Mechanisms in Mudstones and Shales: Implications from the Laboratory and Nature

Louise Marie Duffy

School of Civil Engineering and Geosciences

Newcastle University

Submitted in partial fulfilment of the requirements for

the degree of Doctor of Philosophy.

2011

THESIS CONTAINS

VIDEO

CD

DVD

TAPE CASSETTE

Abstract

This thesis details the analysis of experimental compaction and measurements upon natural samples to quantify the relative roles of mechanical and chemical processes during porosity loss in mudstones and shales, whilst understanding the concepts behind their behaviour at the pore-scale.

The primary controls on the mechanical mechanisms observed are effective stress above the previous maximum, temperature and time. Mechanisms include grain packing/compression and rotation to produce minor fabric development and also thermal hardening. Effects of these mechanisms are quantified in Chapter 3, "Laboratory Simulation of Mudstone Compaction". This work program included extended duration triaxial experiments, testing the results of high effective stresses (max. 50MPa) with varied fluid chemistries and temperatures on compaction behaviour. Primary controls on chemical mechanisms are again stress, temperature and time with the addition of fluid chemistry. The mechanisms include the effects of chemical alteration such as potassium exchange and dehydration, but also the effects of full mineralogical transformation such as the ordering associated with illitization and the proposed link to higher degrees of alignment of phyllosilicates. This is covered in both Chapter 3 and Chapter 4, "Mudstone Compaction in Nature: Malay Basin Case Study", a study to characterise both the chemical/mineralogical and physical properties of fine-grained clastics from a region where chemical processes would be expected to be enhanced.

Other processes in addition to lithology dependant degrees of packing and rotation associated with increased effective stress are not generally incorporated in porosity reduction calculations. Their inclusion may be necessary in more challenging regions such as the Malay Basin.

Acknowledgements

The sponsors of this CASE Studentship, the Natural Environment Research Council and Shell International Exploration and Production BV. are gratefully acknowledged. This study has also benefited from additional grants provided by NERC that allowed key sections of work (HRXTG and Intermediate Tests) to be completed. In addition, Shell has provided placements, laboratory/equipment use, samples and the guidance of their technical staff.

I am very grateful to my academic supervisors Prof. Andrew Aplin and Frans Kets for all of the insight and assistance they have provided throughout the project and to my laboratory supervisor at Shell, Frans Korndorffer who provided vital technical support. I would also like to thank Dr. M Jamaal Hoesni and PETRONAS Research Sdn. Bhd. for useful discussions and providing samples and data.

I extend my gratitude to all of the staff, technicians and researchers I have worked with over the course of the project whilst at Newcastle University, Shell, Durham University and also the University of Michigan. These include: Dr. Claire Fialips; Philip Green, Maggie White, Ian Harrison, Stuart Patterson Fred Beadle, Trevor Whitfield, Yvonne Hall, Kath Liddell, Pauline Carrick (Newcastle University); Fons Marcelis, Arjan Van Der Linden, Axel Makurat, Neil Braunsdorf (Shell); Prof. David Petley, Alison Clark, Chris Longley (Durham University); Prof. Ben Van Der Pluijm, Dr. Anja Schleicher (University of Michigan); Dr. Ruarri Day-Stirrat (University of Texas at Austin).

Finally, I would like to acknowledge my family: Lucia, James, Caroline & Peter Duffy and Therese, Stephen, Nina & Joel Martin, along with Eileen Gallon and Jane Duffy for their patience and support.

Table of Contents

List of Figures

List of Tables

Declaration

The content of this thesis is the original work of the author (other people's work, where included, is acknowledged by reference). It has not been previously submitted for a degree at this or any other university.

L.M. Duffy
Newcastle upon Tyne
September 2011

Chapter 1
Introduction

1. Introduction

1.1 Project Aims

The principle aim of this project was to understand and quantify the relative roles of mechanical and chemical processes during porosity loss in mudstones and shales. Increased focus on mudstone and shale research has developed due to their importance as source and seal for conventional hydrocarbons, their influence on wellbore stability and, more recently, in unconventional gas exploration. This motivation has generated a drive to gain greater understanding of these rocks and the basic principles that control their behaviour, with those that govern the properties of porosity and permability being key. This thesis details the use of experimental and "field" approaches to investigate these principles, both with the final goal of creating qualitative and quantitative models of the mechanisms by which fine grained, clastic ,sediments compact in the burial environment.

The experimental portion of the project was a geotechnical/geochemical program that analysed the alteration of physical rock properties on a laboratory timescale. Previously, stability issues, inadequacy of equipment or lack of impetus in shale research has meant that some key ideas have either not been proven experimentally or not adequately transferred from the discipline of civil engineering to geoscience. In this thesis, this specifically refers to the effects of chemistry and temperature on "mechanical" compaction. This study has allowed the construction of mechanism descriptive, qualitative models of the way in which porosity loss proceeds due to the

influences of temperature and chemistry under normal consolidation at "geological" effective stresses.

The "field" section of the work program comprised a case study of natural samples collected from 2 wells in the Malay Basin, offshore Peninsular Malaysia. Elevated geothermal gradient in this region allowed quantitative comparison of porosity loss in natural samples due to the effects of temperature and chemical/mineralogical change with that predicted by mechanical compaction alone. This could allow for the quantification of porosity loss and better informed use of relationships used to construct models such as those used in petroleum systems analysis.

These dual approaches guided the development of the research program and the structure of this thesis which is discussed further in Section 1.6.

1.2 Porosity in Mudstones and Shales

As stated in Krushin (2005) typical oil-field jargon defines shales as any very fine grained clastic rock, although this definition can sometimes be even broader. In this thesis the definitions used are based on those described in Loucks *et al.* (2009) where the term mudstone is used to describe fine-grained, clastic sedimentary rocks comprised of >50% silt/clay grains of 65μm or less. Rocks would be further defined as shales if they displayed this composition in addition to a degree of fissility (Potter *et al.*, 2005). These classifications would include both siltstones where >50% of the grains are 2-63μm and claystones where >50% of the grains are <2μm (Moore & Reynolds, 1997). However, when discussing clay content, such as in the context of mineralogy with depth, the clay content/total clay was normally based on the abundances of clay minerals from X-ray diffraction measurements. Such focus on definitions may seem pedantic, but as is shown in later chapters, the abundance of clays relative to other minerals in rocks broadly defined as shales can have an impact on important features, such as grain alignment.

As the fine-grained, clastic sediments that form mudstones and shales compact, they undergo reduction in volume and porosity. The porosity of a rock is simply defined as that part of the material that is not occupied by mineral grains (Pearson, 1999) or as a measure of its voids and ability to hold a fluid (Baker Hughes, 2006). The effective porosity is the percentage of interconnected pore space. How the porosity is connected and its ability to transmit fluids (permeability) can influence its measurement and more detailed definitions such as those in Pearson (1999). One definition from that study describes physical porosity as the space that can be

measured with injection techniques such as mercury injection porosimetry. This technique is a very effective tool and is used in this project (see Chapter 2). However, it is only capable of measuring pores down to throat (pore entrance) size of ~3nm (30 Å).

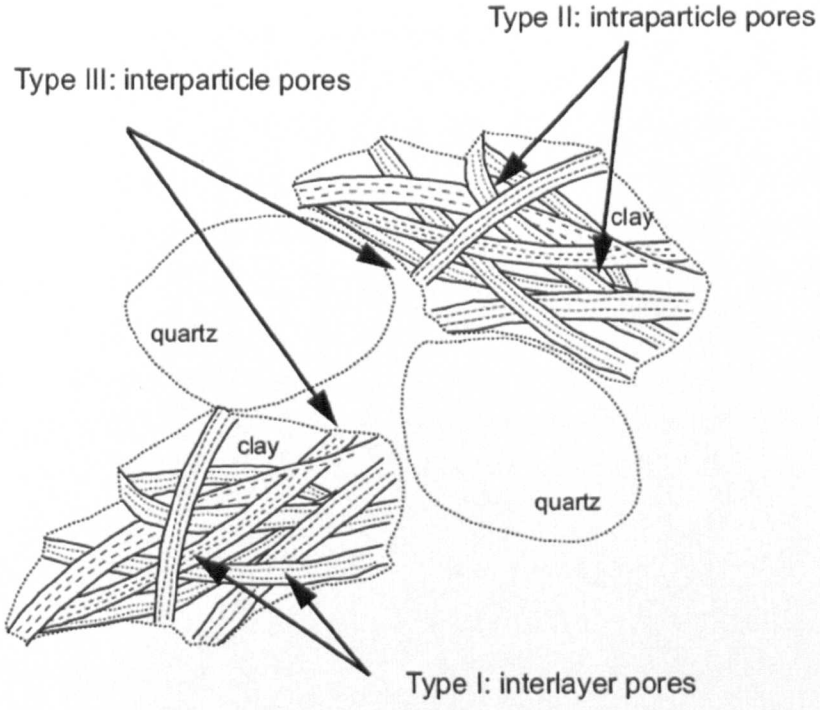

Figure 1.1 Three types of pores present in mudstones and shales from Jin *et al.* (2011) which used small-angle and ultra-small-angle neutron scattering (SANS/USANS) to characterize the evolution of nanoscale features in shales.

A proportion of the fluid-filled porosity in a mudrock can be finer than this and may take several forms. The finest porosity as defined by the IUPAC report (1994) is termed microporosity and comprises pores with widths smaller than 2nm. Mesopores have widths between 2-50nm and macropores have widths larger than 50nm.

The three catagories of pore displayed in Figure 1.1 are based on the definitions described in Jin *et al.* (2011); Allen (1991). Type III interparticle pores are found between grains and tend to be relatively large (nm to μm scale) (Loucks *et al.*, 2009)

so may include some of the mudstone's meso-macro porosity. They are related to the original sediment pore system which is generally connected and provides some of the effective porosity that is measured during MICP analysis. Small angle neutron scattering (Jin *et al.,* 2011) can be utilized to study finer porosity, below the measurable range of MICP but was not part of this study.

Type II intraparticle pores occur within discrete particle boundaries and define a three-dimensional network within the clay grains (Jin *et al.* 2011). They can also occur within organic-matter (Figure 1.3) or other discrete particles such as pyrite framboids, porous phosphate particles etc. (Loucks *et al.,* 2009). They may be primary or secondary pores, forming various morphologies from nearly spherical, to irregular polygons and slightly irregular ellipsoids, which may again range in size on the nm to μm scale (5nm to 0.75 μm observed in Loucks *et al.,* 2009). If connected, this should be within the measurable range of MICP, forming meso-macro porosity. However, some of this porosity may not be effective.

Both Type III and II porosity may form part of the effective porosity network which was modelled in Katsube (2000) as a system of larger storage pores which are interconnected by tortuous, sheet-like connecting pores. This is displayed in Figure 1.2 below and the concept is discussed in more detail in Chapter 4 relating to the mudstones of the Malay Basin.

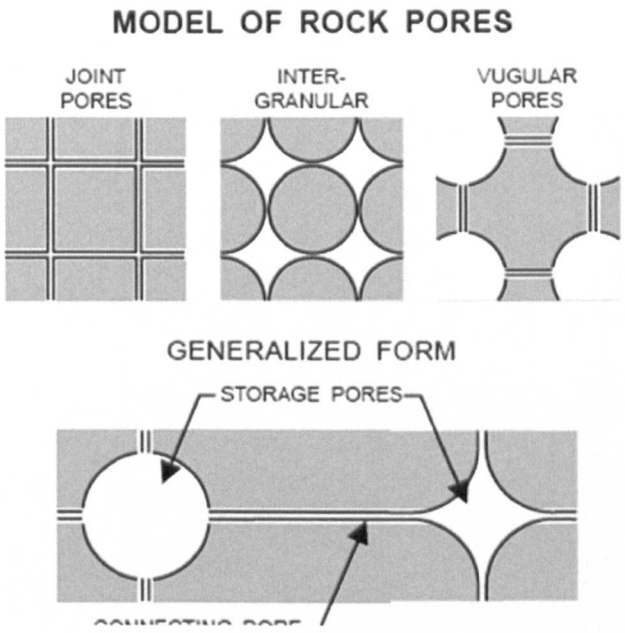

Figure 1.2 From Katsube (2000) showing the storage-connecting pore model of Katsube & Collet (1975) used for characterizing shale porosity.

Type I porosity (from Figure 1.1) is the interlayer porosity and forms between stacked clay layers. These interlayer pores have diameters of only angstroms (Jin *et al.* 2011) and will form microporosity. Therefore, MICP would not be thought to be effective in measuring changes in this type of pore. Baker Hughes (2006) describes the hydration mechanics of clays with particular focus on smectites (see Section 1.3). Hydrated cations are found within the clay interlayers (mainly sodium, calcium, magnesium, and potassium) and are attracted to the negative charge of the clay surfaces which are also surrounded by a thin layer of water. In petrophysics, this is described as the clay-bound water and it would also seem a likely component of Type III and II porosity where some clay-bound water will be found upon the internal and external surfaces of the clays. This does not form part of the effective porosity.

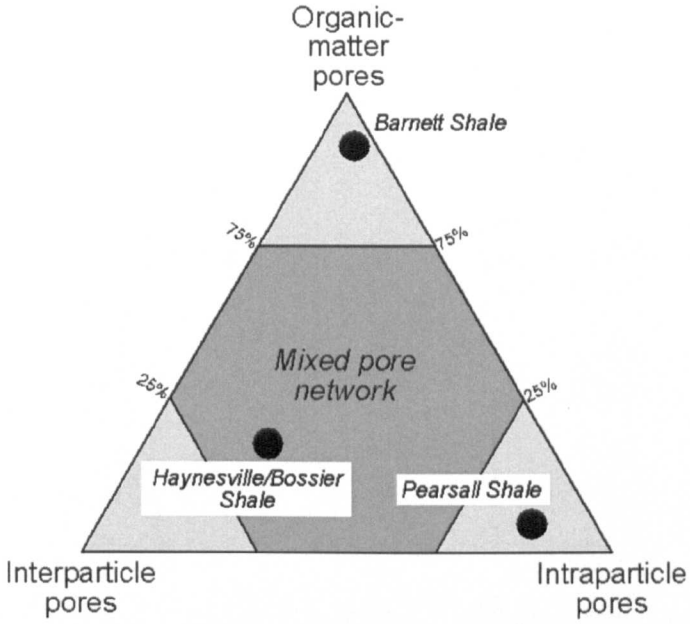

Figure 1.3 Classification of pores in siliceous mudrocks with relative positions of dominant pore-network types in several shale-gas system from Loucks et al. (2010). Both organic matter pores and those described as intraparticle (non-organic) pores can be described as Type II porosity, whereas the interparticle pores are Type III.

Generally, conventional reservoir rocks have effective pore-throat diameters that are > 2μm, compared with 2 - 0.03μm in tight gas sandstones and 0.1 to 0.005μm in shales. This corresponds to hydrocarbon molecules which range in size from 0.01 μm (100 Å) for asphaltenes to 0.00038 μm (0.38nm / 3.8 Å) for methane (Nelson, 2009). The nature of the effective pores in an unconventional reservoir may vary to include Type II and III porosity as is shown in the figure above is from Loucks *et al.* (2010) which shows the dominant porosity types for several of the major US shale gas plays.

1.3 "Mechanical" and "Chemical" Compaction

Pore space within a compacting mudstone is reduced as grain rotation and breakage occur as particles are packed closer, forcing pore fluid to be expelled. Consolidation takes place as the soft, plastic mud matrix and the pore fluid assume an arrangement in equilibrium with the in-situ conditions, compacting the volume of the sediment. However, permeability generally also decreases, reducing the efficiency of fluid flow and if fluid is not expelled, pore pressure will increase leading to overpressure. Despite the relatively low permeability of mudrocks and shales, even at the lower end of their range at 1nD ($10^{-21}m^2$) they do still allow some fluid flow. In Deming (1994) a mudstone with this permeability would allow any large pressure step to decay over a gradual ramp of 1000m width in 1Ma.

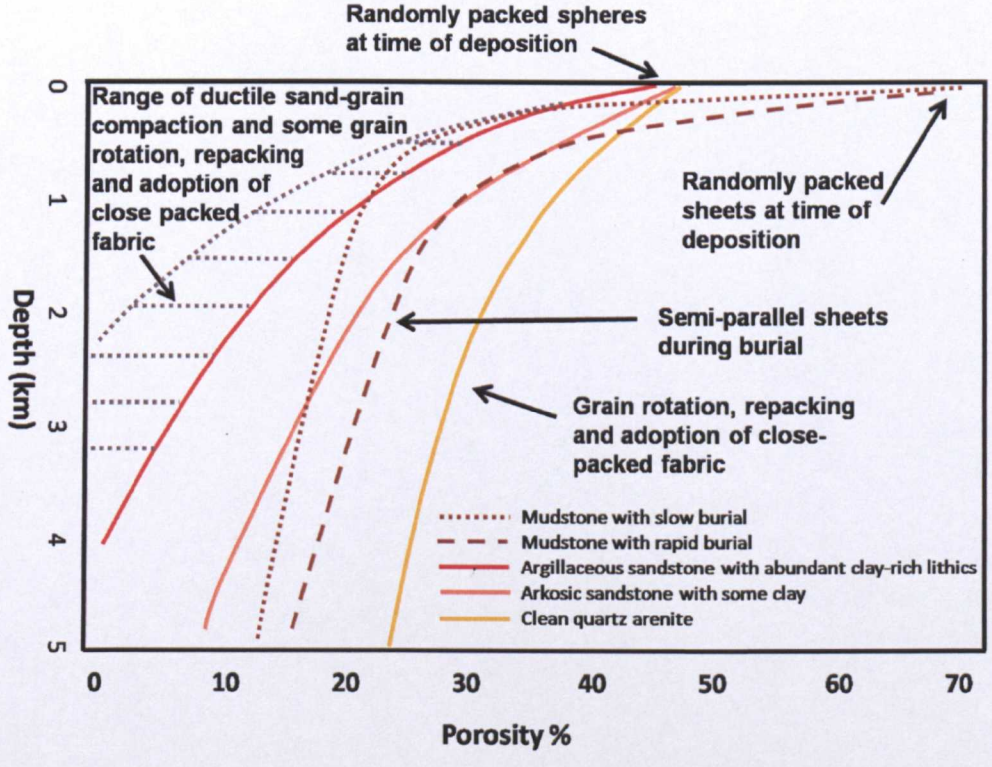

Figure 1.4 Compaction curves from Worden and Burley (2003) for both sandstones of different primary lithologies and mudstones of different compaction rates. These curves are described in Worden and Burley (2003) as showing the effects of compaction only and not cementation.

The differing way in which porosity is lost in a compacting mudstone compared to a sand, with rapid early reduction from relatively large values, can be seen in Figure 1.4 above. The figure displays the effects of the rate of burial and the amount of clay on the degree of porosity loss with depth. The properties are attributed to the same mechanical processes affecting sandstones over this burial range.

Upon initial deposition, sands have a porosity of ~45% compacting to values of ~26% in a clean quartz arenite. This corresponds to the mechanical compaction of quartz as randomly packed, well-sorted spheres rearrange to a structure of close packed spheres. Particle packing also involving clays and silts has been investigated in the studies such as Fies & Bruand (1998), Attou *et al.* (1998). Yang & Aplin (2004) defines the porosity effective stress relationship for the mechanical compaction of mudstones using the following set of equations. The effective stress σ_v' is described as:

$$\sigma_v' = \sigma_V - u$$

where σ_V is the total stress and u is the pore fluid pressure. The relationship between the void ratio e and porosity φ is:

$$\mathrm{e} = \left(\frac{\varphi}{1-\varphi}\right)$$

This means that porosity (and therefore porosity loss during compaction) can be calculated using the following equation :

$$\mathrm{e} = \mathrm{e}_{100} - \beta \ln\left(\frac{\sigma_v'}{100}\right)$$

where e_{100} is the void ratio at 100kPa effective stress and β is the slope of the linear relation between void ratio and the natural logarithm of vertical effective stress. Both of these parameters are related to the clay content through relationships stated in the study. The mechanical loss of porosity in relation to clay content is examined experimentally in Dewhurst & Aplin (1998) and the relation to clay type in Mondol *et al.* (2007), the results of which are displayed as the coloured trends in Figure 1.5.

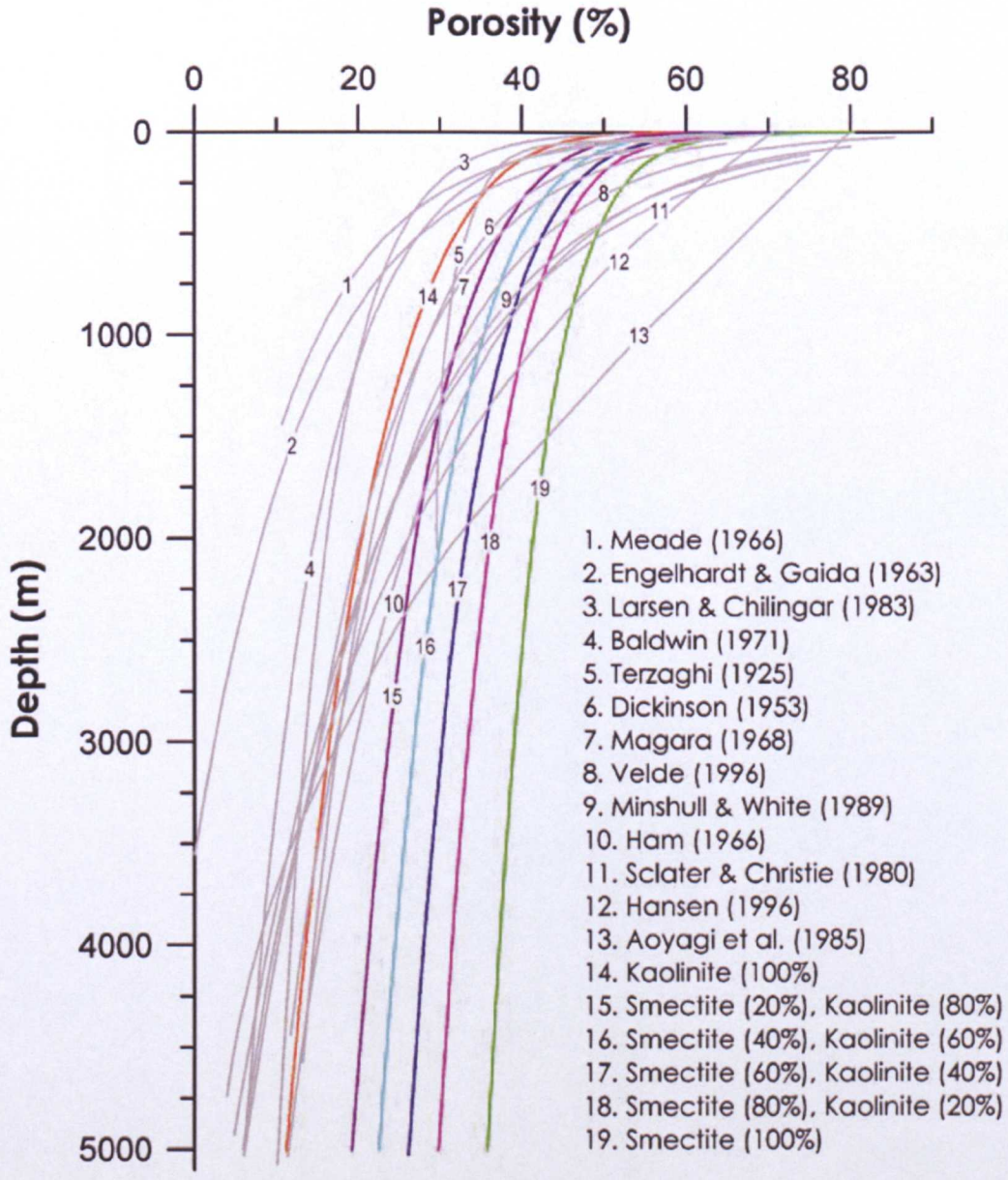

Figure 1.5 A comparison of published porosity–depth trends for shales and argillaceous sediments (gray curves) and experimentally compacted curves of brine-saturated smectite, kaolinite and their mixtures (colour curves), from Mondol *et al.* (2007).

Figure 1.5 shows that there is a clear difference between the trends of porosity loss with depth (effective stress) in the experimentally compacted, wet (1.5x liquid limit) clay mixtures and those of natural muds and shales. This difference was noted in Bjorlykke (1998) and the greater degree of compaction between 2-3km depth explained by chemical compaction.

Chemical compaction is the loss of porosity due to diagenetic chemical/mineralogical processes in the burial environment. In sandstones it is generally associated with cementation processes, particularly quartz cement/overgrowths as shown in Worden & Burley (2003). However, Bjorlykke (1998) attributes chemical compaction in mudstones mainly to the dissolution of smectite and precipitation of mixed-layered minerals and illite above 70°C, with a later contribution from the illitization of kaolinite greater temperatures (see Section 1.4).

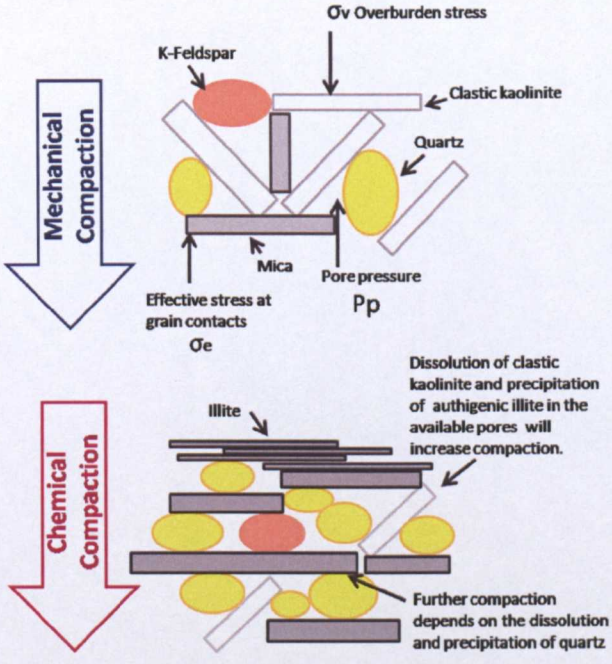

Figure 1.6 Schematic representation of mechanical and chemical compaction of mudstones adapted from Bjorlykke (1998).

The smectites and kaolinites form part of the framework carrying the effective stress and when they dissolve illite precipitates in the available pore space, allowing for more efficient compaction (Figure 1.6).

In Buller *et al.* (2005), the mechanism by which the smectite-illite transformation affects porosity is discussed further. When illite replaces smectite, the illite grains will have a smaller surface area, signifying a likely permeability increase. However, in the subsurface, permeability decreases. The study explains this through smectite dissolution products re-precipitating as pore-bridging fibrous illite throughout a considerable volume of pore spaces in the vicinity of the dissolving smectite mineral. They state that this causes a dramatic reduction in permeability but has little effect on porosity (Figure 1.7).

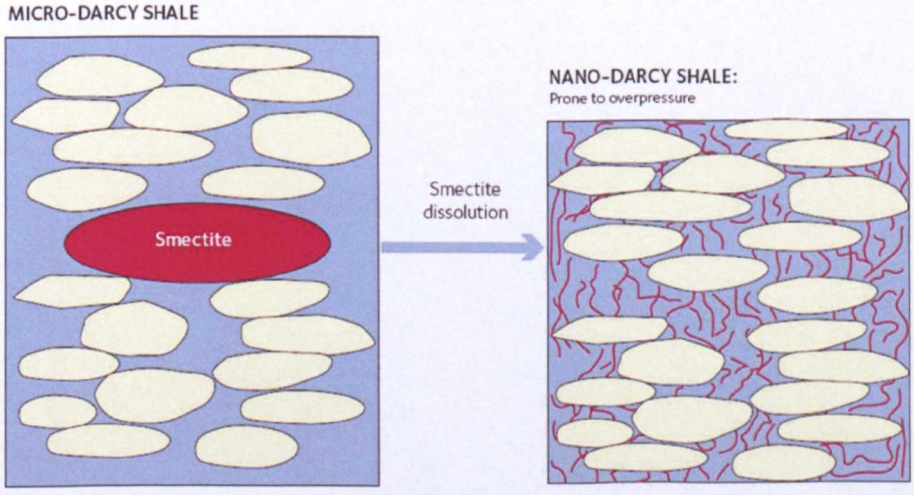

Figure 1.7 From Buller *et al.* (2005) showing the effects of the smectite-illite transition on permeability reduction.

Day-Stirrat *et al.* (2008) links the illitization process with alignment of the phyllosilicate grains (see section 1.5). This provides another mechanism through the development of a more aligned I-S fabric resulting from the dissolution of smectite and the growth of illite with (001) normal to the maximum effective stress. Water is released by illitization and may act as a lubricant for the rotation of all platy minerals

into nanoporosity transiently formed by the illitization reaction, reducing overall porosity.

1.4 Clay Mineral Diagenesis

To give some background to the discussion on chemical compaction, a brief overview of clay minerals and their diagenetic alteration is required. As the definitions in Section 1.2 have stated, clays form an important component of mudstones and shales. They are hydrous phyllosilicates with continuous sheet structures and can be classified on the number of sheets making up their basic structure or unit cell (Potter *et al.*, 2005).

Sheets are composed either of linked silica tetrahedra or linked octahedra, each comprising oxygen and hydroxide ions around an aluminium or magnesium centre. When aluminium ions are in the centres of the octahedra, only two-thirds of the octahedral centres are filled forming a gibbsite (dioctahedral) sheet. When magnesium ions are in the centres, all the octahedra centres are filled creating a brucite (trioctahedral) sheet (Moore & Reynolds, 1997; Potter *et al.*, 2005). The various species of phyllosilicate (with emphasis on clay minerals) of di- and trioctahedral subgroups are tabulated below.

The difference between clay minerals result from the different kinds of cations and amount of OH that hold the sheets together. Cation substitution in the tetrahedral and octahedral sheets can produce a charge deficiency that is compensated by the incorporation of mono- and divalent cations in the interlayer position (Potter *et al.*, 2005). Four of the most common clay mineral groups are represented below in Figure 1.8.

Layer Type	Group	Subgroup	Species
1:1	Serpentine-kaolin z=~0	Serpentines	Chrysotile, antigorite, lizardite, berthierine, odinite
		Kaolins	Kaolinite, dickite, nacrite, halloysite
2:1	Talc-pyrophyllite z=~0	Talc	
		Pyrophyllite	
2:1	Smectite z=~0.2-0.6	Trioctahedral smectites	Saponite, stevensite, hectorite
		Dioctahedral smectites	Montmorillonite, beidellite, nontronite
	Vermiculite z=~0.6-0.9	Trioctahedral vermiculites	
		Dioctahedral vermiculites	
	Illite z=~0.6-0.9	Trioctahedral illites (?)	Ledikite (?)
		Dioctahedral illites	Illite, Fe-illite, glauconite, NH_4-illite, brammalite (?)
	Mica z=~1.0	Trioctahedral micas	Biotite, phlogopite, wonesite
		Dioctahedral micas	Muscovite, paragonite, phengite, celadonite
	Brittle Mica z=~2.0	Dioctahedral brittle micas	Margite
2:1	Chlorite z=variable	Tri, Tri chlorites	Chamosite, clinochlore etc.
		Di, Di chlorites	Donbassite
		Di, Tri chlorites	Sudoite, cookeite
		Tri, Di chlorites (?)	
2:1	Sepiolite-palygorskite z=variable		*Inverted ribbons*

Table 1.1 Classification of phyllosilicates with emphasis on clay minerals (Based on Moore & Reynolds,1997 and Środoń, 1999).

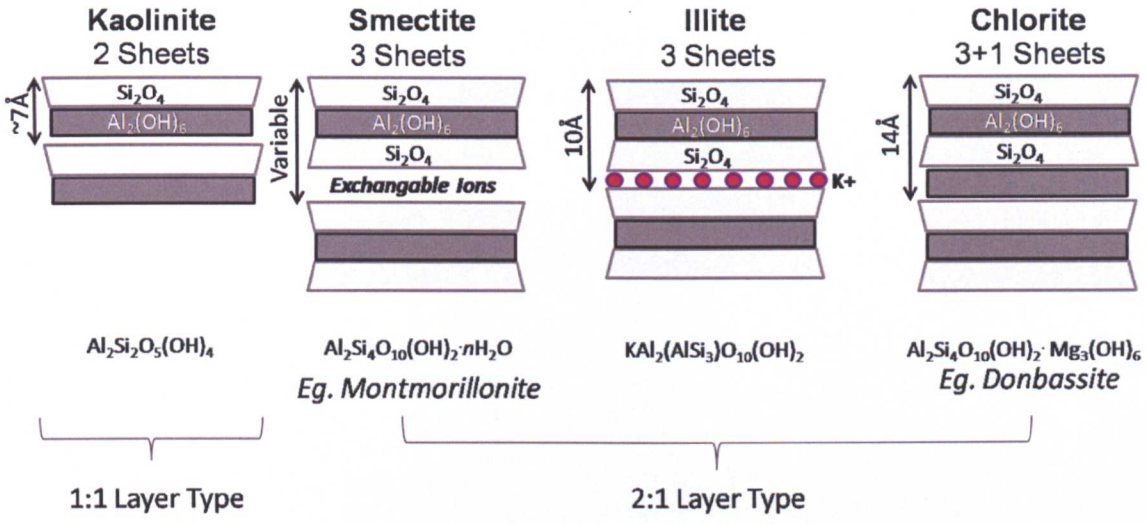

Figure 1.8 Diagram to display basic structural models of clay mineral groups found in this thesis. Based on figures in Moore & Reynolds (1997) and Potter *et al.* (2005). Spacing in the 001 direction (along the Z crystallographic axes) measured in Ångstroms. Formula shown are idealised – the "sheets" have a basic structure of silica tetrahedra and aluminium octahedra with other ions substituted in.

Smectites, already discussed in Section 1.3, are volumetrically the most abundant detrital clay mineral in Cenozoic basins world wide (Mondol *et al.*, 2007) and therefore understanding their diagenetic transformation into illite is key to predicting the behaviour of mudstones and shales in the subsurface. Diagenesis is a broad term involving any post-depositional chemical, physical, or biological change undergone by a sediment prior to metamorphism. It is governed by the pressure-temperature conditions as is shown in Figure 1.9.

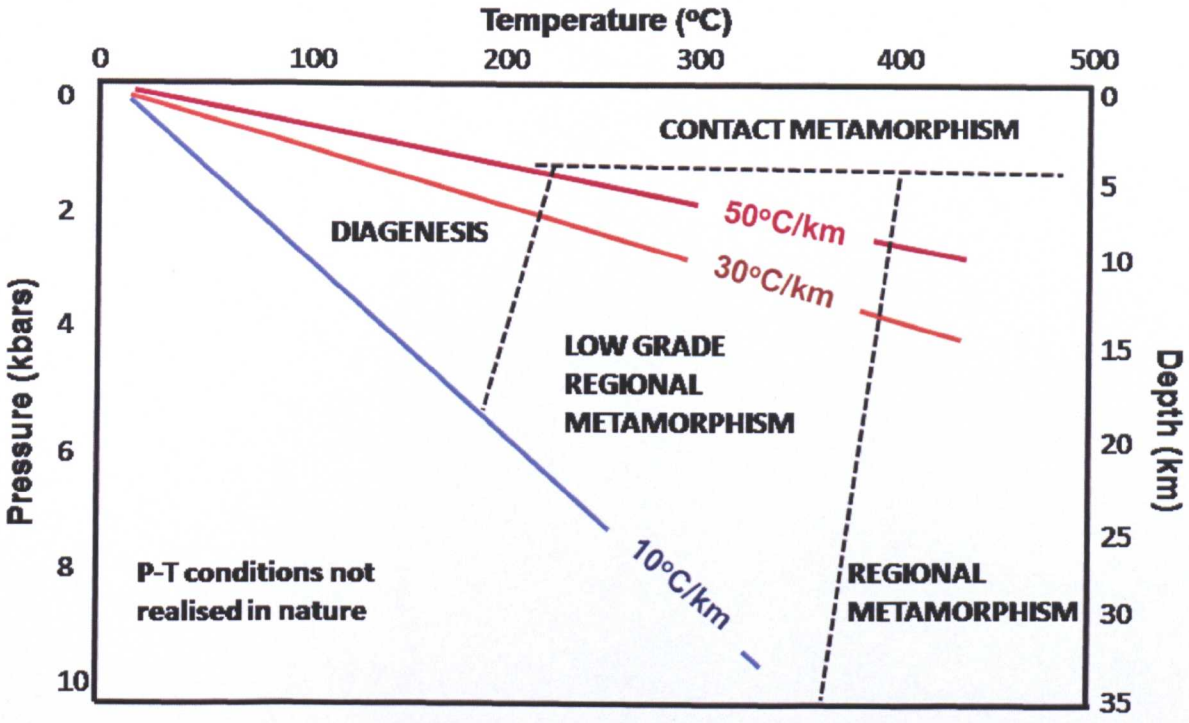

Figure 1.9 Pressure-temperature diagram adapted from from Worden & Burley (2003) defining geological regimes in relation to P-T gradients within the crust. The 10°Ckm^{-1} geotherm is representative of stable cratons and 30°Ckm^{-1} more typical of rifted sedimentary basins such as the North Sea (Chapter 3). The 50°Ckm^{-1} geotherm has been added to illustrate conditions of the Malay Basin which is the subject of Chapter 4. Low pressure, high tempetaure conditions depicted in the upper, right of the diagram are found only in geothermal systems or related to igneous contacts.

Bjorlykke (1998) describes smectite illitization, along with the other diagenetic illitization reactions using the following equations:

smectite + K^+ = illite + silica (*via mixed- layer minerals*)

$$Al_2Si_2O_5(OH)_4 + KAlSi_3O_8 = KAl_3Si_3O_{10}(OH)_2 + 2\ SiO_2 + H_2O$$
kaolinite K-feldspar illite quartz

$$3Al_2Si_2O_5(OH)_4 + 2KAlSi_3O_8 + 2Na^+ = 2KAl_3Si_3O_{10}(OH)_2 + 2NaAlSi_3O_8 + 2H^+ + 3H_2O$$
kaolinite K-Feldspar illite albite

The temperatures at which these reactions are reported to operate show slight variation in different studies, but roughly adhere to those displayed in Figure 1.10.

Worden and Morad (2003) state that high-grade diagenesis (mesodiagenesis) leads to the formation of dickite, illite and chlorite clay minerals in sandstones (although Bjorlykke (1998) shows that the temperatures and pathways also generally apply to mudstones and shales). Kaolinite forms mainly during eodiagenesis (early diagenesis – surface temperatures to ~60°C) and can be cannibalized to form dickite, illite or chlorite. Chlorite seems unlikely to be formed during eodiagenesis and is created by at least 4 main pathways. Illite forms via at least 3 main routes mainly during mesodiagenesis and can also be detrital following incomplete weathering. Its formation via development of interstratification with smectite through mixed-layer compositions of decreasing expandability (decreasing smectite content, increasing illite) is well documented in basins around the world such as the US Gulf Coast, Central Poland, North Africa and the North Sea (Eberl & Hower, 1977; Środoń & Eberl, 1984).

In smectites, water is present on both their surfaces and between the layers of the fine mineral grains (Section 1.2). The loss of this water through systematic dehydration is thought to be part of the illitization process. Colten-Bradley (1987) modelled this process and found that smectites are stable as hydrated phases in compacting shales (under differential pressure as opposed to the hydraulic pressure in a sandstone). Any water layers in excess of 2 will be expelled below 60°C but they continue to be stable as two water layer complexes at temperatures up to 67-81°C. Above this temperature one of the water layers are lost. In Colten-Bradley (1987), one water layer complexes comprise a monovalent cation surrounded by at least 3 water molecules and will persist until temperatures increase to 172-192°C. Dehydration temperatures increase with pore pressure and interlayer water density.

Decreased water content with increasing pressure and temperature may negatively influence the chemical stability of the 2:1 layer and is proposed as important in the initiation of illitization, which starts at temperatures approximately equal to the loss of the second water layer.

As illiization of smectite proceeds, mixed-layer clays form, consisting of random or regularly alternating layers of smectite and illite (often abbreviated to I/S) with increasing stacking order and abundance of the latter. A comprehensive review of mixed-layer clays and their formation/alteration is given in Środoń (1999). The ordering that accompanies the increase in illite is defined as Reichweite and is normally denoted as R0, R1 or R3 (Moore & Reynolds, 1997). It describes the probability given layer A, of finding the next layer to be B (for example, I-S mixed layer clay with R3 ordering means there is likely to be three illite layers between any two smectite layers and it is probable that smectite layers are not directly adjacent in the stacking order). Generally, R0 ordering applies up to ~50% illite in illite-smectite mixed layer clays (I% in I/S), R1 between ~60-80% and R3 at 90% I in I/S and above. Several variables are known to control the reaction, but the actual mechanism by which the transformation proceeds is still debated. Moore & Reynolds (1997) describes different models from a solid-state transformation where the chemistry and structure is remodelled in-situ without disrupting the stack of layers (Hower *et al.*, 1976) to neoformation. This represents particles undergoing dissolution and direct precipitation/crystallization, rather than rearrangement of the structure of the precursor minerals (Boles & Franks, 1979). An intermediate was proposed by Altaner and Ylagan (1993) where the area around the smectite interlayer dissolves and reforms as an illite layer without disrupting the bulk structure.

A fourth mechanism cites direct precipitation of I/S with an illite abundance corresponding to the in-situ conditions.

One separate alternative doesn't just question the mechanisms, but the generally accepted structural characterization. Lanson *et al.* (2009) puts forward the case that smectite illitization does not follow a steady set of reactions forming intermediate compositions of mixed layer clays and that the appearance of this is down to a bias in the use of XRD methodology. During early burial both authigenic smectite and illitic illite-expandable mixed-layer clays (>50% I layers) are formed. With increasing burial I/Exp increases proportionally at the expense of discrete smectite and becomes slightly more illitic.

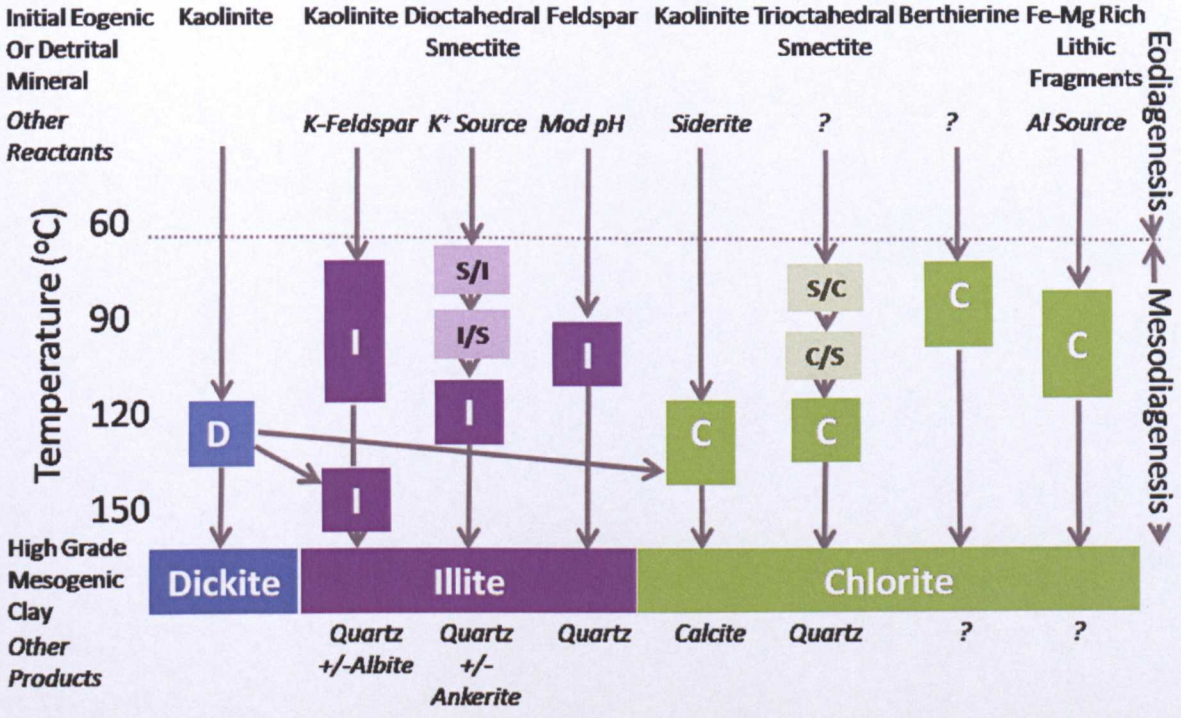

Figure 1.10 Common diagenetic pathways for clay minerals - adapted from Worden and Morad, (2003). D is dickite, S is smectite, I is illite, C is chlorite. Interstratified mixed-layer clays are named with to the most abundant phase listed first.

As shown in Figure 1.8 and the illitization equations above, the availability of potassium is seen as a key control on the rate of illitization and is sometimes put forward as a limiting factor in the final abundance of I% in I/S, impeding the ultimate formation of discrete illite. Berger *et al.* (1999) describe how in the early stages of illitization, illite content is controlled by the presence of feldspar and hence also by the dissolution kinetics of feldspar. However, feldspar does not control the second stage of illitization (R > 0 structures, ca. 50-100% illite content) and potassium is sourced either from within or outside an argillaceous whole-rock system. These different sources of potassium give rise to different rates for I/S conversion. Lynch (1997) shows there is no chemical or mineralogical evidence for a cessation of I/S reaction at ~80% due to potassium supply. That paper also concluded that both chemical and mineralogical changes occur throughout burial and continuous change in the oxygen isotopic composition of I/S implies that the conversion of smectite-layers to illite-layers is a dissolution/precipitation process with an open system required.

Bjørlykke (2011 & 1998) argues that open systems are not likely at the depths generally required for the onset of illitization, even in hot basins. Below the reach of meteoric flow, porewater flow is driven by sediment compaction and the velocity of that flow is then extremely low (in general lower than the sedimentation rate). Thermal convection could potentially increase the fluid flow, but this can be ignored except around igneous or hydrothermal intrusions and only in sandstones not mudstone systems. Day-Stirrat *et al.* (2011) counters that assuming a closed system they are unable to explain the increase in potassium recorded in their samples. There are examples of basins that display a similar trend for potassium and others

that do not. For example, the North Sea (Thyberg *et al.*, 2010) and Podhale Basin of southern Poland (Środoń *et al.*, 2006; Day-Stirrat *et al.*, 2008), show no appreciable change with depth. The lack of a potassium increase with depth increase indicates that these basins may be more closed to solute transport. Given the aims of the high pressure, high temperature triaxial experiments in this thesis, the process and timing of potassium exchange for illitization is an important one and is revisited in Chapter 3.

The effect of a closed system should also be an increase in quartz as illitization proceeds. However, van de Kamp (2008) describes a global dataset that suggests silica removal. Work by Peltonen *et al.* (2009) and Thyberg et al. (2009, 2010 and 2011) shows images of what they attribute to be authigenic silica remaining in the mudstone system following clay mineral reactions. The most recent work of that team, published in Thyberg & Jahren (2011), describe how this authigenic, thin, sheet-like or platelet-shaped quartz cement forms parallel to bedding as flakes at ~ 90–100°C which may evolve into well-developed, near-continuous patchy quartz cement at greater depths/temperatures ~150°C. They state that the quartz cement is probably sourced from silica released by the smectite to illite and kaolinite to illite reactions. The quartz sheets may act as a mudrock stiffening agent, reinforcing and further cementing together the microquartz networks and aggregates and possibly also enhancing the schistosity and anisotropy of these mudstones during increasing burial. This would have a lithifying effect, assisting the transition of mud into a mudstone.

1.5 Grain Alignment

Already mentioned in Section 1.3, grain alignment resulting from clay diagenesis is suggested as another possible mechanism in porosity reduction and the mudstone lithification process (Day-Stirrat *et al.,* 2008; Ho *et al.,* 1999; Haines *et al.,* 2009). During initial deposition, Day-Stirrat (2008) describes two main sedimentation processes operating in the marine environment. Grains that are greater than ~10μm settle as single grains and form a coarser, more anisotropic fabric composed of silt-sized phyllosilicates such as mica, chlorite and kaolinite (Kranck & Milligan, 1985; O'Brien & Slatt, 1990; Kranck *et al.,*1996). Grains that are less than ~10μm are mainly deposited as flocs or as biologically produced aggregates and initially form a fine grained, isotropic fabric.

Some studies such as Meade (1966) describe how preferred orientation of clay minerals develops at a very early stage of compaction, enhanced by greater initial water content, greater amounts of carbonaceous material and lower concentrations of interstitial electrolytes. The paper states that orientation develops under pressure during the early stages of compaction. This stage takes place under overburden loads corresponding to depths of less than half a kilometre. More recent work by Voltolini *et al. (*2009) shows findings similar to this, where alignment was measured on artificially compacted clay mineral/quartz mixtures using different clay contents and exposing them to different levels of stress. The results were increased clay content and stress both generated increased alignment (this is discussed in more detail in later chapters).

However, in the studies of Day-Stirrat *et al.,* (2008 & 2010) and Ho *et al.,* (1999), initial depositional fabric is profoundly transformed by clay mineral diagenesis and later by low-grade metamorphism generating highly aligned fabrics (Jacob *et al.,* 2000 and Ho *et al.,* 2001). Imperfect, wavy smectite layers that show evidence of mechanical processes such as grain rotation and kinking are transformed into straight, defect free illite packages with new growth forming grains that are aligned normal to the principle effective stress. This is not always the case (for example, Aplin *et al.,* 2006), as other influences such as mineralogical heterogeneity can reduce the efficiency of these processes.

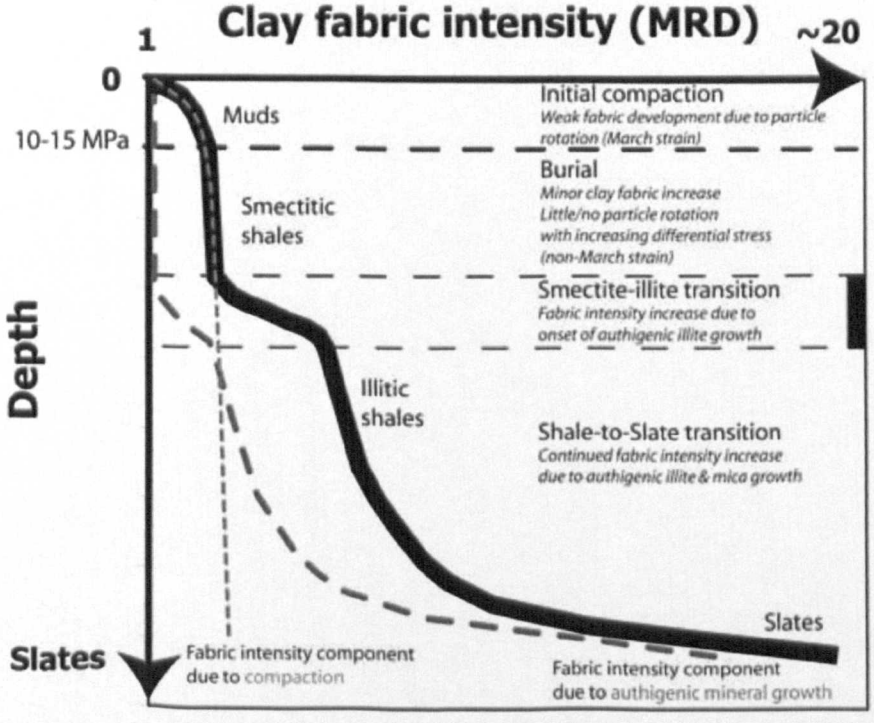

Figure 1.11 From Haines *et al.* (2009) showing clay fabric intensity with depth. Values in MRD are a measurement of alignment expressed in multiples of a random distribution. Thick line is representative fabric intensity evolution in sedimentary basins from deposition to lowgrade metamorphism as inferred from natural data. Fine dashed line is component of measured fabric in sedimentary rocks due to mechanical compaction as inferred from the Haines study, Tullis (1976), and Sintubin *et al.* (1995). Coarse-dashed line is component of fabric in sedimentary rocks due to authigenic mineral growth.

The mechanical and chemical diagenetic processes have been brought together in the study by Haines *et al.* (2009) where a model is shown that accounts for early stress related, minimal levels of alignment in the first kilometre of burial. This is then followed by the development of strongly aligned clay fabrics which are primarily a function of authigenic mineral growth and not compaction induced particle rotation.

1.6 Summary & Thesis Organisation

Following this review of relevant literature and introduction to the central themes discussed in this first chapter, Chapter 2 focuses on methodology. This details the use of various geotechnical equipment, including the HPHT triaxial cells. The capabilities of the latter addressed several of the concerns over equipment inadequacies mentioned previously. Also, a wide variety of rock property techniques were employed to fully characterise results that could be attributed to either mechanical or chemical variables. Chapter 2 also contains details of error minimising practices/calibrations and developmental preliminary testing carried out for procedure optimisation.

The third chapter, "Laboratory Simulation of Mudstone Compaction" details an experimental work program on well characterised North Sea mudstone core aimed at development of the qualitative/quantitative porosity loss models. The laboratory based compaction tests allowed strong constraint of the variables controlling rock properties. The program culminated with a set of 60 day triaxial experiments, testing the effects of high effective stresses (max. 50MPa) with varied fluid chemistries and temperatures on compaction behaviour. This was then followed with the rock property measurement program described in Chapter 2 to identify variation that could be attributed to the compaction experiments and the variables that they tested.

The fourth chapter "Mudstone Compaction in Nature: Malay Basin Case Study" involved a thorough measuring program designed to characterise both the chemical/mineralogical and physical properties of fine-grained clastics from the

Malay Basin, offshore Peninsular Malaysia. The aim was to identify any evidence of chemical compaction. As this chapter focused on analysis of natural samples, less constraint of variables was possible. However, this section was developed as a parallel study to contrast with the experimental program. It provided information on the natural, heterogeous range of burial processes that take place during diagenesis on a geological timescale. The Malay Basin also provided a set of conditions pertinent to this project as the high geothermal gradient allowed the study of the effects of temperature and chemical change prior to the application of high levels of effective stress.

The final chapter brings together the results the experimental and Malay Basin studies, comparing their results with each other and evaluating the ideas that emerged with preexisting ideas and published literature. This highlighted the petrophysical effects of temperature and chemistry and the development of grain alignment, assessed the relative roles of "mechanical" and "chemical" compaction in mudstones and shales and culminated with the identification of areas that would benefit from further research.

Chapter 2

Methodology

2. Methodology

2.1 Introduction

This chapter describes the methodologies employed in studying the effects of compaction in mudstones and shales. The first section describes the orchestration of the various methods of artificial sample compaction used in Chapter 3. The second and third sections describe the various techniques of analysing mineralogical/chemical and physical/textural rock properties respectively. These types of analyses were performed on the artificially compacted samples in Chapter 3 and on the natural mudstone samples from the Malay Basin in Chapter 4.

Several of the techniques used were standard procedures and they are simply recorded with a brief discussion of their aim, as applied to this study and general technical points. However, some investigation was necessary to apply certain practices and meet the specific requirements of this project and additional discussion of those areas is given in the sections below marked as *Method Development Sections*.

2.2 Compaction Systems & Mid-Test Measurements

2.2.1 Low Stress Consolidation:0-5MPa *(METHOD DEVELOPMENT SECTION 1)*

Following review of the literature, particularly that focussing on mechanical compaction of mudstones and clays (Mondol *et al.* 2007; Dewhurst & Aplin, 1998), one of the initial sets of tests focussed on low stress, room temperature consolidation of clay minerals and quartz. Termed the "Shallow Mechanical Consolidations," they were performed using relatively pure clays or artificial mixtures of clays and quartz. Their aims were to test assumptions from previous mechanical compaction studies, optimise conditions for the Compaction Simulation Tests (see 3.2.3) and compare the properties generated with the results of the high stress, high temperature tests that were the main focus of this project.

At moisture contents of 1.5 times their liquid limit (for details see B.S. 1377; Burland, 1990; Mondol *et al.,* 2007) slurries of 100% kaolinite, a 50% mixture of kaolinite and quartz and a 33.3% mixture of kaolinite, quartz and bentonite clay were consolidated and allowed to drain in a standard consolidometer to ~0.238MPa effective stress. Some plugs of these three mixtures were immediately analysed and others were taken for low stress, room temperature, drained consolidations in low stress triaxial cells. However, maintaining higher stresses using that equipment proved impossible, with frequent leaks occurring attempting to achieve the stress range required (low geological stress ~5-15MPa.) Two tests had limited success, consolidating 100% kaolinite to 1MPa and 5MPa and these samples were analysed using mercury injection porosimetry (MICP - 2.4.3).

Test Name & Equipment	Test Material	Effective Stress (MPa)	Temperature (°C)	Pore Fluid Chemistry
Initial consolidations (Consolidometer)	Kaolinite	0.238	20-25	Deionized water
Initial consolidations (Consolidometer)	Kaolinite & quartz	0.238	20-25	Deionized water
Initial consolidations (Consolidometer)	Kaolinite, quartz & bentonite	0.238	20-25	Deionized water
Shallow Mechanical Consolidations (Low stress triaxial cell)	Kaolinite	1	20-25	Deionized water
Shallow Mechanical Consolidations (Low stress triaxial cell)	Kaolinite	5	20-25	Deionized water
Shallow Mechanical Consolidations (Back pressured shear box)	Kaolinite	1	20-25	Deionized water
Shallow Mechanical Consolidations (Back pressured shear box)	Kaolinite	2	20-25	Deionized water
Shallow Mechanical Consolidations (Back pressured shear box)	Kaolinite	2.5	20-25	Deionized water
Shallow Mechanical Consolidations (Back pressured shear box)	Bentonite	1	20-25	Deionized water
Shallow Mechanical Consolidations (Back pressured shear box)	Bentonite	2	20-25	Deionized water
Shallow Mechanical Consolidations (Back pressured shear box)	Bentonite	2.5	20-25	Deionized water
Variable testing: Triaxial Test 1 (HPHT triaxial cell)	North Sea mudstone	6	150	4M KCl
Variable testing: Triaxial Test 2 (HPHT triaxial cell)	North Sea mudstone	6	150	4M KCl
Variable testing:	North Sea	6	150	4M KCl

Triaxial Test 3 (HPHT triaxial cell)	mudstone			
Variable testing: Triaxial Test 4 (HPHT triaxial cell)	North Sea mudstone	30	150	4M KCl
Variable testing: Triaxial Test 5 (HPHT triaxial cell)	North Sea mudstone	6	100	4M KCl
Variable testing: Triaxial Test 6 (HPHT triaxial cell)	North Sea mudstone	6	150	3M KCl 10^{-5}M KOH
Variable Testing: Test A (Reflux condenser)	North Sea mudstone	~0	100	4M KCl
Variable Testing: Test B (Reflux condenser)	North Sea mudstone	~0	100	4M NaCl
Variable Testing: Test C (Reflux condenser)	North Sea mudstone	~0	100	3M KCl 10^{-5}M KOH
Compaction Simulation Tests: Chemical Compaction Test 7 (HPHT triaxial cell)	North Sea mudstone	50	150	3M KCl 10^{-5}M KOH
Compaction Simulation Tests: Mechanical Compaction Test 8 (HPHT triaxial cell)	North Sea mudstone	50	25	4M NaCl
Compaction Simulation Tests: Intermediate Compaction Test 9A (HPHT triaxial cell)A	North Sea mudstone	20	20-25	3M KCl 10^{-5}M KOH
Compaction Simulation Tests: Intermediate Compaction Test 9B (HPHT triaxial cell)	North Sea mudstone	30	20-25	3M KCl 10^{-5}M KOH

Table 2.0 Reference test matrix for all compaction/fluid interaction tests. Note effective stress recorded is axial and HPHT indicates high pressure, high temperature triaxial cell.

As these tests were designed as precursors to the high temperature, high pressure tests, several attempts were made to put the 0.238MPa consolidometer compressed plugs under low stress at room temperature using the HPHT cells (2.2.2). However, it was apparent that even the stress required to seal the cell (ie. push the axial piston past the sealing o-ring) was too high for such soft samples, leading to instant failure.

The final choice of equipment was the GDS Back Pressured Shearbox at Durham University, represented below in Figure 2.1. Slurries of 100% kaolinite and 100% bentonite at 1.5 times their liquid limit were consolidated to 1, 2 and 2.5MPa. The samples were not sheared, instead the equipment was chosen as it was supposed to allow for higher stress consolidations but in application, nothing above 2.5MPa was achievable and even to attain those stresses adaptations had to be made.

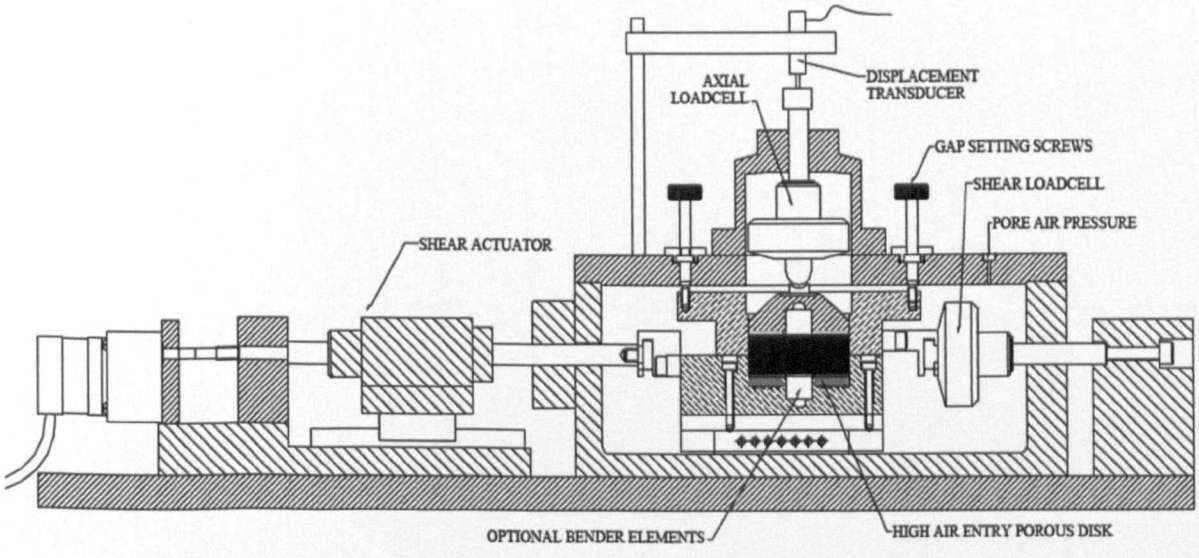

Figure 2.1 Schematic of the GDS Back Pressured Shearbox (BPS) with full unsaturated options from GDSBPS datasheet.

At first, as is the design of the Shearbox, effective stress was determined as the difference between the axial stress applied by the axial piston and the controlled pore pressure using de-aired water as the pore fluid. However, initial attempts

proved that adding water to the sample early in the test to elevate pore pressure created uncontrollable deformation. The normal operating procedures were then altered to allow axial effective stress to be calculated as the axial stress exerted by the axial piston. This was because pore pressure was not controlled and pore water was allowed to drain freely from the compacting sample. This meant that the pore pressure was assumed to be approximately zero. The pore fluid was allowed to drain from the sample and be expelled into the chamber, with saturation maintained as the samples were not open to the air, but to the minimal chamber fluid (expelled de-aired water.) Samples created from these tests were again analysed using MICP to assess differences in porosity with clay type and abundance, along with effective stress.

Porosity results have been used to contrast those of the North Sea mudstone samples in Chapter 5, but the main findings of these tests were used in method development. In Figure 2.2 below, CT scans of selected samples are shown.

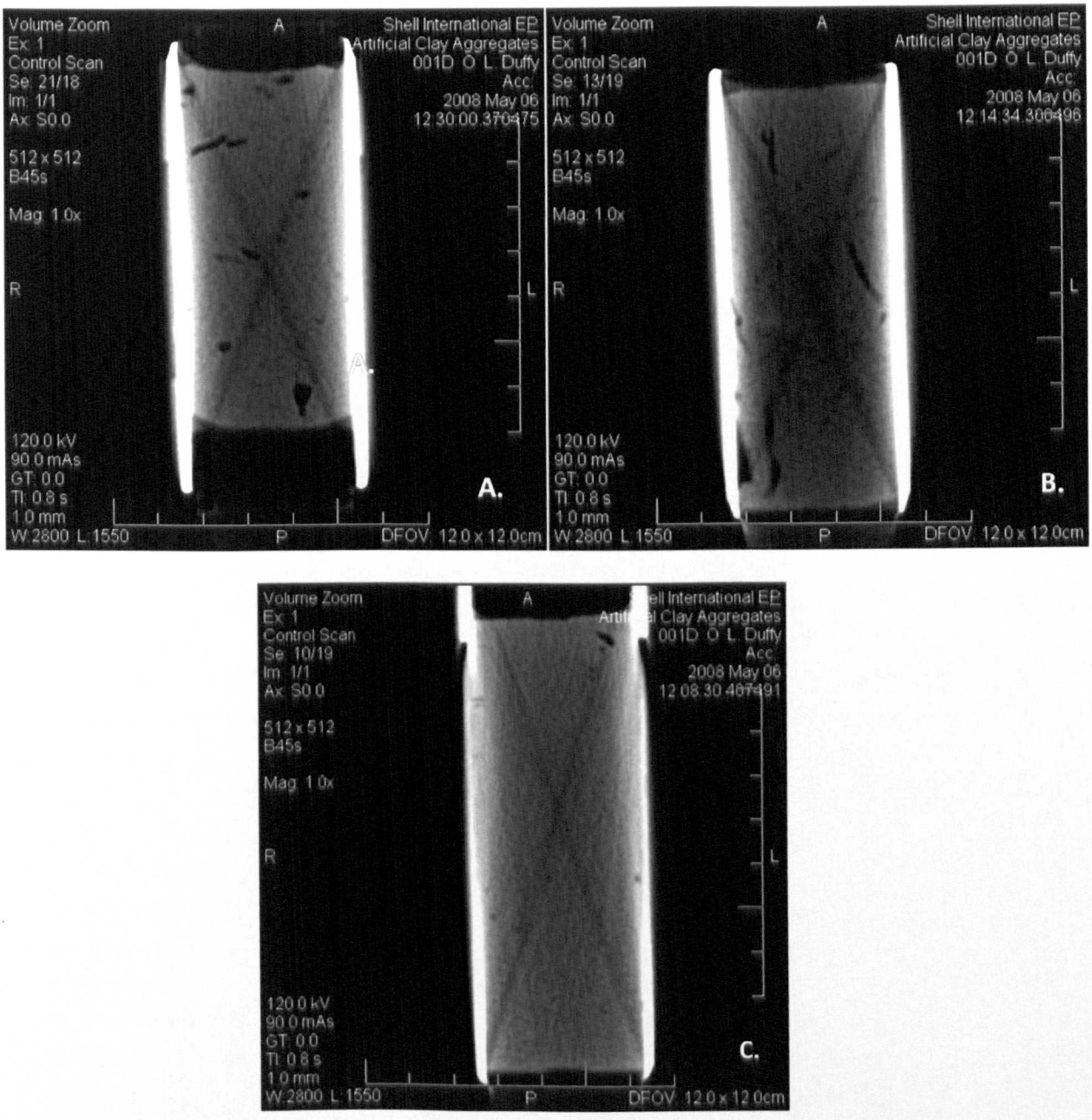

Figure 2.2 CT scan images of samples compressed in the consolidometer to ~238KPa effective stress. A. is 100% kaolinite; B. is a 33% mixture of kaolinite, quartz and bentonite; C. is a 50% mixture of kaolinite and quartz. Scan settings are noted on the diagrams and no magnification was used – carried out at Shell, Rijkswijk. Areas that appear lighter in shade in the images are areas of higher density and darker areas indicate lower density. Cylindrical plugs were encased in steel tubes for transport and sealed with wax – forming the "bright" exterior of the sample.

These images of the three types of clay mixtures consolidated to ~0.238MPa in the consolidometer display the limitations of artificial samples. In Mondol *et al.* (2007), discussed in Chapter 1, an overview of the preparation of artificial clay mixtures for

consolidation describes how the clay powder and water was mixed manually to obtain a homogeneous paste. Trapped air was minimized by constant stirring and shaking and the clay slurries before carefully placing them in their oedometer. This method was used to prepare the samples in this study and yet the CT scans clearly show that it was not successful. The areas that appear dark (black) in the scans are voids that are the result of bubbles trapped in the original slurries.

The 50% kaolinite and quartz mixture was the most homogeneous, but even that was not void free. These kinds of inaccuracies could lead to the discrepancies observed between the way in which porosity is lost at low stresses in artificial samples compared with natural trends (Figure 1.5). These voids should compact rapidly as effective stress increases, producing increased porosity loss and this can be seen in MICP results. Figure 2.3 shows the cumulative porosity and pore size distribution of one of the samples prepared at 0.238MPa effective stress in the consolidometer (equivalent of image B. in Figure 2.2). High porosities and distributions partially outside the range measurable using MICP were observed. The kaolinite samples compacted to just 1 and 5MPa (see Chapter 5) show less anomalous distributions, suggesting rapid compaction to measurable dimensions.

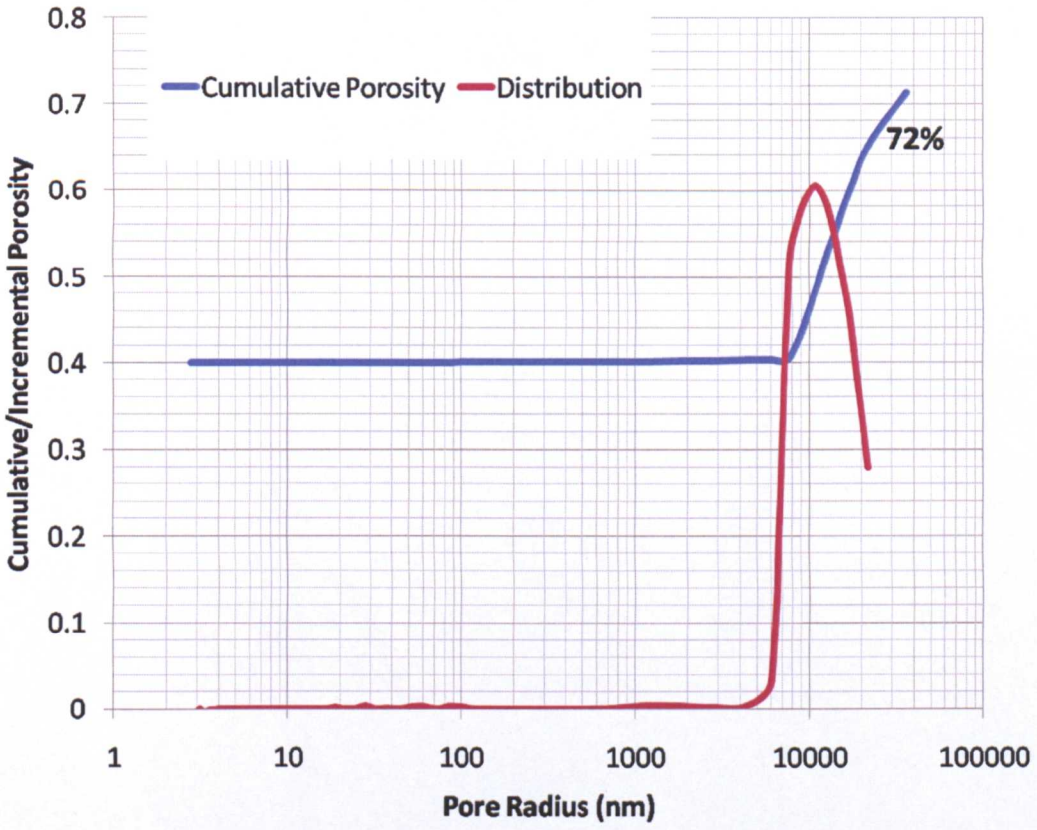

Figure 2.3 Results of MICP analysis on 33.3% mixture of kaolinite, quartz and bentonite consolidated to 0.238MPa. Corrected porosity was calculated as 72%.

MICP analysis of kaolinite samples created in the Back Pressured Shearbox also displayed trends more similar to those of the natural mudstones, but the compacted bentonite showed anomalous distributions as plotted in Figure 2.4.

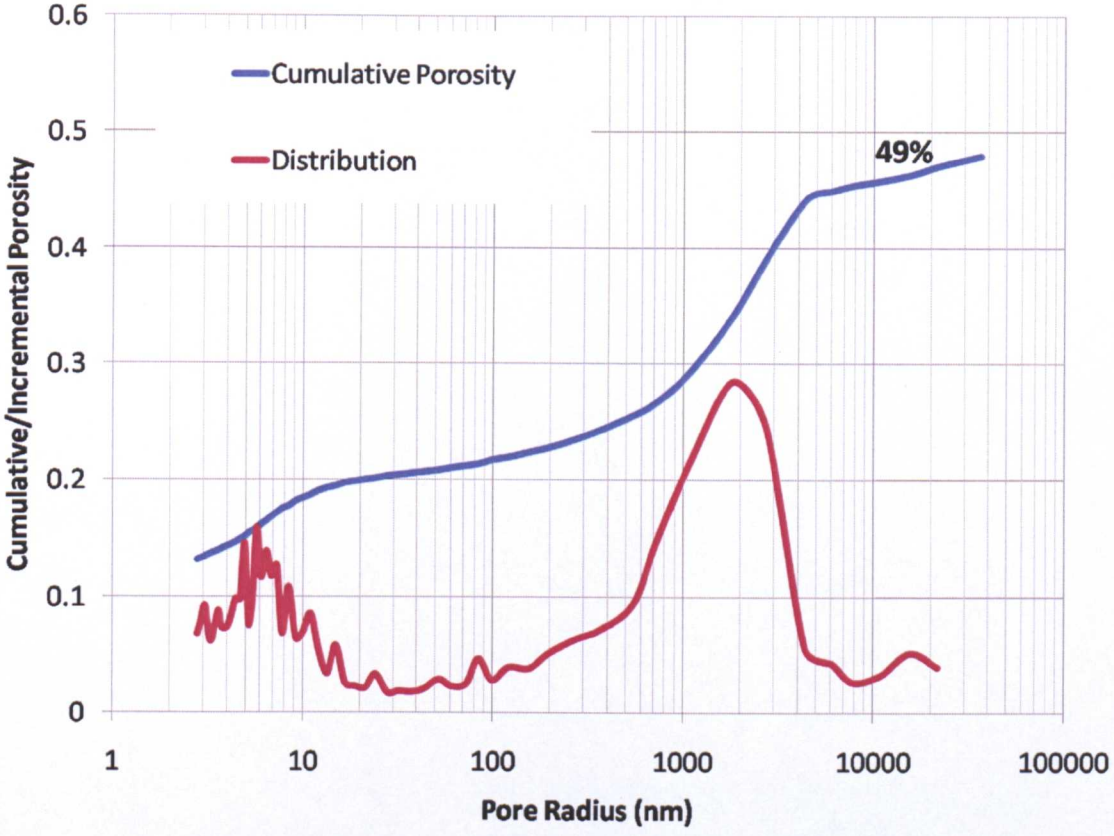

Figure 2.4 MICP (see 2.4.3) data plot for 100% bentonite sample compacted to 2.5MPa in the Back Pressured Shearbox. Corrected porosity was calculated as 49%.

It was observed that following freeze-drying there appeared to be some laminar parallel "fraying" of the samples, speculatively due to the low stress consolidation not providing the strength to withstand the drying process. This did not appear to take place in the kaolinite samples, and was possibly due to grain morphology or higher water content preserved in the bentonites. That the separation/fraying was always perpendicular to the stress applied during the tests indicates some alignment already present in the 100% bentonite samples.

This behaviour may not be unrepresentative of natural, compacting muds in the burial environment but the results in this case were certainly due to sample preparation despite best efforts. These findings were amongst the factors that led to

the decision to use natural samples in the high stress, high temperature triaxial experiments. Figure 2.5 below shows the natural North Sea Mudstone used in Chapter 3 before and after a compaction test (Variable Testing: Triaxial Test 1 – see 3.1.1). Even though the pre-test sample (A.) has experienced moderate burial (core recovered from 1392m) there are no preserved voids visible at this level of magnification. In these samples, some high density areas are pyritized and calcitic fossil material and scanning electron microscopy used in Chapter 3 does reveal some larger void features preserved associated with the fossil tests. This coarser material shows some alignment with bedding (plugs were cut perpendicular to bedding).

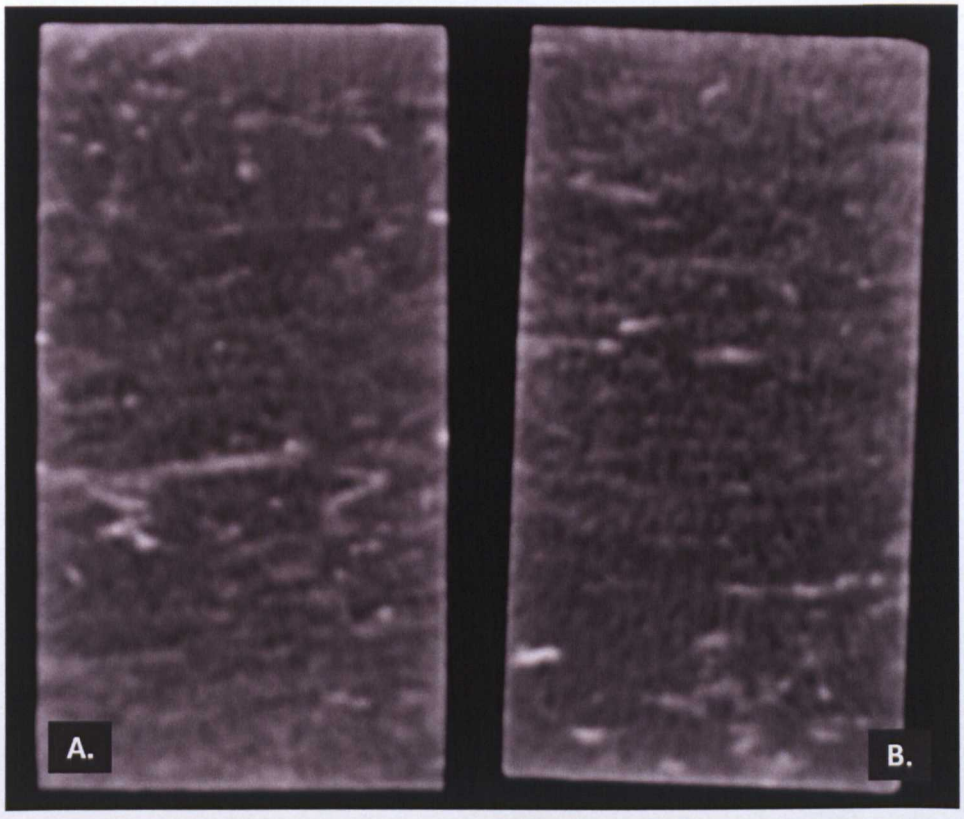

Figure 2.5 CT scans of North Sea mudstone plug used in Variable Testing: Triaxial Test 1 – (see 3.1.1). A. **is the plug scanned immediately prior to going into the cell for testing and B. is the plug when it was removed. Settings used were the same as noted in the scans pictured above (Figure 2.2). Areas that appear lighter in shade in the images are areas of higher density and darker areas indicate lower density.**

2.2.2 Moderate & High Pressure and High Temperature Triaxial Compaction: 6-50MPa Effective Stress

High pressure, high temperature (HPHT) cells were used in all triaxial experiments in Chapter 3. For full testing conditions see the matrices in Table 3.1 (Tests1-6) and Tables 3.4 & 3.5 (Tests 7-9B).

Tests 1-7 were carried out in Triaxial Cell A, Test 8 in Triaxial Cell B and Tests 9A and 9B were completed in Triaxial Cell C, each cell being subjected to its own calibration procedures (see below) to eliminate any variation in the behaviour of individual components. Similar corrected responses in velocity readings under identical conditions at the beginning of Test 7 and Tests 9 (see 3.2.3) indicate comparable performance between cells. All cells had a similar configuration which is simplified in Figure 2.6, to allow axial, radial and pore pressure to be measured and controlled along with temperature (although not in Cell C as an oven was not necessary for the room temperature experiments of Test 9) whilst also recording axial and radial displacements, in addition to axial and radial P and S-wave velocities.

Externally to the cell and oven, pre-test cleaned, filled and de-aired lines carried oil between the axial and radial pumps and the axial piston and radial cavity respectively. The pore-fluid made by design for each test was used to fill the pore pump and lines to the pore-in vessels inside of the cell which fed in through holes in the end-cap at the base of the sample and through a porous disk on either end of the plug (to evenly distribute fluid). As these were all mudstone tests, two layers of (one fine and one coarse) metal gauze were placed around the outside of the plug,

beneath the sleeve to aid consolidation, given the less permeable nature of the mudstone. In the longer tests (4-9), holes were cut in the gauze around the connections for the radial velocity transducers so signals did not have to travel though the gauze as this led to excessive noise.

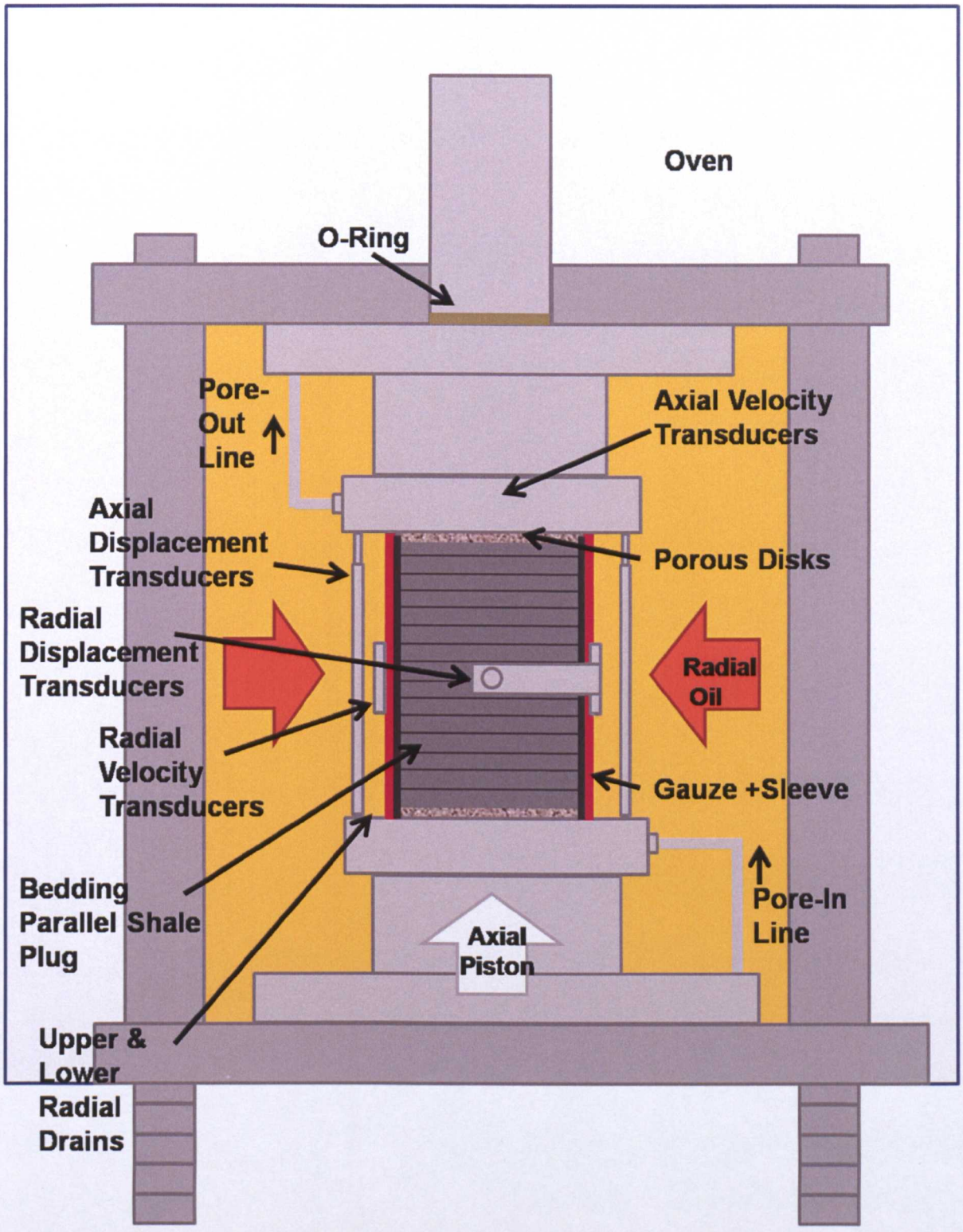

Figure 2.6Simplified diagram to show components of the high pressure, high temperature triaxial cell – wiring and pump system not shown.

Pore-fluid was expected to flow though the samples and along the gauze to reach the pore-out lines leading from the top-cap and out of the cell, to valves beneath the

oven which were closed for the majority of the test. They were only opened when "flushes" of fresh pore fluid were pushed in through the pore-out line which was only carried out over a few minutes during a test at specific intervals (see later).

The "out" lines and external valves for the axial and radial oil were permanently closed throughout all of the tests. Target pressure was set by pre-programmed computer control and the pumps controlled fluid being pushed into the cell or drawn back out via the "in" lines based on readings from sensors at the pump and inside of the cell. Pumps occasionally had to be emptied or filled (for example, following the temperature increase where thermal expansion of the radial oil led to oil being expelled back into the pump to maintain the programmed radial pressure). Under these circumstances, the cell could be "closed-in" by an intermediate valve between the pump and the cell to maintain conditions inside, whilst modifications were made to the volume of the pumps through an "out" valve between the pump and the intermediate cell valve.

Axial stress values always had to be corrected for the friction encountered at the sealing o-ring on the axial piston, upon stress increases a correction of -0.4MPa and upon stress decreases +0.8MPa. During the short periods of data collection where these corrections first took effect the readings can not be used and are subtracted from the data – creating the gaps sometimes observed in the data plots (3.2). The capabilities of the pumps provided pressures of between 0.5-70MPa, although 65MPa was the working maximum to maintain safe conditions. Previous testing have shown the accuracy of the pressure transducers to be 0.1%, with accuracy at the pumps of <0.16% on pressure readings and <0.25% on volume readings.

To maintain the elevated temperatures required in Tests 1-7 (and also for sustaining a constant room temperature in Test 8 – though this was not possible in Tests 9) cells operated inside of an oven. Temperature was controlled via computer program with sensors at the cell and in the oven recording measurements which fed back and programmed the oven temperature. Temperature of the oven was always ramped up to test maximum following a short, initial consolidation period to low stress conditions at the beginning of each test to allow the sample maximum exposure to high temperature. The temperature ramp of the oven was always rapid - ~20-25°C to 170°C in 2 hours. However, temperature readings in the cell showed that it normally took approximately 24 hours for the cell to equilibrate with its surroundings inside the oven and even then whilst the oven stayed at ~170°C for the remainder of the high temperature tests, the temperature in the cell steadied at 150°C. Temperatures quoted in the results chapter are always the cell temperature, not the oven. Accuracy of the temperature device was +/- 0.5°C.

At the end of each test, stress and temperature were ramped down with oven temperature programmed to reduce back to room temperature in 2 hours. The cell was then given a further period of around 24 hours to equilibrate with the oven and cool. Following concerns after the first 2 tests, some stress was still maintained upon the sample during this cooling period for Tests 3-9B. In the high stress tests, care had to be taken due to the probable lag in pore pressure within the mudstone core itself (which cannot be measured) that rapid reduction of the axial and radial pressure did not result in conditions where pore pressure was higher than the confining stresses – resulting in failure of the rock. Therefore, ramping down

procedures at the end of a high pressure test were carried out in stages where a 5 hour ramp took the pressure down from maximum (65MPa axial; 57.5MPa radial; 15MPa pore in Tests 7-9) to 50.9, 43 and 5MPa respectively. This allowed pore pressure to dissipate for around 24 hours before a final 5 hour ramp down of temperature (in the high temperature tests) and stress to 1.5, 1 and 0.5MPa. The cell was then left under these conditions for a further 24 hours as the cell cooled, before building out the sample. Each test's exact parameters are stated in Tables 3.1, 3.3 & 3.4 in Chapter 3.

2.2.3 Mid-Test Measurement

2.2.3.1 Dimensions

During the triaxial tests of Chapter 3, attempts were made to constantly record both axial and radial dimension measurements. In Tests 1-7 (Cell A), axial displacement transducers were inside the cell (as shown in Figure 2.6), inside the radial oil. In cells B and C (Tests 8-9B), external axial displacement transducers were fitted upon the axial piston itself. Previous measurement had shown the error on the displacement transducers to be approximately +/-0.3 μm. Radial displacements were taken by "bridge" mounted transducers around the centre of the plug. The radial measurements suffered from attachment issues once the radial oil (in which it was submerged) reached high temperature. In several tests, readings progressed without problem, but in some tests, most importantly Test 7, the transducer loosened and measured radial results could not be used following the event. Initial dimensions were set by the length and diameter measurements of the plug taken using a micrometer prior to the sample being built-in. These measurements were repeated immediately upon the sample being built-out at the end of each test and the values

checked against the final corrected values from the displacement transducers directly before building-out. There is still some minimal stress upon the sample at this point so some minor difference is to be expected.

As mentioned previously the displacement transducer measurements have been corrected. This is because the cell and its components including the displacement (and velocity – see 2.1.3.2) transducers are subject to change due to pressure and temperature effects that are not the result of changes occurring within the mudstone sample, but simply the equipment itself. Temperature and pressure and corrections for the axial and radial displacement transducers were calculated from calibration tests carried out on Cells A-C using an aluminium plug of known properties and subjecting it to cycles of uniaxial, deviatoric, and isostatic loading/unloading cycles at different temperatures.

2.2.3.2 Velocity

Velocity measurements were attempted in all the triaxial tests, both in the axial and radial direction. P and S wave transmitters were present in the axial end caps above and below the plug inside the cell and also fixed onto either side of the sleeve, half way down the length, at the centre of the plug. These signals were transmitted through a signal amplifier, processed and displayed on an oscilloscope and PC throughout the tests, allowing any adjustments to be made occasionally as the signal changed responding to the deformation of the mudstone during each test. Frequencies used were between 0.1-1MHz.

Velocity measurements also had to be corrected for the influence of temperature and pressure. T_{zero} (the end-cap to end-cap travel time) was measured for a range of frequencies and temperatures. The effects of frequency, temperature and pressure were determined on the radial velocity transducers (as they are submerged in the radial oil) by recording travel times through an aluminium plug of known properties as it was pressurized isostatically under high and low temperature.

Test data was analysed and zero crossing times for each of the waveforms were picked as this was usually easier to identify consistently than the first break (see Figure 2.7 below), particularly for S-waves (Figure 2.8). From this data velocities were calculated.

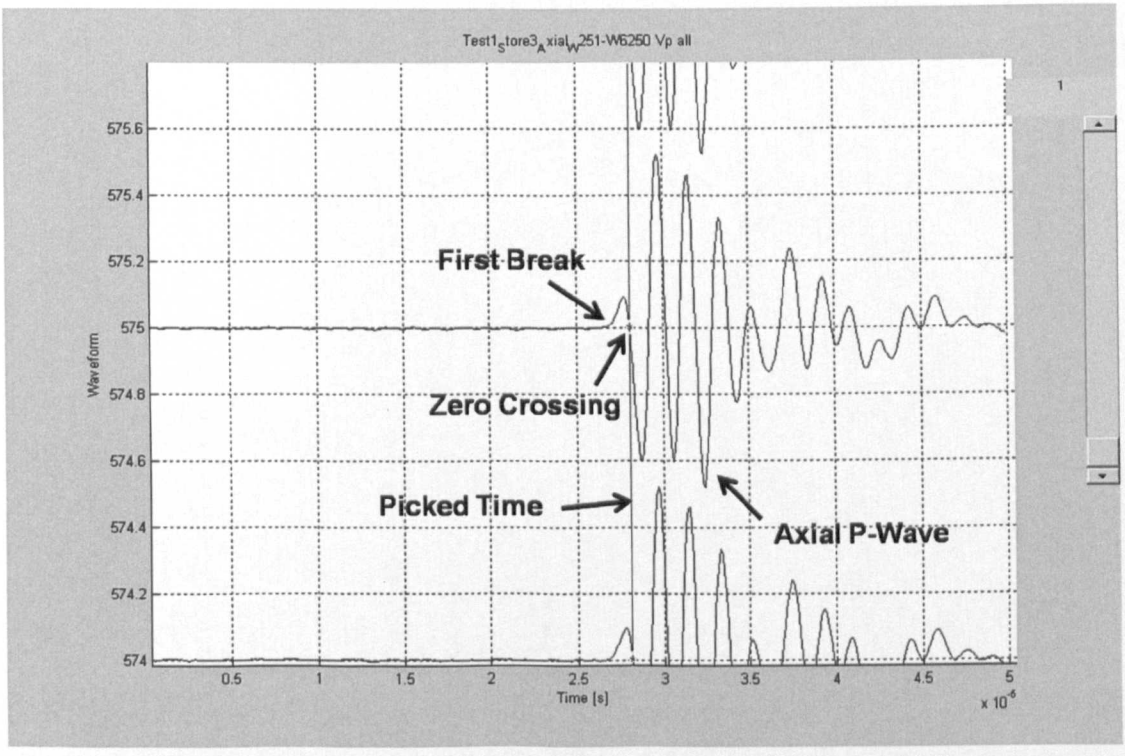

Figure 2.7 Screenshot of picked zero crossing times for axial P-waveforms during Test 1. The waveforms are displayed one above the other in chronological order to allow times to be picked using proprietary software.

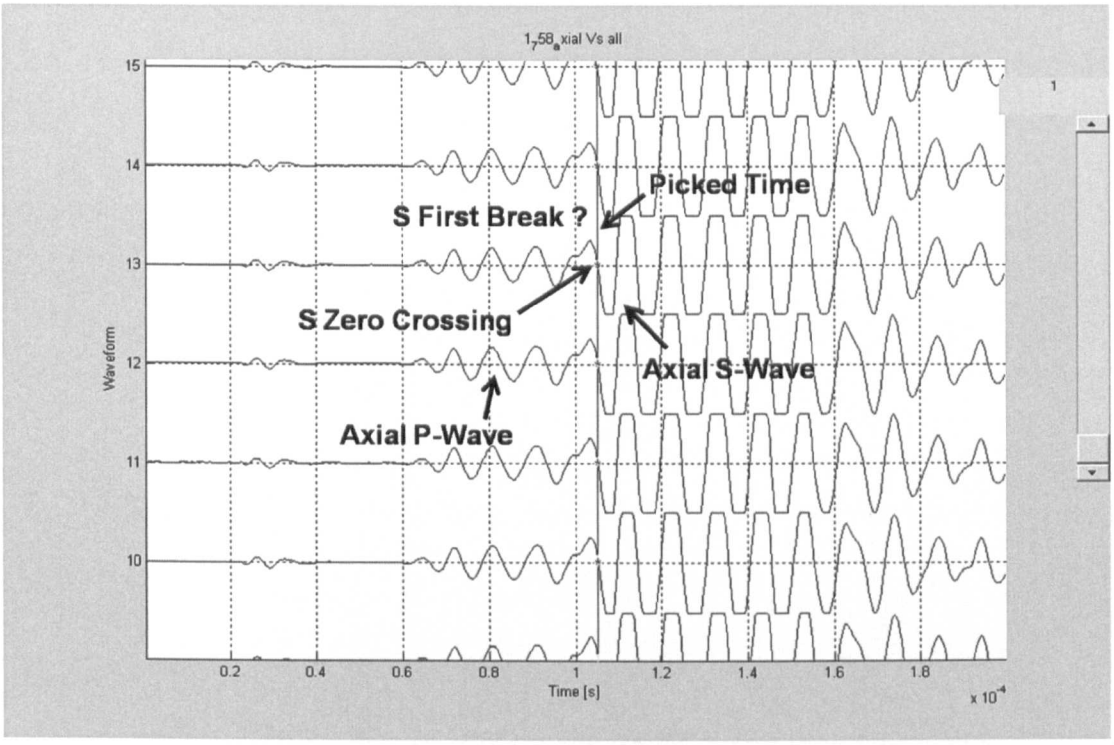

Figure 2.8 Screenshot of picked zero crossing times for axial s-waveforms during Test 3. The waveforms are displayed one above the other in chronological order to allow times to be picked using proprietary software. Picking the S-wave is more problematic due to interference with the faster P-wave and is one of the reasons why zero crossing is used instead of first break.

Plots of the velocity data obtained from these measurements are displayed in Chapter 3 and utilized to calculate various dynamic properties of the mudstones as they compact. The way in which the P and S waves travel through the mudstone gives information on how the properties of the mudstone alter during the test. Several of the dynamic elastic moduli calculated using the velocity data are defined in Mavko *et al.* (2009) below, where ρ is the bulk density, Vp and Vs are the P- and S-wave velocities, respectively.

Bulk modulus *K* is the ratio of the hydrostatic stress to the bulk volume strain or the reciprocal of compressibility

$$K = \rho(V_P^2 - 4/3V_S^2)$$

Shear modulus μ is the ratio of the shear stress to the shear strain

$$\mu = \rho V_S^2$$

Poisson's ratio *v* is minus the ratio of the lateral strain to the axial strain in a uniaxial stress state

$$v = \frac{(V_P^2 - 2V_S^2)}{2(V_P^2 - 2V_S^2)}$$

Young's modulus *E* is the ratio of the extensional stress to the extensional strain in a uniaxial stress state

$$E = \rho V_S^2 (1 + v)$$

2.2.4 Reflux Condenser Tests

To accompany the triaxial tests, which were analyzing the effects of temperature, pressure and pore-fluid chemistry, a small program of tests looking at the effects of temperature and fluid chemistry alone was devised (see Table 3.3 in Chapter 3 for test matrix). In these tests, plugs of the North Sea mudstone core were submerged in each of the 3 main test fluids (4M KCl, 4M NaCl and 3M KCl / 10^{-5}M KOH) at 100°C for a time period equal to that of the high temperature phase of the variable triaxial tests. The swelling nature of the material resulted in the failure of most of the samples during these tests and they were therefore unsuitable for some follow-up analyses such as MICP.

2.3 Measurement of Chemical / Mineralogical Properties

2.3.1 Decontamination

North Sea mudstone samples were preserved in a mineral oil to prevent dehydration, but before preparations began for several of the chemical/mineralogical and physical tests, this had to be removed so as not to interfere with any of the procedures (eg. residue can lead to lower CEC values). This decontamination or cleaning of the mudstone was carried out using an automated Soxhlet technique where samples were submerged in boiling dichloromethane (DCM) on a 120°C hotplate and then rinsed with DCM for an hour. This was simply to clean the material and no extract was collected as all that was expected was storage oil.

2.3.2 Disaggregation

Disaggregation was a necessary preparatory procedure for several of the chemical/mineralogical and physical tests on both the North Sea mudstone samples (Chapter 3) and those from the Malay Basin case study (Chapter 4) to ensure limited damage to the individual grains. Samples were disagreggated using the gentle vacuum, freeze-thaw cycles described in Yang & Aplin (1997). The North Sea samples disaggregated easily following <10 cycles, but Malay Basin samples were very difficult to break-up, particularly Well B (most likely due to siderite cementation). Following >20 cycles of freeze-thaw, they were placed under the ultrasonic probe (in de-ionized water) for 5 minutes. This procedure was just a basic preparatory procedure, but provided additional information on the North Sea mudstone behaviour pre and post-test (3.3.1).

2.3.3 Bulk Fraction X-Ray Diffraction (XRD)

Clay minerals formed important components of the samples in both Chapters 3 and 4. Due to their fine grain size, one of the primary methods for analyzing the mineralogy of these mudstones, both qualitatively and quantitatively, is X-ray diffraction. This is a well known technique based on the idea that minerals are composed of regular, repeating planes of atoms forming a crystal lattice that will diffract a beam of incident X-rays to produce a characteristic diffraction pattern. This is conventionally displayed as intensity against $^{o}2\theta$, where θ is the angle of incidence of the X-ray beam and is related through Bragg's Law to the d-spacing (the distance between adjacent planes of atoms). The basal spacings/reflection positions in Å are often used as a form of "fingerprint" to identify the minerals present (Flohr, 1997).

XRD was used in this study, first upon the whole sample of mudstone material – the bulk fraction and then upon the separated <2 μm clay fraction. The morphology, highly variable chemistry, and reactive behavior of clays makes their study, even with XRD more difficult than with other minerals (eg. oxides and carbonates). In view of this, adaptations have been developed to assist in improving the accuracy of their measurement and have been included in this study.

Samples prepared for bulk fraction XRD were first ground to <500 μm in an agate pestle and mortar and mixed with 20% corundum powder (by weight of total solid). The mixture was ground further and mixed with the emulsifier 0.5 wt.% PVA (polyvinyl alcohol) in a micronizing mill using agate grinding stones. The result is relatively viscous slurry of the sample and the corundum internal standard.

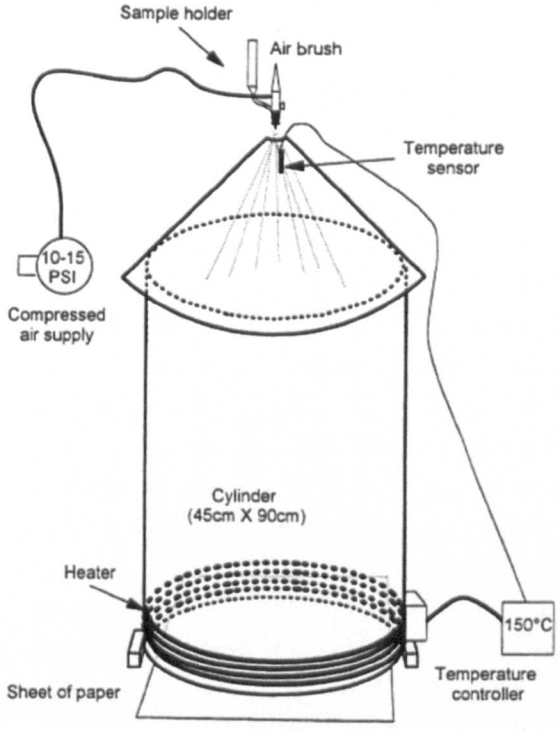

Figure 2.9 Diagram to show operation of the spray-drier used to prepare randomly orientated samples ©1999 The Macaulay Land Use Research Institute. Image from Hillier (1999).

The samples were then spray-dried. This involves the liquid being released through an air gun into the spray dryer which is at a temperature of 110°C (Figure 2.9) and as the drops of liquid dry as they fall through the heated drum, they form the randomly oriented spheres of mineral particles required for quantitative analysis. The spheres were then collected at the base of the drum into glass vials. Initial attempts at the process were checked for the quality of the spray-dried samples and under microscopic examination, the material did appear to have formed the required spheres.

Hillier (2003) states that spray drying material prior to XRD to form spherical granules creates a sample where both the spherical morphology and the way in which spheres pack into the powder holder ensures a random arrangement of the

component particles, increasing the accuracy of quantitfication. Spray dried samples tested in Hillier (1999) were found to be accurate to within 2% regardless of whether or not preferred orientation was refined. This spray drying method described, using an air-gun improves sample recovery to typically ~80%, a significant improvement on earlier methods, but it should be noted this may be as little as ~20% for well dispersed smectites (possibly down to the different suspension concentrations required) (Hillier 1999).

Once prepared, the powder spheres were subject to X-ray diffraction on a PANalytical X'Pert PRO X-ray diffractometer system with X'Celerator for higher speed data collection. The settings used were a step size 0.017°2θ at 0.8 counts per second. The results were processed through PANalytical software X'Pert HighScore Plus to match the peaks observed to the mineral components of the sample through the database. It should be noted that due to some limitations of the reference library specific to clay identification, the Brown and Brindley (1980) reference table was extremely useful and used to solve difficulties and cross check all of the identifications. Once the minerals present were identified they were quantified using the Excel based FULLPAT program developed by Chipera and Bish (2002).This approach merges the reference intensity ratio method with a full–pattern fitting method capable of analyzing all phases in a sample, including the partially ordered or amorphous phases such as the clays, glasses and polymers. The corundum internal standard is present in all prepared samples and also the reference library of standards, minimizing instrumental and matrix effects and a combination of these references are fitted to the sample trace via least-squares minimization (Chipera and Bish, 2002).

2.3.4 Clay Fraction X-Ray Diffraction *(METHOD DEVELOPMENT SECTION 2)*

The <2 μm fractions of selected pre and post-test North Sea mudstone samples and Malay Basin cuttings were prepared as orientated aggregates on glass slides for clay fraction XRD. This allowed clearer identification of the clay mineralogy, including the mixed-layer clays.

All material was subjected to at least 2 "washes" via shaking the sample with deionized water and centrifuging at 10,000 RPM for 85 minutes. Lengthy cycles were primarily necessary for the North Sea mudstones that contained more significant amounts of the very fine, expandable clays. The material was transferred to a beaker and sonicated for 2 minutes to disperse the clays. De-ionized water was added to the beaker to create a column of water 11.2cm high. Sodium hexametaphosphate, $(NaPO_3)_6$ was added to create a solution of concentration of 0.01M, which further dispersed the particles and the mixtures were vigorously stirred and shaken . An initial coarse fraction was settled in 87minutes 39 seconds and the supernatant decanted off and allowed to settle for 9 hours 7 minutes and 49 seconds. The supernatant was collected as the suspension of <2 μm particles. However, due to flocculation issues some of the <2 μm fraction also settled and the settled material was resuspended in a 5.6cm column of fluid and settled over a period of 4 hours 33minutes and 54 seconds. Again the supernatant was collected and the <2 μm suspension transferred to centrifuge bottles.

Following the fractionation, initial rough procedures (to provide indications for the development of triaxial test programs) involved washing the samples with very dilute

NaCl, centrifugation and collection of the viscous <2 μm fraction, which was then pipetted onto a glass slide for analysis. Several issues arose with these methods.

Firstly, pipetting the material onto the slide did not give a particularly even surface once dried and following heat treatment the clays peeled from the edges of the glass. The method also meant that the clays were not likely to be particularly aligned.

Secondly, the "washing" of the sample with dilute NaCl did not allow easy comparison between the pre and post-test North Sea material. This can be seen in Figures 2.10 and 2.11 below. In the "washed" runs there is a large variation between the Pre and Post-Test material. There is a clearly visible elevation at the basal reflection (001/002) glycolated illite/smectite (I/EG-S) position, a glycolated peak at the 002/003 and the ~16.6 Å (5.31°) glycolated peak is intense. In the post-test material of Test 3 (see Chapter 3) the material has been tested in a triaxial cell using a 4M KCl pore fluid and following the wash with dilute NaCl prior to XRD analysis it still shows the effects of potassium in the clay interlayer. The samples do not glycolate to the same extent, to the point that there is no 002/003 glycolated I/S peak.

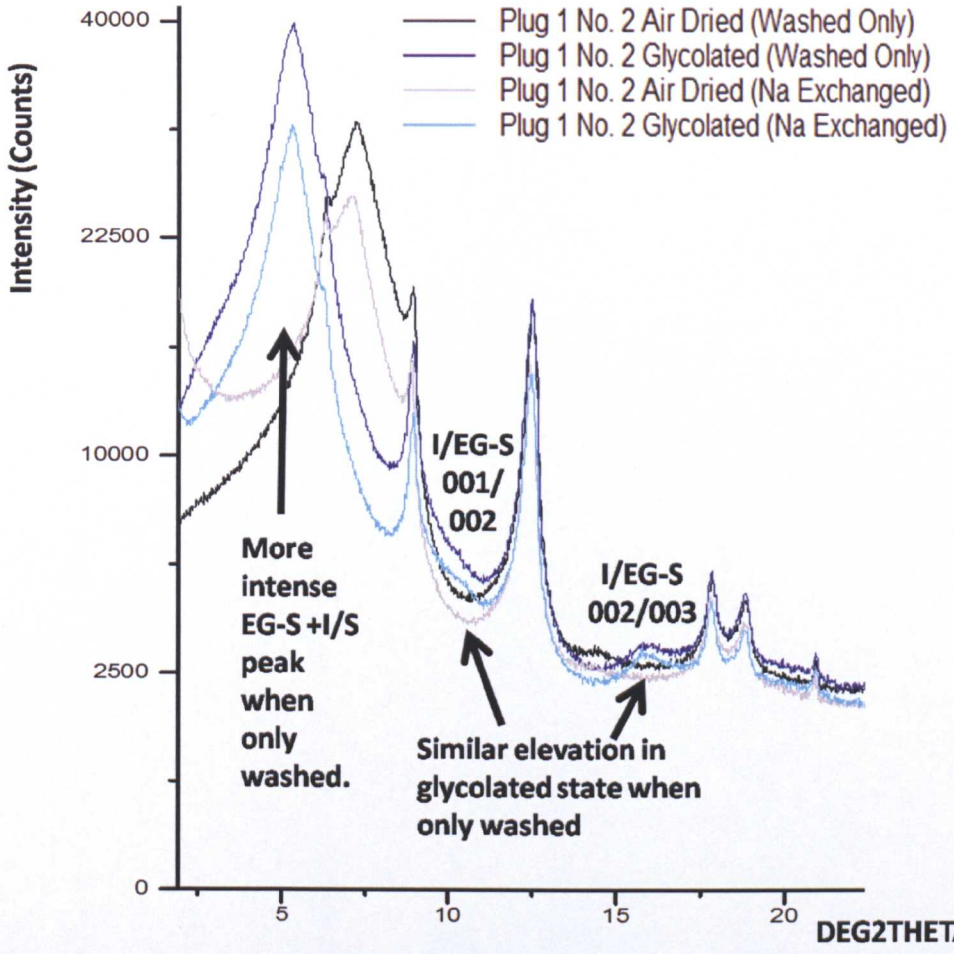

Figure 2.10 Pre-test clay-fraction XRD patterns for air-dried (black/grey) and (EG) glycolated (blue) North Sea mudstone. Dark lines indicate patterns where simple "washing" took place post-fractionation and light lines belong to patterns recorded following full Na-exchange of the samples post-fractionation.

Procedures were adapted when the full analysis for quantification took place. Full exchanges with Na were carried out to assess whether glycolation behaviour was just due to the effects of K exchange (as reported in Mosser-Ruck *et. al.,* 2001) or illitization. This comprised 3 cycles of overnight shaking of the clay-fraction with 1M NaCl solution and washing with 10^{-4}M NaCl solution. The exchanged clay was freeze-dried and then smeared across a glass slide as a very thin paste using the flat end of a spatula. Once air-dried, this gave a very even, thin layer of clay in which the particles were more likely to be aligned than with the pipette method. Having

undergone Na exchange, differences to the pre-test material compared with the "washed" runs were slight (Figure 2.10).

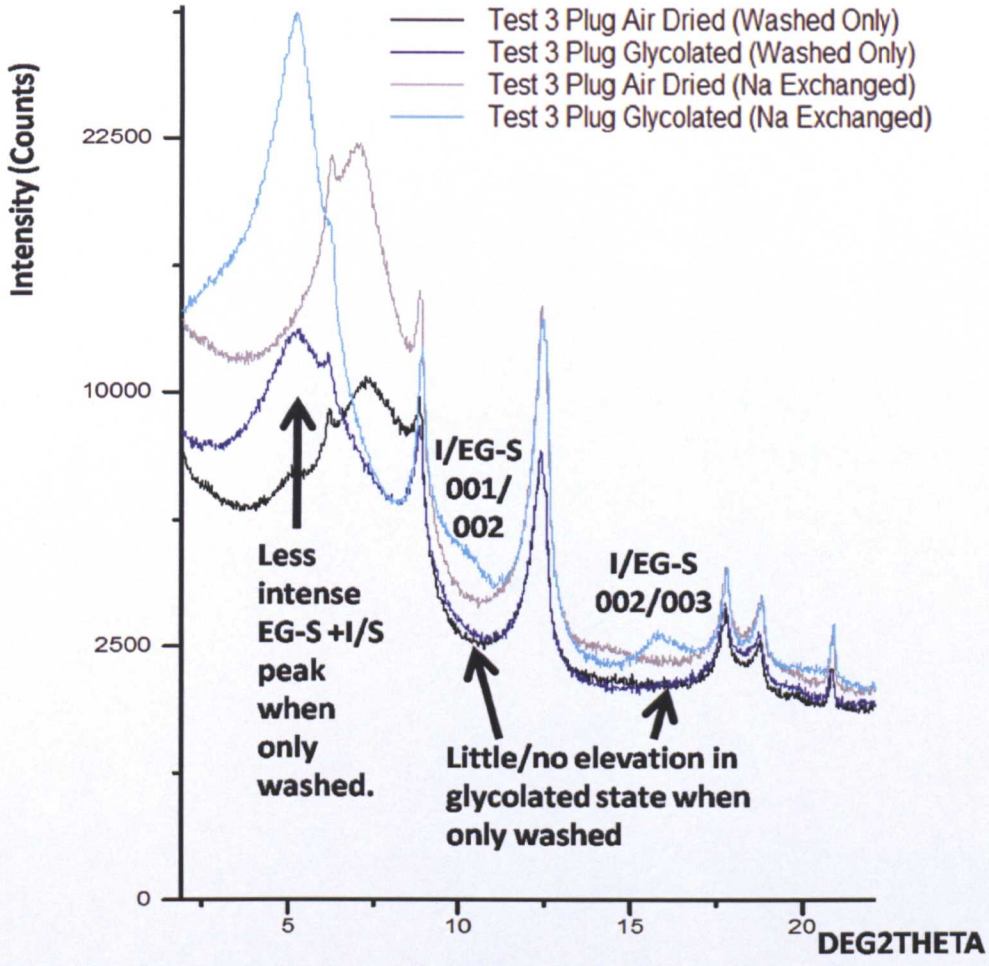

Figure 2.11 Post-Test 3 clay-fraction XRD patterns for air-dried (black/grey) and (EG) glycolated (blue) North Sea mudstone. Dark lines indicate patterns where simple "washing" took place post-fractionation and light lines belong to patterns recorded following full Na-exchange of the samples post-fractionation.

However, the exchange made a significant change to the post-test material (Figure 2.11) intensifying and shifting the ~16Å peak and displaying a 002/003 I/S peak upon glycolation. It was then recognisable that the chemical effects of the triaxial tests were not permanent – no illitization had taken place.

The prominent glycolated I/S 002/003 reflection between 5.10-5.61Å (17.39-15.80°2Theta) in the North Sea diffraction patterns used to estimate I % in I/S is not

visible in the Malay Basin samples (Figure 2.12). This was also the case in the North Sea samples before they were exchanged with Na. The Malay Basin samples were exchanged with Na but still showed lower resolution in this area, perhaps due to the lesser amounts of expandable clays. Similarly to the North Sea samples, the other I/S reflection between 8.58-9.82Å (10.31-9.01°2Theta) used to determine I% in I/S is masked by the presence of mica and illite and its sharp peak at 10Å but elevated intensities in the glycolated state can still be seen.

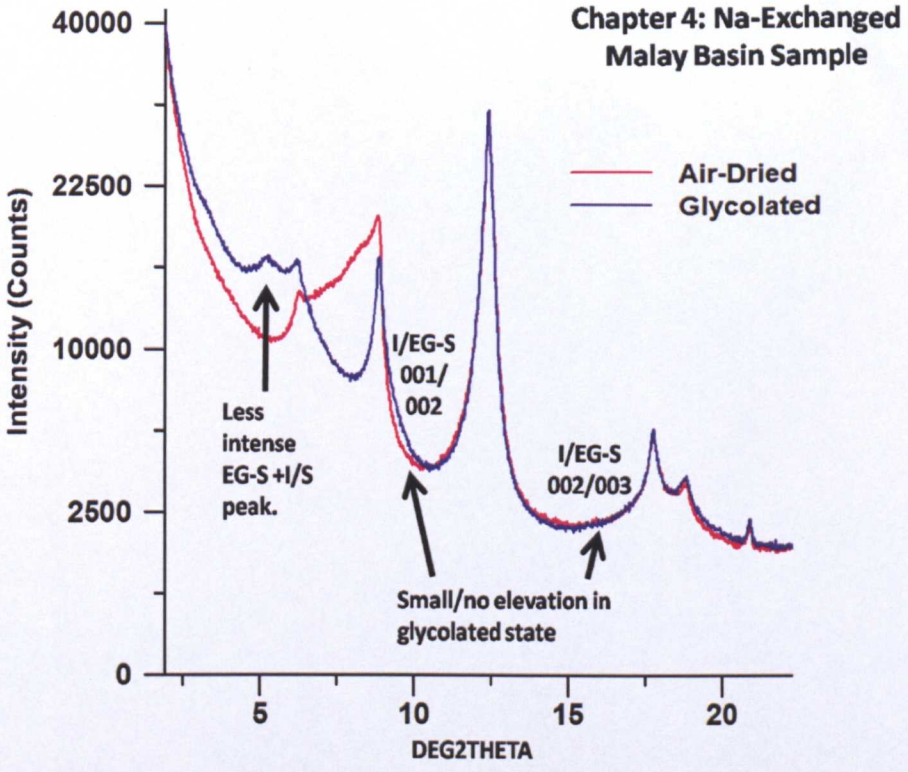

Figure 2.12 Air-dried and glycolated diffraction patterns for the sample from the shallowest sample (1680m) from Well A in the Malay Basin (Chapter 4).

To quantify I% in I/S in the Malay Basin samples, the intensity the air-dried pattern was subtracted from the glycolated trace to reveal the broad "peak" of I/S. Initially, the range in Å at 0.75 intensity peak height was measured and the central point of that range in Å taken and used to calculate I% in I/S using the relationship in Moore & Reynolds (1997). 0.5 intensity peak height is normally used for defining XRD

pattern peaks, but as these are mature samples, the skew on the broad peak meant that the central point at 0.5 intensity peak height did not define the obvious visible peak. Noise in the pattern led to a further method development where a polynomial trendline (Order:6) was fitted to the peak and the position of the maximum peak intensity in Å recorded and again converted into I% in I/S.

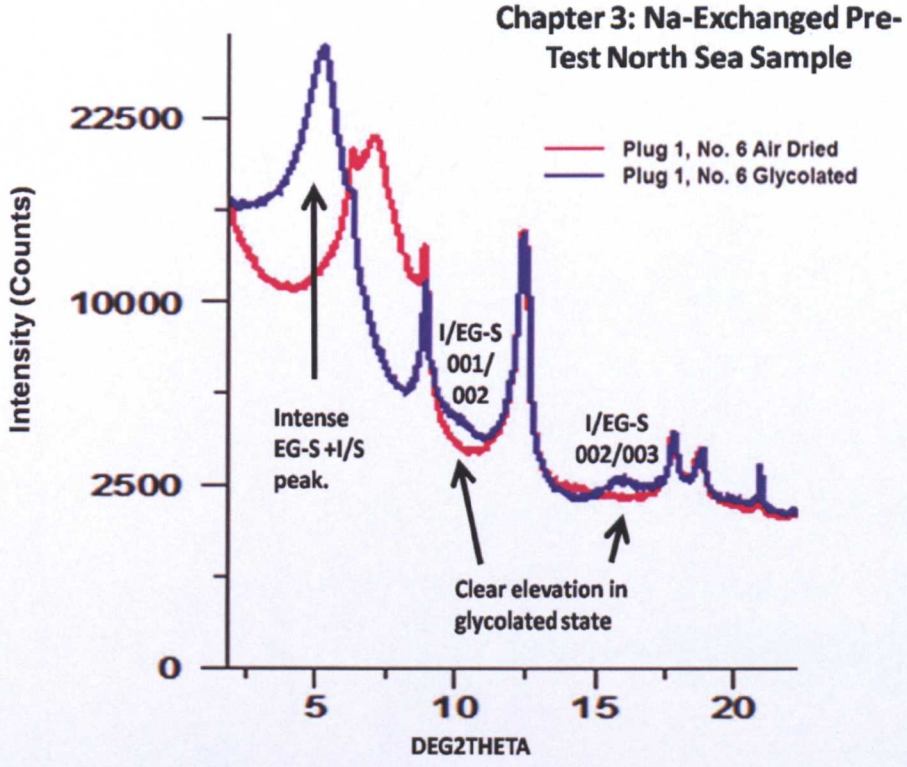

Figure 2.13 Air-dried and glycolated diffraction patterns for the sample from the pre-test North Sea mudstone (Chapter 3).

This methodology was tested on the North Sea mudrocks where both the 8.58-9.82Å elevation on the side of the illite/mica peak and the clearer individual 5.10-5.61Å glycolated peak are present (Figure 2.13). The clear 002/003 peak was defined by fitting a polynomial to the intensity difference between the air-dried and glycolated patterns and recording the position of maximum intensity ($^{o}2\theta$) and converted into I% in I/S using the Moore & Reynolds (1997) relationship. This procedure was repeated on the less obvious 001/002 glycolated elevation on the side of the

illite/mica peak and the difference between I% in I/S calculated from these two peaks recorded in the table below.

NS Pre-Test Sample	002/003 °2 θ	I% in I/S	001/002 °2 θ	I% in I/S	I% in I/S Difference
Plug 1, No. 2	16.02	31.00	10.10	27.64	+3.36
Plug 1, No. 6	16.00	29.13	10.07	30.08	-0.95
Slice 4, No.10	15.96	26.59	10.13	25.58	+1.01
Slice 4, No. 23 & 27	16.00	29.13	9.99	35.47	-6.34
Pre-Test 7 Plug	16.00	29.68	10.13	25.33	+4.35
Pre-Test 8 Plug	16.01	29.99	10.15	24.25	+5.74

Table 2.1 Comparison of I% in I/S calculations using the 001/002 and 002/003 peaks from North Sea mudstone diffraction patterns.

From this pre-test North Sea mudstone sample set (allocation of sample names explained in Chapter 3) the average difference between the I% in I/S calculated from the 002/003 and that from the 001/002 peaks is 3.63% with a maximum difference of 6.34% and a minimum of 0.95%. Accepting these minimal differences subtraction over the 001/002 elevation in intensity where there is no defined glycolated 002/003 peak in the Malay Basin mudstones should still give reasonable estimates of I% in I/S.

It is also worth noting that the standard deviation in °2θ values for the different pre-test samples is only 0.02 at the 002/003 position and 0.06 at 001/002. This is despite the plugs and slices coming from separate areas of the core to the Test 7 and 8 plugs, giving a good indication that geological/experimental hetereogeneity along the 1m length of the core is not great and we have good constraint on the pre-test nature of material, allowing confident appraisal of what changes are due to the triaxial tests.

2.3.5 Cation Exchange Capacity (CEC)

The CEC of a material is a measure of the concentration of unfixed cations in interior and surface layers of a clay mineral (Potter *et al.*, 2005). Measurements of CEC were carried out on selected pre and post-test North Sea samples in Chapter 3 to corroborate mineralogical findings from the XRD analyses.

10g of the bulk mudstone samples was first decontaminated, refluxed with distilled water and 20g barium chloride added to flocculate the clays following refluxing. The sample was then washed by centrifugation three times with 1M barium chloride solution and washed a further five times with distilled water until a test with silver nitrate indicated that no chloride ions were present in the wash water. This was because soluble salts could result in poor titration curves. The clean sample was then transferred to a beaker and 200ml distilled water with 100ml isopropyl alcohol was added whilst the mixture stirred vigorously. Conductance was then measured as a titration with magnesium sulphate solution was carried out. As the barium ions in the clay were replaced by magnesium there was little change in conductance. Once full exchange had taken place there was a sharp change in conductance. The titration curve was then plotted (results seen in Chapter 3) and the titration end point used to calculate CEC.

The purpose of these tests was to give rapid results on the triaxial test samples, looking for change and not necessarily overall values. They were therefore not fractionated to separate the clay fraction. The samples are clay-rich (according to bulk fraction XRD) and therefore their overall CEC gives an indication of the clay types present (see Table 2.2 below).

Clay Mineral	Surface Area (m^2/g)			Cation Exchange Capacity (meq/100g)	
	Internal	*External*	*Total*	*CEC*	*pH Dependence*
Smectite	500-700	70-120	600-820	60-150	Negligible
Vermiculite	500-600	50-100	500-700	100-200	Negligible
Illite	5-10	70-100	70-120	10-40	Low
Chlorite	<10	50-100	50-100	5-40	Low
Kaolinite	~0	10-30	10-30	1-15	High

Table 2.2 Approximate values of surface area and cation exchange capacity for various clay minerals (Fialips, 2007).

As noted in the table above, surface area provides an indication of clay types present and additional surface area measurements were also carried out on pre-test material and post-test 7 and 8 (see Chapter 4) samples by an external contractor. Samples were washed in a fluid with a water activity substantially less than water containing a soluble cation and measurements of the material's dielectric constant was measured at a preselected frequency for comparison to calibration curves. Previously established relationships were then used to calculate surface area from the dielectric constant.

2.3.6 Inductively Coupled Plasma-Optical Emission Spectrometry (ICP-OES)

A small program of ICP measurements were made on samples taken from the 4M KCl fluid prepared as the artificial pore fluid for the early triaxial tests and also upon samples of fluid that had been drained from the cell system following Variable Triaxial Tests 1 and 2. ICP-OES involves subjecting samples to high temperatures, generating excitation and ionization and then allowing relaxation through emission of light at specific wavelengths which are then measured and used to determine the concentrations of elements of interest (Boss & Fredeen, 1999).

The fluid samples were prepared with 1% nitric acid, unequally divided into 3 parts. One part for lower concentration metal analysis, one part for potassium analysis and 1 part spare. For the lower concentration metal analysis, 10ml of sample was diluted with de-ionized water and for potassium analysis, 1ml of sample was strongly diluted with 1% nitric acid solution. The equipment used to run the samples was a Varion Vista MPX ICP-OES which was calibrated using a standard solution diluted with 4M KCl. Further dilution of the samples was necessary for some of the analyses and results belonging to different dilutions are marked in the results table. If the testing had continued, standards more fitting to the concentrated KCl fluid would have been used to prevent high dilution. However, it was decided that the fluid sample analyses with ICP be discontinued. This was because although it gave an indication of chemical changes in the fluid due to its residency in the triaxial system, there was no way of proving conclusively that the increases or loss of certain elements was due to the mudstone itself and not other components of the system.

2.3.7 Optical / Electron Microscopy (SE and BSEM) and Energy-Dispersive X-Ray Spectroscopy (EDX)

Samples of the pre and post test North Sea mudstone core, as well as Malay Basin cuttings were selected and prepared as ~30μm thick thin sections for analysis under a transmitted light, polarising microscope and scanning electron microscopy with EDX measurement to allow chemical testing. This was to visualise and chemically analyse the mineralogical and textural features of the rocks, specifically looking at clay grain morphology and any kind of alignment. Descriptions of orientation of samples for preparation are given in the results chapters, but, generally, attempts were made to slice the cuttings perpendicular to bedding to endeavour to expose

any parallel fabrics. In the North Sea mudstone core bedding was easily identifiable and slides were cut both perpendicular and parallel to bedding for study.
Initial observations under a transmitted light, polarising microscope were made and although analysis of the clays is limited given the zoom capabilities (and sample slide quality as these samples were prepared using traditional techniques) these first observations often gave valuable information on coarser features of the samples.

Samples were then carbon coated and analysed on an FEI XL30 ESEM-FEG. This has a high brightness Schottky field emission source and normal operating conditions for the machine were 20-25 kV with a spot size of 3-4 mm and a working distance of 10-17 mm depending on the sample. An energy dispersive X-ray (EDX) detector was connected and was used to identify the elements present at particular points, over cross-sections and also mapping over whole areas. The spectra were utilized qualitatively to assess mineralogy, but small point count studies were carried out looking particularly at the compositions of the aluminosilicates.

2.3.8 Total Organic Carbon

Pre-test North Sea mudstone and selected Malay Basin cuttings underwent measurement of their total organic carbon content using a standard methodology based on BS7755 Section 3.8. For the material that was to be triaxially tested at temperature, this was mainly to fully characterise the rock as the test temperatures were not expected to reach those of pyrolysis. With the Malay Basin samples, it was carried out to identify potential hydrocarbon source horizons that could influence other measurements.

The North Sea mudstone samples were put through Soxhlet extraction to remove excess storage mineral oil and then both sets of samples ground to <500 μm and air dried.~ 0.1 g of each dried sample was treated with 4M HCl in a porous crucible to remove carbonates, along with 1 empty crucible to act as a blank. The LECO Carbon/Sulphur Analyser was calibrated with a minimum of 5 standard steel rings of certified carbon content and both tungsten accelerator and ironchip accelerator added to each crucible of sample (including the blank). Each sample was then processed in the analyser, with the organic carbon oxidised to CO_2 by combustion in a stream of oxygen and the CO_2 produced quantified by infra-red detection. Error was assessed using the blank and was recorded in all runs.

2.3.9 Rock-Eval

The standard technique based on pyrolyis for screening for potential hydrocarbon source rocks was employed for selected samples from the Malay basin. This was because elevated TOC content was found in two horizons in the Malay dataset and further analysis was deemed necessary to evaluate their potential. 100mg of samples prepared for TOC analysis (decontaminated and ground to <500 μm) was taken and run with THA 200 standard (5.15%TOC; 0.27 S1; 13.59 S2; 430°C Tmax) and a blank on a Rock-Eval system. S peak values (S1 which generated by the release of any free hydrocarbons and S2 resulting from the simulated maturation and generation of new hydrocarbons from kerogen) with Tmax (the maximum temperature required to yield the S2 peak) were recorded.

2.4 Measurement of Physical Properties

2.4.1 Grain Density *METHOD DEVELOPMENT SECTION 3*

Grain densities were measured for all samples in this project. This is because as well as being an important physical property that can show a wide range of values (see Table 2.3 below), it can give an indication of mineralogy, in addition to being an important input parameter for other rock property measurements (for example porosity or grain size distribution).

Mineral	Grain Density (g/cm^3)
Quartz	2.65
Illite	2.6-2.9
Chlorite	2.6-3.3
Kaolinite	2.61-2.68
Montmorillonite group (smectites)	2-2.6*/2.7**
Biotite	2.7-3.3
Pyrite	5.01
Siderite	3.5
Calcite	2.715
Plagioclase Feldspar	2.62-2.76
Orthoclase Feldspar	2.56-2.63

Table 2.3 Grain densities for minerals identified in XRD analyses. Values mainly from Gribble & Hall (1992) and smectite values obtained from *Deer *et al.* (1966) and **webmineral.com.

The basic methodology mainly followed British Standard 733, 1987. ~2g of dried sample was weighed into a pre-weighed pyknometer. The pyknometer was then filled with de-aired water and the weight of the pyknometer with the sample and water was measured at 25°C. The weight of the pyknometer containing only de-aired water was then weighed again at 25°C to measure the volume of the pyknometer.

The volume of water displaced by the sample was then calculated and from the weight of the sample, the grain density. Quartz standards were run with the tests.

In Post (1989) using ASTM Test Method (D 854) smectite grain densities vary as a function of heating temperature and time. Standard procedures require that the sample be dried at 105°C and but other clay-related literature used cooler, slower drying conditions (eg. Mondol *et al.*, 2007 – 60°C for 2-3 days) to preserve the stability of the clays and so this approach was adopted in initial trials for this study. However, an early optimization test where the drying temperature was lowered to 80°C and for a duration of 3 days gave low values for the clays and anomalously low values for both the quartz standard and the silica silt used in the tests described in Section 2.2.1 (see Table 2.4).

Sample	Grain density (g/cm^3) following 3 Days drying at 80°C	Grain density (g/cm^3) following >5 Days drying at 80°C
Quartz Standard	2.59	2.65 -2.68
Silica Silt (Feldspar impurities)	2.39	2.67

Table 2.4 Grain density measurements on quartz samples with different drying times. Actual value should be 2.65 g/cm^3.

Even though what constitutes a dry smectite-rich rock could be open to discussion, for consistency, the quartz standard should always be completely dry and produce a value of ~2.65 g/cm^3. The drying period at 80°C was increased to 5 days and after this period the quartz standard measured 2.65g/cm^3 with the largest error measured as +0.03 g/cm^3. This became the norm for the rest of the study that any dried mudstone samples (not freeze-dried) were placed in an 80°C oven for >5 days.

2.4.2 Grain Size Distribution

Another key physical property is grain size, providing information about the mudstone and being a necessary input for calculations such as those for permeability. Selected samples from all sections of this project were therefore analysed using a sedigraph which records the cumulative distribution of grain sizes as they fall at different rates under Stoke's Law.

Samples prepared for grain size analysis were first decontaminated if stored in mineral oil (North Sea mudstone samples) and then put through the freeze-thaw disaggregation process (North Sea and Malay Basin Mudstones only, materials for low stress consolidations were already powder).

Analysis of different batches of samples were carried out at intervals over the 3 years of the project, but the sedigraph was calibrated using a garnet standard prior to each batch. Testing began when the standard was within the tolerance levels of the mass median equivalent spherical diameter for garnet = 2.47 +/- 0.20 μm, where 10% > 4.80 +/-0.50 μm and 10% < 0.75 +/- 0.20 μm. Once preparation was complete the dried sample was sonicated for 5 minutes and then dispersant (0.24 mol% Sodium-Hexametaphosphate) added. Further de-ionized water was added to make a volume of 50ml (to obtain a final dispersant concentration of 0.05 mol%) and the sample loaded into the Micromeritics Sedigraph 5000ET. Each sample was always left for at least 1 hour prior to every run to allow the sample to equilibrate to the temperature of the machine - approx. 28-35 °C. The rate setting was determined by the measured grain density and the temperature of the chamber, measured from a thermometer inside the chamber prior to all tests.

After each run the equipment was cleaned, the sample collected and poured through a 63μm mesh sieve to gather the material too large for the sedigraph to measure. This was then dried and weighed. Data collected from each run was then loaded into a calibration spreadsheet where the >63 μm material was incorporated into the distribution and first sieve corrected, then pipette corrected. This uses relationships quantified from previous work at Newcastle to calibrate the sedigraph analysis with internal standards (London Clay) which had been previously been analyzed using the pipette method (BS 1377, Part 6, 1990).

2.4.3 Mercury Injection Core Porosimetry (MICP)

As the main aim of this project was to investigate compaction and porosity loss in mudstones, MICP measurements were carried out on all samples to measure porosity and pore size distributions.

Samples prepared for porosimetry were first decontaminated if stored in mineral oil (North Sea mudstone samples) and then all were freeze-dried (Delage and Lefebvre, 1984). Samples were placed inside a penetrometer and run at low pressure and high pressure (up to 39 000 psi – equivalent to a pore radius of ~3nm) in a Micromeritics# Autopore II 9220 mercury intrusion porosimeter. A vacuum is induced and the pores of the sample fill with mercury as pressure is increased in 56 increments where each pressure corresponds to a particular pore size and the volume of intruded mercury with each increment is measured to indicate abundance. Pore diameters were calculated from the mercury injection data assuming a mercury-air contact angle of 141° and an interfacial tension of 0.48 Nm^{-1}. The measured pore volume differs from the total porosity since some pores are <3 nm radius, and some may not form part of

a connected pore network (Day-Stirrat *et al.,* 2008). Total porosities were therefore calculated from bulk volume obtained from the mercury porosimeter value, and the measured grain-density. This is further corrected by analysing distribution data and placing a cut-off at the largest pore radius of the main distribution, eliminating fractures from the total. In the various results chapters the total porosity, the corrected porosity, the chosen cut-off radius (nm), the R_{mean} (mean pore radius in nm) and the $R_{10\%}$ (the mean pore radius at 90% of the cumulative distribution – approximately corresponding to the critical 10% saturation required for migration in a shale, Rudd & Pandey, 1973). These values form key input data for permeability calculations. It should be noted as this study uses both core (North Sea mudstones) and cuttings (Malay Basin samples) that Schowalter (1979) carried out a study on variation in the accuracy of the MICP technique and found that the smaller the sample the more likely the capillary plateau and the displacement pressure estimated at 10% saturation are to be less than that measured on a plug. It does however, also show that the properties of irregular shaped rock-chips as small as drill cuttings can be measured with workable accuracy using standard MICP equipment. Although there was no natural standard that could be run along side this technique repeat measurements were taken on selected samples show repeatability. In addition to this, tests were carried out to examine the accuracy of the equipment in 2010 by P. Green and it was found that values could be reproduced with standard deviations from the mean corrected porosities of 0.0010 and 0.0042% on two different datasets (CV 0.95 and 6.71%).

2.4.4 Permeability Calculations

Pemeability estimates for the samples were important to measure the way in which this property was affected by compaction both in the laboratory tested samples and those compacted naturally in the Malay Basin. However, direct measurement techniques such as pulse-decay tests (Escoffier *et al.*, 2005) were outside the scope of this project. Instead, calculations were made based upon work detailed in Yang & Aplin (1998) utilising grain density measurements, clay abundance from grain size distribution tests and MICP data from results in Chapters 3 and 4.

2.4.5 High Resolution X-Ray Textural Goniometry (HRXTG)

Following literature reviewed in Chapter 1 such as Day-Stirrat *et al.* (2008) and Haines *et al.* (2009) linking the preferred orientation of phyllosilicate minerals with illitization and therefore chemical compaction, grain alignment was first assessed qualitatively in BSEM images and then quantitatively using HRXTG. This was to investigate how the triaxial experiments affected the grain alignment of the North Sea mudstones and also how alignment varied when compared with other rock properties in the natural mudstone samples from the Malay Basin.

High Resolution X-Ray Textural Goniometry (HRXTG) is a method developed at the University of Michigan, USA and is described in Ho *et al.* (1999) and Day-Stirrat *et al.* (2008). Samples were prepared by cutting sections perpendicular to the known bedding in the North Sea core and to any visible lamination in the Malay Basin cuttings, slicing them into ~0.2mm sections and sealing them in a sample holder over the open circular window seen in the second image in Figure 2.14.

An Enraf-Nonius CAD4 single-crystal diffractometer with MoKα – radiation source and scintillation detector was used in the two step process. First, clay mineralogy is determined via a low angle XRD scan. This is followed by a measurement of the degree of alignment of the identified minerals. In transmission mode, the X-ray detector is set to a 2Θ value corresponding to the 001position of the mineral being measured (for example, 10.1Å for illite/mica or 14.2Å for chlorite). The sample is rotated to capture a grid of both diffracted intensity and orientation. Following correction for background and normalisation, relative pole densities are recorded and expressed as multiples of random distribution or MRD.

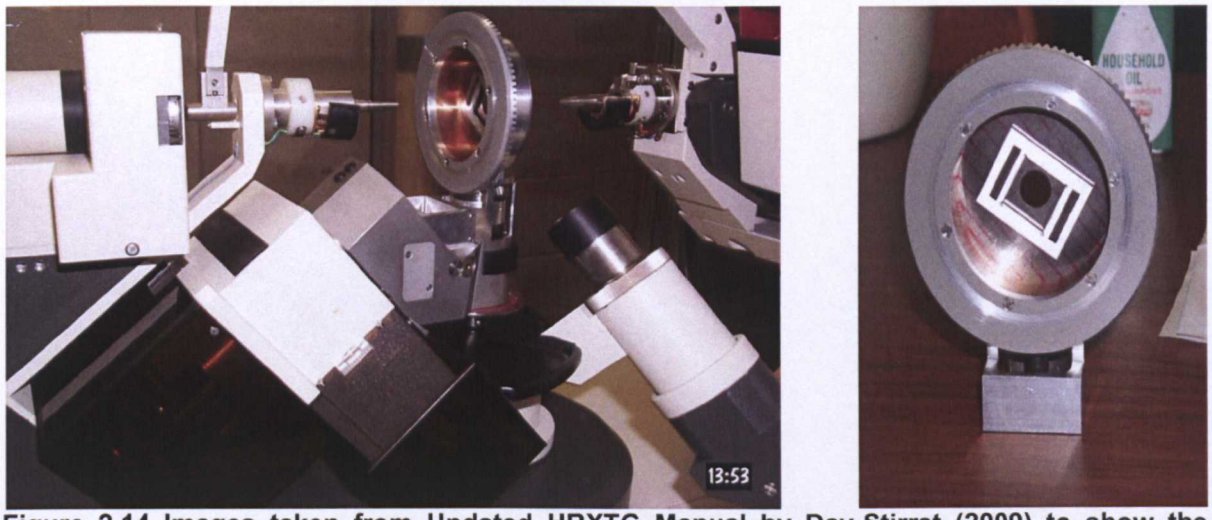

Figure 2.14 Images taken from Updated HRXTG Manual by Day-Stirrat (2009) to show the equipment in working mode and with the stage detached to clearly display the sample holder and window that would normally be covered by a slice of mudstone sample when in working mode.

2.5 Summary

A wide variety of techniques have been employed in this project to attempt to better understand compaction mechanisms in mudstones and shales. First, were those used to simulate geological compaction processes, whilst capturing data that would give insight into the developments taking place during the experiments:

- Low stress consolidometer, triaxial and shearbox consolidations
- Moderate & high pressure and high temperature triaxial compaction with dimension and ultrasonic velocity meaurements
- Reflux condenser temperature and fluid influence tests

Second, were the techniques used to characterize chemical/mineralogical change either due to the experimental compaction tests or due to burial in a high geotherm region:

- Bulk fraction X-ray diffraction (XRD)
- Clay fraction X-ray diffraction (XRD)
- Cation exchange capacity measurement (CEC)
- Inductively Coupled Plasma-Optical Emission Spectrometry (ICP-OES)
- Optical / electron microscopy (SE and BSEM) and energy-dispersive X-ray spectroscopy (EDX)
- Total organic carbon measurement
- Rock-Eval

Third, were the measurements used to assess those changes in physical/textural features of the tested North Sea mudstones or the Malay Basin cuttings:

- Grain density measurement
- Sedigraph analysis
- Mercury injection core porosimetry (MICP)
- High resolution X-ray textural goniometry (HRXTG)

Accuracy of the techniques was under constant scrutiny, wherever possible calibrations were made and errors quoted with results. Some of the largest areas of uncertainty are associated with the less standard testing procedures such as the radial dimension measurements and velocity readings at high temperature. Due to mechanical issues with certain components temperature response, the radial measurements were lost in some tests (Chapter 3). In Test 7 (the "chemical compaction" geological simulation test), a model of radial displacement was constructed. This was one of the occasions when the large variety of techniques used was most effective, as it meant any models could draw on more than one source for calibration. For example the radial displacement model constructed for Test 7 drew upon data from successful, calibrated radial measurements in the other tests, the successful, calibrated axial measurements in Test 7, micrometer pre and post-test measurements, grain density and MICP data (discussed in more detail in Chapter 3). Agreement between independent calibration points gives assurance in models to allow interpretation and confidence in final conclusions.

Chapter 3

Laboratory Simulation of Mudstone Compaction

3. Laboratory Simulation of Mudstone Compaction

3.1 Introduction

3.1.1 Laboratory Compaction Simulations

The aim of the work carried out in this section was to attempt to simulate geologically realistic comditions to generate compaction processes in the laboratory. As discussed in Chapter 1, it is thought that mudrocks and shales compact during burial as a result of both mechanical and chemical processes. Attempts at simulating both types of processes separately have been made in the laboratory to gain qualitative and quantitative understanding of controls. Given the information in Chapter 1 and literature discussed later in this thesis, increasing the key factors listed below (with relevant references) should all contribute to emulating the burial environment:

- **effective stress** *(Mondol et al. (2007); Burland (1990); Al-Wardy & Zimmerman (2004); Swan et al. (1989); Vasseur et al. (1995); Colten-Bradley (1987))*
- **time** *(Horsrud et al. (2004); Eberl & Hower (1976); Bauer & Berger (1998); Howard & Roy (1985); Cuadros & Linares (1996); Velde & Vasseur (1992))*
- **temperature** *(Johnston (1987); Moustafa et al. (2008); (Fjar et al., 2008); Mitchell & Soga, (2005); Hüpers et al. (2010); Sultan et al. (2002); Lynch & Reynolds, (1985); Bauer & Berger (1998); Howard & Roy (1985); Huang et al. (1993); and Eberl & Hower (1976))*

- **potassium concentration of the pore fluid & pH** *(Steiger, (1982); Van Oort, (2003); Yu et al., (2001); Horsrud et al., (1998); Sonstebo & Holt, (2001); Ghassemi & Diek, (2003); Van Gijtenbeek et al., (2006); Mosser-Ruck et al. (2001) Bauer & Velde, (1998); Claret et al. (2002))*

Which, if any of those components are dominant controls is not clear and therefore it was necessary to run additional experiments where variables were run in isolation or in conjunction to test their importance and/or interaction with other controls.

Simulations of mechanical processes such as grain reorganisation, rotation and breakage of clays under stress have long been simulated in studies focussed on civil engineering and later petroleum related geotechnical research. These include Terzaghi (1925), Dewhurst & Aplin (1998), Sintubin *et al.* (2005), Mondol *et al.* (2007), Haines *et al.* (2009). Geochemical processes in mudstones, such as the diagenetic clay mineral transformations have also received intense study with successful synthesis of most authigenic clay minerals possible. A review of this work is given in Manning (2003), with selected study conditions given in Figure 3.1.

However, what has not been simulated extensively in the laboratory is the way in which these processes interact. This has been largely down to equipment constraints. None of the triaxial cell or oedometer compaction studies listed above were performed at geologically realistic temperatures, yet information from civil engineering literature shows that the effects of temperature have a substantial impact on mechanical properties (Mitchell & Soga, 2005).

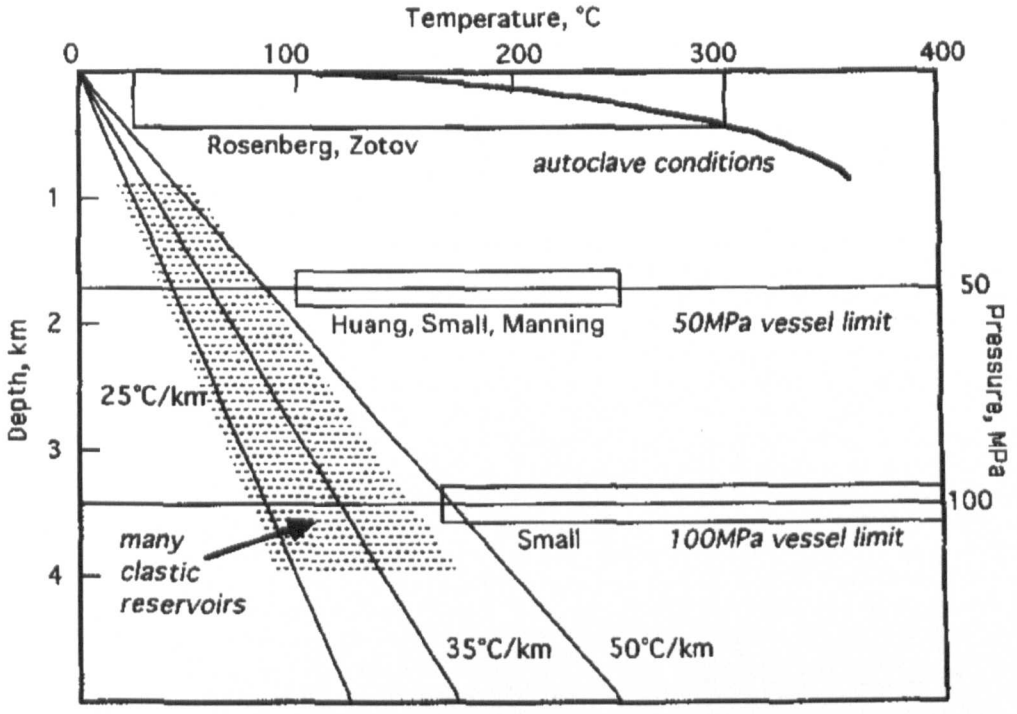

Figure 3.1 From Manning (2003) - General pressure-temperature relationships in petroleum reservoirs (shaded), along typical geothermal gradients in sedimentary basins as used in experimental studies carried out in the laboratories of the researchers named in Manning (2003) The higher, 50°C geotherm is the approximate geothermal gradient in the Malay Basin, the study area in the parallel study on naturally compacted mudstone samples discussed in Chapter 4.

Temperature and fluid chemistry control the diagenetic mineral reactions, yet whilst they have been simulated largely in autoclave equipment/pressure cells, neither the form of sample or pressure in these tests are geologically realistic. Samples used are often disaggregated, separated clays (for example, Drief *et al.*, 2001; Bauer & Velde, 1999; Mosser-Ruck *et al.*, 2001) with their relationship to their normal accessory minerals in a consolidated mudstone (quartz, feldspar, pyrite etc.) disrupted by disaggregation, if not destroyed by fractionation. Also, despite the high vapour pressure that it is possible to exert in an autoclave and the fluid pressure exerted in other pressure cells, this is separate to the differential and effective stresses exerted in compacting mudstones. As noted in Colten-Bradley (1987), the type of stress has an influence on chemical clay mineral processes. In addition to

this, without exerting effective stress on transforming clay minerals, the development of textural features, such as alignment (linked to the smectite-illite transition through analysis of natural samples), cannot be studied.

This chapter contains several different forms of laboratory simulation of clay / mudstone compaction designed to understand the processes observed in previous mechanical / chemical research and culminating in three longer term tests to try to bring the two forms of study together. The outlines of all of the compaction simulations are given below:

- ***"Shallow" Mechanical Consolidations*** - Room temperature, low pressure consolidometer, triaxial and shear box consolidations of clays and clay mixtures from slurry form with selected accompanying property measurements. Designed to test assumptions from previous mechanical compaction studies and optimise procedures for the Compaction Simulation Tests. These tests were discussed in Section 2.2.1 and selected results are discussed later in Chapter 5, largely for comparison purposes.
- ***Variable Testing: Triaxial Tests*** *(Tests 1-6)* - High temperature, moderate effective stress triaxial compactions of North Sea mudstone using optimized pore fluids with comprehensive program of accompanying rock property measurements on pre, mid and post-test samples. Designed to highlight any obvious controls from variables tested and optimize conditions for the Compaction Simulation Tests.

- ***Variable Testing: Reflux Condenser Tests*** *(Tests A-C)* - High temperature tests essentially boiling the North Sea mudstone in fluids used in the triaxial experiments as pore fluid with selected pre and post-test property measurements. Designed to highlight any obvious controls from variables tested without the applied effective stresses of the triaxial experiments and again, to optimize conditions for the Compaction Simulation Tests.
- ***Compaction Simulation Tests***
    - Test 7 – "Chemical Compaction Test";
    - Test 8 – "Mechanical Compaction Test";
    - Tests 9A and 9B – both attempts at an "Intermediate Test")

Test 7 was a high temperature, high effective stress, long term triaxial test on North Sea mudstone core using a potassium-rich, elevated pH pore fluid. This test was designed to combine aspects of previous mechanical and chemical research into mudstone diagenesis to simulate conditions promoting chemical compaction.

Test 8 was a room temperature, high effective stress, long term triaxial test on North Sea mudstone core using a sodium-rich pore fluid. This test was designed to follow more closely aspects of previous mechanical research into mudstone diagenesis to simulate conditions promoting mechanical compaction as a comparison for Test 7.

Tests 9A and 9B were both attempts at simulating conditions intermediate to Test 7 and 8, where long term triaxial tests on North Sea mudstone core were run only at room temperature, but still under high effective stress, using a potassium-rich, elevated pH pore fluid. These tests were added to the testing program to clearly

identify the controls on differences in properties generated by Test 7 and 8, i.e. whether differences were due to temperature or fluid chemistry. Both tests A and B failed due to issues with the cell, but 9B ran for the whole first consolidation stage to 30MPa axial effective stress (the lower stress plateau in Tests 7 & 8) so provides some useful data.

The triaxial tests on the North Sea mudstone utilised the high pressure, high temperature triaxial equipment in the geotechnical laboratories at Shell International Exploration and Production BV. (for cell capabilities see Sections 2.2.2 & 2.2.3). Intact smectite-rich North Sea mudstone (recovered from a depth of ~1400m) was compacted under moderate/high effective stresses at room temperature or elevated temperature and supplying artificial pore fluid designed to limit or promote chemical change in the smectites. A comprehensive program of accompanying property measurements on pre, mid and post-test samples was run for all of the Geological Simulations.

Of course, such pore fluids and the timescale employed when working in the laboratory are not geologically realistic, but this study has achieved results combining more geologically realistic conditions with a wide range of chemical and physical/textural property measurements to record changes in the mudstone attributed to the various simulated controls.

3.1.2 Work Flow Design

Given the multiple variables described as influencing compaction in the literature, deciphering the relative importance of each factor in a natural mudrock sample becomes difficult. For this reason, the Variable Testing: Triaxial Tests were designed to vary each parameter as independently as possible. These parameters included time (and testing procedures) in Tests 1-3, stress in Test 4 (but also time due to extended consolidation period for high stress), temperature in Test 5 and fluid chemistry in Test 6 and the reflux condenser tests A-C. The aim was to separate out their particular impact through their characteristic effects. Following the results of these tests, the conditions were optimized for the Compaction Simulations - "chemical compaction simulation", Test 7 (high temperature, K-rich pore fluid and elevated pH) and for the "mechanical compaction simulation", Test 8 (low temperature, no additional K supply, no additional hydroxide to elevate pH) in another with both under simulated geological conditions (extended time period and high effective stress). A later addition to the program was Test 9 with conditions intermediate to Tests 7 and 8.

A well preserved, shallow buried, natural mudstone was to be selected as the test material. This was to be chosen so that natural mechanical re-organisation processes (where much initial porosity is lost) had already taken place, but the main diagenetic clay mineral transformations would not have yet begun. This was to allow fair testing of the mechanisms behind the later stages of porosity loss, without any interference from inaccuracies in simulating initial mechanical compaction.

Distinguishing the effects characteristic of the different factors varied during the tests requires that the initial character of the material prior to testing is well defined to allow accurate comparison. Even at the centimeter scale, physical behavior and mineralogical composition of geological strata may differ both laterally and vertically due to depositional or diagenetic variation. So a set of measurements were taken to quantify the original properties of the mudstone prior to testing. The pre-test material and the post test plugs were put through the same range of rock property analyses to try and quantify the initial heterogeneity and see if changes post-test were statistically significant.

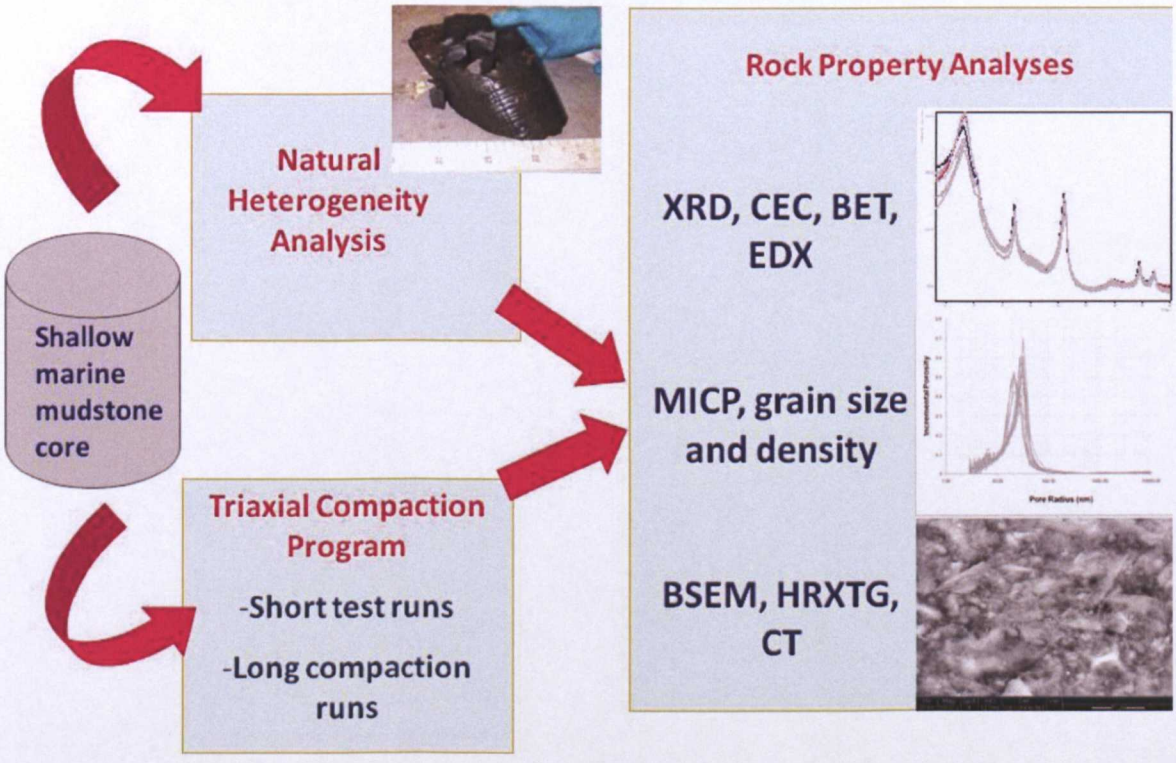

Figure 3.2 Triaxial compaction program work flow. Short test runs covers the Variable Testing experiments (Tests 1-6) and the Long compaction runs describe the Compaction Simulations (Tests 7-9).

3.1.3 Sample Selection

1 metre of Cretaceous, marine mudstone core from a depth of ~1400m was chosen from a selection of North Sea samples (central core in Figure 3.3). Present day geothermal gradients in the North Sea vary mainly between 30-40°C/km only and are not likely to have been higher since the Mesozoic/ Lower Tertiary (Bjorlykke, 1998). Sea floor temperatures in the cored area are 4.9-11.1°C

Figure 3.3 Selected core (centre) upon temporary removal from kerosene. Markings along the length and the diagonal fracture (parallel to bedding) are due to the coring process.

It was chosen as it had been well preserved (kerosene and then mineral oil), CT imaging showed it to be the most homogeneous (fewer high density areas indicating mineralisation or low density fracture areas – Figure 3.4) and previous research on the material had shown it to have a significant proportion of swelling clays.

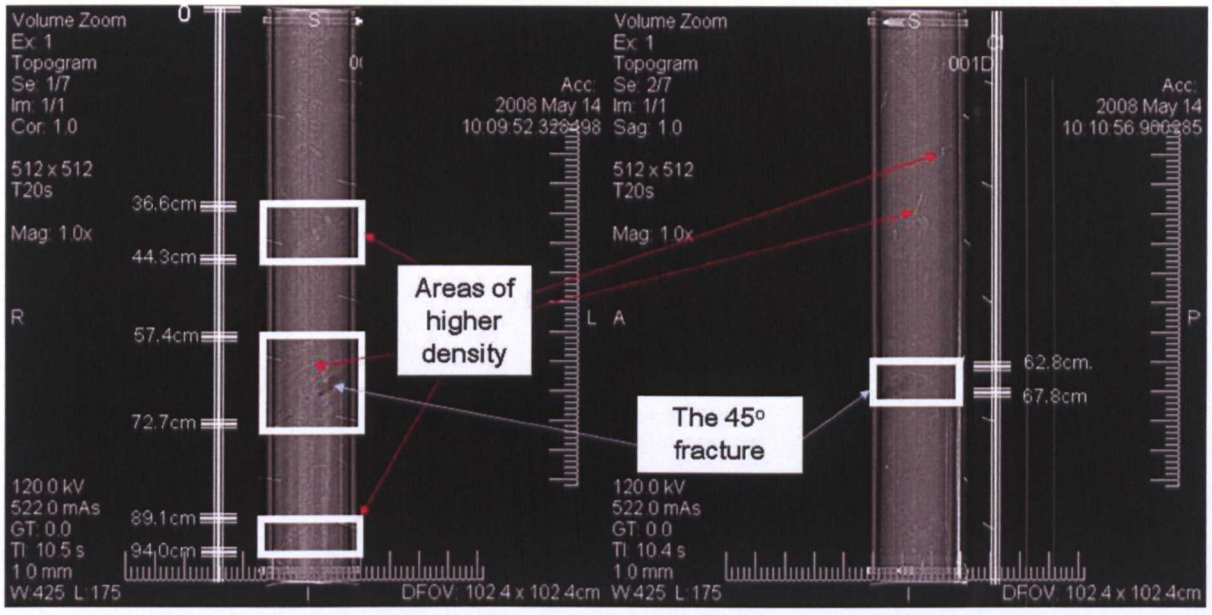

Figure 3.4 CT images showing the length of selected mudstone from 2 sides inside its container. The core was the most homogenous available and those areas highlighted above as higher or lower density were avoided when taking samples for the tests.

Some uplift (<<600m) had occurred in the cored source area during the Cenozoic and despite the current value of approx 30°C /km, the Paleogene geotherm would have been significantly higher. In view of this, the selected sample was also one of the shallowest cores. This met the requirements of the test both mineralogically and structurally, as the higher expandable clay content was a positive sign that has not been subject to mineralogical change due to excessive burial and internal fractures should be minimised as the shallower section was from a tilted fault block, whereas the earlier Cretaceous section was obtained near a zone of shearing. Basic calculation detailed further in the discussion (3.5.1.4), showed that the maximum vertical effective stress that the North Sea mudstone has been subject to in the burial

environment was in the range of 17MPa (no uplift) to 24MPa (600m uplift). This means it was heavily overconsolidated in many of the earlier variable testing triaxial experiments (bar Test 4), but consolidating normally in the later runs (Tests 7-9B). Again, this is discussed in more detail later (3.5.1.4).

3.1.4 Sample & Test Preparation

First, the material was sectioned, cutting with oil, so as not to damage the core prior to testing and second, cylindrical plugs were cut perpendicular to bedding (Figure 3.5) for maximum strength in the high pressure tests (see section 3.1.4.2) aiming for a ratio of length to diameter of 2:1.

Figure 3.5 Preparation of the material at Shell, Rijswijk A. Sectioning the mudstone perpendicular to bedding B. Cutting the test plugs

To complete the heterogeneity analysis, 5 extra plugs (cut perpendicular to bedding) and 4 slices of mudrock (cut parallel to bedding) were also drilled and divided up into 20mm^3 blocks. Sets of the blocks were then each allocated to the mineralogical and textural rock property analyses employed to quantify the initial variability of the core.

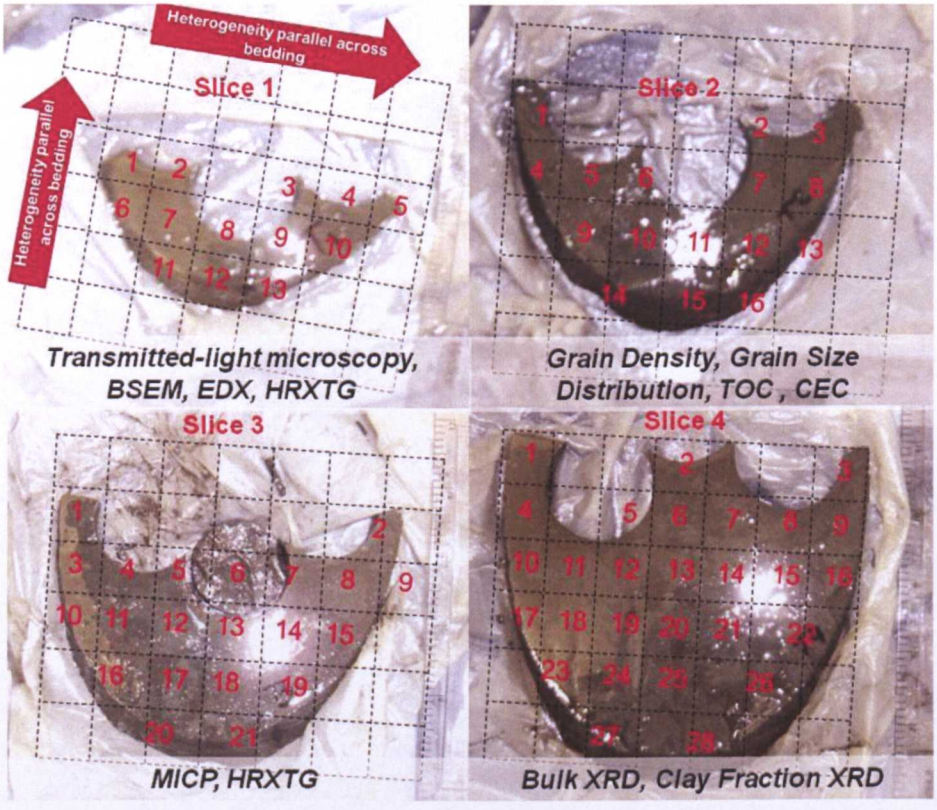

Figure 3.6 Allocation of bedding parallel samples to rock property analyses

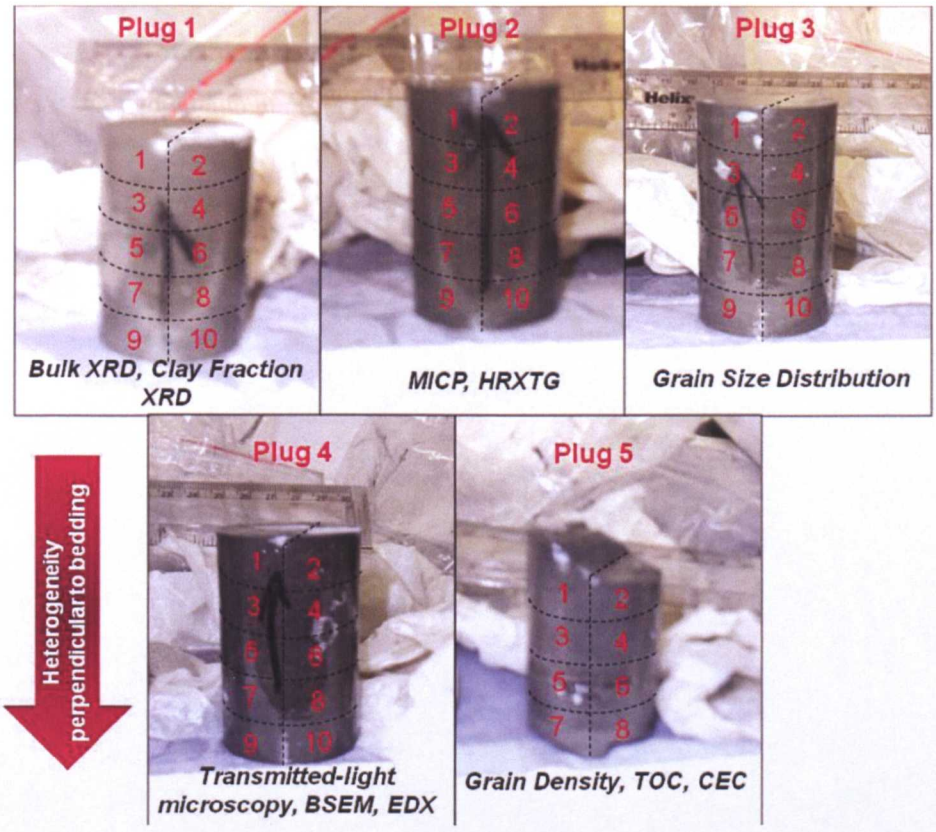

Figure 3.7 Allocation of bedding perpendicular samples to rock property analyses

3.1.4.1 Fluid Compatibility

Attempts to maintain the original pore fluid composition of mudstone were made from the initial recovery of the core to the point at which the samples were positioned in the triaxial cell prior to testing. Potassium (K) content and pH were the important factors when deciding the artificial pore fluid to be flushed into the sample during the tests.

Compatibility tests submerging the untested mudstone into various fluids showed that high molar K fluids gave the greatest stability to the sample and the best was the 3M KCl 10^{-5}M KOH. This was the optimum result as both high K concentration and elevated pH were both factors that promote illitization of smectite and were already requirements for the tests.

For the experiments that were to attempt to simulate non-chemical related compaction (no illitization) a choice of pore fluid was required. Submersion of the smectitic clay rich mudstone into tap water, deionized water or weak NaCl solutions saw rapid disaggregation of the sample. The 4M NaCl gave greatest stability without providing K cations to facilitate illitization (see Figure 3.8 below).

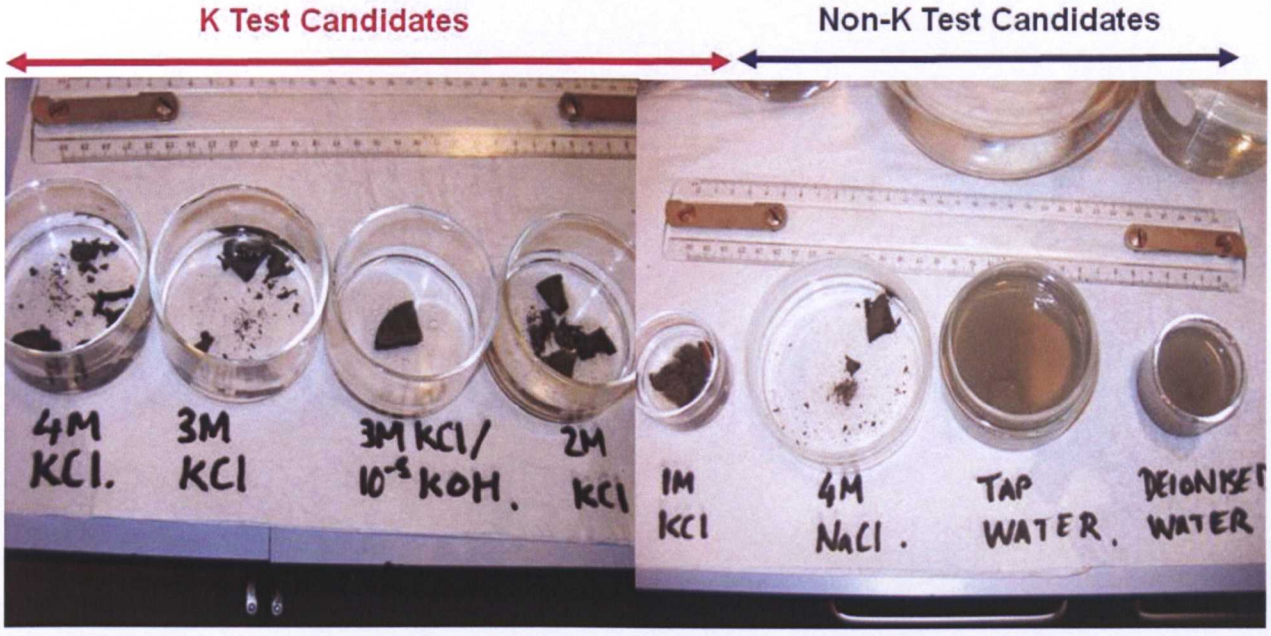

Figure 3.8 Compatibility testing to select optimum extended test fluids

3.1.4.2 Material Strength

Geomechanical testing of the mudstone had previously been carried out by other workers. This strength data was used to calculate a stress path for the triaxial compaction experiments that would not result in failure of the sample, important as tests were an attempt to evaluate compaction related phenomenon only.

Material from the cored section used in this study was only tested at various angles to bedding (with increased angles displaying decreased measured strength). This

information was behind the decision to ensure test plugs were cored perpendicular to bedding and the calculated Mohr-Coulomb envelope was used as a guide to the upper limits of stress increases during the 9 triaxial tests.

3.2 Compaction Simulations and Mid-Test Measurements

3.2.1 Variable Testing: Triaxial Experiments

The initial phase of testing of the North Sea mudstone comprised a set of shorter period experiments varying different conditions thought to influence compaction and/or chemical change. Table 3.1 shows how these conditions varied in each test.

Test	Variable Tested	Max. Axial Stress (MPa)	Max. Radial Stress (MPa)	Max. Pore Pressure (MPa)	Temp. (°C)	Pore Fluid	Time At Max. P&T (Days)
1	***TIME***	10	8.5	4	150	4M KCl	***11 (14 days at high temp)***
2	***TIME***	10	8.5	4	150	4M KCl	***22 (26 days at high temp)***
3	***TIME / END PROCEDURE***	10	8.5	4	150	4M KCl	***11 (14 days at high temp)***
4	***STRESS***	***50***	***40***	***20***	150	4M KCl	11 *(34 days at high temp)*
5	***TEMP.***	10	8.5	4	***100***	4M KCl	11 *(14 days at higher temp)*
6	***FLUID CHEMISTRY - pH***	10	8.5	4	150	***3M KCl /10^{-5} M KOH***	11 *(14 days at higher temp)*

Table 3.1 Test matrix for Variable Testing: Triaxial Experiments, with the parameter being investigated highlighted in bold, italics. Final column states the number of days the test ran at the maximum temperature and pressure conditions, with the time spent at elevated temperature (either 150 or 100°C in Test 5, whilst the stress was being ramped up in stages) is bracketed below.

Stress conditions stated are those that the sample was left to consolidate to over an extended period of time (marked in the final column). As this was the initial phase of testing and strength tests were not specific to this section of core, caution was taken over how these stresses were reached and a stepped increase or ramp of stress was employed and is demonstrated in Figures 3.9-3.11. The samples were to be

exposed to high temperature for the longest duration possible and temperature was increased as soon as was practical (the system had to be closely monitored over this period and drained due to radial oil expansion – 2.2.2).

3.2.1.1 Dimension Variation

Figures 3.9-3.11 also show the measured dimension responses of the mudstone plugs due to the triaxial program. Problems with the radial displacement and velocity transducers are discussed in 2.2.2 and 2.2.3, but Tests 3, 4 and 6 showed reasonable radial results when calibrated with the actual post-test micrometer dimension measurements (good fit was generally found in all tests axially). However, the radial results of Test 4 in particular should be treated with caution and used as a rough guide only.

All variable testing triaxial tests showed an initial expansion of the sample upon heating both radially and axially, followed by a sharp decrease during the stress ramp. Axial and radial decreases differ, in that the sharp decrease in length occurs following the final stress increase in tests (excluding Test 4) where axial pressure is increased alone. The decrease following expansion in the diameter responds earlier to the initial stress increases. At the end of the tests, all acceptable measurements show some elastic response upon the removal of stress.

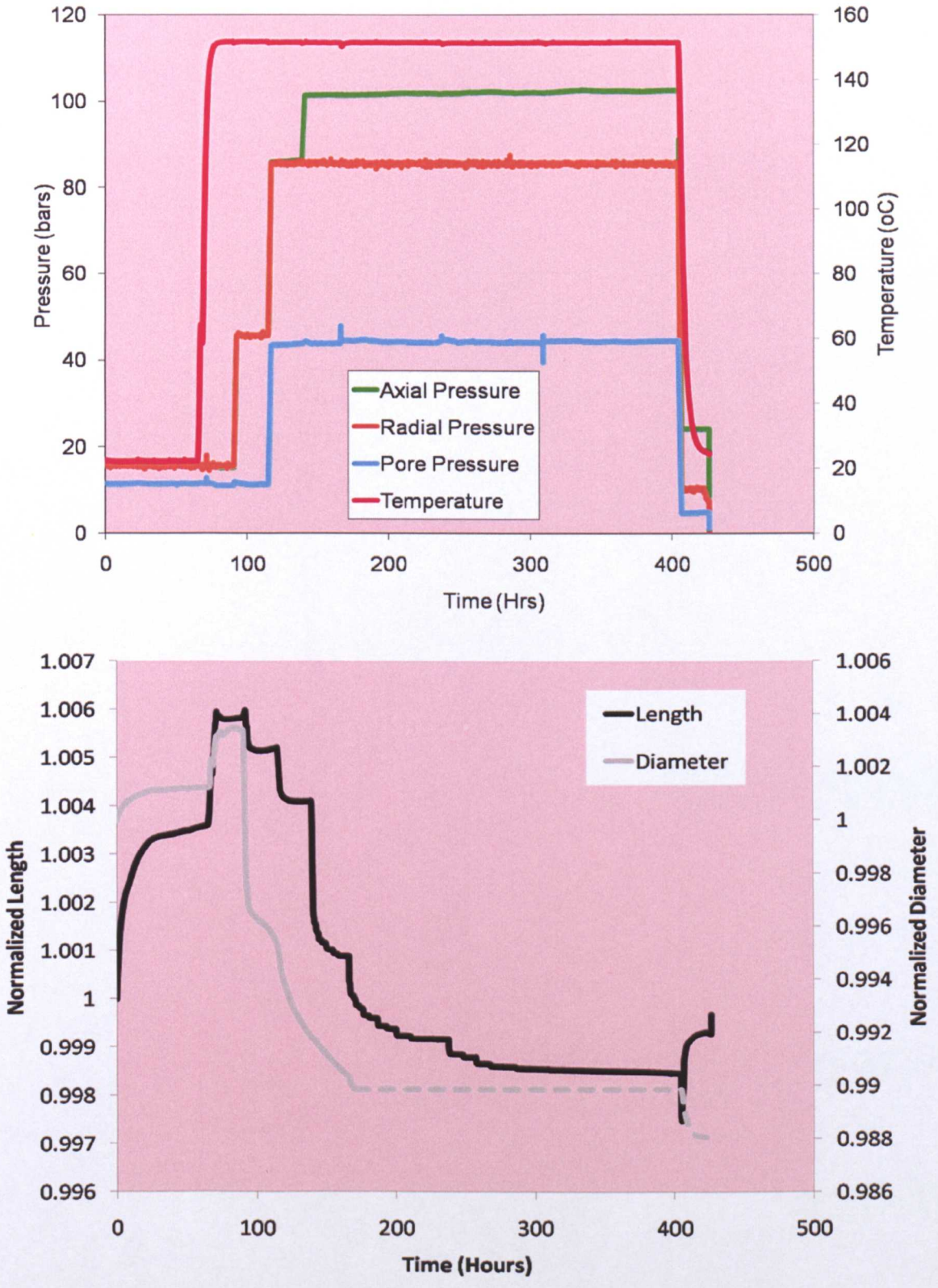

Figure 3.9 Test 3 (Time/Procedure): Upper plot is axial, radial, pore pressure and temperature with test time. Lower plot is normalized plug dimensions with test time. Dashed diameter response is region where anomalous zero change occurs.

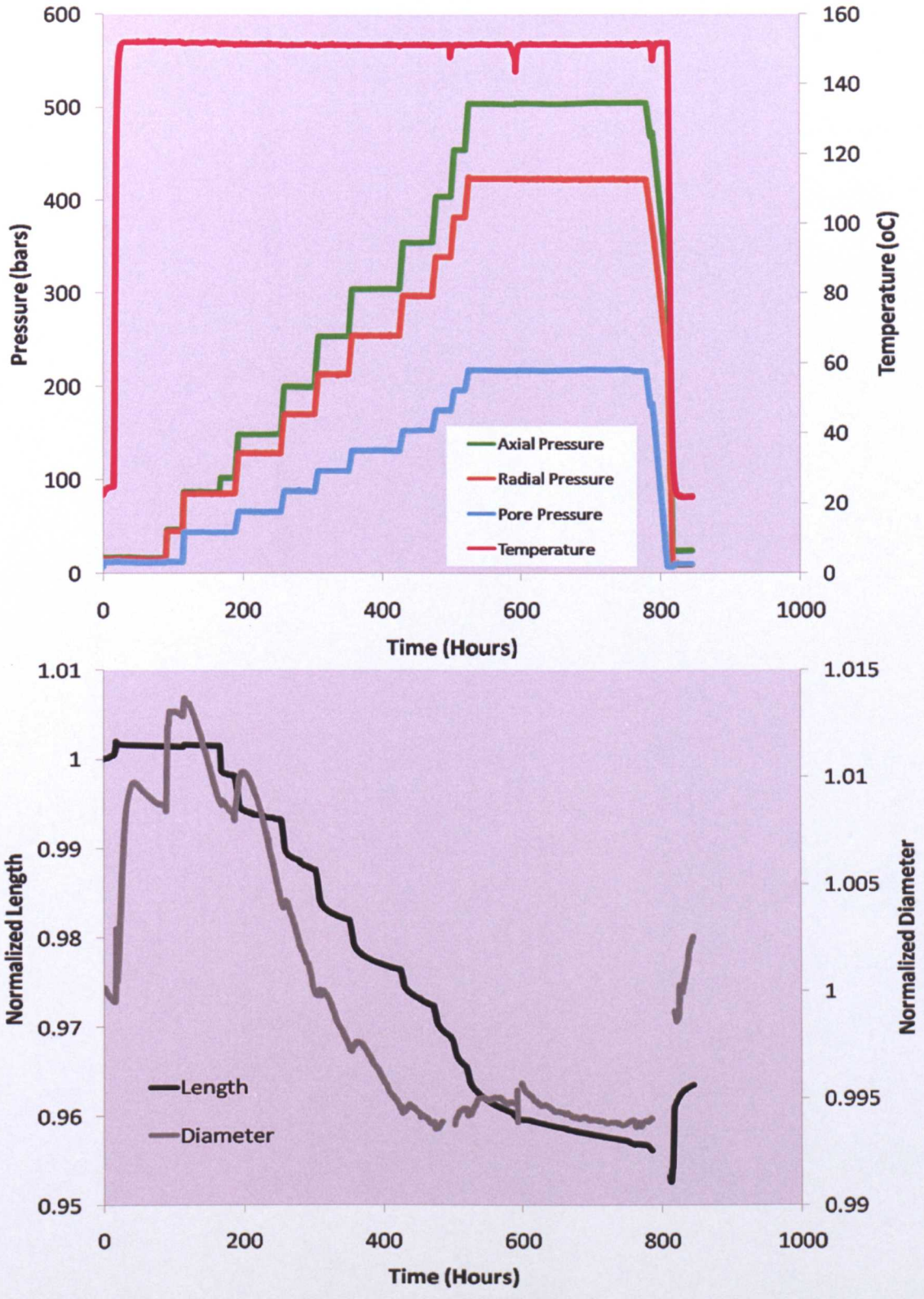

Figure 3.10 Test 4 (High Stress): Upper plot is axial, radial, pore pressure and temperature with test time. Lower plot is normalized plug dimensions with test time.

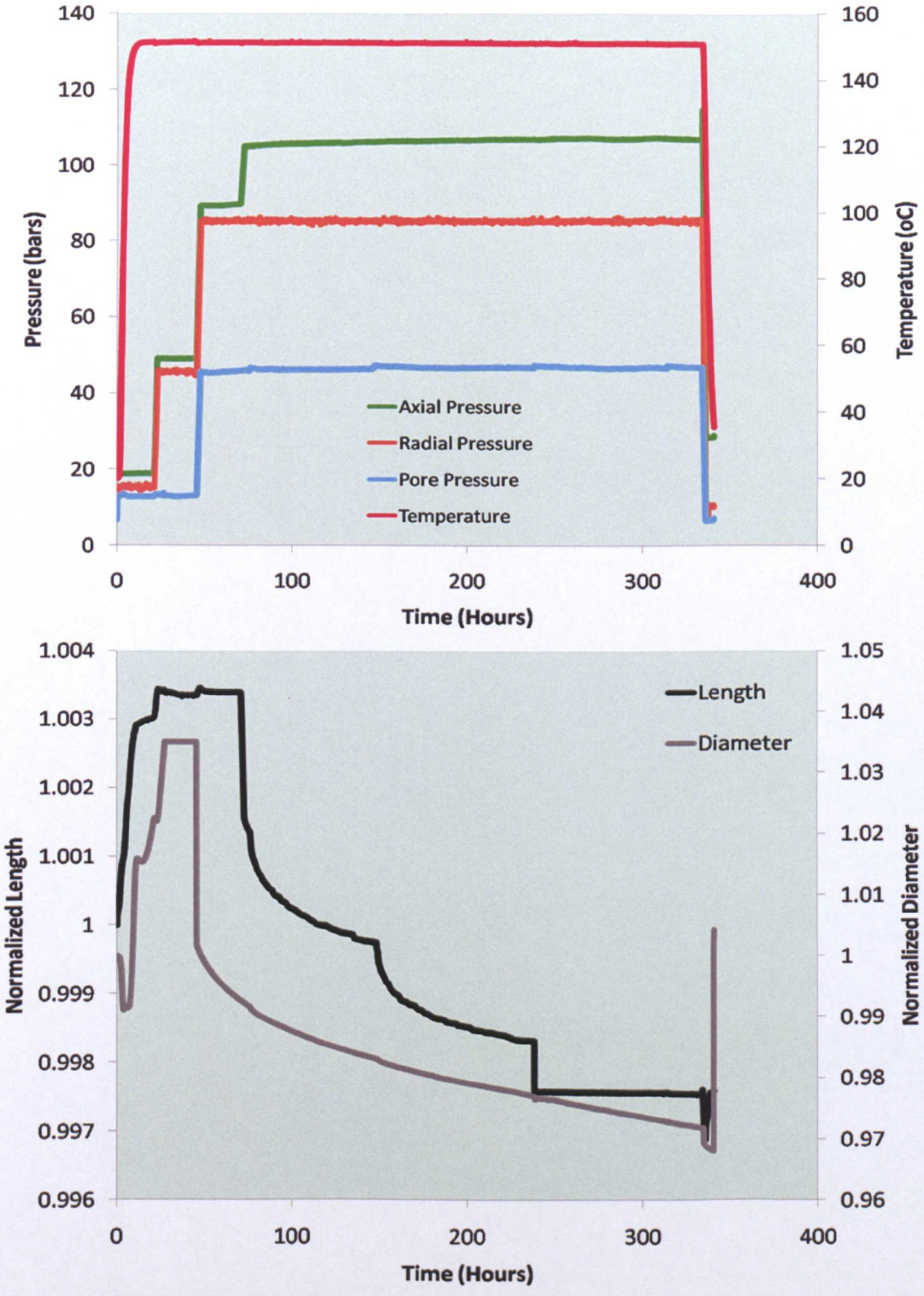

Figure 3.11 Test 6 (Fluid Chemistry): Upper plot is axial, radial, pore pressure and temperature with test time. Lower plot is normalized plug dimensions with test time.

Test	Initial Length (mm)	Final Length (mm)	Length Difference (mm)	Initial Diameter (mm)	Final Diameter (mm)	Diameter Difference (mm)	Volume Change (%)
1	65.7	66.8	-1.1	36.1	36.7	-0.6	5.1% Expansion
2	64.8	64.4	+0.4	36.0	35.8	+0.2	1.7% Reduction
3	62.5	62.6	-0.1	36.0	36.0	0.0	0.2% Expansion
4	64.5	62.7	+1.8	36.0	35.8	+0.2	3.9% Reduction
5	63.7	64.2	-0.5	35.7	35.8	-0.1	1.4% Expansion
6	63.8	63.7	+0.1	35.9	35.9	0.0	0.2% Reduction

Table 3.2 Plug dimensions before and after the Variable Testing: Triaxial Experiments

Table 3.2 shows the micrometer measured dimension changes due to each of the tests. Tests 1, 3 and 5 showed expansion which is recorded by the displacement transducers as the stress was removed from each test. The compaction in Test 6 is minimal and in Test 2 could be associated with the longer consolidation period tested in that experiment or may be due to some open internal fractures that it displayed on CT scans of the pre-test plug that were closed post-test. Test 4, the high effective stress variable test, shows the most significant reduction. Despite some elastic response post-test, more permanent compaction effects had taken place in that plug.

This is also supported by the calculated porosity values mid-test as seen in Figure 3.12. Final MICP measured porosities approximate the final calculated porosities following elastic expansion for the post-Test 6 plug (which also showed minimal permanent compaction in micrometer dimension measurements). Whereas the MICP measured porosity following Test 4 displays greater porosity loss calculated whilst the plug was still at high temperatures and pressures.

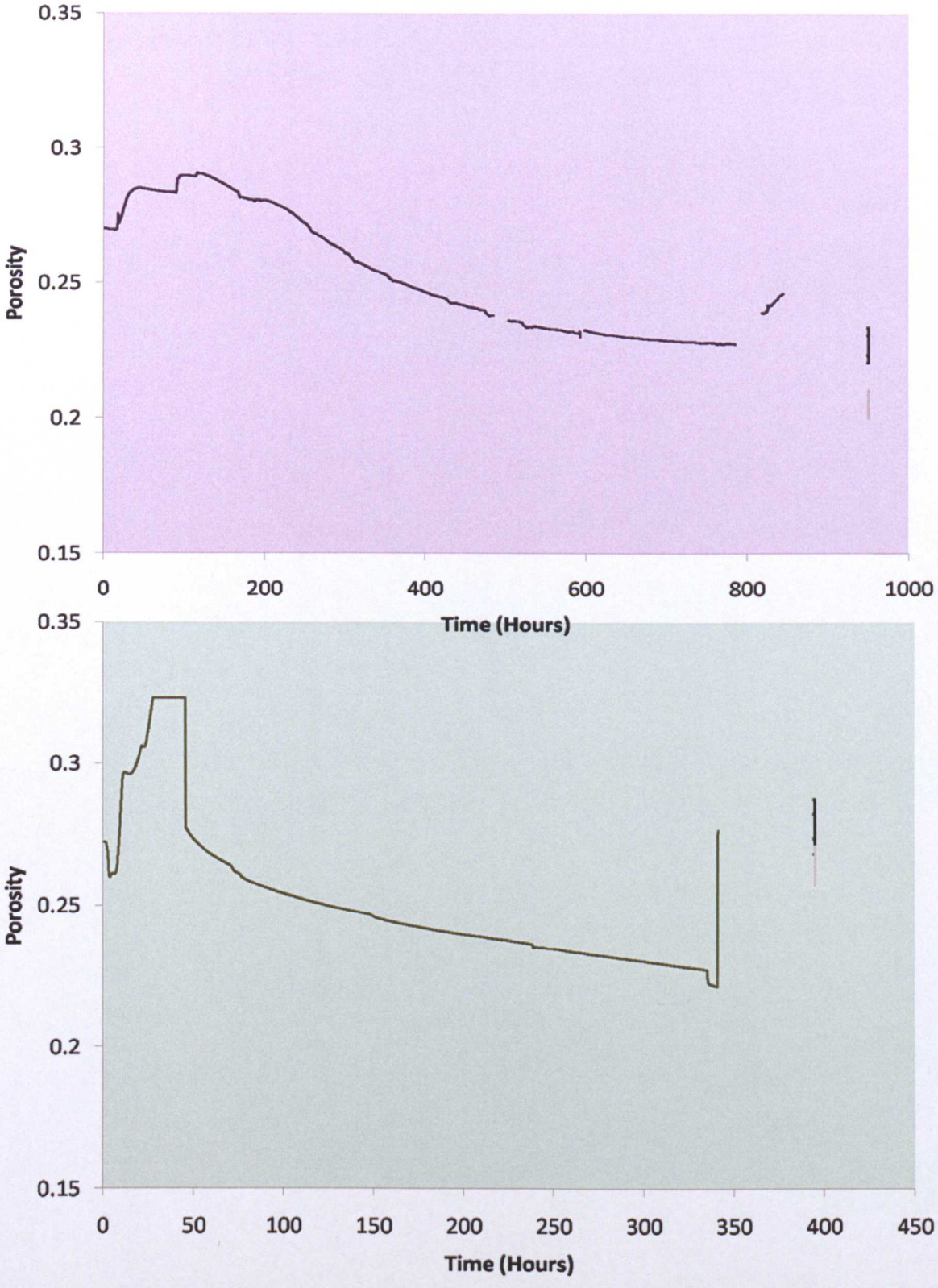

Figure 3.12 Porosity change calculated during variable test 4, the high stress test (purple) and Test 6, the pH 9 pore fluid test (green). Black and grey vertical error bars display the MICP measured uncorrected and corrected porosity values, with the black bars using grain density values measured upon the actual test plugs and grey error bar using the pre-test average 2.66g/ml. The time position of these values is arbitrary. The use of grain densities in MICP porosity determination is discussed below.

Input parameters for these calculations are important to understand to assess their validity. Porosity (φ_C) was calculated from the measured grain density ($\rho_{G\ Meas}$) the measured initial bulk density ($\rho_{B\ Meas}$) and the initial pore fluid density ($\rho_{F\ Initial}$ ~1.03g/cm3):

$$\varphi_C = \frac{(\rho_{G\ Meas} - \rho_{B\ Meas})}{(\rho_{G\ Meas} - \rho_{F\ Initial})}$$

The bulk density during the test ($\rho_{B\ Test}$) was then calculated using the normalized dimension measurements (M_A and M_R), along with the test fluid density ($\rho_{F\ Test}$ ~1.18g/cm^3 at 25°C and ~1.26g/cm^{3}once at 150°C temperature) and the calculated initial porosity (φ_C):

$$\rho_{B\ Test} = \frac{(\rho_{B\ Meas} - \varphi_C * \rho_{F\ Initial} + \varphi_C * \rho_{F\ Test} + (M_A * M_R * M_R - 1) * \rho_{F\ Test})}{M_A * M_R * M_R}$$

$\rho_{B\ Meas}$ was 2.22g/cm^3 in all tested plugs apart from Test 3 which was known to contain excess pyrite and was measured as 2.23g/cm^3. During the tests the fluid densities were calculated according to the chemistry of the fluid being used and the temperature of the test. From this, the test values were substituted into the first equation and porosity during the test was calculated:

$$\varphi_{Test} = \frac{(\rho_{G\ Meas} - \rho_{B\ Test})}{(\rho_{G\ Meas} - \rho_{F\ Test})}$$

The $\rho_{B\,Test}$ was also used in the calculation of the dynamic moduli during the tests. In the lower stress, tests axial strain measurements indicate consolidation to 6MPa axial effective, but radial deformation appears to be ongoing. In Test 4, attaining the higher effective stress of 30MPa for the first time was approached with caution via several stress steps. This increased the overall time that the sample spent at high temperature, but it was only left to consolidate to a stress believed to be above in-situ conditions for the North Sea mudstone for the specified period of 11 days.

As a result both axial and radial strain is ongoing at the point at which the stress/temperature ramp-down took place in Test 4. The Test 4 plug, with its permanently decreased dimensions, porosity and velocity response shows that mechanical compaction controls such as effective stress and time are vital. Test 4 was the only variable testing, triaxial test to surpass in-situ stress and it is the only plug to show significant, permanent compaction. This is despite all variable tests (1-6) using K-rich fluid and being ran at elevated temperature.

3.2.1.2 Ultra-Sonic Velocity Variation

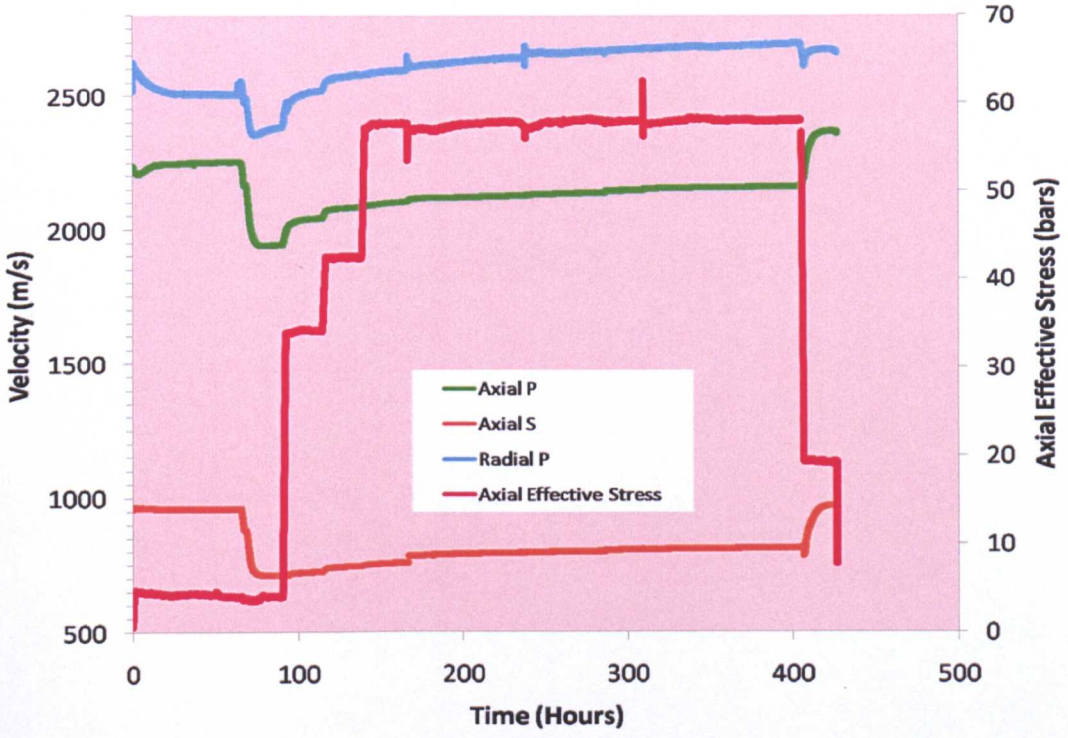

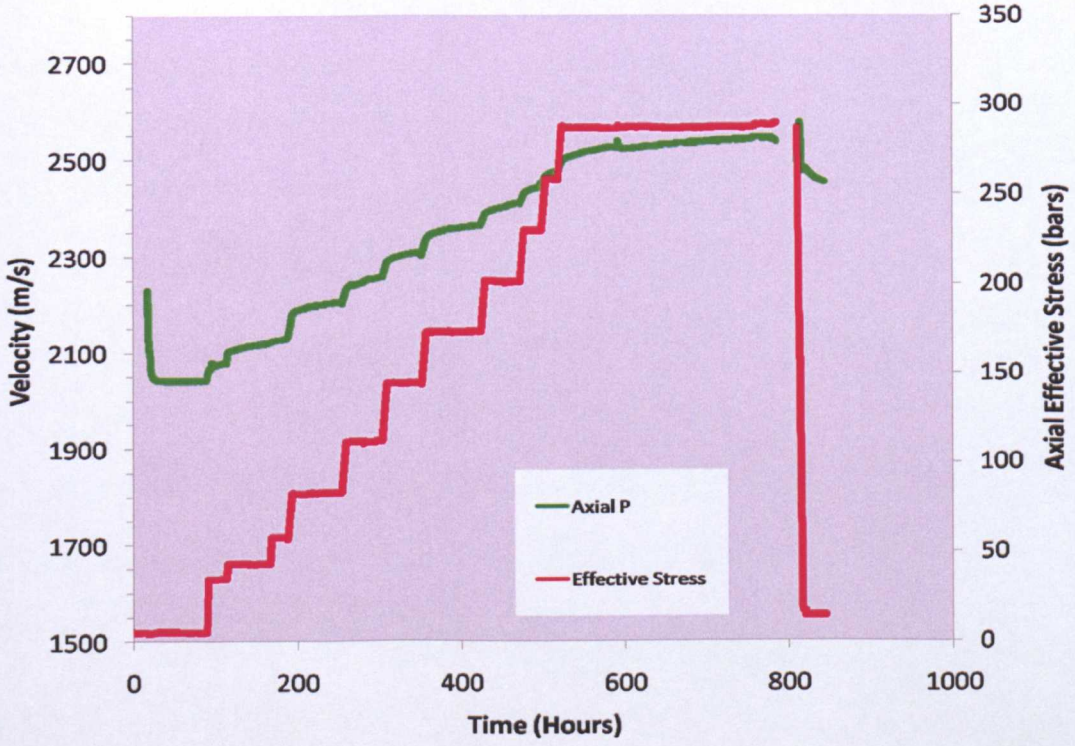

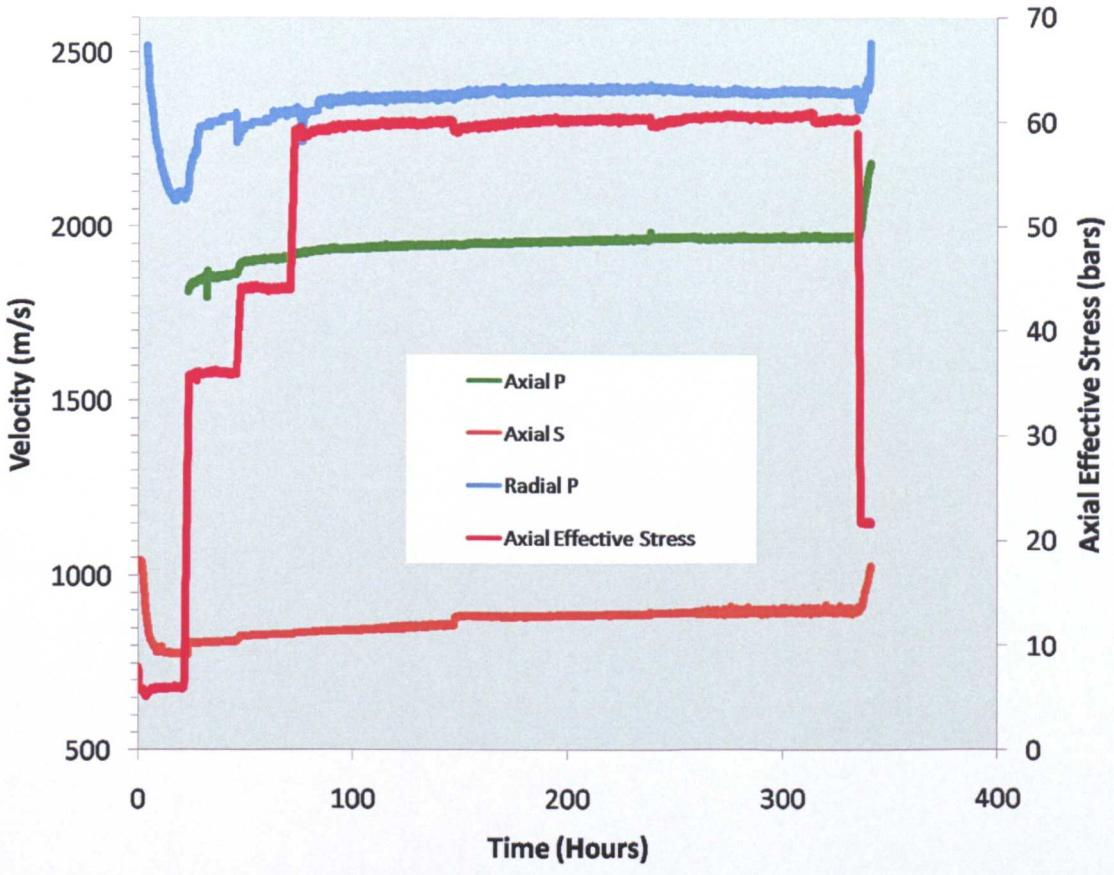

Figure 3.13 Selected wave velocities with axial effective stress against time, recorded during variable tests 3 (testing increased time take off procedures- red), 4 (with high stress - purple) and Test 6 (using pH9 pore fluid - green).

Ultrasonic velocity measurements display responses to test conditions consistent with the behavior observed in the dimension measurements/porosity calculations. There is always a reduction in velocity associated with the expansion of the sample upon heating. This can be attributed to the separation of grain contacts as the pore fluid expanded during the elevation of temperature. As stress is applied to the system, matrix grain contacts are increased and cracks (observed in CT scanning and micro-cracks along elongate grain boundaries such as those of micas - observed in BSEM images) may close.

Also, as with the dimension measurements, the velocities generally decrease with the reduction of pressure, post test, to initial values. Some variation according to test

conditions can be seen (Figure 3.13). The Test 4 plug is again the exception with final velocity readings considerably above those at the start of the test. This is attributed to the permanent compaction recorded in the Test 4 plug due to consolidation to high effective stress (30MPa).

3.2.2 Variable Testing: Reflux Condenser Experiments

Information from the literature pointed to the importance of the pore fluid chemistry both in chemical alteration (eg. Mosser-Ruck *et al.*, 2001; Bauer & Velde, 1999) and the physical stability of mudstones (Steiger, 1982; Van Oort, 2003). In response to this, a short program of tests were carried out as described in 2.2.4. where the effects of temperature and fluid chemistry could be observed without the constraints of effective stress. The program followed the conditions detailed in Table 3.3.

Test	Effective Stress (MPa)	Temp. (°C)	Time At Max. T (Days)	Pore Fluid
A	Zero Control	Approx. 100	14	***4M KCl***
B	Zero Control	Approx. 100	14	***4M NaCl***
C	Zero Control	Approx. 100	14	***3M KCl /10^{-5} M KOH***

Table 3.3 Test Matrix for Variable Testing: Reflux Condenser Experiments with the varied parameters highlighted in bold, italics.

Any chemical change due to the tests is exchange related only – no permanent illitization took place. One of the main outcomes of these tests was related to the physical stability of the mudstone at temperature in the separate fluids. Test A (4M KCl) showed partial disaggregation of the sample with some blocks remaining in a quantity of saturated powder at the base of the container post-test. A repeat of Test A using a small amount of Teflon tape to secure the sample axially and radially showed the same decreased stability.

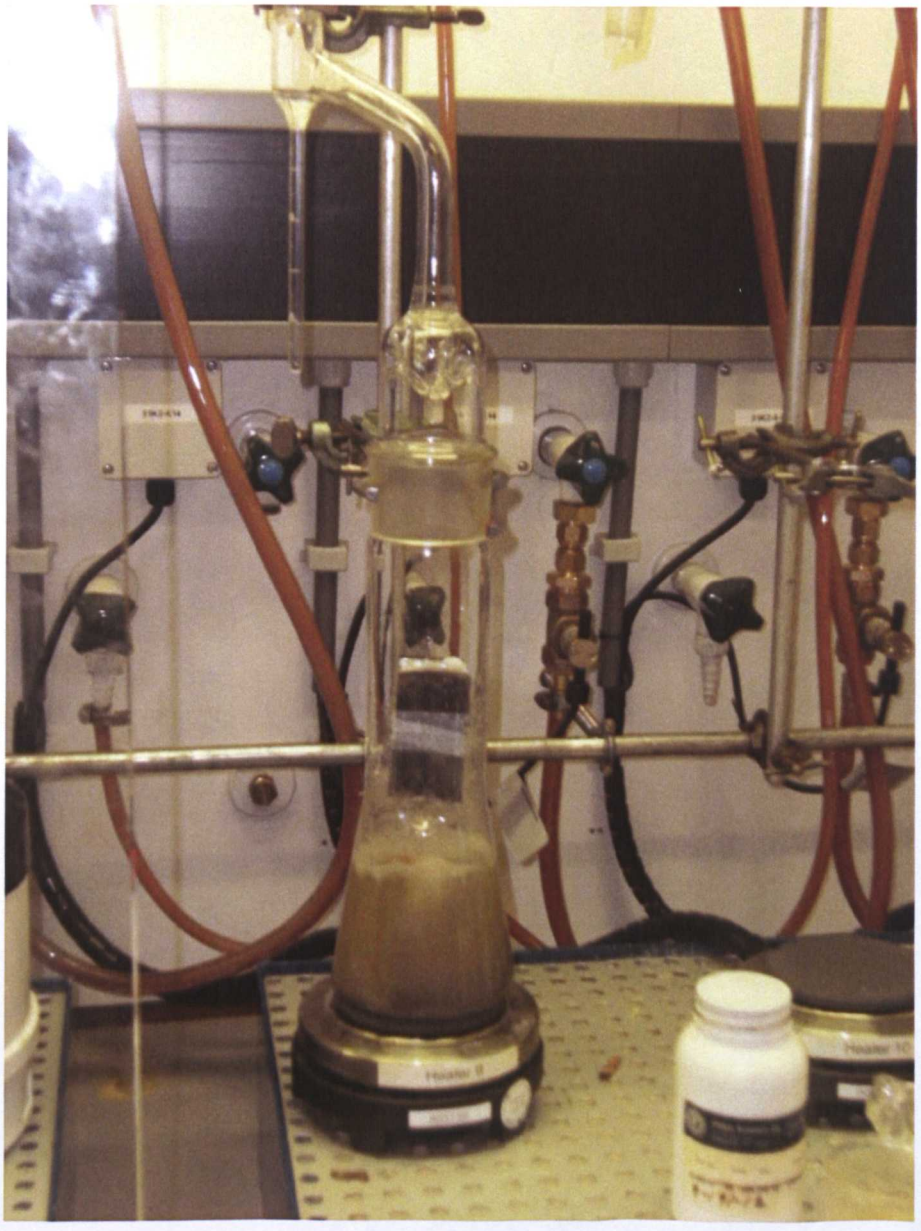

Figure 3.14 Final image of intact mudstone plug positioned on glass ledge in the center of the equipment following the second repetition of Test C (using 3M KCl /10^{-5} M KOH fluid - Variable Testing: Reflux Condenser Experiments).

Test B using 4M NaCl showed complete disaggregation with only saturated powder remaining post-test. This is most likely attributed to the swelling of the material upon exchange with hydrated Na^{+}. However, following Test C, very little disaggregation

had taken place and the plug remained intact despite being boiled vigorously in the 3M KCl /10^{-5} M KOH fluid for 11 days (Figure 3.14 – image taken during draining/ dismantling of the equipment). A shorter repeat of Test C showed the same stability characteristics.

In Figure 3.8, the stability difference between 4M and 3M KCl did not appear to be significant. Therefore, the increased pH of the 3M KCl /10^{-5} M KOH fluid emerges as the controlling variable. The difference is important to remember in qualitative assessments of the behaviour of Tests 6, 7 and 9 compared with the other tests.

3.2.3 Compaction Simulation Tests

All of the tests described previously were intended to contribute to the design of the final stage of experiments, the Compaction Simulation Tests. Table 3.4 details the test matrix designed to assess the relative roles of "chemical" and "mechanical" compaction by providing the optimum conditions for each (Tests 7 and 8). As fluid chemistry and temperature were both varied, an intermediate test, Test 9, was designed to identify the separate effects of those variables

Test	Variable Tested	Max. Axial Stress (MPa)	Max. Radial Stress (MPa)	Max. Pore Pressure (MPa)	Temp (°C)	Pore Fluid	Time At Max. P&T (Days)
7	"Chemical" Compaction Test	65	57.5	15	150	3M KCl /10^{-5} M KOH	23 days at target 57 days high temp 47 days stable elevated pressure
8	"Mechanical" Compaction Test	65	57.5	15	25	4M NaCl	23 days at target 47 days stable elevated pressure
9	Intermediate Test	65	57.5	15	25	3M KCl /10^{-5} M KOH	23 days at target 47 days stable elevated pressure

Table 3.4 Main Triaxial Testing Program - Compaction Simulation Tests. Test 9 conditions (shaded in grey) were never reached as both attempts at completing this simulation failed due to mechanical issues with the pressurizing pumps. The actual conditions of both attempts at Test 9 are noted in Table 3.5.

Test 9 was carried out in a newer cell and some components of the system proved unequal to the task of maintaining high stress conditions for the period required for the extended duration test. The first attempt at Test 9 (A) failed during the initial ramp-up of stress following an issue with pump control.

Another plug was prepared, and a second attempt, Test 9B was made. Some early problems establishing pore pressure occurred, where there was a drop in pore pressure to near zero for a period of 24 hours - similar to that occurring in Tests 7 and 8, but earlier in the program. Following this, the consolidation at 30MPa effective stress progressed smoothly and the test completed the first consolidation plateau. However, during the second stress ramp to 50MPa effective stress, one of the high-pressure feed throughs broke and the test was lost. Therefore, the actual conditions met by Test 9 (both Test 9A – stress ramp 1 break and Test 9B - stress ramp 2

break) are detailed in Table 3.5 below. The stress/temperature programs for Tests 7, 8 and 9 are shown in Figure 3.15.

Test	Variable Tested	Max. Axial Stress (MPa)	Max. Radial Stress (MPa)	Max. Pore Pressure (MPa)	Temp (°C)	Pore Fluid	Time At Max. P&T (Days)
9A	Intermediate Test	35	29.8	14	20-25	3M KCl /10^{-5} M KOH	0 days at target 0 days stable elevated pressure (+15 days of ramp)
9B	Intermediate Test	50	42.5	20	20-25	3M KCl /10^{-5} M KOH	0 days at target 28 days stable, elevated pressure (+13 days of ramp)

Table 3.5 Actual triaxial simulation Test 9 conditions for attempts 9A and 9B. Test 9A failed during the initial stress ramp, but 9B stabilized at the first extended consolidation stage at 30MPa (axial effective stress) before failing due to mechanical issues with the pressurizing pumps during the second ramp to 50MPa axial effective stress.

In both cases, the plugs did not remain intact. However, the mid-test data collected on the dimension and velocity changes prior to failure is still valid. This information can be compared directly to similar sections of Test 7 and 8. The plugs were not completely disaggregated, but broken into large sections. These sections were taken and prepared for some post-test analyses, which meant there was useful data post-test (MICP and grain density) that could be evaluated cautiously considering the possibility of additional deformation resulting from the failure. Because of the lower consolidation stress reached, the post-test data was consequently more analogous to the initial triaxial experiments examining the influence of the different variables. Most notably, Test 9B reaches the same effective stress as Test 4 and utilizes a K-rich fluid.

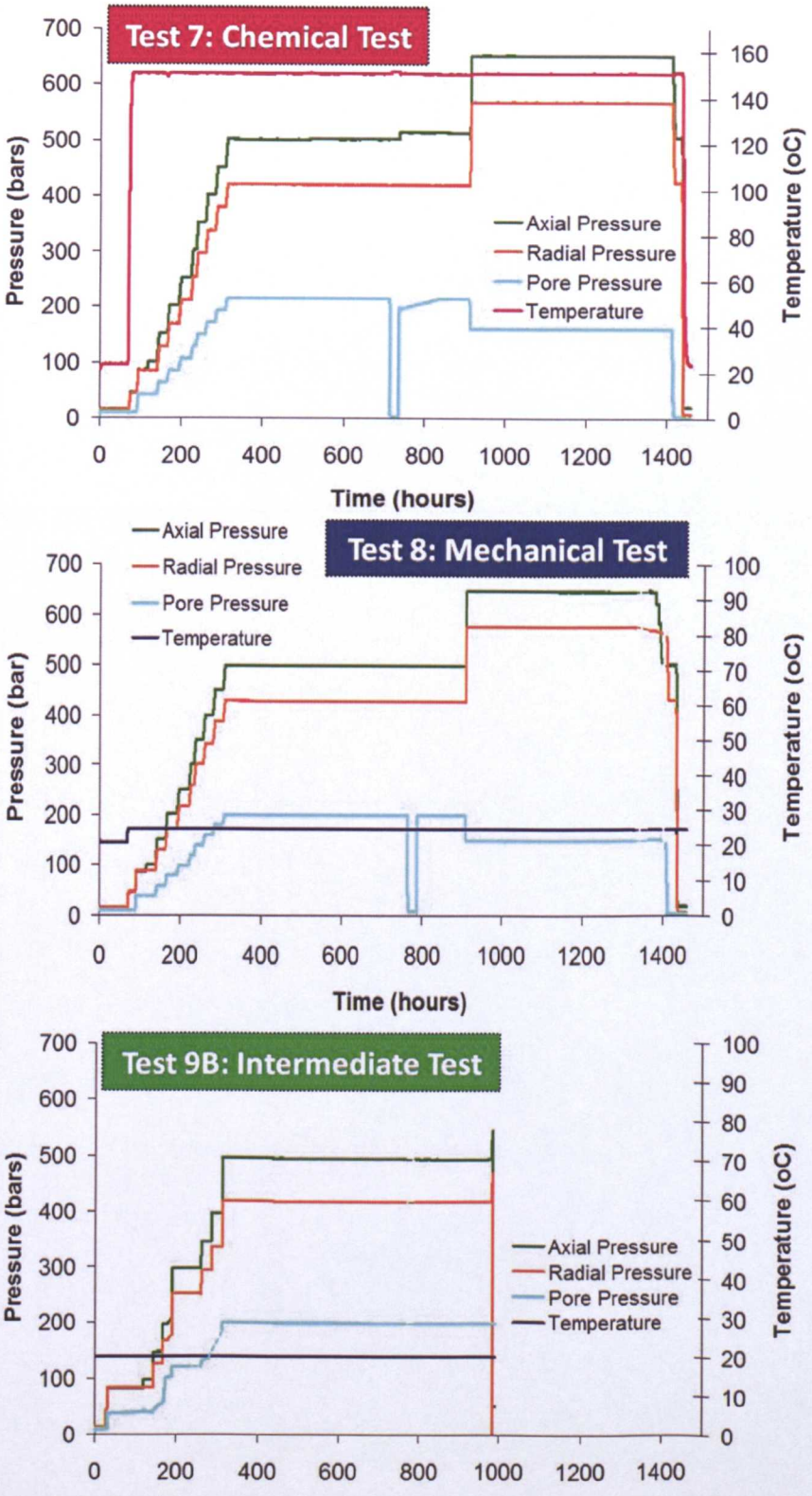

Figure 3.15 Pressure and temperature program during Test 7 (chemical compaction simulation) using a pore fluid of 3M KCl $^{10\text{-}5}$M KOH, Test 8 (mechanical compaction simulation) using 4M NaCl and Test 9 (intermediate compaction simulation) using 3M KCl $^{10\text{-}5}$M KOH Temporary decreased pore-pressure ~700 hrs into Test 7 & 8 reflect a pump issue in Test 7 that was rectified and simulated in Test 8 for consistency. Dashed pore pressure line in Test 9 over pore pressure decrease period (unreliable data).

3.2.3.1 *Relative Dimension Variation*

Initial and final micrometer readings of the test plugs immediately before and after the tests are recorded in Table 3.6 as with the Variable Testing Triaxial Tests. Break-up of the plug following Test 9 meant that this could not be included in Table 3.6.

Test	Initial Length (mm)	Final Length (mm)	Length Difference (mm)	Initial Diameter (mm)	Final Diameter (mm)	Diameter Difference (mm)	Volume Change (%)
7	63.6	60.7	+2.9	35.8	35.0	+0.8	8.8% Reduction
8	59.8	59.5	+0.3	35.9	35.7	+0.2	1.6% Reduction

Table 3.6 Plug dimensions before and after the main Compaction Simulatations – Tests 7 and 8. Test 9 plugs were not measurable post-test as they were broken due to equipment failure.

The minimal 1.6% reduction in Test 8 plug represents the lowest degree of compaction. Test 7 shows the greatest with 8.8% reduction. This reduction mainly occurs in the axial direction, reducing the length of the plug (closing along/parallel to bedding). The mid-test behavior leading to this discrepancy can clearly be seen in Figure 3.16. Drawing on this information, Test 9B, the more successful intermediate test, shows an intermediate degree of axial compaction. Despite only consolidating to 30MP effective stress (same as Test 4) which is 20MPa less than Test 8, it shows a greater degree of compaction. Tests 8 and 9B are both at room temperature, but use different fluid chemistries. The lowest reduction is associated with the 4MNaCl fluid, where as Tests 7 and 9 both used the 3MKCl/10^{-5}M KOH solution. Test 7 where this fluid is used at high temperature shows the greatest reduction in length and the largest volume reduction of all tests.

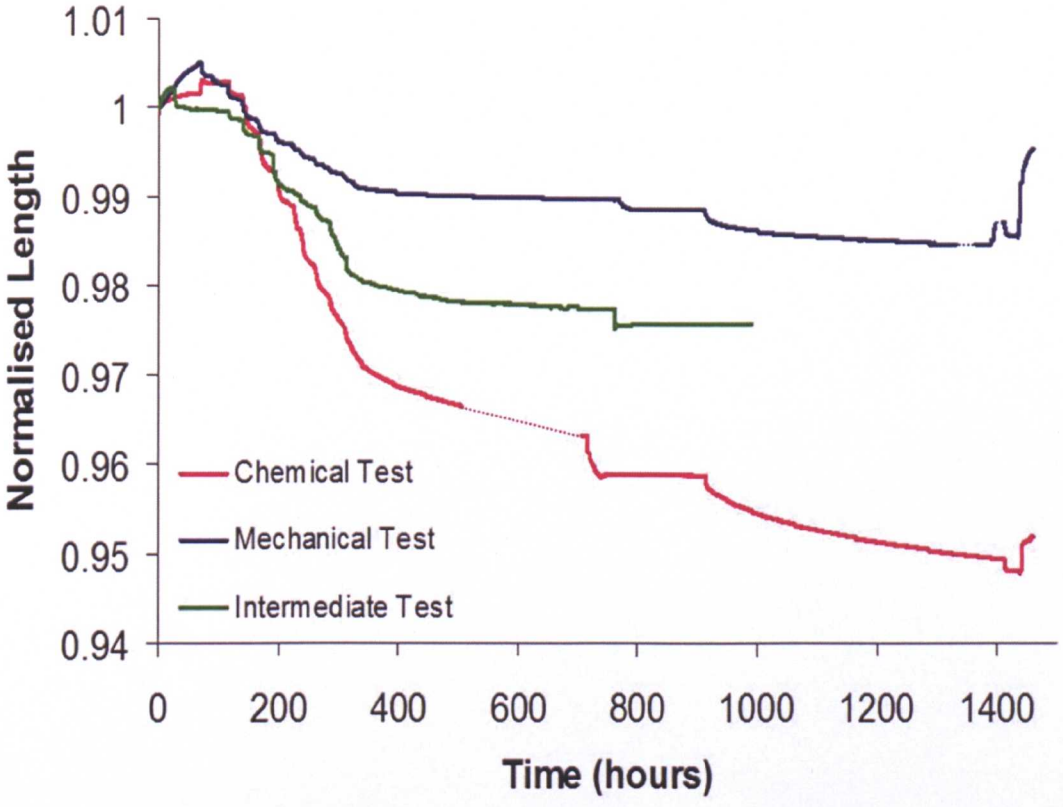

Figure 3.16 Decrease in length of sample normalized to initial sample dimensions for Test 7 (chemical test – 150°C), Test 8 (mechanical test – 25°C) and Test 9 (intermediate test-25°C). Missing sections in test 7 and 8 trends are infilled by dashes and represent periods where dimension measurements were uncertain. Equipment failed in test 9 at the final stress increase.

During all tests a short period of swelling can be seen prior to the stress increase. A small, more rapid swelling can be seen due to temperature increase and fluid expansion in Test 7. From this point all samples compact whilst under stress. Much of the reduction in size occurs during the stress ramps with a lower rate of shortening during the longer consolidation stages. Whilst stress-strain data show near consolidation at the final stress states of Tests 8 and 9, in the high temperature test (Test 7) strain is ongoing.

At the end of the tests, stress was ramped off (with temperature and the cell allowed to cool at minimal pressure in Test 7) before building the sample out. Over this final

period, the Test 7 sample shows a small amount of swelling but is still markedly compacted from original dimensions. This is contrasted by the greater elastic response displayed by the Test 8 plug, accounting for the smaller degree of permanent compaction measured upon removal from the cell.

Radially, issues with connectivity of the radial displacement transducer at temperature arose during Test 7 and a model of the radial displacement had to be constructed (Figure 3.17). This used the relationship with axial measurements established in other tests and constrained using the known pre- and post-test diameter from the micrometer measurements (see Appendices). Although the majority of mid-test behavior for Test 7 is a model, the additional radial compaction is definite as it was measured directly upon removal from the cell.

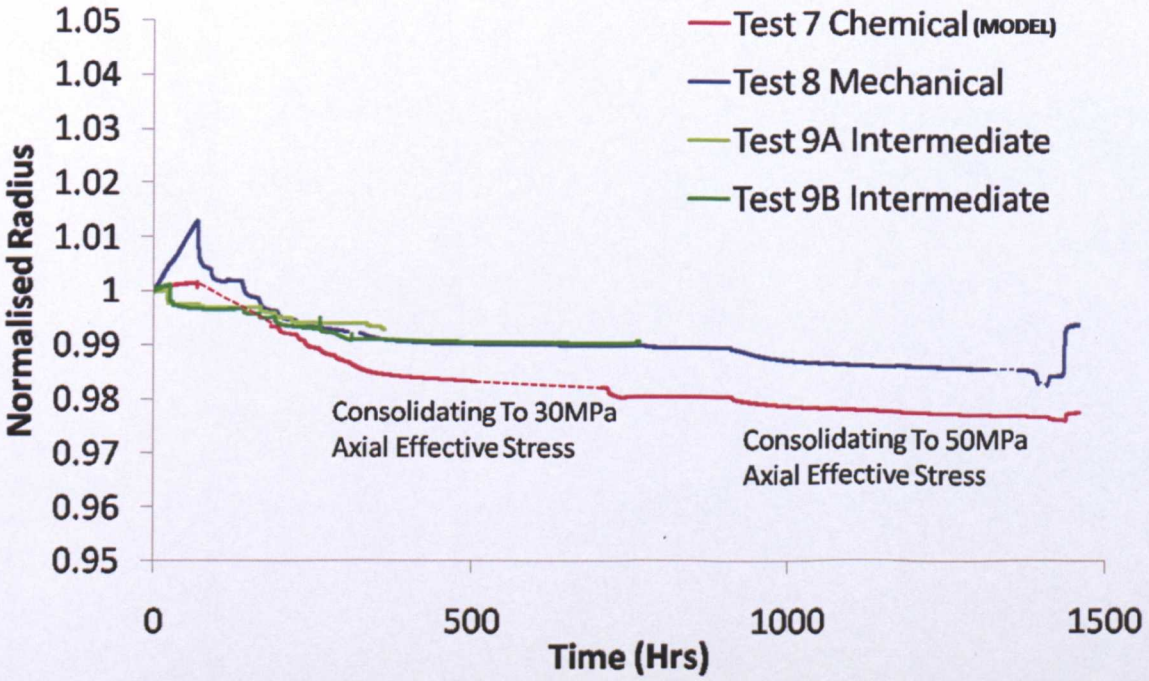

Figure 3.17 Decrease in diameter of sample normalized to initial sample dimensions for Test 7 (chemical test -150°C), Test 8 (mechanical test - 25°C) and Tests 9A and 9B (intermediate tests- 25°C). Missing sections with dashed lines represent periods where dimension measurements were uncertain. Equipment failed in test 9 at the final stress increase. Mechanical problems with the radial displacement transducer attachment means that the Test 7 trend is mainly a model. It was necessary for the calculation of bulk density and therefore porosity and several of the elastic moduli calculations. Constrains on this model are described above.

The radial measurements indicate that while Test 7 compacts significantly radially as well as axially, Test 9 no longer shows the same intermediate relationship, but is similar to Test 8. Test 9A is under ~10MPa less effective stress when it failed than 9B at the equivalent time due to a lag in the program (temperature increases/large stress increases were not carried out over weekends). This is why it appears to show lesser reduction, when corrected for equivalent stress it does not. This means that both Tests 9A and 9B, in addition to Test 8, the three room temperature tests have similar radial responses to stress.

Calculated porosity behavior during the tests follows the dominant trends of the axial compaction and overall volume loss, where Test 9 is intermediate to Test 7 (greatest porosity loss) and Test 8 (smallest porosity loss). Figure 3.18 first displays the way in which MICP porosity measurements correspond to the calculated values immediately prior to the end of the tests. Whilst Test 7 measurements correspond more to the reduced porosity, the MICP corrected porosity of the Test 8 plug shows that is is more representative of the expanded dimensions of the plug, rather than the values reached whilst at high stress. Figure 3.19 shows the calculated porosity normalized to initial dimensions and displays the relative change due to the different test conditions.

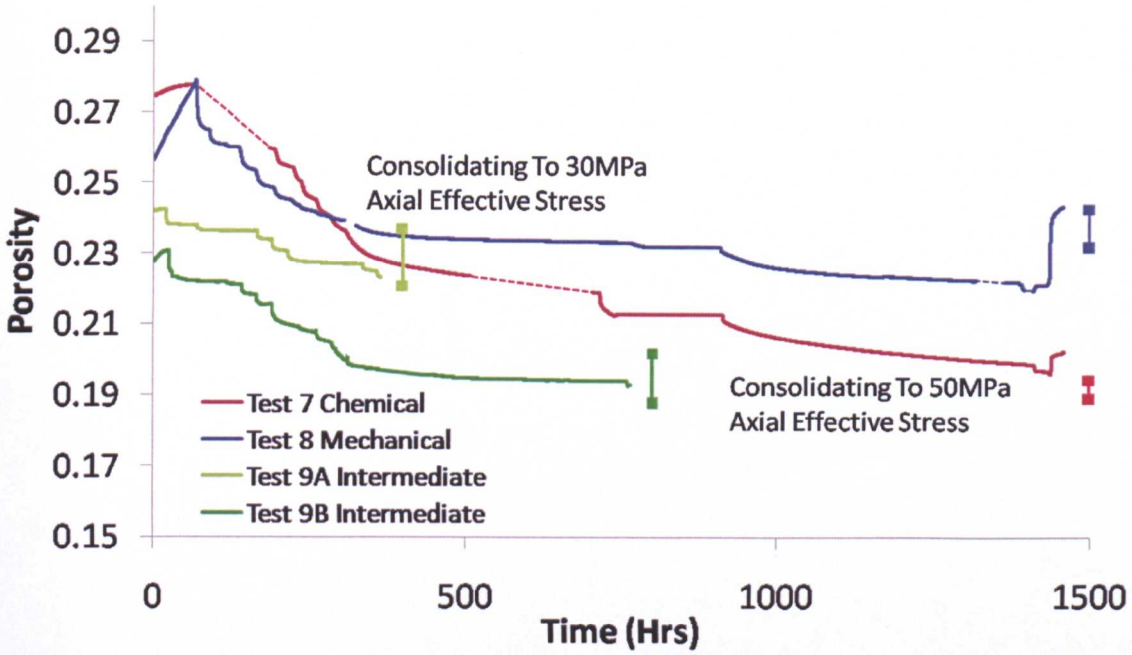

Figure 3.18 Calculated porosity during Test 7 (chemical test), Test 8 (mechanical test) and Tests 9A and B (intermediate tests). Missing sections with dashed lines represent periods where dimension measurements were uncertain. Final (vertical) error bars represent the MICP determined porosities where the upper point is the uncorrected value and the lower point is the corrected porosity. Time positions of the MICP measurements are arbitrary.

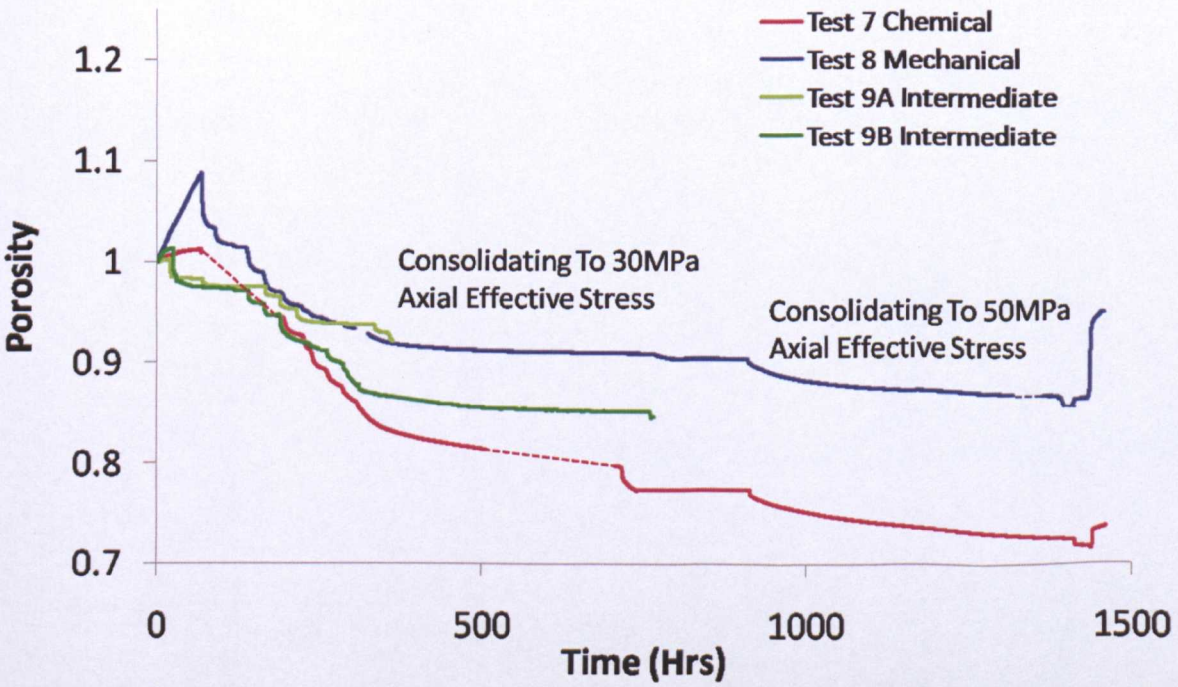

Figure 3.19 Calculated porosity normalized to initial calculated values during Test 7 (chemical test), Test 8 (mechanical test) and Tests 9A and B (intermediate tests). Missing sections with dashed lines represent periods where dimension measurements were uncertain. Note that this plot is against time and due to time constraints, the stress program in 9A lagged behind that of 9B. This meant that at the last recorded points of Test 9A, effective stress was only ~20.7MPa, whereas at the same point of test time in Hours, Test 9B had already reached the 30MPa effective stress consolidation stage.

The average differences in the test responses over the two main consolidation stages can be seen in Figure 3.20 and provides quantification of the relative impacts of the variables tested.

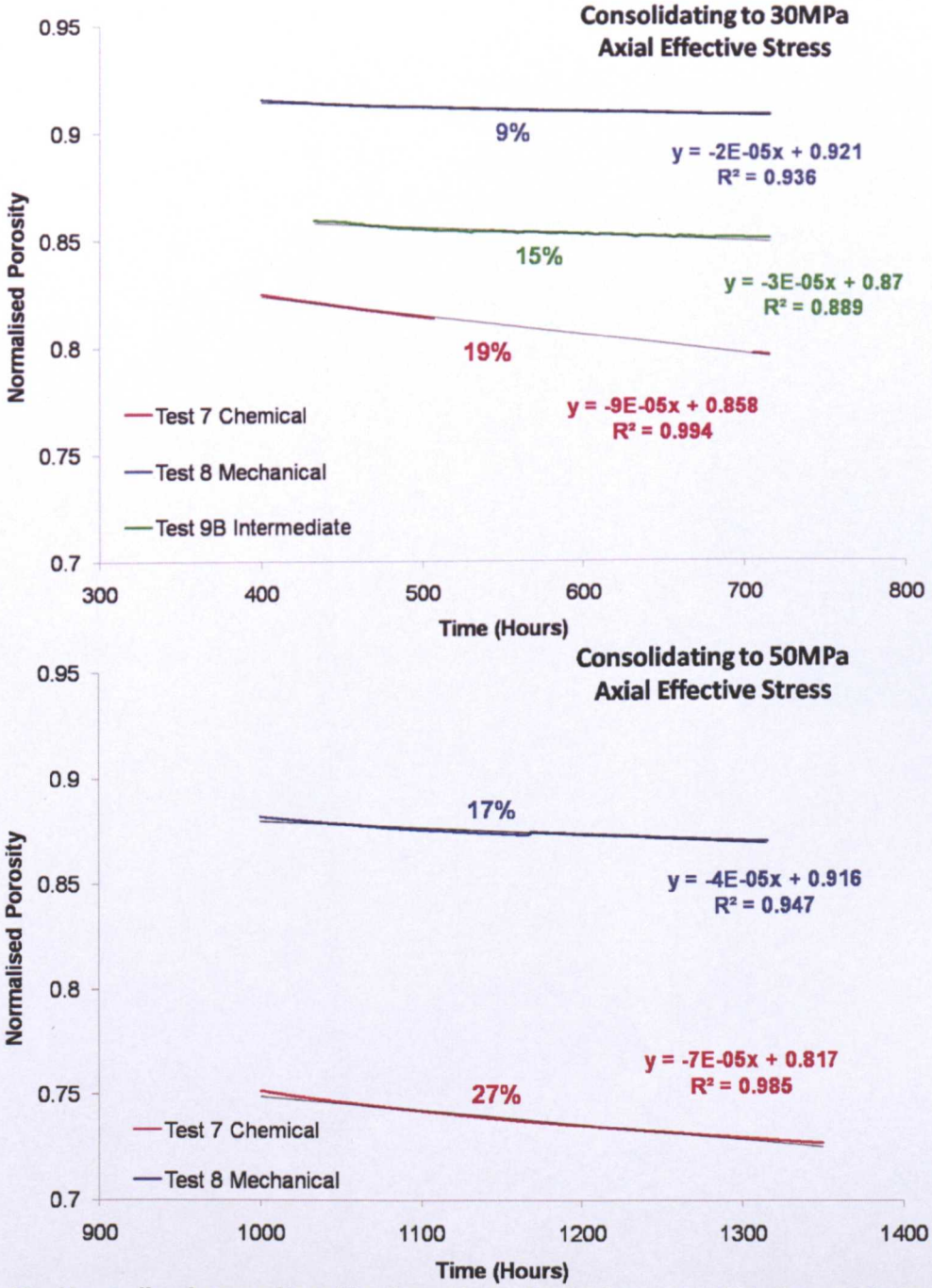

Figure 3.20 Normalized porosity with time plots displaying consolidation periods between 400-715 hours of Tests 7, 8 and 9B consolidating to 30MPa and between 1000 to 1350 hours of Tests 7 and 8 consolidating to 50MPa. Trendlines were fitted to the datasets and their equations displayed.

Where the variable testing triaxial tests showed that effective stress (>in-situ) was a key control on compaction of the material, when all tests surpass the in-situ stress state of the mudstone, other variables exert the most control. Whilst consolidating to 30MPa, stress without the effects of K-exchange or increased temperature reduces the porosity by only 9%. With the additional effects of K-exchange, this increases to 15% and with the combined effects of stress, K-exchange and elevated temperature this increases again to 19%. With greater addition of stress, the same relationship is displayed but stress is still an important control, compacting the material further in Test 8 to lose 17% porosity and 27% in Test 7.

The relative effects of stress once in-situ conditions for the material are surpassed do not seem to be a dominant control on the permanent behaviour of the material. This is because although Test 8 compacts further than Test 9B during the tests, it's elastic behavior post-test means that the final corrected porosity of the mudstone is lower following Test 9B than Test 8.

3.2.3.2 Ultra-Sonic Velocity Variation

Further information is gained through the velocity measurements carried out during the Compaction Simulations (Figures 3.21 and 3.22).

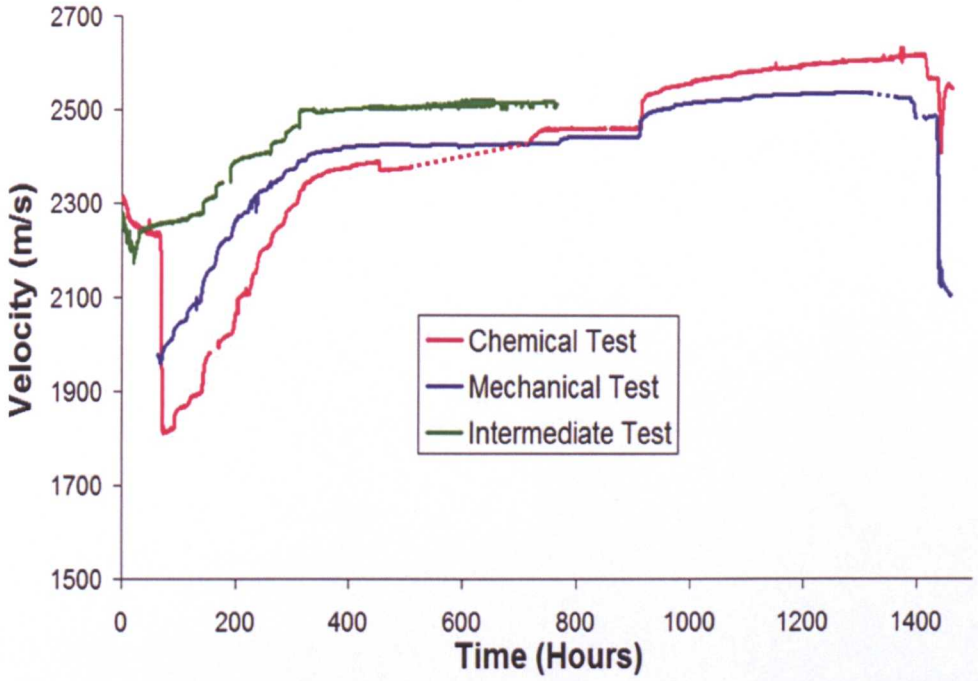

Figure 3.21 Axial P wave velocities recorded during Test 7 (chemical test), Test 8 (mechanical test) and Test 9B (intermediate test). Missing sections depicted by dashed lines in trends represent periods where dimension measurements or velocity responses were uncertain. Equipment failed in test 9 at the final stress increase.

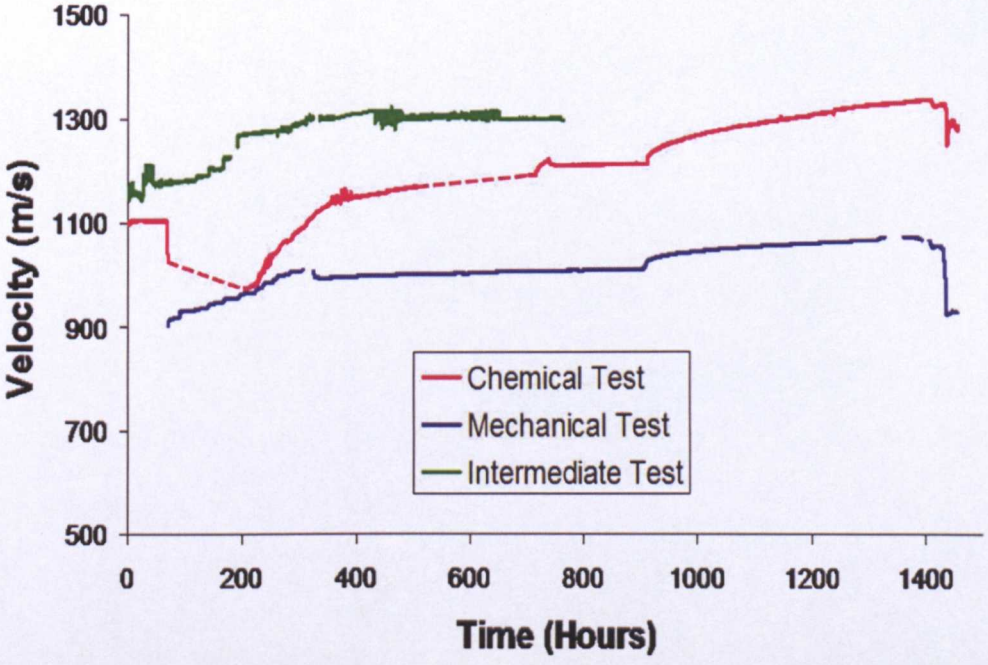

Figure 3.22 Axial S wave velocities recorded during test 7 (chemical test), test 8 (mechanical test) and test 9 (intermediate test). Missing sections depicted by dashed lines in test 7 and 8 trends represent periods where dimension measurements were uncertain. Equipment failed in test 9 at the final stress increase.

The Test 7 plug shows a large decrease in velocity following the fluid expansion associated with the temperature increase, despite relatively small dimension expansion. The velocity decrease at the start of Test 8 cannot be quantified as the initial signals were not clear enough to measure zero crossing of the waveforms. However, initial recorded velocities in Test 8 are significantly lower than those measured at the start of Tests 7 and 8, indicating there has likely been a decrease associated with the larger dimension expansion exhibited by Test 8 prior to loading. Osmotic effects should be minimizing this behavior at that point. Without the effects of temperature or the onset of hydrated Na^+ exchange, Test 9 shows minimal early expansion and the axial P and S wave velocities remain at ~2300 and 1200m/s.

Following the initial phase, all tests show increased P and S wave velocities during the stress increase. The relative velocity responses of the tests during this stage shows that Test 7, despite the intial velocity drop due to temperature and beginning the stress ramp at ~1800m/s, axial P wave velocity increases more rapidly, surpassing those measured in Test 8. This most probably reflects the greater compaction occurring in the test 7 sample seen in Figure 3.16. Although the increased fluid density with temperature in Test 7 may have an impact (see below). The axial S waves are slower than the axial P waves as is expected but show roughly similar trends.

Test 9 recorded the highest velocities whilst it ran, having not been influenced by a temperature increase, but undergoing the additional compaction associated with use of the K-rich fluid. Test 9B was the only Compaction Simulation which also generated usable radial P wave velocity data (Figure 3.23).

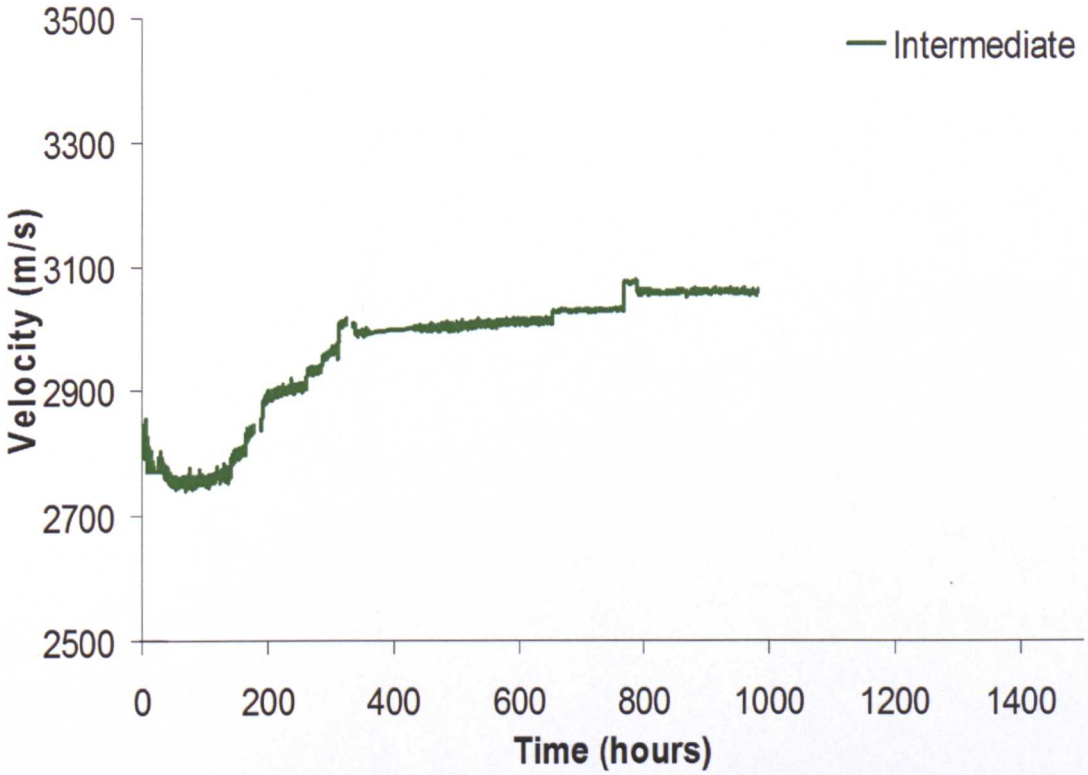

Figure 3.23 Radial P wave velocities recorded during test 9 (intermediate test). Radial waves from tests 7 and 8 were unusable. Equipment failed in test 9 at the final stress increase.

Radial P wave velocity is initially recorded ~2800m/s, increasing to ~31,00m/s, displaying anisotropy with the axial P wave velocities. The greatest velocities are recorded parallel to bedding in the radial direction. This was an effect also recorded in the variable tests and despite the considerably greater effective stresses applied in these tests (24MPa more in Test 9 than Tests1,2,3,5 & 6) the difference between the axial and radial p waves is approximately 500m/s in both the variable testing triaxial experiments and the compaction simulations.

The Vp/Vs ratio (Figure 3.24) shows an initial increase over the stress ramp in Tests 7 and 8 followed by a gradual decrease in Test 8 and a sharper decrease associated with the consolidation in Test 7. Following an initial decrease, the Test 9 ratio remains relatively constant. Decreasing Vp/Vs indicates increasing consolidation

(Duffaut & Landrø, 2007) and the trends during the each of the tests, in addition to their relationship to each other correlates to previously discussed compaction behavior.

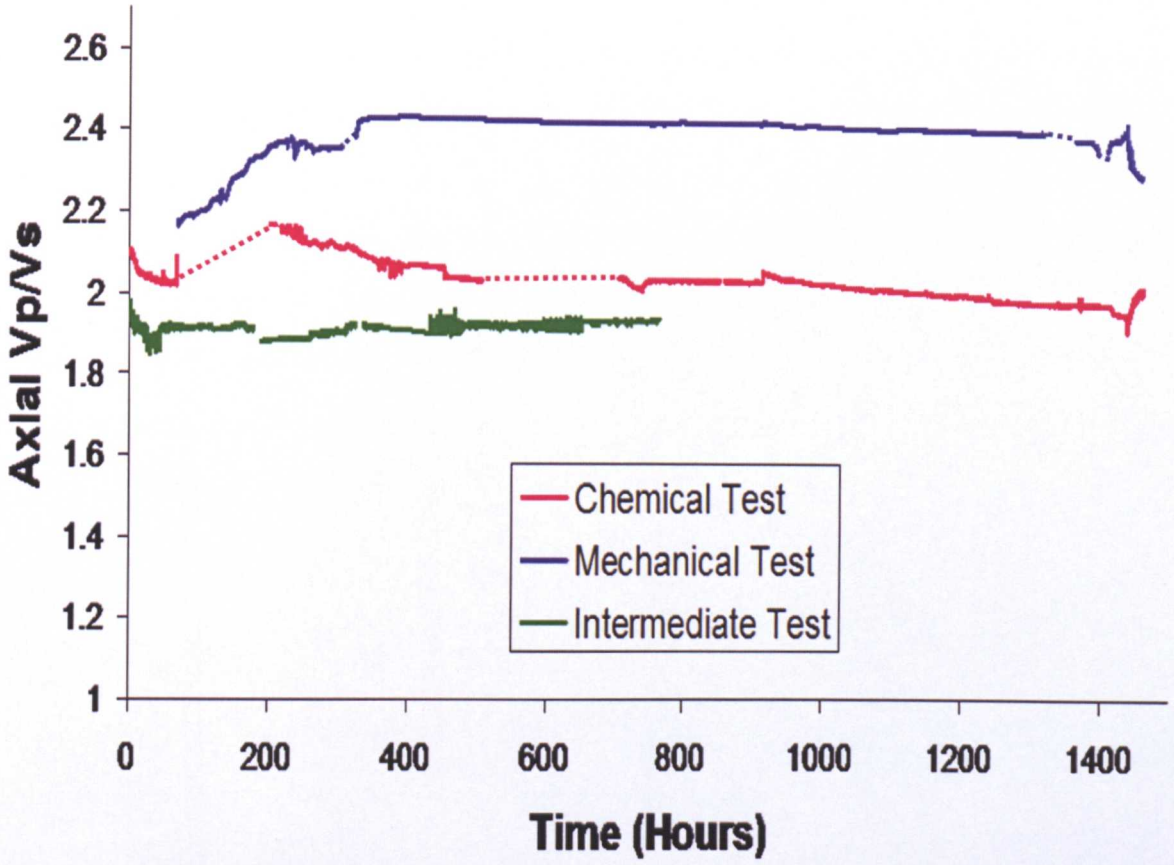

Figure 3.24 Axial Vp/Vs recorded during Test 7 (chemical test), Test 8 (mechanical test) and Test 9 B (intermediate test). Dashed sections in test 7 and 8 trends represent periods where dimension measurements were uncertain. Equipment failed in test 9 at the final stress increase.

As stress is ramped down at the end of Test 8, the material rebounds back to almost pre-test dimensions. This is accompanied by a sharp decrease in both P and S-wave velocities. A 0.2 decrease in Vp/Vs ratio, indicating consolidation, is measured. However, this does not reduce the ratio below pre-test values. Test 7 material showed more minimal rebound and less of a decrease in P and S wave velocities as

stress and temperature were decreased. The ratio shows an opposite response in Test 7, showing a slight (0.2) increase, however, the final value is less than the initial ratio and lower than the final ratio calculated for Test 8.

The dynamic elastic moduli were calculated for the comapction simulations using the equations in 2.2.3.2 and are plotted in Figures 3.29 with the dynamic Young's Modulus and Poisson's Ration in Figure 3.26.

Fluid density is used in the calculation of bulk density which in turn is used along with the velocity data to determine the dynamic elastic moduli. Test 7 and 9A & B flowed a test fluid of 3M KCl with 10^{-5}M KOH. If 3M KCl is as an approximation for the overall salinity then the calculated value is 223680mg/l, which at 25°C creates a fluid density of 1.18g/cm^3 in Test 9. This is calculated to increase to 1.26g/cm^3 at 150°C in Test 7. Although the NaCl solution concentration in Test 8 is 4M, this corresponds to a salinity of 223680mg/l which at 25°C also gives a fluid density of 1.18g/cm. Therefore prior to the temperature increase, the calculated artificial fluid density (the natural salinity of the North Sea mudstone pore fluid was unknown) is 1.18g/cm^3 for all three of the Compaction Simulations. This should only vary later in Test 7, following the temperature increase when the density is calculated as increasing to ~1.26g/cm^3.

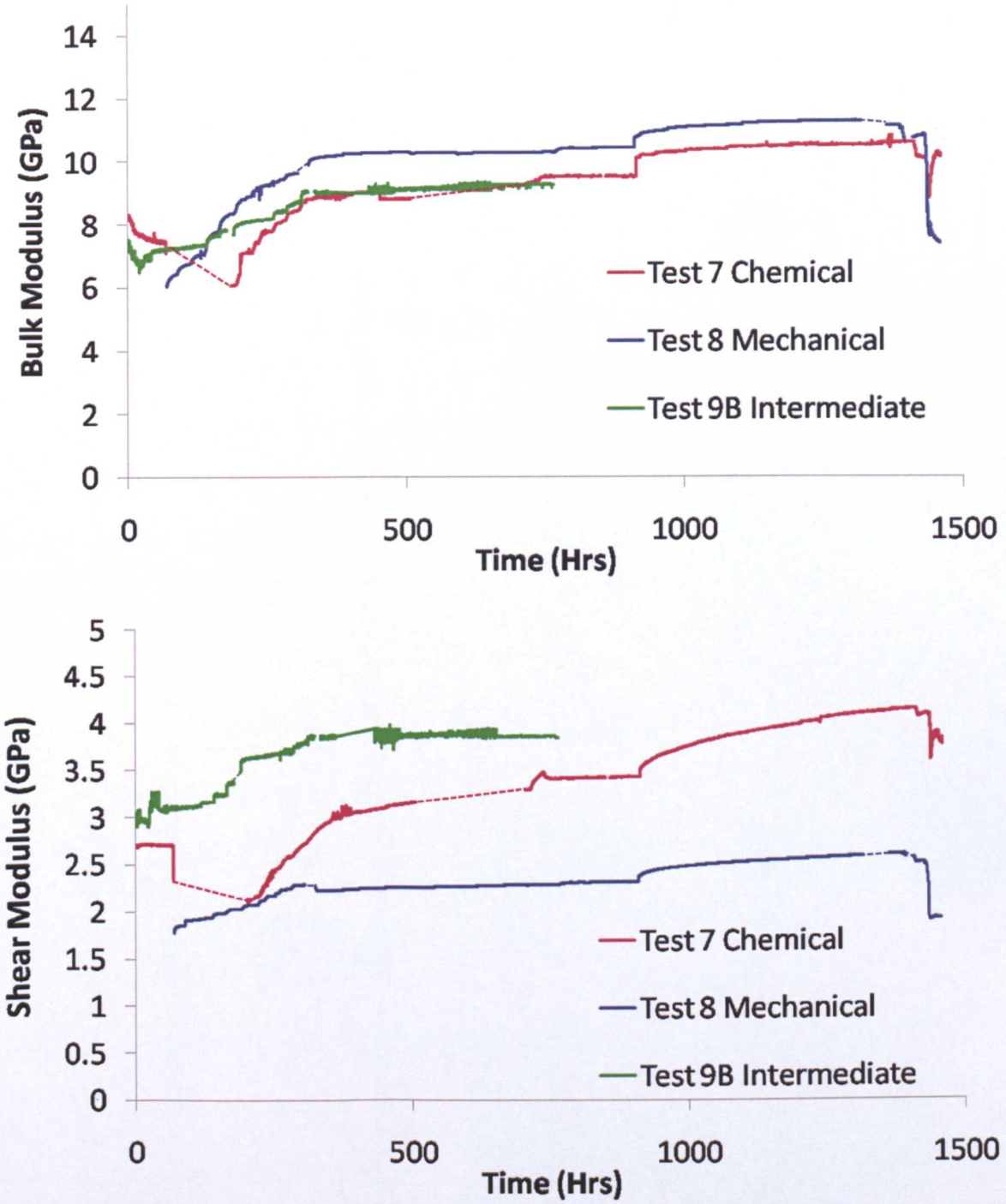

Figure 3.25 Dynamic bulk modulus and shear modulus calculated during test 7 (chemical test), test 8 (mechanical test) and test 9 (intermediate test). Dashed sections in test 7 and 8 trends represent periods where dimension or velocity measurements were uncertain. Equipment failed in test 9 at the final stress increase.

The bulk modulus represents the resistance of a system to compression. Given the salinities of the fluids used and the calculated elevation of fluid density in Test 7 with temperature, it may have been expected that Test 7 may show a separate response,

if the bulk modulus was being controlled by the fluid density. However, following the stress ramp (and temperature ramp in Test 7) Tests 7 and 9 appear to show similar bulk moduli of ~9GPa. It is Test 8 that shows a separate response, with a higher value at equivalent effective stresses. This appears to be independent of the fluid density / low temperature conditions which it shares with Test 9. It would seem that use of the NaCl solution is the determining factor in its divergent response, where the exchange of hydrated Na^+ into/onto the matrix clays makes the material less compressible.

The shear modulus represents the resistance of a system to shearing. This is greatest in the room temperature, K-rich fluid test, Test 9, followed by Test 7 and then Test 8. The shear modulus of Test 7 is increasing the most during the test period and it is unknown if it would have surpassed or followed Test 9 if the intermediate test had continued. What can be inferred is that use of the 3M KCl with 10^{-5}M KOH solution and the K^+ exchange that it promotes would appear to strengthen the mudstone, increasing its resistance to shearing.

Figure 3.26 displays plots of the Poisson's Ratio and Young's Modulus with time through the three Compaction Simulations. The Poisson's Ratio as regards these simulations describes the change in lateral strain due to the axial effective stress compressing the sample. The consistently higher value of Test 8 (mechanical test) is another example of the Na-exposed material showing less compressibility, whilst

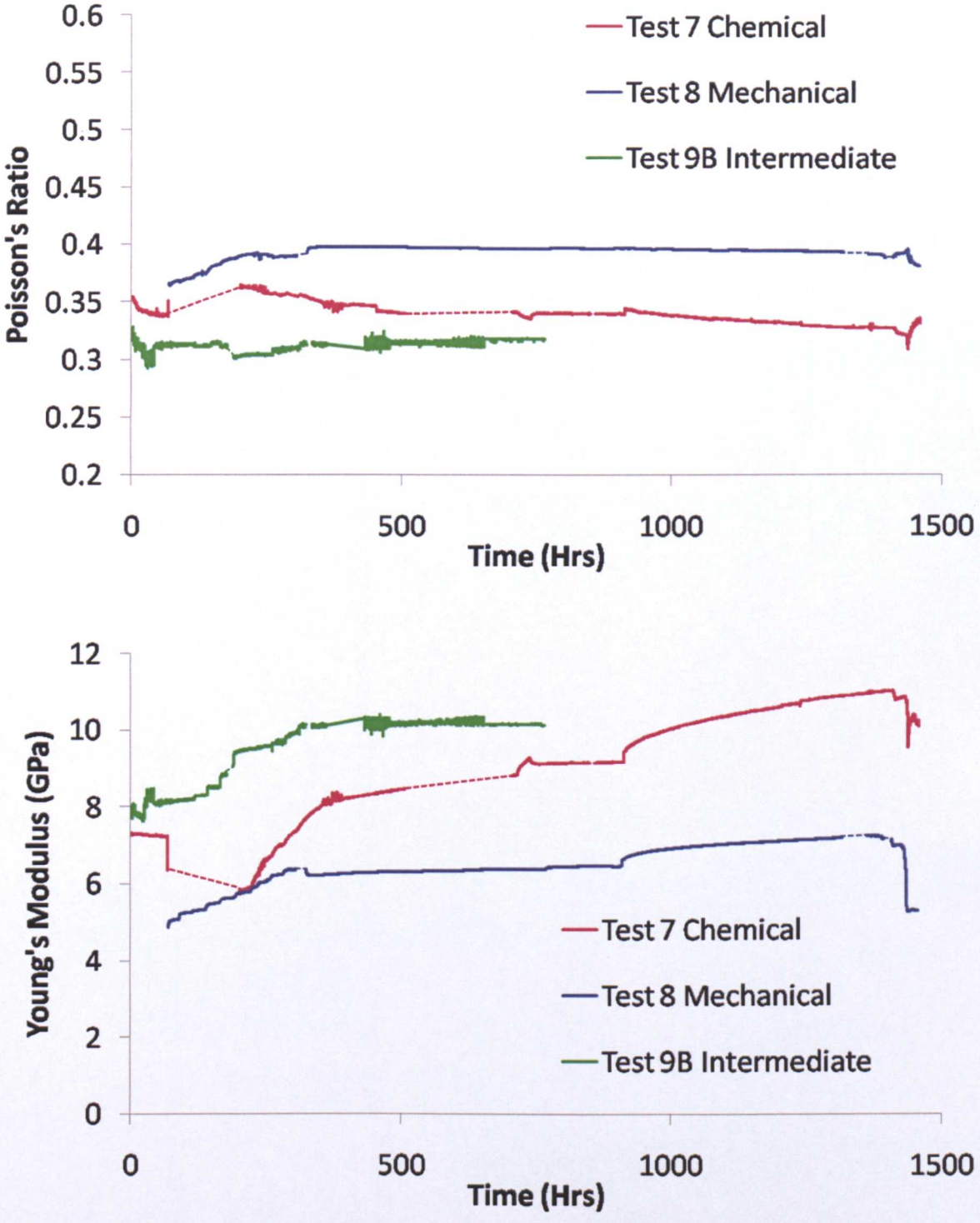

Figure 3.26 Dynamic Poisson's ratio and Young's modulus throughout test 7 (chemical test), test 8 (mechanical test) and test 9 (intermediate test). Dashed sections in test 7 and 8 trends represent periods where dimension or velocity measurements were uncertain. Equipment failed in test 9 at the final stress increase.

Test 9 shows the lowest ratio initially indicating the least lateral deformation, with Test 7 (chemical test) showing an intermediate trend that is increasing in

compressibility throughout the test. This could be a response to the higher fluid densities involved in Test 7 whilst it is at 150°C and/or recovery behavic the expansion of the material due to temperature increase.

The Young's modulus quantifies the stiffness of a material and similarly to the shear modulus results, Test 9 shows the greatest stiffness, followed by Test 7 which increased during the test, approximately doubling its stiffness following the temperature increase which reduced it. Test 8 shows some increase in the modulus during the stress ramp and consolidation periods. However, not to the same degree as Test 7 and following a rapid decline as stress was removed, the final Young's Modulus of Test 7 is approximately double that of Test 8.

3.2.4 Fluid Tests

Samples of the artificial pore KCl pore fluid were taken prior to its use in the tests and following draining procedures for the cell system (mid-test, this was usually associated with necessary draining following "flushes" filling the pore pump.) These samples were then prepared for ICP analysis as described in 2.3.6.

	Ca mg/L	Mg mg/L	Fe mg/L	Mn ppm	Al mg/L	Zn mg/L	Si mg/L	K mg/L
Blank	0.00	0.00	0.00	0.00	0.00	0.00	0.00	0.00
Standard 1	5.00	2.50	2.50	1.00	1.00	1.00	5.00	25.00
Standard 2	10.00	5.00	5.00	2.50	2.50	2.50	10.00	50.00
A	1166.94	132.54	5.47	5.12	0.27	0.91	10.91	108342.00
B	1473.65	161.64	6.48	5.41	0.22	0.87	14.16	117829.00
C	665.70	138.94	8.98	2.29	0.17	1.39	5.97	108072.00
D	1198.00	112.30	8.45	8.40	0.71	1.27	18.46	105969.00
E	1.33	11.96	0.15	0.06	0.11	0.25	11.53	126284.00
F	1.68		0.15	0.06	0.09	0.39	11.40	121159.00
G	2.41		0.15	0.07	0.08	0.24	9.72	123152.00

Run 1
Run 2
Run 3
Run 4

A Cell End Test 2
B Cell Mid Test 2
C Cell Mid Test 1
D Cell Start Test 2
E Flask Mid Test 2
F Flask Early Test 2
G Flask Late Test 1

Table 3.7 ICP results for tests on pre-test fluids (samples E, F & G) and those collected in association with tests 1 and 2 (samples A,B,C & D). Runs 1 and 2 were made following the initial dilutions described in 2.3.6, but elevated concentrations of Mn and Mg required more dilution, with analysis of Ca requiring further dilution again prior to Run 4.

Basic analysis of this data shows that pre-test fluids show high levels of potassium with low levels of the other elements tested (only Ca, Mg and Si show levels >1mg/L). Following differing residency times in the cell system, the amount of potassium drops and most other element concentrations increase, bar Si, with particularly strong increases in Ca and Mg. Calcitic fossil material is present in all analysed samples of the North Sea mudstone (see BSEM images/EDX) and could have supplied a proportion of the Ca, which shows the most significant increase. However, KCl solution (used in Tests 1&2) pH was tested and found to be approximately neutral/borderline acidic at room temperature. Mg and Fe are known to form part of the clay matrix along with K and Na. Na concentrations were so high

that following all dilutions, they were still not measurable. A separate preparation similar to that for the high concentration K analyses would have been required.

The high pressure, high temperature triaxial cells used for these tests are generally used for engineering purposes and cannot be prepared as rigorously as would be desirable prior to ICP. The purpose of these ICP runs was, therefore, not to obtain exact quantitative analyses of the fluid samples, rather to give a relative indication in the first set of variable triaxial tests of chemical influences. As discussed in 2.3.6 a decision was made not to continue these analyses. This was because initial tests had yielded the required information that fluid composition altered during its residency in the cell system, but the source/point of loss could not be clarified due to the design of the cell system and the points from which fluid could be collected.

3.2.5 Compaction Simulations and Mid-Test Measurements: Summary

Variable Testing: Triaxial Tests (Tests 1-6)

- 6 variable testing, triaxial tests were completed investigating the effects of varying time at temperature and pressure, effective stress, temperature and fluid chemistry (with 1 repeat – Test 1/Test 3). All showed initial expansion upon heating both radially and axially, followed by a sharp decrease in dimensions during the stress ramp and consolidation periods.
- An elastic response is generally measured upon the removal of stress at the end of each test. Final dimension measurements showed that either negligible, permanent compaction or actual expansion of the sample occurred once samples were removed from the cell. This is despite all variable tests (1-6) using K-rich fluid and being ran at elevated temperature.

- The main exception was Test 4, the high effective stress test that surpassed the in-situ stress of the North Sea mudstone, reaching 30MPa axial effective stress and showing 3.9% reduction in volume. Axial and radial strain is ongoing at the point at which the stress/temperature ramp-down took place in Test 4. Test 2, the longer time period test, also reduced in dimensions – this is thought to be related to closure of fractures observed in pre-test CT scanning.
- Calculated porosities throughout the test reflect the dimension reduction observed in Test 4 and calibrate to the MICP measured porosities (see later).
- Ultrasonic velocity measurements display responses to test conditions consistent with the behavior observed in the dimension measurements/porosity calculations. There is always a reduction in velocity associated with the expansion of the sample upon heating. This can be attributed to the separation of grain contacts as the pore fluid expanded during the elevation of temperature. As stress is applied to the system, matrix grain contacts are increased and cracks (observed in CT scanning and micro-cracks along elongate grain boundaries such as those of micas - observed in BSEM images – see later) close.
- As with the dimension measurements, the velocities generally decrease with the reduction of pressure, post-test, to approximate initial values.
- The Test 4 plug is, again, the exception with final velocity readings considerably above those at the start of the test. This is attributed to the permanent compaction recorded in the Test 4 plug due to consolidation to high effective stress (30MPa).

- Following differing residency times in the cell system, the amount of potassium drops and most other element concentrations increase, bar Si, with particularly strong increases in Ca and Mg. Na concentrations were so high that following the dilutions carried out, they were still not measurable.
- Fluid composition altered during its residency in the cell system, but the source/point of loss could not be clarified due to the design of the cell system and the points from which fluid could be collected.

Variable Testing: Reflux Condenser Tests (Tests A-C)

- Three fluids tested at temperature with the North Sea mudstone assessing the role of fluid chemistry and temperature without effective stress. Test fluids were 4M KCl 4M NaCl and 3M KCl /10^{-5} M KOH, (2 repeat tests).
- Main finding was the increased stability provided by the 3M KCl /10^{-5} M KOH solution and that increased pH along with K appear to control the sample.

Compaction Simulation Tests

- 3 main tests to assess the effects of conditions designed to simulate chemical compaction (Test 7 – 50MPa effective stress, 150°C, 3M KCl /10^{-5} M KOH) and mechanical compaction (Test 8 - 50MPa effective stress, 25°C, 4M NaCl).
- The third set of conditions were intermediate and designed to differentiate between the effects of K-rich/elevated pH fluid and temperature (designed to reach 50MPa effective stress, 25°C, 3M KCl /10^{-5} M KOH. These tests, the Intermediate Tests 9A and 9B both failed due to mechanical issues. However, usable mid-test data is provided by both tests (providing repeatability) and 9B completed the first consolidation stage to 30MPa providing comparison with

Tests 7 and 8 and the nature of failure meant samples were still intact enough to be analysed for selected properties whilst exercising caution.

- During all tests a short period of swelling can be seen prior to the stress increase. A small, more rapid swelling can be seen due to temperature increase and fluid expansion in Test 7. From this point all samples compact whilst under stress.
- Test 7 compacts most in the axial direction, followed by Test 9B (and 9A when plotted against effective stress, not time) and Test 8 compacts the least. Radially, Test 7 compacts significantly, whilst Test 9B and Test 8 compact to a similar degree.
- Calculated porosities quantify the relative compaction attributed to the varying conditions. Whilst consolidating to 30MPa, stress without the effects of K-exchange or increased temperature reduces the porosity by only 9%. With the additional effects of K-exchange, this increases to 15% and with the combined effects of stress, K-exchange and elevated temperature this increases again to 19%. With greater addition of stress, the same relationship is displayed but stress is still an important control, compacting the material further in Test 8 to lose 17% porosity and 27% in Test 7.
- Upon removal of stress and temperature, Test 7 shows some elastic behavior but not to the same degree as Test 8. Final volume reductions are 8.8% following Test 7 and only 1.6% reduction in the Test 8 plug (not measurable for Test 9).
- Tests 7 and 8 appear to show an initial velocity reduction associated with temperature increase and Na-exchange respectively. All tests show increased

P and S wave velocities during the stress increase. Test 7 increased more than Test 8, probably reflecting the greater compaction measured. Test 9 recorded the highest velocities whilst it ran, having not been influenced by a temperature increase, but undergoing the additional compaction associated with use of the K-rich fluid.

- The greater elastic reponse in Test 8 dimensions post-test is reflected in the velocity measurements with Test 8 velocities decreasing back to approximate initial values. Test 7 does not.
- The anisotropy observed in the variable testing triaxial tests can be seen in Test 9 (radial velocities not available for Tests 7 and 8).
- The Vp/Vs ratio shows an initial increase over the stress ramp in Tests 7 and 8 followed by a gradual decrease in Test 8 and a sharper decrease associated with the consolidation in Test 7. Following an initial decrease, the Test 9 ratio remains relatively constant. Decreasing Vp/Vs indicates increasing consolidation.
- Tests 7 and 9 appear to show similar bulk moduli of ~9GPa. Test 8 shows a separate response, with a higher value at equivalent effective stresses. It would seem that use of the NaCl solution is the determining factor in its divergent response, where the exchange of hydrated Na^+ into/onto the matrix clays makes the material less compressible.
- Use of the 3M KCl with 10^{-5}M KOH solution and the K^+ exchange that it promotes would appear to strengthen the mudstone, increasing its resistance to shearing.

- Test 9 shows the greatest stiffness, followed by Test 7 which increased during the test, approximately doubling its stiffness following the temperature increase which reduced it. Test 8 shows some increase in Young'smodulus during the stress ramp and consolidation periods. However, not to the same degree as Test 7 and following a rapid decline as stress was removed, the final Young's Modulus of Test 7 is approximately double that of Test 8.

3.3 Chemical / Mineralogical Rock Properties

3.3.1 Pre/Post Test Fluid Compatibility

Following the freeze-thaw disaggregation process (2.3.2) a stability difference was noted between the pre-test material and the samples of post-test (K-rich pore fluid tests only) plugs. Pre-test material disaggregated rapidly upon contact with de-ionized water, replicating the results of the earlier fluid compatibility tests (3.1.4.4). However, post-test (K-rich fluid tests only) samples show greater stability in de-ionized water. They remained stable over several cycles of freeze-thaw whilst the pre-test mudrock swelled and disaggregated in the first cycle (see below figure 3.27). Given information in the literature *(*Steiger, *1982;* Van Oort, *2003)*, this was inferred as qualitative evidence for exchange of potassium in the tested material even following the shorter period tests such as Tests 1 and 2.

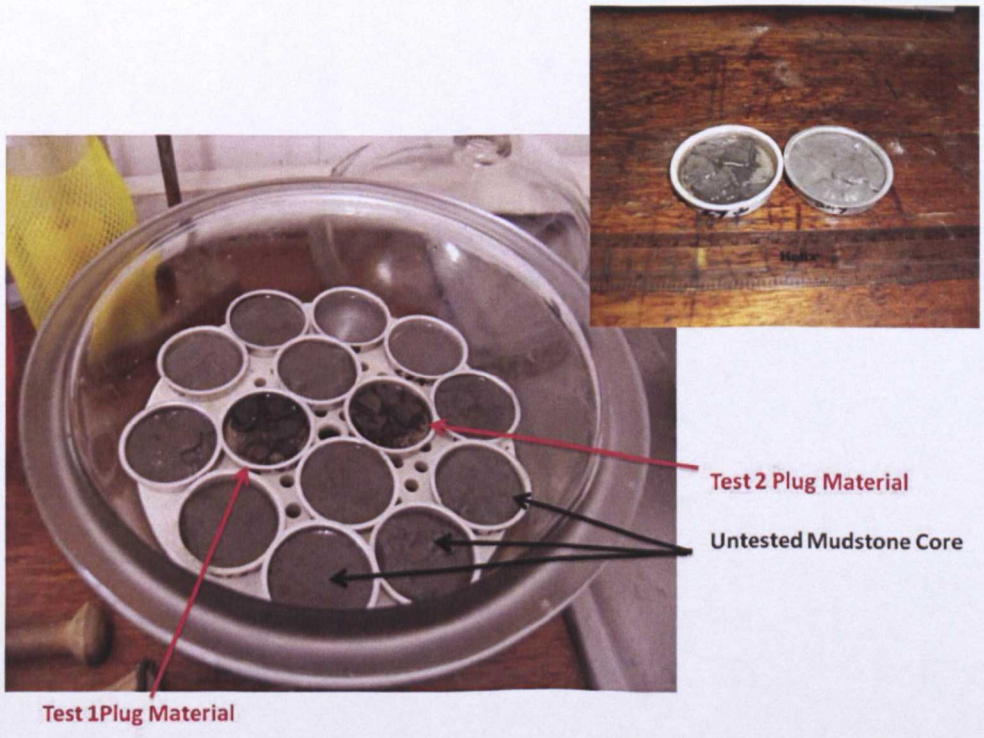

Figure 3.27 Sample behaviour following cycle 1 of freeze-thaw disaggregation, highlighting the difference between pre and post-test samples.

3.3.2 Bulk Fraction X-Ray Diffraction (XRD)

3.3.2.1 Pre-Test Mineralogy

Bedding parallel and perpendicular sections of untested North Sea mudstone were prepared and analysed using XRD (Chapter2). Mineralogy was identified using X'Pert HighScore Plus (Figure 3.28)

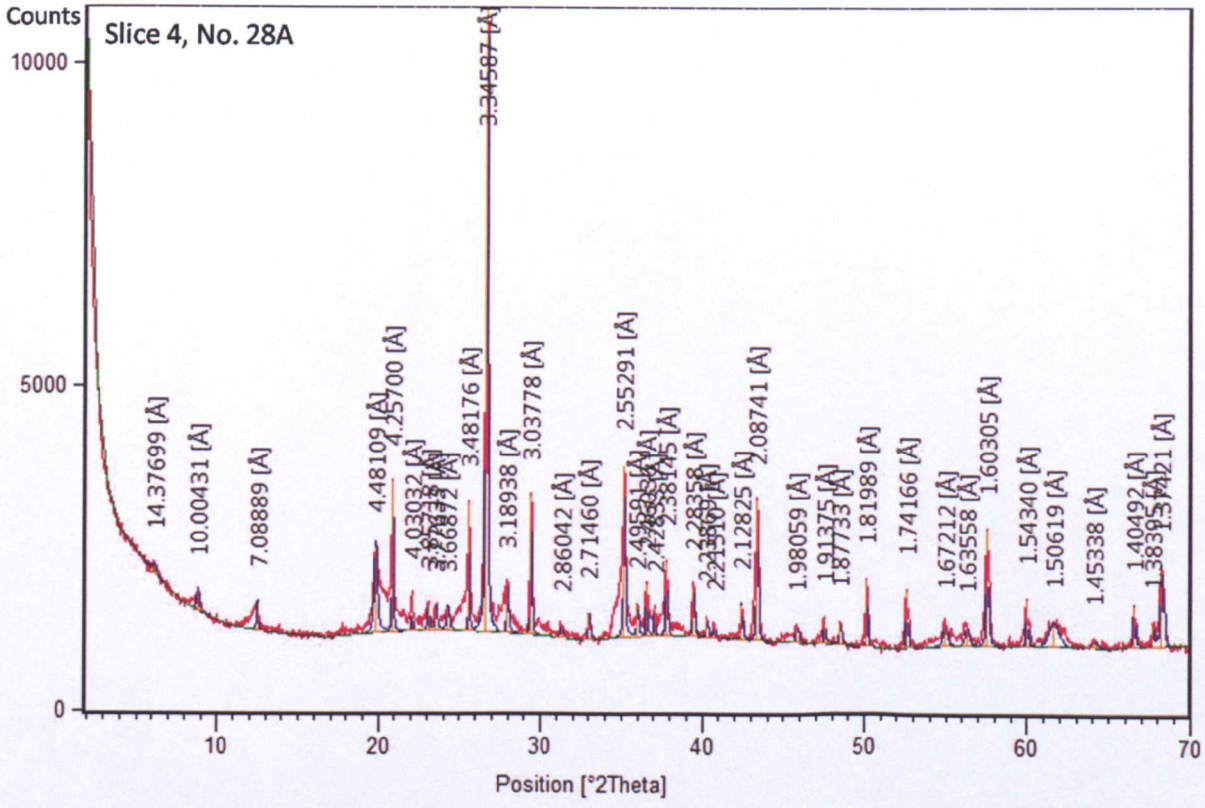

No.	V..	Ref. Code	Compound Name	Chemical Formula
1	✔	01-086-1560	Quartz low	Si O2
2	✔	01-071-0958	Corundum	(Al.948 Cr.052)2 O3
3	✔	01-071-0053	Pyrite	Fe S2
4	✔	01-072-1937	Calcite	Ca C O3
5	✔	01-076-0927	Albite calcian low	(Na0.84 Ca0.16) Al1.16 Si2.84 O8
6	✔	00-029-1488	Kaolinite-1\ITMd\RG	Al2 Si2 O5 (O H)4
7	✔	00-026-0911	Illite-2\ITM#1\RG	(K , H3 O) Al2 Si3 Al O10 (O H)2
8	✔	01-076-0825	Potassium-Feldspar CA1A	K.886 Na.099 Ca.009 Ba.012 Al1.005 Si2.995 O8
9	✔	00-012-0232	Montmorillonite	(Na , Ca)0.3 (Al , Mg)2 Si4 O16 (O H)2 !x H2 O
10	✔	00-013-0003	Chlorite	Mg2 Al3 (Si3 Al) O10 (O)8

Figure 3.28 Example diffraction pattern for bedding parallel, pre-test sample Slice 4, No 28A with background fitted, peaks identified and labelled in Å. Below minerals subset identified via scoring (X'Pert HighScore Plus screenshots).

Scoring according to fit of a reference pattern to the observed trace identified the basic mineralogy of the pre-test mudstone to be quartz, pyrite, calcite, plagioclase, K-feldspar, chlorite, kaolinite, illite/mica and an expandable phase fitted by a montmorillonite reference pattern. Modelling of the data then took place using FULLPAT (Chapter 2 for details) to quantify abundance (Table 3.8).

Sample	Quartz	Pyrite	Calc.	Albite	Kaol.	Illite/ Mica	K-Feld	Smectite	Chlor.	Total
Pl.1 No.1A	14	6	5	2	7	19	3	38	5	101.8
Pl.1 No.3A	14	3	5	4	7	18	3	38	7	100.2
Pl.1 No.5A	14	5	5	4	8	10	3	45	6	100.2
Pl.1 No.7A	14	6	3	4	8	9	3	46	6	97.2
Pl.1 No.9A	12	6	6	3	8	10	3	47	6	102.4
Sl.4 No.1A	14	5	6	4	7	11	3	44	6	99.1
Sl.4 No.3A	13	6	6	3	7	8	3	48	6	98.8
Sl.4 No.5A	13	3	3	4	7	21	3	36	7	101.2
Sl.4 No.7A	14	5	4	4	7	9	3	47	7	107.0
Sl.4 No.9A	14	5	5	4	8	16	2	41	6	101.6
Sl.4 No.11A	14	6	6	3	8	9	0	55	1	99.0
Sl.4 No.15A	15	5	5	4	7	7	4	47	6	100.2
Sl.4 No.17A	14	4	6	4	7	16	3	39	6	100.9
Sl.4 No.19A	14	3	5	4	8	22	4	34	6	103.8
Sl.4 No.21A	14	5	4	4	8	9	3	46	6	101.9
Sl.4 No.23A	14	3	5	4	7	24	4	34	6	103.8
Sl.4 No.25A	14	5	4	4	7	11	3	45	5	100.7
Sl.4 No.28A	15	5	5	4	8	10	3	44	6	99.3

Table 3.8 Modelled pre-test abundances using FULLPAT normalised to 100% with the original (pre-normalisation) totals in the final column.

The average pre-test composition (± standard deviation modelled phase abundance for this sample set – error on the method discussed separately in Chapter 2) was 14±0.7% quartz, 5±1% pyrite, 5±1% calcite, 4±0.6% plagioclase, 3±0.9% K-feldspar, 7±0.5% kaolinite, 13±5% illite/mica, 43±6% smectite and 6±1% chlorite. The smectite abundance across a bedding plane and perpendicular, through bedding are plotted in Figure 3.29. There is variation between a minimum of 34% to a maximum of 55% parallel to bedding, but no obvious grouping. In the plug analysed, there was an increase from 38% to 47% smectite down the length of the plug, through bedding. The average pre-normalised model total was 101±2%, where the maximum difference from 100% was +7 and minimum -3.

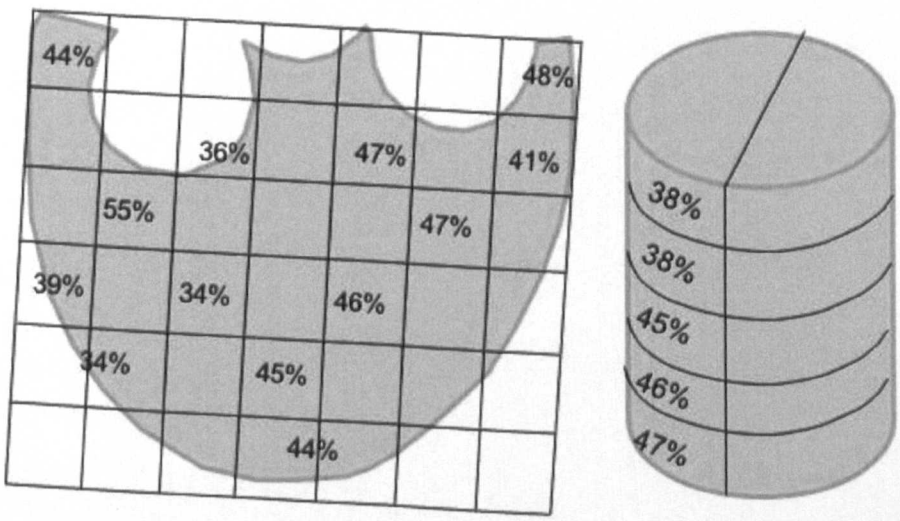

Figure 3.29 Modelled pre-test smectite phase abundance parallel to bedding in Slice 4 and perpendicular to bedding in Plug 1.

3.3.2.2 Post-Test Mineralogy

The same procedures were applied to the post-test material after the plug was sectioned and prepared.

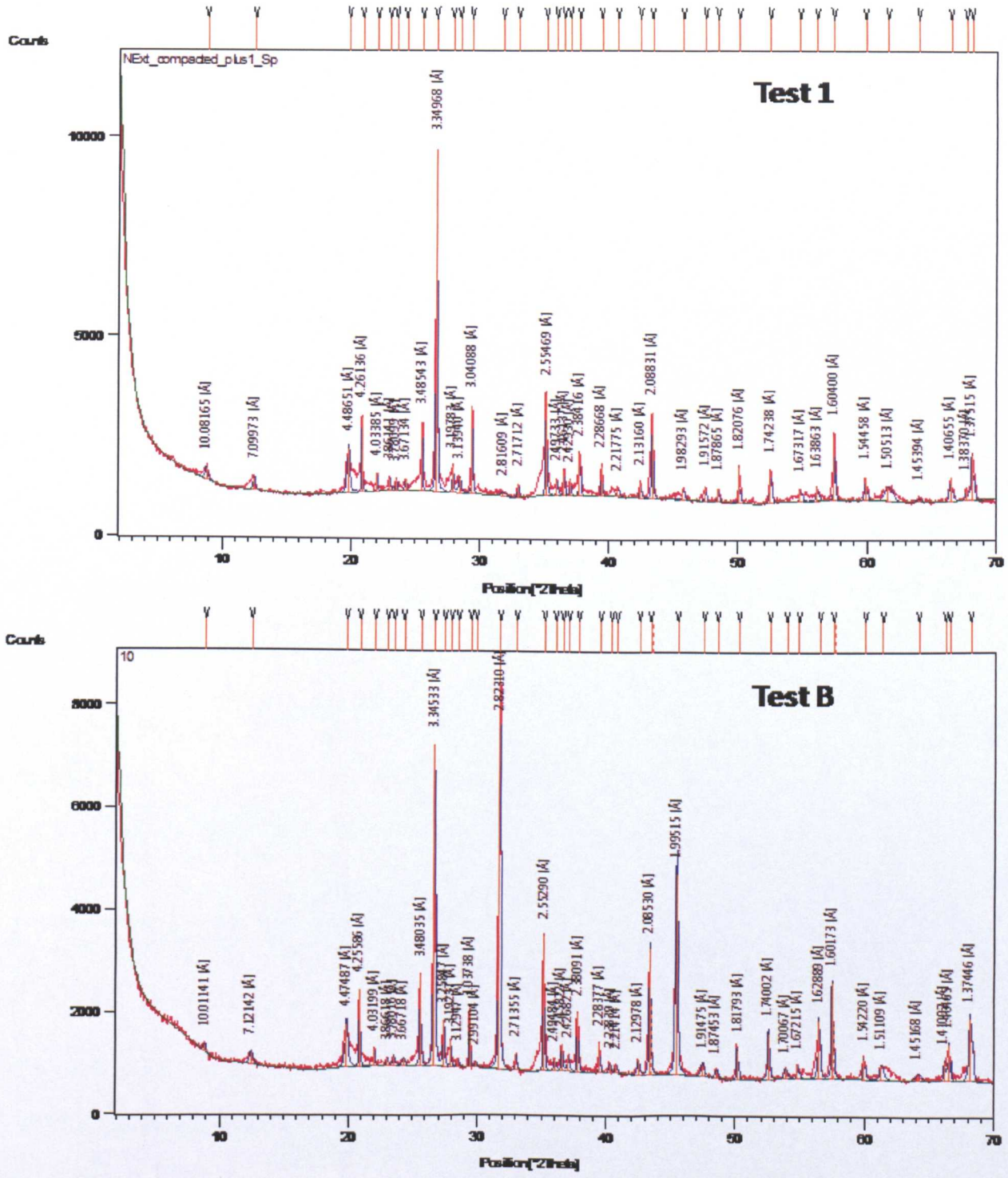

Figure 3.30 Example diffraction pattern for bedding post-test samples from Test 1 and Test B with background fitted, peaks identified and labelled in Å (X'Pert HighScore Plus screenshots).

Sample	Quartz	Pyrite	Calc.	Albite	Kaol.	Illite/ Mica	K-Feld	Smectite	Chlor.	Total
Test 1	14	2	6	5	7	30	4	27	6	103.5
Test 2	15	2	6	5	6	29	4	27	6	97.8
Test 3	15	2	4	5	7	48	3	14	3	100.4
Test 4	15	0	1	5	7	52	5	13	2	102.4
Test 5	14	3	6	4	6	20	4	38	6	106.5
Test 6	14	1	9	4	7	47	2	12	3	89.8
Test 7	14	2	6	4	7	38	3	22.5	5	98.4
Test 8	12	6	6	4	8	8	3	48	7	96.7
Test A	13	4	2	5	5	12	4	47	5	106.6
Test B	10	4	3	2	3	0	4	51	8	89.1
Test C	16	1	6	6	7	42	1	20	0	92.9

Table 3.9 Modelled post-test abundances using FULLPAT normalised to 100% with the original (pre-normalisation) totals in the final column.

The average (4M KCl fluid) post-triaxial test composition was 15±0.5% quartz, 2±1% pyrite, 5±2% calcite, 5±0.4% plagioclase, 4±0.7% K-feldspar, 7±0.5% kaolinite, 36±14% illite/mica, 24±10% smectite and 5±2% chlorite.

The average (3M KCl, 10^{-5}M KOH fluid) post-triaxial test composition was 14% quartz, 2±0.7% pyrite, 8±2% calcite, 4% plagioclase, 3±0.7% K-feldspar, 7% kaolinite, 43±6% illite/mica, 17±7% smectite and 4±1% chlorite.

The (4M NaCl fluid) post-triaxial test composition was 12% quartz, 6% pyrite, 6 calcite, 4% plagioclase, 3% K-feldspar, 8% kaolinite, 8% illite/mica, 48% smectite and 7% chlorite.

Whilst Test 8, which used 4M NaCl pore fluid, retained mineral abundances within the error margin on each mineral's pre-test mean (apart from quartz which was only

1% below), the other tests showed significant variation. The largest change was in the relative abundances of illite/mica and smectite. In the pre-test material illite comprised 13±5% of the North Sea mudstone, whereas following the 4M KCl pore fluid triaxial tests (Tests 1,2,3,4 and 5) this increased to 36±14% and following the 3M KCl, 10^{-5}M KOH pore fluid triaxial tests (Tests 6 and 7 – Chemical Test) this figure increased to 43±6%. 43±6% was the initial abundance of smectite in the pre-test material which decreased to 24±10% following the 4M KCl pore fluid triaxial tests and 17±7% the 3M KCl, 10^{-5}M KOH pore fluid triaxial tests.

Normality and equal variance of the datasets were tested prior to running two-sample t-tests. This was chosen, as opposed to paired t tests, as although the pre-test plugs and slices provided data on the pre-test material, direct before and after measurements on the same section of mudstone were obviously not possible due to the destructive procedures of the property analyses. The tests showed the difference in smectite content following the 3MKCl with 10^{-5}M KOH fluid tests (Test 7 – the chemical compaction simulation, Tests 6 and Test A) to be statistically significant at the 95% confidence level (95% CI for difference:(17.69, 29.69) and P-Value = 0.000). Following the Mechanical Test, statistical testing determined that it had not altered the smectite content at the 95% confidence level (95% CI for difference:(-15.36, 2.24) and P-Value = 0.134). This gave an initial positive indication of smectite illitization in the K-rich pore fluid tests. However, analysis of (Na-exchanged) clay fraction XRD data and CEC measurements shows that the difference in modelled illte/mica and smectite abundances does not represent true illitization, merely exchange with potassium.

3.3.3 Clay Fraction X-Ray Diffraction (XRD)

3.3.3.1 Pre-Test Clay Mineralogy

Following optimization of preparation procedures (Chapter 2), the <2μm fraction of the pre-test material was analysed using XRD.

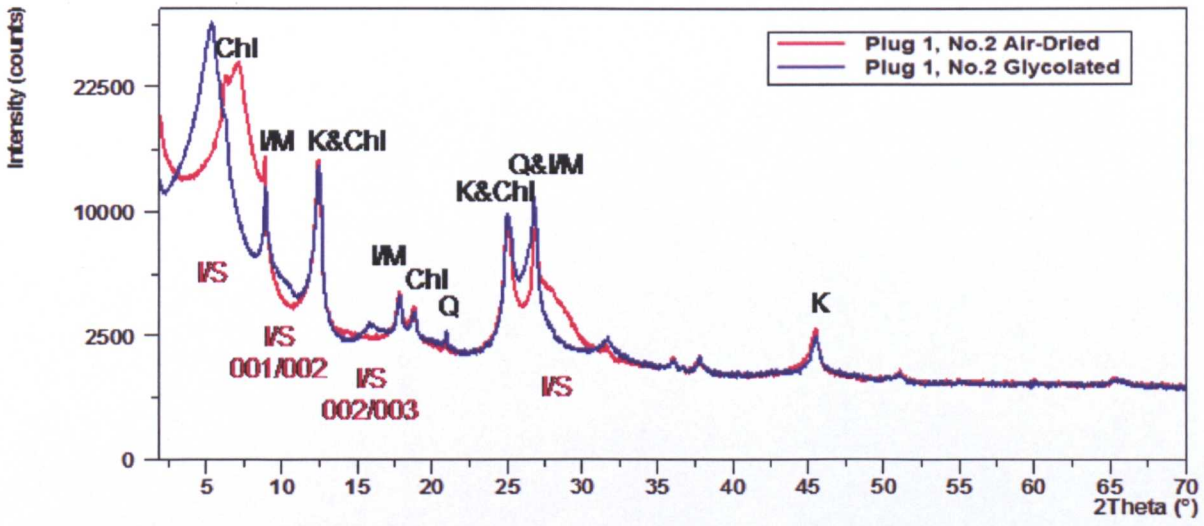

Figure 3.31 Pre-test example diffraction pattern for sample Plug 1, No. 2 following air-drying and glycolation. I/S mixed layer clay peaks are labelled, as are the other minerals present in the clay fraction – illite/mica (I/M), kaolinite (K) chlorite (Chl) and a small amount of quartz (Q).

From this data, the illite% in I/S mixed-layer clays was calculated from the position of the I/S 002/003 peak in the glycolated state as described in Chapter 2 and is displayed in Table 3.10.

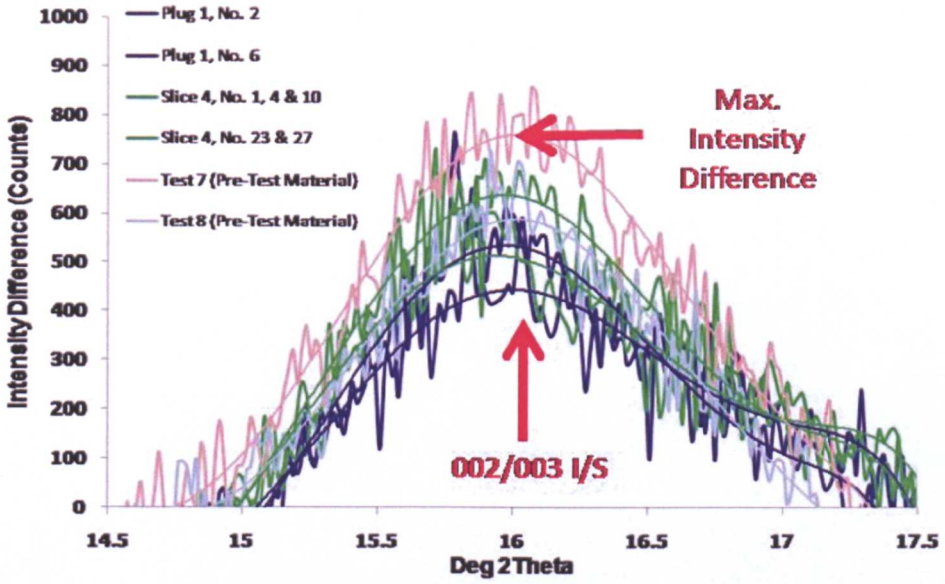

Figure 3.32 Difference plots between the air-dried and glycolated intensities for pre-test samples over the I/S 002/003 peak fitted with 6th order polynomials The position of maximum intensity difference was used to calculate I% in I/S.

Sample	Illite % in I/S
Plug 1 No. 2	29
Plug 1 No. 6	30
Slice 4 No. 1, 4 & 16	26
Slice 4 No. 23 & 27	32
Test 7Plug (Pre-Test material)	28
Test Plug 8 (Pre-Test material)	27

Table 3.10 Calculated illite% in I/S mixed-layer clays in pre-test material.

The average I% in I/S is 29±2%. The samples analysed included two sections from the bedding perpendicular plug and two from the bedding-parallel slice analysed in the bulk fraction XRD measurements. It also included slices removed from the top of the plugs that underwent Tests 7 and 8 (the Chemical and Mechanical Tests) as they were taken from different sections of the original 1m core. The results show that

there is little variation in the metre of core as the latter two measurements are within the range recorded within the slice and plug which is only 6%.

I/S mixed-layer clay reference patterns were modelled in the bulk fraction quantification procedures, but were found to produce lesser fits. Yet I/S is identified in the clay fraction. The reason for this is likely to be that the reference pattern for I/S was for an illitic I/S (~70% I in I/S) and the data above shows that the North Sea mudstone contains smectite-rich I/S which is likely to have been quantified as bulk smectite.

3.3.3.2 Post-Test Clay Mineralogy

Samples underwent identical preparations for clay fraction XRD post-test and the diffraction patterns are displayed below.

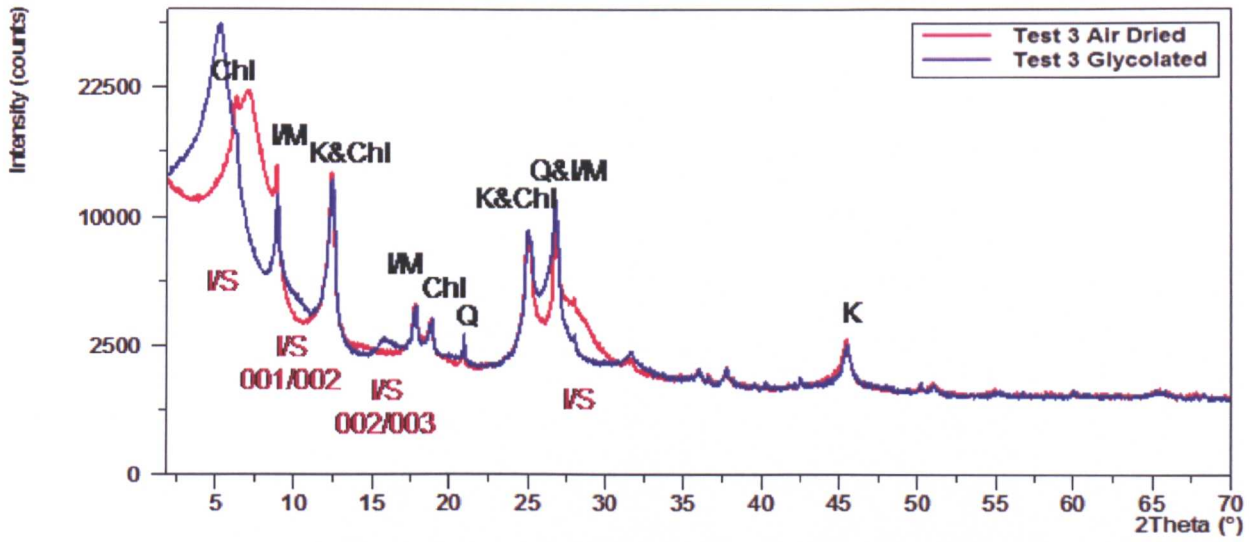
Test 3 Air Dried
Test 3 Glycolated
Intensity (counts)
22500
10000
2500
0
Chl
I/M
K&Chl
Q&I/M
K&Chl
I/M
Chl
Q
K
I/S
I/S
001/002
I/S
002/003
I/S
5
10
15
20
25
30
35
40
45
50
55
60
65
70
2Theta (°)

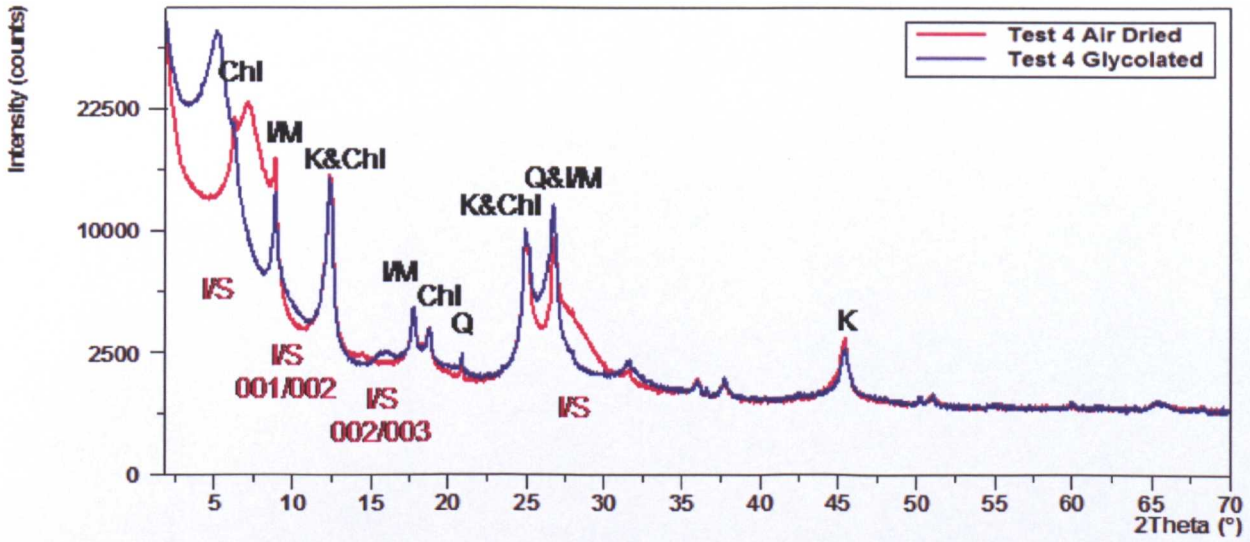
Test 4 Air Dried
Test 4 Glycolated
Intensity (counts)
22500
10000
2500
0
Chl
I/M
K&Chl
Q&I/M
K&Chl
I/M
Chl
Q
K
I/S
I/S
001/002
I/S
002/003
I/S
5
10
15
20
25
30
35
40
45
50
55
60
65
70
2Theta (°)

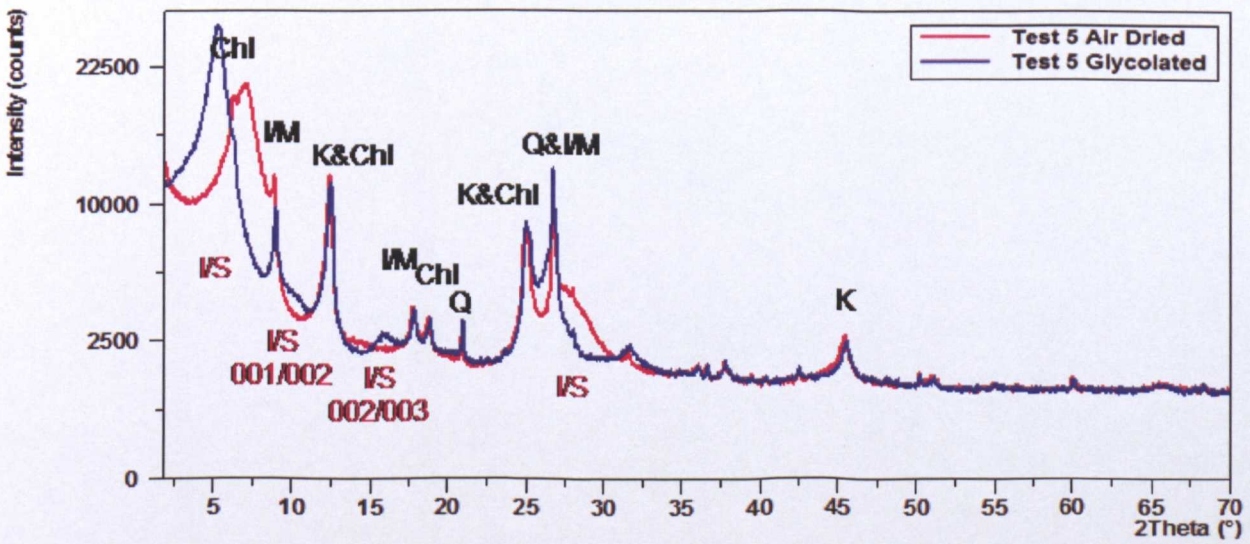
Test 5 Air Dried
Test 5 Glycolated
Intensity (counts)
22500
10000
2500
0
Chl
I/M
K&Chl
Q&I/M
K&Chl
I/M
Chl
Q
K
I/S
I/S
001/002
I/S
002/003
I/S
5
10
15
20
25
30
35
40
45
50
55
60
65
70
2Theta (°)

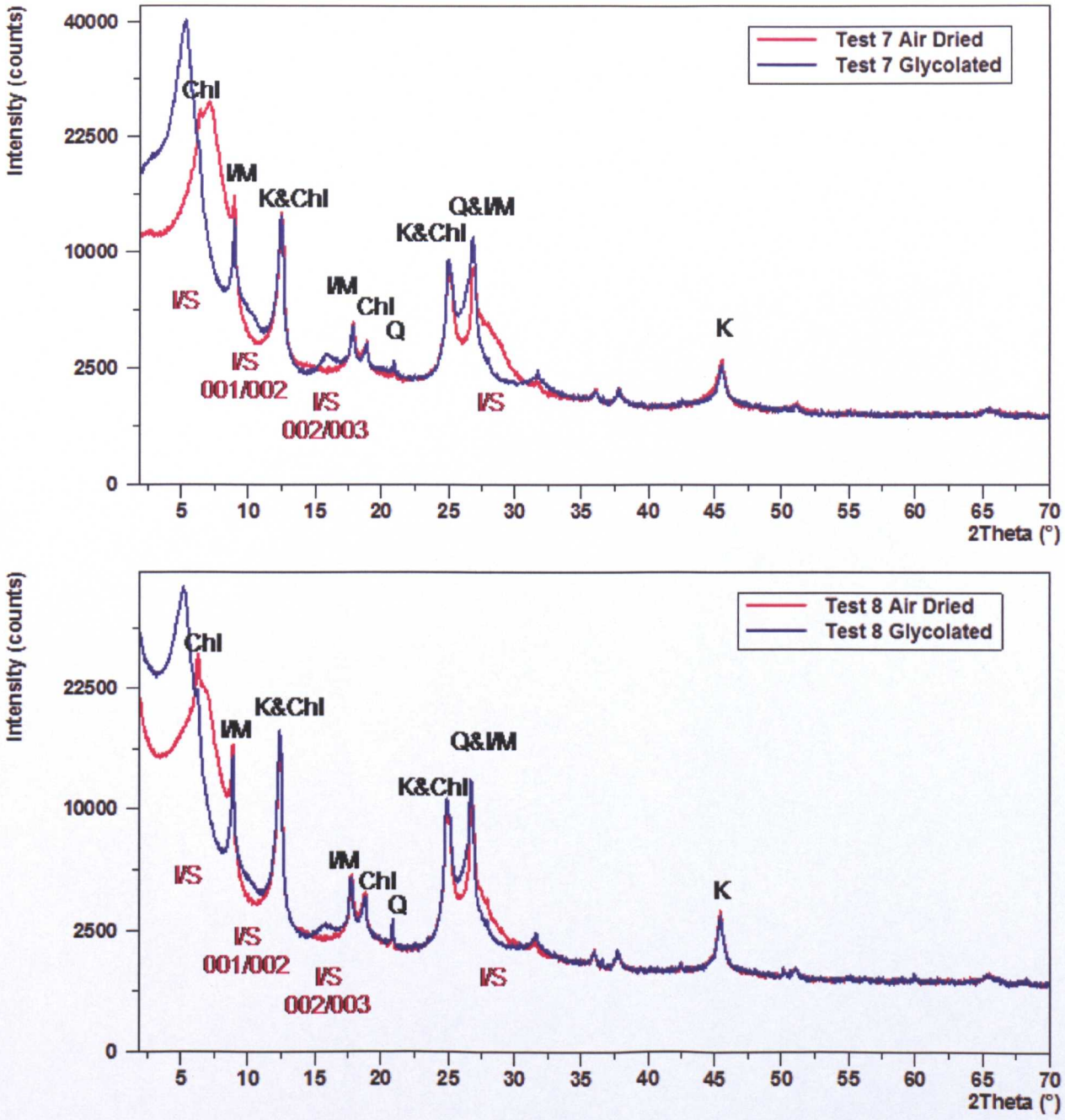

Figure 3.33 Post-test diffraction patterns following air-drying and glycolation. I/S mixed layer clay peaks are labelled, as are the other minerals present in the clay fraction – illite/mica (I/M), kaolinite (K) chlorite (Chl) and a small amount of quartz (Q).

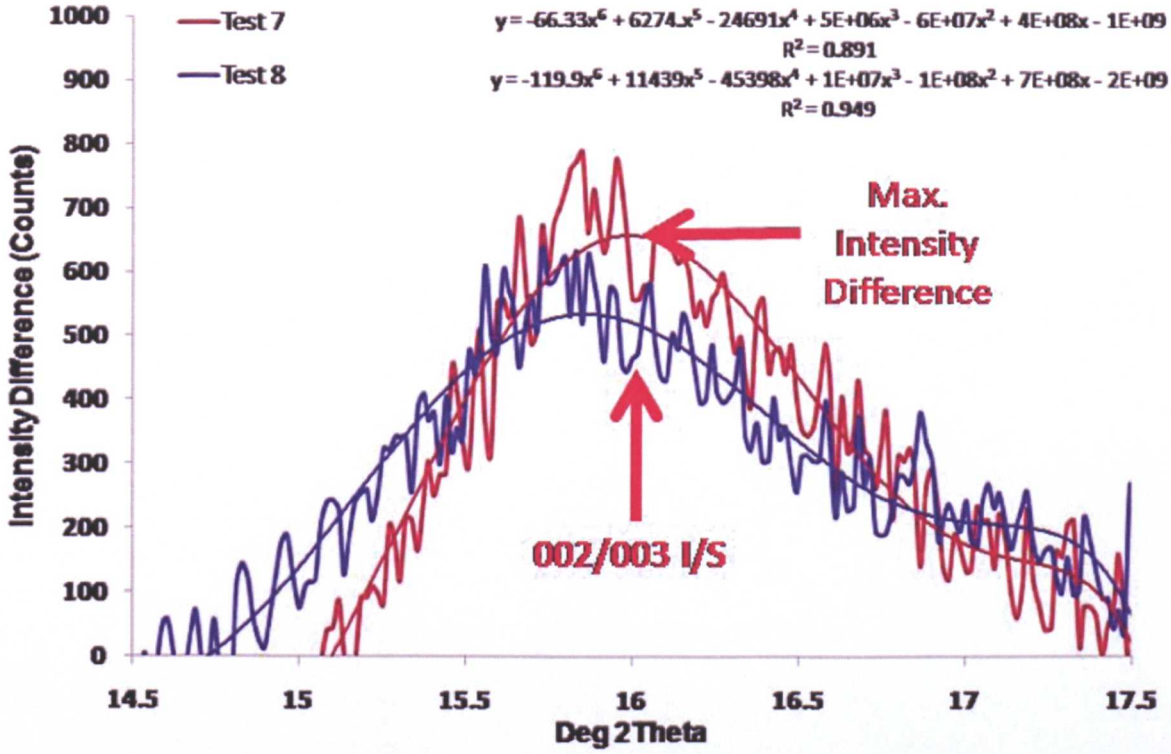

Figure 3.34 Difference plots between the air-dried and glycolated intensities for post-test 7 and 8 samples over the I/S 002/003 peak fitted with 6th order polynomials The position of maximum intensity difference was used to calculate I% in I/S .

Sample	% Illite in I-S
Test 3	29
Test 4	35
Test 5	28
Test 7	31
Test 8	23

Table 3.11 Calculated illite% in I/S mixed-layer clays in pre-test material.

Illite % in I/S is within the error of the mean of the pre-test material in Tests 3, 5 and 7 (Chemical Test). It is above the error margin in Test 4 and below in Test 8 (Mechanical Test). However, statistical testing the I% in I/S on post-test material from Tests 3, 4, 5, 7 and 8 was found to show no statistically significant change

given the range of pre-test values (95% CI for difference: (-5.10, 4.04) and P-Value = 0.798).

Initial XRD runs on the separated fine fraction of the compacted mudstone material gave similarly positive indications of illitization to the bulk fraction measurements, where a greatly reduced glycolated smectite peak is found in comparison to that of the pre-test material. This was only in indication runs where the samples from the tests using K-rich pore fluid most likely still contained K exchanged in the smectitic clay inter-layer as all samples (pre-test material and tested) had only been subject to sodium hexmetaphosphate used as a dispersant and the samples rinsed with weak NaCl. However, when a thorough exchange with Na-rich fluid had been completed for all samples (Chapter 2) there was no change in the intensity of the glycolated smectite peaks. Because of this, the I% in I/S could be calculated from 23-35% for the tested material compared to 26-32% in the pre-test mudrock. It is therefore concluded from the fine fraction data that no significant illitization has taken place due to the tests.

The only notable change that can be interpreted from the fine-fraction results is a decrease in the 002 chlorite peak/ 001 kaolinite peak relative to illites 001 peak at 10Å in tests 4 (the high stress variable test) and 7 (the chemical test). The ratio is 1.07 in test 4 and 0.97 in test 7 compared with an average of 0.85 (range: 0.81-0.89) in the uncompacted pre-test material. Reduction of the 7.10Å peak can indicate a decreased iron content in chlorite. This change is only very slight and bulk fraction data does not indicate a change in the overall abundance of chlorite or kaolinite so its relevance is not certain, but a change in the chlorite chemistry cannot be ruled

out. This could have provided some of the additional Fe in the fluid samples whilst it is known there was increased Mg content in the artificial fluid (from the sample or the system) available to the sample

3.3.4 Cation Exchange Capacity (CEC) and Surface Area

3.3.4.1 Pre-Test CEC and Surface Area

Pre-test samples were prepared for cation exchange capacity measurements as detailed in Chapter 2 and the results shown below.

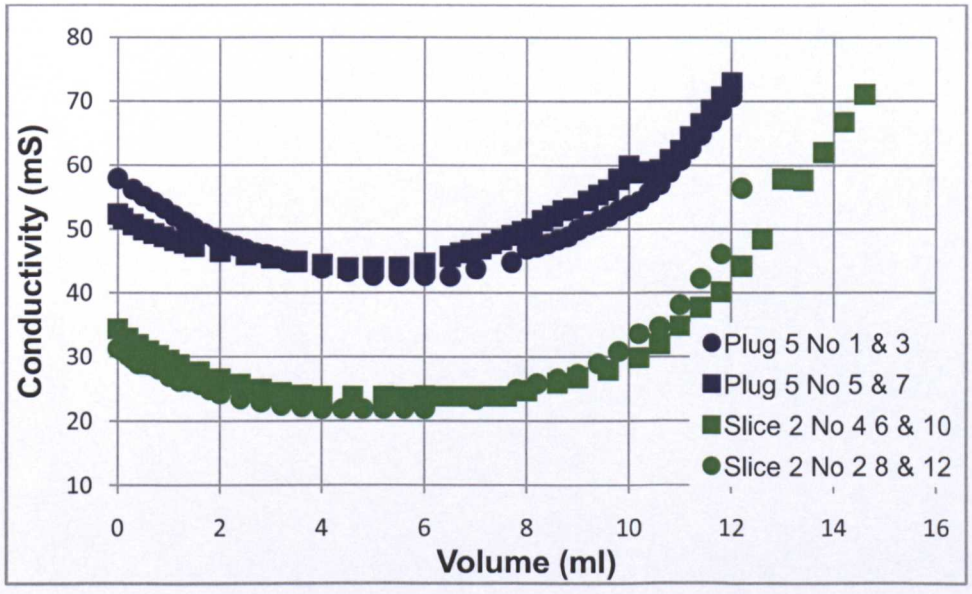

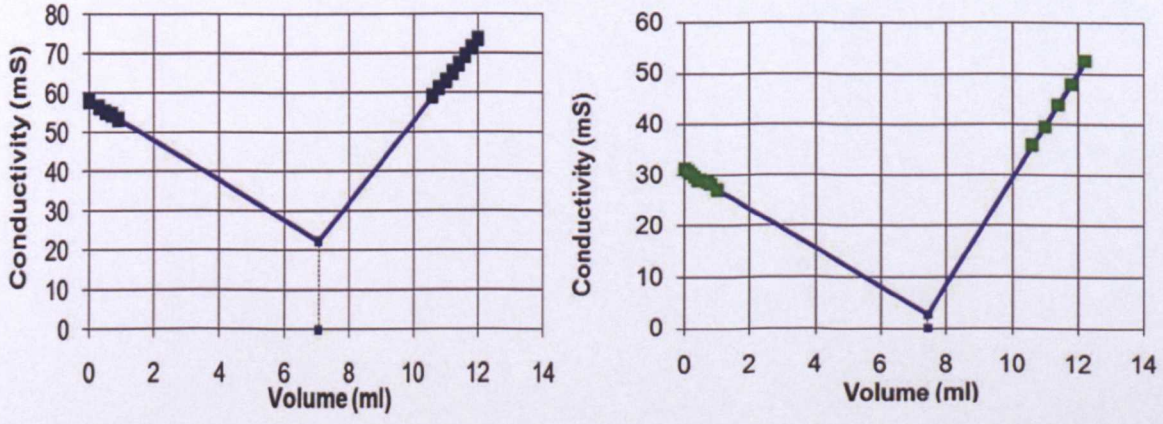

Figure 3.35 Conductivity with volume $MgSO_4$ added and examples of corrected titration data for Plug 5 No 1 & 3 and Slice 2 No 2 8 & 12 with intercept for CEC calculations

Sample	Intercept *(ml)*	CEC *(meq/100g)*
Plug 5 No. 1 & 3	7.07	19.8
Plug 5 No. 5 & 7	7.26	21.4
Slice 2 No. 4, 6 & 10	8.14	21.9
Slice 2 No. 2, 8 & 12	7.42	21.7

Table 3.12 Pre-test cation exchange capacity (CEC) experimental data

These values appear relatively low for smectite-rich material and are more in the range of illite clays. However, these tests were not carried out on fractionated clays, but the bulk sample and this will influence the values which range from 19.9-21.9meq/100g with an average of 21.2 ± 0.9meq/100g.

3 sections of the untested mudstone (from a section adjacent to the plugs and slices cut for the other tests) were sent to an external contractor (En Laboratories) and following dielectric constant measurements (DCM – see Chapter 2) specific surface area was calculated.

Sample	Aliquot 1		Aliquot 2		Surface Area Average (m^2/g)
	D.C.M.	S.A. (m^2/g)	D.C.M.	S.A. (m^2/g)	
A	64.80	235	66.10	243	239
B	75.41	307	71.70	281	294
C	68.44	259	70.40	272	266

Table 3.13 Dielectric constant measurements (DCM) on pre-test material and calculated surface areas (SA).

Duplicate DCM measurements made and were within 10% for all samples. Mineral classification information supplied by the contractor showed the smectite to be associated with values of 600-800m^2/g, illites 80-120 m^2/g but also listing values associated with illite-smectite mixed layer clays as having values between 200-250 m^2/g. The other components of the rock have minimal surface area by comparison, so the bulk rock SA of with and average 266±28m^2/g indicates I-S clays are an important component of the initial mudrock.

3.3.4.2 Post-Test CEC and Surface Area

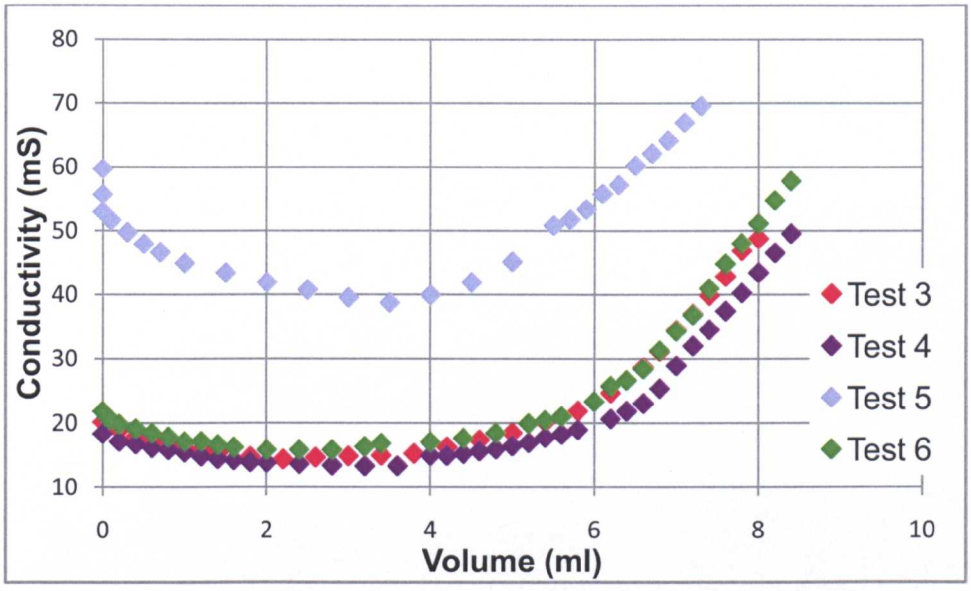

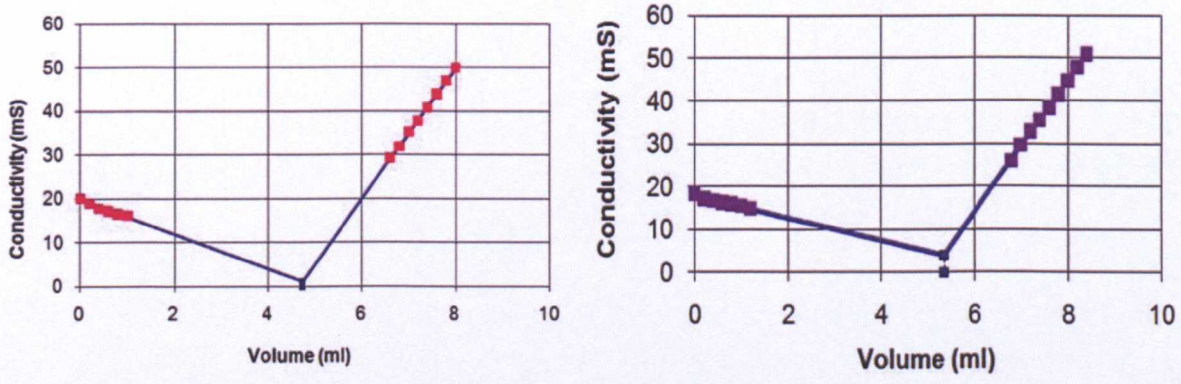

Figure 3.36 Conductivity with volume $MgSO_4$ added and examples of corrected titration data for Test 3 and Test 4 material with intercept displayed for CEC calculations.

Sample	Intercept *(ml)*	CEC *(meq/100g)*
Test 3	4.73	21.7
Test 4	5.35	24.1
Test 6	4.97	22.6

Table 3.14 Post-test cation exchange capacity (CEC) experimental data

CEC measurements carried out on variable test material show no real change in the ability to exchange cations post-test. Although the values for Tests 4 and 6 are outside of the pre-test range, the differences are not on a scale indicating changes to the clay mineralogy. They are most probably linked to the range in smectite content found in the bulk fraction XRD measurements carried out on a greater number of samples.

Sample	Aliquot 1		Aliquot 2		Surface Area Average (m^2/g)
	D.C.M.	S.A. (m^2/g)	D.C.M.	S.A. (m^2/g)	
Test 7	67.40	252	72.65	288	270
Test 8	71.67	281	68.43	259	270

Table 3.15 Dielectric constant measurements (DCM) on post-test material and calculated surface areas (SA).

The average surface area measurements of 270.0 m^2/g indicate smectitic I-S as the dominant clay component in the high stress chemical test (test 7) and mechanical test (test 8) material. Values lie within the range measured on the untested mudstone (239.2 - 294.4 m^2/g). Although the wide range means change due to the triaxial tests cannot be ruled out, there has been no statistically significant alteration. This supports the fine-fraction XRD results.

3.3.5 Microscopy and EDX

3.3.5.1 Pre-Test Microscopy and EDX

Thin sections of pre-test material were prepared as described in 2.3.7. As with the Malay Basin samples, discussed in Chapter 4, preliminary observations were made using transmitted-light microscopy. However, the fine-grained, smectitic nature of the North Sea mudstones meant that this method met with less success than in the coarser Malay cuttings.

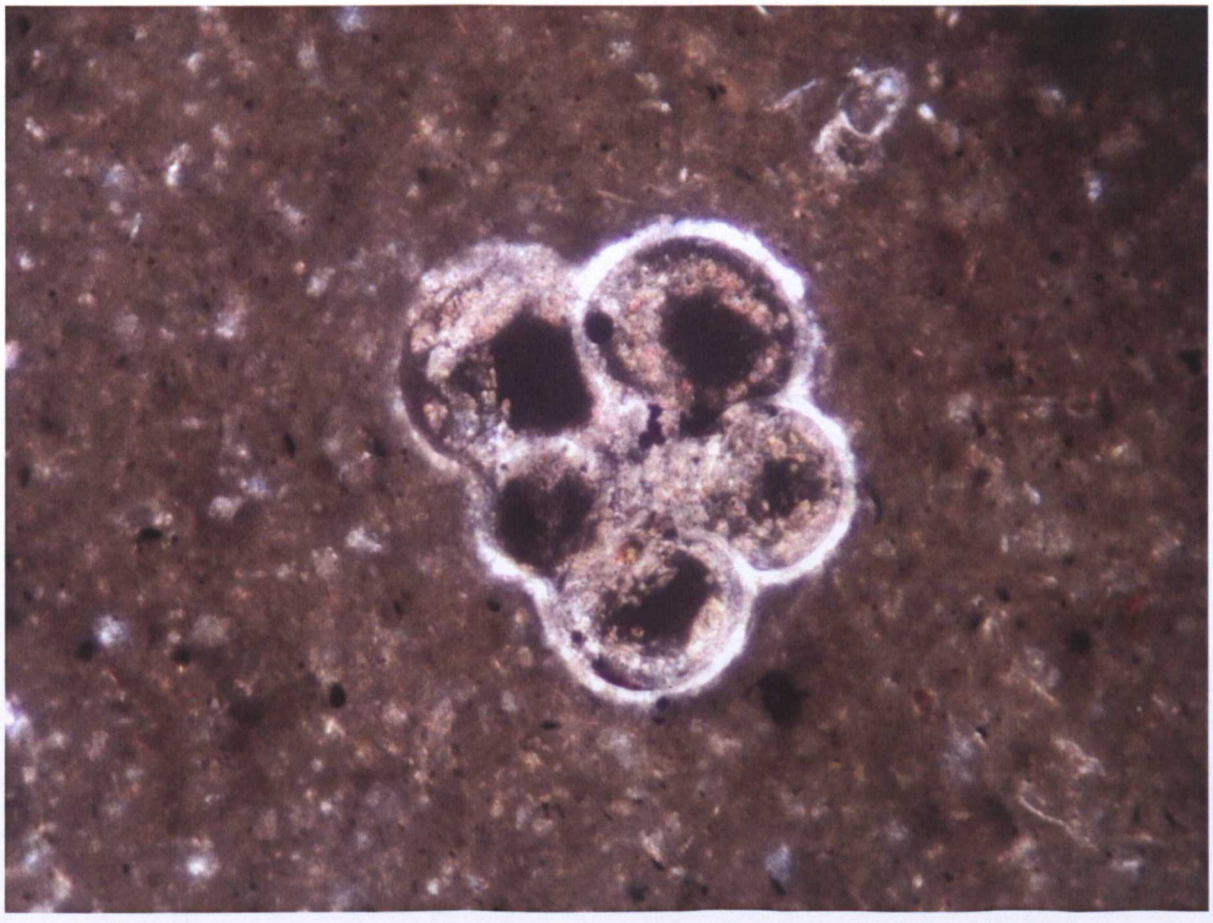

Figure 3.37 Transmitted-light microscopic image maximum zoom, magnified under PO A20/ 0.40 160/0.17 lens showing a calcitic test, with pyritization in a fine, mud-rich matrix.

Figure 3.37 shows a calcitic fossil test, identified by its high, 4th order birefringence with opague pyrite grains both inside and outside the shell. Fossils and pyrite were observed in many of the slides, but they were amongst the only coarse features along with selected feldspar and quartz grains, where even the latter were relatively

fine grained. Little information could be gained on the nature of the matrix as discussed in 2.3.7 and therefore the slides were prepared for electron microscopy, particularly BSEM and EDX.

BSEM imaged the coarser features with more clarity and several of the calcitic tests were identified as benthic forams. Pyrite is distributed throughout the matrix, occasionally replacing fossil material or infilling associated voids, indicating a diagenetic origin (Figure 3.38). Fossil voids and well preserved tests are identified in several slides and support the information identifying the mudstone as not having been previously exposed to high effective stress/deep burial. However, not all tests remain intact (Figure 3.42).

The matrix is phyllosilicate-rich with EDX spectra identifying the presence of Na, Mg and K- aluminosilicates. Fe and Ca peaks were also associated with Si and Al and may form part of the clay component and/or may be related to pyrite and calcite with Si and Al responses due to the spot size taking in abundant, surrounding clay matrix. This matrix appears very fine grained and well sorted apart from the coarser shells (and diagenetic pyrite). Feldspar and quartz form fine, silt sized grains (Figure 3.42) and are matrix supported.

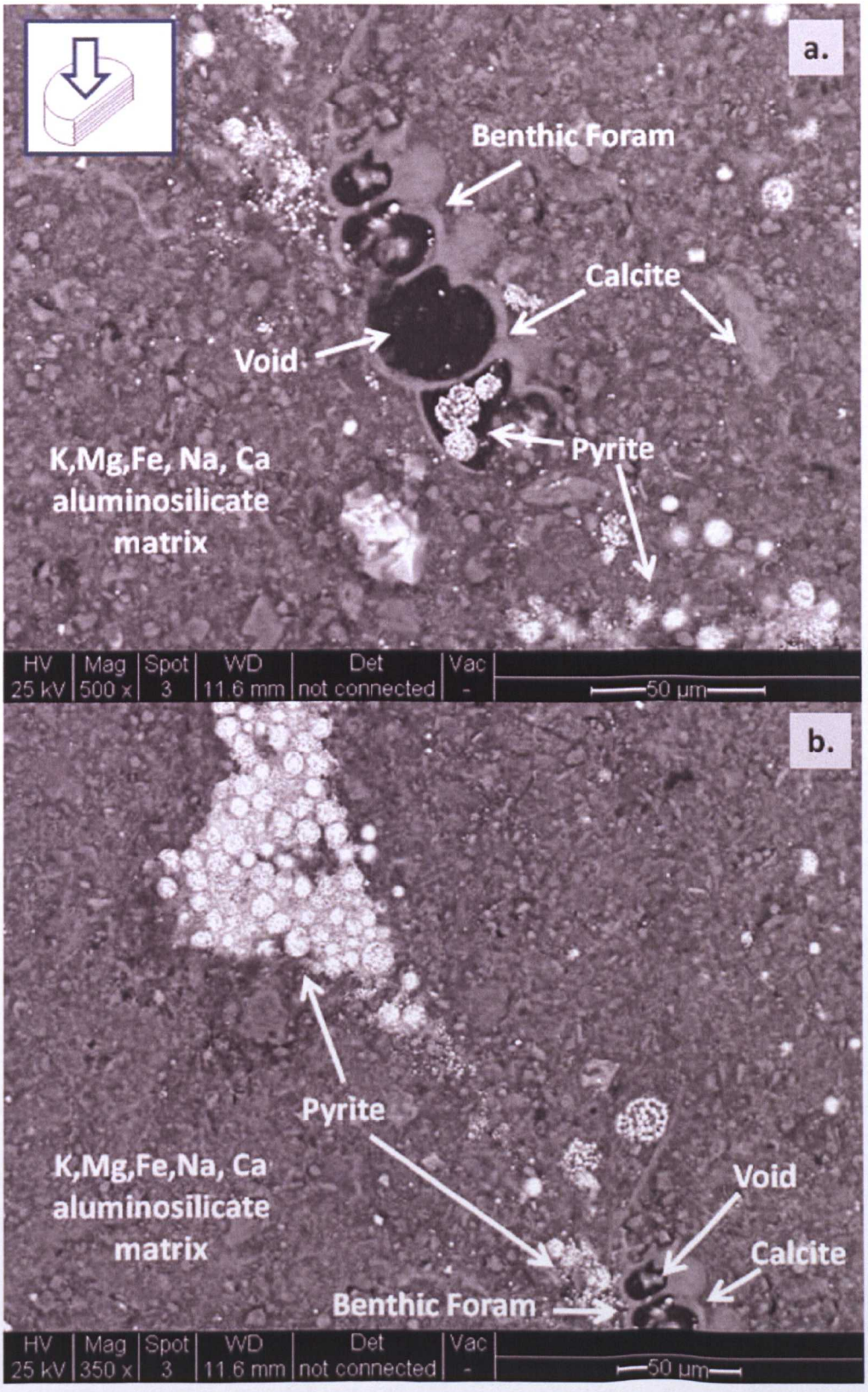

Figure 3.38 Pre-Test Plug 4, No.8, bedding parallel, plan section.

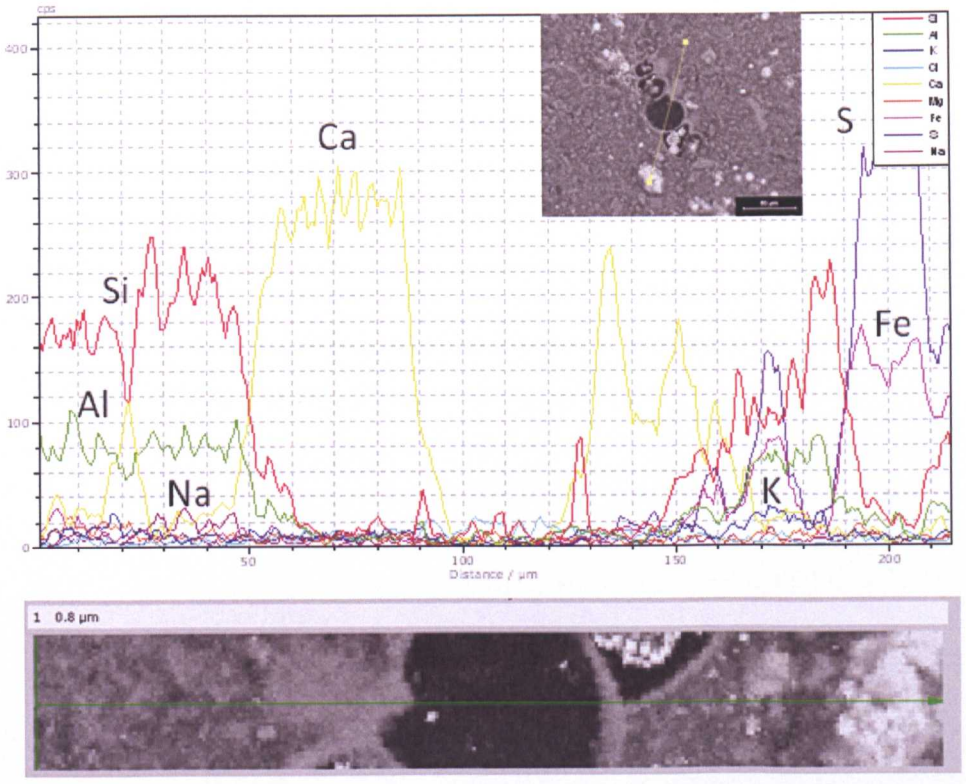

Figure 3.39 Pre-tst Plug 4 No.8, Line scan of multiple elements spectra capturing grain composition.

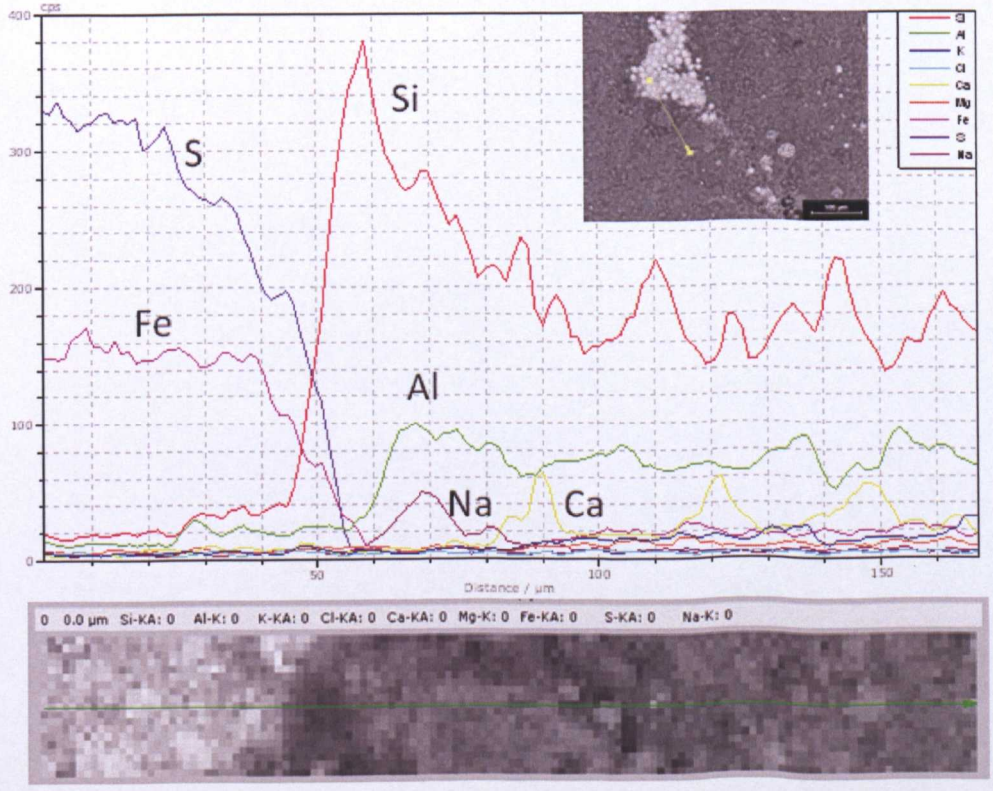

Figure 3.40 Pre-test Plug 4 No.8, Line scan of multiple elements spectra capturing grain to matrix composition

In bedding perpendicular sections, allowing a cross-sectional view through bedding some of the larger K-phyllosilicates are seen to be elongate mica grains. This means that not all of the 10Å material recognized in the XRD analyses (3.3.2) is part of the clay fraction. Micas could be described as forming a weak fabric with grains lying parallel with the overall bedding of the core in some areas. However, there does not appear to be any clear fabric developed in the clay matrix (Figure 3.41). These are qualitative assessments and required further quantification (addressed later). Also, often associated with the elongate mica grains, though not in the example displayed in Figure 3.41, are elongate voids/cracks. These features may be associated with slide preparation procedures or they may be real characteristics of the unloaded mudstone following its retrieval from the subsurface or coring of the plugs. CT scans of the intact plugs tend to rule out the first option as internal cracks are occasionally observed prior to sectioning.

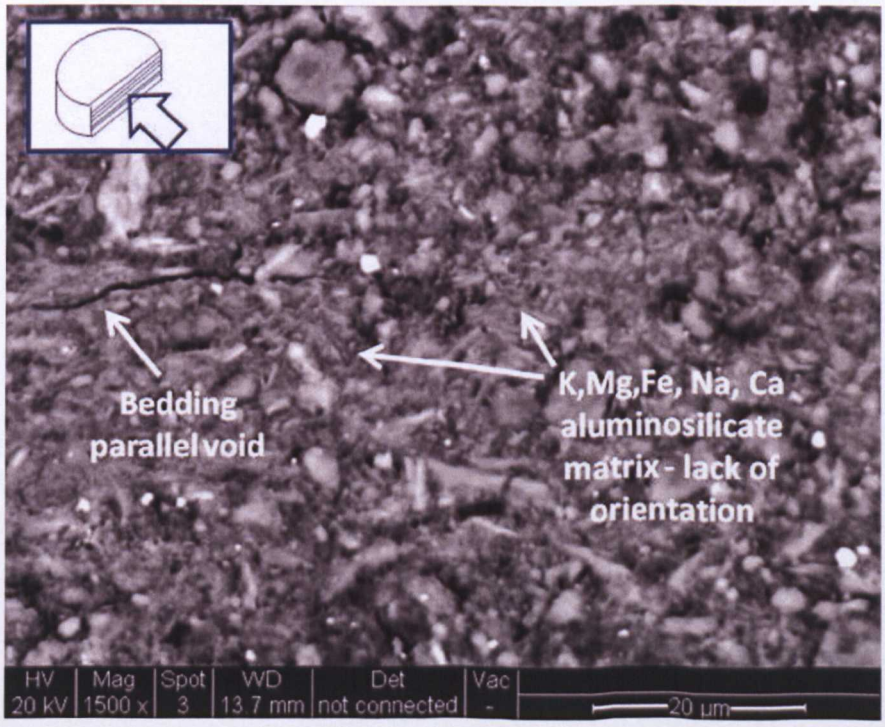

Figure 3.41 Pre-test Plug 4, no. 6, bedding perpendicular side section

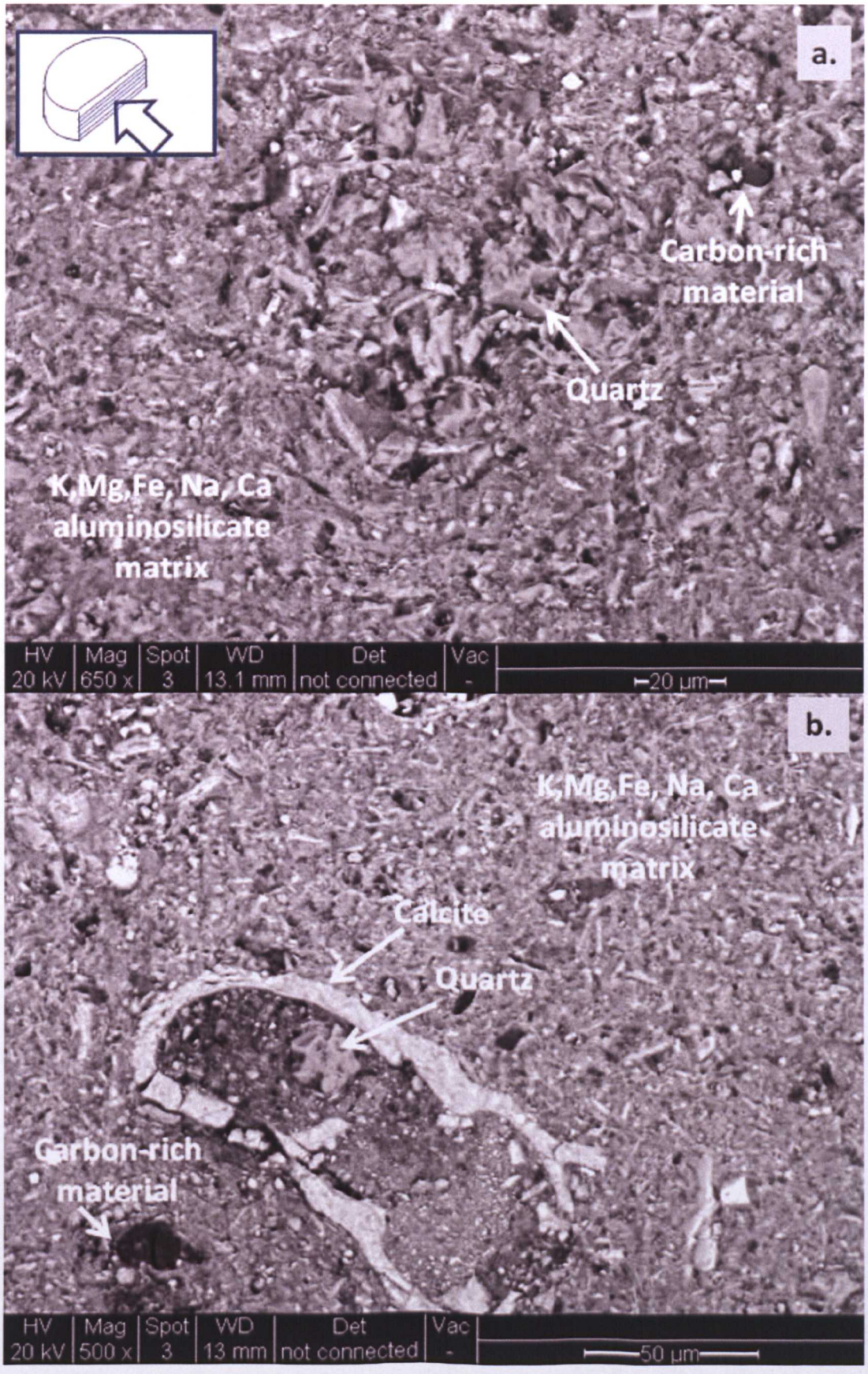

Figure 3.42 Pre-test Plug 4, No.4, bedding perpendicular - side section

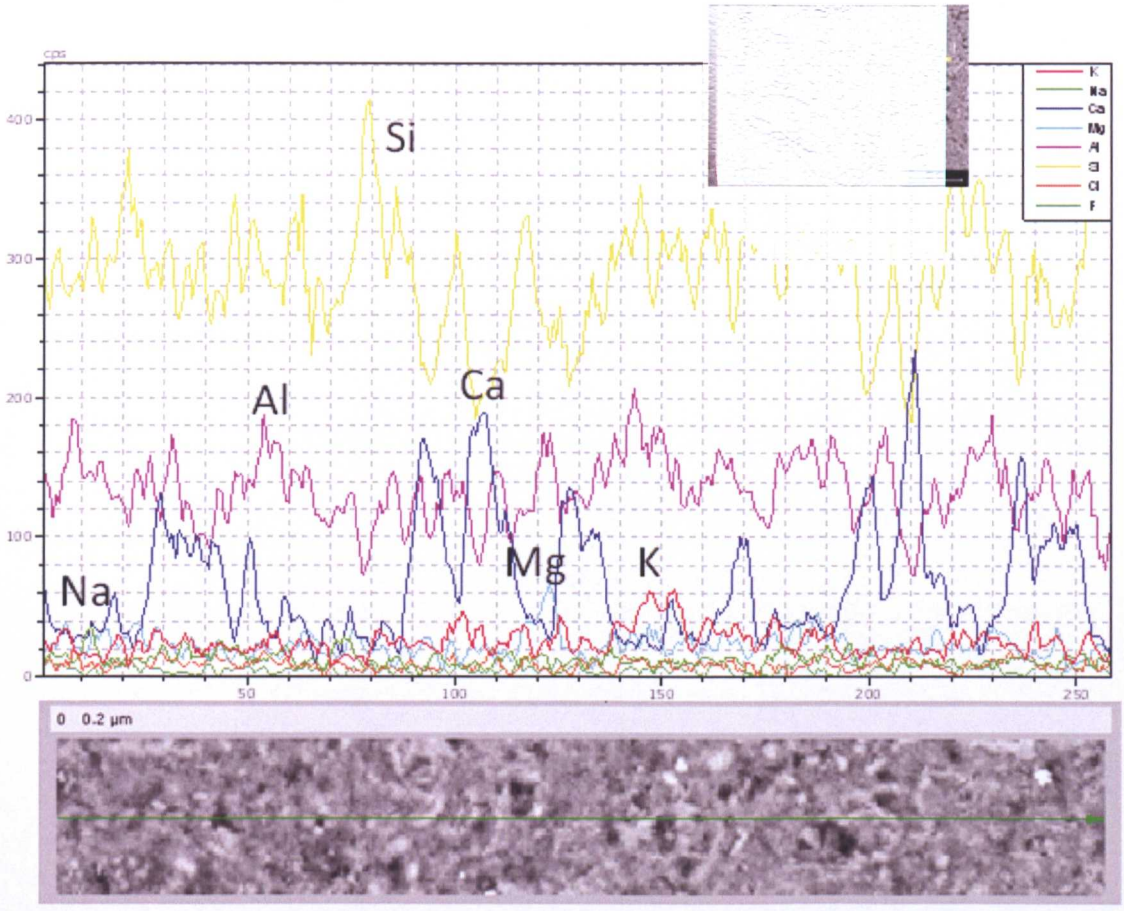

Figure 3.43 Pre-test Plug 4, No.4: Line scan of multiple elements spectra capturing matrix composition.

Occasional "dark" grains are observed in the matrix (Figure 3.42) and EDX showed this to be carbonaceous material, visible in spectra as counts elevated significantly higher than that of the carbon coating. This resulted in TOC measurements being taken to quantify any organic carbon in light of the organic material related compaction mechanisms identified in Johnson (1987).

3.3.5.2 Post-Test Microscopy and EDX

BSEM images and EDX analyses of post-triaxial test material showed many of the features of the original material left unchanged. Pyrite framboids and a

carbonaceous grain can be seen in Figure 3.44 which shows mudstone following Test 1.

These framboids can be seen infilling a calcitic foram, both the fossil and pyrite preserved from the pre-test material. However, what is also visible below the foram in the lower image (Figure 3.44) is a vein of solidified KCl solution, following what was presumably a plane of weakness between the fossil and the matrix. The curved nature of this boundary in cross-section appears compaction induced, around the harder, pyritised fossil although whether or not this occurred during the test or during its original burial is not known. Solidified KCl crystals were also found in Test 2 material. The "ramp-down" procedures were altered following these images being taken, so that in Tests 3-8 a pore pressure (plus axial and radial pressure) was maintained on the system as the cell temperature equilibrated with the reduced oven temperature at the end of each test. This was to maintain saturation and appears to have been successful as these veins of KCl were not found in later post-test material.

The KCl veins did indicate that the artificial pore fluid was finding its way into the matrix, but EDX analysis of the matrix indicated K-exchange into the clays had taken place. Element mapping confirmed that K was pervasive in the matrix following the tests (Figure 3.45) and line/ point spectra showed that it was associated with Si, Al and O as well as Mg and Fe. Cl was not generally found associated with K in test material from Test 3 onwards suggesting that K responses were not from emplaced KCl, but where it had exchanged into/onto the expandable clays.

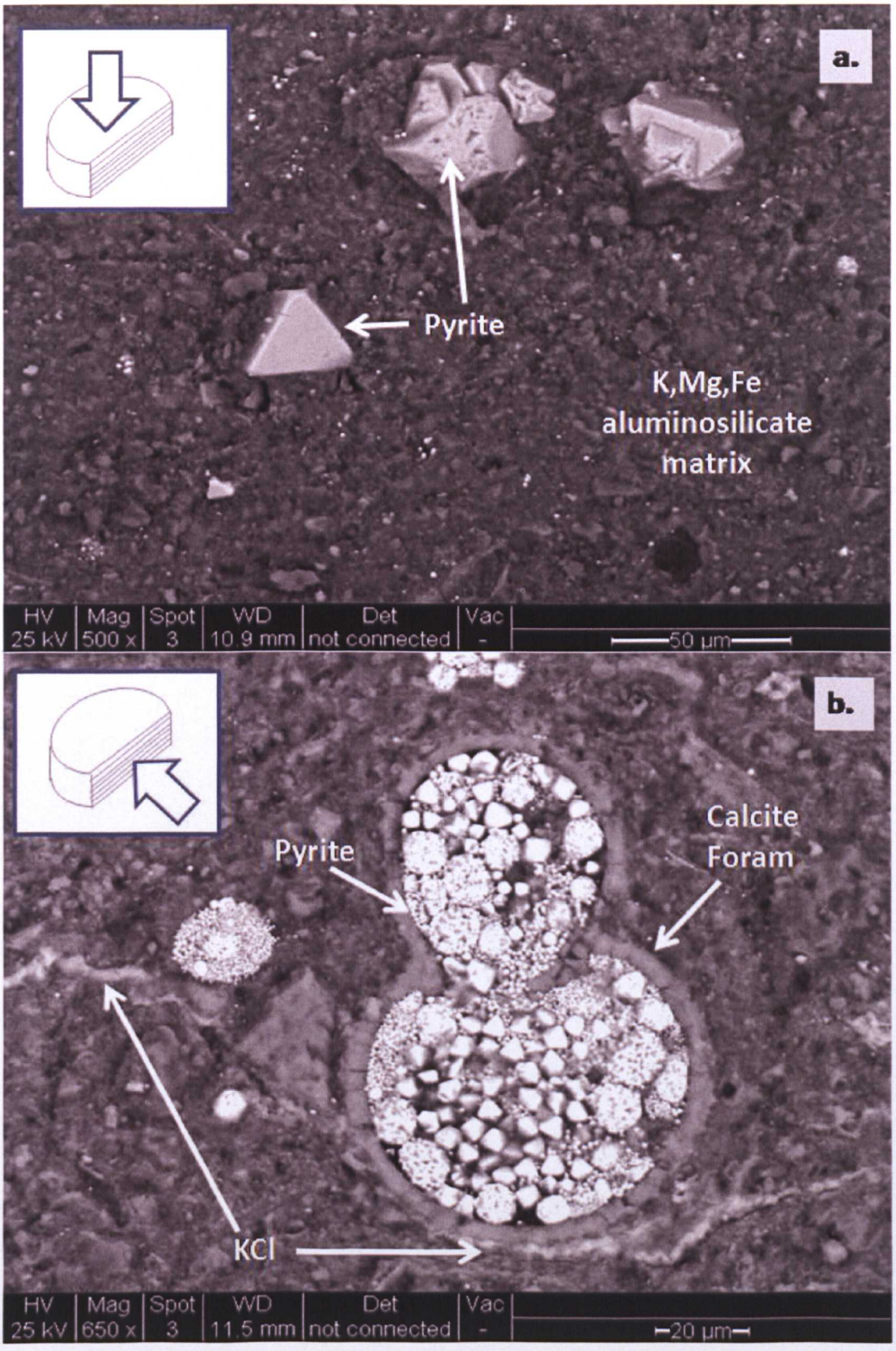

Figure 3.44 Post Test 1 material displaying bedding parallel and perpendicular - side section views at 500x and 650x magnification.

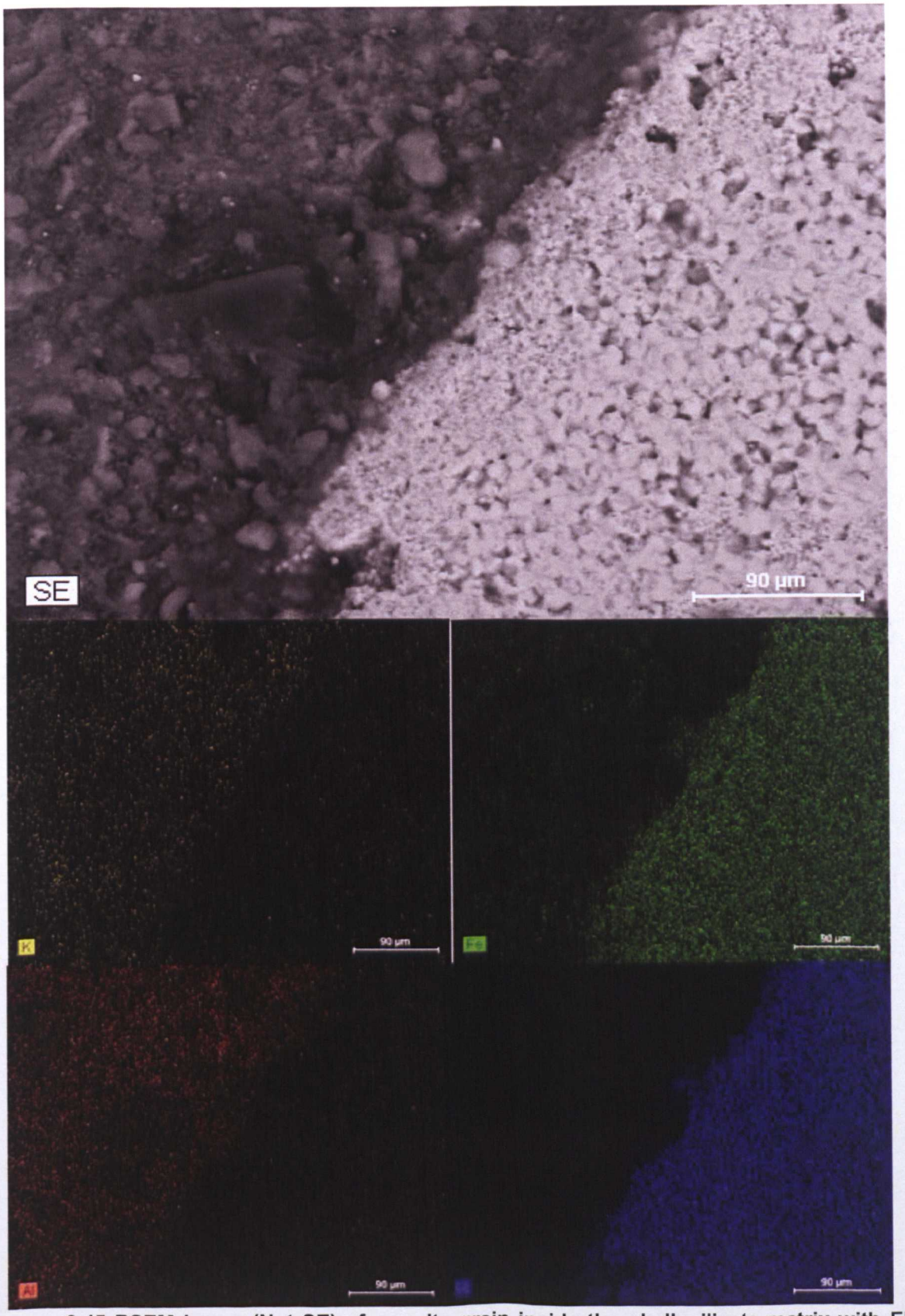

Figure 3.45 BSEM image (Not SE) of a pyrite grain inside the phyllosilicate matrix with EDX maps of potassium (K – yellow), iron (Fe – green), aluminium (Al – orange) and sulphur (S – blue). Matrix region displays higher density of K compared to Fe or S.

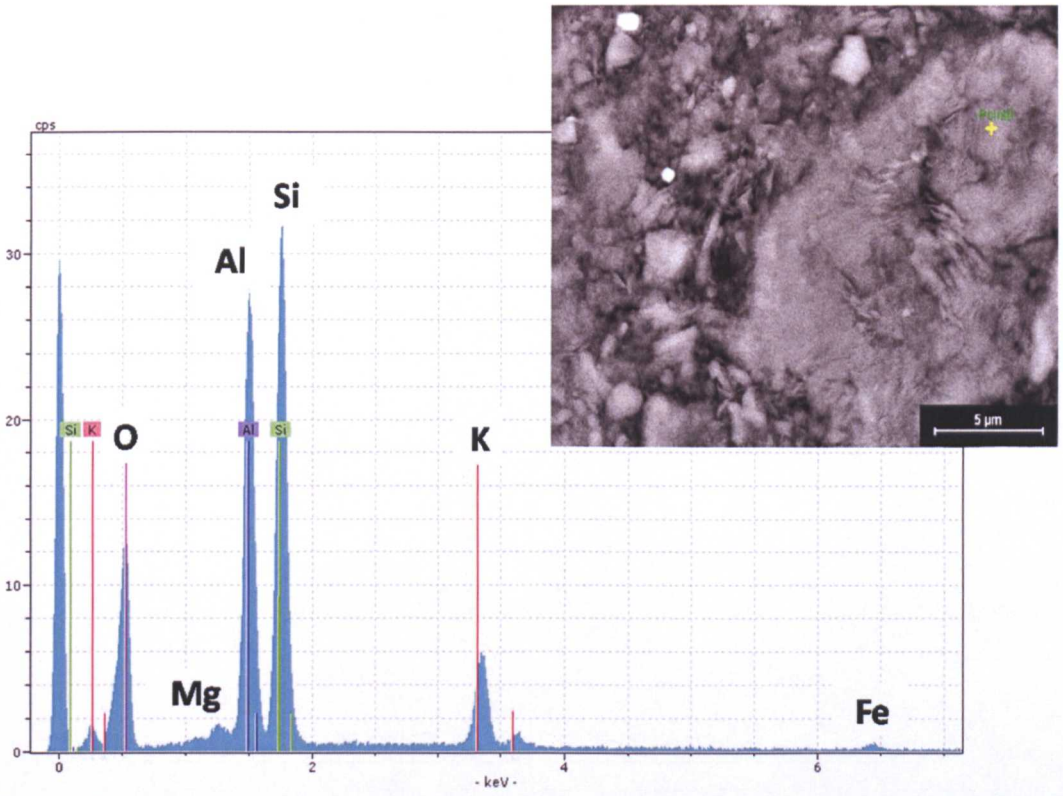

Figure 3.46 Test 7 plug material spectra showing the K-exchanged nature of the aluminosilicate.

The boundary between pyrite framboids and the aluminosilicate matrix can be seen in Figure 3.45. The element maps over this area show the dense Fe and S content of the pyrite, but also iron present in the matrix. However, the iron content of the matrix is lower than that of the other two elements mapped, K and Al. Figure 3.46 shows typical matrix point spectra for Test 7 (the Chemical Compaction Test) of a K-rich aluminosilicate. The Test 8 mudstone (Mechanical Compaction Test) was not dominated by Na exchange as appears to have occurred following the K-rich fluid tests. Figure 3.47 shows a typical response where although Na shows the highest counts, Ca, K, Mg and Fe are all still significant. However, Na is not always present in matrix EDX spectra following Test 8.

Al was used to distinguish the aluminosilicate areas as Si is more prevalent due to its presence in quartz also. Quartz appears to be unchanged by the tests, with fine, silt sized detrital grains randomly distributed through the matrix. One anomalous feature was identified in post-test material following Test 4. This was what appeared to be a quartz vein. In a section perpendicular to bedding, the side view of what appeared to be a linear feature was picked out by the crack along its upper boundary (due to slide prepartation difficulties resulting from the large difference in hardness between the minerals) (Figure 3.48). Given the lack of illitization and the timescales used in this test it appears unlikely that this feature was generated by the test, however, such features were not noted in the pre-test material. It could perhaps be the remnants of a much larger grain.

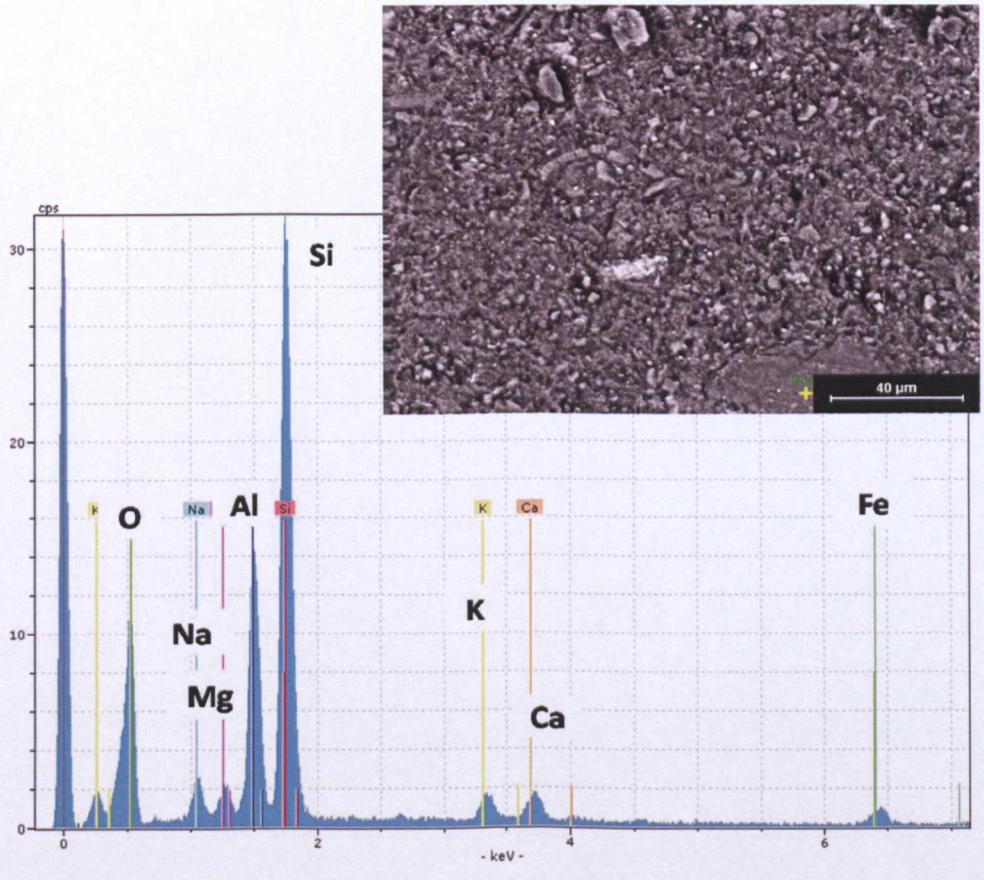

Figure 3.47 Test 8 spectra showing the varied elemental composition of the aluminosilicate matrix.

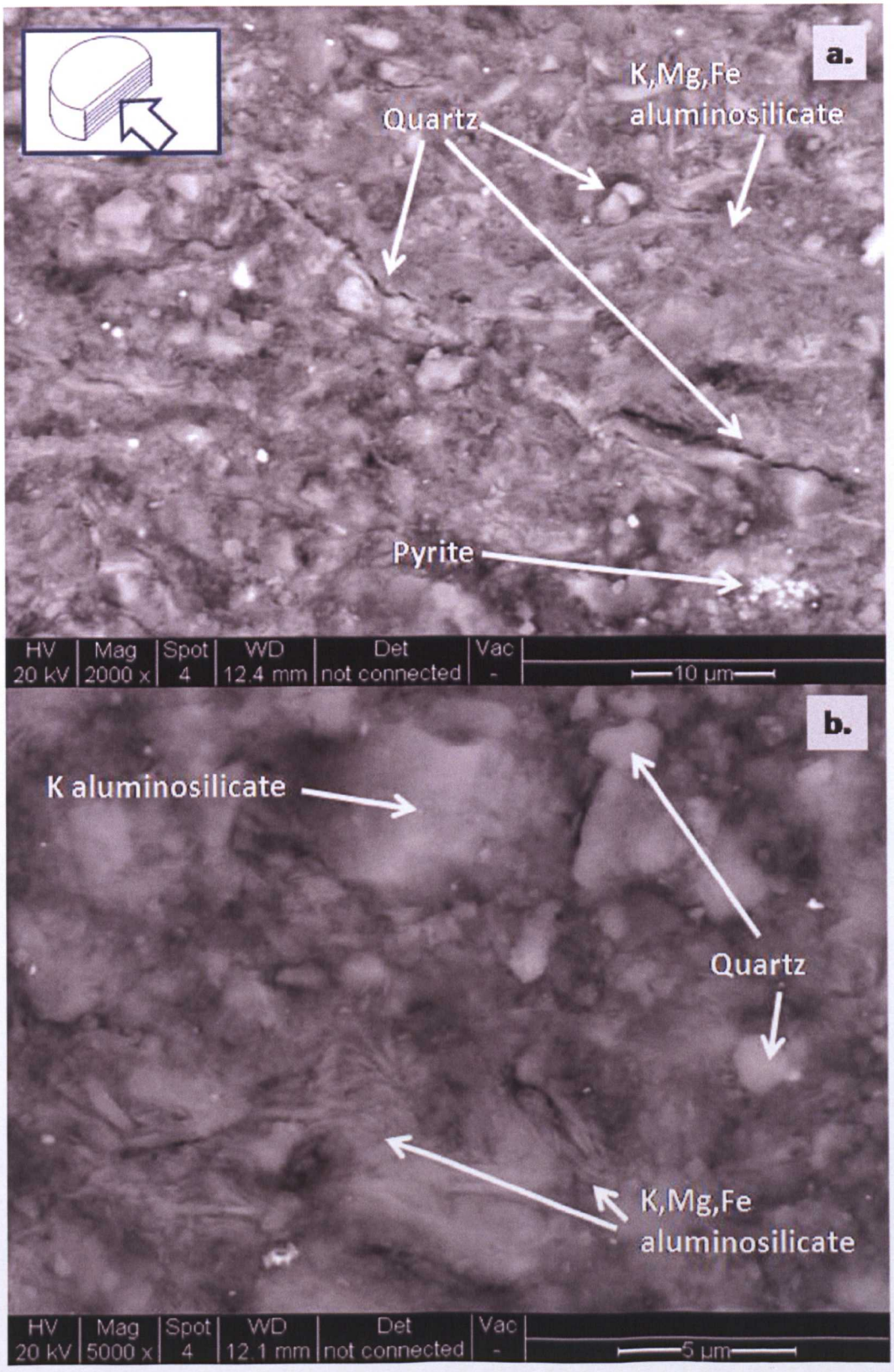

Figure 3.48 BSEM images of post-test 4 mudstone. Upper image shows the elongate quartz feature and lower image displays the fine, whispy aluminosilicates.

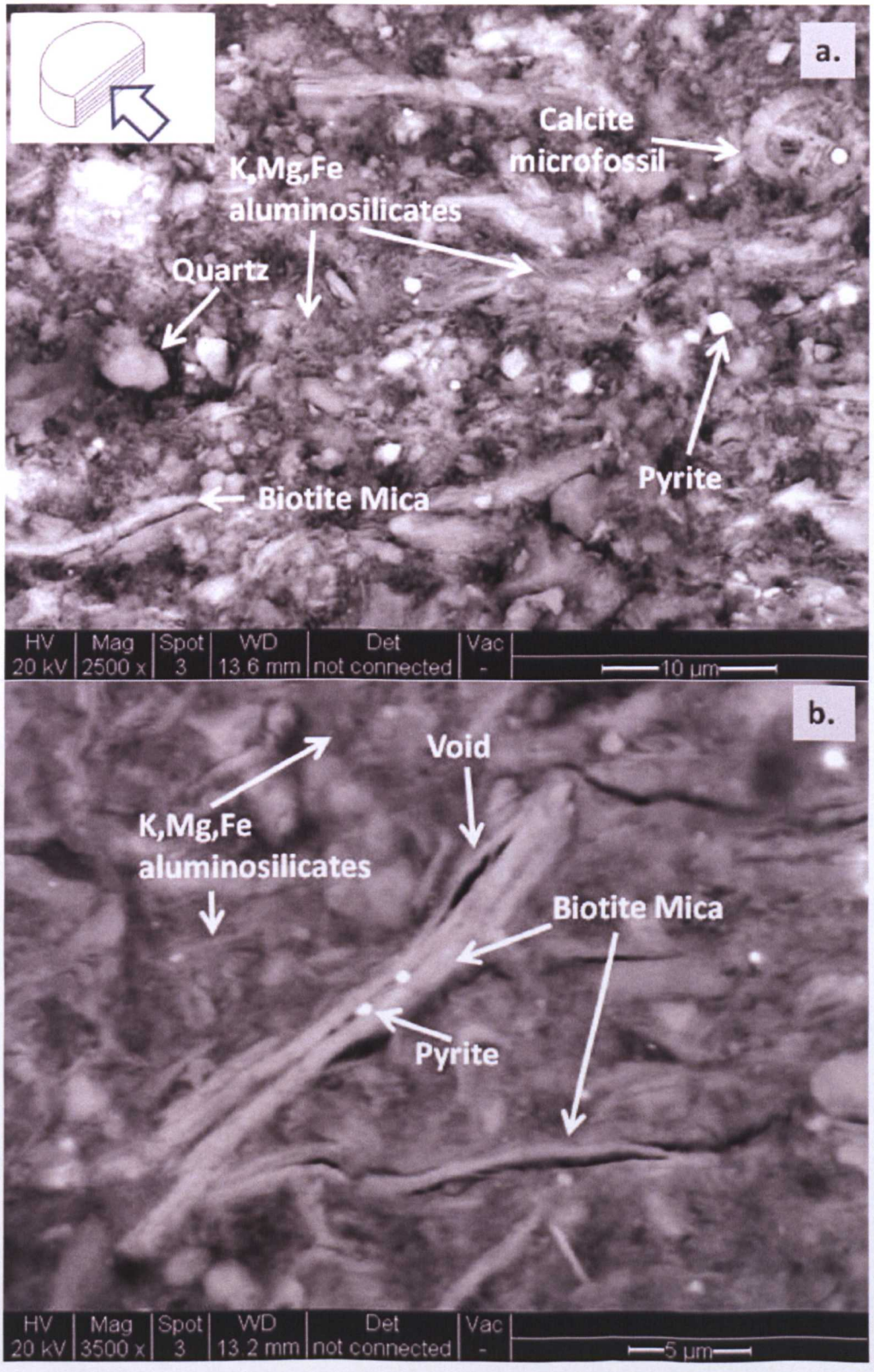

Figure 3.49 BSEM images of post-test 2 mudstone. Upper image shows the matrix at 2500x zoom and lower image displays elongate voids associated with mica. Pyrite grains present in voids.

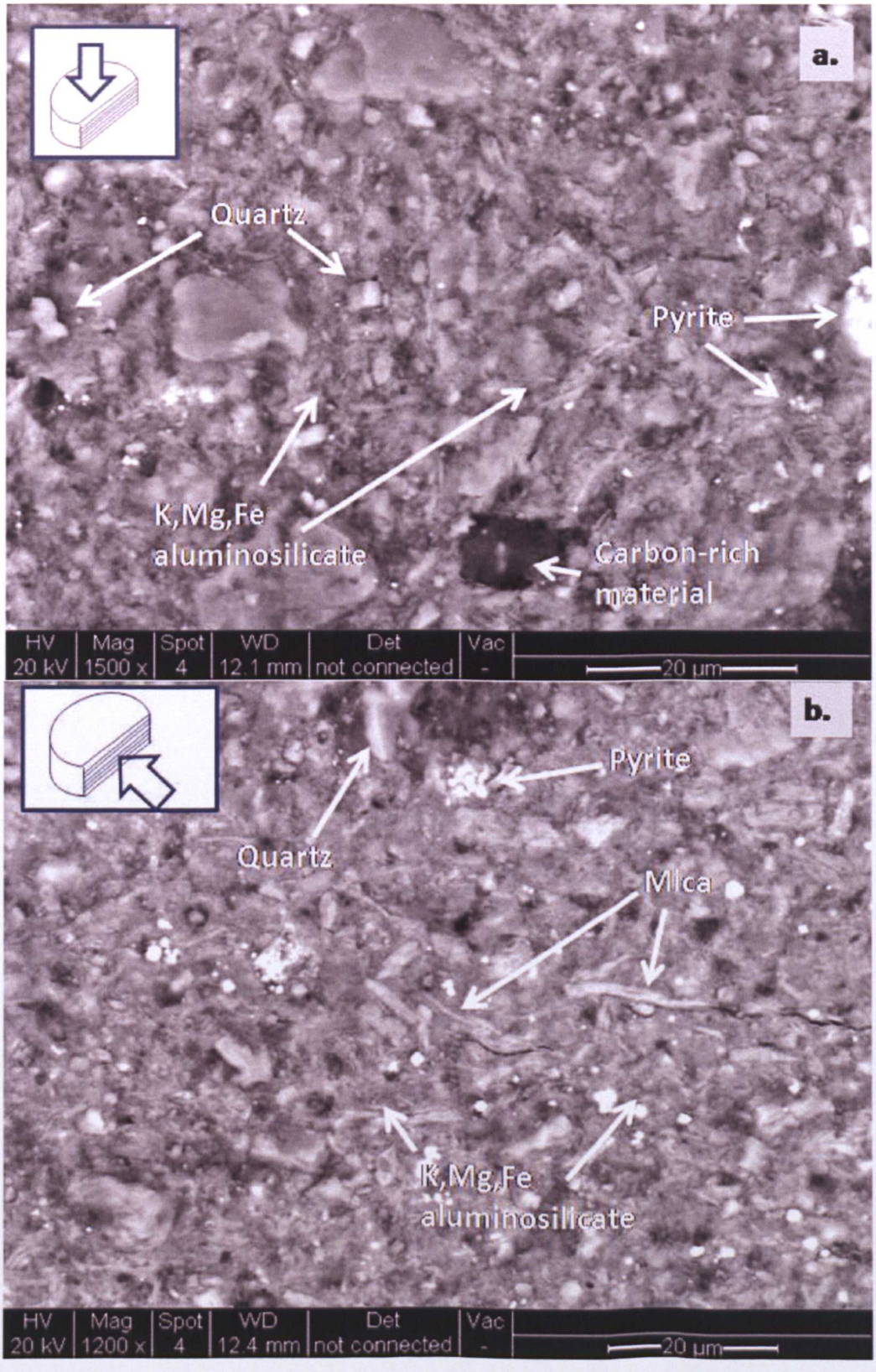

Figure 3.50 BSEM images of post-test 4 mudstone. Upper image is a plan view showing "patches" of organic material in the matrix and lower image shows the conformance of elongate, coarse grains of mica to bedding.

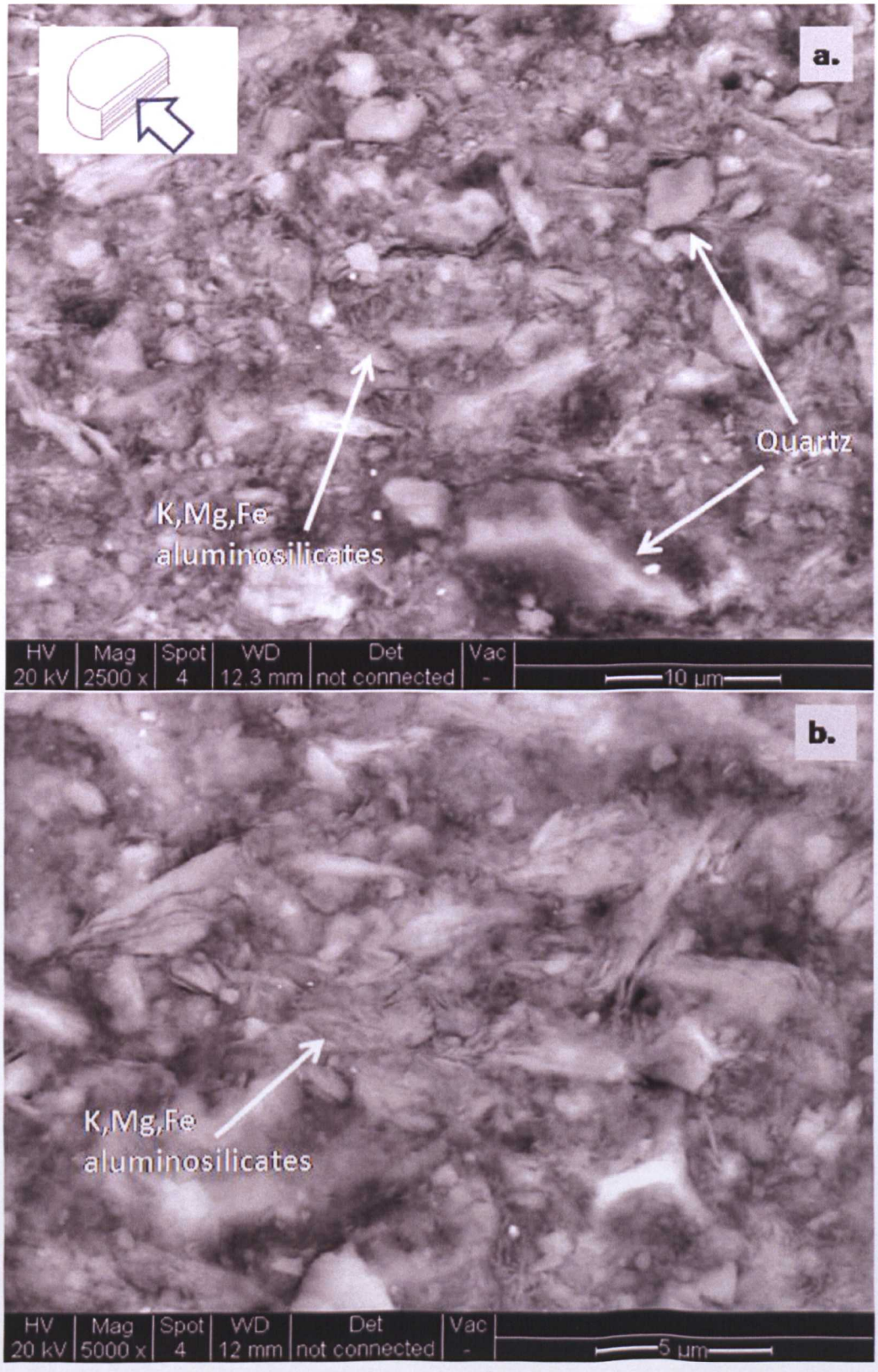

Figure 3.51 BSEM images of post-test 3 mudstone to show lack of alignment of fine, aluminosilicate grains.

Cracks were also present in their pre-test form, associated with elongate mica grains as seen in Figure 3.49 where pyrite grains appear to be infilling an elongate void in the same way that they infill the fossils. This could be a result of slide preparation, the cracks being open in the subsurface to allow growth of pyrite or movement of particles during the tests. Focussed ion beam techniques could generate more conclusive interpretations.

Carbonaeous areas are not visible in bedding perpendicular sections, only when viewing the material in plan section. From this view, the sub-rounded "patches" do not appear significantly different post-test. Whether any change to morphology has taken place along bedding planes – plastic flow of organic material (as described in Johnston, 1987) is not clear. However, the material does not appear significantly abundant and how much difference this limited component could make to the behavior of the overall matrix is not thought to be significant.

Figures 3.48, 3.49, 3.50 and 3.51 show high magnification images displaying the morphology of the clay grains as "whispy" elongate particles and there does not appear to be any increased alignment of these grains. Figures 3.52 and 3.53 show lower magnification images comparing the alignment of coarser features in the post test material. Whilst alignment of the finer particles appears minimal, coarser grains such as micas show some conformance to original bedding.

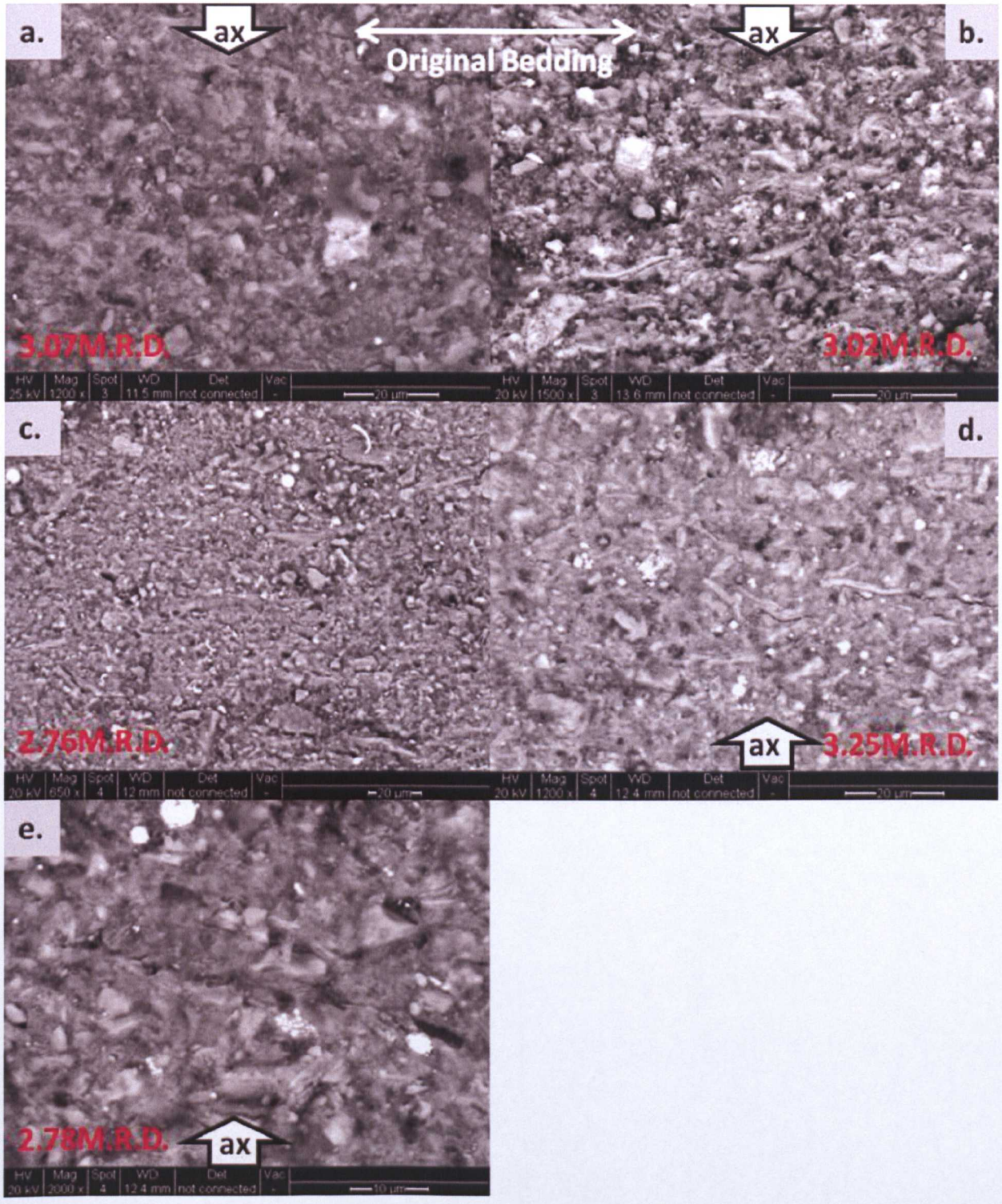

Figure 3.52 BSEM images of mudstone following tests 1-5 orientated to axial stress during test (up-down) and showing cross-section through original bedding at relatively low magnification with alignment measurement: a. Test 1, 1200x; b. Test 2, 1500x; c. Test 3, 650x; d. Test 4, 1200x; e. Test 5, 2000x.

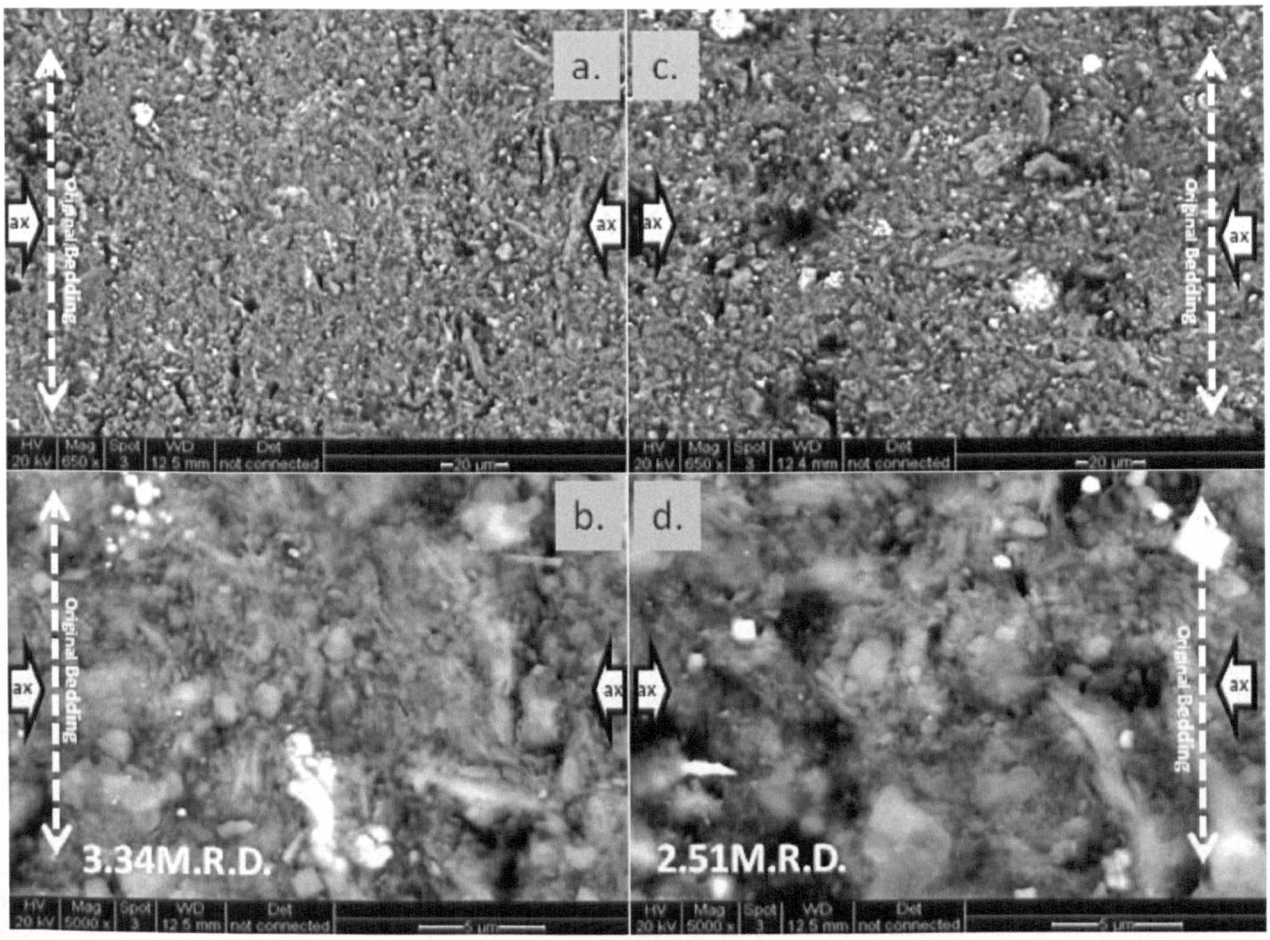

Figure 3.53 BSEM images of Test 7 (chemical test) and Test 8 (mechanical test) post-test at low and high magnification with alignment measurement: a. Chemical test material, 650x; b. Chemical test material, 5000x; c. Mechanical test material, 650x; d. Mechanical test material, 5000x. Images show sections cross-cutting original bedding (running up-down), perpendicular to axial stress during test (left-right).

3.3.6 Total Organic Carbon (TOC)

As pyrolising temperatures were not reached during the experiments, pre-test only samples were analysed for TOC content.

Sample	TOC (wt. %)
Plug 5, No. 1	1.72
Plug 5, No. 3	1.63
Plug 5, No. 5	1.83
Plug 5, No. 7	1.58
Slice 2, No 4	1.86
Slice 2, No 8	1.55
Slice 2, No 10	1.65
Slice 2, No 12	1.79

Table 3.16 Measured TOC values for pre-test bedding parallel (slice) and bedding perpendicular (plug) sections of mudstone.

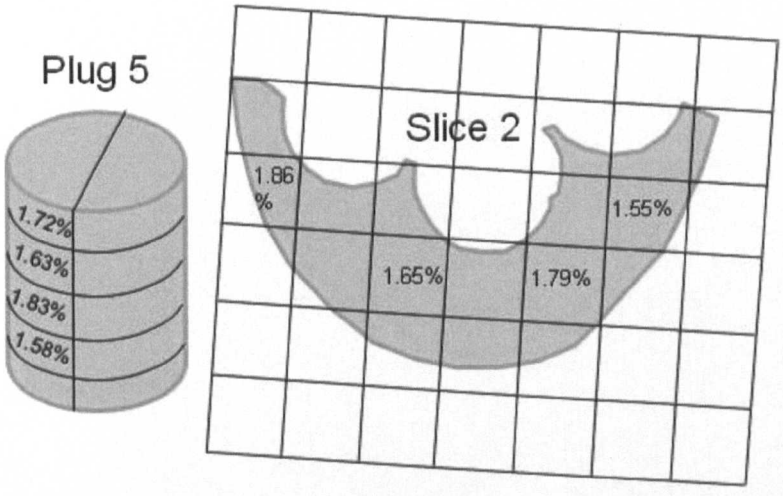

Figure 3.54 Schematic of TOC variation in the mudstone plug and slice sections.

The mean total organic carbon (TOC) of the North Sea mudstone was 1.7±0.1 wt %. The deviation is an order of magnitude greater than the experimental error established by a blank sample that gave a value of 0.021 wt %. The material is similarly heterogeneous both laterally and vertically within the core (Figure 3.54), with similar error margins.

Given the classification schemes below, the material is of fair – good source rock quality. However, it is considerably less organic rich than major North Sea source rocks of the Upper Jurassic, the Kimmeridge Clay / Mandal Formations. Organic matter rich facies contain 2 - > 15 wt % TOC, with the average "hot shale" containing 5 wt% (Gautier, 2005). The comparison in organic content becomes pertinent when evaluating compaction mechanisms in this study and Johnston (1987). TOC is significantly below that of the material tested in Johnston (1987) and therefore temperature-organic material related mechanisms are not thought to be behind the test results documented in 3.2.

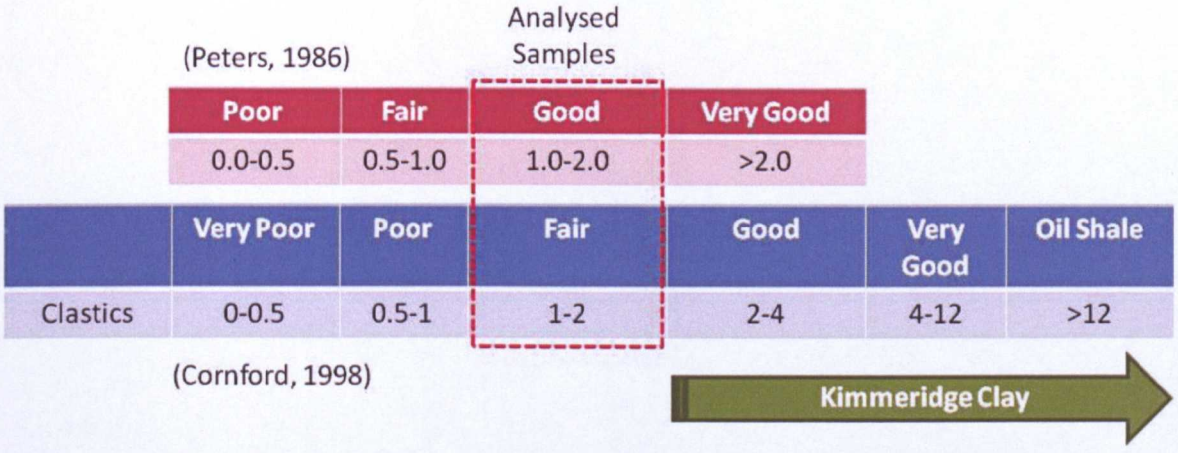

Figure 3.55 Classification schemes of Peters (1986) and Cornford (1998) for source potential with the organic content of the North Sea mudstone highlighted in red.

3.3.7 Chemical/Mineralogical Rock Properties: Summary

- Freeze-thaw disaggregation shows that post-test (K-rich pore fluid tests only) plugs showed a marked increase in stability compared to pre-test material. Qualitative evidence that K-exchange has taken place.
- In the pre-test material illite comprised 13±5% of the North Sea mudstone, whereas following the 4M KCl pore fluid triaxial tests (Tests 1,2,3,4 and 5) this increased to 36±14% and following the 3M KCl, 10^{-5}M KOH pore fluid triaxial

tests (Tests 6 and 7 – Chemical Compaction Test) this figure increased to 43±6%. 43±6% was the initial abundance of smectite in the pre-test material which decreased to 24±10% following the 4M KCl pore fluid triaxial tests and 17±7% the 3M KCl, 10^{-5}M KOH pore fluid triaxial tests.

- Bulk fraction XRD shows an apparent increase in illite/mica content with corresponding decrease in modelled smectite content following triaxial tests utilizing a K-rich pore fluid. Tests flowing a Na-rich fluid did not display any increase.
- Material modelled as smectite in bulk fraction XRD will include I/S as the mixed-layer clays present are smectitic (unlike the I/S reference in FULLPAT at the time of measurement). The average I% in I/S is 29±2%.
- Clay fraction XRD upon Na-exchanged samples shows that no permanent illitization has taken place as there is no statistically significant increase of I% in I/S in any of the post-test samples. Bulk fraction XRD measurements are interpreted as reflecting K-exchange only.
- A decrease in the 002 chlorite peak/ 001 kaolinite peak relative to illites 001 peak at 10Å in tests 4 (the high stress variable test) and 7 (the chemical test) may indicate a change in iron content of the chlorites.
- Cation exchange capacity measurements and dielectric constant measurements calculating specific surface area confirm that no illitization appears to have taken place as values are unchanged in a significant manner following the triaxial experiments.

- BSEM/EDX analyses showed that the mudstone was Na, Mg and K - phyllosilicate-rich with coarser grains of quartz, feldspars, mica and pyrite visible, along with calcitic foram tests supported by the fine-grained matrix.
- Element mapping confirmed that K was pervasive in the matrix following the tests and line/ point spectra showed that it was associated with Si, Al and O as well as Mg and Fe.
- KCl veining was observed in post-test 1 and 2 samples and led to a change in ramp-down procedures in the following triaxial tests. The veining was subsequently not observed in later samples.
- Micas and elongate cracks sub-parallel to original bedding, but no strong fabric is visible in the fine grained matrix.
- Carbonaceous "patches" were observed when looking in plan-view to bedding. They did not appear pervasive.
- Quantitative analysis of this organic content showed that the mean total organic carbon (TOC) of the North Sea mudstone was 1.7±0.1 wt %.
- Whether any change to morphology has taken place along bedding planes, ie. plastic flow of organic material (as described in Johnston, 1987) is not clear. However, the material does not appear significantly abundant and how much difference this limited component could make to the behavior of the overall matrix is not thought to be significant.

3.4 Physical Rock Properties

3.4.1 Grain Density

3.4.1.1 Pre-Test Grain Density

Following preparation described in 2.4.1, grain densities were determined for selected bedding parallel and perpendicular, pre-test samples and the results displayed below.

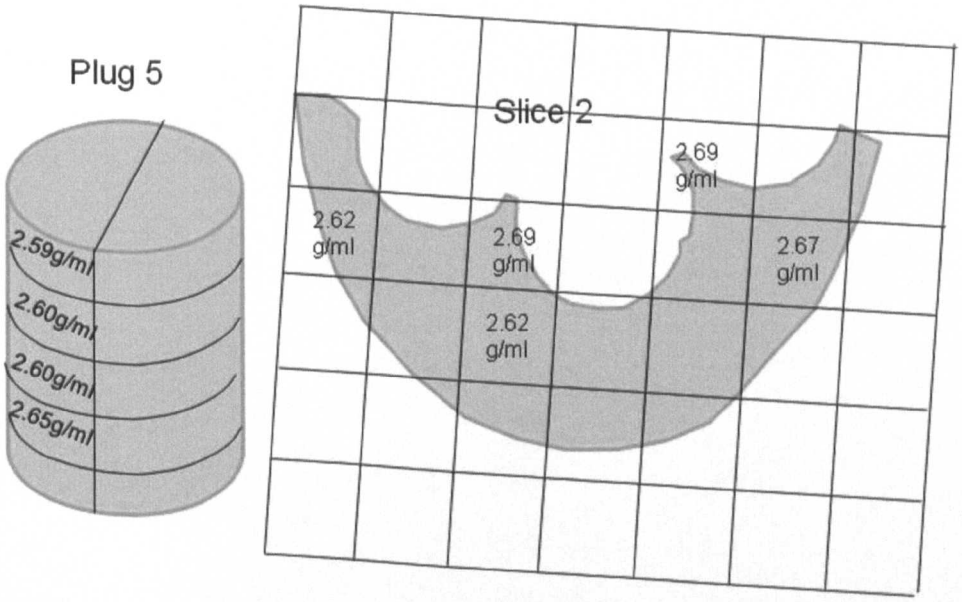

Figure 3.56 Bedding perpendicular (Plug 5) and parallel (Slice 4) variation of grain density in the pre-test North Sea mudstone.

The average grain density for the pre-test plug material is 2.61±0.03 g/cm^3, with values increasing down the plug (increasing depth in the original core). Variation in grain density laterally along bedding shows an average of 2.66±0.04 g/cm^3 showing no obvious trends/grouping. Variation in mineralogy is the likely cause of density deviations, particularly pyritized fossils observed in BSEM images.

3.4.1.2 Post-Test Grain Density

Post-test samples were prepared as described in 2.4.1 and grain densities were determined and tabulated below.

Sample	Grain Density (g/cm^3)
Test 1	2.77
Test 2	2.71
Test 3	2.80
Test 4	2.74
Test 5	2.78
Test 6	2.72
Test 7	2.69
Test 8	2.64
Test 9A	2.62
Test 9B	2.59
Test A	2.75
Test B	2.66
Test C	2.76

Table 3.17 Grain density results for all post-test samples.

A quartz standard was run with all sample batches, with average results of 2.67±0.009g/cm^3. Repeat measurements were made on samples from Variable Tests 6 and C, in addition to the main Compaction Simulations (Tests 7, 8, 9A & 9B) and the value stated in Table 3.17 is the average value.

The pre-test range was 2.59-2.69 g/cm^3, but post-test samples from test plugs 1,2,3,4,5,6, A and C were all above this range. The Test 3 sample which shows the highest grain density, contained an anomalous amount of pyrite. Plugs were CT scanned prior to testing to ensure this did not usually occur, but due to time

constraints this plug had to be utilised for the repeat variable test using 4M KCl pore fluid at 150°C under low effective stress (Test 3). Figure 3.57 shows the localised nature of the pyritisation (usually associated with fossils) and this is reflected in the discrepancy between the XRD quantification and grain density result. Material for grain density (and porosity) measurement came from the upper, pyritized section resulting in the 2.80 g/cm^3 value whilst the XRD sample came from the lower half of the plug with little mineralization and was modelled as containing only 2% pyrite.

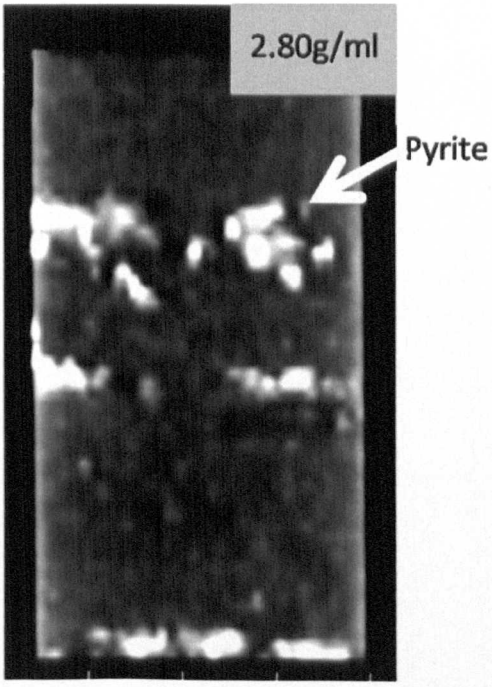

Figure 3.57 CT Scan image of pyritized mudstone prior to Test 3. Settings similar to those displayed in Figure 2.2. The plug was 62.5mm in length by 36mm in diameter. Grain density was measured as 2.80 g/cm^3.

This should not have been the case for the other test plugs and Figure 2.5 in Chapter 2 showed the more homogeneous nature of the plug used in Test 1, which was more indicative of those used in the other tests. Yet the post Test 1 material showed a grain density of 2.77 g/cm^3. On a microscopic scale, observed in BSEM images, pyrite was identified in most samples and could be behind this variation.

An alternative is the effect of potassium exchange on the mudstone as both NaCl solution tests (Test 8 and B) had grain densities within the pre-test range. However, Tests 7, 9A and 9B were also within range and used 3M KCl 10^{-5}M KOH solutions. Tests 6 and C both used these fluids also, but had grain densities exceeding the pre-test range. If there are influences from factors other than bulk mineralogy, they are not clear.

Grain densities are basic but important measurements as they provide input data for other tests such as MICP (3.4.3). Test 7 (the Chemical Compaction Test) showed the largest decrease in porosity and pore size, but corrected porosity would be influenced by variation in the grain density from the measured value of 2.69±0.01 g/cm^3. Using this value, post-test porosity following Test 7 was 19.3%. If grain density was reduced to the minimum value measured (2.59 g/cm^3 – pre-test Plug 5, No 1 and Test 9B) then porosity would be 16.2%. If it was increased to the maximum recorded in the anomalously pyritized sample (2.80 g/cm^3 – Test 3), porosity would increase to 22.5%. However, the latter case is unlikely as, following Test 3, plugs were CT scanned at several "slices" through the plug to ensure minimal coarse pyritization and selection of the best plugs (particularly those used in the final Comapction Simulations). Even if it were the case, the porosity loss due to Test 7 would still be significant as 22.5% is below the pre-test range and it also shows reduced R_{mean} (due to loss of the largest pores in the distribution) – see 3.4.3.

3.4.2 Grain Size Distribution

3.4.2.1 Pre-Test Grain Size Distribution

Plug 3 and Slice 2 pre-test samples underwent grain size distribution measurements using the Micromeritics Sedigraph 5000ET (2.4.2). The results were corrected via calibration procedures (sieve and pipette correction) and plotted below.

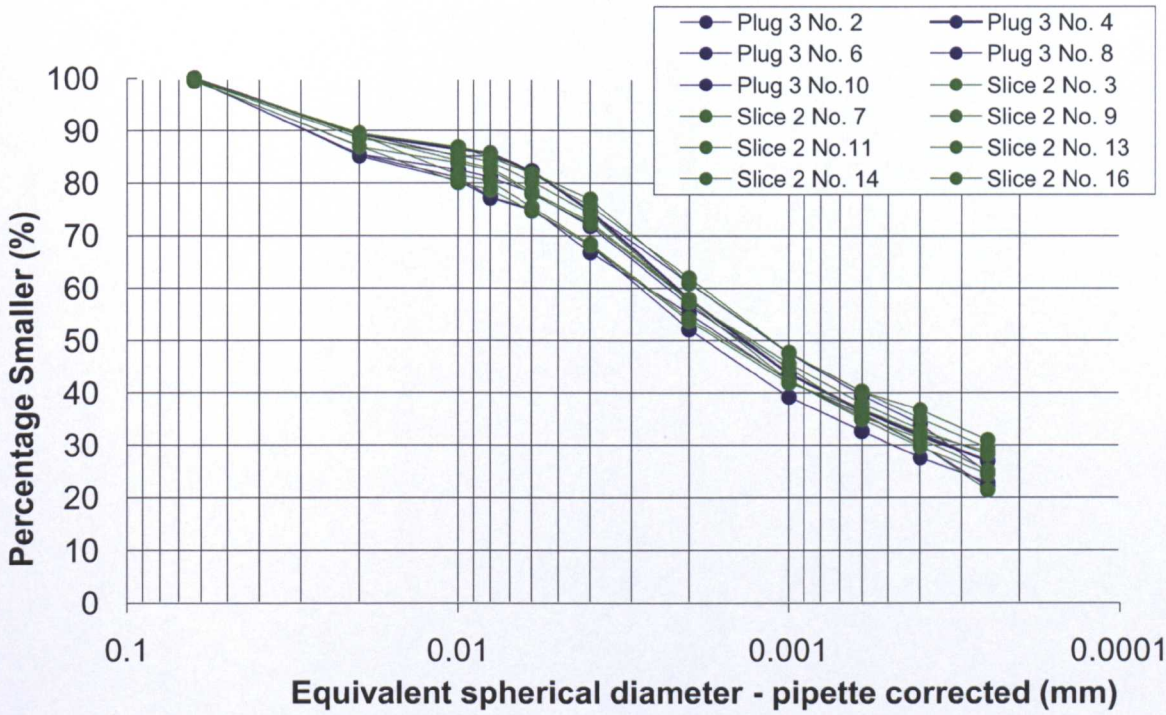

Figure 3.58 Grain size distribution of mudstone core material for analysis of natural heterogeneity

D_{50} (50% smaller) for the material ranges from 1.2-1.8μm with an average of 1.5μm and D_{60} ranges from 1.9-3.0μm with an average of 2.4μm. The effective size or D_{10} could not be read as the minimum measurable size was 0.25μm and 21-31% by mass of the material is smaller than this equivalent spherical diameter. Extrapolation gave unreliable results and without the effective size, the coefficients of uniformity and curvature could not be calculated. However, visual interpretation of the distribution profiles and their change from convex to concave/straight at 2μm indicate

the material is clay-rich. This is substantiated by the D_{50} and D_{60} values which show that the clay sized particles (<2μm) form a dominant component of the material (average 57±3%), though a significant proportion is therefore between 2-63μm.

It was noted that the material collected in the >63μm fraction was a very minor component (so small that the final correction recalculated it to zero in all but one sample, Slice 2, No.14: >63μm =1%) and was mainly composed of hard, black particles, speculatively identified as pyrite. No real trends emerge in the distribution of the amount of fine fraction material (<0.25 μm), but as with other characteristics the smallest range in values (5%) can be seen in the plug, perpendicular to bedding, whereas 10% range can be seen across bedding in Slice 2.

3.4.2.2 Post-Test Grain Size Distribution

Post-test samples were analysed using the same procedures as the pre-test material (2.4.2) and are plotted together for comparison in Figures 3.59-3.61.

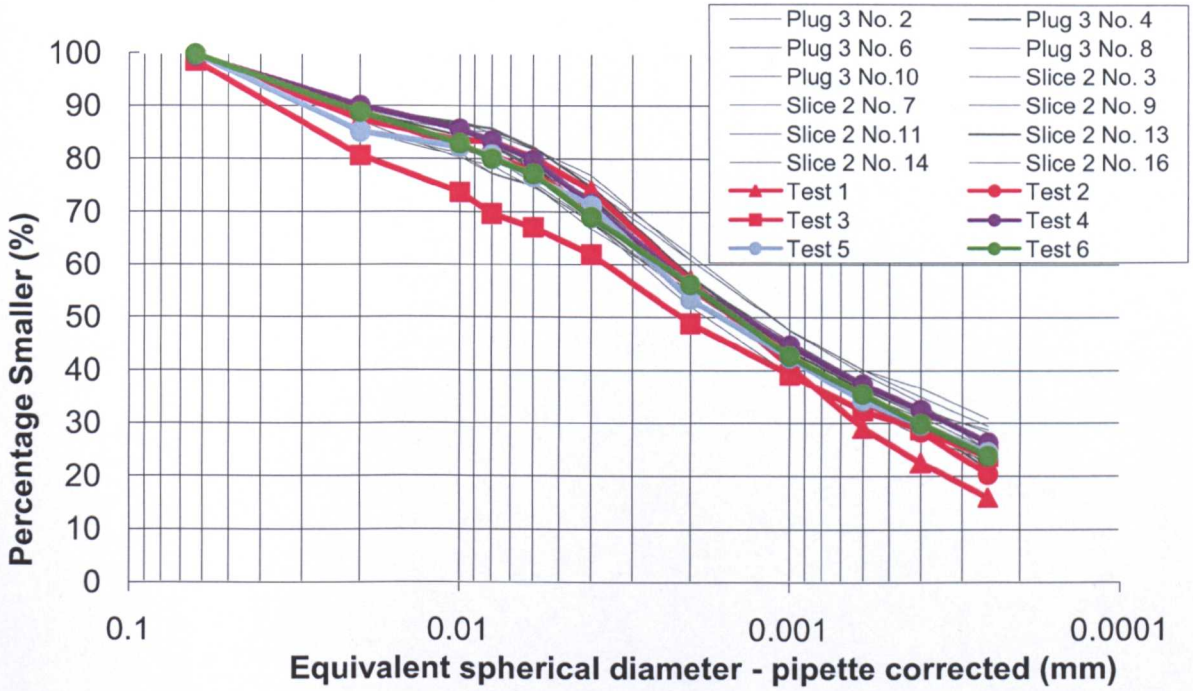

Figure 3.59 Grain size distributions for Tests 1-6 material (Variable Testing -Triaxial Experiments).

Generally post-test material fell within the pre-test range over most of the 63-0.25 μm distribution. The main exceptions were Test 3 (Figure 3.59) and 8 (the Mechanical Compaction Test – Figure 3.61) which have straighter trends as opposed to the general convex distribution, indicating that they comprise more silt sized particles. However, both trends move back into the pre-test range by 0.25 μm. Variation from the general range does not seem to be associated with the finest fraction, likely to be the smectite/smectitic I/S component. The only triaxial test that shows variation in that area is Test 1, but there is only 3% less <0.25 μm in the Test 1 plug than the minimum measured on the pre-test material.

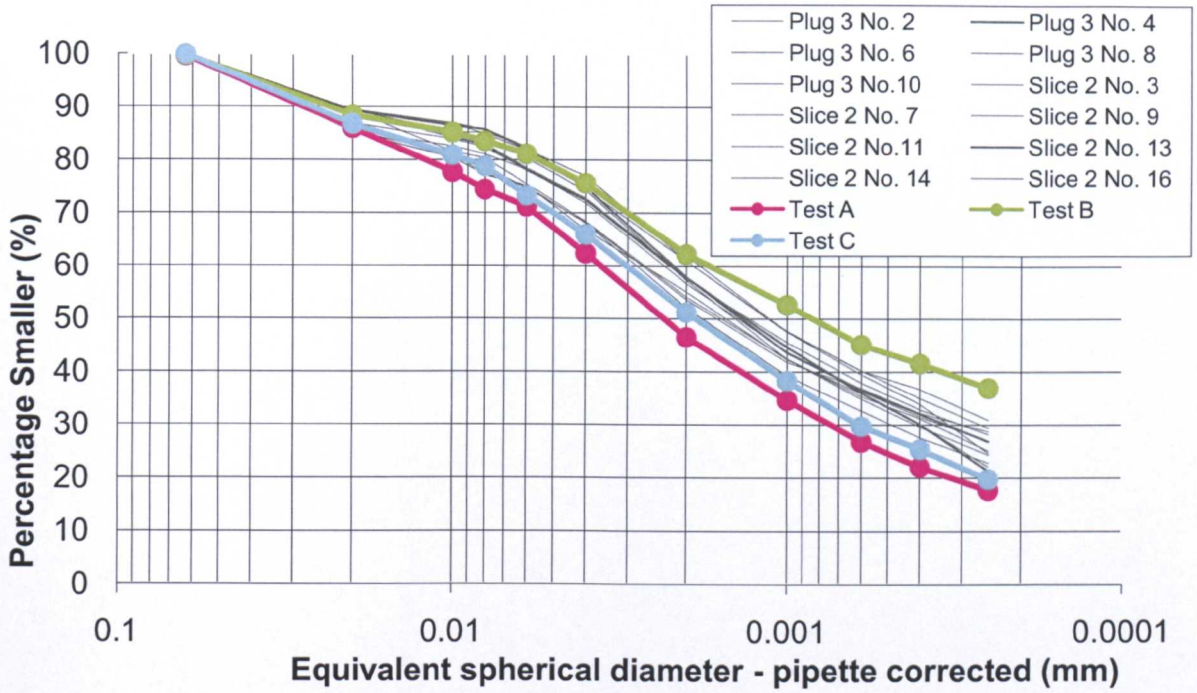

Figure 3.60 Grain size distributions for Test A, B and C material (Variable Testing - Reflux Condenser Experiments).

The material collected following the reflux condenser tests (Tests A-C) display distributions outside the pre-test range. These results are unreliable as the most divergent trends are those of Tests A and B which disaggregated during the reflux condenser test and collection of the sample may have been an issue. If not, then the NaCl fluid test (Test B) contained the largest clay fraction, diverging below 2 μm and with with a <0.25 μm fraction 5% greater than the pre-test maximum.

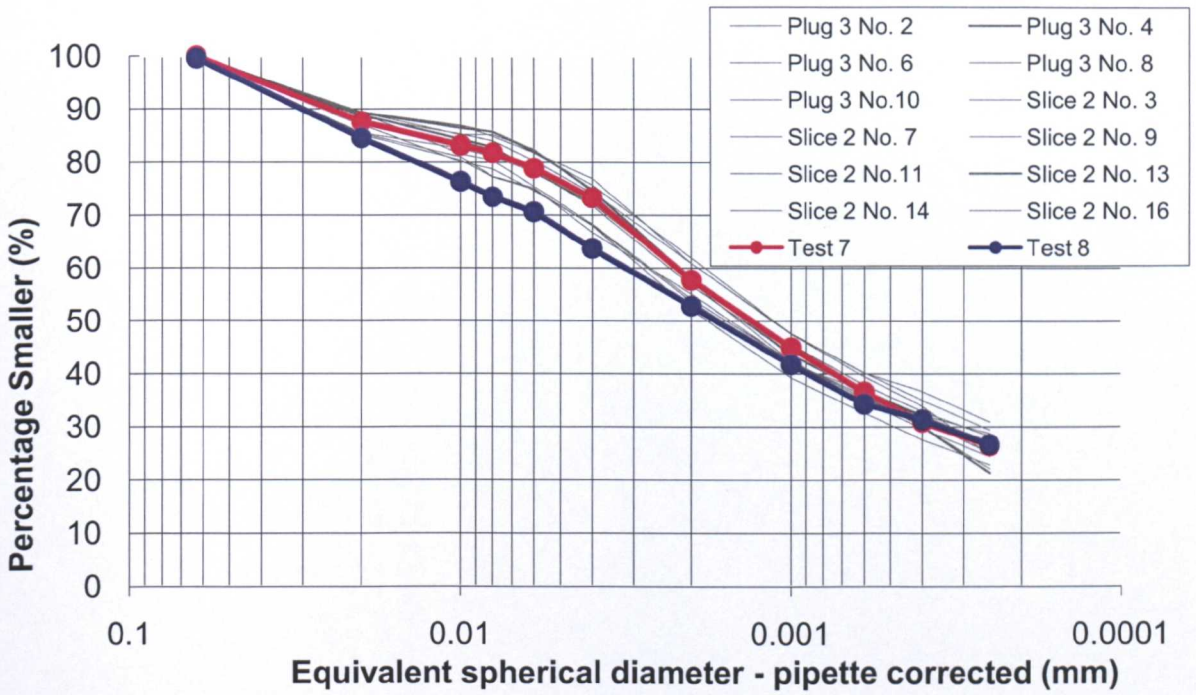

Figure 3.61 Grain size distributions for Test 7 and 8 material (Main Compaction Simulatations).

3.4.3 MICP Measured Porosity

3.4.3.1 Pre-Test Porosity

Pre-test samples were prepared for mercury injection porosimetry (MICP) to determine porosity as described in 2.4.3 and the data obtained displays the natural porosity heterogeneity in the North Sea mudstone core (Table 3.18).

Sample	Total Porosity (%)	Corrected Porosity (%)	Cut-Off Radius (nm)	R_{mean} (nm)	$R_{10\%}$ (nm)
Plug 2, No.2	24.8	23.9	121.5	21.6	35.4
Plug 2, No 4	25.6	24.5	198.8	27.5	44.7
Plug 2, No.6	25.1	23.9	273.4	27.3	41.9
Plug 2, No.8	25.1	23.7	121.5	26.1	42.8
Plug 2, No.10	25.6	24.5	156.2	28.2	44.3
Slice 3, No.1	24.5	23.2	121.5	22.6	38.4
Slice 3, No.4	24.1	23.2	198.8	26.4	41.3
Slice 3, No.6	27.0	25.3	546.7	34.8	56.7
Slice 3, No.8	24.6	23.7	156.2	23.7	37.2
Slice 3, No.10	26.2	25.1	198.8	26.5	45.4
Slice 3, No. 12	26.2	25.1	364.5	25.5	40.4
Slice 3, No. 14	25.2	24.4	156.2	20.1	32.5
Slice 3, No. 16	24.9	24.0	273.4	28.3	43.3
Slice 3, No. 18	25.9	25.1	156.2	26.3	41.3
Slice 3, No. 21	24.5	23.5	121.5	21.1	34.1
Average (Mode*)	25.3	24.2	121.5*	25.7	41.3
Maximum	27.0	25.3	546.65	34.8	56.7
Minimum	24.1	23.2	121.5	20.1	32.5

Table 3.18 Pre-Test Mudstone porosity values measured using MICP. Also used as input data for permeability calculations. Third column indicates MICP measured porosity corrected to exclude larger cracks/fractures delimited by the cut-off radius. * indicates use of mode instead of mean.

The distribution of corrected porosity parallel and perpendicular to bedding is displayed in Figure 3.62. There does not appear to be any strong patterns/groupings, with values varying between a maximum of 25.3 and a minimum of 23.2 approximately 2cm apart. The overall pre-test average corrected porosity was

24.2±0.7%, with little difference between the plug or slice averages of 24.1± 0.4% and 24.3± 0.8% respectively.

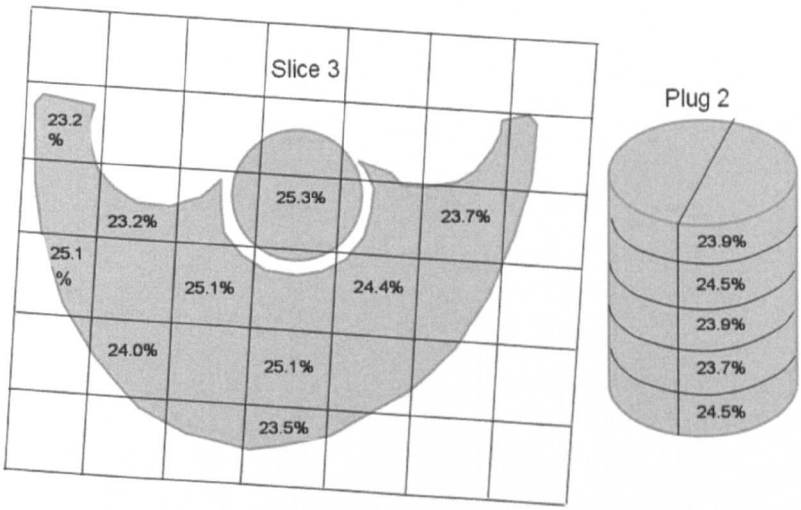

Figure 3.62 Bedding perpendicular (plug 2) and parallel (slice 3) variation of porosity in the pre-test North Sea mudstone.

The overall mean pore radius was 25.7 ± 4 nm, with 26.1±3nm and 25.5±4nm the plug and slice average pore radii. Similar values in the plug and slice indicate that there is similar heterogeneity both laterally and vertically on the scales measured. Example pore throat distributions, as well as cumulative porosity are displayed in Figure 3.63. They show that the size distributions range from a small amount of pores approaching the minimum measurable values (<10nm) up to ~100nm.

Rather than use all 15 measurements in the post-test comparison plots, the cumulative porosity and distribution for pre-test samples Slice 3 No. 1, Slice 3 No. 16 and Slice 3 No. 6 have been plotted (Figure 3.64). This is because they display corrected porosities closest to the minimum, average and maximum values for the whole dataset, respectively.

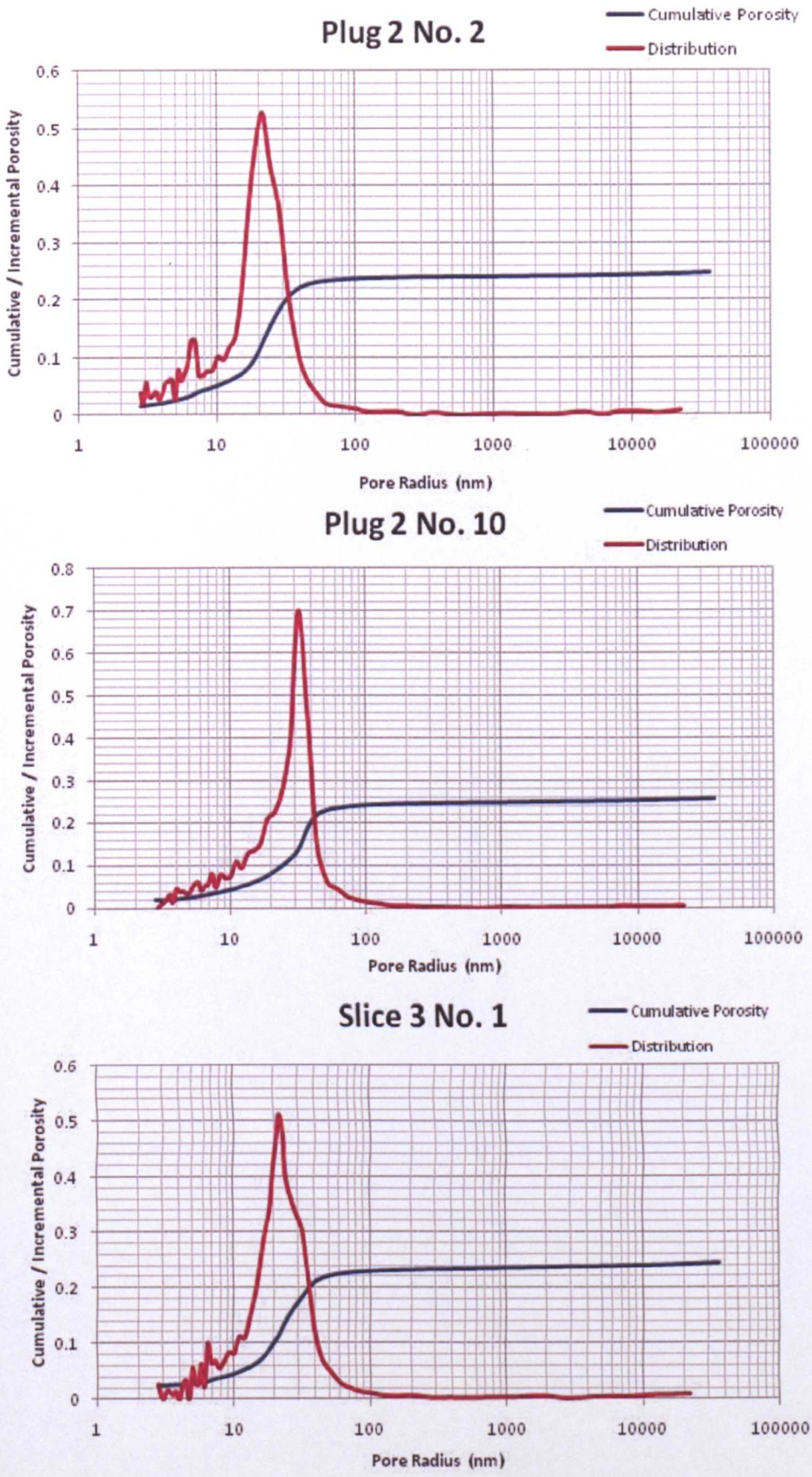

Figure 3.63 Example plots of cumulative porosity with pore radii distribution for pre-test material.

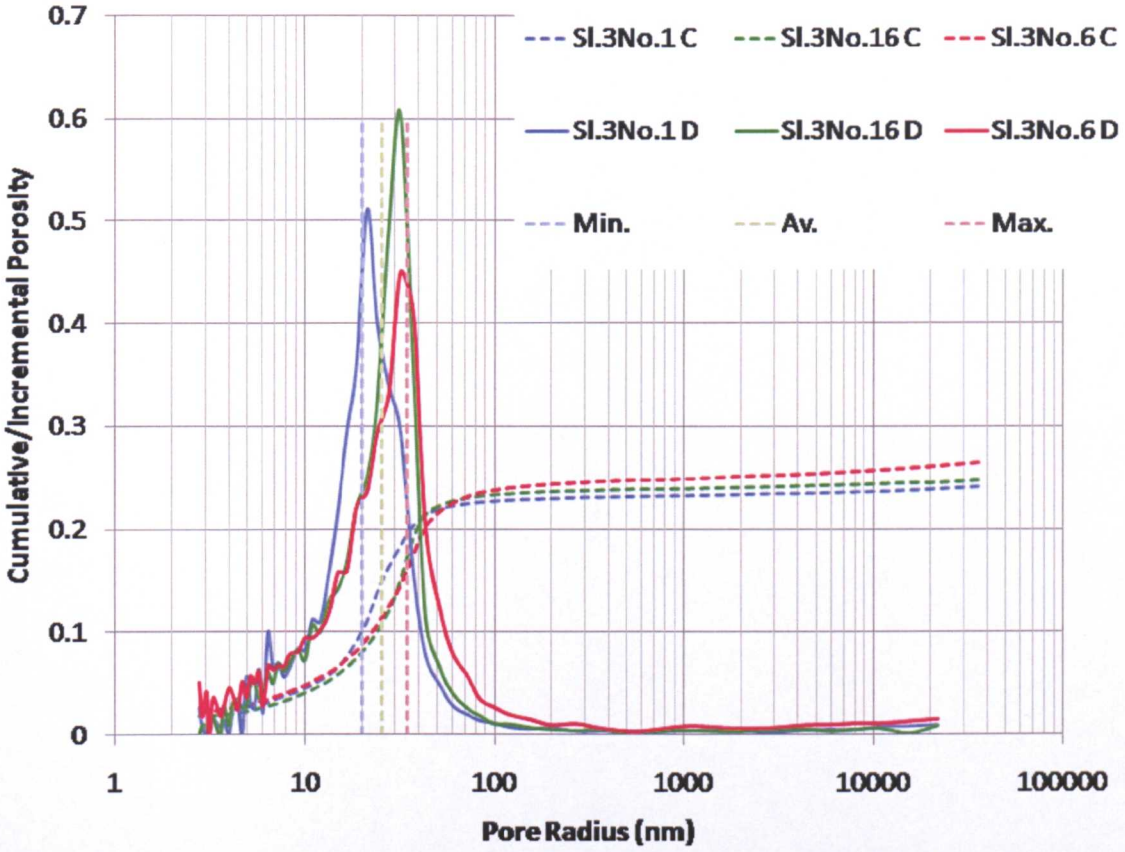

Figure 3.64 Plot to show cumulative porosity (C) and distribution (D) for Pre-Test samples: Slice 3, No. 1; Slice 3, No. 16 and Slice 3, No. 6 which have corrected porosities closest to the minimum (23.2/23.2%), average (24.0/24.2%)and maximum (25.3/25.3%)values for the whole dataset respectively. The minimum (min.), average (av.) and maximum (max.) R_{mean} positions for the whole dataset are also marked over the actual sample distributions.

3.4.3.2 Post-Test Porosity

All triaxially tested material underwent the same porosity measurement preparation and techniques as the pre-test material. Samples from Tests A-C were not viable for MICP measurement. The results for samples from the variable testing, triaxial tests (Tests 1-6) are tabulated in Table 3.19 below.

Sample	Total Porosity (%)	Corrected Porosity (%)	Cut-Off Radius (nm)	R_{mean} (nm)	$R_{10\%}$ (nm)
Test 1	30.6	27.2	546.7	30.3	48.5
Test 2	24.7	22.6	546.7	27.2	41.0
Test 3	27.1	25.8	546.7	25.4	42.8
Test 4	23.3	22.3	156.2	15.2	27.8
Test 5	31.4	30.4	273.4	20.0	38.6
Test 6	28.7	27.3	84.1	16.5	34.7

Table 3.19 Post-Variable Triaxial Tests mudstone porosity values measured using MICP. Also used as input data for permeability calculations. Third column indicates MICP measured porosity corrected to exclude larger cracks/fractures delimited by the cut-off radius.

Figure 3.65 shows the distributions and cumulative porosities for pre-test and post–Variable Test samples. Pre-test samples, Slice 3 No. 1, Slice 3 No. 16 and Slice 3 No. 6 which have corrected porosities closest to the minimum, average and maximum values for the whole Pre-Test dataset are displayed for comparison with the measurements for samples following the Variable Triaxial Tests. None of the corrected porosities are within the range of the original pre-test material (23.2 to 25.3%), although Test 2 and 3 are close. Test 1, 5 and 6 all appear to show increased porosities. These correlate with the final post-test dimension measurements for these samples which showed slight expansion.

Test 4 (the high stress test) has reduced porosity, which is also shown in the decreased R_{mean} (along with Test 6 – the pH 9 test). The R_{mean} measurements for Tests1, 2, 3 and 5 are within the range of the pre-test material. The only test that appears to have significantly reduced both the corrected porosity and R_{mean} is the high stress test, Test 4. This is displayed most clearly in A. of Figure 3.65.

Several statistical tests were carried out to analyse the significance of the various changes generated by tests under different conditions. In a broad comparison of the pre-test values with those measured following the variable testing triaxial experiments, Tests 1, 3, 5 and 6 showed statistically significant differences in corrected porosity, but not in R_{mean} (with Test 2 included) at the 95% confidence level.

The results tabulated below are the MICP measurements on the post-test material following the Compaction Simulations (Tests 7-9).

Sample	Total Porosity (%)	Corrected Porosity (%)	Cut-Off Radius (nm)	R_{mean} (nm)	$R_{10\%}$ (nm)
Test 7 (I)	19.9	19.3	72.9	15.1	24.0
Test 7 (II)	20.1	19.7	43.8	13.9	22.8
Test 7 Av.	20.0	19.5	-	14.5	23.4
Test 8 (I)	25.4	24.1	273.4	28.0	49.6
Test 8 (II)	23.7	22.9	99.4	20.6	32.6
Test 8 Av.	24.6	23.5	-	24.3	41.1
Test 9A (I)	21.9	20.3	156.2	22.2	36.3
Test 9A (II)	26.6	25.0	364.5	22.6	93.6
Test 9A Av.	24.3	22.7	-	22.4	65.0
Test 9B (I)	21.3	19.6	546.7	29.3	44.1
Test 9B (II)	20.2	19.1	546.7	27.0	39.3
Test 9B Av.	20.8	19.4	-	28.2	41.7

Table 3.20 Post-Main Compaction Simulations mudstone porosity values measured using MICP. Also used as input data for permeability calculations. Numerals indicate repeat measurements on different sections of the same plug and Av. is the average. MICP measured porosity corrected to exclude larger cracks/fractures delimited by the cut-off radius.

Test 7 (Chemical Compaction Test) shows a reduction in corrected porosity and R_{mean} when compared to pre-test values. Test 8 (Mechanical Compaction Test) material has an average corrected porosity and R_{mean} that are within the calculated errors of the pre-test averages; there is apparently limited change to porosity due to Test 8.

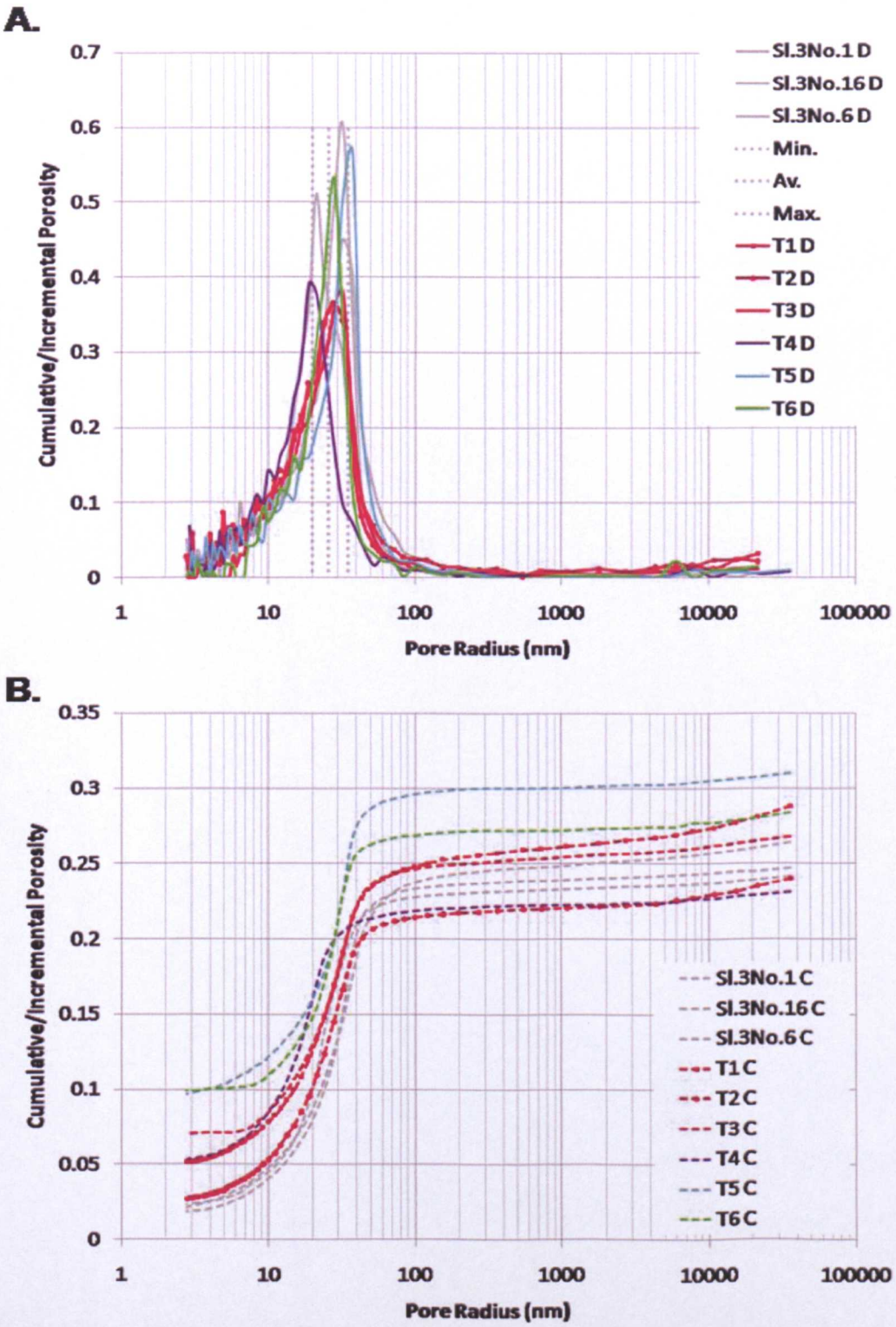

Figure 3.65 Plots to show (A.) distribution (D) and (B.) cumulative porosity (C) and for Pre-Test and Post–Variable Test samples. In grey are Slice 3, No. 1; Slice 3, No. 16 and Slice 3, No. 6 which have corrected porosities closest to the minimum, average and maximum values for the whole Pre-Test dataset. The minimum (min.), average (av.) and maximum (max.) R_{mean} positions for the whole dataset are also marked in grey over the actual sample distributions in A. In colour are the measurements for Variable Tests 1-6

Test 9A, the failed Intermediate Test, shows a relatively large difference between repeat measurements of corrected porosity. The average is below the range of pre-test porosities, as is the average corrected porosity of the the second Intermediate Comapction test, 9B. Test 9B consolidated at 30MPa before failing during the stress increase to 50MPa. 30MPa was the same effective stress Variable Test 4 reached, yet Test 9B (or Test 9A) does not show a similar reduction in the R_{mean}. Test 4 ran at 150°C (and used 4M KCl pore fluid), whereas Test 9B ran at room temperature (using 3M KCl 10^{-5}M KOH).

The corrected porosities and values of R_{mean} measured following Test 7, the Chemical Compaction Simulation, both showed statistically significant difference to pre-test values at the 95% confidence level (*Corrected Porosity*: 95% CI for difference: (3.599, 5.814)and P-Value = 0.000 / R_{mean}: 95% CI for difference: (5.57, 16.90) and P-Value = 0.001). Whereas the corrected porosities measured following Test 8, the Mechanical Compaction Simulation, were not found to show a statistically significant difference at the 95% confidence level (95% CI for difference:(-0.450, 1.863) and P-Value = 0.212, the null hypothesis that the difference is zero is accepted).The R_{mean} value following Test 8 was also found to show no change and groups with Test 9B (the Intermediate Compaction Simulation), which also shows no statistical change at the 95% confidence level. However, Test 9B groups with Test 7 for corrected porosity change, showing statistically significant differences to pre-test porosities at the 95% confidence level.

The difference between the main Compaction Simulation results is clearly observed in plots of the cumulative porosity and pore size distribution (Figure 3.66). Test 7

shows a reduction in the larger pore throats which shifts the distribution to a lower R_{mean}. The distribution of Test 8 plug data is similar to the pre-test distributions also plotted for comparison. Both Test 9 distributions show a trend not observed in any other post-test MICP distribution, a loss of smaller pore throats (approximately <10nm), with little change to the larger, resulting in the within pre-test range R_{mean} values.

Tests 9A and 9B were the only tests where failure occurred and its influence cannot be ruled out. However, care was taken to select samples for MICP from within the solid blocks of plug recovered and also porosity calculated from mid-test dimension measurements confirms the MICP measured porosities were reached during the test prior to failure (Figure 3.18). Therefore, this allows some confidence in the interpretation that the anomalous distribution is also likely to be due to test conditions and not failure. Tests 9A and 9B were the only tests that used K-rich pore fluids at room temperature. Figure 3.19 also shows that despite the final corrected porosity of Test 9B being lower than/approximately equal to Test 7, when normalised to calculated initial porosity values the final porosity value shows an intermediate reduction, with Test 7 showing the largest and Test 8 showing the least. This is supported by the R_{mean} data.

A.

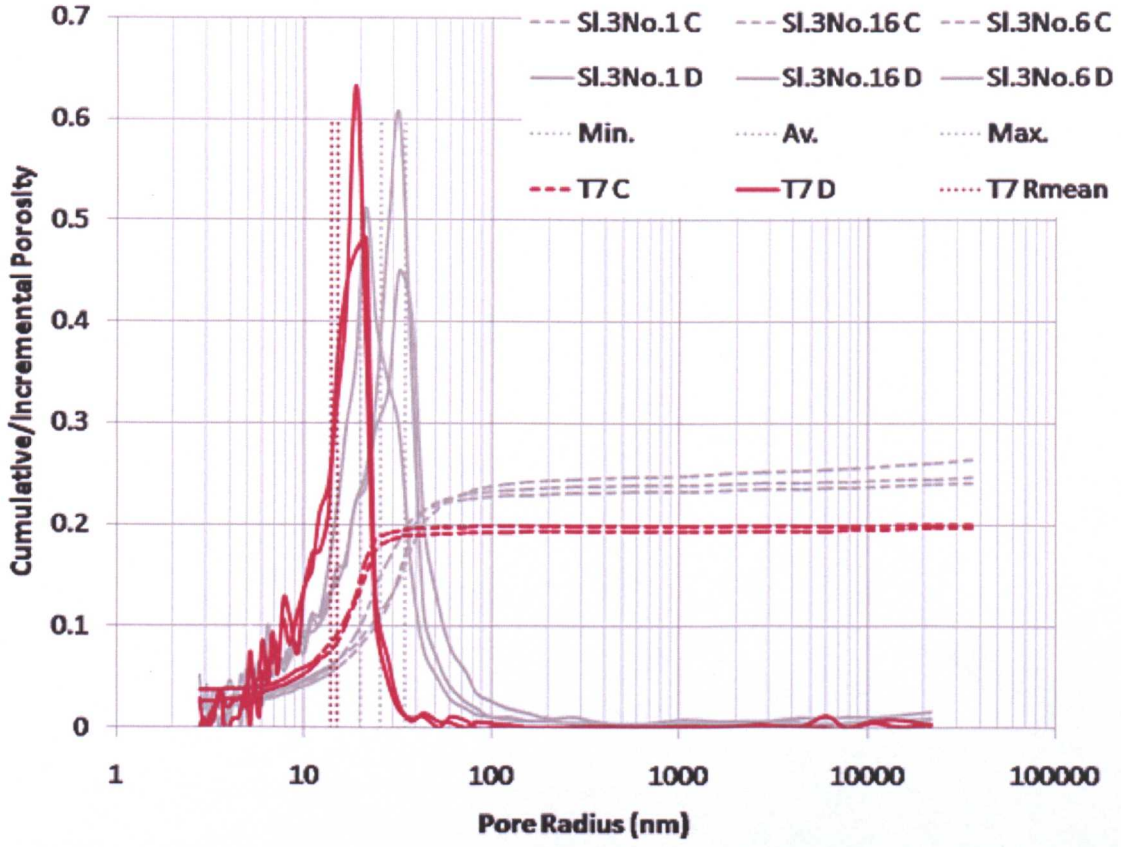
Sl.3No.1 C
Sl.3No.16 C
Sl.3No.6 C
Sl.3No.1 D
Sl.3No.16 D
Sl.3No.6 D
Min.
Av.
Max.
T7 C
T7 D
T7 Rmean
Cumulative/Incremental Porosity
0.7
0.6
0.5
0.4
0.3
0.2
0.1
0
1
10
100
1000
10000
100000
Pore Radius (nm)

B.

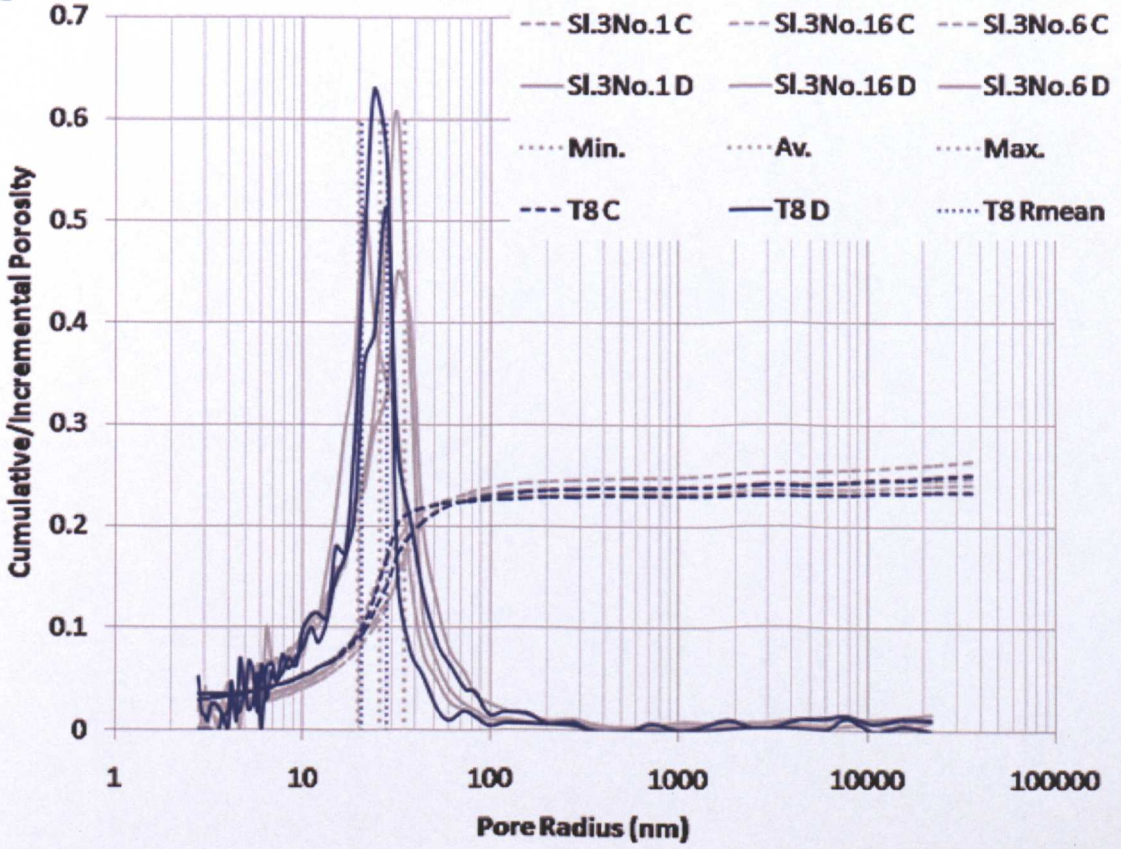
Sl.3No.1 C
Sl.3No.16 C
Sl.3No.6 C
Sl.3No.1 D
Sl.3No.16 D
Sl.3No.6 D
Min.
Av.
Max.
T8 C
T8 D
T8 Rmean
Cumulative/Incremental Porosity
0.7
0.6
0.5
0.4
0.3
0.2
0.1
0
1
10
100
1000
10000
100000
Pore Radius (nm)

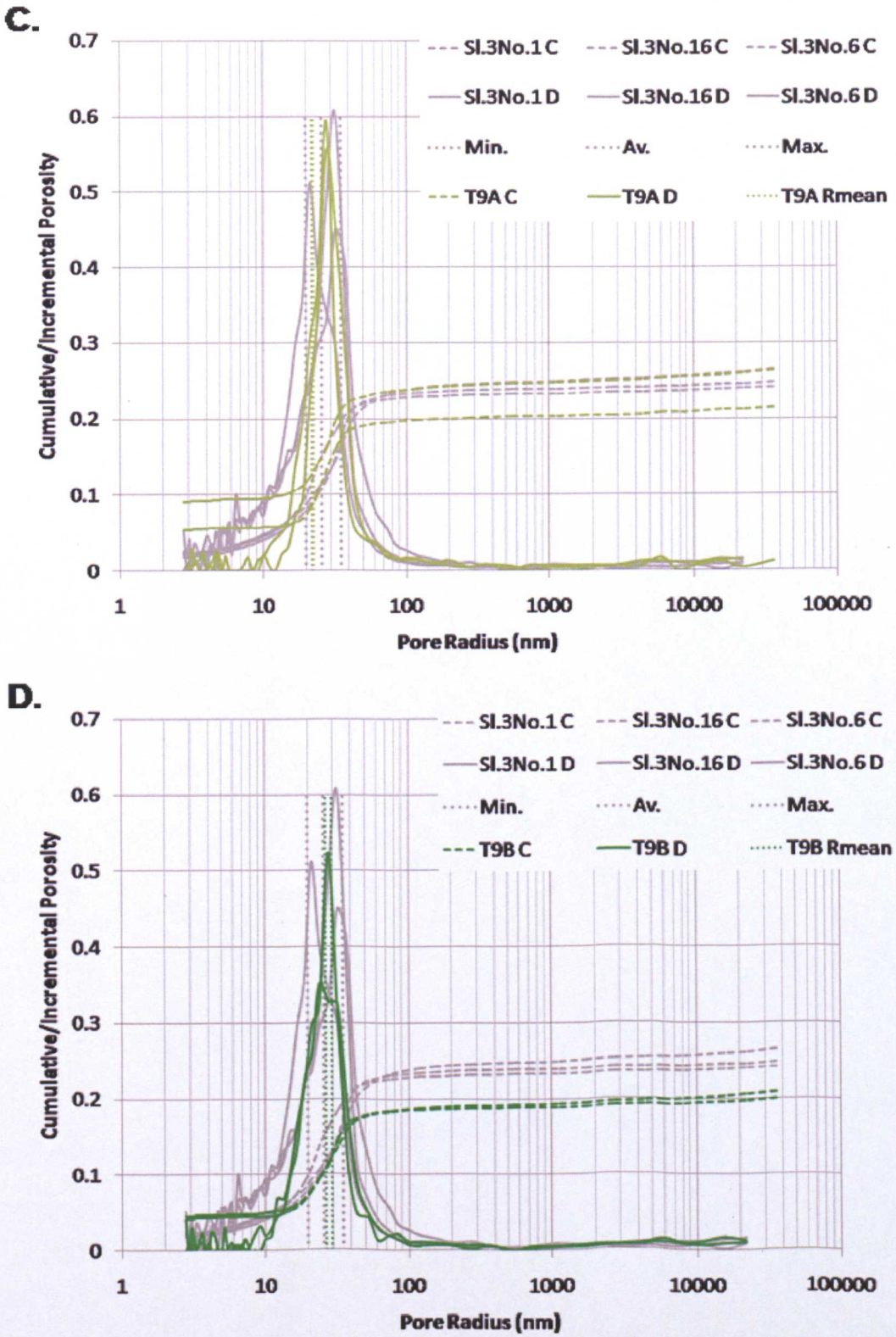

Figure 3.66 Plots to show cumulative porosity (C) and distribution (D) for Pre-Test and Post–Main Test samples. In grey are Slice 3, No. 1; Slice 3, No. 16 and Slice 3, No. 6 which have corrected porosities closest to the minimum, average and maximum values for the whole Pre-Test dataset. The minimum (min.), average (av.) and maximum (max.) R_{mean} positions for the whole dataset are also marked in grey over the actual sample distributions. In colour are the measurements for (Fig. A.) Main Tests 7 (Chemical Test); (Fig. B.) 8 (Mechanical Test) and the two failed Intermediate Tests 9A (Fig. C.) & 9B (Fig. D.).

3.4.4 High Resolution X-ray Textural Goniometry (HRXTG)

3.4.4.1 Pre-Test HRXTG Alignment

BSEM images (3.3) had previously identified some bedding parallel alignment of coarser features, such as mica grains, in both the pre-test and post-test material. However, the finer clay grains were difficult to image in the North Sea mudstone and HRXTG was undertaken to quantify any alignment. The classification taken from Day-Stirrat (2006) gives some guide to interpretation.

M.R.D Value	Alignment Classification
<1.8	No alignment / Very Weak alignment
2-3	Weak alignment
3-4	Moderate alignment
4-5	Strong alignment
>5	Very strong alignment

Table 3.21 Classification for alignment measured in multiples of random distribution (MRD) (Day-Stirrat, 2006)

The average illite/mica alignment is 3.13±0.01 MRD, for smectite/smetitic I/S the average is 2.99±0.24MRD and for chlorite is 2.90±0.28 MRD. Therefore, the pre-test mudstone already displays weak to moderate alignment of the clay minerals. There is also a positive correlation between the alignment of the different phases, mainly provided by the I/S with chlorite relationship (Figure 3.67).

Sample Depth (m)	I Kα ave. d-spacing (Å)	I Max. Pole Density (MRD)	I/S Kα ave. d-spacing (Å)	I/S Max. Pole Density (MRD)	Ch Kα ave. d-spacing (Å)	Ch Max. Pole Density (MRD)
Plug 2 No. 3	-	-	12.3	2.60	13.9	2.56
Plug 2 No. 7	-	-	x	3.06	14.2	3.10
Plug 2 No. 9	-	-	12.9	2.78	14.0	2.78
Slice 1 No 7	10.2	3.14	12.6	3.14	-	-
Slice 3 No 5	-	-	12.1	3.18	13.9	3.16
Slice 3 No 15	10.0	3.12	11.1	3.19	-	-

Table 3.22 HRXTG data for pre-test material with alignment measured in MRD for illite/mica (I), smectitic I/S (I/S) and chlorite (Ch).

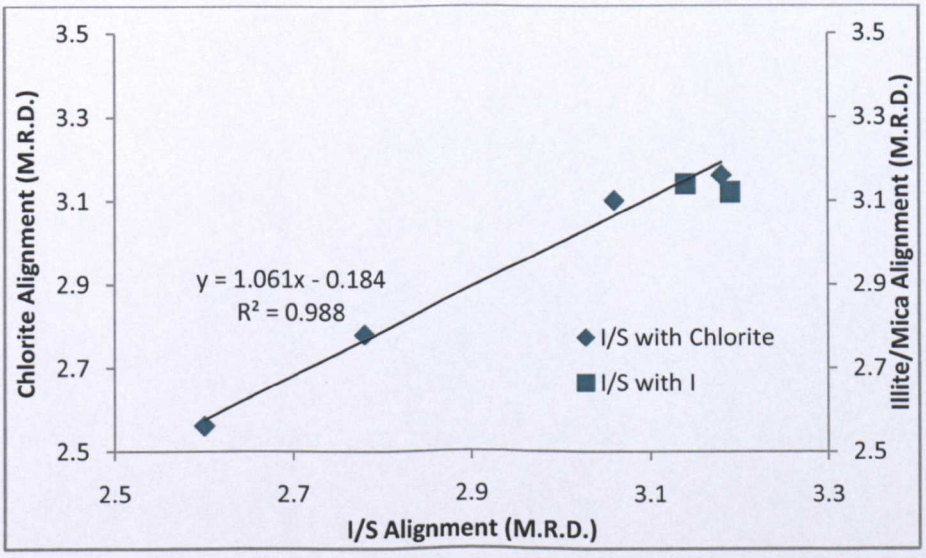

Figure 3.67 Alignment of I/S with chlorite and I/S with illite/mica from HRXTG measurements.

3.4.4.2 Post-Test HRXTG Alignment

Post-test mudstone samples showed alignment values that were largely within the range measured on the pre-test samples.

Post-Test Sample	I Kα ave. d-spacing (Å)	I Max. Pole Density (MRD)	I/S Kα ave. d-spacing (Å)	I/S Max. Pole Density (MRD)	Ch Kα ave. d-spacing (Å)	Ch Max. Pole Density (MRD)
Test 1	10.0	3.14	11.4	3.07	-	-
Test 2	9.9	3.15	11.4	3.02	-	-
Test 3	-	-	12.2	2.76	13.3	2.68
Test 4	10.0	3.26	12.3	3.25	13.3	3.17
Test 5	10.5	2.82	12.3	2.78	-	-
Test 6	9.9	2.58	12.4	2.65	-	-
Test 7	10.0	3.34	12.4	3.08	14.0	3.14
Test 8	10.0	2.51	12.4	2.53	-	-

Table 3.23 HRXTG data for pre-test material with alignment measured in MRD for illite/mica (I), smectitic I/S (I/S) and chlorite (Ch).

Test 4 (High stress Variable Test) and 7 (Chemical Compaction Test) show values of alignment slightly above the maximum recorded on the pre-test material, with Test 7 showing the highest, 3.34MRD for illite/mica. These samples were also the only plugs that showed significant loss of larger pores and statistical testing was carried out to analyse whether this difference was significant given the large range in values.

Statistical tests on the pre-test material HRXTG results and the post-test data showed that the null hypothesis should be accepted and there was no statistically significant change to the alignment of I/S grains measured in MRD at the 95% confidence level following any of Tests 1- 8 (95% CI for difference:(-0.132, 0.433) and P-Value 0.266).

Similarly to the pre-test material, the tested samples show a positive correlation between the alignment of the different clay minerals. However, there does not appear to have been any statistically significant increase in alignment, despite the high effective stresses applied to the samples (in addition to other conditions).

3.4.5 Physical Rock Properties: Summary

- The pre-test grain density range was 2.59-2.69g/cm^3, but post-test samples from test plugs 1,2,3,4,5,6, A and C were all above this range. Compaction Simulations 7, 8, 9A and 9B were all within range. Variation is likely to be attributed to variation in pyrite content.
- Grain size distributions show that D_{50} (50% smaller) for the pre-test material ranges from 1.2-1.8μm with an average of 1.5μm. Post- triaxial test material generally lies within the range of the pre-test material over much of the distribution and all (bar Test 1) are within range in the clay fraction. The reflux condenser tests show differing distributions, but results are questionable due to sample recovery issues.
- The overall pre-test average corrected porosity was 24.2±0.7%. For the variable testing, triaxial tests, none of the corrected porosities are within the range of the original pre-test material (23.2 to 25.3%), although Test 2 and 3 are close. Test 1, 5 and 6 all appear to show increased porosities. This correlates with the final post-test dimension measurements for these samples which showed slight expansion. Test 4 (the high effective stress test) had reduced porosity, which is also shown in the decreased R_{mean}.

- Test 7 (Chemical Compaction Test) shows a reduction in corrected porosity and R_{mean} when compared to pre-test values. Test 8 (Mechanical Compaction Test) material has an average corrected porosity and R_{mean} that are within the calculated errors of the pre-test averages, there is apparently limited change to porosity due to Test 8. Test 7 shows a reduction in the larger pore throats which shifts the distribution to a lower R_{mean}. The distribution of Test 8 plug data is similar to the pre-test distributions also plotted for comparison.
- Test 9B consolidated at 30MPa before failing during the stress increase to 50MPa. 30MPa was the same effective stress Variable Test 4 reached, yet Test 9B (or Test 9A) does not show a similar reduction in the R_{mean}. Test 4 ran at 150°C (and used 4M KCl pore fluid), whereas Test 9B ran at room temperature (using 3M KCl 10^{-5}M KOH).
- Both Test 9 distributions show a trend not observed in any other post-test MICP distribution, a loss of smaller pore throats (approximately <10nm), with little change to the larger, resulting in the within pre-test range R_{mean} values. Porosity calculated from mid-test dimension measurements confirms that the MICP measured porosities were reached during the test prior to failure, indicating that the distribution is condition related and not due to failure.
- When normalised to calculated, initial porosity values, the final porosity for Test 9B shows an intermediate reduction, with Test 7 showing the largest and Test 8 showing the least. This is supported by the R_{mean} data.
- The average pre-test illite/mica alignment is 3.13±0.01 MRD, for smectite/smetitic I/S the average is 2.99±0.24MRD and for chlorite is 2.90±0.28 MRD. Therefore, the pre-test mudstone already displays weak to

moderate alignment of the clay minerals. There is also a positive correlation between the alignment of the different phases, mainly provided by the I/S with chlorite relationship.

- Test 4 (High stress Variable Test) and 7 (Chemical Compaction Test) mudstone shows values of alignment slightly above the maximum recorded on the pre-test material, with Test 7 showing the highest, 3.34MRD for illite/mica. The difference is not calculated as being large enough to be statistically significant.

3.5 Discussion

3.5.1 Porosity Behavior

3.5.1.1 Triaxial Compaction

The variable testing triaxial experiments were mainly carried out at low effective stresses of 6MPa. Despite compacting whilst under pressure in the cell, mudstone samples rebounded, with Test 1,3,5 and 6 showing virtually no change or actual expansion in post-test dimension measurements, confirmed by MICP analysis which showed that those tests appeared to show slightly larger porosities when compared to pre-test values (for example, 27.2% following Test 1 compared to 25.3% maximum in pre-test material). The major contradiction to this trend was Test 4 which elevated the effective stress to 30MPa over an increased time period. It ran at 150°C, using a 4M KCl pore fluid. The tests listed above ran under similar conditions, bar the stress and time factors. Yet Test 4 was the only test to show significant dimension reduction post test (3.9%), again confirmed by its reduced porosity in MICP testing as well as a lower mean pore radius. The effect of stress is integral to compaction, but in this case, the key is surpassing of the in-situ stress as this is a natural mudstone so some degree of stress must be applied before normal compaction may resume.

Supporting this interpretation of Test 4, none of the main compaction simulations showed expansion on pre-test dimensions and porosities remained at or below pre-test values. This is because the samples in Tests 7 (Chemical Compaction Simulation), 8 (Mechanical Compaction Simulation) and 9B (Intermediate Test)

surpassed the in-situ stress conditions of the North Sea mudstone and normal consolidation was taking place.

3.5.1.2 Chemical Compaction Simulation (Test 7)

In Test 7, the Chemical Compaction Simulation, the mudstone plug consolidated at higher than in-situ stress, flowing a 3MKCl with 10^{-5}M KOH pore fluid at 150°C. During the triaxial test, the mudstone shows a limited degree of swelling in response to exposure to the 3MKCl with 10^{-5}M KOH fluid with further expansion due to increased temperature. However, it then shows the largest degree of porosity loss, exhibiting the greatest compaction in both the axial and radial dimensions. As stress and temperature were ramped down, the Test 7 sample showed the least rebound and post-test MICP measurements found that statistically significant porosity reduction had taken place through an apparent decrease in larger pores (measured as pore throats), shifting the mean pore radius (R_{mean}) to a smaller pore size. This compaction does not, however, result in any increased in alignment of the matrix.

In the soil mechanics literature, parts of this behavior are explained by the temperature-volume relationships described in Mitchell & Soga (2005). As the clay-rich sample consolidates normally (ie. under > previous maximum stress) under drained conditions with the temperature raised, a significant positive pore pressure develops due to the greater volumetric expansion of the pore fluid compared to the mineralogical solids. The relationship between temperature and illitization described in Chapter 1 meant that temperature increases in the triaxial tests were always carried out at the beginning of the test and relatively rapid (~24hrs). The lower the hydraulic conductivity of the mudstone, the longer the time required for this pore

pressure to dissipate. Though the North Sea mudstone used in the tests was well consolidated, its porosity of ~25% is not low in comparison to some of the values recorded for the Malay Basin mudstones (see Chapter 4). Also, as described in Chapter 2 radial gauze drains were used aid the dissipation of this pore pressure and decrease consolidation time. Water drains from the sample over this period due to temperature in a way analogous to the normal consolidation curve associated with changes in applied stress.

As temperature increases, the shearing resistance decreases at individual particle contacts resulting in partial collapse of the of the mudstone matrix. This is accompanied by a decrease in the void ratio (and porosity) until a sufficient number of additional contacts are formed to allow the mudstone to accommodate the stress at higher temperature. When temperature is decreased, differential thermal contractions between the clay matrix and the pore fluid generate a pore pressure reduction. The clays absorb fluid, but there is no secondary volume change as the temperature decrease causes a strengthening/hardening of the matrix and no further structural change is required to accommodate the effective stress (Mitchell & Soga, 2005).

3.5.1.3 Intermediate Compaction Simulation (Test 9B) ,

However, the results of Test 9B (the Intermediate Test) show that temperature is not the only factor behind the compaction seen in Test 7. Test 9B consolidated at higher than in-situ stress, flowing a 3MKCl with 10^{-5}M KOH pore fluid at room temperature (20-25°C).The sample in the Intermediate test showed a small degree of swelling in

response to exposure to the 3MKCl with 10^{-5}M KOH fluid similarly to the sample in Test 7, but without the further expansion due to increased temperature as Test 9B remained at room temperature. Despite this, the Test 9B plug does not compact to the same degree as that in Test 7, but shows an intermediate porosity loss between Test 7 and Test 8.

This intermediate behavior only appears to apply in the axial direction, perpendicular to bedding as Test 9B shows a similar radial response to effective stress as Test 8. As the cell system failed during this test, the sample consolidated to a lower effective stress than in Tests 7 and 8 and its controlled ramp-off behavior was unrecorded. MICP measurements found that statistically significant porosity reduction had taken place, but displayed a different distribution to the porosity loss in Test 7 through an apparent decrease in smaller mesopores (measured as pore throats), without shifting the mean pore radius (R_{mean}) (Figure 3.68). Again, this compaction does not result in any increase in alignment of the matrix.

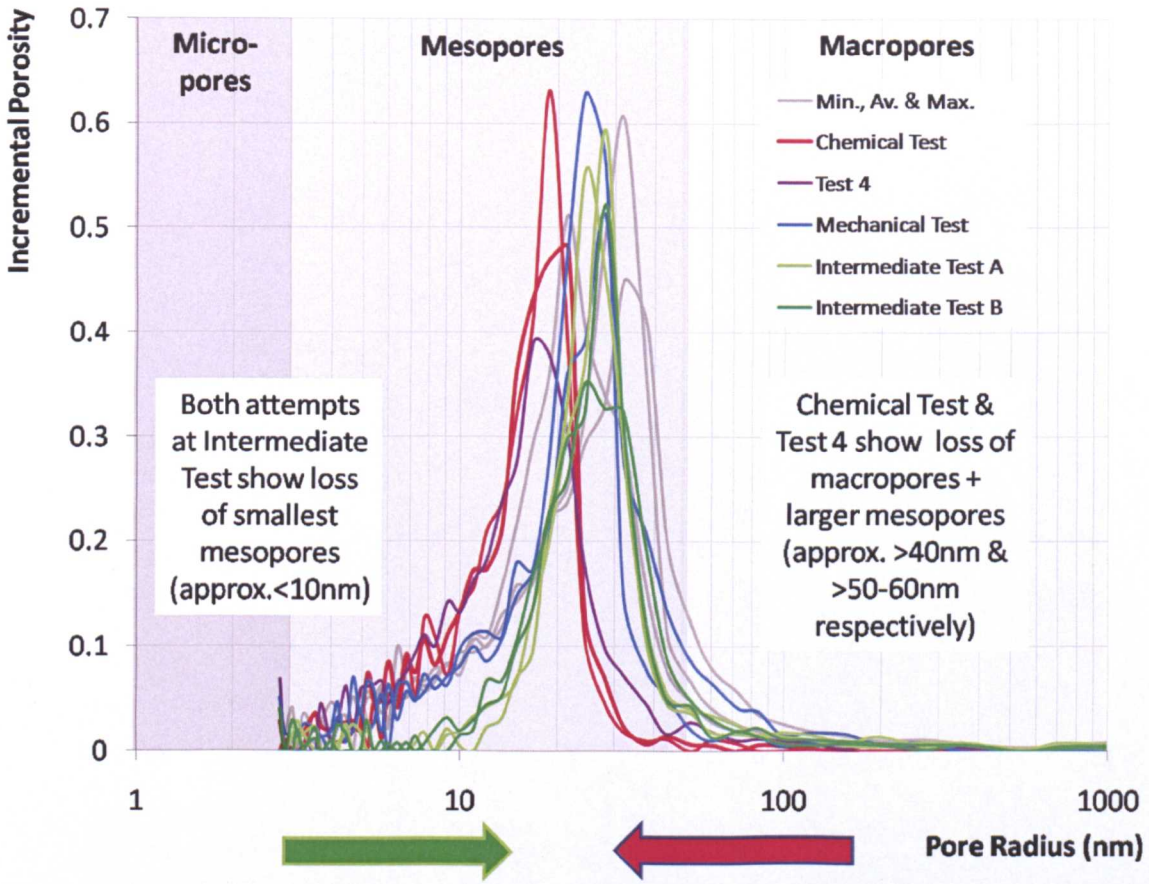

Figure 3.68 Pore radius distributions for pre-test (minimum, maximum and average), Test 4 of the "Variable Tests" and the Chemical, Mechanical and both Intermediate Compaction Simulations.

The corrected porosity value post-Test 9B is similar to that following Test 7. However, the porosity calculated during the test (which corresponds to the MICP data) shows that this is only because Test 9B starts the test at a lower porosity (calculated from the bulk, fluid and grain densities). This may be related to an elevated smectite content as it has one of the lowest grain densities measured (grain density exerts a strong control on the porosity calculation). Its porosity loss is therefore calculated to be intermediate to Tests 7 and 8 (see Figure 3.69).

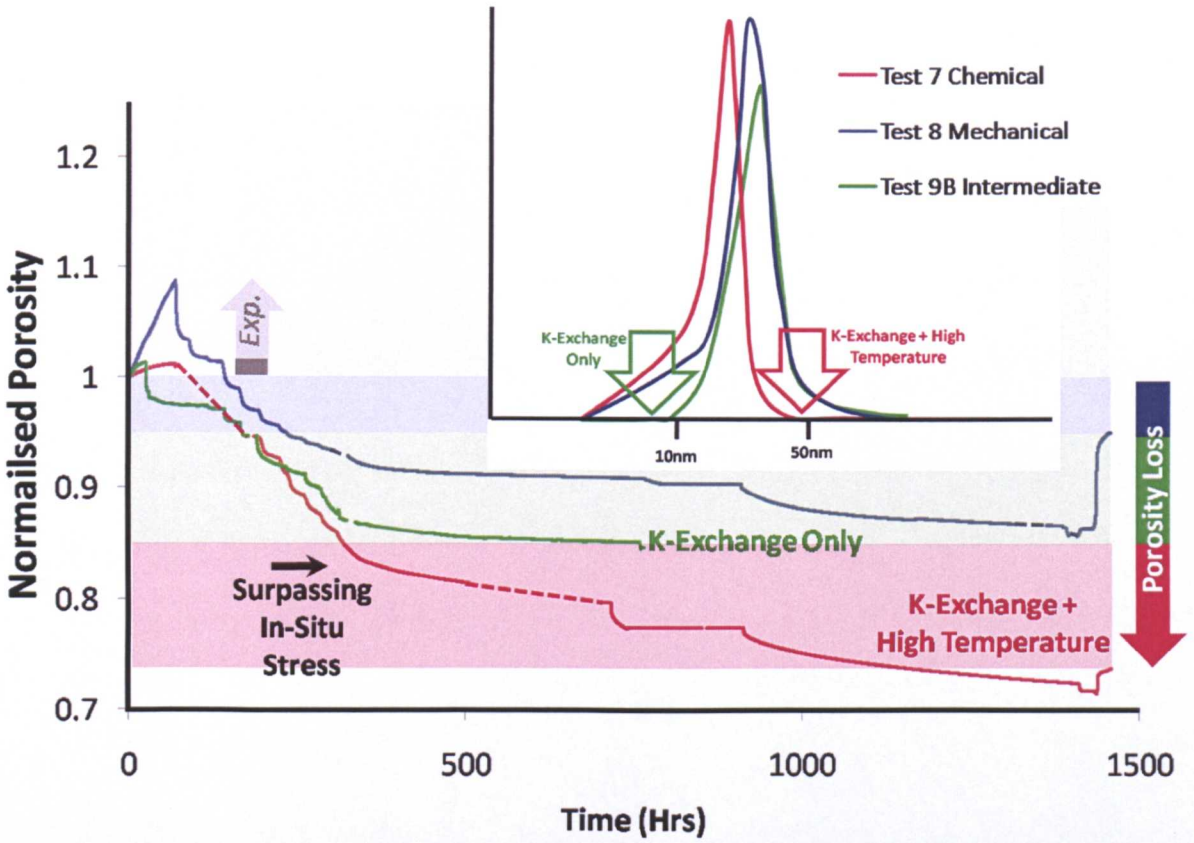

Figure 3.69 Simplified sketch of Figure 3.19 superimposed onto annotated normalized porosity plot from Figure 3.68. Arrow shaded according to porosity loss, right of image shows permanent loss of porosity due to compaction at 50MPa effective stress in Test 7 and 8 (red and blue, respectively), but green section is porosity loss at 30MPa (Test 9B). Speculatively, at 50MPa, the green shading would move lower, into the red section. Greyscale shaded arrow, left of image, shows the relative initial expansion. This behavior is only seen during normal consolidation (ie. beyond the in-situ stress of the North Sea mudstone).

If the compaction behavior observed in Test 9B is related to normal consolidation using the 3MKCl with 10^{-5}M KOH pore fluid, then the mechanisms behind it should also be operating in Test 7, contributing to the larger compaction measured in that sample. Yet, as seen in Figure 3.68, the distribution in Test 7 plug pore sizes shows no decrease in the smallest mesoporosity. In fact, it shows a greater amount than the pre-test representative distributions and those following Test 8.

To understand this, the mechanism behind the loss of the smallest mesopores in Test 9B must be identified. It would appear to be linked to the use of the K-rich fluid

and given the literature discussed in Chapter 1, potassium exchange into and onto the clays in the mudstone matrix (observed in EDX mapping in previous tests). The shrinkage of the clays in response to exchanging the less hydrated potassium cations is on an Ångstrom scale of change (in the range ~20-10Å). 20Å is 2nm and the lowest measurable pore throats using MICP are 3nm. Referring back to Chapter 1, MICP will not be measuring the interlayer porosity. However, the shrinkage associated with reduction of the interlayer "pores" and exchange on the clay surfaces will reduce the associated portion of the microporosity and smaller mesoporosity in the inter and intra particle network of the clay matrix. This could explain the observed loss of the <10 μm pore throats observed in Figure 3.68.

This compaction mechanism should also be operational in Test 7, yet it is not observed in the Chemical Compaction Test distributions. Despite the fact that these tests were carried out on a consolidated mudstone and not a soil, the high temperature related mechanism of structural collapse to increase particle contacts would appear to be operating in Test 7. This would cause re-organisation of the whole matrix including the larger mesopores and macropores which are "closed" following Test 7. This difference in the scale of effects appears to be borne out by the difference in radial compaction in Test 7. Test 9B only reduces radially to the same extent at Test 8 due to effective stress. Its compaction occurs in the axial direction or rather perpendicular to the modest layering (~3MRD alignment, also in evidence in the anisotropic velocity response – discussed later). This is the direction affected by the reduction of a proportion of the clay inter-layers in partially aligned clays. Test 7 compaction takes place in the axial and radial directions and the whole matrix is affected. The larger pores collapse to create more grain contacts and the

mean pore radius reduces. Inter and intra particle pores that were once mesopores or even small macropores are reduced to form more smaller mesoporosity. Evidence of this process occurring is present in the form of the excess <10 μm porosity, not only in Test 7, but also Variable Test 4 where this mechanism would also be predicted to be operational due to its high temperature, K-rich fluid (4M KCl) and >in-situ stress conditions. That the process appears to be functioning in Test 4 indicates that potassium content in the fluid is the control and there does not appear to be a porosity-related influence from the elevated pH used in Tests 7 and 9B.

If "new" smaller mesoporosity is being created by the temperature related mechanism, then it will mask the exchange related mechanism, despite both contributing to the overall loss of porosity and will not be clearly detected in Test 7 and this is what is observed in Figure 3.68.

3.5.1.4 Mechanical Compaction Simulation (Test 8)

Understanding the interplay of these mechanisms is integral to explaining the behaviour of the mudstones as they compact in these tests and a simplified conceptual model is displayed in Figure 3.70. The uppermost image depicts the state of the matrix in Test 8, the Mechanical Compaction Simulation. In Test 8, the mudstone plug was consolidated at higher than in-situ stress, flowing a 4M NaCl pore fluid at 25°C. During the triaxial test, the mudstone shows initial swelling in response to exposure to the 4M NaCl, greater than the expansion due to increased temperature in Test 7, despite the hypothesized osmotic effects of the Na^+ concentration of the fluid. It then shows the lowest degree of compaction under

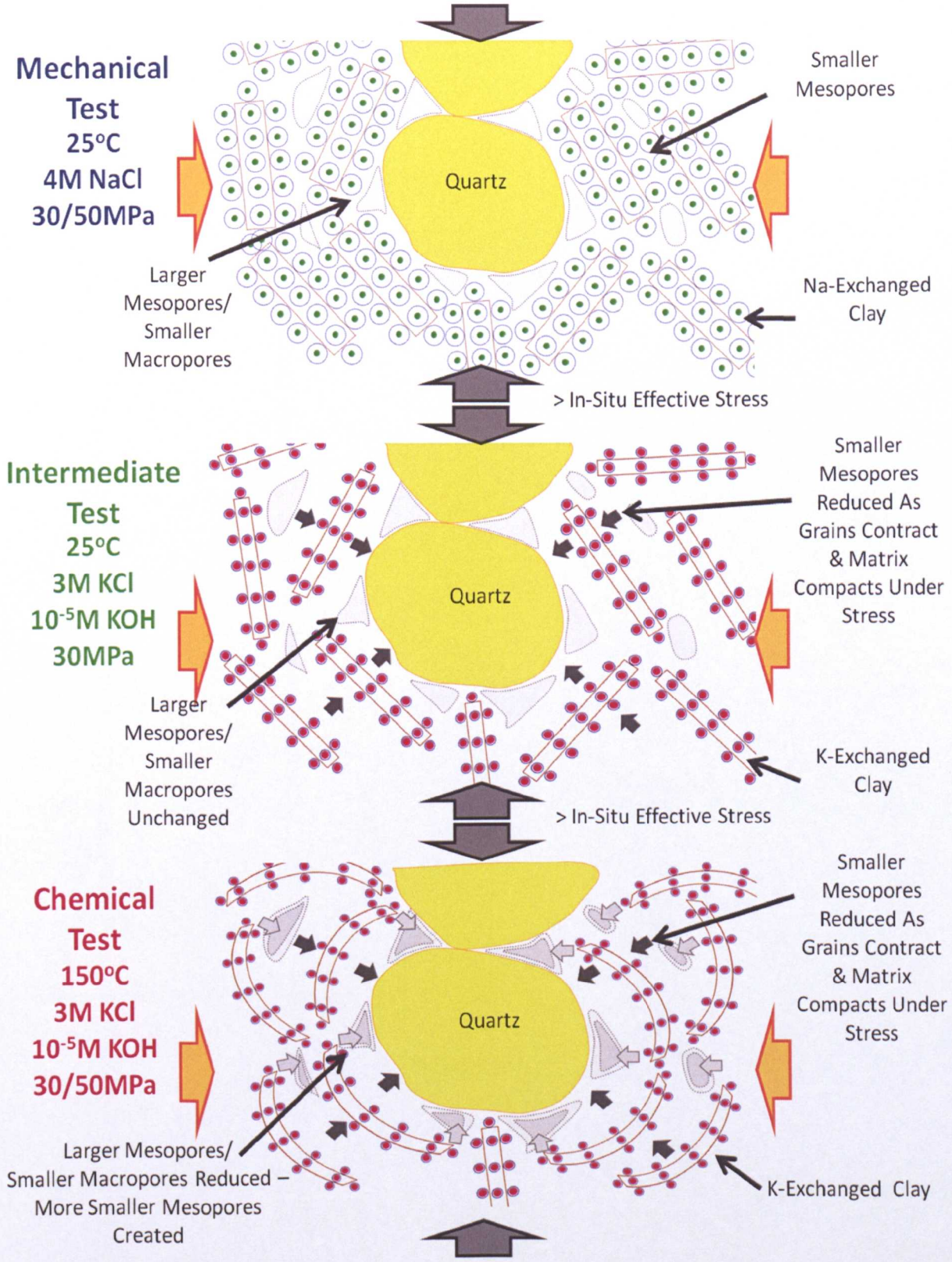

Figure 3.70 Cartoons of suggested grain and pore behavior during the Main Compaction Simulations (Mechanical – Test 8, Intermediate – Test 9 and Chemical – Test 7).

stress, despite being subject to the same level of effective stress as the other compaction simulations.

Given the excess pore pressure described as being inherent in the temperature increase, Test 8 may for a period, even be at higher effective stress than Test 7. As stress and temperature were ramped down, the Test 8 sample showed a large degree of rebound, resulting in post-test dimensions that were almost equal to initial measurements. This was reflected in the post-test MICP measurements that found no statistically significant porosity reduction had taken place due to the test and the mean pore size was within range of the pre-test samples. There was similarly no change to alignment.

This minimal level of compaction was found despite surpassing the calculated in-situ stress conditions by ~25-30MPa. Taking a step back to look at Test 8 in the context of the other tests and soil mechanics theory is useful. Stress history has large influence on the volume (Hueckel & Baldi, 1990). Applying soil mechanics to this work, the highest stress that a mudstone has been subjected to is called the preconsolidation stress. The over consolidation ratio (OCR) is the maximum stress experienced by the mudstone divided by the current stress. When the mudstone is experiencing its greatest level of stress it is termed normally consolidated (OCR=1). When it is at a level of stress less than that it has already experienced, it is termed overconsolidated (OCR>1). Mitchell & Soga (2005) describe that for normally consolidated to moderately overconsolidated clay, the permanent component of the volume reduction is observed through structural degradation (radial and axial compaction in Test 7) and an increase in shear strength (increased shear modulus in

Test 7). In heavily overconsolidated clay (at stresses below in-situ) the sample will expand upon heating, the rate of which increases with overconsolidation ratio; this is observed in the moderate stress ranges tested in the Variable Tests (1,2,3,5 and 6). Using simple calculations and assumptions that the hydrostatic gradient is 0.0105MPa/m and the lithostatic gradient is 0.0226MPa/m and that there has been no more than 600m uplift in the region (this value is actually likely to be $\ll$ 600m given geological background), the maximum effective stress that the North Sea mudstone has been subject to in the burial environment can be found. The range is 17MPa (no uplift) to 24MPa (600m uplift). This means that for most of the variable tests where the effective stress is 6MPa, the overconsolidation ratio is between 3-4. This means that the mudstone in the variable testing, triaxial tests can be described as heavily overconsolidated and volume expansion could be expected upon testing at high temperature. This was precisely the response of those tests, displayed in both their dimension changes and MICP measured porosity.

Whereas in variable Test 4 and 9B where the effective stress reached a maximum of 30MPa, the OCR is 0.6-0.8 and in the Chemical and Mechanical tests, 7 and 8, at 50MPa effective stress, the OCR is 0.3-0.5. This means that the samples (given that the pore pressure generated by the maximum load should have had time to dissipate and therefore the samples should not be undercompacted) are normally compacted and volume would be predicted to permanently reduce.

Yet Test 8 does not significantly, permanently compact despite having a low OCR. However, the test ran at 25°C and rough estimates of the maximum in-situ temperature range between 57-78°C. The OCR was calculated from effective stresses resulting from the stress due to the total stress minus the stress exerted by the pore pressure only. That the Test 8 plug only lost a recorded 1.8% volume (and was still expanding) and a statistically insignificant amount of porosity, means that the volume lost during its natural burial to ~17-24MPa axial effective stress is not significantly increased (greater volume loss) during its stress ramp to 50MPa. Therefore, the processes that decreased the volume due to stress and temperature by ~17-24MPa and 57-78°C are more effective than just increasing stress by a further 26-33MPa as there does not appear to be the additional permanent reorganization of grain contacts. The real effective stress exerted upon the samples during natural burial from ~17-24MPa and the effects of temperature are apparently close to 50MPa effective stress without temperature.

The irrecoverable volume reduction due to temperature depends on the pressure range. The pre-consolidation pressure (previous maximum stress sustained) of natural soft clay depends on temperature, where there is ~1% decrease in pre-consolidation pressure per 1°C increase in the range of 5-40°C and then to a lesser degree at higher temperatures (Leroueil & Hight, 2002). The equations for pore pressure behavior during compaction under temperature state that they are based on assumptions that do not apply to a consolidated mudrock as opposed to a clay soil. The ideas underpinning these equations are therefore not applied conceptually in effective stress related geological compaction models. However, in models such as Yang & Aplin, (2004), the calculation of coefficients based on statistical analysis

of natural datasets should incorporate their influence without necessarily citing all of the causal mechanisms. The influence of the mechanical effects of temperature and the chemical effects of K-exchange are not credited in chemical compaction literature either. Yet given the results of this thesis, they do contribute to the volume/compaction behavior of mudrock mechanics as well as soil mechanics. Given the Leroueil & Hight (2002) relationship, temperature effects at least should be operating even in the rapid porosity loss region at shallow depths. This could explain why previous mechanical compaction experiments such as Mondol *et al.* (2007) do not match the early porosity loss of natural mudstones. Increasing temperature will further elevate pore pressure, decreasing the gradient initially compared with experimental trends, but ultimately decreasing porosity at a rate higher than experimental trends whilst the temperature related collapse mechanisms operate in addition to those of effective stress. This could contribute to why the trends don't match natural data at further depth, previously interpreted as being the result of mineralogical change only. The lack of temperature effects are certainly a detrimental loss in studies similar to Mondol *et al.* (2007) as they actually start as saturated soils and so should certainly be governed by well established soil mechanics principles.

Incorporation of temperature effects into a consolidation model exist in the form of the adapted Cam Clay model discussed in Chapter 5 where this relationship is examined further in relation to the North Sea mudstone and Malay Basin datasets. This is because comparison with a natural dataset becomes vital as even with the combined effects of elevated temperature and K-exchange final porosities were not reduced to natural levels. However, Figure 3.69 shows that Test 7, at least, was

clearly not finished consolidating under its imposed conditions and this is evaluated with the control of a geological timescale and the proposed effects of illitization through the Malay Basin samples in Chapter 5.

3.5.2 Ultra-sonic Velocity Change and Fluid Interaction

3.5.2.1 Ultra-Sonic Velocities and Calculated Elastic Moduli

The variation in ultra-sonic velocities recorded through the samples correlate with other mid-test data such as dimension changes (to be expected as they form part of the calculation), but also tie in with post-test rock properties such as porosity. As temperature is increased at the beginning of Test 7, expansion of the sample is linked to a rapid reduction of compressional and shear wave velocities. Despite poor waveforms recorded at the start of Test 8 ruling out a conclusive view, it would appear that the expansion of the sample as it came into contact with the NaCl solution also caused a decrease in velocities. Limited expansion upon contact with the KCl and KOH in Test 9B generated only limited expansion (as also observed in Test 7 prior to the temperature increase) and only minor velocity decrease is noted. This means that Test 9B starts the stress ramp-up at the highest velocities and maintains that maximum position throughout the test. All tests show velocity increase as the stress ramp and consolidation periods continue with Test 7 showing the most rapid increase, surpassing the velocity increase measured in Test 8. This is likely to be associated with the greater volume reduction discussed in the previous section. At the ends of the Tests 7 and 8 where the response of the samples to controlled stress reduction was monitored, Test 8 showed the larger rebound effect in velocities as the sample dimensions returned to just under their initial values. Test 7 showed

less rebound and the final velocities recorded are above those initially measured at the beginning of the experiment.

A brief overview of the elastic moduli trends, calculated from a calculated bulk density and the velocity results can be made as follows. The bulk modulus representing resistance to compression, shows that Test 8 material shows the least compressibility during the experiment, whilst Tests 7 and 9B (both K-rich fluids used) show similar, greater compressibility. The shear modulus, as the resistance to shearing, is greatest in Test 9B, intermediate in Test 7 (though rapidly increasing) and lowest in Test 8. The Poisson's ratio, or the change in lateral strain due to the axial compression, shows the reverse ordering where Test 8 has the highest ratio, Test 7 is intermediate and Test 9B shows the lowest. Therefore, Test 9B shows the greatest lateral strain with compression, where as Test 8 shows the least. The Young's Modulus calculations show test 9B to be the "stiffest" material, followed by an increasing Test 7 trend, with Test 8 material being the least stiff.

These results indicate certain consistant behaviours in each of the Triaxial Compaction Simulations that are linked to the test conditions. Moduli comparisons are made at the same effective stress, ie. only comparing Test 9 to the 30MPa stages in the other tests. Test 7, the Chemical Compaction Test, carried out at 150°C, first under an axial effective stress of 30MPa and then at 50MPa using a 3MKCl with 10^{-5}M KOH fluid is one of the most compressible plugs and shows intermediate characteristics for the other properties. This is likely to be linked to the mechanisms operating in the material discussed in the previous section where the temperature effect of matrix collapse will make the material less stiff and less

resistant to shearing that the plug in Test 9B. The Intermediate Compaction Test was carried out at 20-25°C, under an axial effective stress of 30MPa only using a 3MKCl with 10^{-5}M KOH fluid) is stiffer and more resistant to shearing than in Test 8 (the Mechanical Compaction Test carried out at 25°C, first under an axial effective stress of 30MPa and then at 50MPa using a 4MKCl fluid), but more compressible due to the shrinkage and stabilizing effect of potassium exchange.

3.5.2.2 Transport Properties

As is clear from the last statement, the artificial fluid used to control a pore pressure throughout the triaxial experiments plays a large role in the behavior of the mudstone. Literature review prior to the tests had already highlighted the fact that in low permeability materials such as mudstones and shales, diffusion is the most rapid form of transport as opposed to Darcy flow in more permeable media (van Oort, 2003). Calculations based on the equations of Yang & Aplin (1998) were carried out using measured rock properties to assess the permeabilities of the North Sea mudstone both pre and post-test. K_x and K_z were calculated and results are displayed in Figure 3.71 plotted against calculated effective stress.

The pre-test range was calculated using the minimum porosity/maximum clay data to calculate the minimum permeability, averages for the whole Pre-Test dataset were used to calculate the average and the maximum porosity/minimum clay data was used to estimate the maximum. These results are marked in grey in Figure 3.71. Post-Test data was taken directly from measurements and in the Compaction Simulations (Test 7 and 8) the 2 porosity measurements carried out on each post-test plug were used for individual calculations and plotted.

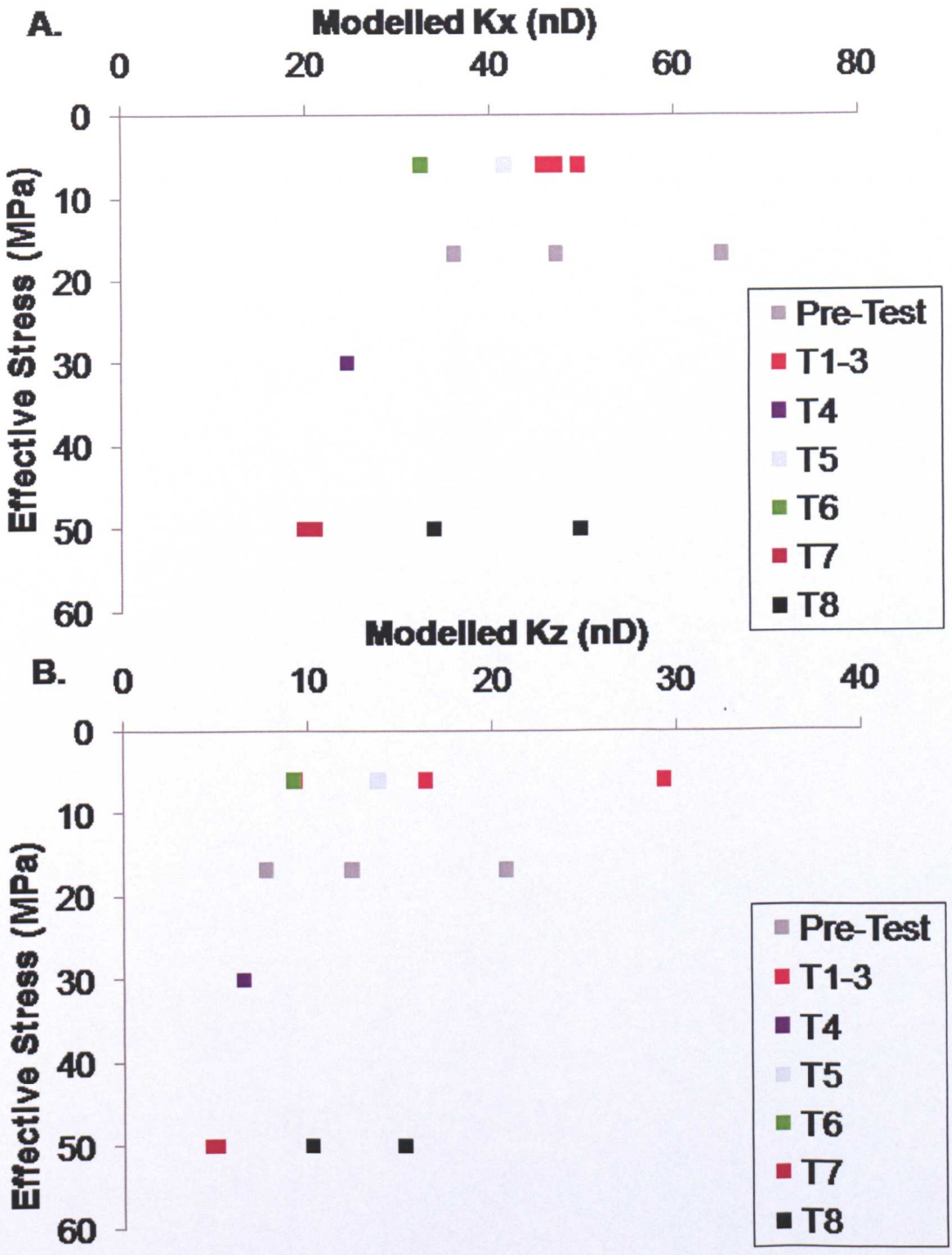

Figure 3.71 Estimated effective stress with modelled K_x and K_z (nD) for pre-test data and post-triaxial test samples.

These calculations show first, that permeabilities are low, despite the moderate porosities as these samples are clay-rich and second, variation can be seen between different tests.

For K_z or vertical permeability, the variable testing, triaxial experiments are generally within range of the pre-test range (with the exception of Test 1). Test 4, the 30MPa effective stress Variable Test, shows a permeability below the pre-test range. As does Test 7 (both porosity results used to give individual calculations). Repeat porosity measurements of Test 8 showed more variation than Test 7. However, calculations using either porosity following Test 8 show permeability to be within the original pre-test range. Given the previous discussion, it is noteworthy that despite being subject to 20MPa higher effective stress, permeability in the Test 8 plug remains higher than in Test 4 which was subject to high stress, K-rich fluid and high temperature. Values of K_x or horizontal permeability are higher, but follow a generally similar relationship with a few exceptions. The lowest permeability estimate for Test 8 is just below the pre-test range. However, the Test 8 average K_x still lies within range.

Given the low permeabilities, it is likely that diffusion is the main transport process. van Oort (2003) estimates that solute/ion diffusion in mudstones and shales takes place at centimeters per day, which is one to two orders of magnitude faster than Darcy flow of mud filtrate/bulk water which proceeds at millimeters per day under down wellbore conditions. This effect is also mentioned in Yu *et al.* (2001). It is likely to be this diffusion that supplied potassium ions to the matrix for exchange to take place (observed in EDX element concentration maps/spectra) and increasing the bulk density of the pore fluid used in calculation of the moduli discussed previously.

3.5.2.3 Fluid Interaction Stability Effects

The stability effects of potassium exchange are well known and persistant. As discussed in the work of Di Maio & Fenelli (1994) and Di Maio (1996) samples

exchanged prior to testing exhibited the same mechanical behavior as those exposed to brine during the testing, ie. diffusion is efficient enough to alter mechanical properties. Also, while the effects of NaCl were reversible, KCl effects persisted even when re-exposed to pure water some months after continuous testing. This accounts for the K-echanged characteristic persisting in through processes such as wet grinding and spray drying prior to bulk fraction XRD, or through fractionation and washing (without rigourous Na exchange) prior to initial clay fraction XRD measurements.

However, a further stabilisation effect was observed when adding the small amount of KOH to the artificial test fluids. Fluid compatibility tests showed that the smectite-rich mudstone was more stable in a fluid composed of 3M KCl and 10^{-5}M KOH than it was in just 3M KCl. This effect was shown to be significant when the reflux condenser tests in the latter fluid (Test C) remained intact throughout repetitions of the test, where as Test A (with 4M KCl solution) and Test B (4M NaCl solution) broke up. The effects of pH on cation exchange behaviour and therefore swelling and stability is known. However, pH dependence is normally associated with kaolinites and its effects approximated as negligible in smectites and illites which form the dominant component of this material. It operates as the higher the pH, the greater the tendancy of the H^+ from the hydroxyls (OH^-) exposed on the surface or edges of clay particles to go into solution. This leads to a greater effective negative charge on the clay particles leading to enhanced interaction with cations such as K+. Smectite particles with small thickness to length ratios do not normally support a large effect on total charge from the OH termination sites at the edges of particles (Mitchell & Soga, 2005). The North Sea mudstone has pre-test average clay abundances of

7±0.5% kaolinite (high pH dependence), 13±5% illite/mica (low pH dependence), 43±6% smectite (negligible pH dependence) and 6±1% chlorite (low pH dependence). Yet this minor component of kaolinite (and to some extent illite and chlorite) are enough to make have a meaningful stabilising effect on the material. This is noteworthy as, although pH is often elevated in drilling fluids to prevent equipment corrosion, it has not been previously linked with mudstone/shale stability in the borehole stability references cited in this thesis.

4.5 Conclusions

- Despite compacting whilst under pressure, variable testing triaxial experiments produced negligible change or actual expansion in post-test dimension measurements due to overconsolidation effects. Surpassing the in-situ stress/ preconsolidation stress of a natural mudstone is vital for further compaction to take place even when exposed to other compaction agents such as increased temperature or potassium.
- Once in-situ stress has been passed, the mechanism for compaction in Test 9B/Intermediate Test is the shrinkage associated with reduction of the interlayer "pores" and exchange on the clay surfaces which reduce the associated portion of the microporosity and smaller mesoporosity in the inter and intra particle network of the clay matrix, perpendicular to bedding. Diffusion is efficient enough to alter mechanical properties and KCl effects are persistent. Further stabilisation appeared to be generated by the small pH increase and its effect on the clay minerals. This is despite the prevalence of the finer clay minerals in the North Sea mudstone.
- These mechanisms also operate in Test 7/, the Chemical Compaction Test, along side the additional effects of temperature increase. This involves shearing resistance decrease at individual particle contacts resulting in partial collapse of the of the mudstone matrix. The larger pores collapse to create a sufficient number of additional contacts to allow the mudstone to accommodate the stress at higher temperature and the mean pore radius reduces. Inter and intra particle pores that were once mesopores or even

small macropores are reduced to form additional, smaller mesoporosity, also reducing permeability of the matrix.

- The compressional effects of surpassing in-situ stress in Test 8/Mechanical Compaction Test without the operation of the mechanisms associated with K-exchange or elevated tempertaure does not significantly, permanently compact the mudstone and a largely elastic response occurs as stress is reduced. The processes that decreased the volume due to stress and temperature in the North Sea burial environment are more effective than simply significantly increasing stress and surpassing in-situ stress alone does not appear to be associated with the additional permanent reorganization of grain contacts to a more stable state.
- Velocites respond to the separate mechanisms at work during the tests in different ways. The K-shrinkage effect associated with loss of the smaller mesoporosity, perpendicular to bedding created a more compressible material due to the shrinkage and stabilizing effect of potassium exchange. It also resulted in velocity responses relating to the mudstone becoming stiffer and more resistant to shearing than in Test 8/Mechanical Compaction Test.
- The additional effect of increased temperature and matrix destabilization and associated with reduction of mesopores/small macropores and the formation of additional, smaller mesoporosity gives velocity responses and dynamic moduli trends that indicate that the most compressibility is generated via these mechanisms.
- Despite compression during the test, without the operation of the other mechanisms, the expansion of the material back to approximate pre-test

dimensions and porosity distribution, meant that velocities also decreased, responding to the elastic component of the response.

Chapter 4

Mudstone Compaction in Nature: Malay Basin Case Study

4. Mudstone Compaction in Nature: Malay Basin Case Study

4.1 Introduction

4.1.1 Background and Aims

Focussing on the main goal of this thesis, which was to understand the relative roles of different compaction mechanisms in mudstones, the Malay Basin, offshore Peninsular Malaysia, offers an excellent opportunity to study compaction in a high heat flow environment. This is of interest because under normal basin conditions geothermal gradient is between 20-40°C/km (Gluyas & Swarbrick, 2004) and under hydrostatic conditions, rocks can be found at depths of several kilometres and under significant vertical effective stresses by the onset of clay mineral reactions such as the smectite to illite transition at ~80°C (83-88°C in Freed & Peacor, 1992). This is an obstacle to studying the influence of increased temperature and mineralogical reactions on porosity loss in natural samples as any potential non-mechanical cause cannot be isolated from the extensive physical stress the rocks have already been exposed to.

To mitigate the influence of high stress at the onset of illitization temperatures, samples were obtained for this study from the Malay Basin where the geothermal gradient can reach up to 63°C/km. Samples at 80°C could therefore in theory be found at depths of only ~1032m (assuming seabed temperature of 15°C, Hoesni, 2004) and under only ~12.5MPa of vertical effective stress (if normally pressured). According to the composite porosity with depth plot (Figure 1.5), at these depths

some mudstones can still retain >50% porosity and therefore any effects due to temperature-related processes should be clearer to observe.

Also, in a previous study examining wireline log data from wells in the Malay Basin (Hoesni, 2004), the possible role of chemical compaction was proposed in explaining rock properties and high pore pressures found at depth.

This is investigated further in this work where the chemical/mineralogical properties of samples from the basin, associated with the Hoesni (2004) study were analysed and compared with the physical properties such as porosity with the aim of assessing any link. In addition, any variation of trends from the laboratory work of Chapter 3 or published studies from other basins was gauged to understand and quantify the role that enhanced temperature and/or chemical compaction may play in porosity loss.

4.1.2 The Malay Basin

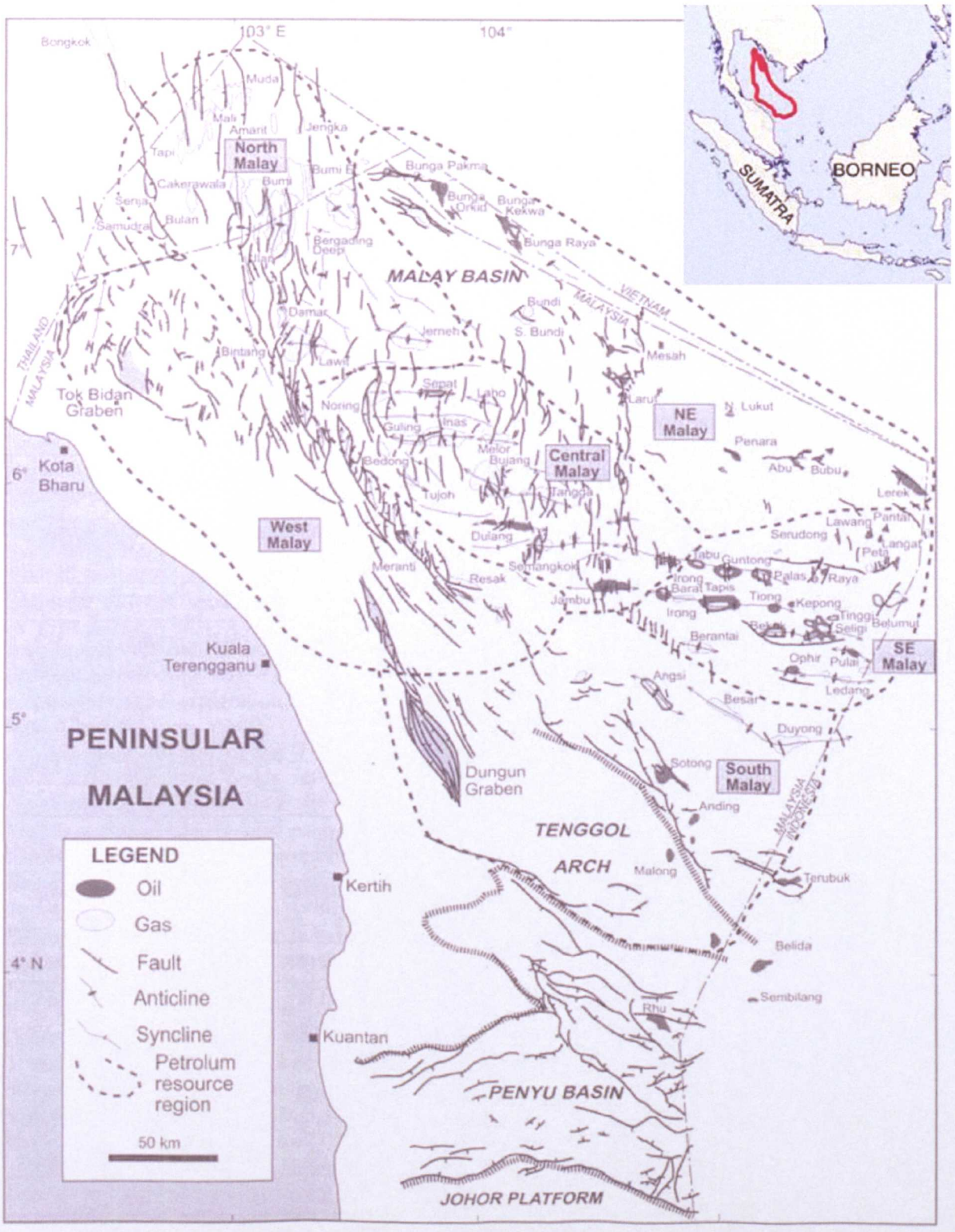

Figure 4.1 Location map with the Malay Basin marked in red (Bishop, 2002) embedded in a map to show the six petroleum regions of the basin with their oil and gas fields/discoveries (Tan, 2009).

The Malay Basin is located offshore Peninsular Malaysia in SE Asia. It is an asymmetric rift basin, ~500km in length by ~200km in width (Bishop, 2002) and is orientated NW-SE in the South to NNW-SSE in the North (Tan, 2009). The basin has been a prolific hydrocarbon producing area for several decades, with offshore exploration for oil and gas starting in 1968 (Tan, 2009). The samples samples provided for this study came from 2 wells (Wells A & B) in the South Malay region.

Several models have been proposed for the origins of the basin and are briefly reviewed in Tan (2009) and Madon (2007). They include regional thinning of the continental crust (White & Wing, 1978); a back-arc basin system (Kingston *et al.,* 1983); crustal extension over a hotspot or aulacogens, failed rift arms of a triple junction over the Malay Dome mantle plume related hot spot (Tan, 2009). Another proposal is a simple pull-apart basin on a releasing bend of a major sinistral strike-slip fault zone, reactivated by the eastward extrusion of Indochina following the collision of India with Eurasia during the Late Eocene based on the model of Tapponnier *et al.* (1982). The escape tectonics model has been modified in later work with studies such as Ngah *et al.* (1996) describing oblique rifting or shear from transtensional extension of the E-W basement faults along a broad NW–trending shear as opposed to a discrete strike-slip fault.

The extensional phase resulted in the E-W trending grabens and half-grabens which subsided through the Oligocene until the Middle Miocene when regional stresses changed and the Axial Malay Fault became dextral. Inversion followed creating thrust faults and the anticlines that later became structural traps for the hydrocarbons, its effects being greatest in the SE of the basin (Tan, 2009). During

the Pleistocene lowstands, some erosion took place (Bishop, 2002), but generally from the Pliocene onwards gentle subsidence and deposition has resumed. Between <3000m to >12000m of sediment has now been deposited in the basin overall and the surface lies under a water column of <200m (Bishop, 2002).

Understanding the basin tectonics is important to this study as the maximum depth that the mudstone samples have been buried to will be integral to interpreting controls on their porosity. During the inversion event of the Late Miocene, the sampled horizons would have experienced uplift and lower porosities compared to current depth could be expected. Burial history modelling carried out outside of this project shows that this period of inversion lasted between approximately 8 to 7.1Ma and over this period the sampled horizons from Wells A and B were uplifted by around 650 and 275m respectively. From 7Ma to the present the area has been subsiding again with the top of the sampled horizon in Well A now reaching 5m below its previous maximum burial depth at the present day and reaching 450m below in Well B.

Although the uplift was significant, particularly in Well A and may have had an effect on overpressure generation (see later) both wells are now approximately at or below their previous maximum burial so if the models are correct, porosities in both wells should reflect their current burial depth.

4.1.3 Geothermal Gradient

As mentioned earlier in 4.1.1, one of the features of the Malay Basin pertinent to this study is the high geothermal gradient. Given the models of tectonic development, there are several explanations put forward for the high heat flow and geothermal gradient in the Malay Basin. Dome formation in the Late Cretaceous from the emplacement of a mantle plume could be associated with high heat flow (Tan, 2009). The effect of this could be compounded by the composition of the emplaced material which is thought to be granitic and could therefore contain substantial radioactive, heat producing minerals. Also, the relatively young age of the basin could allow elevated gradients as it is probably still undergoing post-rift thermal re-equilibration (Madon, 2007) following simple rifting 35-25Ma or more a more recent heat-pulse event within last 100,000 yrs (Waples *et al.*, 1995).

An average of 51.8°C/km for the basin is recorded in Mohd Firdaus Abdul Halim (1994) and the degree to which that varies with location can be seen in Figure 4.2 below from that study. Bishop (2002) reports from an earlier study maximum gradients of 63°C/km in the northwest to a minimum of 36°C/km in the southern region of the basin. This is roughly the trend observed in the map in Figure 4.2 with the maximum and minimum values possible within the 60°C/km and 40°Ckm contours in the northwest and southeast.

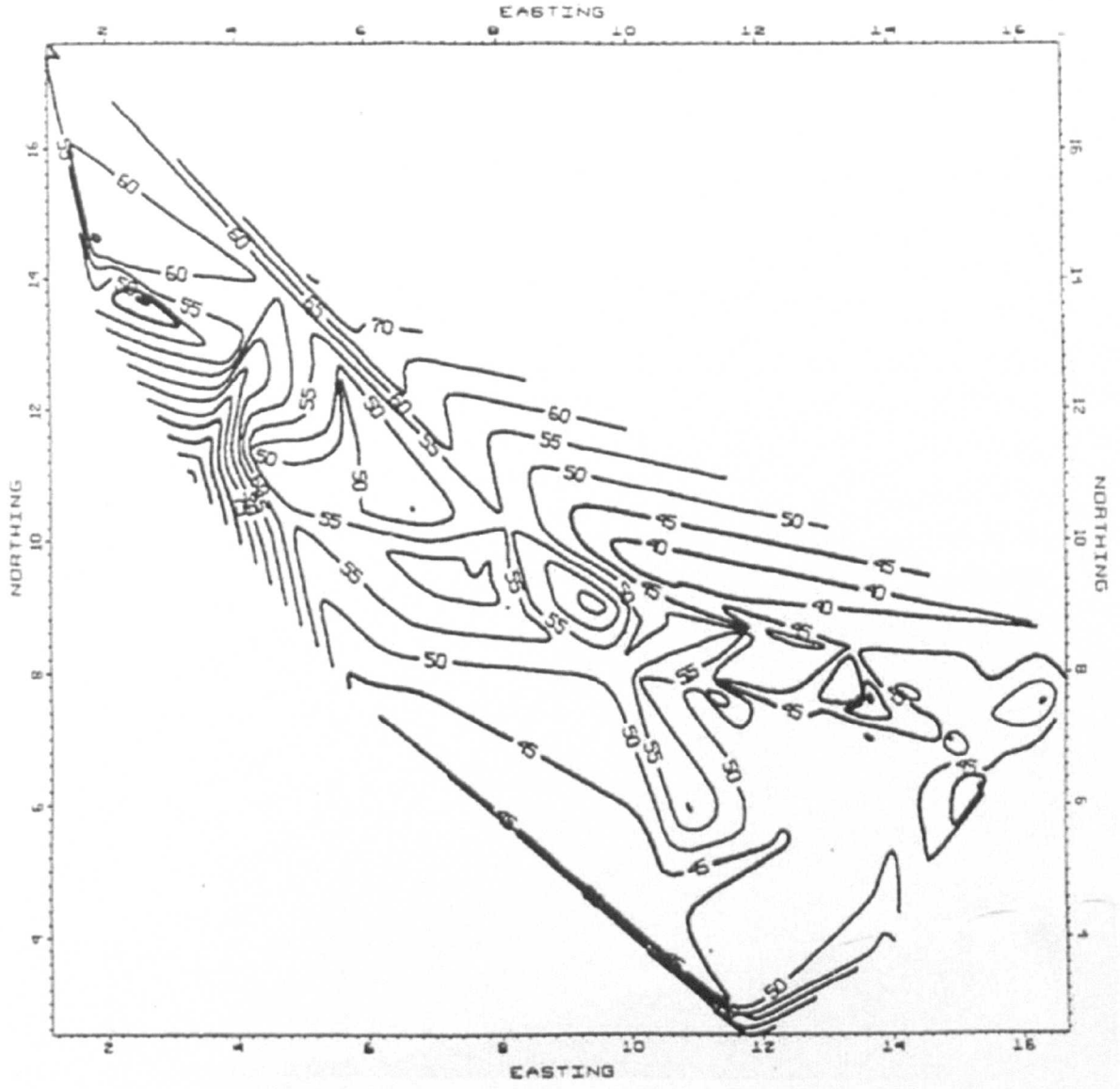

Figure 4.2 Geothermal gradient map of Malay Basin from Mohd Firdaus Abdul Halim (1994). Contours in °C/km.

The wells in this study are located in the South and are therefore cooler than the maximum, but are not in the coolest southeastern area. Estimates from location on the maps above and below (Figures 4.2 & 4.3) were that the wells would have present day gradients between 45-50°C/km (still relatively high) and this is in agreement with measured borehole data provided.

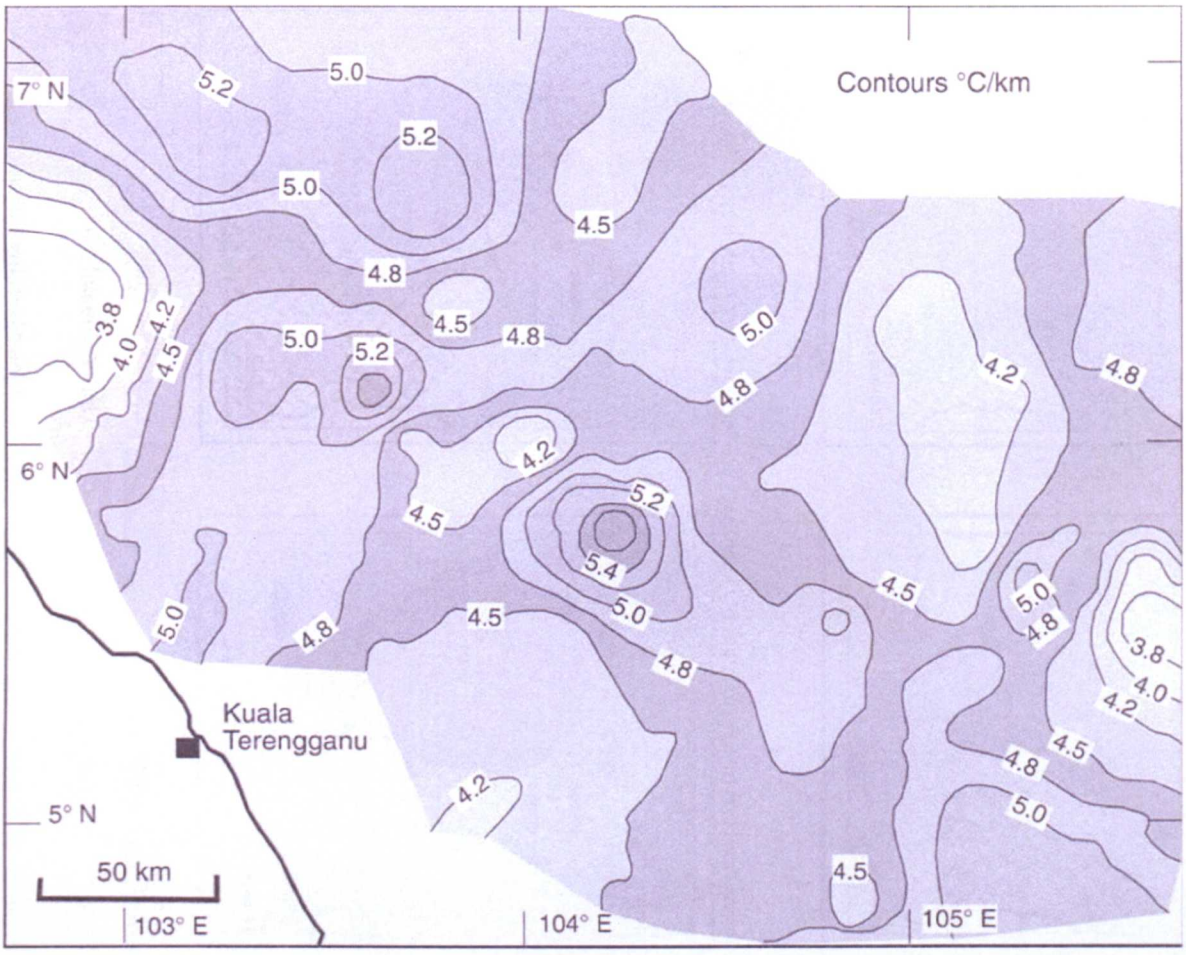

Figure 4.3 Map from Tan (2009) showing geothermal gradient across the Malay Basin. Contours in °C/100m not km.

4.1.4 Stratigraphy

The different phases of tectonic development are represented in the stratigraphy of the basin. As the basin developed in the Late Eocene or earlier, the syn-rift phase began and sedimentation rates were high with alluvial systems and lakes forming within half-grabens, depositing locally sourced clastics, associated with braided streams (synrift image Figure 4.4). As early subsidence continued, alluvial influence lessened and fluvial-lacustrine depositional environments dominated (early subsidence image Figure 4.4). In the South sediment was generally sourced from

the South-West and further South-East, sediment is arrived from the East via fluvial systems and lacustrine deltas. Subsidence progressed through to the Lower Miocene and marine incursion began as the South China Sea transgressed to form a marine basin (late subsidence image Figure 4.4) with clastics supplied from the NW, W and E topographic highs. A large river system, the Paleo Chao Praya, entered the basin in the North setting down fluvial deposits comprising many of the coal and coaly source rocks and reservoir, whilst in the South sediment was being deposited at a marine shoreline (Bishop, 2002).

As inversion began in the Middle-Late Miocene (early and late inversion images Figure 4.4) marine water depths shallowed and more swamp like conditions prevailed over much of the basin with sediment mainly being received from the North-East. From the Pliocene to recent times as gentle subsidence resumed and open marine conditions became established (Tan, 2009).

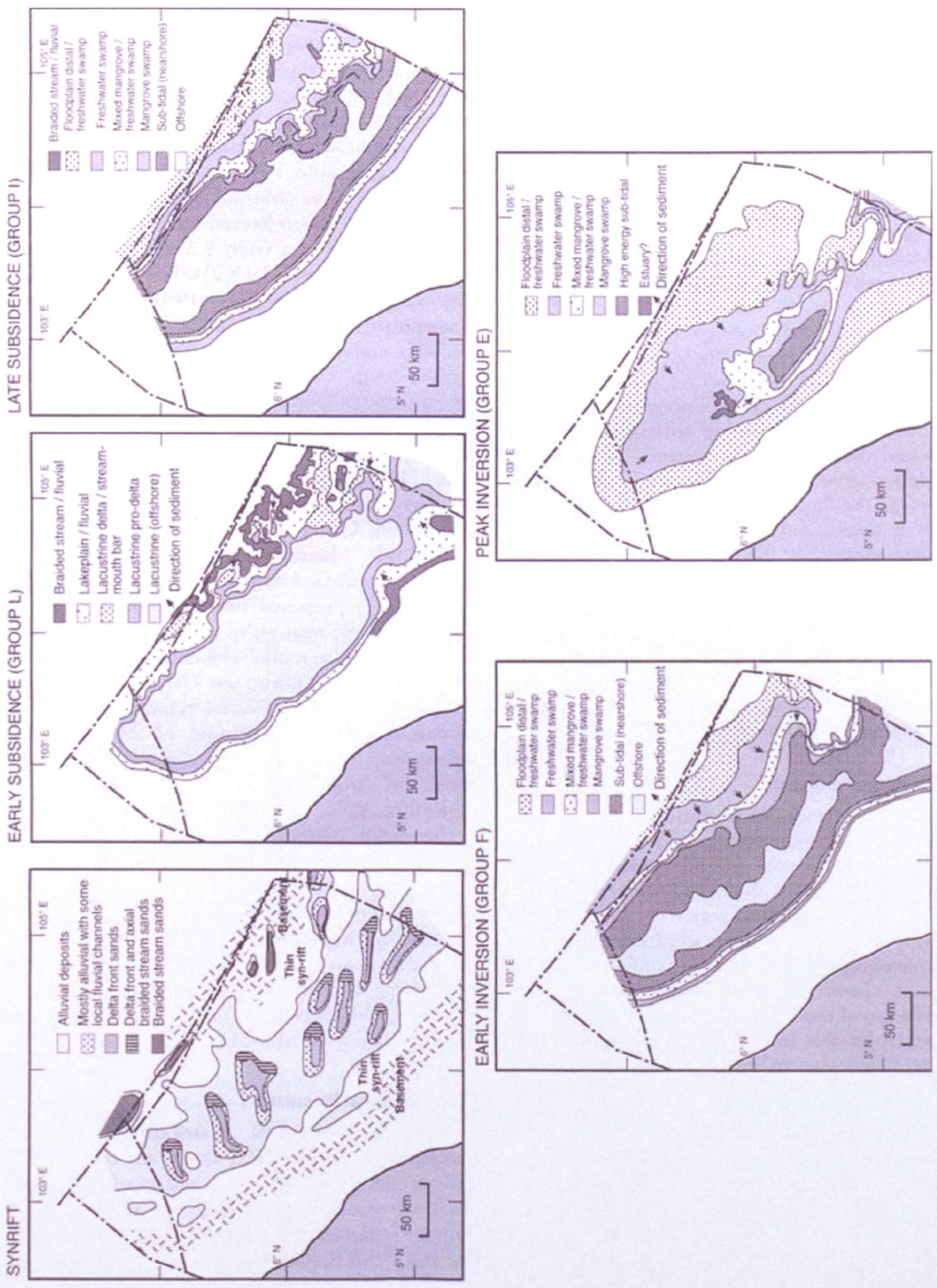

Figure 4.4 Malay Basin palaeogeographic maps (Tan, 2009).

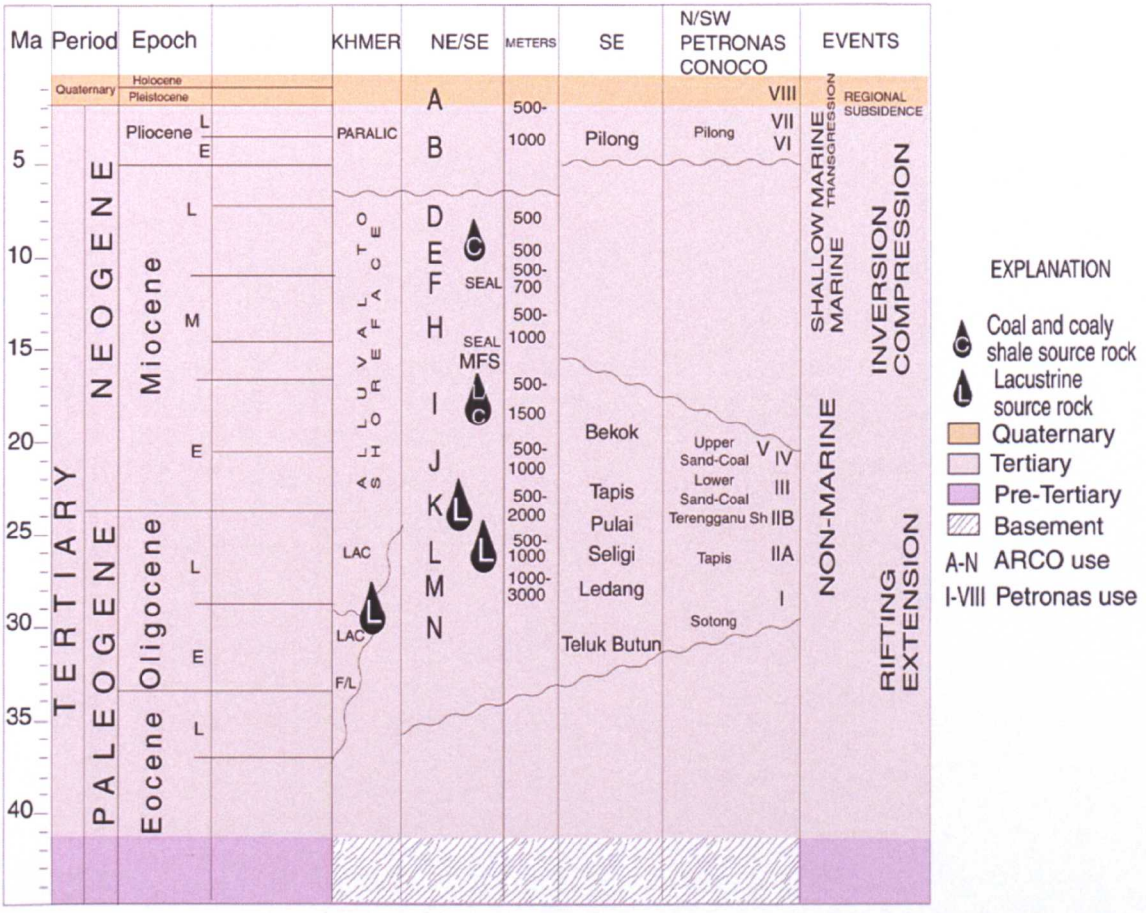

Figure 4.5 Simplified stratigraphy from different areas fo the Malay Basin region (Bishop, 2002).

The lettered groups in Figure 4.5 represent the stratigraphic classification scheme used, though what exact epochs are associated with each group differs with different operators/authors mainly due to unresolved issues regarding the initiation of the basin and the age of the oldest sediments. Generally the EMPI seismic derived groupings are followed (column 1 in Table 4.1).

A/B	• Deposited during the post-inversion period of gentle subsidence in a nearshore to shallow marine environment • Mainly marine clay and silt • Group B may form a seal for Group D and E reservoirs
D	• Youngest of the inversion period groups • Comprises coal, siltstone, shale and glauconitic sandstone deposited in a shallow marine environment • The sands were likely depsotied in offshore sand bars and reservoir porosities in this group range ~17-24% • Coals have similar source potential as Groups F and E
E	• Inversion period group • Deposited in low energy coastal plain, marine environment depositing sandstone in delta front, delta plain, distributary mouth bar, shore face and channels which provides good reservoir in the Central and North Malay • Porosities are between 27-31% and permeability is generally good • Other lithologies present include siltstone, carbonaceous shale and coal • Similar source potential to Group F
F	• Inversion period - deposition continued in the central and northern regions of the basin where low energy coastal plains, peat swamps, estuarine systems and tidal were the dominant environments • Lithologies include sandstone, siltstone, carbonaceous shale and coal • F shale - regional shale controlling overpressure in the centre of the basin • Does not have well developed reservoir facies and the sands are fine to occasionally coarse grained with average porosities of 15-16% but are not particularly permeable. • The F shale has excellent oil potential despite its coaly influence, with TOC ~3-20% and HI ~400-900 mg/HC/g TOC and the coals themselves can have HI of up to ~700 mg/HC/g TOC.
H	• At the top of Group I inversion of the basin began, sea-level rose and Group H sediments were deposited in a deltaic-marine environment with fluvial/estuarine channels. • The uplift proceeded until the Pliocene with folding and truncation of Group H and older horizons in the SE of the basin. • Reservoirs have average porosities of 24-25% • Similar source potential to Group I • Possibly providing a regional seal to older reservoirs.
I	• South China Sea transgressed the region from SE to NW with clastics supplied from the northwetsern, western and eastern topographic highs • Post-rift phase, mudstone, coaly mudstone, coal and sandstone were laid down in fluvial-deltaic systems of braided channels, offshore delta front, sandy tidal estuarine • Sands are fine-very fine grained and matrix-rich • Mechanical compaction has allowed deformation of ductile grains to reduce porosity significantly. Early porosity loss inhibited further diagenesis and quartz overgrowths are rare in these sandstones where porosity ranges 10-30%. • As a source, Group I contains coals and high TOC &HI shales (TOC >20% and HI >350-<700 mg/HC/g TOC) (Figure 5.9). • This unit is one of the sources for the lower coastal plain/Miocene coaly strata petroleum system along with Groups H-D.

J	• First marine incursion occurred as the basin sagged and moved into the post-rift phase • Sandstone, silty-sandstone, siltstone and mudstones and coal were deposited in tidal and offshore bars, sub-tidal shoals and lower shoreface • Reservoir is generally tidally dominated paralic to shallow marine, well sorted fine-medium grained sands with porosities 15-28%
K	• Braided rivers, alluvial fans and delta complexes • Distributary and tidal channel sandstones with crevasse-splay, interdistributary, lagoonal and tidal flat sandstone, siltstone and shales with the thickest deposits in the West and Central areas of the South Malay Basin • Medium grained sands - generally good porosities 15-25% in channel facies. • Porosity loss has taken place following mechanical compaction and quartz cementation/precipitation of authigenic clays. • One of the sources for the Oligocene-Miocene lacustrine petroleum system along with Groups M and L but shows the best potential of the non-marine facies with ~1-3% TOC and HI up to <800 mg/HC/g TOC • May also form effective seals for older reservoirs
L	• Initial subsidence - continental, fluvial-lacustrine setting and comprises facies/sediments similar to those in Group M. • Reservoir is generally gas prone with 8-15% porosity • Regional shale controlling overpressure in towards the basin margins. • As a source Group L mudstones generally have ~1-2% TOC but can have high HI values of ~400-700 mg/HC/g TOC.
M	• Deposited in the extensional phase • Sandstones and shales deposited in an alluvial-lacustrine, continental setting • Braided delta system - texturally and compositionally immature sandstones with the best reservoir within channel fill and mouth bars • Other facies include alluvial fans, paleosols and lacustrine mud in the grabens Porosities range 8-15%. • Low potential source <1 to 2% TOC and HI <200 to 300 mg/HC/g TOC perhaps because of the stronger alluvial influence in this group.

Table 4.1 Overview of the environments of deposition, reservoir, source and seal characteristics for the various groups using references from Hoesni (2004), Madon (2007), Tan (2009) and Bishop, (2002).

Previous reservoir quality studies on the sands of the basin have highlighted petrographic features such as dissolution, particularly of feldspar grains in the sandstones where it has generated secondary porosity, high percentage micro-porosity preserved between clay matrix and authigenic clays (particularly kaolinites) and diagenetic products including calcite and siderite cements with glauconite, chlorite and smectite observed less.

4.1.5 Overpressure

The Malay Basin suffers significant problems with overpressure with 80% of exploration and appraisal wells terminated due to pressure issues (Madon, 2007). Exploration drilling in SE Asia as a whole has fallen over the past three years and discovered volumes have declined even faster (Chan & Mair, 2011). However, the study shows the region still has significant potential, but overpressured play concepts need to be developed. It appears that understanding the mechanisms generating and controlling the overpressured systems will be key to utilizing those plays and consequently important for the future potential of the basin.

Disequilibrium compaction is thought to be the dominant mechanism for overpressure generation in the central and northeastern sections of the basin (Singh & Ford, 1982). The same study also states that in the southeastern area, the uplift within the basin could also have generated overpressure via the inversion of deep, normally pressured horizons being elevated to shallower depths creating inflationary overpressure and that lateral flow via faults could be redistributing high pressure from depth to shallower strata.

The Madon (2007) study described the current state of overpressure over the basin with overpressure beginning at depths of 1900-2000m in the basin centre in Group E, being influenced by the Group F regional shale (noting the Madon, 2007 Group F covers the same time period as both Groups E and F in the EPMI scheme). This top of overpressure deepens away from the centre, creating a convex profile (Figure 4.6).

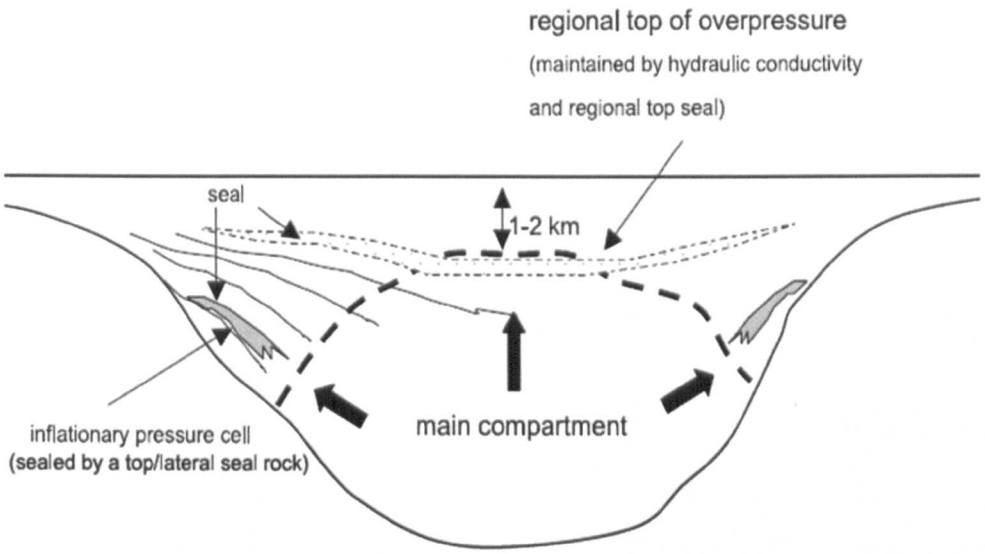

Figure 4.6 Model of current overpressure from Madon (2007) showing the main overpressure compartment in the basin centre.

What can also be seen in the first image of Figure 4.7 is that the top of overpressure then deepens again at the outer margins of the basin and the Madon study describes the overpressure at greater depth in the northeastern flank of the basin at depths 2600-3000m as a separate pressure compartment sealed by the stratigraphically deeper Group L. Regional shales are described as having a strong influence on overpressure and disequilibrium compaction as a result of high subsidence and sedimentation rates (>1000m Ma $^{-1}$) during the syn-rift phase in the basin centre. This subsidence and sedimentation decreases away from the centre, creating the domal top to the onset of overpressure. Sedimentation rates decrease in the post-rift phase (~<500m Ma $^{-1}$) and it is concluded from the modelling that the initial overpressures then dissipated up through the post-rift strata and through faults to separate pressure compartments on the basin flanks as seen at the northern edge of the cross-section of Figure 4.7.

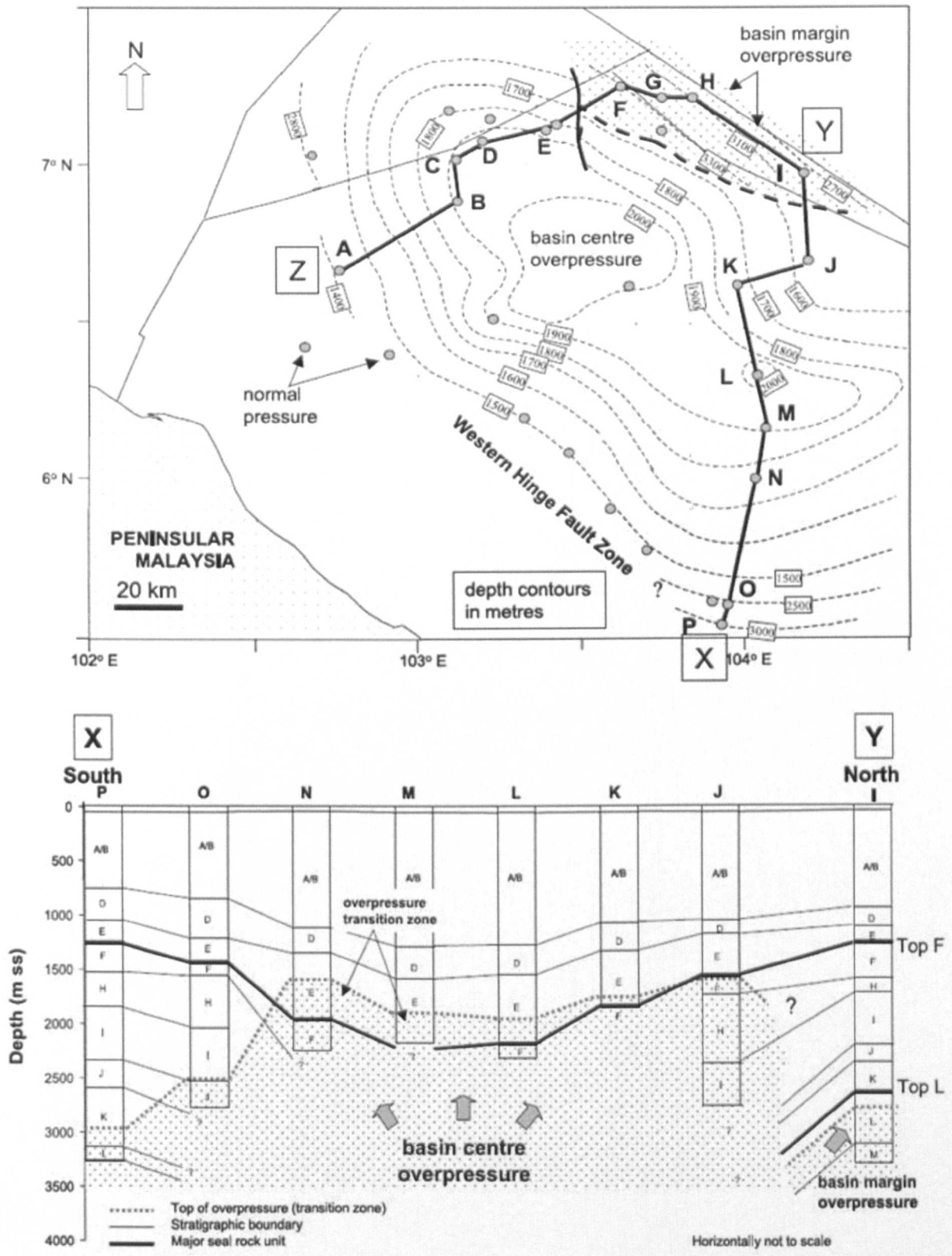

Figure 4.7 Map of depth to top of overpressure in the Malay Basin displaying the main, basin centre pressure compartment and a smaller one on the northeastern margin (shaded). Below is a cross-section of the line XY showing top of overpressure in relation to stratigraphy. Both images from Madon (2007).

5.1.6 Wireline log analysis

In addition to those mechanisms described above, the work by Hoesni (2004) also adds chemical compaction/ mineralogical change as a mechanism for the generation of overpressure. The author states that Heng (1985) suggested that overpressure in the North of the Malay Basin may result from the conversion of smectite to illite. The evidence for the operation of this mechanism in some areas is based on work that was carried out on wire-line log data from wells in the basin. It suggested that there was a wireline "signature" indicative of chemical compaction.

Pressures for the wells were estimated using the empirical Eaton ratio method and the deterministic equivalent depth method that assumes shales of equal porosity have similar composition and have been subjected to the same maximum vertical effective stress. This assumption is valid only if disequilibrium compaction has created any overpressure and that the ratios between the principal effective stresses do not vary with depth (Goulty, 2004). The results of these methods were compared with direct pressure measurements (RFT and MDT) and it was found that whilst shallow sections show modelled pressures consistent with direct measurements, in lower sections both methods underpredict the measured pressures.

On velocity-density cross plots, some wells revealed a move away from normal compaction trends not explained by unloading. Rapid increase in density with small velocity increase was then followed by a rapid increase in velocity with little associated increase in density. In the lower sections of these wells, pore pressures based on mechanical models are underestimated/effective stress overestimated. An unloading wireline signature of rapid velocity decrease with lesser density decrease

is not observed in these wells and it was concluded that the actual observed velocity/density patterns were best explained by chemical compaction (Hoesni, 2004). Either by mechanisms of continuous matrix collapse with partial dewatering, clay mineral transformations with associated fabric re-orientation or sequential cementation of storage and connected pores (referencing the Katsube, 2000 model discussed in Chapter 1).

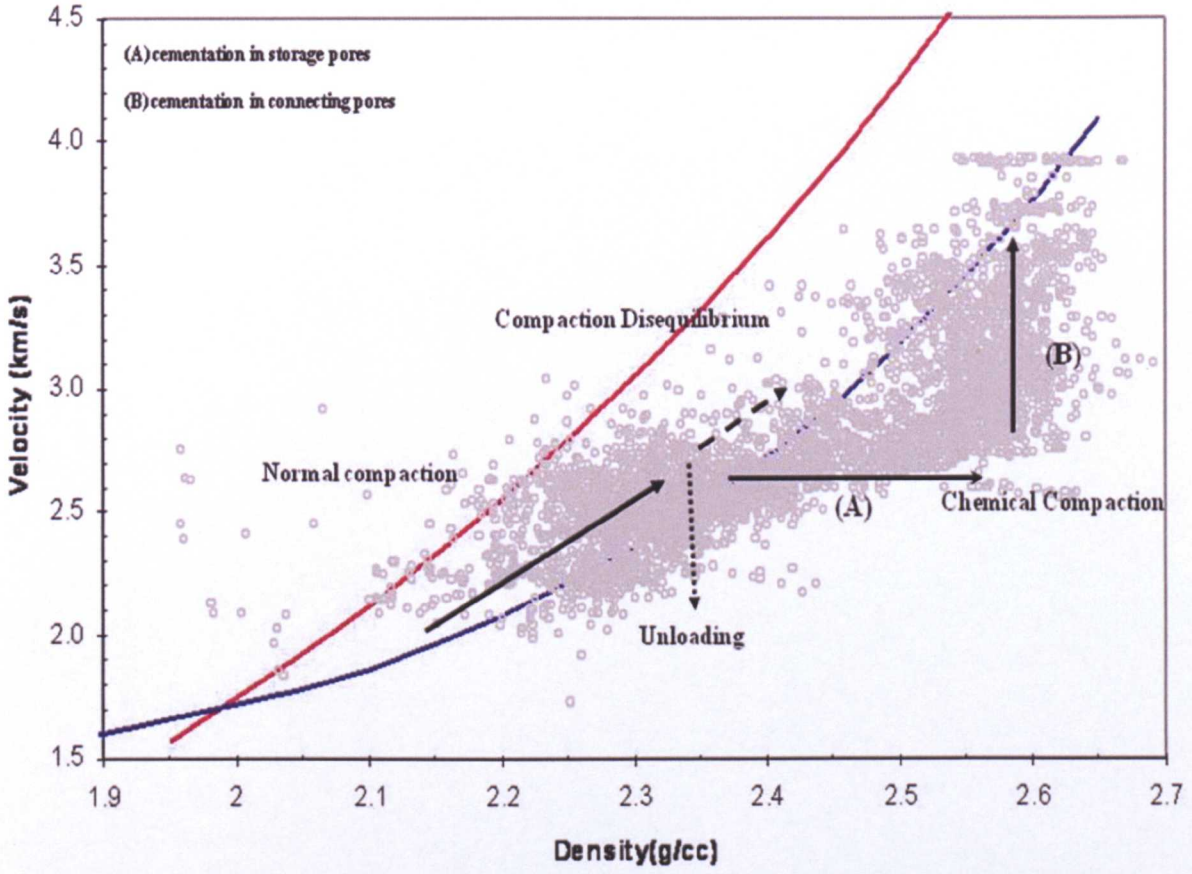

Figure 4.8 Generalised velocity – density cross-plot displaying the "chemical compaction" trend. Responses to suggested mechanism are: (A) represents response over cemented storage pores; (B) the response through cemented connecting pores. The upper and lower bound curves (solid lines) are taken from Bowers (2001) for normal compaction for different shales.

The samples from the 2 South Malay wells that have been supplied for this study correspond to two wells from the Hoesni (2004) study that showed the suggested chemical compaction trend in their wireline responses (Figure 4.9).

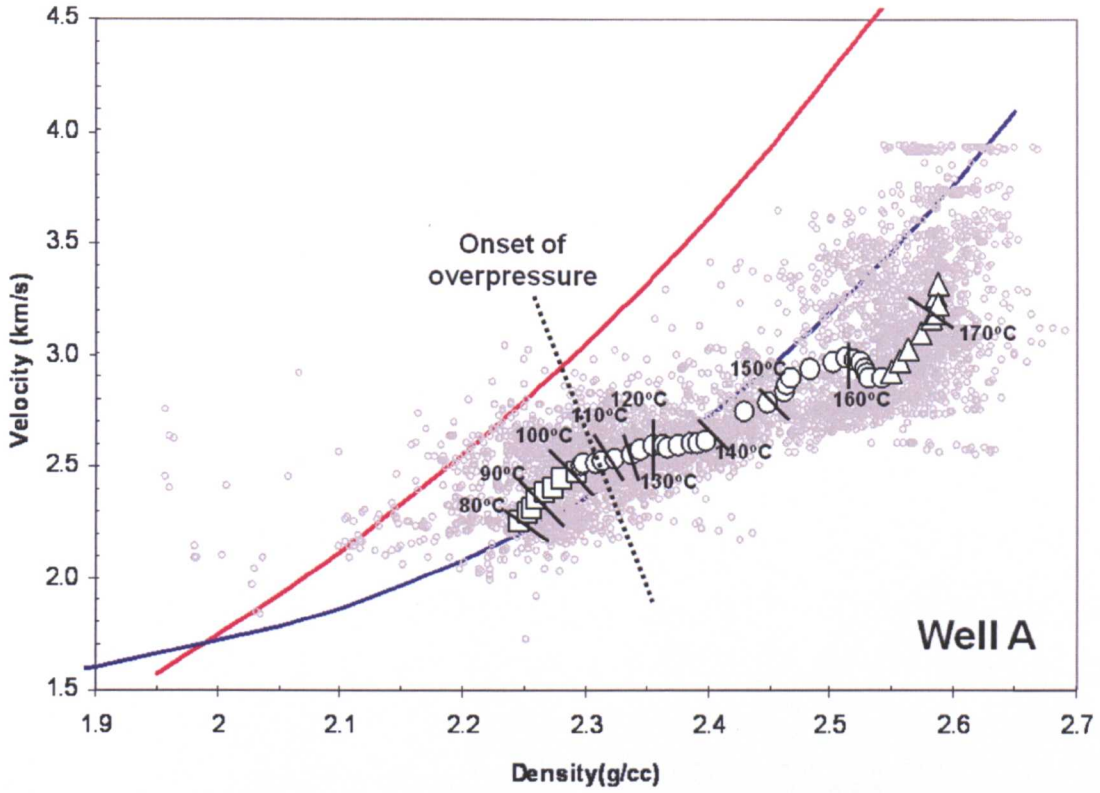

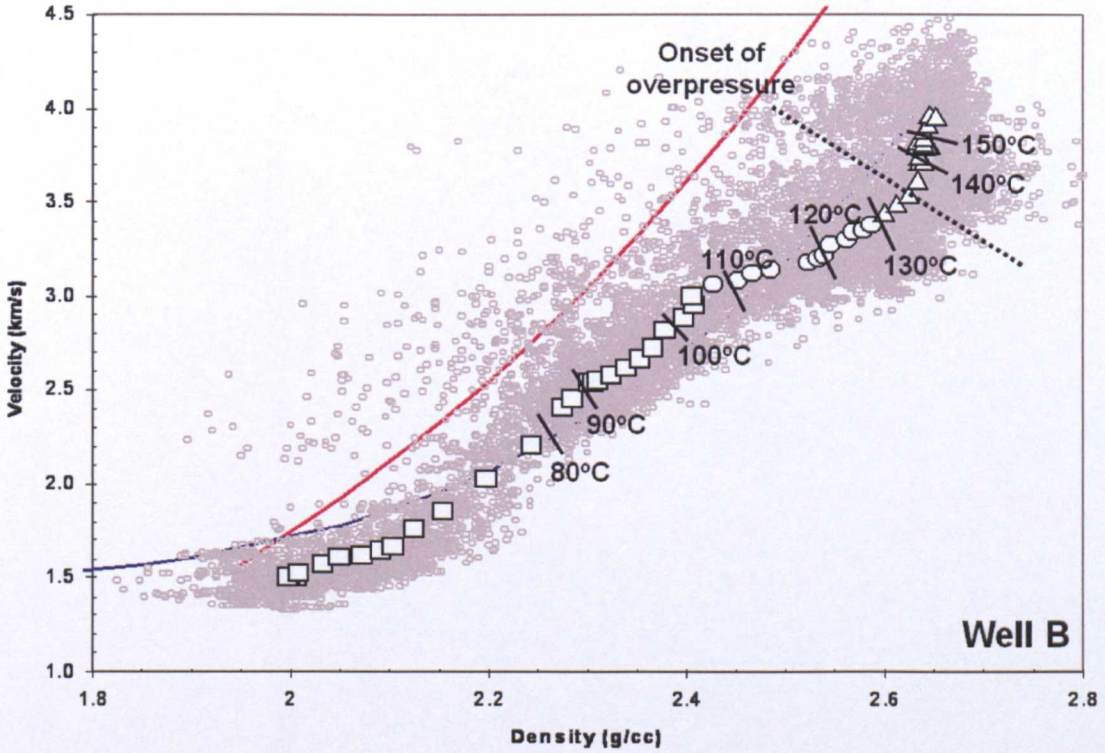

Figure 4.9 Velocity – density cross-plots from Hoesni (2004) for Wells A and B studied in this thesis. The upper and lower bound curves (solid lines) are taken from Bowers (2001). Compaction trends are represented by different symbols.

Both wells are marked on Figure 4.10 below which also shows the distribution of the wells studied by Hoesni (2004) and overpressure mechanism categorized according to their wireline log responses.

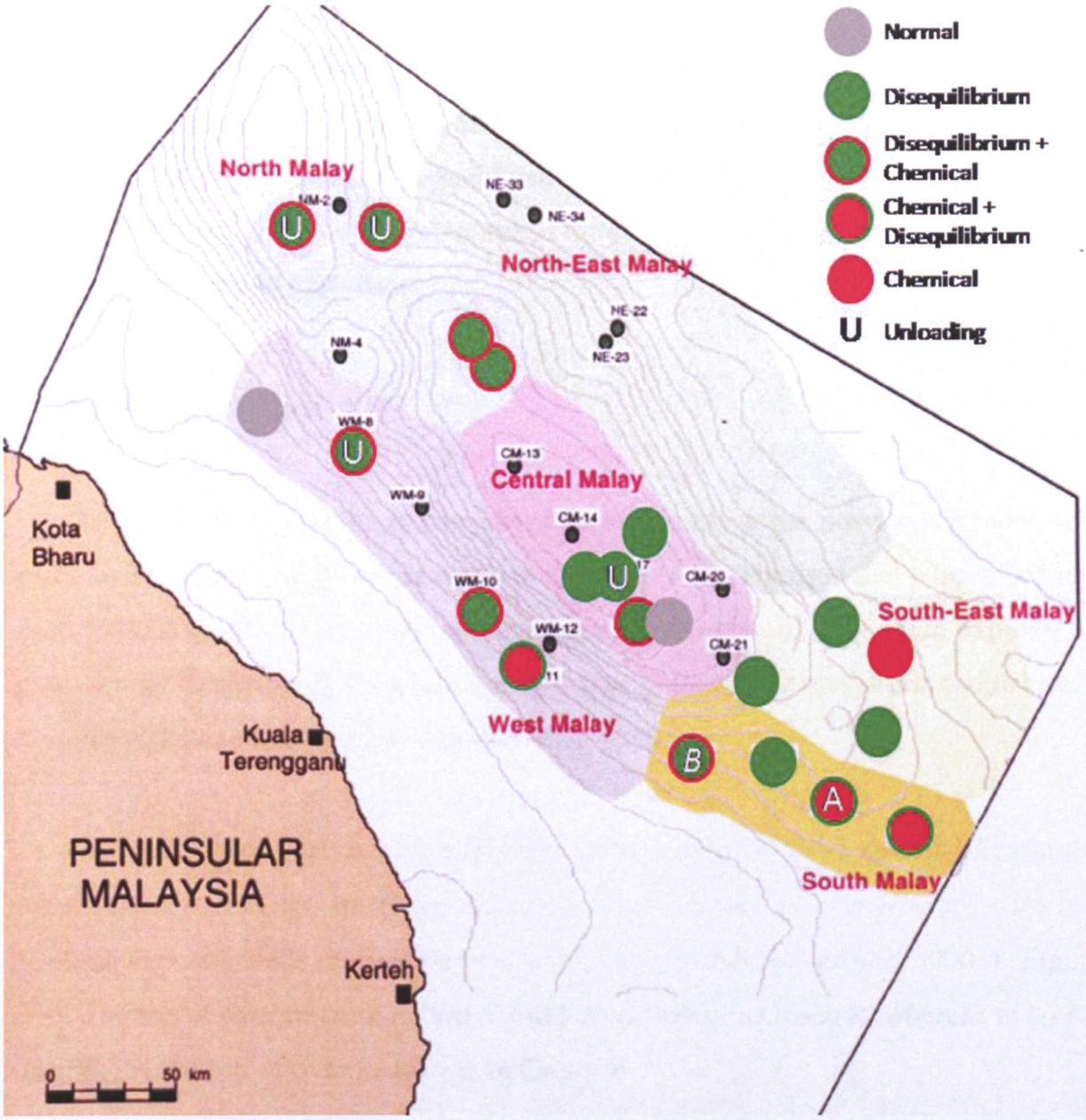

Figure 4.10 Overview map modified from Hoesni (2004) to identify study wells A and B and show the interpreted origins of overpressure from velocity-density crossplots for the study wells of Hoesni (2004). Grey circles indicate a normal compaction signature, green show disequilibrium compaction origin, green with red line show a signature of disequilibrium compaction with chemical compaction and red with green line indicates chemical compaction with disequilibrium compaction. Red circles alone mark a chemical compaction trend. Wells where unloading was indicated by the pressure profiles are additionally marked with a U. This study's sampled wells are similarly marked A and B in italics. Tertiary sediment thickness is contoured in km.

4.1.5 Study Wells A and B: Sample overview

4.1.5.1 Well A samples

Samples provided from Well A were from depths between 1619 – 2621m +/-3m). These depths cover a stratigraphic range of units J, K and L meaning that the very earliest syn-rift alluvial fan/plain sediments are not sampled in this well. Sediment deposited in the other 2 major palaeoenvironments occurring in the Malay basin, fluvial-lacustrine and tidal-marine are just captured in Well A. The shallowest sample is from a depth of approximately 1619m and is therefore inferred as belonging to unit J which forms one of the tidal-marine units, but below this all other samples are taken from units K and L.

The samples were apparently dry cuttings. The initial appearance of the J sample was quite different from all other Well A samples, comprising 2 solid blocks of material that was dark grey/dark purple appearance and up to 5cm in length. The samples from units K and L were mainly small, dark grey centimeter scale shards of sub-angular to sub-rounded material.

4.1.5.2 Well B samples

Samples from Well B cover a greater range of depths from 1350m to 3000m. Based on data supplied, this section would include Units H, I, J and L. This means that again the alluvial section is not sampled but the deposits of the later palaeoenvironments are.

Again the samples were dry cuttings but there was more variation in appearance between samples from different depths than Well A. Generally, there was more

remnant powder and the fragments were smaller and more sub-rounded than Well A samples which could be due to geological controls or simply different drilling techniques.

Figure 4.11 Sample bags containing cuttings from Well A and B. Note the large, blocky fragments comprising the sample from 5313ft (1619m) in Well A and the general shape and colour difference between Well A and B.

There was more light, pale-sand coloured material in all bags compared to Well A and it formed the dominant component in some samples, notably those from 1600m (see Figure 4.11), 2010m, 2200m, 2320m, 2500m, 2620m and 2840m. As the aim of this study was to analyse any change in clay mineralogy and initial observations of the samples indicated a higher sand content, a decision was made upon the sampling process for Well B prior to rock characterization tests. The bags of cuttings were first coned and quartered to obtain a representative sample. Then a second

sample was taken of the remaining material where the lighter, coarser grained fragments were removed as far as was visually possible. The coned and quartered, representative sample was used for the initial description above and the selective sample was used for all other tests. This process was not necessary for Well A samples that were merely coned and quartered prior to testing.

4.2 Chemical / Mineralogical Properties

4.2.1 X-Ray Diffraction (XRD) Measurements

4.2.1.1 Bulk fraction XRD Measurements

The initial attempts to characterize the samples focused on X-ray diffraction analysis as described in the previous chapters. The main aim was to assess any mineralogical change that could contribute to chemical compaction. Preparation was carried out as noted in Chapter 2 on the samples of Well A and Well B. Diffraction patterns for 9 depth intervals in Well A and 10 in Well B were recorded and the mineral phases present identified. This was completed via a combination of manual identification using the d-spacing table from Brown and Brindley (1980) and analysis with X'Pert HighScore Plus database software (Figure 4.12 below). The amount of each identified phase in the different samples was quantified using FULLPAT as described in Chapter 2 (Figure 4.13).

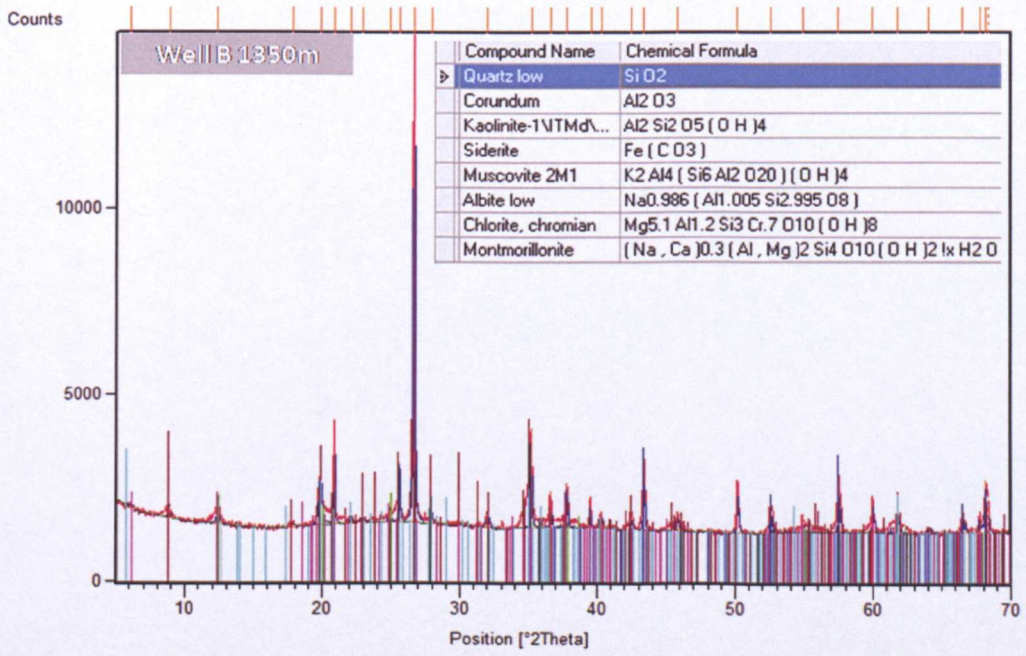

Figure 4.12 Image of mineral standards match with peaks of sample diffraction pattern for 1350m Well B in X'Pert HighScore Plus software.

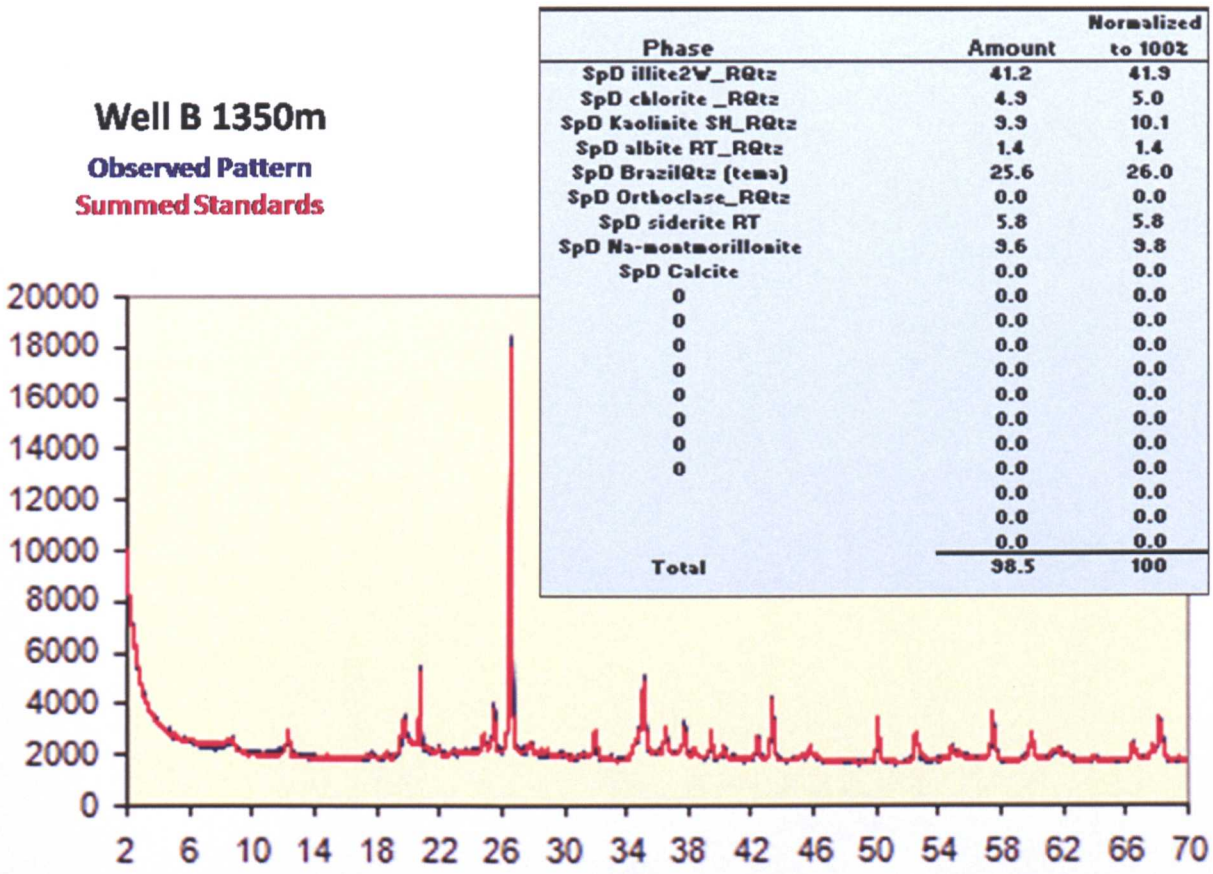

Phase	Amount	Normalized to 100%
SpD illite2W_RQtz	41.2	41.9
SpD chlorite _RQtz	4.9	5.0
SpD Kaolinite SH_RQtz	9.9	10.1
SpD albite RT_RQtz	1.4	1.4
SpD BrazilQtz (tema)	25.6	26.0
SpD Orthoclase_RQtz	0.0	0.0
SpD siderite RT	5.8	5.8
SpD Na-montmorillonite	3.6	3.8
SpD Calcite	0.0	0.0
0	0.0	0.0
0	0.0	0.0
0	0.0	0.0
0	0.0	0.0
0	0.0	0.0
0	0.0	0.0
0	0.0	0.0
0	0.0	0.0
	0.0	0.0
	0.0	0.0
	0.0	0.0
Total	98.5	100

Figure 4.13 Image of summed mineral standards match with peaks of sample diffraction pattern for 1350m Well B in FULLPAT software. Y axis shows intensity in Counts and X axis shows °2Theta. Blue table shows modelled mineral quantities with normalisation to 100%.

The quantified bulk fraction mineralogical compositions for Wells A and B can be found in tables 4.2 and 4.3 below. Modelled totals had an average difference of 1.8% from 100%, bar the 1619m sample in Well A where fluorescence due to the high iron content elevated the baseline and could be making it more difficult to simulate with the standards. Previous work on the method indicated accuracy +/- 10%.

Sample Depth ft. (m)	Qtz.	Py.	Calc.	Alb.	Kaol.	Illite/ Mica	K-Feld	Smec.	Chl.	Sid.	Total
1619	21	-	1	2	4	32	1	-	4	34	110.4
1750	25	-	-	-	17	55	-	-	3	-	98.7
1932	24	4	-	-	20	45	-	1	6	-	97.5
2140	27	7	-	--	14	48	-	-	4	-	100.5
2280	23	6	-	-	12	53	-	-	7	-	100.0
2408	17	9	-	-	16	50	1	-	7	-	97.3
2530	29	2	1	-	11	51	-	-	7	-	98.8
2582	24	5	-	-	14	51	-	1	6	-	99.6
2621	22	5	-	-	13	54	-	-	6	-	100.0

Table 4.2 Well A quantified mineralogy from FULLPAT modelling normalized to 100% with original total prior to normalization in final column.

Sample Depth m.	Qtz.	Py.	Calc.	Alb.	Kaol.	Illite/ Mica	K-Feld	Smec.	Chl.	Sid.	Total
1350	26	-	-	1	10	42	-	10	5	6	98.5
1680	34	-	-	2	9	42	1	-	5	7	98.5
1970	44	1	-	3	9	29	-	8	2	5	93.8
2110	37	-	-	3	8	35	-	10	2	6	99.5
2240	47	-	1	1	7	38	-	-	3	2	99.1
2320	52	1	-	2	6	27	-	4	2	5	94.6
2500	52	-	-	-	-	48	-	-	-	-	102.3
2620	54	7	-	3	9	24	-	-	3	-	100.2
2840	52	5	-	5	5	29	-	-	3	-	98.2
3000	44	-	-	2	10	34	1	-	4	5	95.9

Table 4.3 Well B quantified mineralogy from FULLPAT modelling normalized to 100% with original total prior to normalization in final column.

Basic interpretation of the bulk fraction XRD data confirms the initial visual interpretations showing Well A samples are more clay-rich with lower quartz content (average 24%). Whereas, though the shallowest samples in Well B are clay-rich, quartz content increases to surpass the clay content by the lower fluvial-lacustrine section. In the very deepest samples clay content rises again but is very close to the amount of quartz.

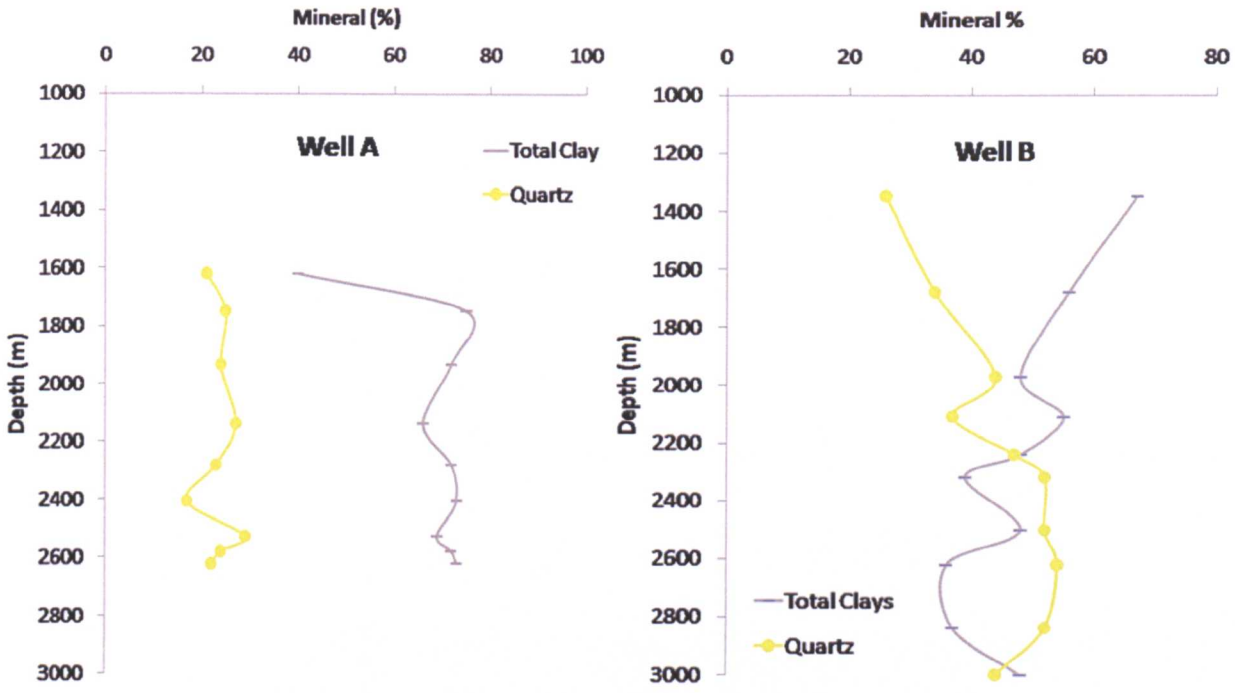

Figure 4.14 Plots of total clay content with sample quartz content with depth for Well A and B.

In comparing the 2 wells it is important to remember that selective samples were used from Well B to try and eliminate sandy layers. The comparison is still useful as samples in Well A are confirmed as clay rich and it can still be said that Well B is more quartz-rich than Well A, just that a non-selective sample would likely make the quartz totals even larger. These representative samples are still preserved if required for future study.

Analysis of the individual mineralogy with depth in Well A (Figure 5.17) shows that most of the clay content comprises illite/mica although kaolinite is also more prevalent in Well A. Small amounts of what is modelled as smectite are seen in 2 samples, but given the issues described in Chapter 3 surrounding the chemical composition of smectite (the presence of potassium) and its effect on modelled bulk

fraction XRD quantity, caution should be taken with values and comparison with exchanged clay-fraction XRD results should be made.

Siderite is present only in the shallowest sample in Well A where it forms 34% of the rock and explains the nature of the 1619m cuttings (section 4.1.5). This is the only sample in Well A of the tidal-marine unit. All other samples are derived from the earlier fluvial–lacustrine facies. Iron minerals are also found in these strata, however the phase present is pyrite.

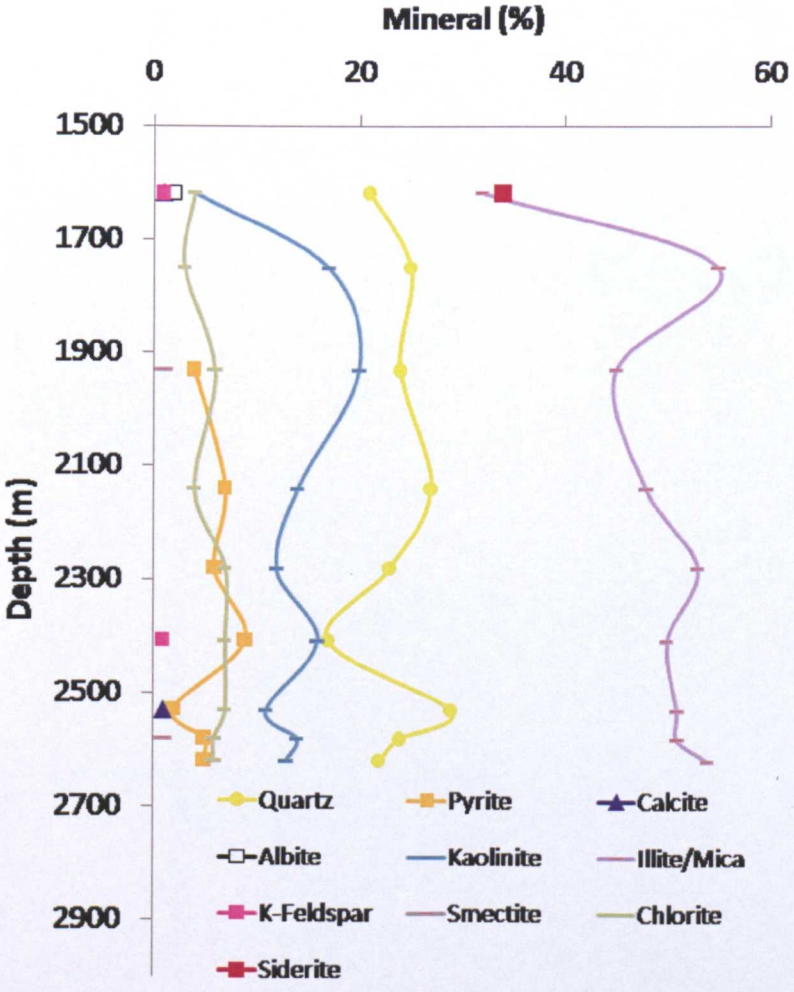

Figure 4.15 Bulk mineralogy from FULLPAT modelling with depth in Well A.

Again, in Well B the dominant clay mineralogy is illite/mica although it should be noted from microscopic work, detailed in later sections, that some of this material is mica, not clay. Smectite content in the shallower section of the well appears higher, which given previous results indicates that the smectite present is not fully K-exchanged.

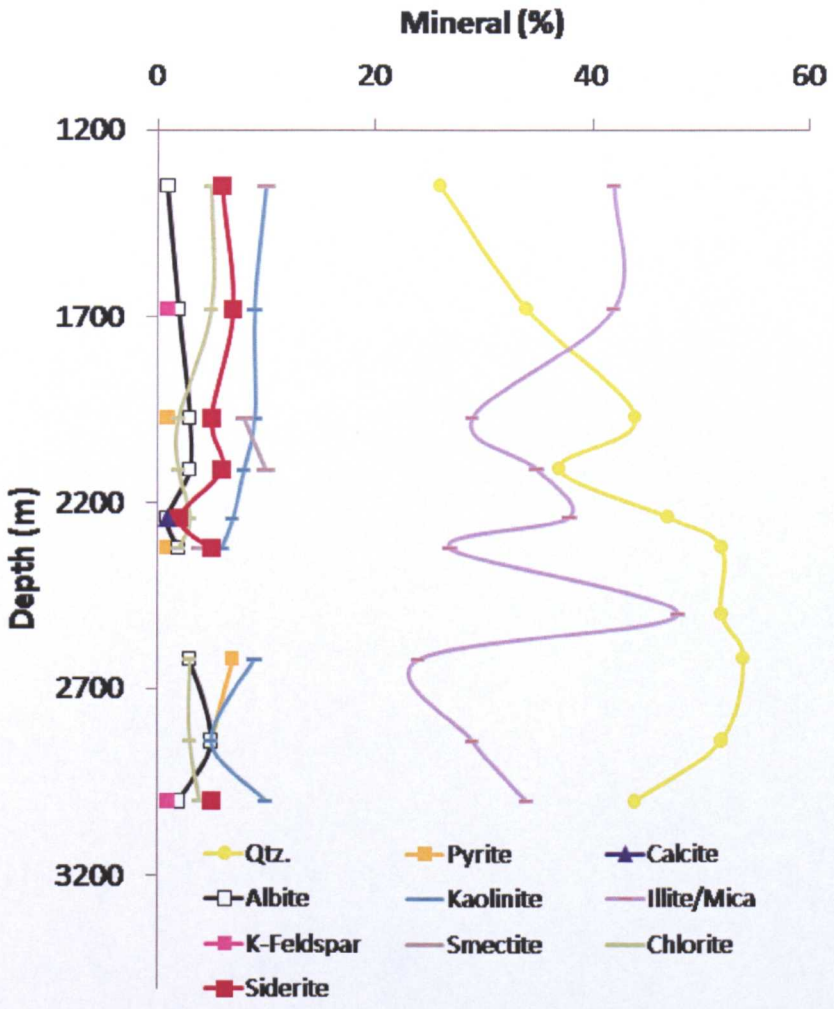

Figure 4.16 Bulk mineralogy from FULLPAT modelling with depth in Well B.

Kaolinite content is lower in Well B and there is generally more quartz despite visual removal in the Well B samples. In the BSEM images much of the quartz appears of silt size or smaller which means it may not have been removed via visual

identification. The deeper, quartz-rich, fluvial – lacustrine horizons are also associated with pyrite whereas the more clay-rich, shallower, tidal marine sections represented by more samples in Well B, contains siderite (Figure 5.19). The more clay rich section at the base of the well sampled at 3000m also contains siderite.

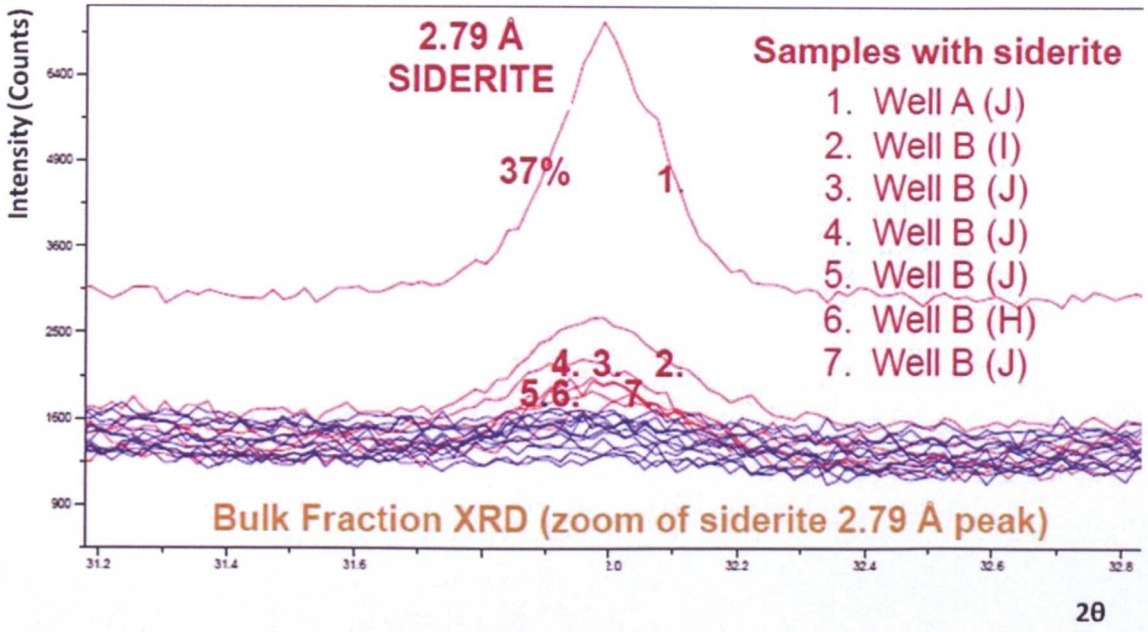

Figure 4.17 Bulk Fraction XRD (zoom of siderite 2.79 Å peak) with well and stratigraphic group annotation of significant intensities at 2.79 Å. Peaks are also found at 2.34, 2.13, 1.962, 1.736 Å.

4.2.1.2 Clay Fraction XRD Measurements

The clay fraction (<2 μm particles) of samples from the 2 wells were prepared and analysed following initial air-drying, glycolation and for selected samples also following heat treatment. As shown in Chapter 3, the difference between air-dried and glycolated diffraction patterns gives information about the expandable clays present. The bulk fraction measurements show that there is considerably less expandable clays (smectite or smectitic mixed layer I/S) than can be found in the North Sea mudstone in Chapter 3. However, looking at the patterns for Wells A and B some differences are noted (selected samples shown in Figure 4.18).

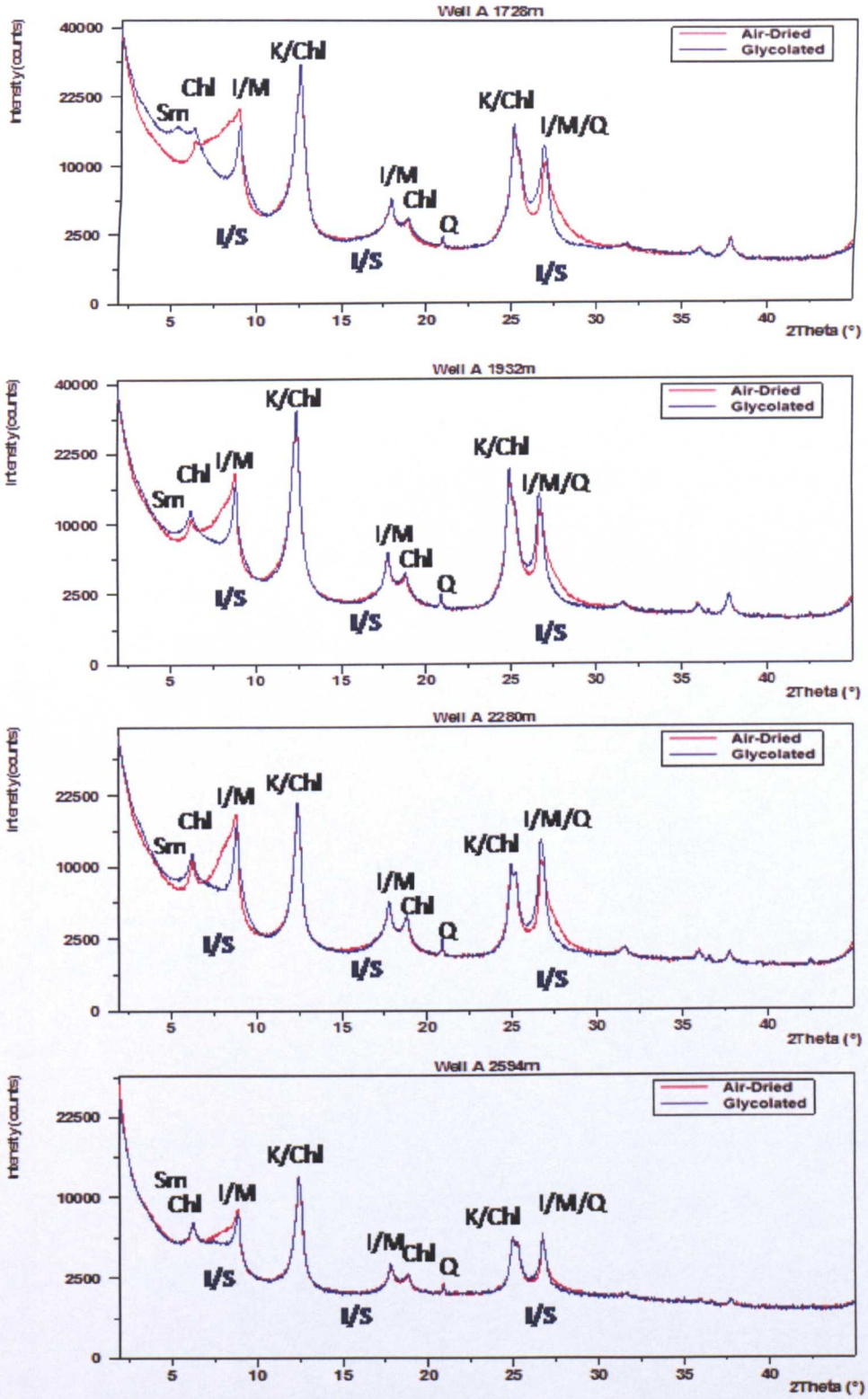

Figure 4.18 X-ray diffraction patterns for clay fraction (<2μm) of selected samples from Well A. Patterns shown for the samples following preparation stages - air-drying (red) and glycolation (blue). Black captions show interpreted mineral peaks: Sm – smectite / I/S; Chl-chlorite; I/M – illite/I/S/mica; K – kaolinite; Q – quartz. Blue captions mark the regions used in defining I% in I/S.

The 2 shallowest samples from 1728m (shown Figure 4.18) and 1795m have no individual smectite or smectitic I/S peak in the air-dried state, but there is a broad "ramp" from the 14 Å chlorite peak up to the illite peak near 10 Å (far left I/M peak). Upon glycolation an individual peak does form at 16.8Å (far left Sm peak Figure 4.18) indicating the presence of smectitic I/S in the 2 shallowest samples.

In the third shallowest sample at 1932m there is no longer an individual smectite peak even in the glycolated state. 1932m does follow the 1728m and 1795m samples in that the chlorite/kaolinite peak at 3.57Å (far right K/Chl peak in Figure 4.18) is more intense than the 3.33/34Å illite/mica (and fine quartz) peak.

Despite the lack of an individual smectite peak there is still a shift in intensities between the air-dried and glycolated state for the sample from 1932m and those below. The "ramp" up to the illite/mica 10Å peak when air-dried becomes narrower and shifts closer to 10Å as can be seen in the samples from 1932 and 2280m in Figure 4.18. Only one of the deeper samples shows some broadening of this area and this is the sample from 2582m, but it is not comparable with the shallowest samples. This is also one of only 2 samples from the bulk fraction measurements that shows any smectite content (albeit minimal). In the two deepest samples from 2594 and 2621m there is a "flatter", less intense elevation in the air-dried state prior to the 10Å peak. The 2594m sample the 16.8Å region doesn't show an individual glycolated smectite peak and also does not show any elevation from the air-dried pattern as the intermediate depth samples all do. The 2621m diffraction pattern is very low resolution (similar to a couple of the Well B samples) possibly due to small sample amounts available for use in the original fractionation of the clays.

Overall, it would appear that there is some change to the expandable clays and illite with depth but quantifying that change was difficult. As discussed in detail in Chapter 2, the 8.58-9.82Å (10.31-9.01°2Theta) region was used to calculate the amount of illite in interlayered I/S. Intensity of the air-dried pattern was subtracted from the glycolated trace to reveal the broad "peak" of I/S. Initially, the range in Å at 0.75 intensity peak height (columns 4 & 5 in Table 4.4) was measured and the central point of that range in Å taken and used to calculate I%in I/S (column 3 in Table 4.4) using the relationship in Moore & Reynolds (1997). Noise in the pattern led to a further method development where a polynomial trendline (order:6) was fitted to the peak and the position of the peak intensity in Å recorded and again converted into I%in I/S (column 2 in Table 4.4).

Sample Depth (m)	Illite (%) in I-S (I)	Illite (%) in I-S (II)	"Minimum" Illite (%) in I-S	"Maximum" Illite (%) in I-S	Range of Illite (%) in I-S
1728	79.5	74.6	64.1	85.1	21
1795	84.2	81.8	73.9	89.7	16
1932	85.5	85.6	80.9	90.1	10
2082	82.2	78.7	68.9	88.6	20
2280	86.6	85.8	79.5	92.1	13
2316	87.4	87.6	83.0	92.1	9
2408	88.6	90.7	88.6	92.8	4
2530	87.4	87.2	83.0	92.1	8
2582	87.4	88.7	84.7	92.8	8
2594	85.1	85.4	83.8	87.0	3
2621	89.3	91.8	90.4	93.1	2

Table 4.4 Calculation of Illite (%) in I-S for samples from Well A. (I) is calculated from position in Å of peak intensity on polynomial trendline through measured difference between glycolated and air-dried patterns. (II) is calculated from position in Å of the central point of range at 0.75 maximum peak intensity of measured difference between glycolated and air-dried patterns. Maximum and minimum values are calculated from the position in Å of the minimum and maximum position of that range at 0.75 maximum peak intensity. This range is also converted to % in the final column

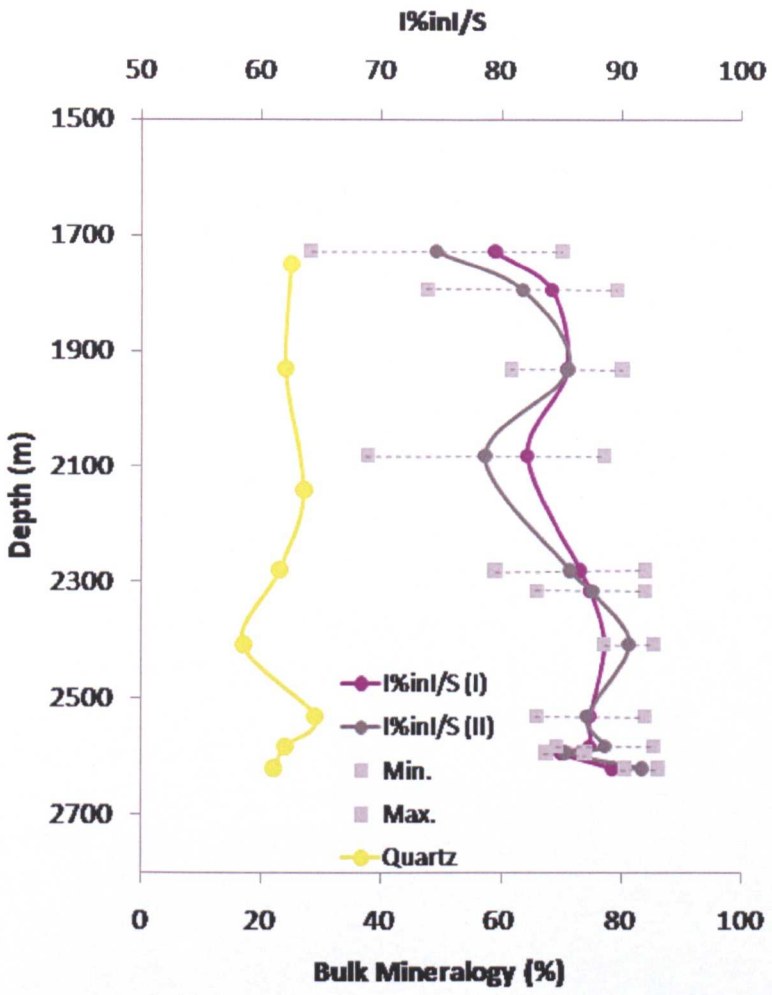

Figure 4.19 Representing Table 4.4 data with bulk fraction quartz amounts for comparison

Bulk fraction XRD measurements were not made on the 2 shallowest clay-fraction samples. 1932m has both clay and bulk fraction and is the only sample in Well A to contain any modelled smectite bar 2582m. This lack of material that would be modelled as end-member smectite is supported by the clay-fraction values which show calculated I% in I/S is already considerable even in the shallowest samples with a "minimum" of 64% and 73%. These are the samples which have individual glycolated 16.8Å peaks. As such, the early section of the transition is not represented in the sampled intervals but change can be seen over those depths.

The least "mature" samples from the shallowest depth will be just over the threshold for *R*1 ordering (~>50% = *R*0 to *R*1). The rest of the Well A samples should have *R*1ordering also, until the deepest samples which at ~90% I in I/S could possess *R*3 ordering. There is a decrease in the range also seen with an average range of 16% at 2280m and above to an average of 6% below and only 2% in the deepest sample. Also, superimposed on any depth trend there also appears to be an inverse relationship with bulk quartz content (Figure 4.19).

Well B samples show less obvious trends in the clay-fraction data. Bulk fraction data showed more modelled smectite in the shallower strata, but this is not clear in the clay-fraction. 1350m sample was modelled as containing 10% smectite, yet shows virtually no glycolated elevation at 16.8 Å or in the <10 Å region used to calculate I% in I/S. It should be noted that the amount of 1350m sample available for fractionation was very small, like 2621m in Well A and gives a similarly high I% in I/S figure.

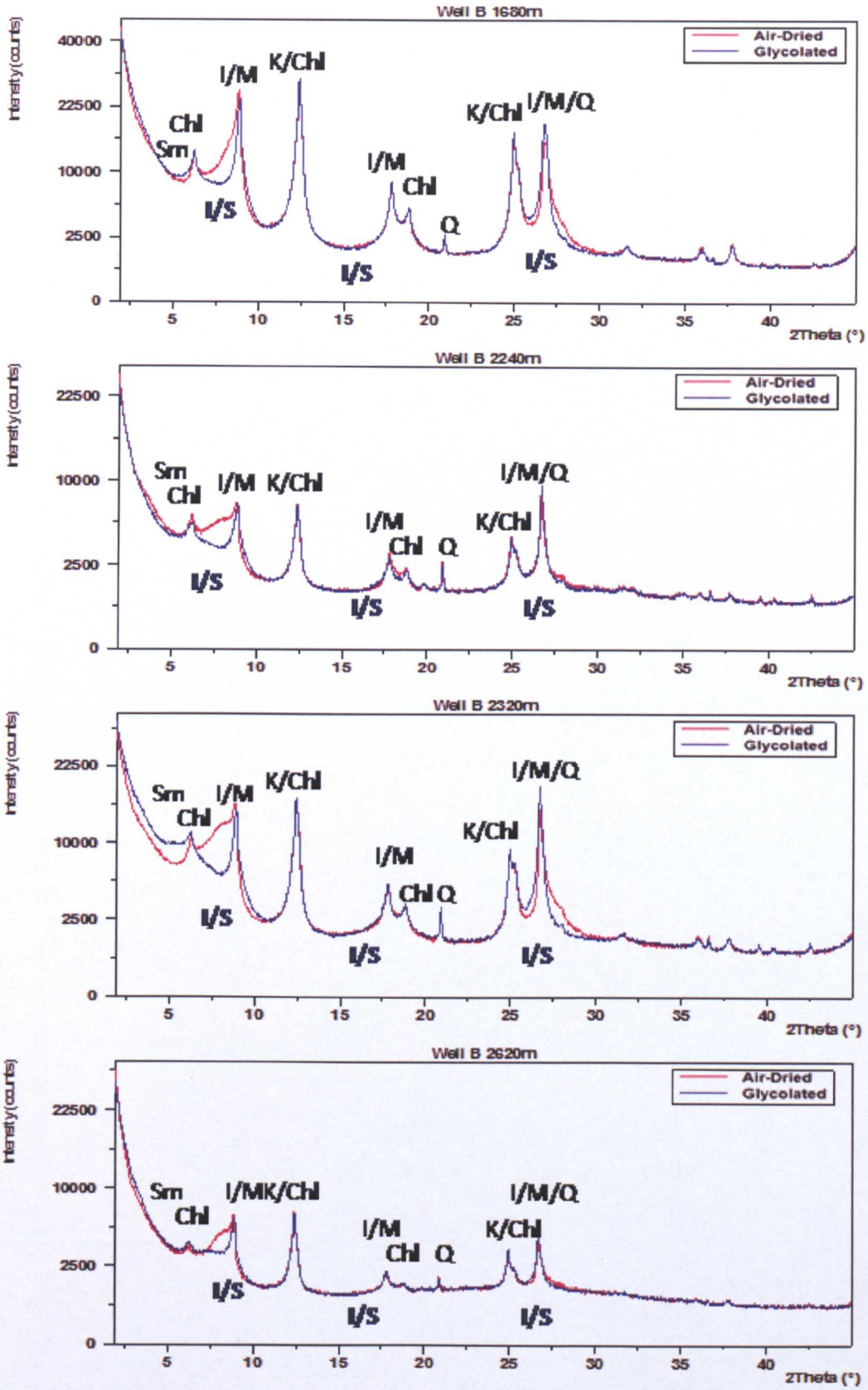
Well B 1680m
Air-Dried
Glycolated
Intensity(counts)
2Theta (°)
Sm
Chl
I/M
K/Chl
I/S
I/M
Chl
Q
K/Chl
I/M/Q
I/S
Well B 2240m
Air-Dried
Glycolated
Intensity(counts)
2Theta (°)
Sm
Chl
I/M
K/Chl
I/S
I/M
Chl
Q
I/S
K/Chl
I/M/Q
I/S
Well B 2320m
Air-Dried
Glycolated
Intensity(counts)
2Theta (°)
Sm
Chl
I/M
K/Chl
I/S
I/M
Chl
Q
I/S
K/Chl
I/M/Q
I/S
Well B 2620m
Air-Dried
Glycolated
Intensity(counts)
2Theta (°)
Sm
Chl
I/MK/Chl
I/S
I/M
Chl
Q
I/S
I/M/Q
K/Chl
I/S

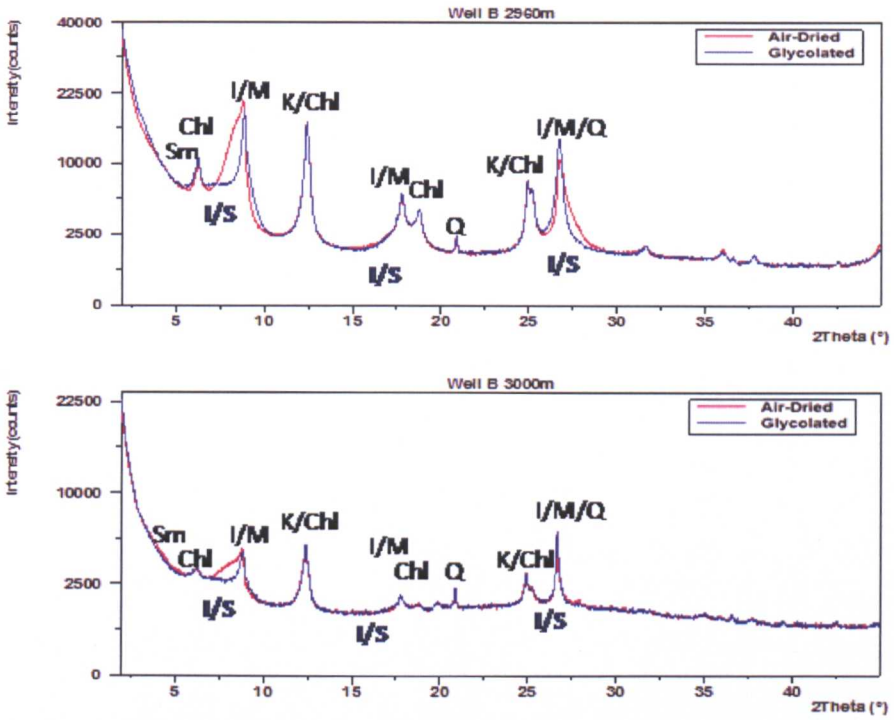

Figure 4.20 X-ray diffraction patterns for clay fraction (<2μm) of selected samples from Well B. Patterns shown for the samples following preparation stages - air-drying (red) and glycolation (blue). Black captions show interpreted mineral peaks: Sm – smectite / I/S; Chl-chlorite; I/M – illite/I/S/mica; K–kaolinite; Q– quartz. Blue captions mark the regions used in defining I% in I/S.

Sample Depth (m)	Illite (%) in I-S (I)	Illite (%) in I-S (II)	"Minimum" Illite (%) in I-S	"Maximum" Illite (%) in I-S	Range of Illite (%) in I-S
1350	87.8	90.7	90.4	91.1	1
1680	84.2	81.3	73.0	89.7	17
1970	87.0	86.9	81.7	92.1	10
2110	88.1	89.0	85.9	92.1	6
2180	84.2	83.0	76.3	89.7	13
2240	87.4	88.7	85.9	91.4	6
2320	83.0	77.9	66.8	88.9	22
2620	87.8	90.7	88.6	92.8	4
2730	87.8	90.0	87.8	92.1	4
2840	87.0	90.0	87.8	92.1	4
2960	85.5	83.7	76.3	91.1	15
3000	88.9	90.9	88.9	92.8	4

Table 4.5 Calculation of Illite (%) in I-S for samples from Well B. (I) is calculated from position in Å of peak intensity on polynomial trendline through measured difference between glycolated and air-dried patterns. (II) is calculated from position in Å of the central point of range at 0.75 maximum peak intensity of measured difference between glycolated and air-dried patterns. Maximum and minimum values are calculated from the position in Å of the minimum and maximum position of that range at 0.75 maximum peak intensity. This range is also converted to % in the final column

Samples have commonly high I% in I/S and strong trends of either mean or minimum or range of I% in I/S with depth do not emerge and it looks likely that there are multiple influences on the clay mineralogy in Well A . One such influence could be depositional mineralogy variation and cements, but there is not the same clear relationship with quartz as seen in Well A (Figure 4.21).

The other shallower samples do indicate the presence of some expandable material with significant elevated intensity (only when glycolated – far left Sm elevation) at 16.8 Å in 2320m (Figure 4.20), a corresponding wide 22% range of I% in I/S and this sample was modelled as containing 4% smectite and 27% illite, but generally intervals of higher or lesser range do not show any correlation with depth.

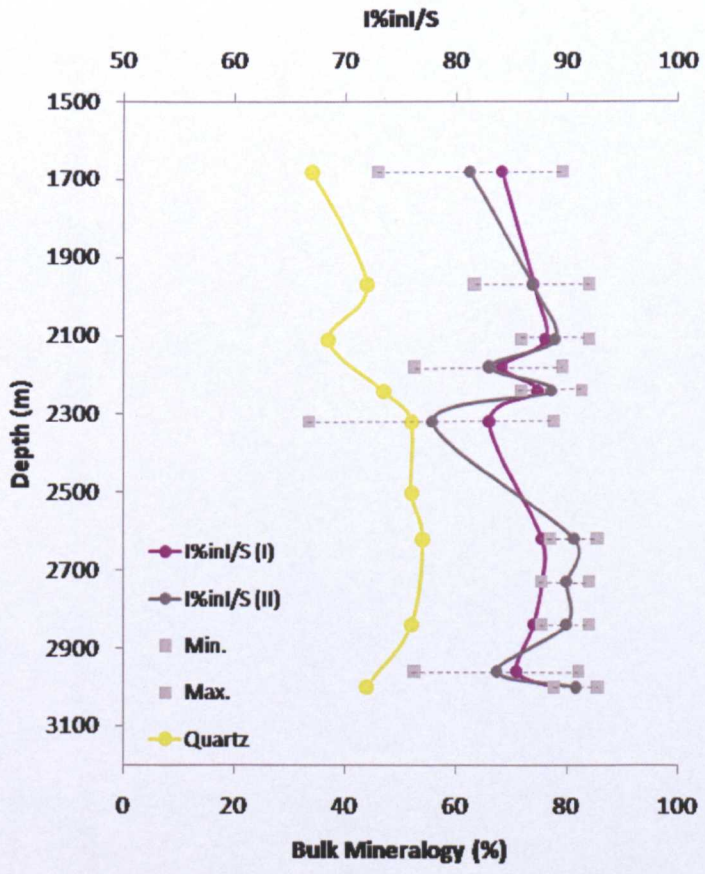

Figure 4.21 Representing Table 5.4 data with bulk fraction quartz for comparison.

4.2.2 Microscopic Petrography

4.2.2.1 Transmitted-Light Microscopic Analysis

As described in Chapter 3, information that may be gained from use of transmitted light microscopy on samples as fine as mudrocks can be limited without preparation of very thin sections (20–25 μm thick – Macquaker *et al.*, 2010) which was not possible in this study. However, to give initial insight into broad petrological characteristics (the coarser composition and texture), a brief study was carried out on thin sections (~ 30 μm thick) of samples from Well A and Well B.

Slides from Well A showed the material to be fine grained and little information could be gained on the matrix. Shallow slides tend to look similar to the image of 2140m in Figure 4.22. Larger grains with low birefringence that may be quartz or feldspars are distributed throughout the matrix as sub-angular to sub-rounded particles. Small amounts of brown coloured material is also sparsely distributed in the matrix. This sometimes shows higher birefringence but is masked by a strong brown body colour and displays parallel extinction. This material is therefore identified as biotite mica. In other places, the material is darker with no birefringence and this is interpreted as organic matter.

Several of the deeper slides contain a greater abundance of the brown material often displaying an elongate grain morphology. This includes 2326m, 2530m, 2582m 2621m (with 2530m shown in Figure 5.25). The 2326m "browns" do also show birefringence under crossed polars and parallel extinction so can be interpreted as biotite.

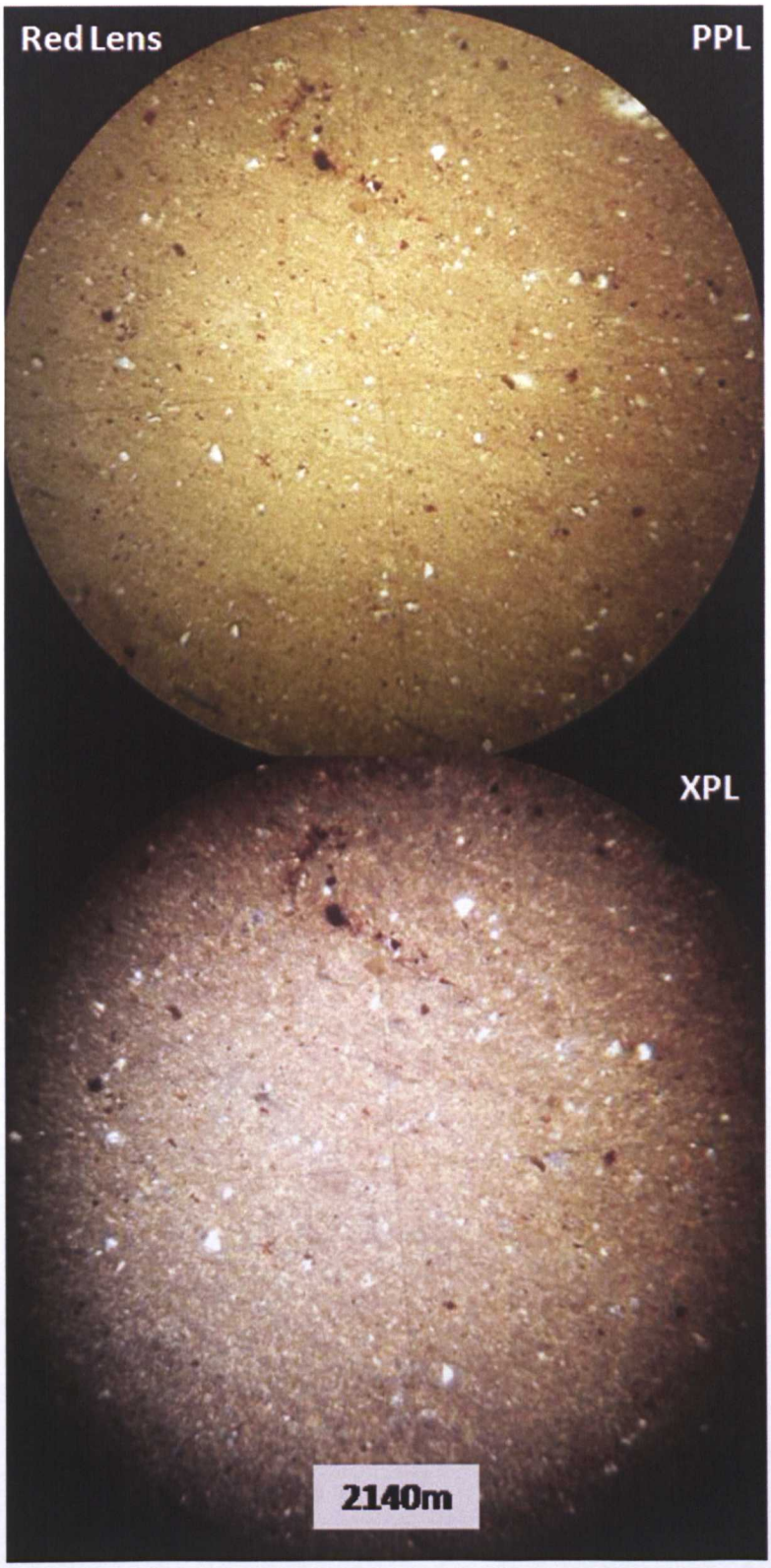

Figure 4.22 Images of sample 2140m under plane and crossed-polar views. Images were taken at minimum zoom, magnified under the PO A4 / 0.10 160 lens. White/grey angular grains possibly quartz or feldspar within phyllosilicate matrix. Dark brown features possibly organic matter, some will be biotite with masked birefringence.

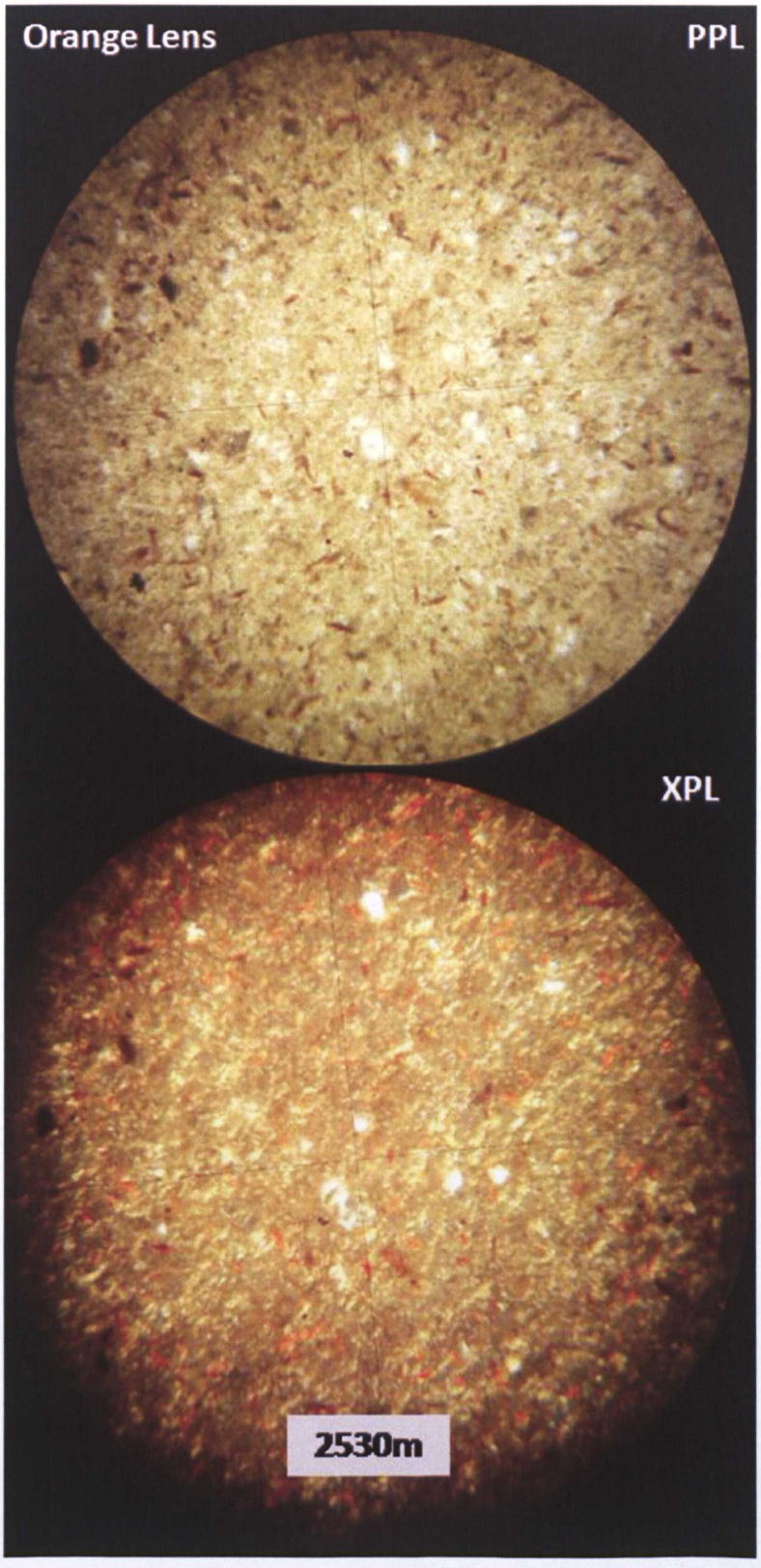

Figure 4.23 Images of sample 2530m under plane and crossed-polar views. Images were taken at maximum zoom, magnified under the PO A20/ 0.40 160/0.17 lens. White/grey angular grains possibly quartz or feldspar within phyllosilicate matrix. Dark brown features possibly organic matter, some will be biotite with masked birefringence. On some elongate grains birefringence can be seen and parallel extinction is observed indicating biotite content.

2472m is very fine grained and does not contain the same quantity of "browns" but all 3 deeper slides do with some being designated as biotite, some as organic material. 2530m and 2582m are slides of the samples that show TOC >1%. The difference in coarser mineralogy will also reflect the depositional variation seen in the different fluvial-lacustrine groups. Sample 2326m and those below are from the L Group and those samples above are from the K.

So despite the more homogenous mud-rich nature of the samples in Well A in comparison with the larger variation seen in Well B, it is important to remember that there is variation in mineralogy associated with depsositional facies. Indeed, the transition from the K to L Group samples is also the point that the calculated range of I% in I/S reduces to single figures (though the individual16.8Å glycolated peak is lost at shallower depths within the K).

The slides of the samples from Well B unsurprisingly show more variation than those from Well A. Shallow samples are dominated by "mud" matrix with some white/grey grains possibly quartz or feldspar. On some elongate grains birefringence can be seen and parallel extinction is observed indicating biotite content, though some "browns" may be organic content (Figure 4.24).

In slides of samples 1680 to 2240m (Figure 4.25) the material is fairly opaque and the images, very dark. Slide 2010m is almost completely opaque under crossed polars. These layers correspond to the >1% TOC measurements (see later section) and the dark material is likely to be organic matter. This is the tidal-marine section

and source rocks from these strata are generally composed of type III kerogen which may explain the coarseness of the opaque material.

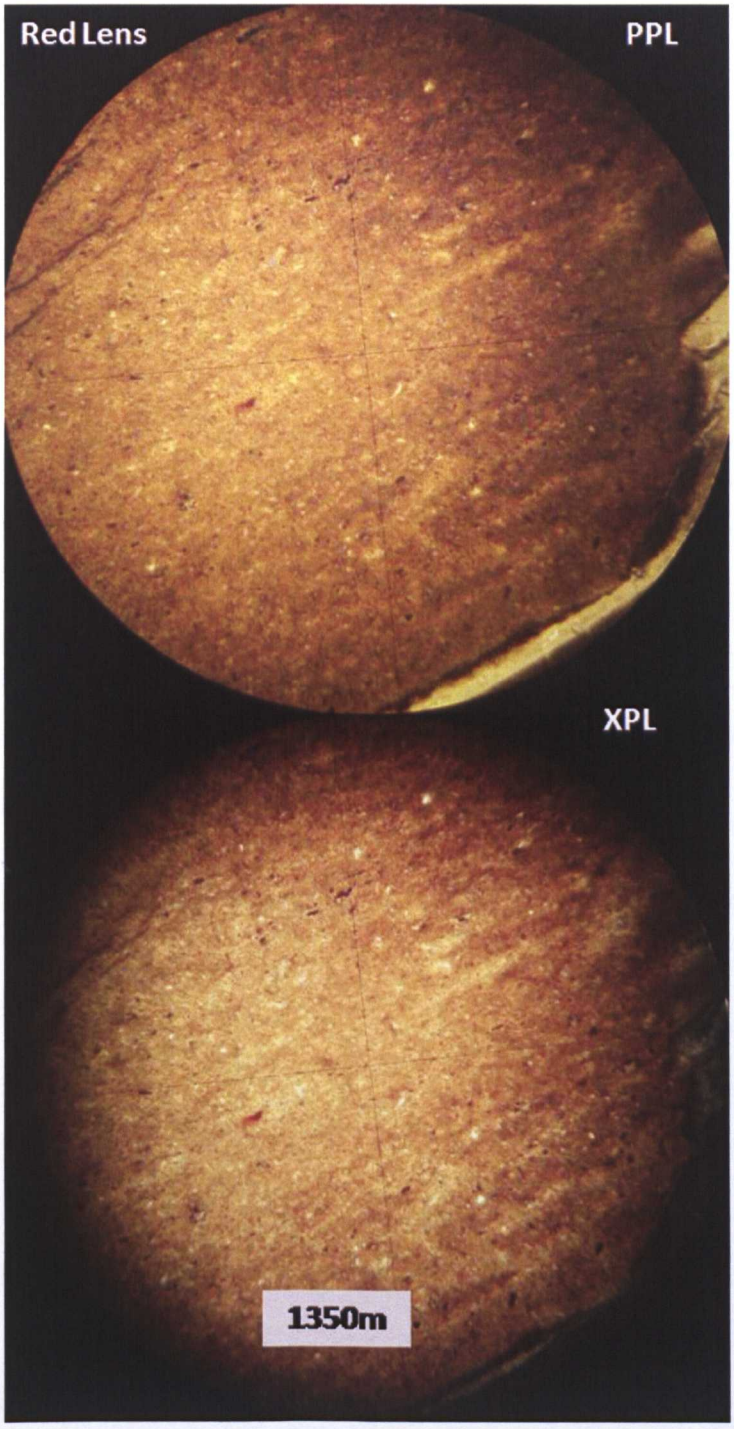

Figure 4.24 Images of sample 1350m under plane and crossed-polar views. Images were taken at minimum zoom, magnified under PO A4 / 0.10 160 lens. Dominated by "mud" matrix with some white/grey grains possibly quartz or feldspar. On some elongate grains birefringence can be seen and parallel extinction is observed indicating biotite content.

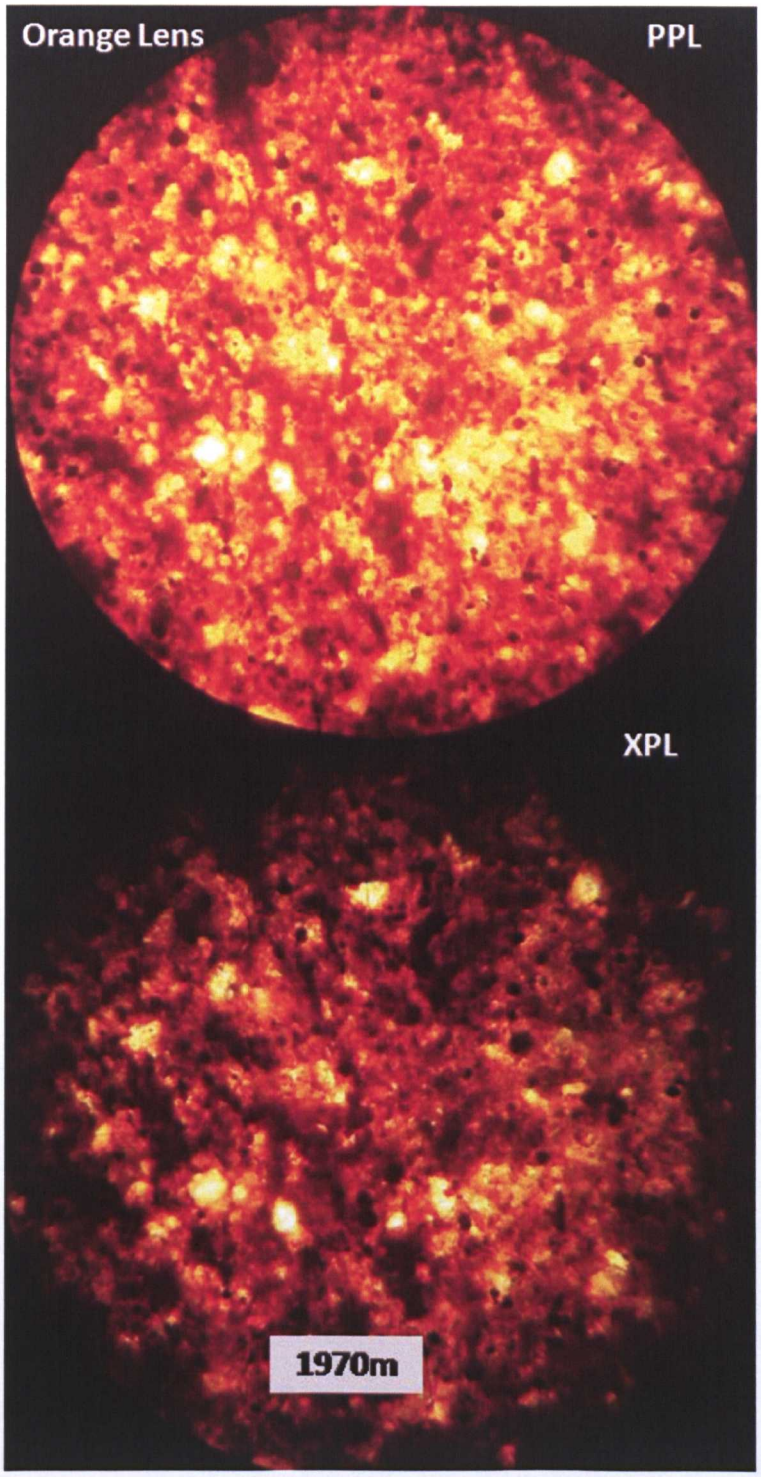

Figure 4.25 Images of sample 1970m under plane and crossed-polar views. Images were taken at maximum zoom, magnified under PO A20/ 0.40 160/0.17 lens. Very dark sample even under plane polars – dark brown material likely to be organic matter. White/grey angular grains possibly quartz or feldspar within phyllosilicate matrix.

Below these samples, the coarser, more quartz-rich samples of the fluvial-lacustrine system can be seen in Figures 4.26. Some images from these strata also display a more mud-rich appearance. Again, it should be remembered that Well B samples were selected for their lack of visible sand, so this may influence some of the variation. 3000m appeared to have the coarsest general grain size observed in any of the slides with lighter material preliminarily described as quartz with darker patches of material for closer observation under the scanning electron microscope.

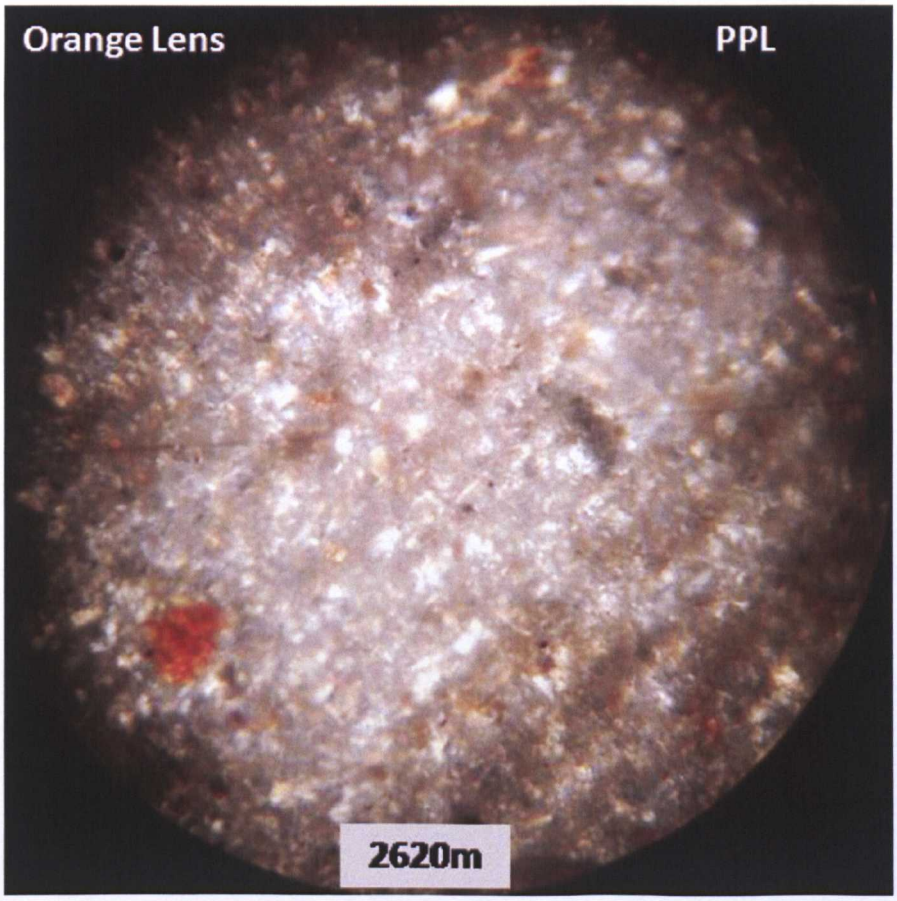

Figure 4.26 Images of sample 2620m under plane and crossed-polar views. Images were taken at maximum zoom, magnified under PO A20/ 0.40 160/0.17 lens. Dominated by white/grey angular grains possibly quartz or feldspar within phyllosilicate matrix. Dark brown features possibly organic matter, some will be biotite with masked birefringence.

4.2.2.2 Scanning Electron Microscopy and Energy-Dispersive X-Ray spectroscopy

Samples identified as of interest following the transmitted-light study and those required to give balanced coverage of the depths sampled were prepared for SEM imaging (see Chapter 2). In Well A samples from 1728m, 1795m, 2140m, 2530m and 2621m were studied.

Transmitted light microscopy had shown the 1728m (5670ft) sample to be representative of the shallowest samples in Well A, in that little could be seen apart from abundant matrix and some quartz and/or feldspar with dark brown/red material that was preliminarily identified as organic matter. These features can be confirmed and seen in more detail using BSEM and EDX (Figure 4.27).

Quartz is present, along with K-aluminosilicate which given the grain morphology and chemistry is likely to be orthoclase feldspar, Na-aluminosilicate which could be plagioclase feldspar ($NaAlSi_3O_8$), pyrite and a rather large (>20 μm) fragment of carbonaceous material (Figure 4.27). The matrix is clay-rich and along with Si, Al and O tends to contain K, Mg and Fe with some Na. This will represent the illite ($K_{1-1.5}Al_4[Si_{7-6.5}Al_{1-1.5}O_{20}](OH)_4$)/mica, chlorite ($(Mg,Al,Fe)_{12}[(Si,Al)_8O_{20}](OH)_{16}$), kaolinite ($Al_4[Si_4O_{10}](OH)_8$) and expandable I/S clays containing some smectite ($(1/2Ca,Na)_{0.7}(Al,Mg,Fe)_4[(Si,Al)_8O_{20}](OH)_4.nH_2O$) – though K may be exchanged in as I/S is already well developed).

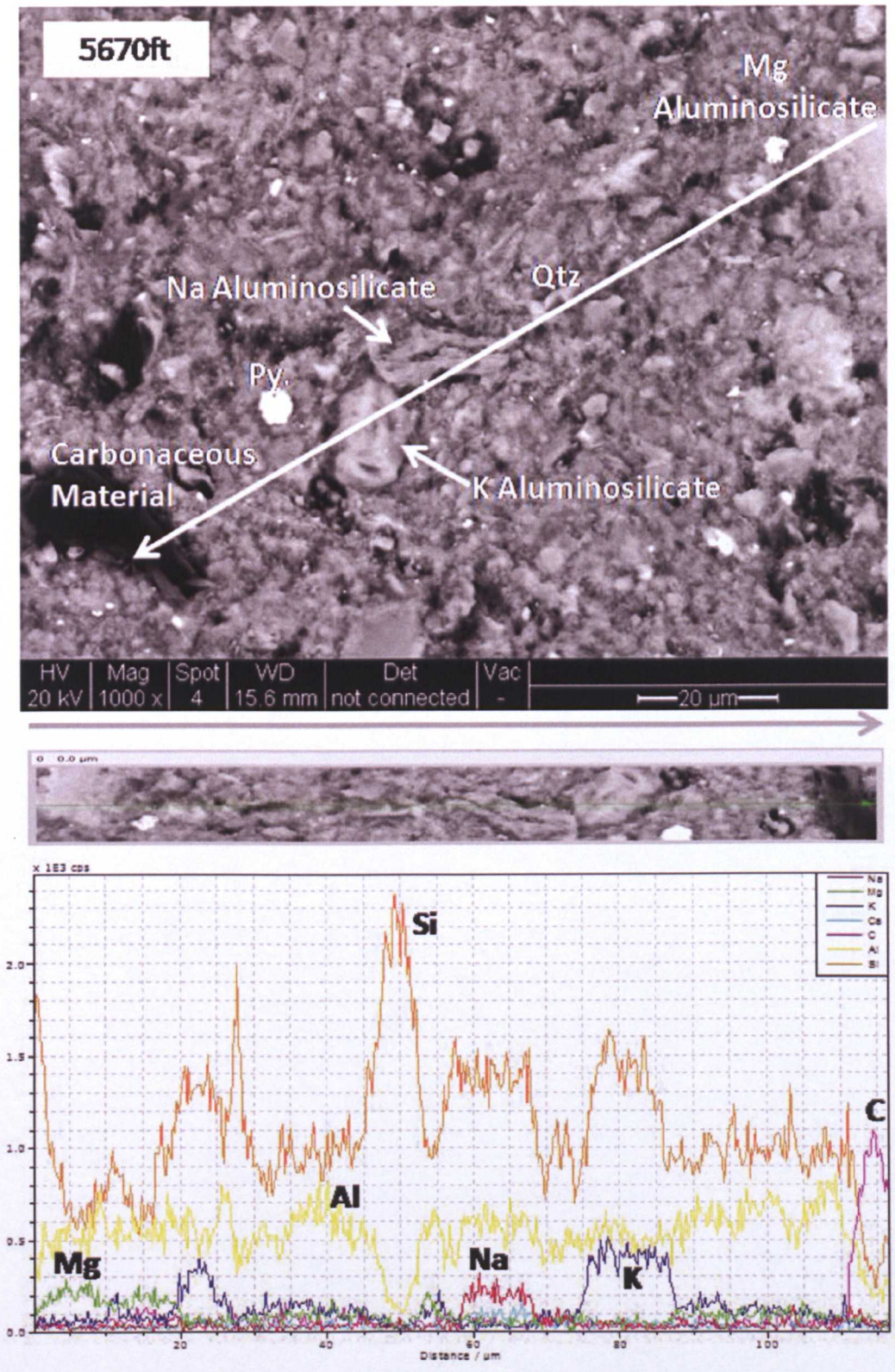

Figure 4.27 BSEM image of sample 1728m (5670ft) with EDX spectra displayed below for cross-section marked by white arrow (and shown in central strip-image). EDX measured presence of Si, Al, Mg, Na, K, Ca and C. Slides were carbon coated, but peak far greater than base-line identified the carbonaceous grain.

No alignment or specific texture can be described. As could be seen in the transmitted light microscopy, coarser grains (but still relatively fine ~20 μm) seem randomly distributed in a dominantly clay matrix.

The 1795m (5890ft) sample, along with 1728m, shows the individual 16.8 Å peak upon glycolation in the clay-fraction XRD results. A small point-count was carried out using the EDX software and along with Si, Al and O, the matrix tends to contain K, Mg and Fe with some Na. The most intense response is K in 87% of counts and Mg in 13%. The 5000x zoom on the matrix shows whispy, fine grains that are dominantly K-rich aluminosilicate and are thought to be I/S or illitic material (Figure 4.28). Generally the matrix does not appear to show any strong alignment, but amongst packages of clay/mica some parallel grains can be seen. Coarser mineralogy is similar to 1728m and again, just appears to show scatter throughout the dominant clay matrix.

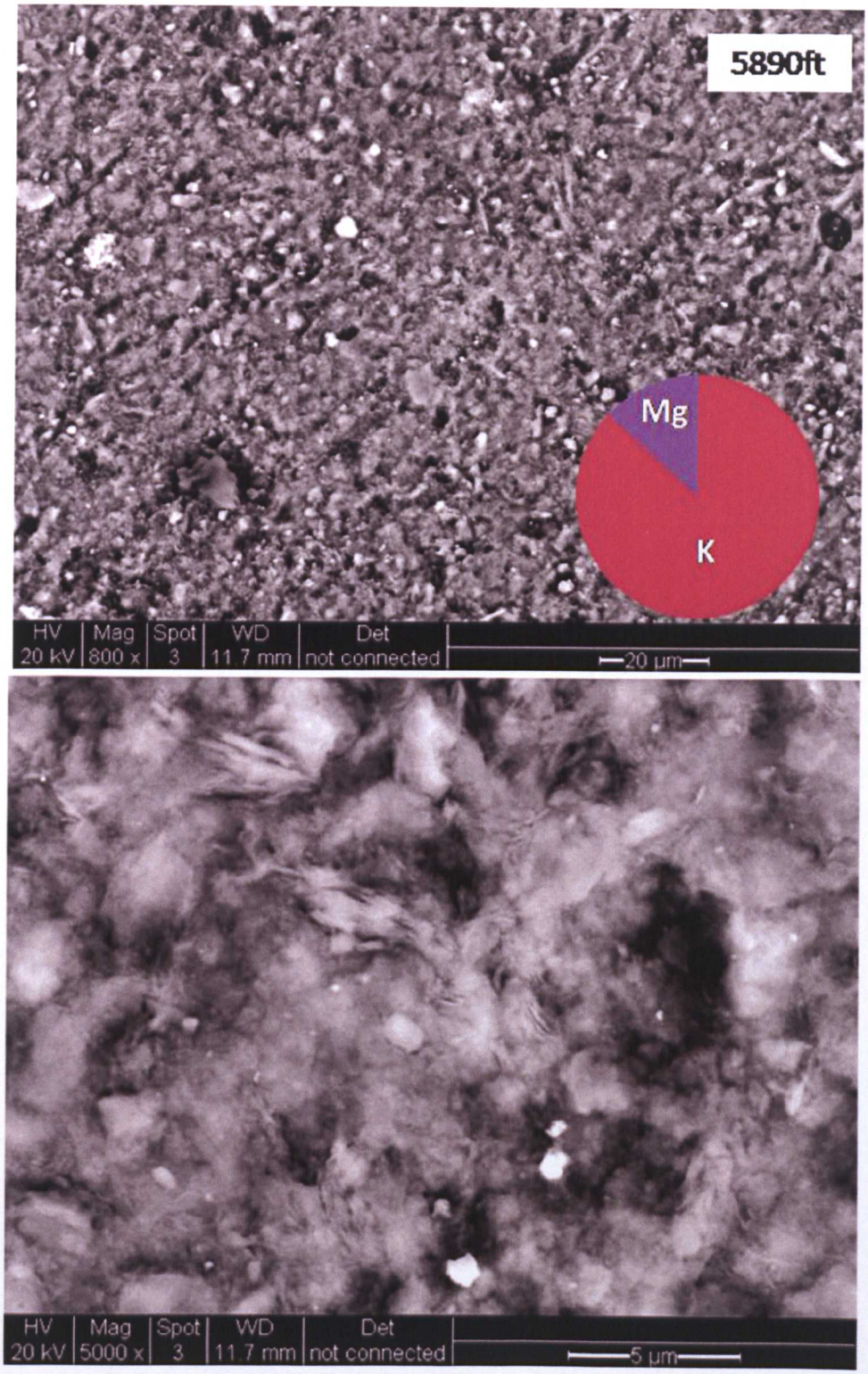

Figure 4.28 BSEM image of sample 1795m (5890ft) at lower (800x) and higher (5000x) magnifications with pie diagram to display dominant non-Si/Al/O element from EDX point counts.

The slide of 2140m (Figure 4.29) is mineralogically similar to the shallower samples but does seem to show higher amounts very fine, sub-rounded quartz (<10 μm) which is in keeping with the bulk fraction XRD analysis which shows this sample to have the second largest quartz content (27%). Again, no strong alignment is visible but within areas of clay, some parallel grains can be seen.

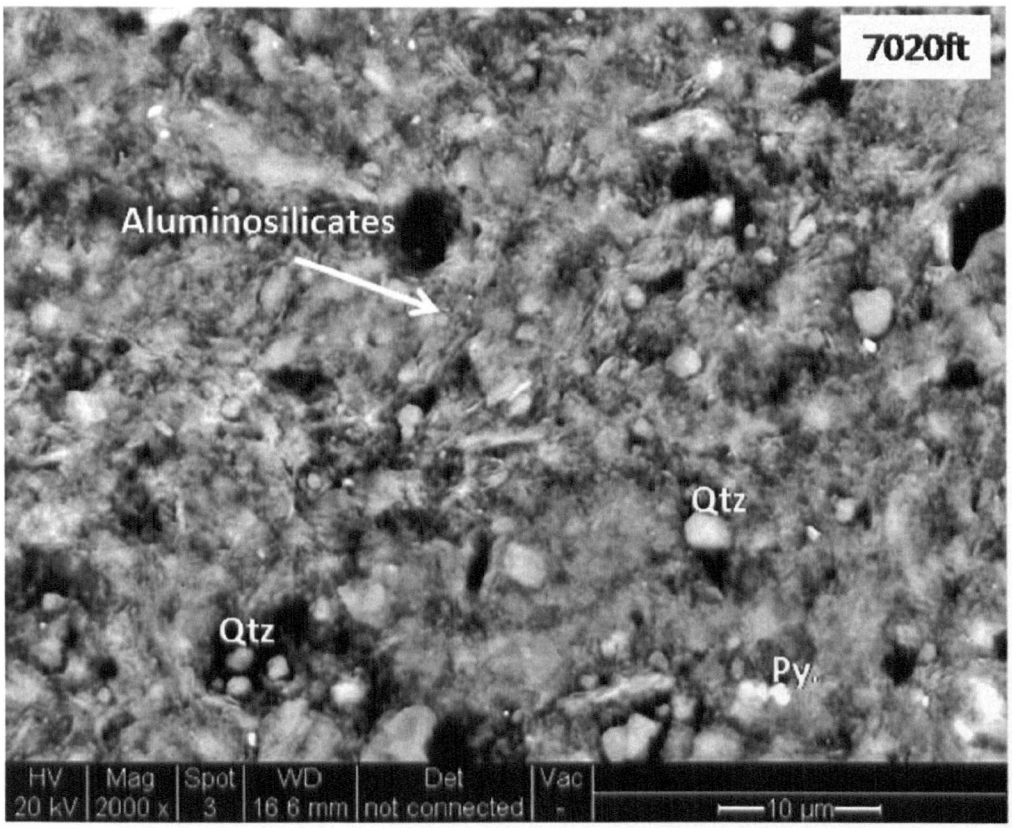

Figure 4.29 BSEM image of sample 2140m (7020ft) at 2000x magnification and mineralogy identified using EDX point analyses.

The 2530m (8300ft) sample contains TOC >1%, but although EDX point analyses revealed some carbonaceous grains, they were not dominating the slide. Instead as indicated in the initial microscopy, some of the "browns" are biotite mica (observed Figure 4.30) where the central "bright" grains contain Mg, Fe, Ti (higher atomic

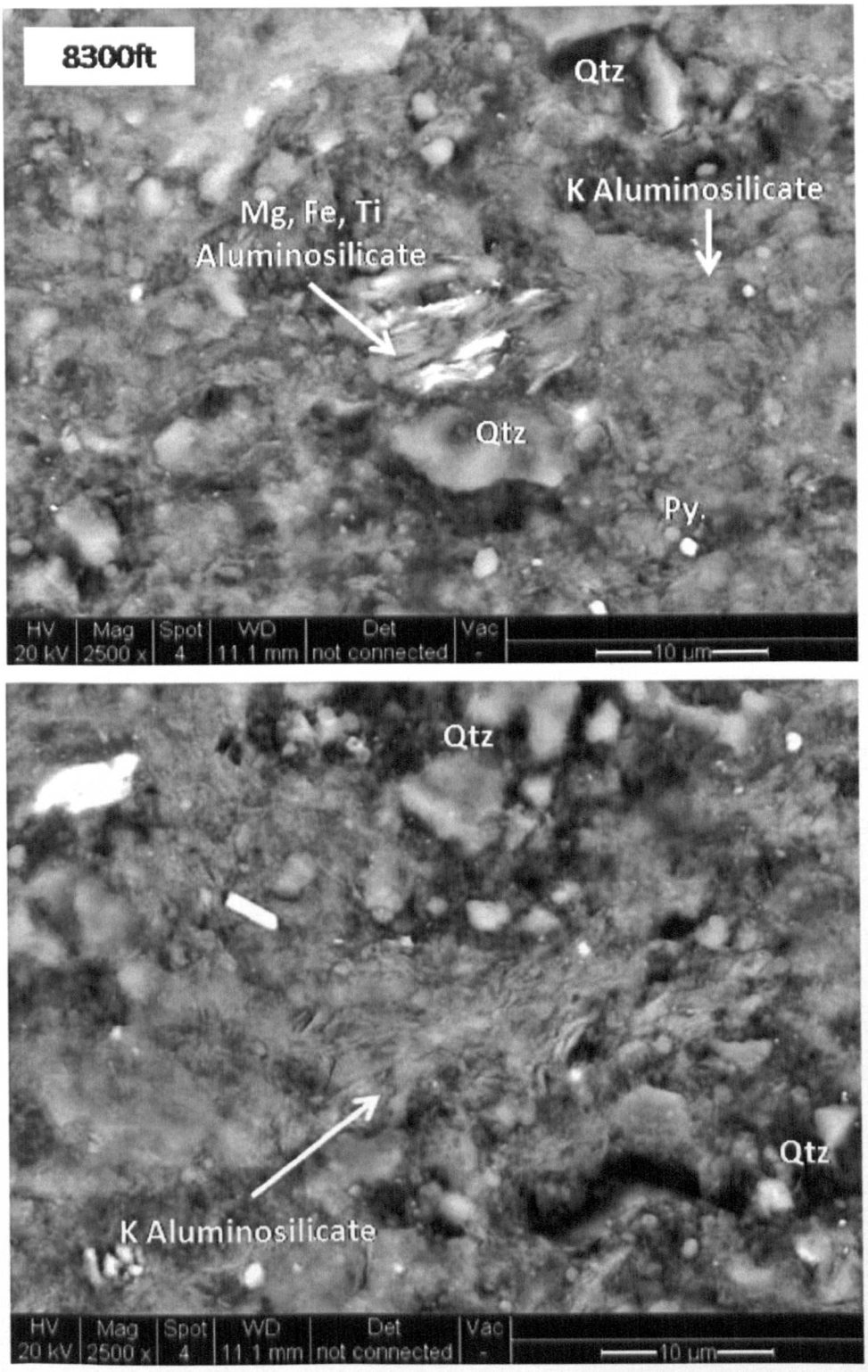

Figure 4.30 BSEM image of sample 2530m (8300ft) at 2000x magnification and mineralogy identified using EDX point analyses (Qtz: quartz; Py: pyrite).

mass) aluminosilicate. Packages of sub-parallel whispy K-rich aluminosilicate grains (illitic I/S or illites) can be seen in the second image of Figure 4.30, but in the first

image they can be seen showing more random orientation and overall there is not a very strongly aligned appearance.

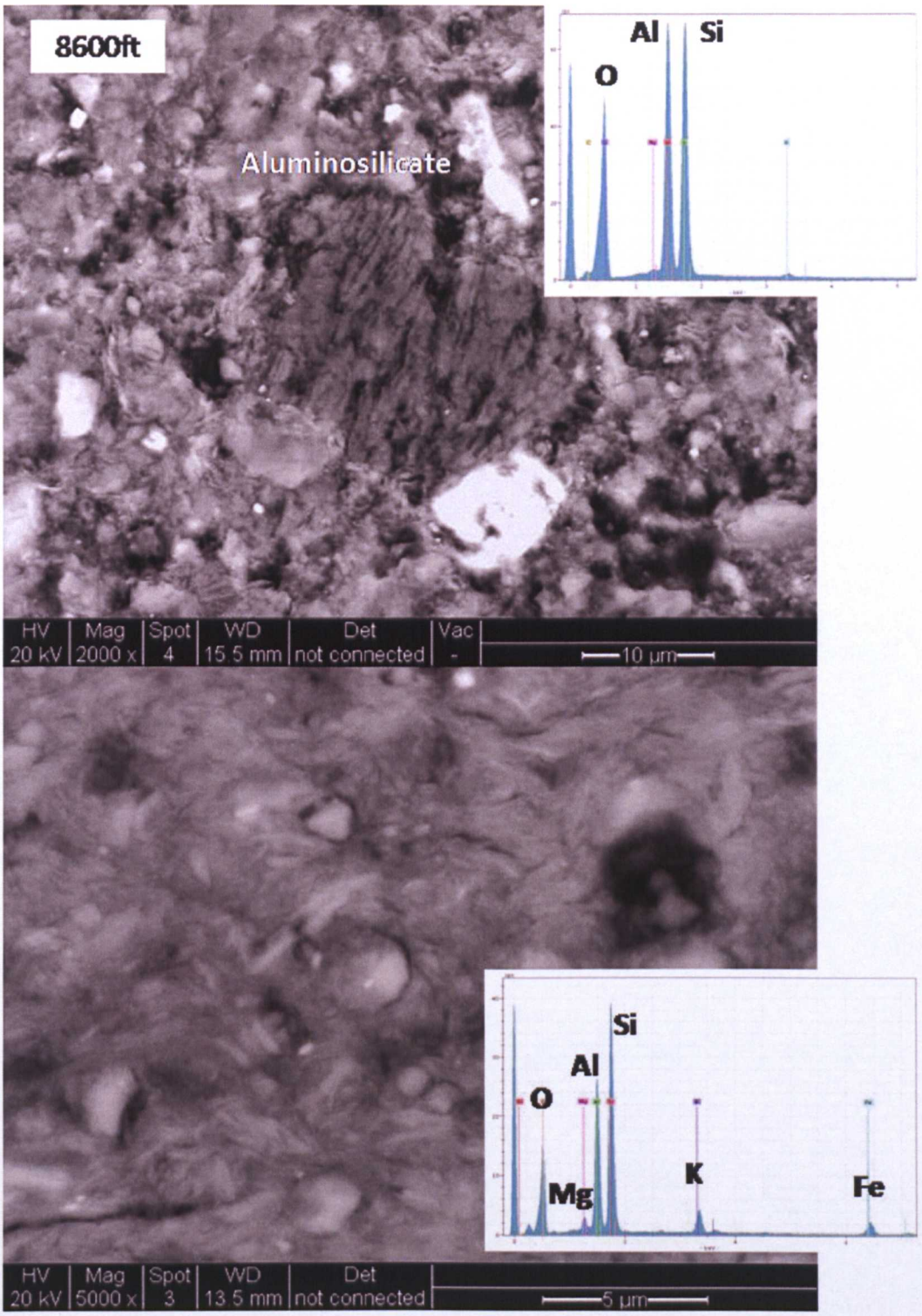

Figure 4.31 BSEM image of sample 2621m (8600ft) at lower (2000x) and higher (5000x) magnifications with thumbnail EDX spectra to display composition of central, darker grain in upper image and composition of the whispy matrix in the lower image.

The deepest sample of Well A from 2621m (8600ft) is shown in Figures 4.31 and 4.32. In the former, the central, darker grain in the upper image is a kaolinite grain that looks cracked and does not look in equilibrium within the matrix. Its appearance may be due to slide preparation, but a border of very fine lighter grey contrast (K-rich aluminosilicate) appears to be present around part of its edges and it may be a grain undergoing alteration. General mineralogy is similar to that encountered in shallower samples with matrix, quartz and pyrite, and some organic matter. Feldspars were not identified regularly in the deeper sample slides.

The matrix is K, Fe, Mg aluminosilicate with 78% of EDX point analyses showing K to be the most intense peak followed by Fe (15%). Grains show "flowing" sub-parallel behaviour in many areas. This is occasionally picked out as linear cracks as can be seen in Figure 4.32 presumably opening along grain boundaries following stress release. The term "flowing" is subjectively used, as when the elongate grains encounter the sub-rounded quartz grains, they appear to orientate around the grains (Figure 4.32). Due to slide preparation, the areas immediately around the quartz grains are sometimes missing due to the difference in hardness between the quartz and the matrix.

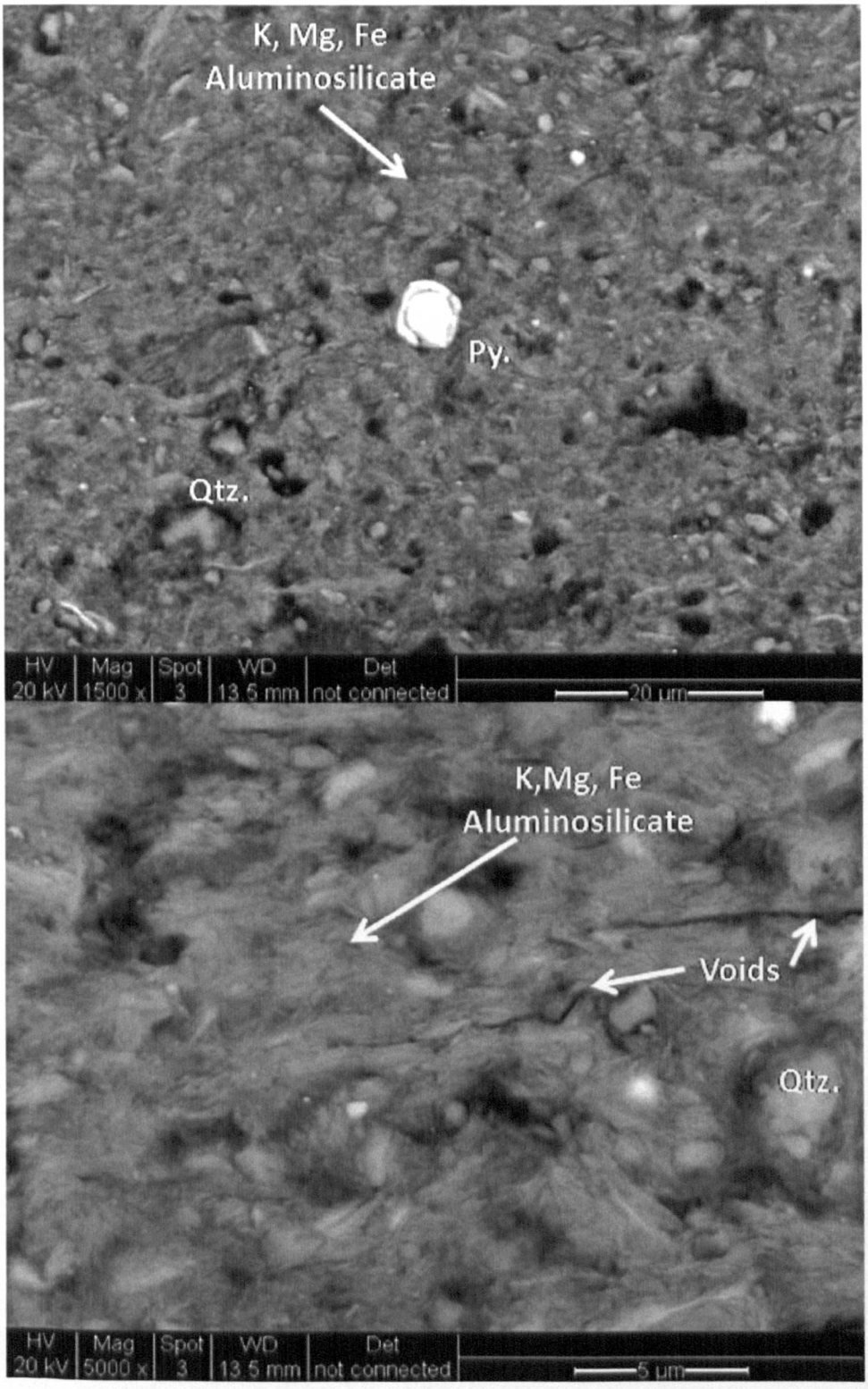

Figure 4.32 BSEM image of sample 2621m (8600ft) at lower (1500x) and higher (5000x) magnifications mineralogy identified using EDX point analyses (Qtz: quartz; Py: pyrite).

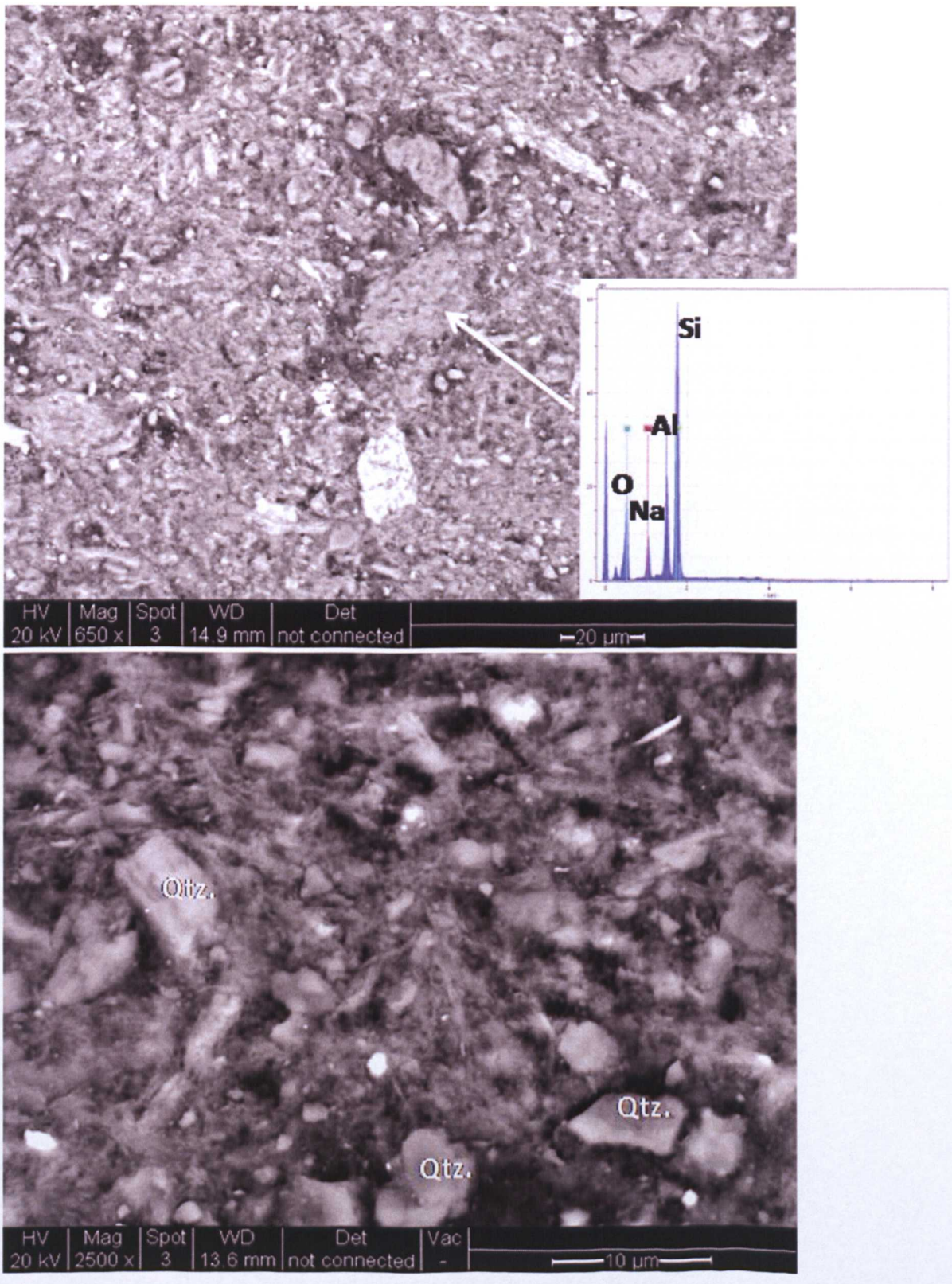

Figure 4.33 Well B - BSEM images of sample 1350m at lower (650x) and higher (2500x) magnifications with thumbnail EDX spectra to display composition of central region in upper image and mineralogy identified using EDX point analyses (Qtz: quartz).

In Well B, samples from 1350m, 1680m, 2730m, 2960m and 3000m were studied. The shallowest sample from 1350m displayed a matrix-rich slide but with more coarse and mineralogically varied grains compared with Well A (evident in EDX maps). Coarser, more sub-angular quartz is present as is feldspar with "bright" contrast, coarser grains of biotite and clusters of fine "bright" grains interpreted as siderite. Amorphous patches of Na-rich aluminosilicate could be the smectite material identified in the bulk fraction XRD, but have patchy distribution shown by the EDX analysis point count. This found the matrix is generally a mix of Ca, K, Fe, Mg and Na aluminosilicate with 38% of EDX point analyses showing Ca to be the most intense peak followed by K (27%) and then Na (19%) plus Mg (15%). Visually there is no appearance of strong alignment amongst the clay grains and coarser grains seem randomly distributed through the matrix.

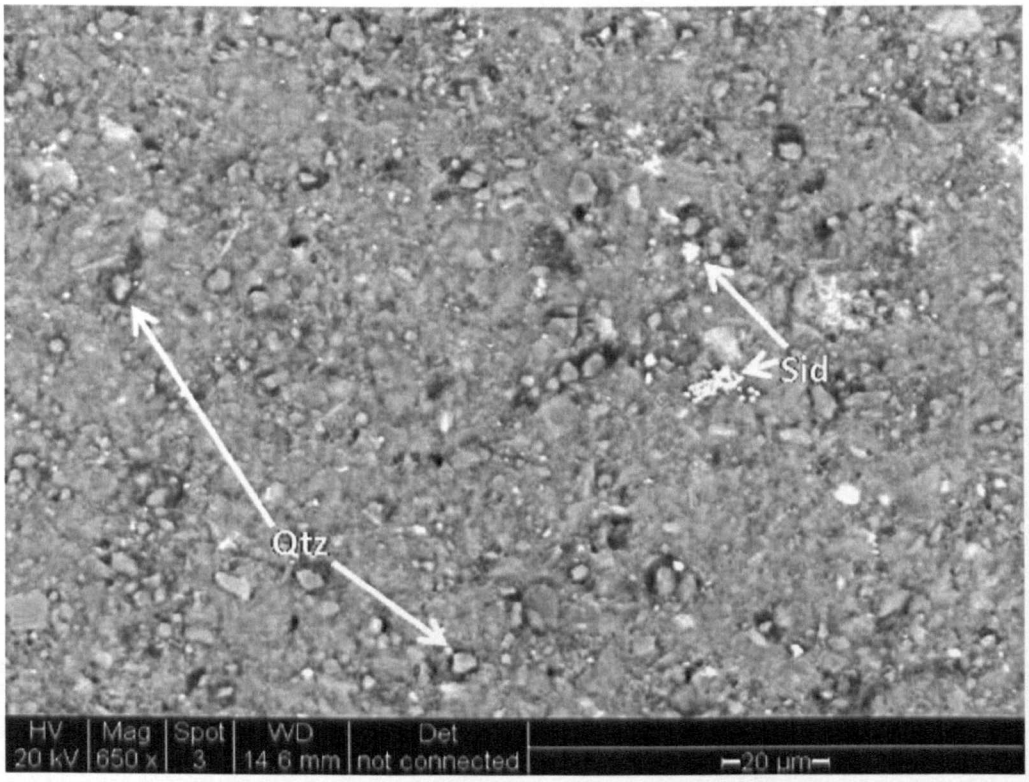

Figure 4.34 BSEM images of sample 1680m at lower (650x) magnification with mineralogy identified using EDX point analyses (Qtz: quartz; Sid:siderite).

The 1680m samples (Figure 4.34) shows some biotites and organics, but is mainly comprised of clay matrix and quartz with some feldspars. The matrix is generally a mix of Ca, K, Fe, Mg and Na aluminosilicate with 78% of EDX point analyses showing K to be the most intense peak. Siderite is very noticeable throughout the matrix showing "bright" clusters of grains that in some areas become more dispersed – infilling the matrix.

The 2730m slide was one of the samples marked as being more matrix rich, in the generally more quartz-rich deeper section of Well B and this is held up by its appearance in Figure 4.35. The K, Fe, Mg aluminosilicate matrix showed 93% of points to be K dominant. This matrix does not appear to show strong alignment but amongst clay clusters sub-parallel grains can be seen. Brights appear to be biotite and pyrite, although siderite is also occasionally picked up using EDX point analyses.

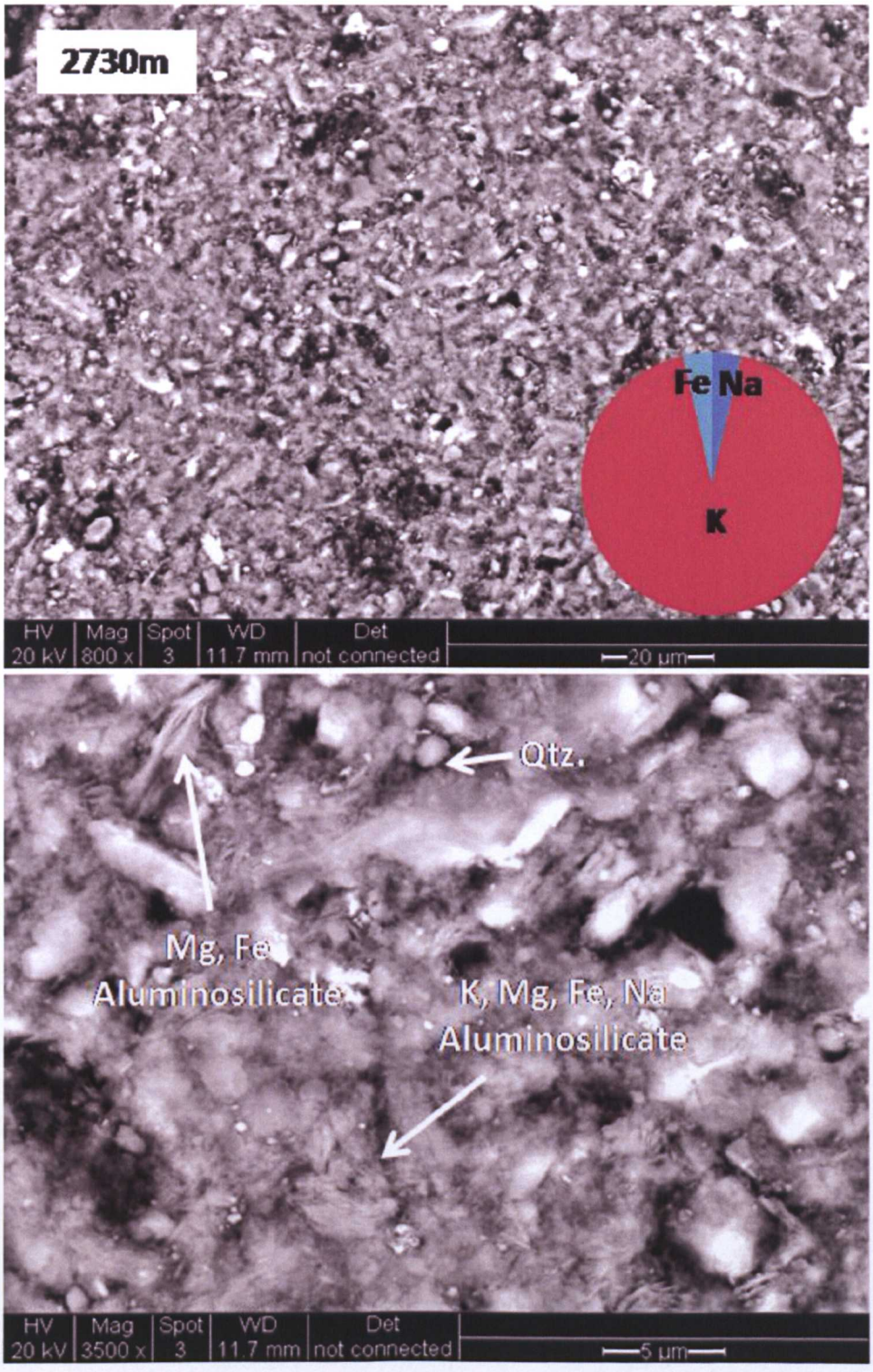

Figure 4.35 BSEM images of sample 2730m at lower (800x) and higher (3500x) magnification with mineralogy identified using EDX point analyses (Qtz: quartz) and pie diagram to display dominant non-Si/Al element from EDX point counts.

In the second deepest sample from 2960m, EDX maps of Al and Si identify the quartz grains in red (containing Si only) and the mixed areas belong to the clay matrix (Figure 4.36). Higher magnification images of the matrix does show alignment of the grains as can be seen in the upper BSEM image in Figure 4.36. The generally K, Fe, Mg aluminosilicate matrix comprises 88% of points showing K as the most intense peak.

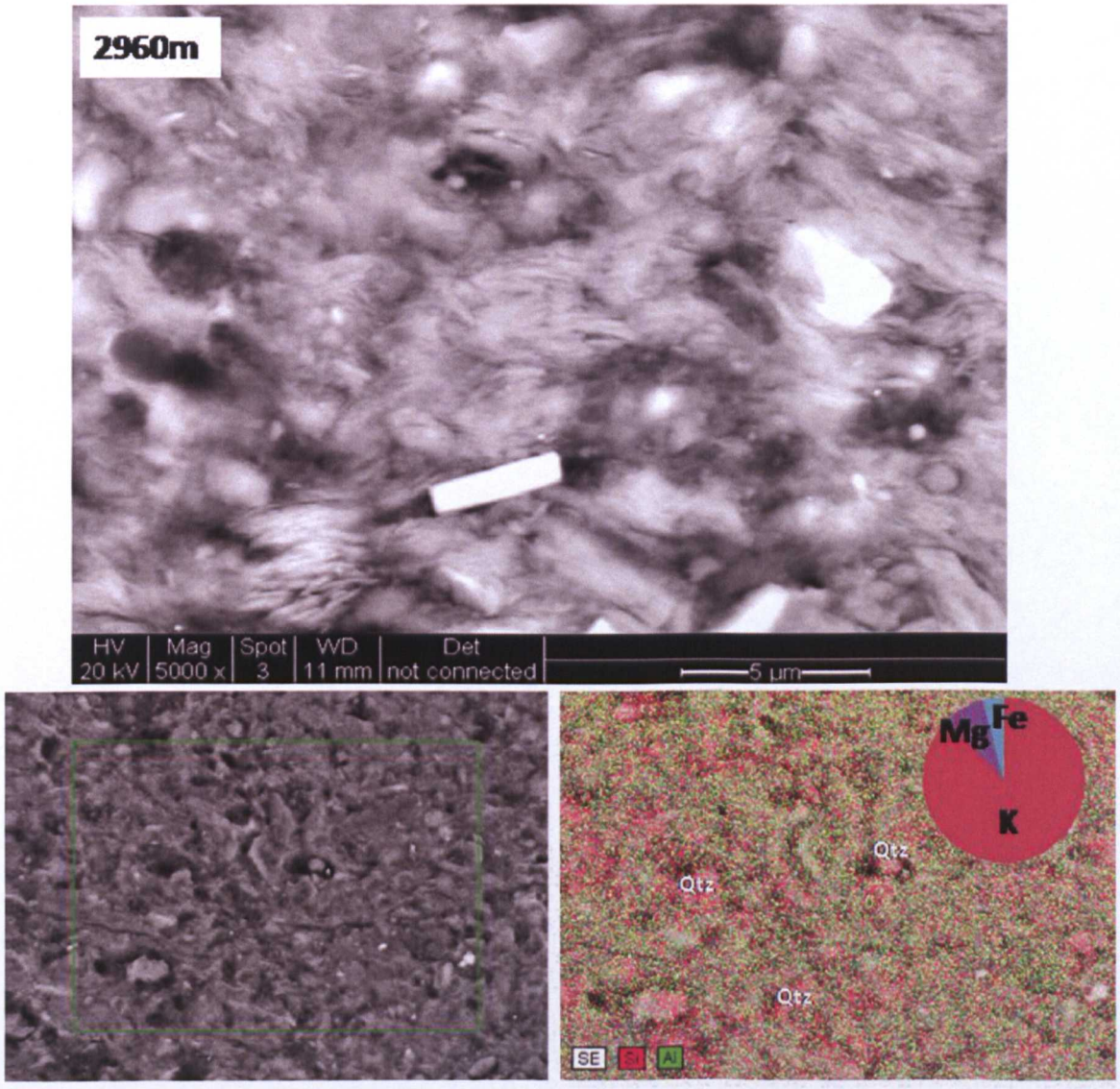

Figure 4.36 BSEM images of sample 2960m at higher (5000x) and lower magnification with EDX maps of Si and Al content of lower magnification image. Mineralogy identified (Qtz: quartz) and pie diagram to display dominant non-Si/Al/O element from EDX point counts.

The deepest sample from 3000m was shown to be quartz-rich and one of the coarsest grained slides studied in the initial transmitted light microscopy. However, abundant clay matrix/cement can be seen in BSEM images and EDX maps of Si and Al. A generally K, Fe, Mg aluminosilicate matrix with 87% of points showing K as the most intense peak (typical spectra shown in Figure 4.38). In the matrix areas, clay grains are very well formed and and aligned as can be seen in the images a,b and d in figure 4.38.

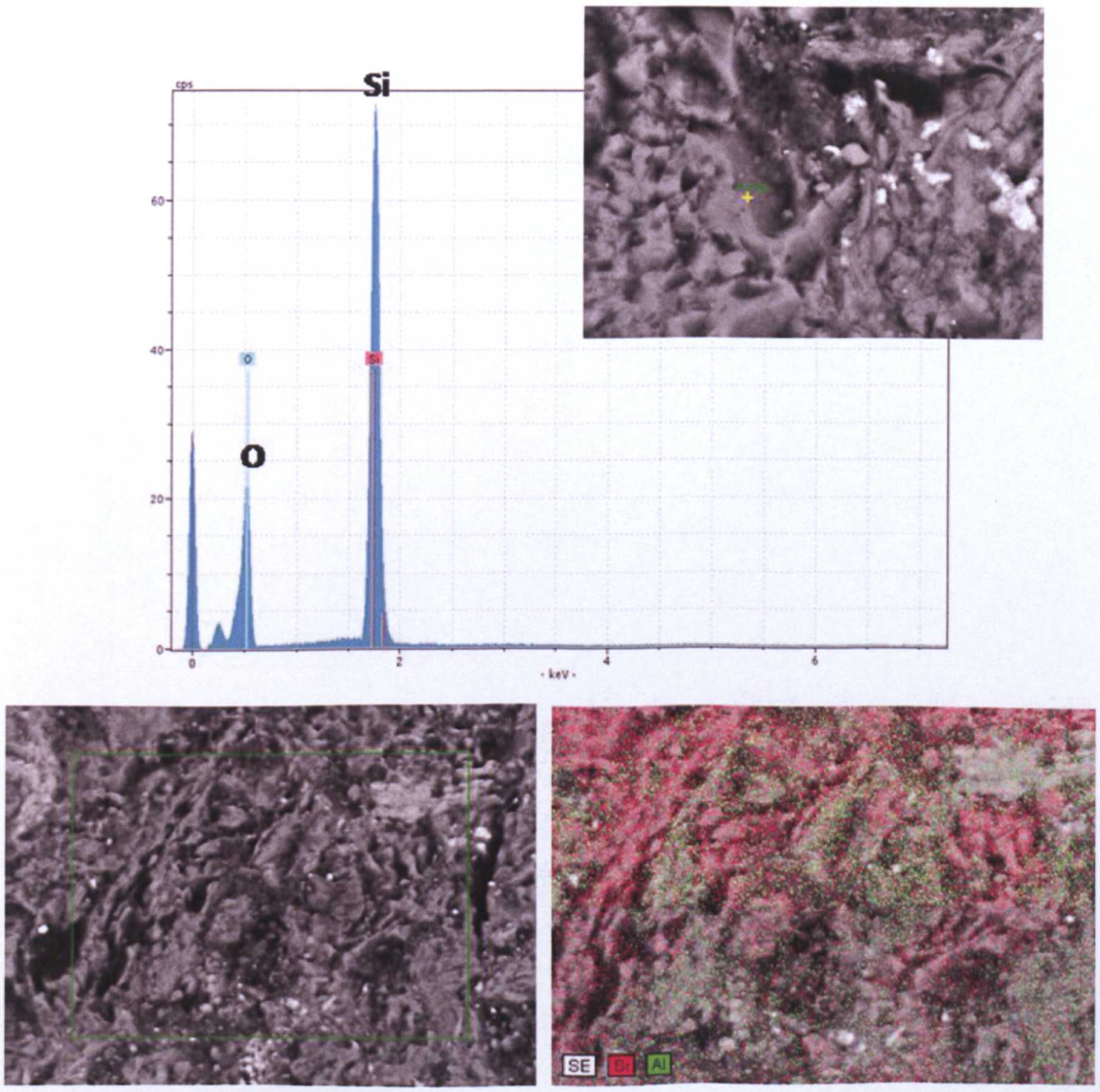

Figure 4.37 BSEM images of sample 3000m with a point spectra of a quartz "grain" and EDX maps of Si and Al content of high magnification image.

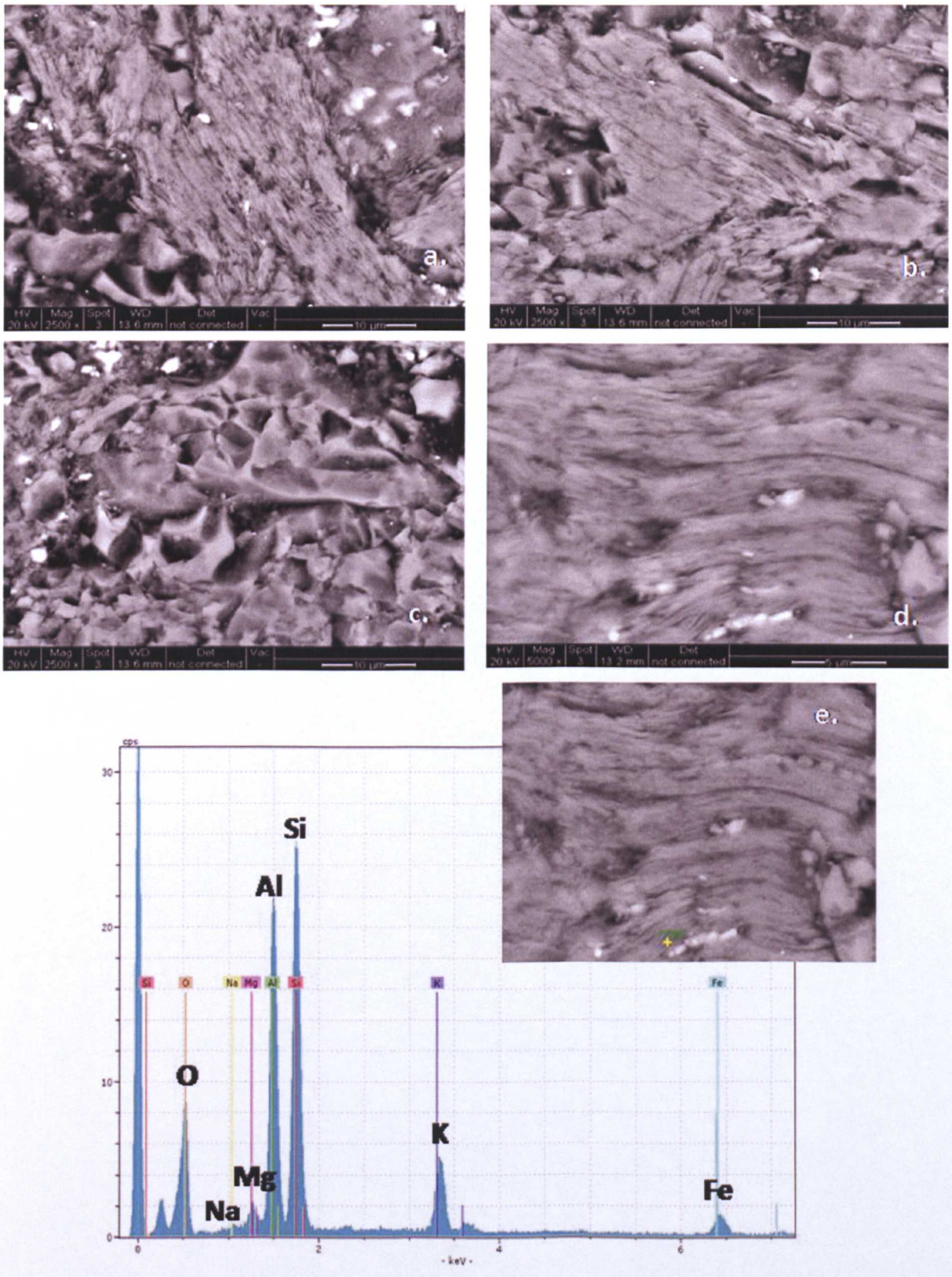

Figure 4.38 BSEM images of sample 3000m a, b & d. show clay packages with chemistries similar to those recorded in the spectra below (actual spectra for d/e). Image c. at 2500x shows the abundant quartz with its blocky, angular surface.

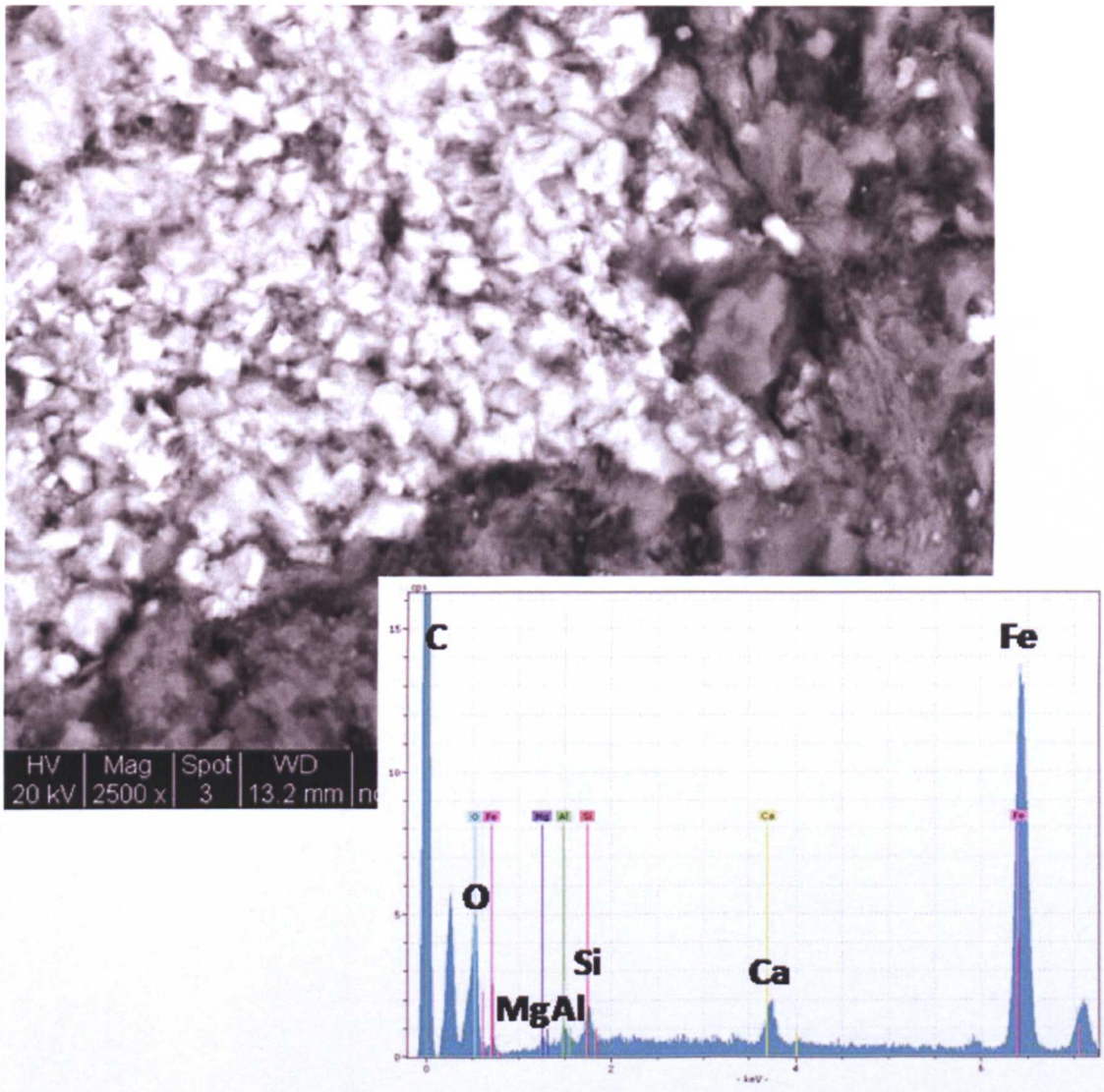

Figure 4.39 BSEM images of "bright" grains at 3000m (2500x) and associated EDX spectra.

Figure 4.39 shows a 2500x magnification of a cluster of siderite closely associated with the matrix. The BSEM images in Figure 4.40 show the intergrowth and/or alteration of minerals from sample 3000m. In the upper image the lighter coloured Fe, Mg aluminosilicate is likely to be chlorite given its spectra and the material that is interspersed with it is the more typical K, Mg, Fe aluminosilicate (I/S or mica). In the lower image some of the "brights" are siderite, but other sections are chlorite that is interspersed with I/S or mica. The textures observed in 3000m are quite different from those observed in other samples and there was initial speculation over whether

they were natural. It would appear that this is actually just a coarser sandstone/siltstone with abundant matrix/cements some quartz, siderite and clays.

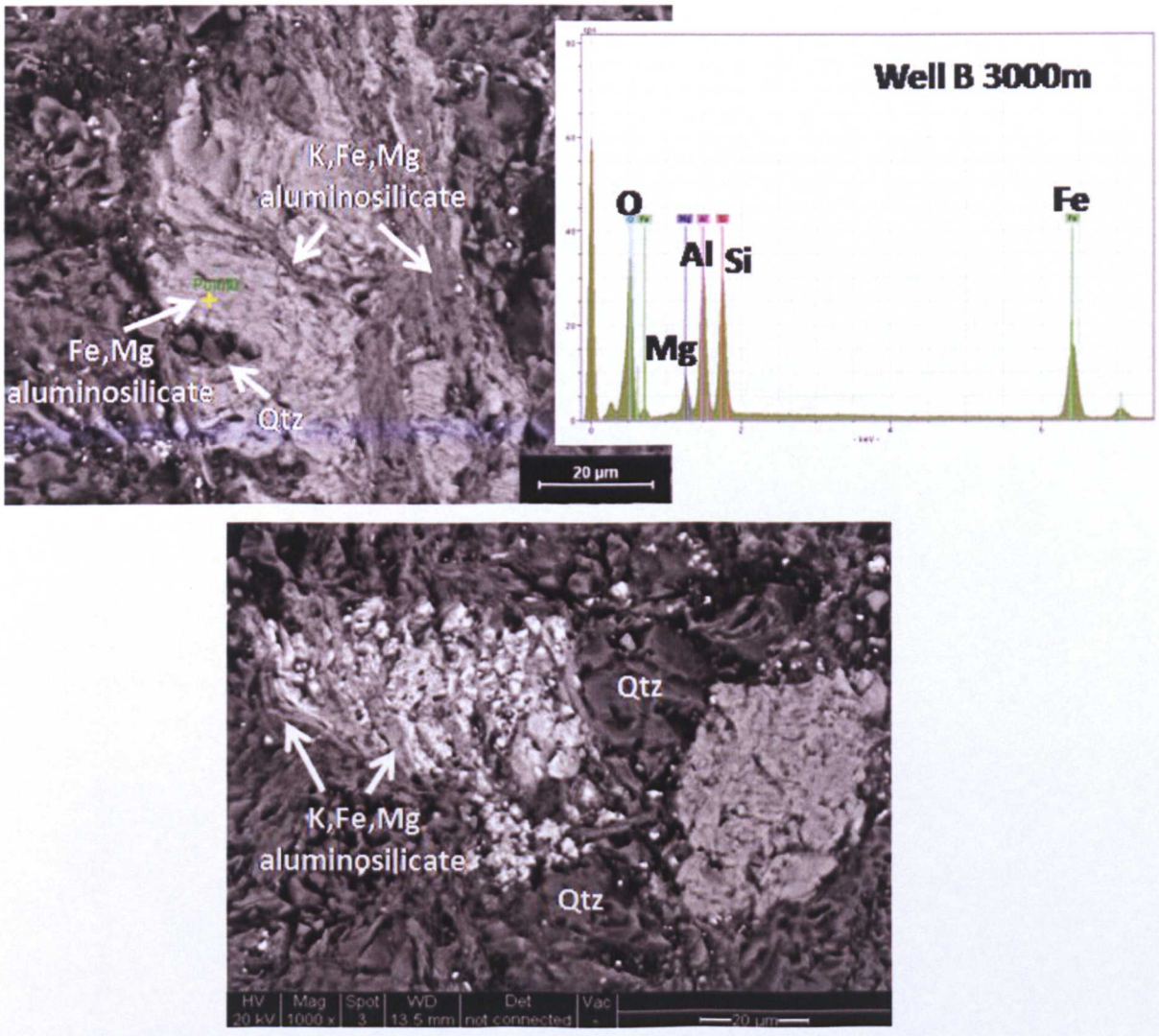

Figure 4.40 BSEM images of sample 3000m with EDX spectra for bright grain in upper image.

4.2.3 Organic Properties

4.2.3.1 Total Organic Carbon (TOC) Content

Sample depth (m)	TOC (%)
1728	0.94
1795	0.76
1932	0.70
2140	0.85
2316	0.90
2472	0.89
2530	1.02
2582	1.53
2621	0.79

Table 4.6 Measured TOC for samples from Well A. Samples with TOC >1% highlighted in green.

The error on the procedures was measured using an inorganic reference soil (+/- 0.11%) and a blank sample (+/- 0.03%). The highlighted samples from Well A in Table 4.6 have 1-2% TOC indicating their potential as fair source rocks for hydrocarbons (see classification Chapter 3). However, generally organic matter-rich facies contain 2 - > 15 wt % TOC, with the average "hot shale" containing 5 wt% (Gautier, 2005), so their quality should not be overestimated. 2530-2582m (8300-8420ft) lies in the Upper Oligocene/Lower Miocene fluvial – lacustrine deposited strata of Unit L where the lacustrine, Type I source rock is found in some areas of the basin. As described in 4.1, Group L sources have ~1-2% TOC but can have high HI values of ~400-700 mg/HC/g TOC.

Sample	TOC (%)
1350	0.68
1680	1.45
1970	4.02
2110	3.94
2240	0.41
2470	0.51
2520	0.56
2620	0.59
2840	0.62
3000	0.78

Table 4.7 Measured TOC for samples from Well B. Samples with TOC >1% highlighted in green.

In Well B, 1680-2100m covers an interval in the in the tidal-marine deposited Units I/J. These are among the units that can hold the lower coastal plain source rocks of the Lower-Mid Miocene. These units contain coal and carbonaceous shales that can have TOC >20% and HI >350-<700 mg/HC/g TOC. This horizon corresponds to the opague slides from the transmitted light microscopy and the elevated C content from EDX.

4.2.3.2 Rock-Eval Pyrolysis

Rock-Eval pyrolysis was carried out to examine the samples, to see how values changed through the horizons and also to assess the real source potential of horizons already identified as havin >1% TOC as the hydrogen index is also key.

Sample Depth (m)	TOC (%)	Oil (S1) (mg hc/g)	S2 (mg hc/g)	Tmax (oC)
1728	0.94	0.03	0.67	442
1795	0.76	0.02	0.21	443
1932	0.70	0.02	0.40	442
2140	0.85	0.02	0.63	444
2316	0.90	0.02	0.85	446
2472	0.89	0.22	1.11	443
2530	1.02	0.14	0.84	443
2566	*NM*	0.05	0.47	446
2582	*1.53*	0.53	1.43	440
2582 *(RI)*	*1.53*	0.13	0.88	442
2582 *(RII)*	*1.53*	0.10	1.11	444
2594	*NM*	0.22	1.17	444
2621	0.79	0.04	0.71	445

Table 4.8 TOC (from previous, separate measurements - not repeated) with S1, S2 and Tmax from RockEval analysis for depths sampled in Well A. RockEval analysis repeated for 2582m (highest TOC content) .

The error on the procedures was measured using an organic reference average +/- 0.11 and a blank sample average+/- 0.03 for TOC and for Rock-Eval the blank ran at 0.00mg hc/g and the standard (see Chapter 2) at +/- 0.00 mg hc/g.

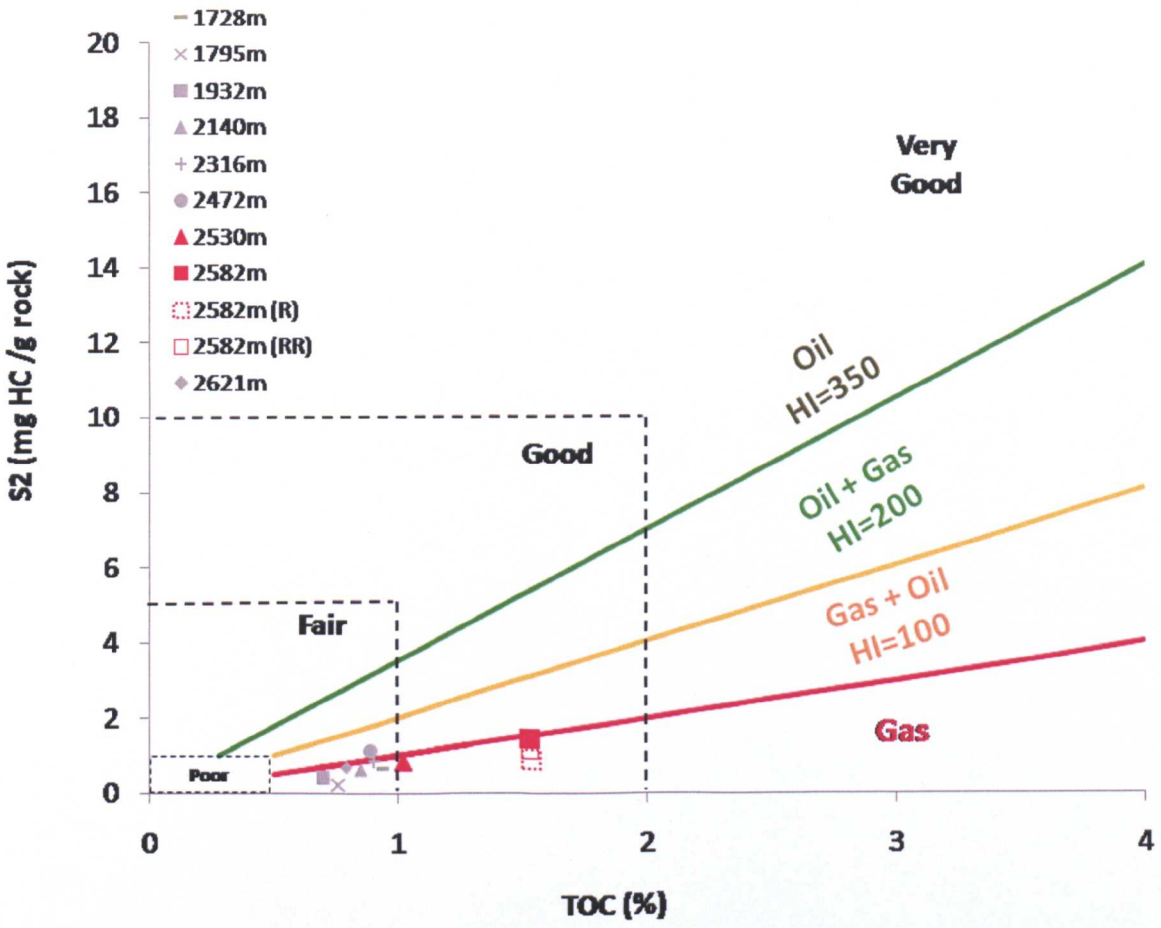

Figure 4.41 S2 vs. TOC plot of Langford & Blanc-Valleron (1990) displaying variation in potential quality of source and hydrocarbon type (Ro~0.6%) with rock eval data for Well A samples.

The data in Figure 4.42 gives TOC values from the previous measurements and S2 from the Rock-Eval analysis. According to the diagram, both >1% TOC samples plot near the Gas / Gas + Oil bound line and are therefore classified as a good gas source. This may be optimistic by comparison with other classification schemes.

Sample Depth (m)	TOC (%)	Oil (S1) (mg hc/g)	S2 (mg hc/g)	Tmax (oC)
1350	0.68	0.06	0.19	445
1680	1.45	0.08	0.57	442
1970	*4.02*	0.12	3.51	437
1970 *(RI)*	*4.02*	0.15	3.44	438
2110	3.93	0.11	2.80	444
2240	0.41	0.23	0.15	446
2620	0.59	0.06	0.29	456
3000	0.78	0.05	0.17	471

Table 4.9 TOC (from previous separate measurements - not repeated) with S1, S2 and Tmax from RockEval analysis for depths sampled in Well B. RockEval analysis repeated for 1970m (highest TOC content).

In Well B, of the samples with greater than 1% TOC, 1680m plots as good gas prone and 1970-2110m are classified as very good gas prone sources (Figure 4.42). Whether or not either of these sources have generated any hydrocarbons requires looking at Tmax data provided. Tmax, as seen in Table 4.9, appears to decrease over the potential source horizons, but is still relatively high indicating generation could have taken place.

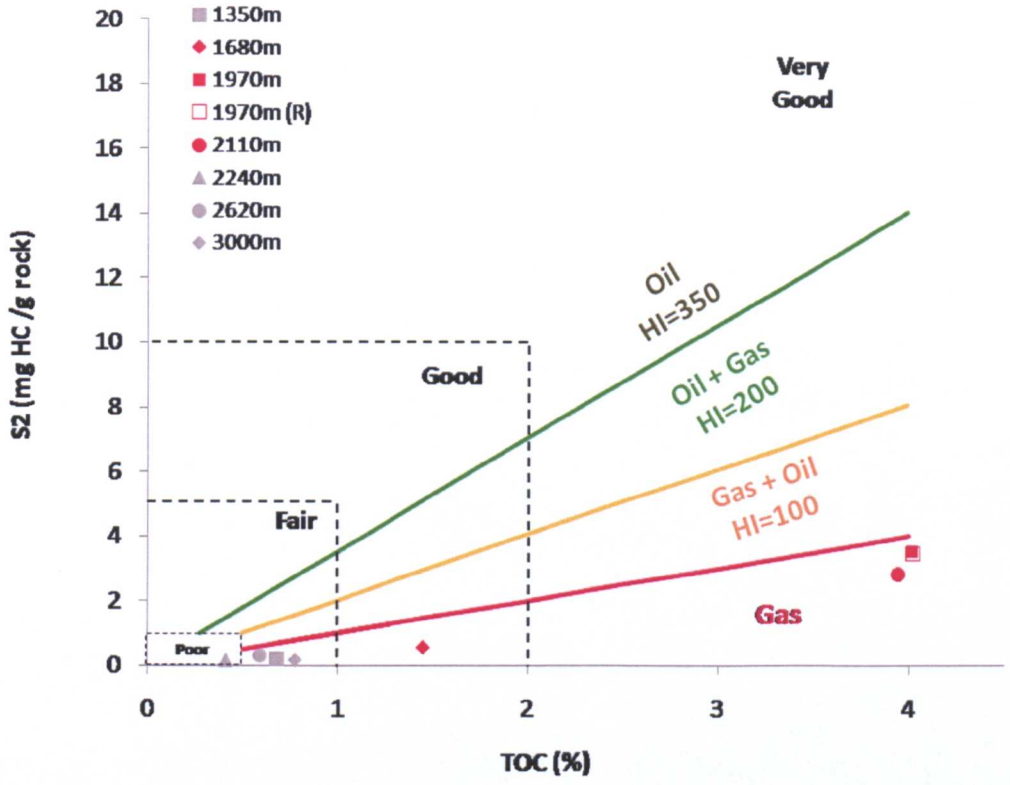

Figure 4.42 S2 vs. TOC plot of Langford & Blanc-Valleron (1990) displaying variation in potential quality of source and hydrocarbon type (Ro~0.6%) with rock eval data for Well B.

4.2.4 Summary of Chemical/Mineralogical Properties

There are many controls on the chemical/mineralogical properties of the samples from Well A and B as is to be expected from the natural, burial environment. These include spatial and group dependant depositional compositions, diagenesis and possibly catagenesis.

- Bulk fraction XRD showed Well A to be more clay-rich than the sampled horizons in Well B. Illite-mica is the dominant clay mineral presnt in both wells, but this is outweighed by the quartz content of the deeper Well B samples (even following selective sampling). Fe-rich mineralogy appears to show some correlation with depositional environment with more samples of the tidal-marine environment bearing siderite and the fluvial-lacustrine groups mainly bearing minor pyrite.

- Clay fraction XRD showed that the shallowest samples in Well A displayed individual16.8Å glycolated smectite peaks that were not visible in deeper samples. The I% in I/S is generally high, however, the range of expandable material present in each if the samples decreases with depth. The least "mature" samples from the shallowest depth will be just over the threshold for *R*1 ordering (~>50% = *R*0 to *R*1). The rest of the Well A samples should also have *R*1 ordering, until the deepest samples which at ~90% I in I/S could possess *R*3 ordering. Depth related trends are not observed in Well B.
- Transmitted light microscopy served to highlight the higher TOC samples between 1680-2110m in Well B. More detail was obtained from the BSEM images of the samples, in combination with EDX spectra to show that there was a K-rich aluminosilicate matrix, with increasing richness observed in Well B which covered a greater depth range, appearance of mineral alteration at depth and a speculative increase in the alignment of the fine, aluminosilicate particles in the deeper samples. Well B could be seen to be more quartz rich and apparent loss of alignment was interpreted around silica grains.
- Organic measurements show that the deeper Upper Oligocene/Lower Miocene fluvial – lacustrine source horizon may be present between 2530-2582 in Well A, but it has corresponding low HI and is gas prone. Tmax of 440-444°C would indicate generation. The lower coastal plain source rocks of the Lower-Mid Miocene may also be sampled between 1680-2110m in well B, showing a gas prone character in TOC and rock eval analyses with Tmax between 437-444°C.

4.3 Physical properties

4.3.1 Grain density

Grain densities were measured for all samples using the adapted, small pyknometer method as described in Chapter 2 and results are tablulated in Table 4.10 below.

Well A Sample Depth m. (ft.)	Grain Density (g/cm^3)	Well B Sample Depth m.	Grain Density (g/cm^3)
1619 (5313)	3.02	1350	2.77
1728 (5670)	2.69	1600	2.73
1750 (5740)	2.71	1680	2.91
1795 (5890)	2.71	1900	2.83
1887 (6190)	2.68	1970	2.77
1932 (6340)	2.67	2010	2.90
2082 (6830)	2.73	2110	2.71
2140 (7020)	2.75	2180	2.77
2280 (7480)	2.77	2200	2.92
2316 (7600)	2.78	2240	2.75
2408 (7900)	2.81	2260	2.78
2472 (8110)	2.80	2320	2.87
2481 (8140)	2.89	2470	2.83
2530 (8300)	2.76	2500	2.77
2566 (8420)	2.70	2520	3.01
2582 (8470)	2.70	2620	2.79
2594 (8510)	2.76	2730	2.76
2621 (8600)	2.84	2840	2.78
		2960	2.81
		3000	2.75

Table 4.10 Grain densities of all samples from Wells A and B. The measured error with reference to the quartz standard used in all runs was +/- 0.014 (min.+/-0.001, max.+/-0.029).

Many of the grain densities have relatively high values for mudstones. Given the consistency of the higher readings and the known presence of iron bearing minerals such as siderite and pyrite, this is thought to refect the genuine character of the mudrocks. A number of calculations were made using the mineral densities tabulated

in Chapter 2, with the modelled mineral abundances from bulk fraction XRD and the measured sample grain densities were always within a sensible range of error (for example, > the minimum calculated value possible or within -0.03g/cm^3 of it), bar the more organic rich samples 2530 and 2582m in Well A and 1680m, 1970m and 2110m in Well B which required the reduced density of the organic component to be included in the calculation.

When plotted against depth, the samples in Well A show a number of separate trends and have been grouped arbitrarily into Horizons I-IV (Figure 4.43).

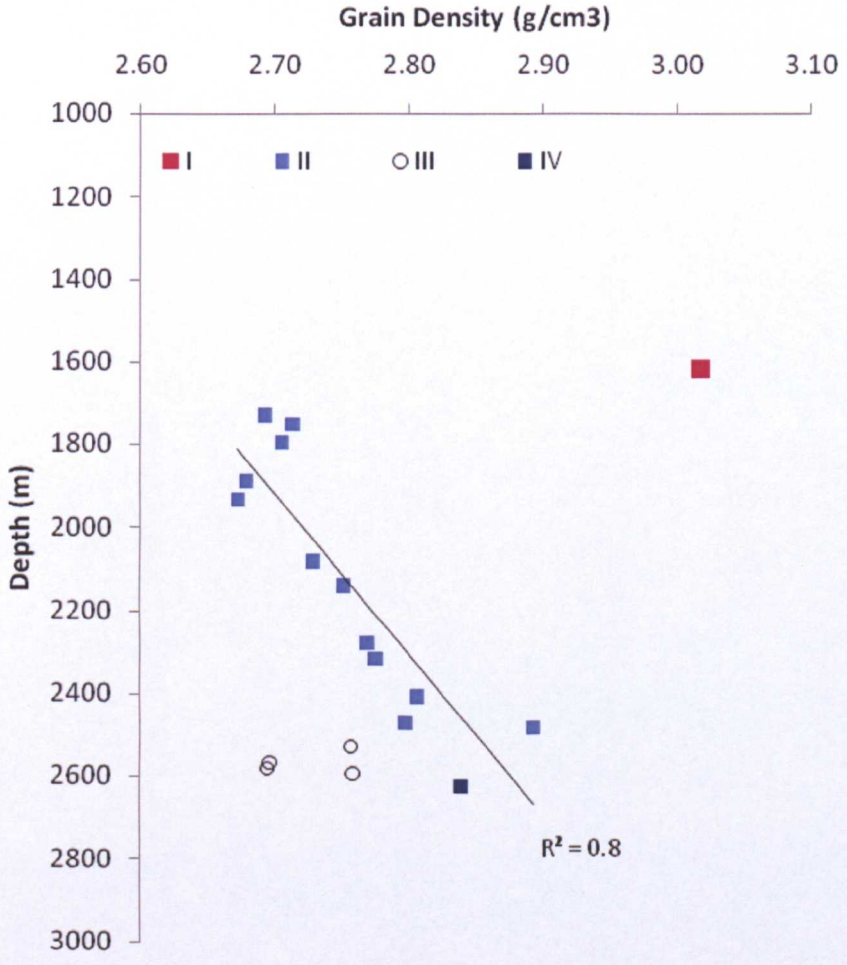

Figure 4.43 Grain density data with depth of sample for Well A categorized into horizons I-IV.

I is a shallow, high density sample from 1619m and is the only sample from the tidal/marine deposited facies. It contains 34% siderite which contributes significantly to its density. The second horizon, II, contstitutes the bulk of the Well A samples increasing in density with depth. The upper 3 samples of II (IIa) lie slightly above trend and in other properties, form a separate trend (see later). They lie between 1728 and 1795m and are the shallowest samples of the fluvial-lacustrine Unit K. The 2 samples measured using clay-fraction XRD from this upper interval displayed a separate, glycolated smectite peak. The remaining samples of horizon II (IIb) lie between 1887 and 2581m, covering the lower section of K and the earlier Unit L. These samples show a distinct increase in grain density with depth which shows some correlation with pyrite content (Figure 4.44).

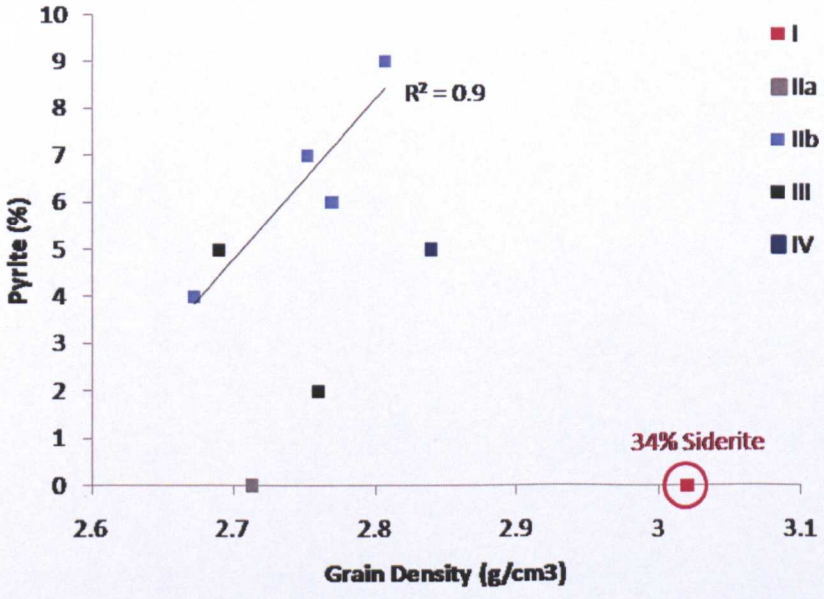

Figure 4.44 Grain densities for Well A with pyrite content from bulk fraction XRD measurement. Colours indicate an arbitrary classification (horizons I-IV) based on general behavior in the rock property analyses.

However, the density is not entirely controlled by the pyrite content in Well A. III denotes a horizon of lower density samples at depths between 2530 and 2594m and

contains the samples identified in 4.2.3 as containing possible gas prone source material which could explain the lower densities observed. IV is the deepest sample, beneath III and has a density that returns to the main trend of IIb (Figure 4.43).

On Figure 4.44 it can be seen that the pyrite content, though elevating the general value due to its presence, is not the only control. Siderite content is affecting horizon I and minor organic content has a distinctive effect on the horizon III samples. Horizon IV, despite being a pyrite bearing sample on the main increasing trend of the plot in Figure 4.43, has a higher density than the samples of horizon IIb, yet has approximately half the pyrite content of the densest IIb sample. The general relationship seen in Figure 4.43 for horizons II and IV does indicate some homogeneity of the material at least at a bulk lithology scale. There is a clear increase in density with depth which is not entirely related to iron mineral content.

Well B shows no such general trends, the densities represent a complicated interplay of siderite, pyrite, organic matter and quartz content. For example, the samples showing a higher TOC content such as those from 1970 and 2110m have relatively low grain densities (2.71 and 2.77g/cm^3), but other samples such as that from 2500m also have lower densities, most probably due to the higher quartz content and lack of iron minerals. The other higher TOC sample from 1680m also contains the highest measured siderite content and has a high grain density of 2.9g/cm^3 that reflects this. These grain densities were used in determining the correct rate for sedigraph analysis and for use in the MICP porosity calculation.

4.3.2 Grain size distribution

12 samples from Well A and 13 samples from Well B were prepared, analysed and the distribution of grain sizes present in each depth interval recorded and pipette method corrected as described in Chapter 2.

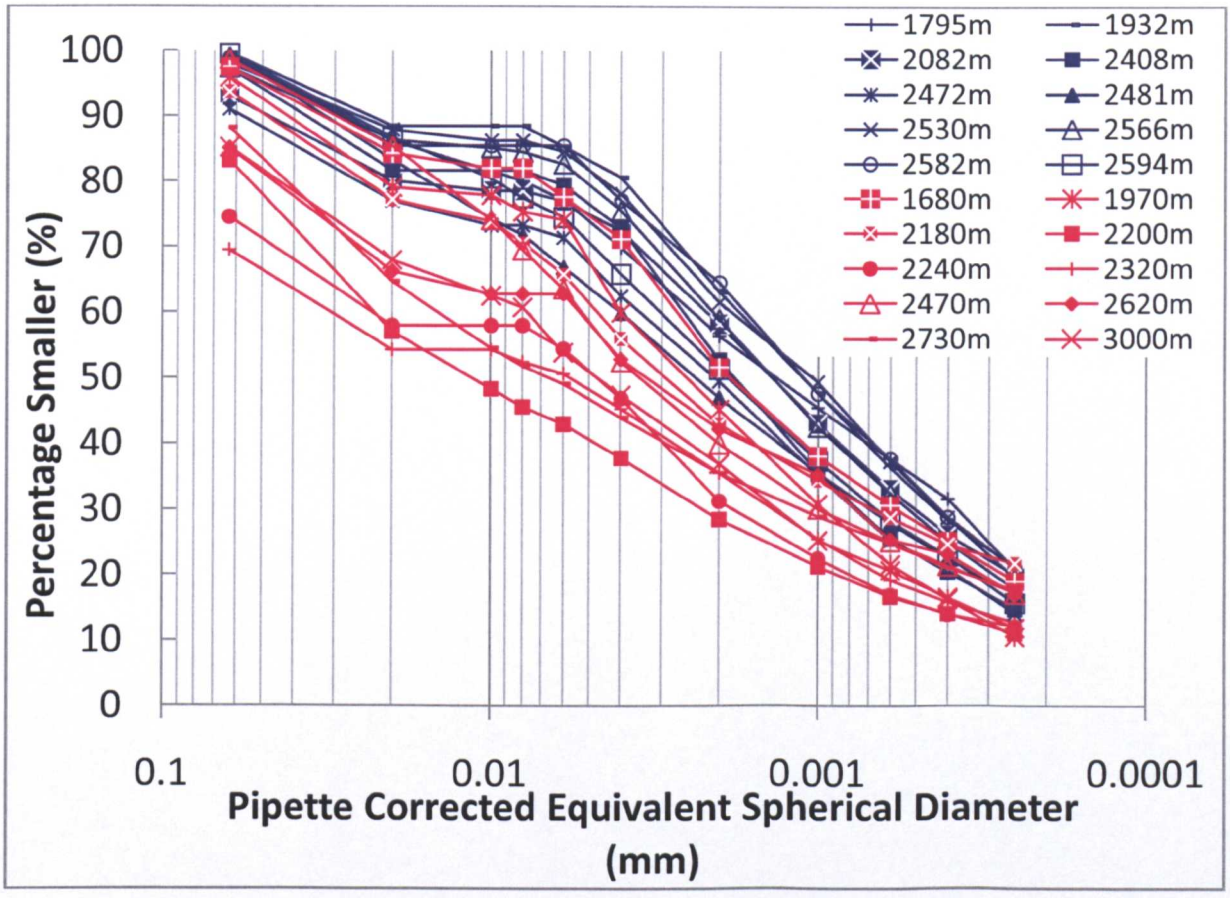

Figure 4.45 Grain size distributions of samples from Well A (Blue) and B (Red) from sedigraph analysis.

Despite some overlap, distinction can be made in Figure 4.45 between samples from Well A and those from Well B. Well A material is more uniformly clay-rich, supporting the XRD quantification, whereas Well B is more variable with some samples showing coarse distributions despite the selective sampling procedures. Exact correlation between total clay from XRD and the <2 μm fraction from sedigraph measurement is not found, most probably due to the significant kaolinite content and some of the

XRD identified illite/mica actually being coarser grained mica as is visable in the BSEM images.

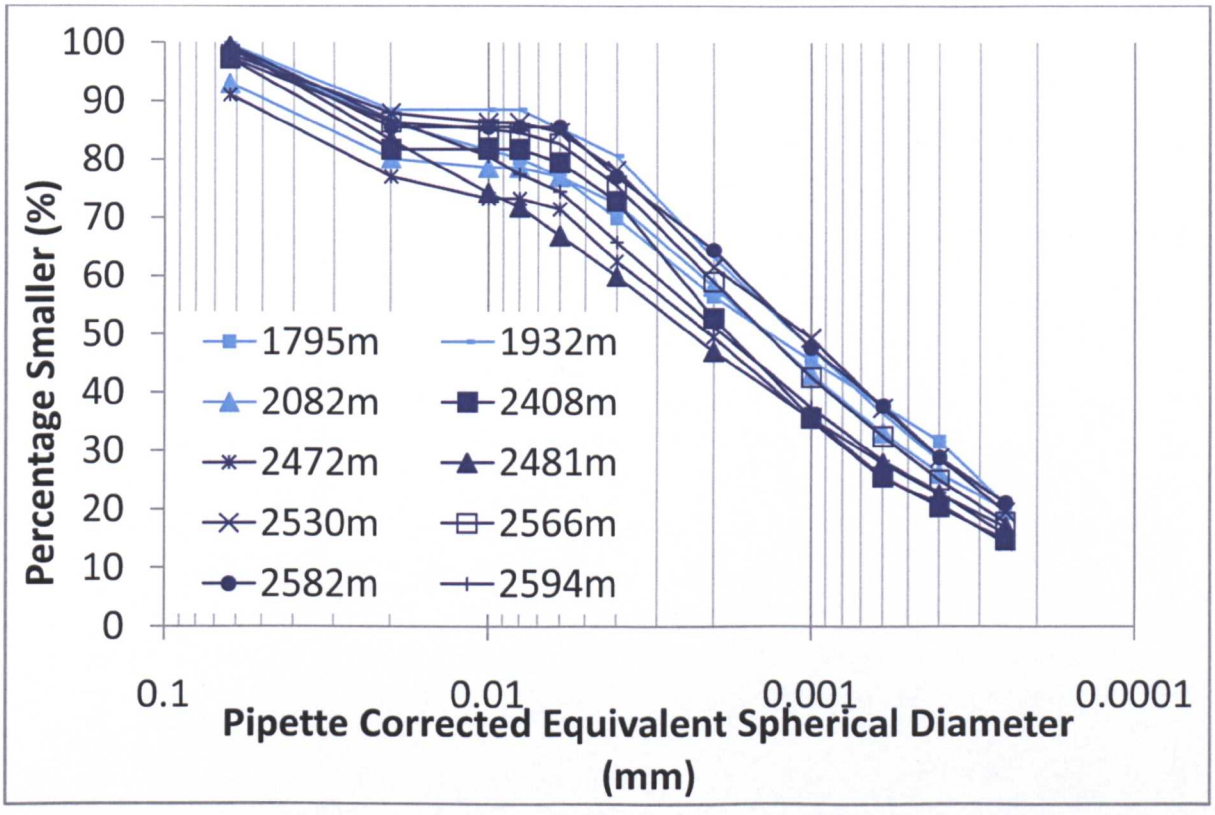

Figure 4.46 Grain size distributions of samples from Well A colour coded according to group (Light Blue: Group K; Dark Blue: Group L)

Separating the distributions for the 2 wells in Figures 4.46 and 4.47 show clay rich distributions that are relatively similar independent of depth or group in Well A with D_{50} is between 2.5-1 μm for all samples apart from the shallowest at 5740ft which is finer grained with a D_{50} of 0.6 μm. The least clay rich sample is 8140ft (2481m) and although an XRD measurement was not carried out at this depth, the nearest sample tested at 2530m shows the highest quartz content and lowest total clay in Well A and so a coarser, more quartz rich horizon is inferred at this depth.

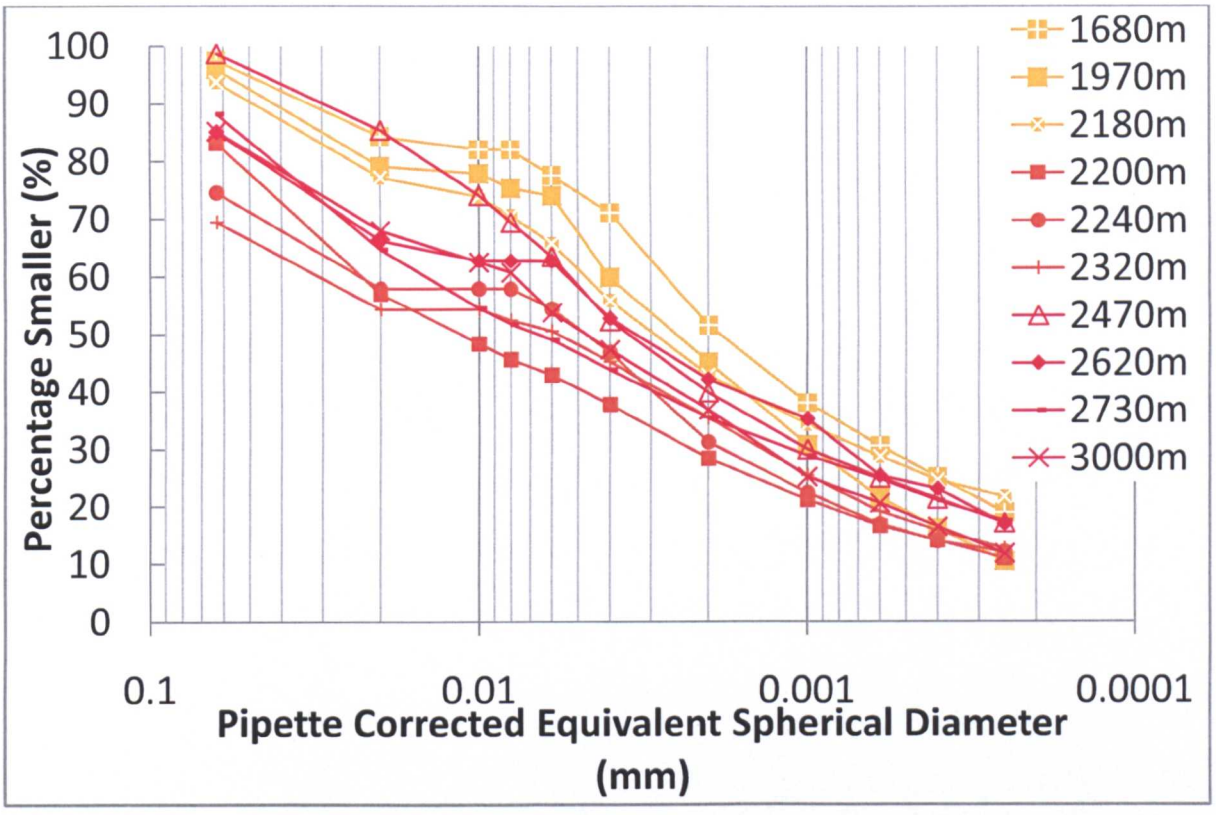

Figure 4.47 Grain size distributions of samples from Well B colour coded according to depth (Yellow: Groups I-J; Orange: Sandier Group J; Red: Group L)

Some samples from Well B are more clay rich, plotting in with the Well A distributions and the distinction can be made with depth or group. The 4 shallowest samples, from Groups I-J form the main area of overlap with Well A in the more clay-rich region of the plot.

The coarsest section is the lower Group J (2200-2320m), previously highlighted as the sandier samples in the initial visual identification of the samples. This broadly ties in with XRD, which for example shows 2320m to contain 52% quartz. However, the upper section of Group L is more quartz rich, so combining this with the sedigraph data it is inferred that despite the quartz content it is finer grained.

4.3.3 Mercury Injection Porosimetry (MICP)

All samples were prepared for MICP analysis of porosity using the procedures described in Chapter 2 although a problem occurred in measuring the sample from 2730m (Well B).

Data from Well A is compiled in Table 4.11. This includes the total porosity, the porosity corrected for fractures using the cut-off radius, the mean pore (throat) radius and the pore (throat) radius at the 10% saturation threshold (see Chapter 2). This data is required for the permeability calculations.

Sample	Total Porosity (%)	Corrected Porosity (%)	Cut Off Radius (nm)	R_{mean} (nm)	$R_{10\%}$ (nm)
1619	19.2	18.2	546.7*	28.6	42.1
1728	14.3	12.7	32.2	6.3	12.6
1750	15.3	12.5	28.1	5.7	10.2
1795	14.9	12.4	52.1	6.1	12.5
1887	12.2	10.3	32.2	5.5	8.7
1932	11.4	9.6	28.1	5.6	8.6
2082	12.2	11.2	32.2	4.9	8.8
2140	13.4	12.1	28.1	3.8	8.2
2280	14.3	12.7	28.1	3.9	8.3
2316	22.0	11.6	28.1	3.9	7.7
2408	13.1	12.5	24.3	3.4	7.1
2472	13.7	12.5	52.1	4.1	7.6
2481	16.3	14.9	52.1	4.1	9.0
2530	10.0	9.1	37.7	3.9	7.9
2566	10.2	9.5	43.8	4.6	7.5
2582	8.4	7.3	52.1	5.5	10.5
2594	11.1	9.7	84.1	4.8	9.1
2621	14.8	13.8	52.1	3.8	8.4

Table 4.11 MICP data Well A measurements. Also used as input data for permeability calculations. Third column indicates MICP measured porosity corrected to exclude larger cracks/fractures delimited by the cut-off radius.

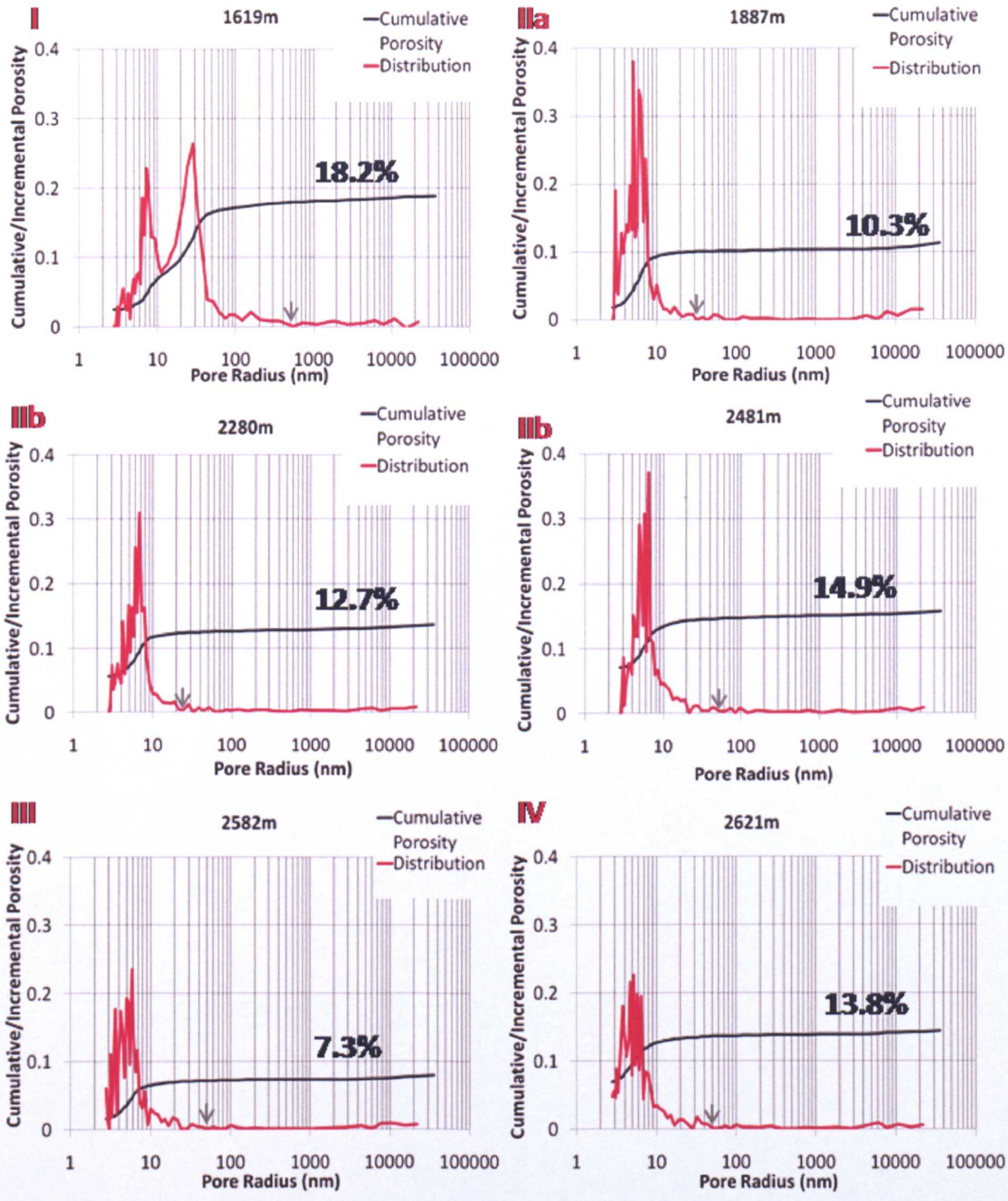

Figure 4.48 Cumulative and Incremental porosity plots for selected depths in Well A. Porosity (%) shown in blue adjacent to cumulative porosity line and grey arrows mark chosen cut-off values of pore size. Red numerals indicate which trend samples belong to in previous measurements.

The tabulated data shows that porosity is generally tight, given the relatively shallow depths they represent. Also, bar some exceptions, the corrected porosities are similar between the upper section of the interval to those from the base. Sample

1619m or trend I may show anomalously large porosity due to the different distribution of siderite within the matrix (Figure 4.48). Trend IIa, IIb and IV could be interpreted at maintaining a similar porosity with depth or that IIb and IV form a reverse trend, where porosity increases with depth. The apparent increase does correlate roughly to a slight increase in quartz content over this interval, so may be lithology related. The mean pore radius decreases from 5.7-6.3nm in the horizon IIa (with the separate expandable clay peak) to <6nm below. This can be seen visually in Figure 4.48 above in the distributions and variation from the trend can be seen in Figure 4.49 below. However the most significant porosity reduction is seen over the higher TOC and adjacent samples (2530-2594m), where porosity reduces to its minimum 7% at 2582m.

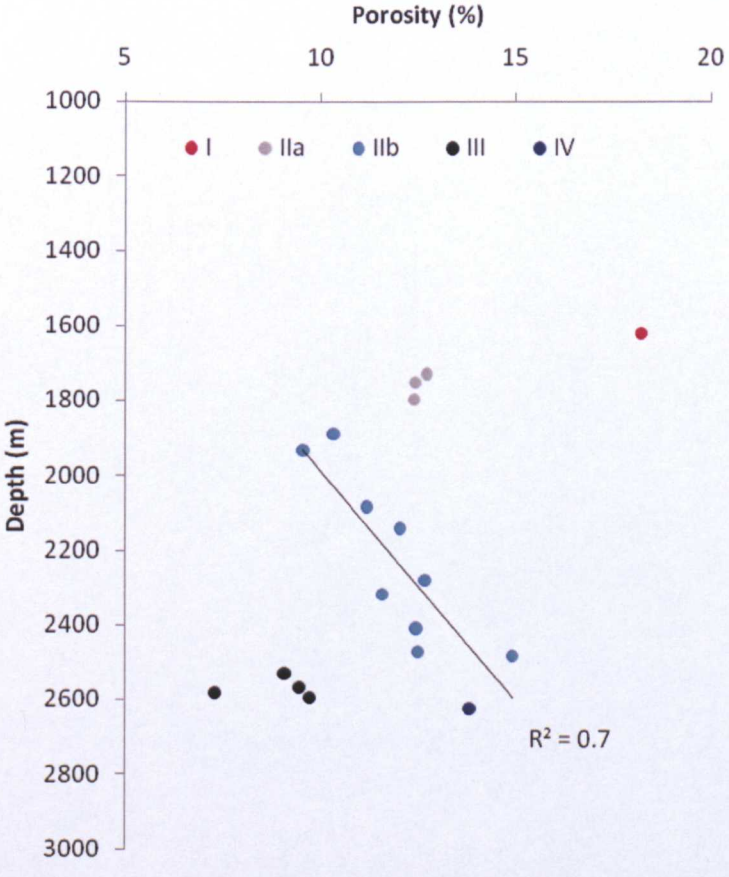

Figure 4.49 Porosity with depth in Well A catagorised into trends I-IV.

Sample	Total Porosity (%)	Corrected Porosity (%)	Cut-Off Radius (nm)	R_{mean} (nm)	$R_{10\%}$ (nm)
1350	20.4	18.5	364.5	21.2	34.6
1600	16.6	15.8	52.1	6.9	13.4
1680	19.9	18.7	84.1	5.7	12.7
1900	16.1	14.5	18.9	3.9	9.3
1970	16.2	14.9	546.7	20.2	27.1
2010	21.5	19.6	546.7*	11.9	12.8
2110	15.3	14.7	36444.8	1157.4	1586.4
2180	17.0	15.6	6074.1*	184.2	218.5
2200	20.9	19.5	36444.8	1442.9	2560.7
2240	12.7	9.1	728.9*	29.8	90.6
2260	11.2	7.9	60.78*	6.5	13.6
2320	14.0	12.8	18.9	4.2	9.5
2470	13.9	12.7	156.2	7.0	15.5
2500	13.1	12.1	10933.4	340.4	568.0
2520	42.5	33.3	36444.8	10717.0	$1.27x10^{15}$
2620	10.0	9.1	546.7*	21.7	45.0
2840	12.9	11.9	1822.3*	139.7	451.3
2960	9.3	8.4	546.7*	27.8	80.3
3000	11.0	9.1	546.7*	33.0	104.6

Table 4.12 MICP data Well B measurements. Also used as input data for permeability calculations . * denotes where the cut-off radius is not certain. Third column indicates MICP measured porosity corrected to exclude larger cracks/fractures delimited by the cut-off radius.

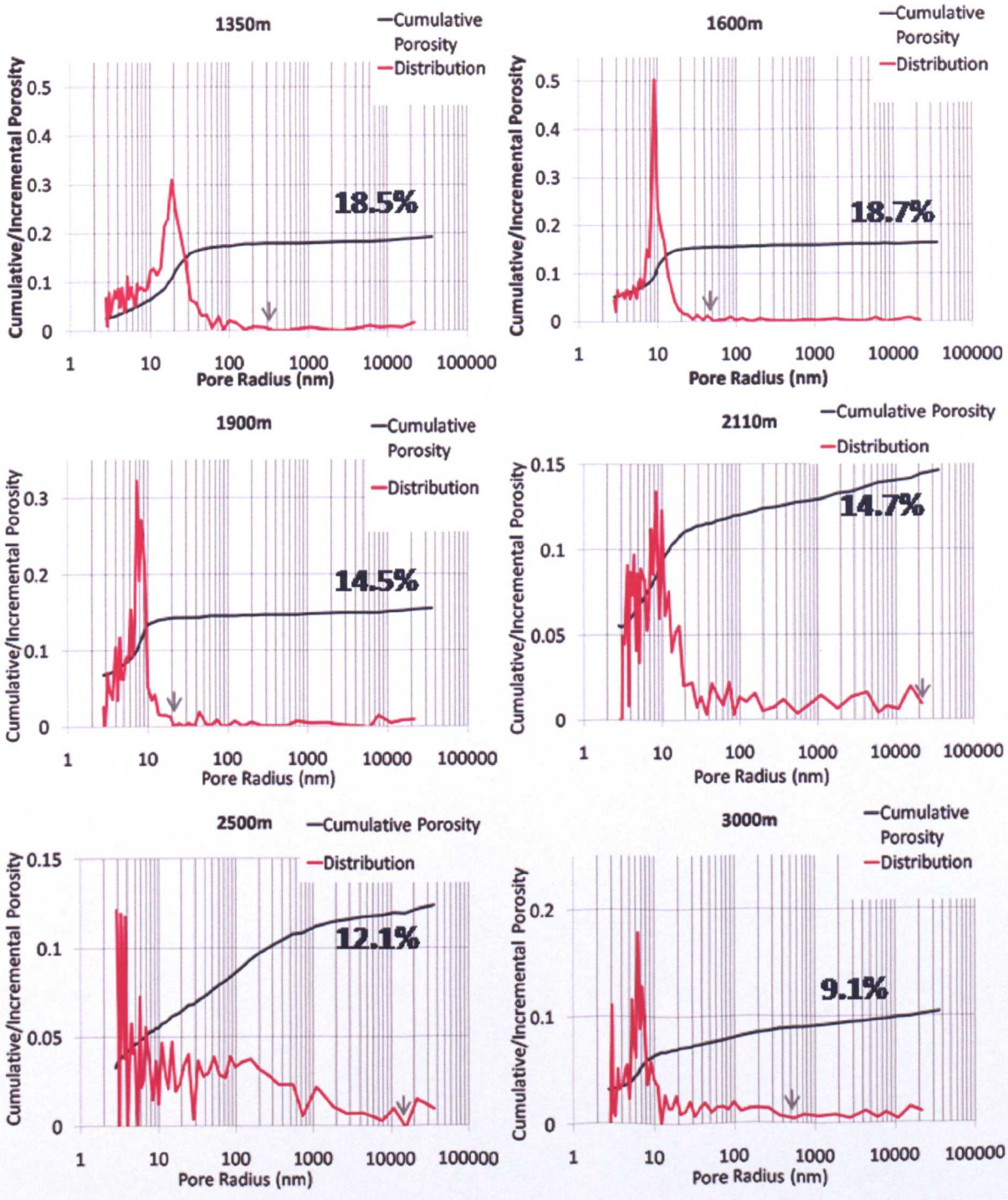

Figure 4.50 Cumulative and Incremental porosity plots for selected depths in Well B. Porosity (%) shown in blue adjacent to cumulative porosity line and grey arrows mark chosen cut-off values of pore size

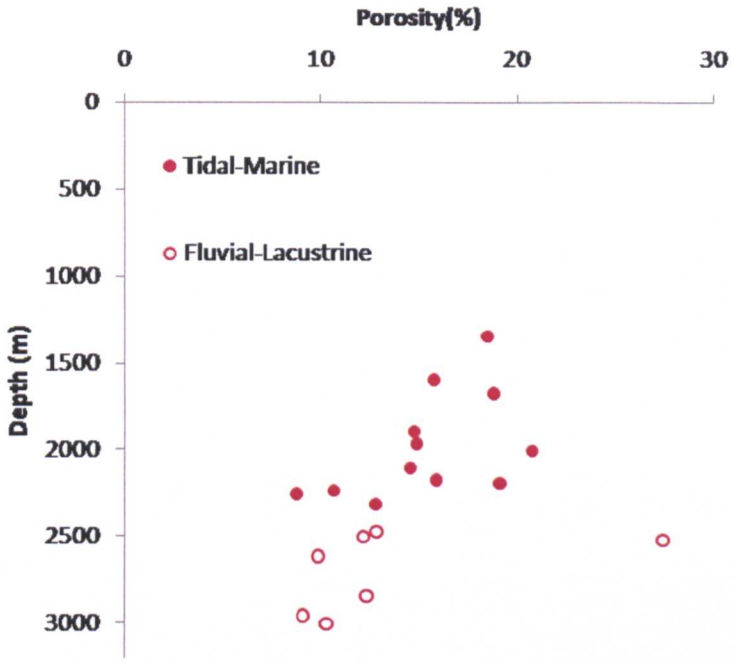

Figure 4.51 Porosity with depth in Well B catagorised according to depositional environment.

The samples of Well B could be said to show a general decrease with depth. However, lithological variation in this well is greater and the samples show more of a grouped distribution with most of the shallow samples deposited in the later tidal-marine environment showing larger porosities and the deeper samples mainly of the fluvial-lacustrine groups showing the lowest porosities. This larger porosity in the shallower samples is despite the siderite content of these samples which could have been thought to be cementing and may indicate that the larger porosity seen in 1619m sample of Well A may indeed more be representative of the siderite bearing horizons. It should be noted that such porosities are still relatively tight considering the depths sampled (see 4.4 for comparison with other basins), but are generally greater than Well A samples at equivalent depths.

The anomalously high porosity sample at 2500m also diverges in the XRD models as the only sample constituting quartz and illite/mica alone. Combining the MICP and XRD data it could be inferred that this is a porous, micaceous sandstone horizon.

It may be inferred that varied lithology has a stronger control on porosity change in Well B than Well A. Whether this is depostional or diagenetic is difficult to conclude.

4.3.4 High Resolution X-Ray Textural Goniometry (HRXTG)

Following XRD analysis of mineralogical composition sections of selected samples were prepared for HRXTG measurements (Chapter 2) to attempt to quantify alignment of clay minerals as in Chapter 3.

Sample Depth (m)	I Kα ave. d-spacing (Å)	I Max. Pole Density (MRD)	I/S Kα ave. d-spacing (Å)	I/S Max. Pole Density (MRD)	Ch Kα ave. d-spacing (Å)	Ch Max. Pole Density (MRD)
1728	10.0	3.51	11.4	3.29	13.9	3.17
1750	10.0	5.35	10.5/12.1	5.28/5.06	-	-
1795	10.1	5.63	11.7	5.05	14.0	4.63
2280	10.1	5.54	12.4	5.08	14.0	4.94
2408	10.2	6.60	11.4	5.34	14.0	5.17
2472	10.2	4.47	11.3	4.31	14.2	3.87
2530	10.1	5.55	11.2	5.37	14.0	4.90
2566	10.2	5.72	11.7	5.27	14.0	4.74
2582	-	-	10.4	4.67	13.9	3.63
2594	10.0	7.24	10.4	7.53	14.0	6.32
2621	10.2	6.57	12.1	6.61	-	-

Table 4.13 HRXTG data for Well A

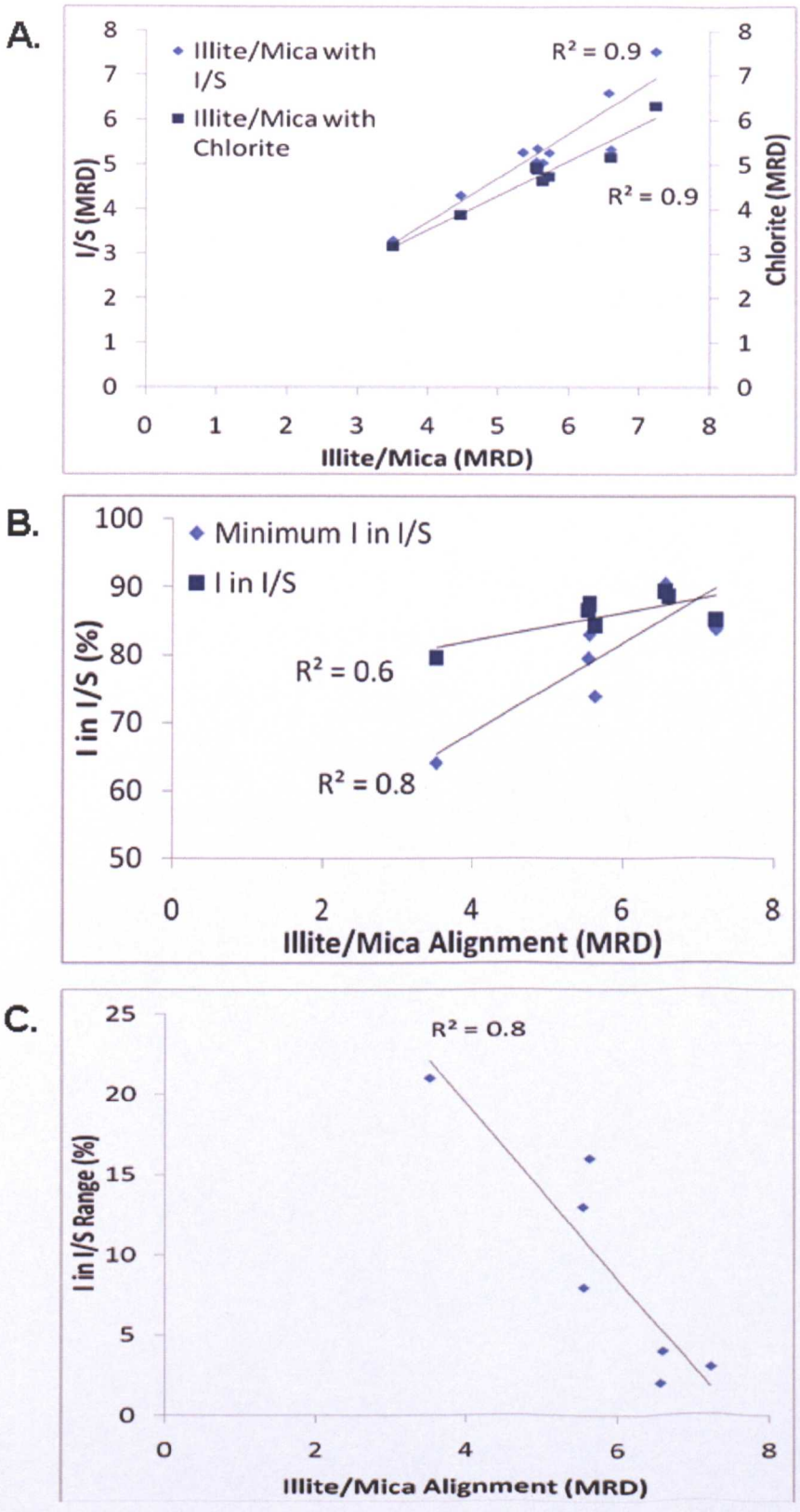

Figure 4.52 Various alignment correlations for Well A data. A. shows correlation between I/S with illite/mica alignment and between chlorite with illite/mica alignment; B. shows correlation between I% in I/S with illite/mica alignment; C. displays the correlation between I% in I/S range calculated from 0.75 peak height with illite/mica alignment.

Compared to the North Sea mudstone of Chapter 3, Malay basin samples showed higher alignment values measured in multiples of a random distribution. Broadly, the shallowest sample measured 1728m shows the lowest alignments at all 3 positions measured (for illite/mica, I/S and chlorite) and the 2 deepest samples at 2580 and 2621 show the highest (Figure 5.59).

However as can be seen in the table above, this analysis may be over simplistic. The sample from 1728m can be classified as weak-moderate alignment (Day-Stirrat, 2006), the sample from 2472m is moderate to strongly aligned and all others are classified as strong to very strong. This generall strong alignment does not exclude a link to porosity reduction as porosity is also largely tight with other influences and the two samples with the lower classifications are also the two samples amongst the largest porosities.

Illitization is also well advanced in most samples, but the clearest signal from the clay fraction XRD of any ongoing change over the interval was the range in I/S calculated from 0.75 intensity peak height. This shows a correlation with the measured alignments (Figure C in 4.52). Also, the weak to moderate alignment belongs to the sample which showed the strongest individual glycolated smectite peak.

In addition, there is good correlation between the alignments measured for different clay minerals (separate peaks) on the same samples (Figure A in 4.52).

Sample Depth (m)	I Kα ave. d-spacing (Å)	I Max. Pole Density (MRD)	I/S Kα ave. d-spacing (Å)	I/S Max. Pole Density (MRD)	Ch Kα ave. d-spacing (Å)	Ch Max. Pole Density (MRD)
1350	10.2	3.87	-	-	14.0	3.53
1680	10.0	4.97	-	-	14.0	4.15
2110	10.2	4.98	-	-	13.7	3.95
2320	10.2	8.29	-	-	-	-
2470	10.0	7.21	11.2	6.79	13.9	6.12
2730	10.2	4.39	12.4	3.44	14.0	3.40
2840	10.2	3.28	-	-	14.0	3.06
2960	10.2	4.98	-	-	-	-
3000	10.0	7.37/7.22	11.2	6.71	14.0/14.2	5.99/6.14

Table 4.14 HRXTG data for Well B

As with Well A, the shallowest sample measured showed a relatively low value of alignment 3.87 m.r.d. and the deepest, 7.37 m.r.d. but again this is simplistic. The trends displayed in Well B show an increase in alignment with depth in the shallower tidal-marine section 1350-2470 with an r^2 of 0.7 between 3.87 and 7.21 for illite/mica. Over the quartz-rich section of the fluvial-lacustrine facies, alignment decreases again to values of 4.39 and 3.48, returning to 7.37 in the more clay rich sample in 3000m. Well B samples were generally more quartz-rich with an overall average total clay for Well B of 48% (72% in Well A). This is discussed further in 4.4.

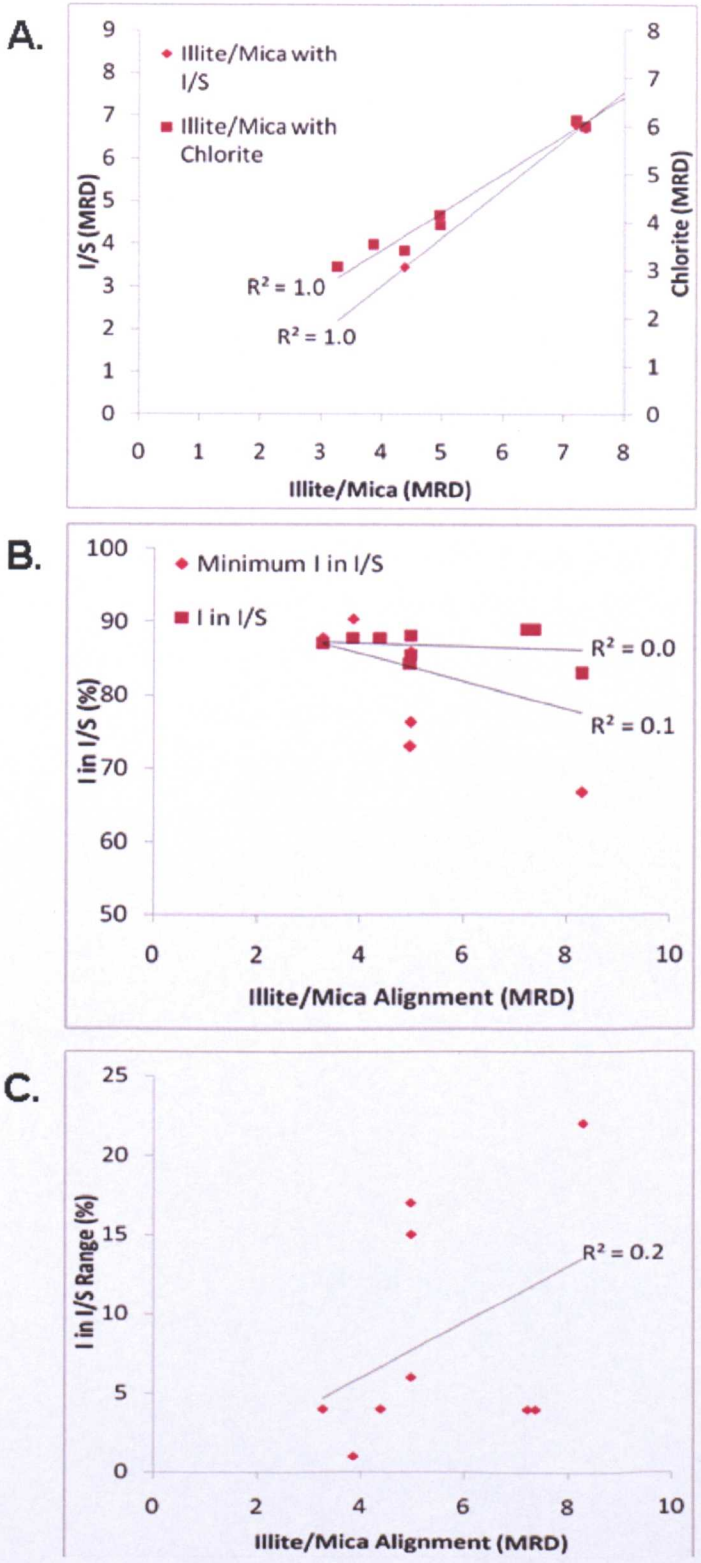

Figure 4.53 Various alignment correlations for Well B data. A. shows correlation between I/S with illite/mica alignment and between chlorite with illite/mica alignment; B. shows correlation between I% in I/S with illite/mica alignment; C. displays the correlation between I% in I/S range calculated from 0.75 peak height with illite/mica alignment.

Plots that displayed significant correlations in Well A data show different behaviour for Well B points. Figure A in 4.53 shows the relationship between alignment values for separate clay peaks where I>I/S>Chlorite and the correlations are even stronger (though the I/S with illite/mica relationship lacks data). However, there is no correlation between I% in I/S with alignment, shown by either the modal, minimum or range values (Figures B & C in 4.53).

BSEM images of the matrix allow visual identification of the alignment measured with HRXTG and comparison with initial interpretations show reasonable agreement (Figure 4.54). However, not all results were comparable. The sample from 2960m did appear to display a stronger alignmenment of the matrix than shallower samples and yet it was not classified amongst the strongest alignments. Visual interpretation may therefore be misleading or heterogeneity of sample at this depth created the discrepancy.

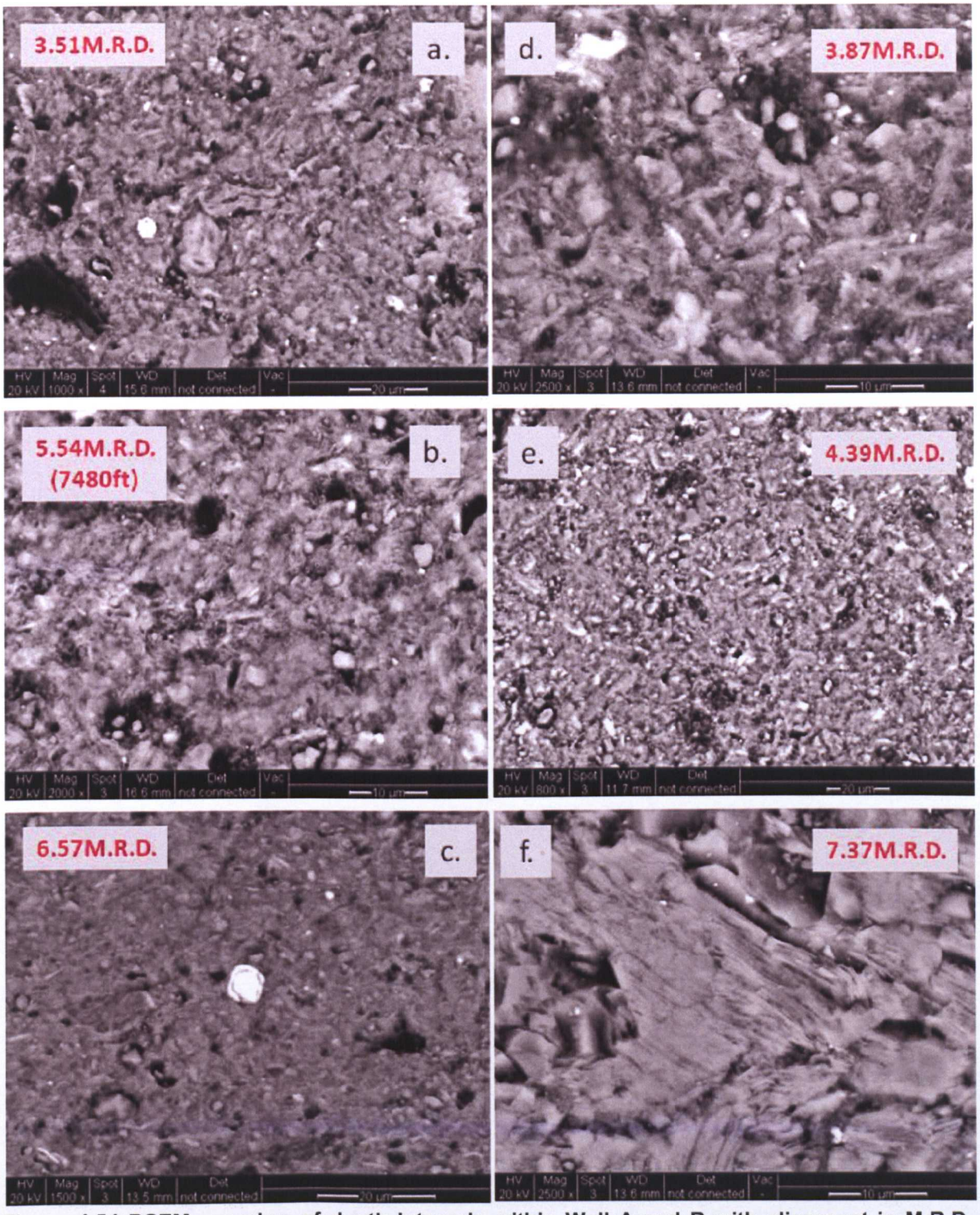

Figure 4.54 BSEM overview of depth intervals within Well A and B with alignment in M.R.D. Images taken at relatively low zoom (800-2500x) to give view of clay behavior in the matrix in the shallowest, intermediate and deepest samples: a. Well A, 5670ft (1728m) at 1000x; b. Well A, 7020ft (2140m) at 2000x (with MRD for 7480ft); c. Well A, 8600ft (2621m) at 1500x; d. Well B 1350m at 2500x; e. Well B 2730m at 800x; f. Well B 3000m at 2500x

4.3.5 Permeability Calculations

Using data compiled in the grain density, grain size distribution and porosity measurements, calculations of modelled permeability were completed using the method of Yang & Aplin (1998).

Depth (m)	Modelled K_x (m^2)	Modelled K_z (m^2)
1728	$5.1x10^{-21}$	$1.2 x10^{-21}$
1750	$4.5 x10^{-21}$	$2.9 x10^{-22}$
1795	$4.8 x10^{-21}$	$1.1 x10^{-21}$
1932	$3.4 x10^{-21}$	$5.6 x10^{-22}$
2082	$3.4 x10^{-21}$	$7.1 x10^{-22}$
2280	$3.2 x10^{-21}$	$4.2 x10^{-22}$
2408	$2.5 x10^{-21}$	$6.4 x10^{-22}$
2472	$3.0 x10^{-21}$	$8.8 x10^{-22}$
2481	$3.6 x10^{-21}$	$1.2 x10^{-21}$
2566	$2.7 x10^{-21}$	$5.2 x10^{-22}$
2582	$2.5 x10^{-21}$	$3.8 x10^{-22}$
2594	$2.7 x10^{-21}$	$7.3 x10^{-22}$

Table 4.15 Modelled permeabilities for Well A samples.

Depth (m)	Modelled K_x (m^2)	Modelled K_z (m^2)
1680	$6.8x10^{-21}$	$2.0 x10^{-21}$
1970	$2.0 x10^{-20}$	$6.7 x10^{-21}$
2110	$1.6 x10^{-18}$	$3.5 x10^{-19}$
2180	$2.2 x10^{-19}$	$8.0 x10^{-20}$
2200	$2.2 x10^{-18}$	$1.3 x10^{-18}$
2240	$6.8 x10^{-21}$	-
2320	$2.9 x10^{-21}$	$1.3 x10^{-21}$

2470	5.0×10^{-21}	2.0×10^{-21}
2620	1.2×10^{-20}	4.3×10^{-21}
2840	1.3×10^{-19}	2.7×10^{-20}
2960	1.6×10^{-20}	3.0×10^{-21}
3000	1.8×10^{-20}	7.4×10^{-21}

Table 4.16 Modelled permeabilities for Well B samples

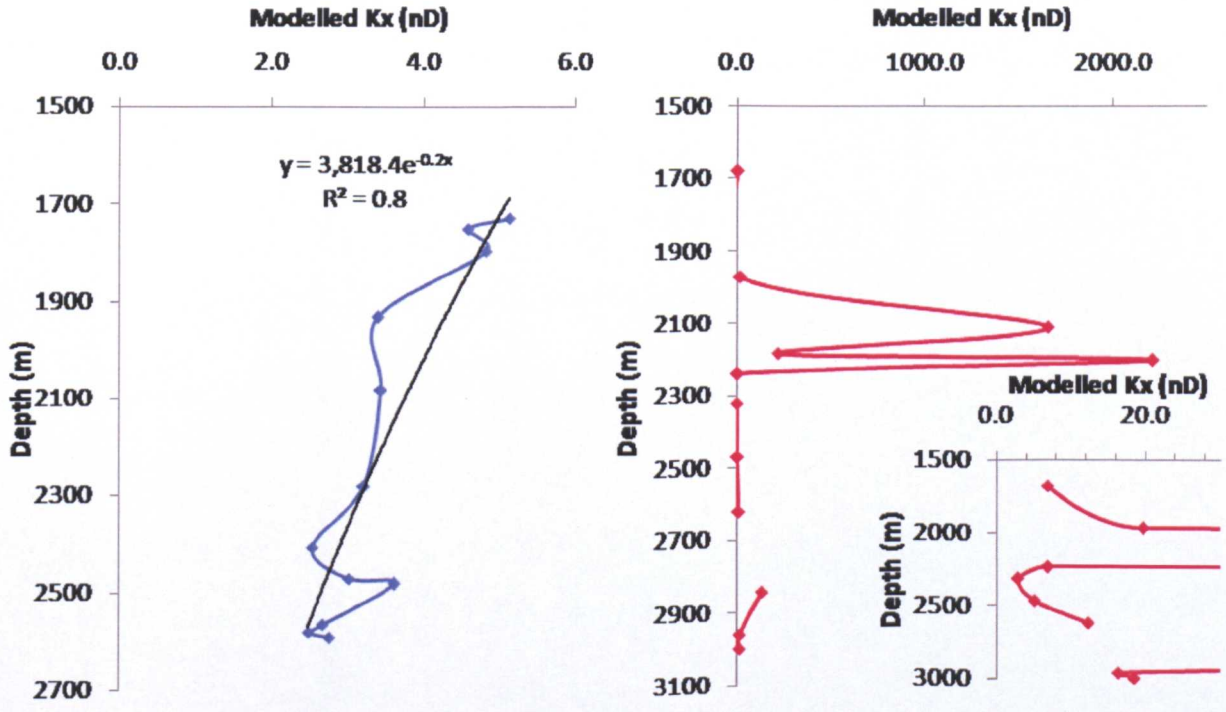

Figure 4.55 Modelled Kx results for Well A (blue) and Well B (red) in nanoDarcies. Thumbnail plot (lower, right of figure) of Well B lower permeablility samples (red).

Porosity in Well A mudstones over the sampled interval is generally tight and the calculated porosity is generally low. However, despite variability in the porosity data, modelled K_x results displayed in Figure 4.55 show an overall decreasing permeability with depth trend. The lowest permeability samples belong to the horizon around 2582m, which were the samples with >1% TOC. This in keeping with their lower porosity.

Well B shows selected horizons of higher permeability in the μD range as opposed to nD around 2100-2300m (Figure 4.55). Even in the lower permeability strata (nD range) values are generally greater than those in Well A , with 89% of all samples above the range observed in Well A.

4.3.6 Summary of Physical Properties

- Grain densities are generally high for mudstone-shale lithologies and this will be influenced by the iron mineral components determined in XRD analyses. Well A shows an increasing trend with depth, where as Well B is not as clear. Other controls can be inferred such as the decreased densities over the interval of minor TOC increase in Well A.
- Grain size distribution shows that whilst Well A is uniformly clay-rich, Well B is more variable. Well B distributions differ according to the stratigraphic groupings.
- Porosities in both Well A and B are tight given their burial depth. The porosities in Well A are related to the high siderite content in the upper section and the lowest porosities are related to the minor elevated TOC interval. Values in Well B tend to cluster according to their stratigraphic group/depositional environment.
- Alignmnent measurements are higher than those recorded for the North Sea mudstones and in Well A, alignment is generally strong to very strong, with moderate values only in the shallowest sample. A link to porosity reduction and/or illitization is not ruled out. Alignment in Well B is more varied and appears lithologically controlled with more quartz rich intervals (despite selective sampling) showing decreased values. There is good correlation

between the alignments measured for different clay minerals from the same sample in both wells.

- Modelled K_x in Well A is low and within the nD range, whilst displaying a overall decreasing permeability with depth trend. The lowest permeability samples belong to the horizon around 2582m, which were the samples with >1% TOC. This in keeping with their lower porosity. Well B shows selected horizons of higher permeability in the μD range and even in the lower permeability strata (nD range) values are generally greater than those in Well A.

4.4 Discussion

4.4.1 Mudstone porosity and compaction in the Malay Basin

Porosity values measured upon samples from this study vary about the porosity log trends used in Hoesni (2004) confirming the relatively tight nature of Malay Basin mudrocks with depth noted in that study (Figure 4.56).

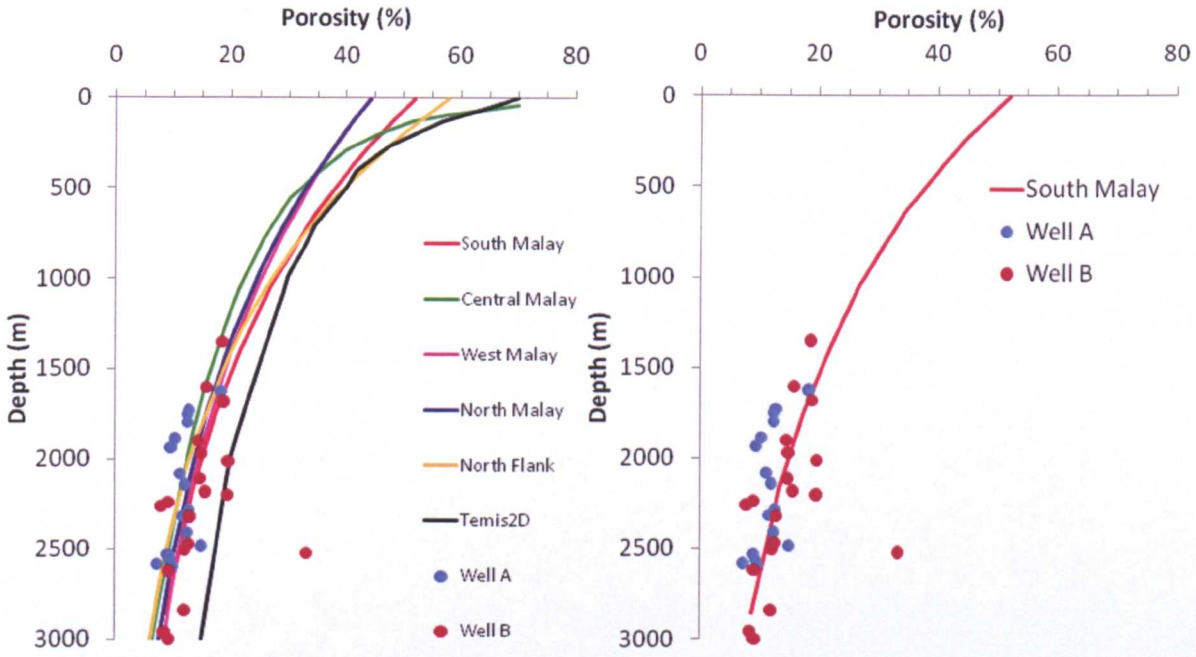

Figure 4.56 Regional porosity-depth trends used in Hoesni (2004) with MICP porosity measurements from this study. The second image separates the most relevant trend from the South Malay to show fit with the measured data.

Most of the samples that fall to the right of the trend, at higher porosities, belong to Well B. As described in the grain size distribution and XRD results, many of the samples in the deeper section of Well B are coarser and quartz-rich. Well A samples were true clay-rich, fine grained mudstones and their porosities are plotted with "mechanical" compaction trends generated from experimental results (Figure 4.57).

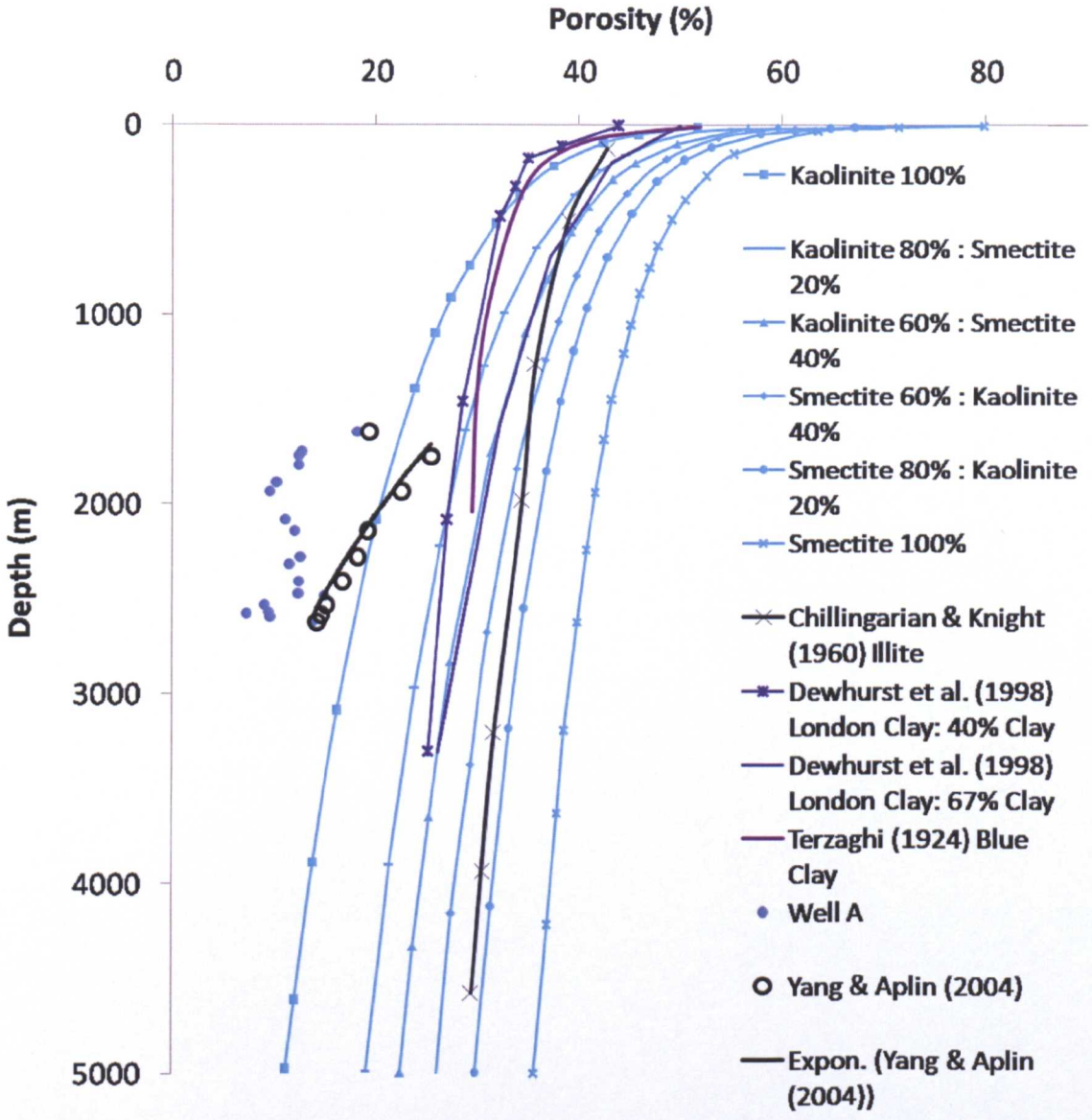

Figure 4.57 Porosity – depth plot to show variation in Well A porosities in comparison with those of samples compacted mechanically in the laboratory from the studies of Mondol *et al.* (2007), Dewhurst *et al.* (1998), Chillingarian & Knight (1960) and Terzaghi (1924). Black circles indicate calculated porosities using relationships defined in Yang & Aplin, (2004).

Samples from Well A show a marked reduction in porosities measured on mechanically compacted samples. The average difference between the MICP data from Well A and their depth equivalent values in the illite trend of Chillingarian & Knight (1960) measured from a fitted exponential ($Y=14762497e^{-0.027}$, $R^2=0.98$) is a substantial 21±2%. The 100% kaolinite trend shows the closest relationship, but

even that is on average is 8±2% greater than the real porosity values and most importantly, is not representative of the XRD measured mineralogy. Illite is the dominant clay phase in Well A. It is therefore concluded that the mechanisms behind the compaction seen in Well A are not simulated in mechanical consolidation experiments at room temperature. Excluding one sand sample, the Well B porosities also lie below the kaolinite trend.

Despite being based on effective stress relationships, the porosities calculated using the equations detailed in Yang & Aplin (2004) approach the natural dataset Figure 4.57). This is likely to be as they utilise coefficients based on natural datasets, other non-mechanical mechanisms may be included by proxy. However even these predicted values based on the rock property data were too high in Well A. Using the total clay content from XRD measurements to calculate the coefficients, the measured porosities are 7±5% less than predicted. Using the <2 μm fraction from the sedigraph results, the average difference is 7±4%. This shows good agreement between rock property measurements of the clay fraction. The porosities were calculated using the equations in 1.3 and assuming effective stresses based on a hydrostatic fluid pressure. The difference between MICP measured porosities and the modelled data is greatest in the upper samples (maximum difference of 14%), showing closer correlation in the lower section (one sample has equal porosity to the model). This is likely to be an artefact of the use of normal pressures. Due to discrepancy between the modelled pressures in Hoesni (2004) and the measured high overpressure at depth, an arbitrary hydrostatic pressure gradient was used to calculate the vertical effective stress, simply to give an idea of correlation. The

gradual increase in fit with the modelled porosities is likely to represent the decreasing accuracy of using a hydrostatic model.

If the highly overpressured conditions were respresented, effective stress would decrease and the modelled porosities would be higher, maintaining a relationship with the measured values in a manner similar to those up section, which are themselves mildly overpressured. An attempt was made to use the mudweight data and formation pressures from nearby horizons to calculate a more realistic effective stress and the linear relationship is displayed in Figure 4.58. This was used to recalculate the porosities (based on the sedigraph measured clay fractions) and the results are also plotted on Figure 4.58.

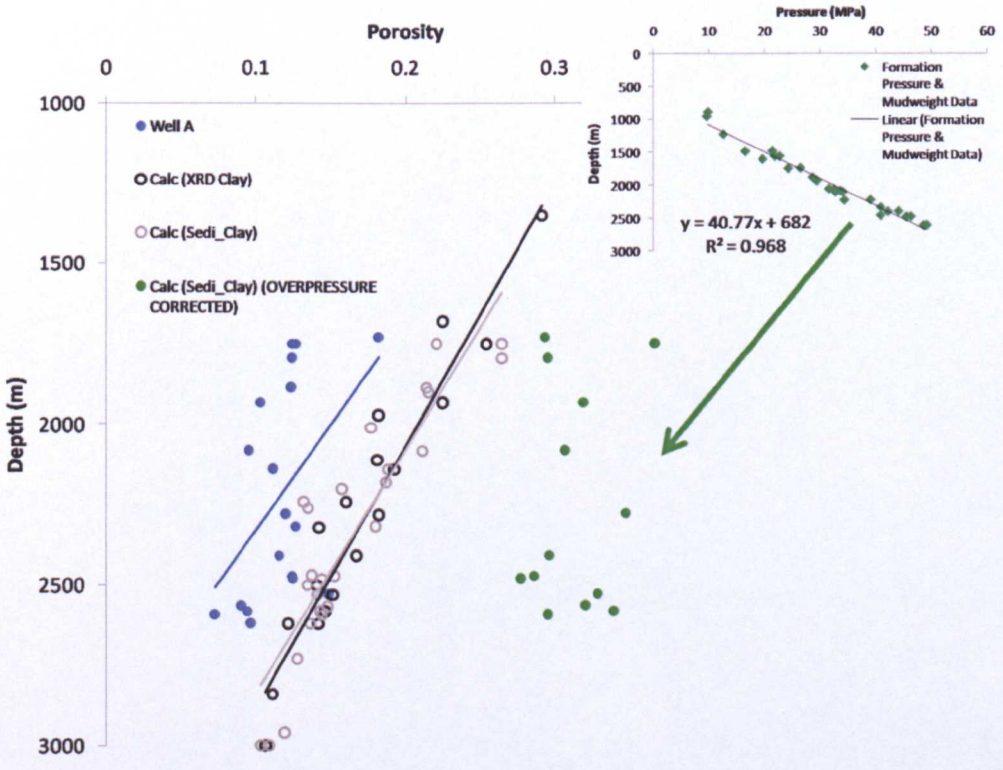

Figure 4.58 Main plot displays the close results of calculated porosity using XRD and sedigraph measurement derived clay totals with the MICP measurements on Well A cuttings. Also shown in green are the calculated porosities corrected for approximated overpressure. The new effective stress was calculated using the linear relationship through nearby formation pressure and mudweight data (thumbnail image) to estimate pore pressure which was then subtracted from the calculated lithostatic stress.

Once this correction was made, calculated values showed values more similar to the experimental datasets and less fit with the actual sample measurements. However, the validity of this correction depends upon the timing of overpressure development. The coarser samples of Well B show a closer fit with modelled data. Well B is essentially normally pressured over much of the well.

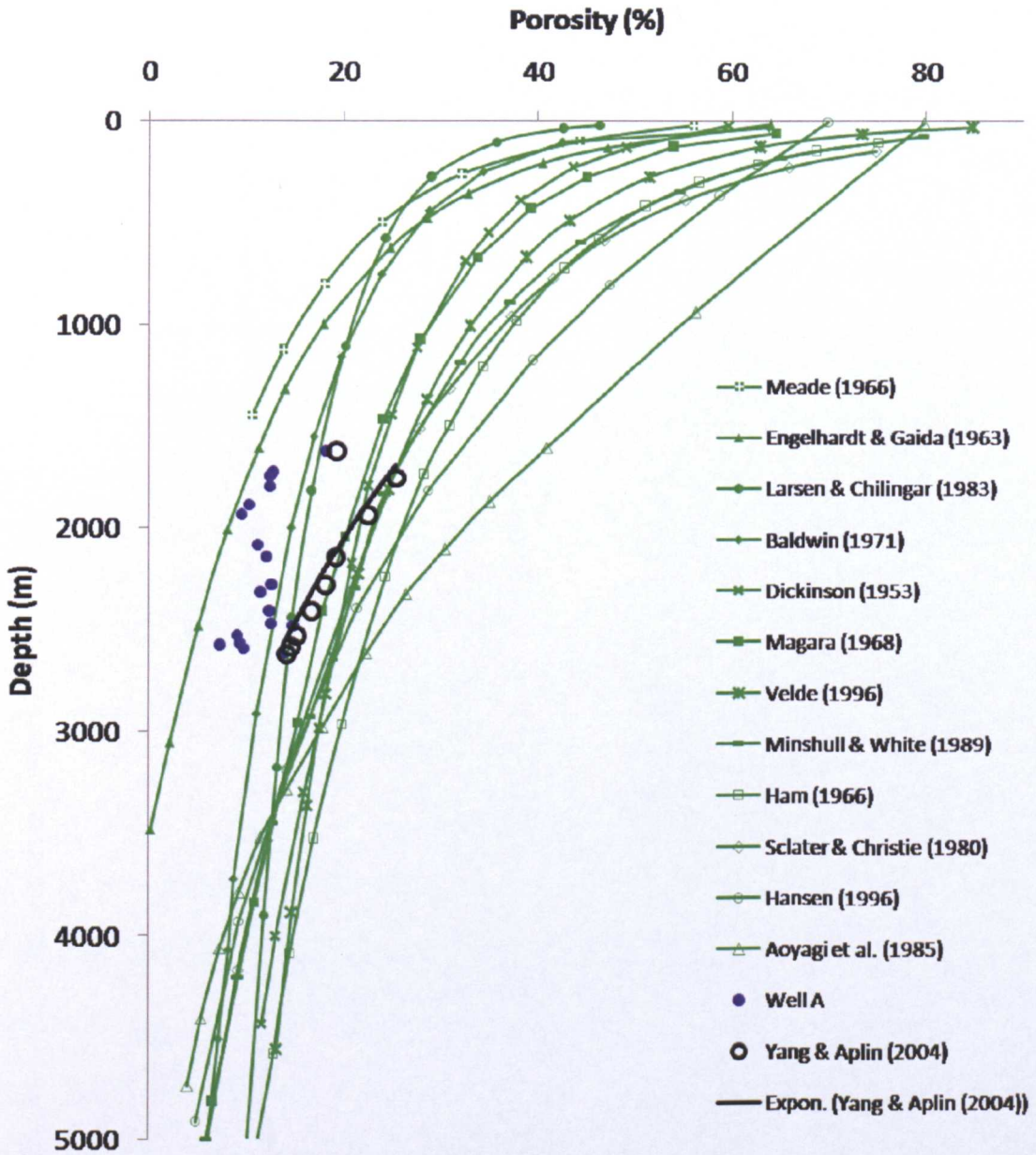

Figure 4.59 Porosity with depth for Well A and natural mudstones with relationships from the studies plotted in Mondol (2007). Also, black circles indicate calculated porosities using relationships defined in Yang & Aplin, (2004).

When plotted with natural compaction curves, the calculated Yang & Aplin (2004) (hydrostatically pressured model) modelled porosities appear much more typical, than when compared with the experimental datasets (Figure 4.59) cutting through, along 5 of the published trends. However, the Well A dataset persists in its separate trend even when compared to other natural trends. Of the curves displayed, only those of Meade (1966) and Engelhardt & Gaida (1963) plot at such low porosities at shallow depth. The first is taken from a composite of other trends and the second is based on values apparently from the Po Valley. The Malay Basin samples plot in between these trends and the others, at generally lower values than ten of the other curves. With the possibility of the rocks in Well A being significantly above their maximum burial depth ruled out (see 4.1), this is evidence that compaction mechanisms are at work in the mudstone sections of the Malay Basin that are not generally observed at similar depths in other previously studied locations. These are mechanisms which are not only controlled by effective stress, as demonstrated above. As the geothermal gradient of the Malay Basin is known to be anomalously high (~48°C/km at Well A), this seems a likely candidate to be facilitating mechanisms behind the atypical porosity behaviour.

Following the discussion in Chapter 3, it remains a possibility that increased temperature at shallower depths may be contributing to further mechanical compaction via matrix destabilisation mechanisms. Whilst temperature related effects may normally be compensated for in the use of statistically derived coefficients (from natural data) under more average geothermal gradients, they may not if the geotherm is significantly elevated.

The main temperature related mechanism is that defined as chemical compaction in Chapter 1. This involves porosity loss via the clay mineral transformations that occur in the burial environment.

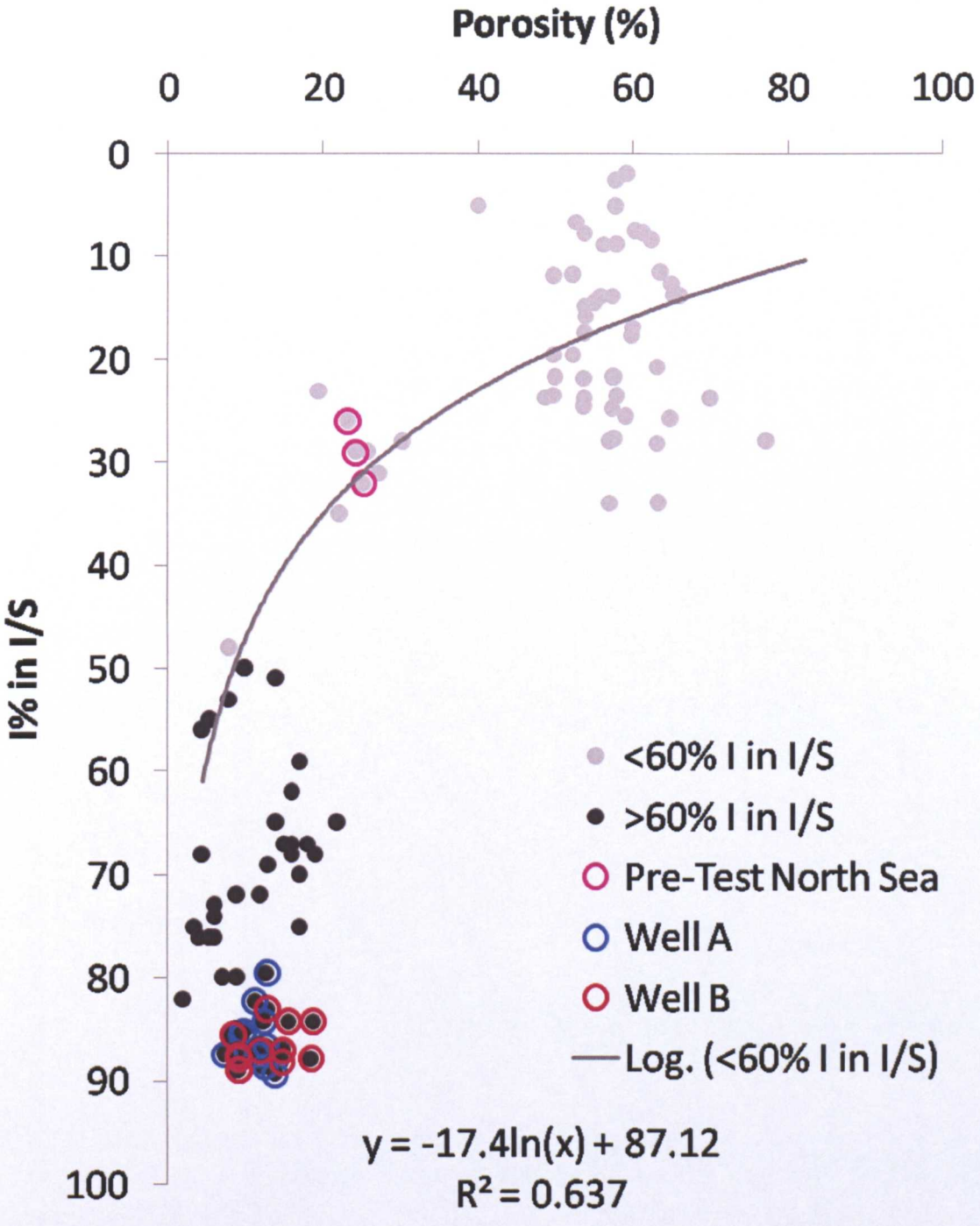

Figure 4.60 Composite plot with data from Schoonmaker Tribble (1990), Day-Stirrat et al. (2008); Aplin et al. (2006) and Day-Stirrat et al. (2010) and this study. Samples are shaded according to illitization. The pre-test North Sea average, minimum and maximum values from Chapter 3 are highlighted in purple and the data from Wells A and B in the Malay Basin are highlighted in blue and red, respectively.

The Malay Basin porosities that looked anomalous when plotted against depth, now look on trend when plotted with I% in I/S (Figure 4.60). Even when the ranges of some of the shallowest Well A samples are taken into account they still fall above 60% I in I/S and therefore in the vertical section of the trend.

4.4.2 Compositional Variation With Depth

The kinetic controls on illitization, links between the process and temperature are strong. To further demonstrate this, Figures 4.61 and 4.62 have been constructed.

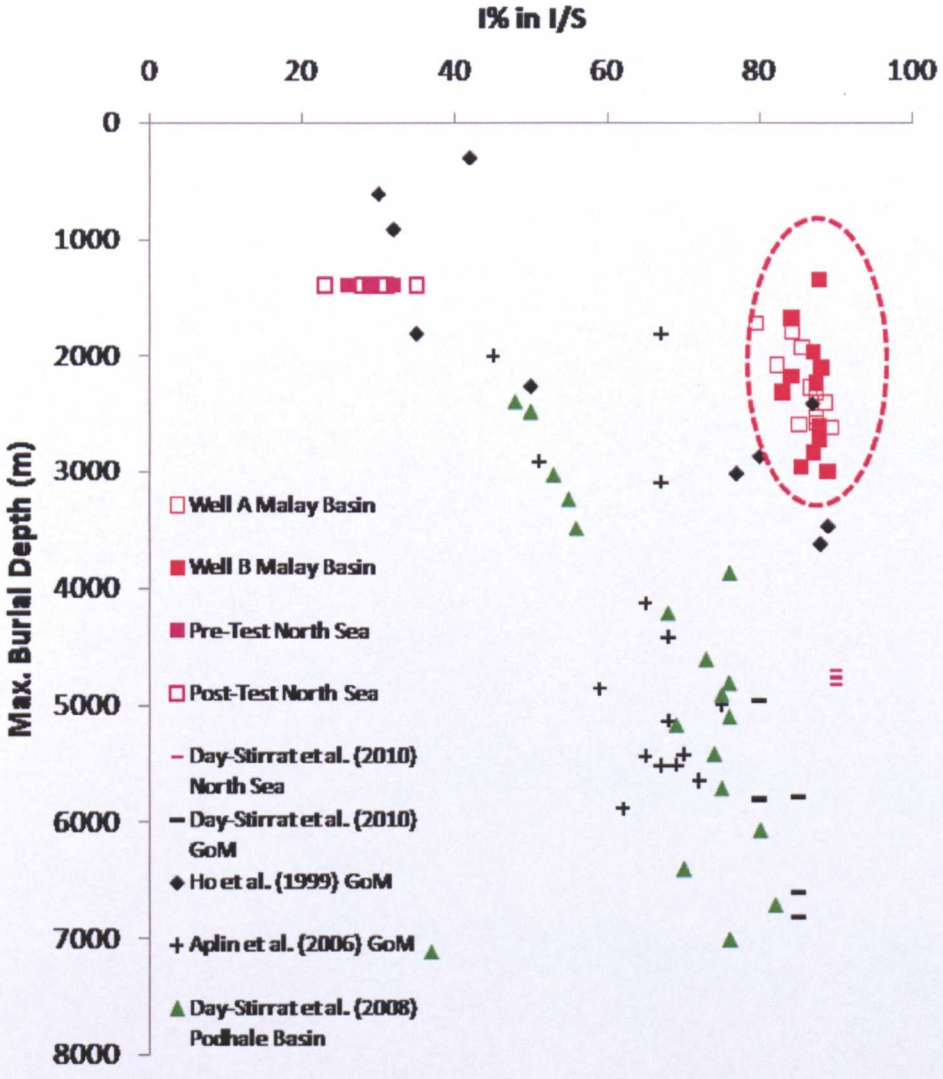

Figure 4.61 I% in I/S mixed layer clays with maximum burial depth for Well A and B samples from the Malay Basin (ringed in red), in addition to the North Sea mudstones (Chapter 3) and other published data sets listed.

When plotted against maximum burial depth, the Malay Basin samples appear considerably more mature than those from other locations. The mixed layer clays (I/S) in North Sea samples from Chapter 3 and the Gulf of Mexico samples from Ho *et al.* (1999) at roughly similar burial depths are pre-transition.

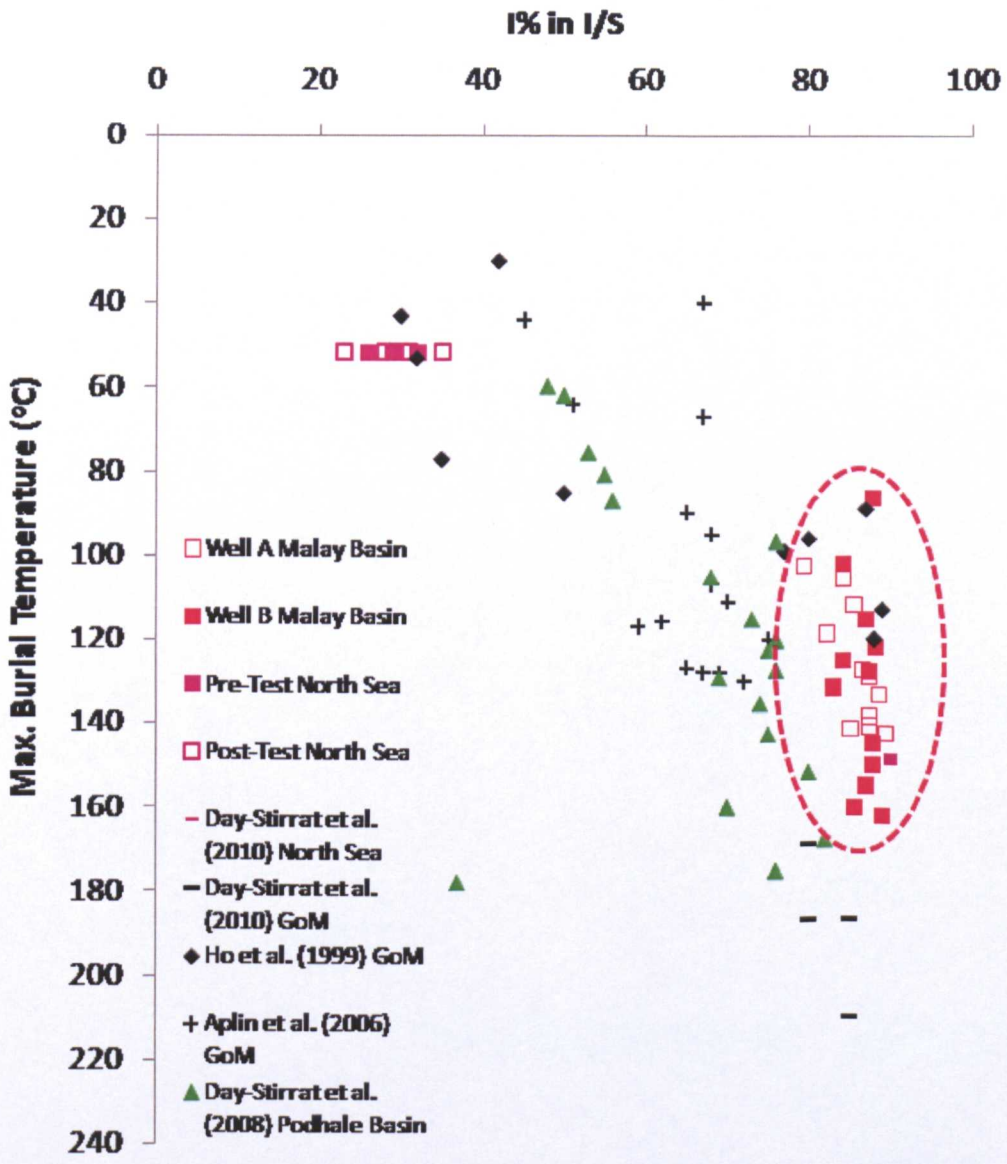

Figure 4.62 I% in I/S mixed layer clays with maximum burial temperature for Well A and B samples from the Malay Basin (ringed in red), in addition to the North Sea mudstones (Chapter 4) and other published data sets.

Once plotted against temperature, as opposed to depth, the Malay Basin datset now shows fit with several of the other studies from different locations. Points show

similar values to the post-transition North Sea samples of Day-Stirrat *et al.* (2010) and the post-transition Gulf of Mexico samples from Ho *et al.* (1999). The Podhale Basin samples generally show slightly less mature samples at equivalent maximum temperature, but several points are not dissimilar.

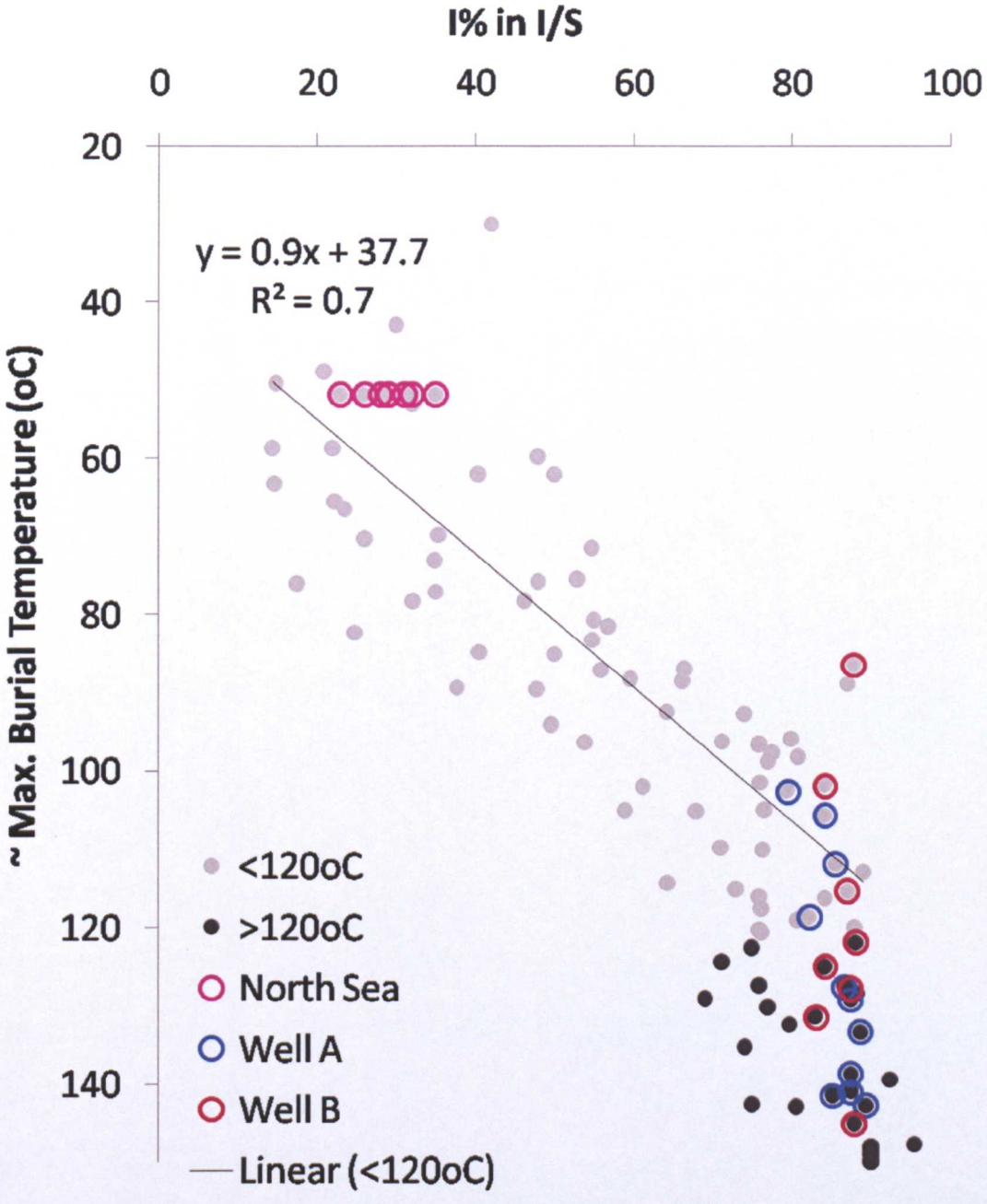

Figure 4.63 Composite plot using data from Eberl & Srodon (1984), Day-Stirrat *et al.* (2008), Aplin *et al.* (2006), Day-Stirrat et al. (2010) and Ho et *al.* (1999) and this study. Samples are shaded according to maximum temperature. The North Sea values from Chapter 3 are highlighted in purple and the data from Wells A and B in the Malay Basin are highlighted in blue and red, respectively.

The data from this study was added to a larger dataset comprising more studies from different geographic locations to form Figure 4.63. The inclusion of data from Eberl & Srodon (1984) adds further data from the North Sea, the Douala Basin (Africa), Central Poland and the Gulf of Mexico. This trend is fitted with a linear relationship over the main illitization window, although there could still be some argument for using the stepped trend shown in Ho et al. (1999). In this image, any step would probably be around the point where scatter about the line decreases at ~50% I in I/S.

The persistent question over whether the illitic nature of the samples is depositional or diagenetic cannot be comprehensively answered by this study as shallower samples were not available. However, the presence of the glycolated 16.8 Å peak in the shallowest samples of Well A and that this material is associated with mixed-layer clays (observed prior to glycolation) does give some indication of the final stages of a diagenetic process. Given all of the above relationships, mechanisms associated with the diagenetic alteration of clays remain a stong candidate behind the advanced porosity loss observed in this study.

Bulk fraction XRD shows the mineralogy in the samples provided from Well A to be significantly different to that in Well B and the original depositional facies undoubtedly exerts strong control on the current rock properties. Only the shallowest sample from Well A appears to contain siderite (and is in fact a concretion), whereas in Well B all of the shallowest samples 1350-2320m do. This range in both wells generally corresponds to groups of the same depositional environment – the tidal-marine horizons (Group J in Well A and Group H-J in Well B). Siderite's presence is also indicated by elevated grain densities. The chemical requirements for siderite

precipitation include formation waters of high bicarbonate activity, low oxidation potential and extremely low concentrations of dissolved sulphide (Garrels and Christ, 1965). Siderite precipitation is common where tropical weathering is occurring, supplying Fe^{2+}. The latitude at time of deposition and the tidal environment (which can allow lower concentrations of SO_4^{2-}) can explain the presence of this mineral in these sections.

The overall effect of siderite precipitation on porosity reduction over the analysed section is minimal. This is based on evidence that the porosities exhibited in Wells A and B where siderite is present are amongst the largest porosities measured. Porosity is lowest in the fluvial/lacustrine section below, in both wells. However, the porosity, even in the siderite-bearing section is already tight and siderite precipitation may have some influence on this, chemically shutting down porosity via the precipitation of the new mineral

4.4.3 Evaluation with log data and Implications for Overpressure Development

4.4.3.1 Inorganic Chemical Compaction

One of the initial motivations for conducting rock property analyses on these samples was that wireline log analysis of Wells A and B highlighted features of the velocity-density trends supposedly linked to chemical compaction. This chemical compaction of the mudstones was cited as an overprssuring mechanism in the deeper sections of the wells. Figure 4.64 below shows the pressure with depth in Wells A and B.

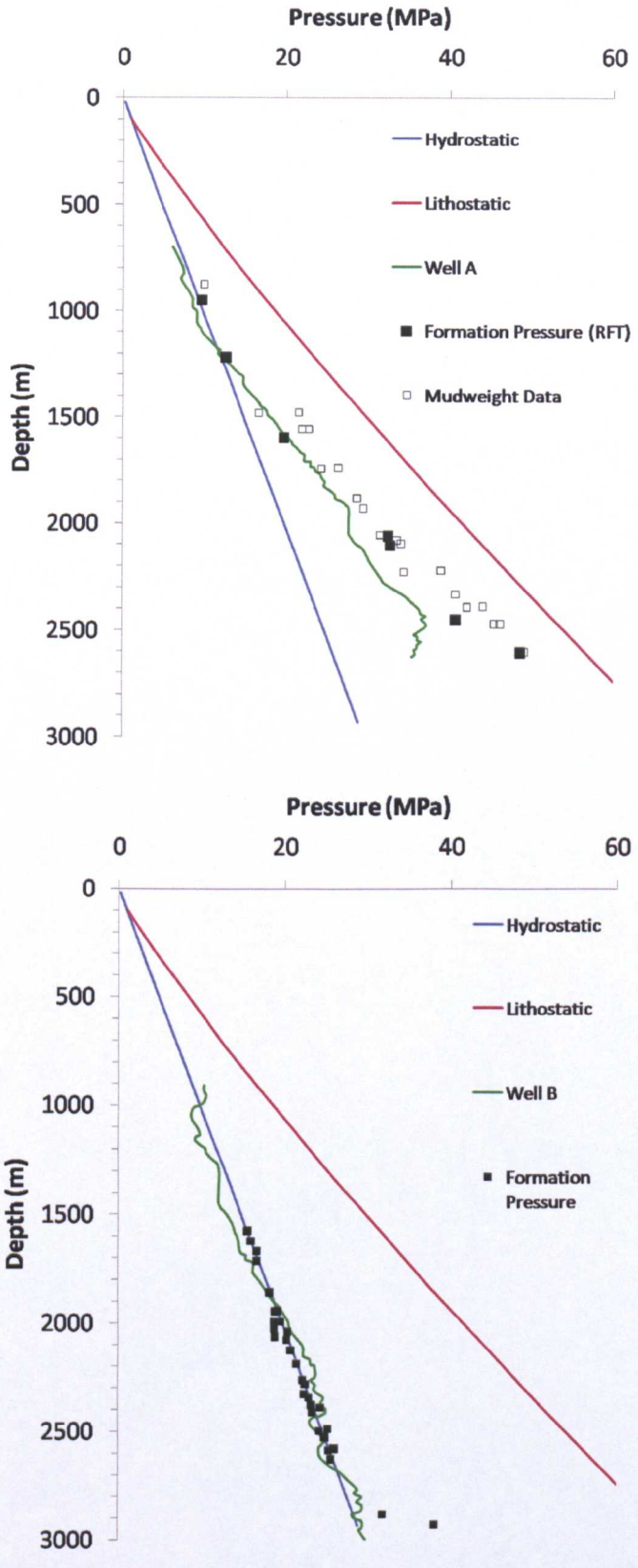

Figure 4.64 Pressure data from Hoesni (2004) for Wells A and B. Fluid pressure was calculated using the equivalent depth method. Formation pressure data is also plotted for both wells, along with mudweight data for Well A.

Sampled intervals in the wells range between 1619-2621m in Well A and 1350-3000m in Well B. Given this range and the information in Figure 4.64, all Well A samples are from overpressured sections, with overpressure increasing with greater depth. Well B samples are largely from normally pressured sections until formation pressures indicate some overpressure development at depths >2800m. Three samples are from below that depth, 2840, 2960 and 3000m. The equivalent depth method calculates a fluid pressure that correlates to the formation pressures measured in adjacent sections in the upper section of Well A, but starts to underpredict the high overpressures with greater depth. The modelled fluid pressure also does not meet the measured formation pressures at the base of Well B. It is this discrepancy between modelled fluid pressures and the measured deep overpressure that is cited as part of the evidence for the operation of chemical compaction in the mudstones, as these processes would not be included in the pressure models.

On the velocity-density cross-plots in Section 4.1 (Figure 4.9), an increasing density trend moves away from the normal compaction bound curves, without showing significant increase in velocity and then shows a rapid increase in velocity, without increasing density. In Well A the initial density increase coincides with the onset of overpressure and in Well B it it is concurrent with the increase in velocity. These trends are cited as being representative of chemical compaction in Hoesni (2004). Several ideas as to how the illitization process may bring about such log responses are stated. These include matrix collapse with partial dewatering, shale fabric re-orientation or sequential cementation of pores. The latter process could be linked to the velocity-density trends as cementation of the storage pores could lead to the observed sharp increase in bulk density, while the sharp increase in velocity is due

to cementation of the connecting pores (for image of storage and connecting pores see Chapter 1).

In the previous sections, composite plots of the Malay Basin data measured in this study did appear to suggest that temperature related mechanisms including illitization could have influenced the formation of the low porosities measured at relatively shallow depth if the prerequisite mineralogy was available whilst the sampled section was at shallower burial depths. Bulk fraction XRD showed variation but no depth / temperature related increases or decreases, with strong depositional control on quartz content in Well B likely.

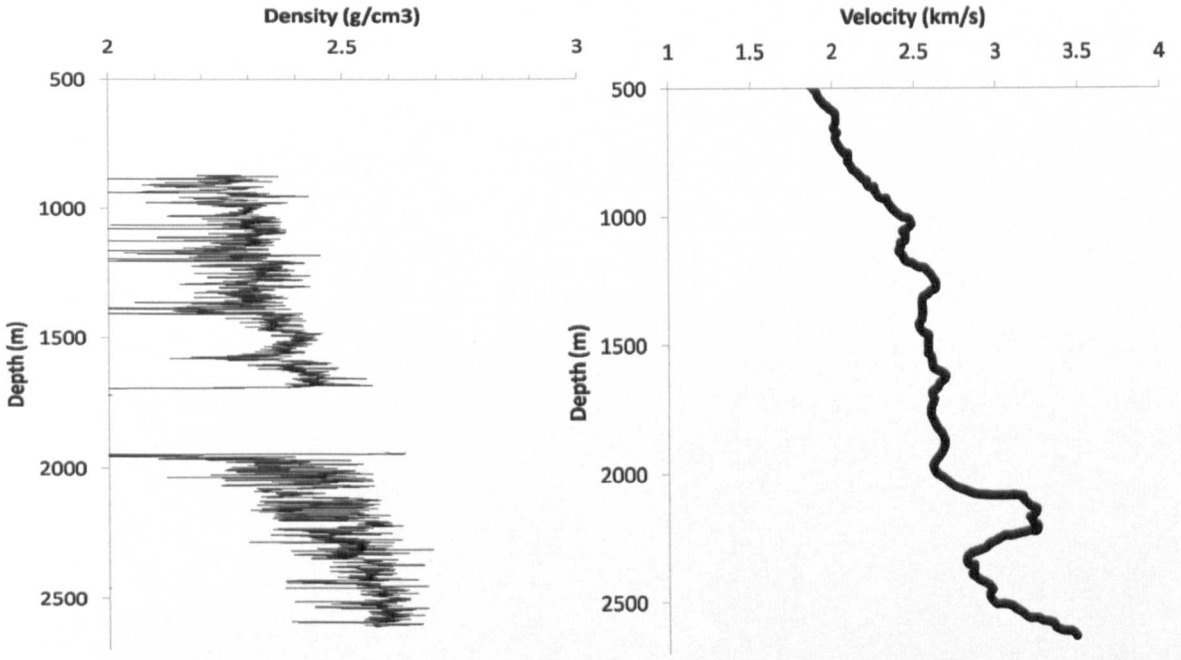

Figure 4.65 Plots of density and velocity with depth based on the work of Hoesni (2004) for Well A. Density trend is a moving average through the unfiltered density log data and velocity data are calculated from the filtered sonic log data displayed in the thesis of Hoesni (2004).

In the clay fraction XRD measurements on Well A, the reason behind this may be found in what could be interpreted as the latter stages of illitization taking place. Illitization in Well A would start above the sampled section, but so does overpressure

and the density increase. They all appear roughly coincident at ~1200-1400m. In well B shallower samples do not show evidence of progressive illitization. However, Well B samples are generally less clay-rich with several samples appearing to be quartz siltstones.

As samples in Well A are in the latter stages of illitization, the I% in I/S is high and on composite plots they tend to form the end member of general trends. However, on a more detailed scale with log data some variation can be observed (Figure 4.66).

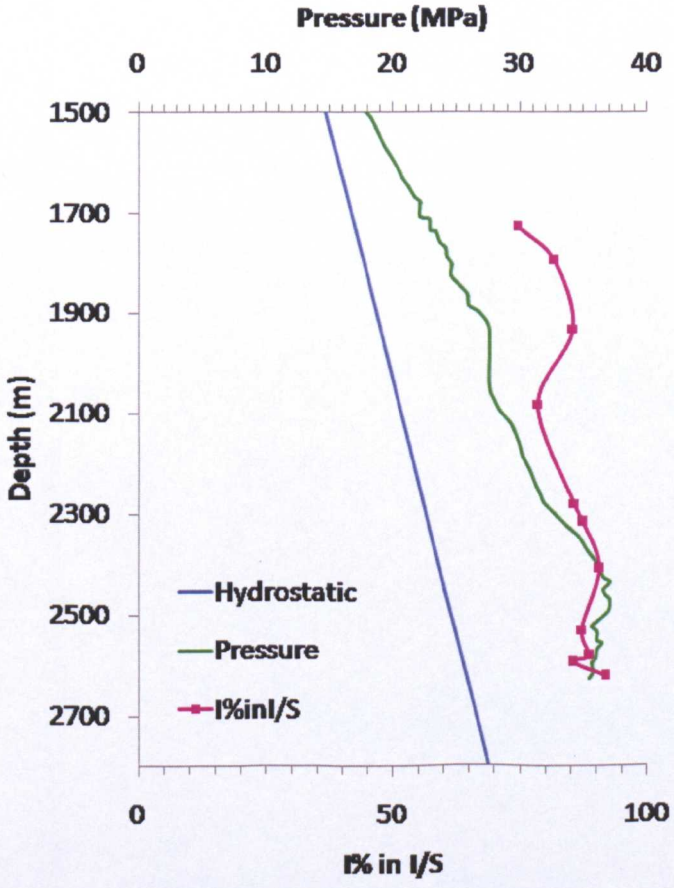

Figure 4.66 Pressure data from Hoesni (2004) for Wells A with I% in I/S from this study. Fluid pressure was calculated using the equivalent depth method.

As noted above the calculated pressures do not agree with the measured formation pressures, yet seem to show a general correlation to I% in I/S (Figure 4.67).

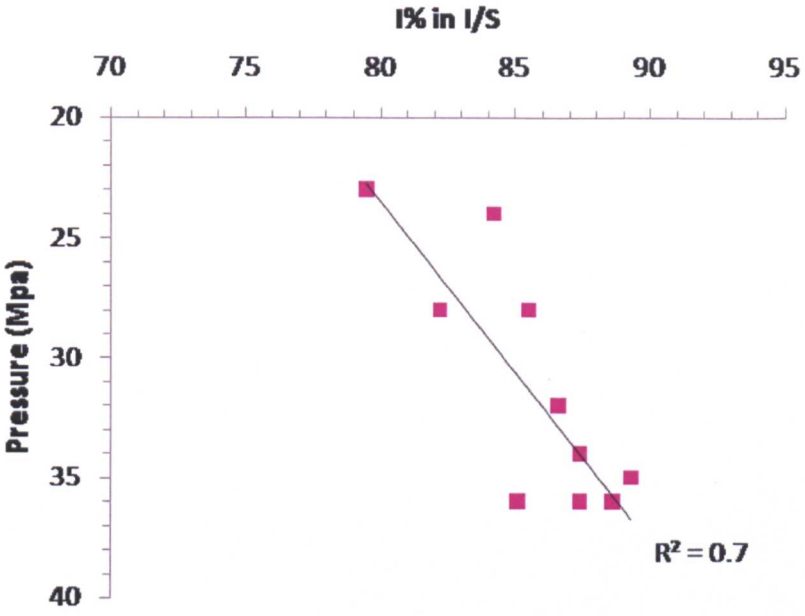

Figure 4.67 Calculated fluid pressure from Hoesni (2004) with I% in I/S for Well A from this study.

The equivalent depth method used to calculate the fluid pressure is based on sonic derived shale porosity related to either the vertical or mean effective stress as described in Hart et al. (1995) and Harrold et al. (1999). One of the assumptions with this method is that shales of equal porosity and similar composition, have been subjected to the same maximum vertical effective stress, regardless of their burial depth (Hoesni, 2004). It may be that the variation in calculated pressures is incorporating some compositional variation in the strata, with I in I/S following more mud-rich horizons. Alternatively, supporting the chemical compaction suggestion, the more illitized strata are more compacted.

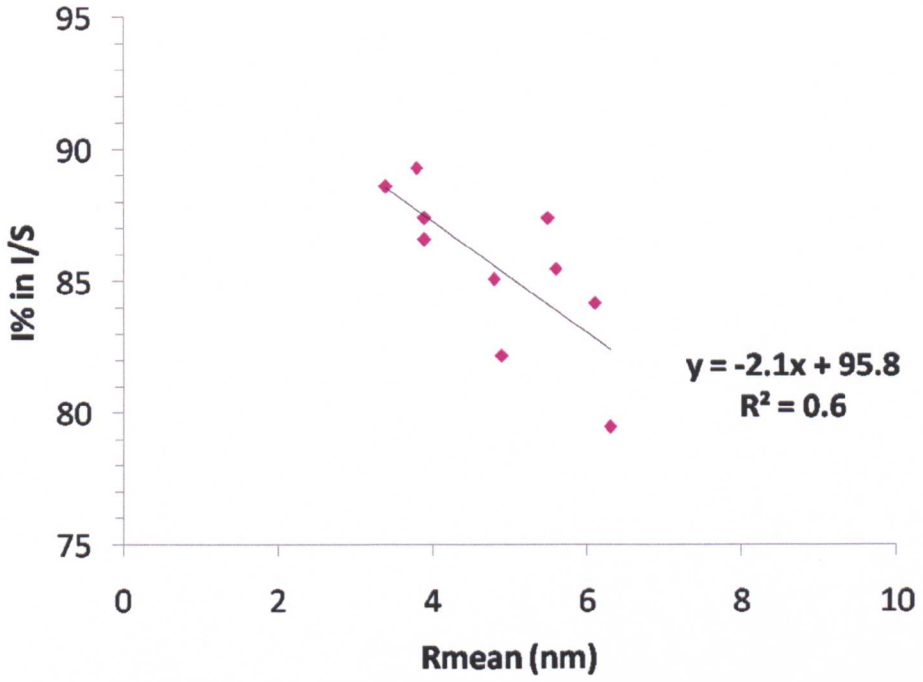

Figure 4.68 I% in I/S with Rmean from MICP measurements for Well A.

The dataset is not comprehensive, but from those samples analysed, I% in I/S shows scatter with corrected porosity values. However, when plotted with R_{mean} some correlation emerges where the most illitized samples have the smallest pore throats. The reduction of R_{mean} is similar to the compaction behaviour observed in the high temperature, potassium exchanged experimental plugs from Tests 4 and 7 in Chapter 3. Although, this is on a much finer scale as the samples with the highest I% in I/S have R_{mean} values that are approaching the minimum that it is possible to measure with MICP. These mudstones are very tight, especially considering their relatively shallow burial. It is therefore to be expected that if such porosities are used to calculate fluid pressure making the assumptions of the equivalent depth method, then it would be assumed that these rocks had been subject to high effective stresses and the fluid pressure would be underpredicted.

4.4.3.2 Compaction of organic material

Another chemical factor related to observed compaction, is the reduced porosity observed associated with increased TOC towards the base of Well A. Between 2530-2582m, TOC increases to 1.53% and grain densities correspondingly drop to a minimum of 2.70g/cm^3. This follows the general increase in grain densities seen over the section above it. TOC values are not particularly high, but it has been noted as the samples of this horizon show the lowest corrected porosities measured on the Malay Basin samples and this is related to the region of calculated highest overpressure (Figure 4.69).

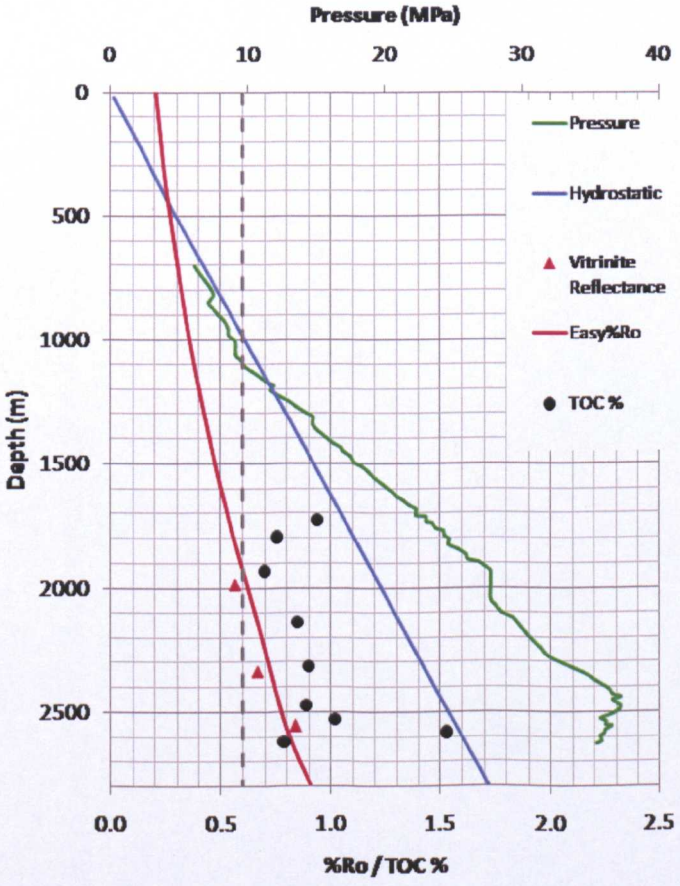

Figure 4.69 Vitrinite reflectance/modelled %Ro with TOC% and pressure with depth.

Vitrinite reflectance measurements and Easy%Ro modelling from Hoesni (2004) shows this horizon (Figure 4.69) to be approximately 0.8%. This makes the material immature/early mature, though HI values indicate this is not a particularly high quality horizon and any potential source would be gas prone.

Speculatively gas generation effects could contribute to overpressure, but a link between organic content and the lowest porosities at this level could also point towards either the effects of chemical compaction of organic matter and/or the additional mechanical compaction that comes with plastic strain of organic matter at high temperature (Johnston, 1987). The permeability is also reduced and through that mechanism, may generate overpressure through disequilibrium compaction. This effect does not appear to take away from the link between I% in I/S and the decreasing R_{mean}, in fact removing the higher TOC samples from that dataset increased the correlation to r^2=0.7.

Linking these two effects back to the velocity-density trends, the initial density increase in the log data corresponds to a pattern of measured grain density increase. The cessation of the increase in the log bulk density, is roughly over the same interval as the grain density decrease over the higher TOC interval (Figure 4.70).

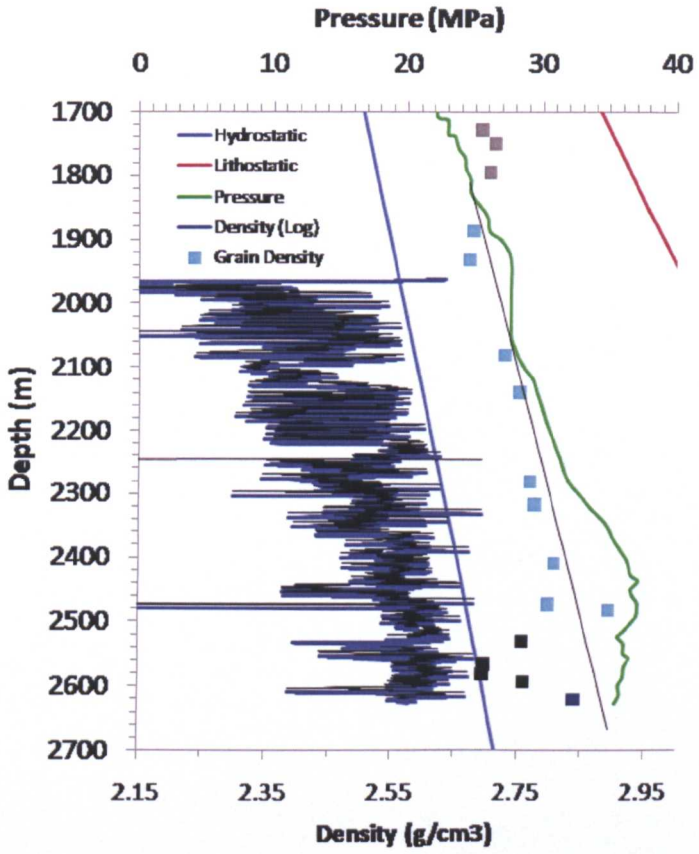

Figure 4.70 Well A calculated pressures and density log from Hoesni (2004), with measured grain densities.

over this interval, corrected porosity reaches its minimum and may therefore be related to the increased velocities as grain contacts increase. In Well A the overall high density is likely linked to the iron mineralogy measured with XRD, but increasing density and velocity trend may be linked to the final stages of illitization, as Figure 4.72 shows, illite mineralogy is interpreted as denser and associated with higher velocities. The velocity trend may also be linked to compaction in the higher TOC horizon. There is also the possibility that if any gas generation has taken place then the rapid velocity change could also be viewed as a decrease from the normal compaction curve if read conversely (Figure 4.71). This would make it more similar to the study of Ramdhan & Goulty (2010) in the SE Asian, Cenozoic,

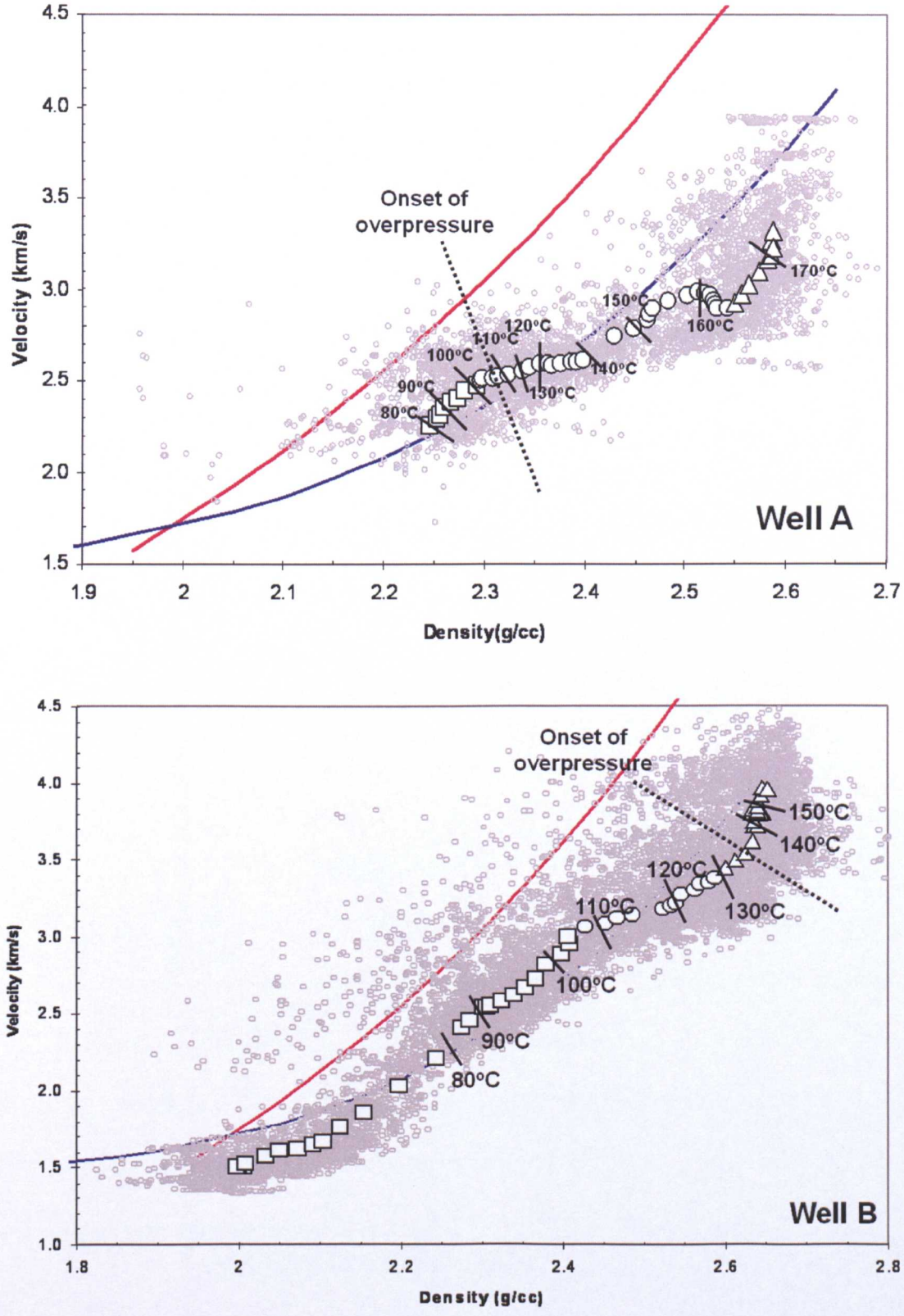

Figure 4.71 Repeat of Figure 4.9 Velocity – density cross-plots from Hoesni (2004) for Wells A and B studied in this thesis. The upper and lower bound curves (solid lines) are taken from Bowers (2001). Compaction trends are represented by different symbols.

Peciko Basin. The study concludes that that gas generation and chemical compaction are the mechanisms behind a rapid velocity decrease recorded in log data and overpressure generation.

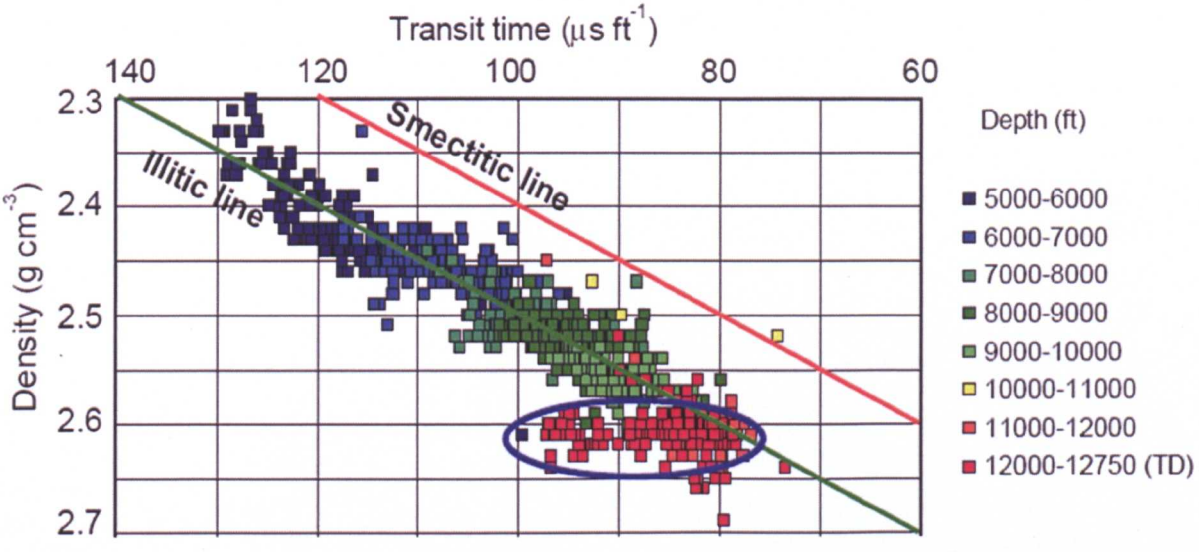

Figure 4.72 From Ramdhan & Goulty (2010) Crossplots of density against sonic transit time for well NWP-9 in the Peiko Field. Data points on unloading trends are encircled in blue.

Well B is generally normally pressured until the deepest section >2800m and any deviation from the normal compaction trend on the velocity-density cross-plots appears minimal (Figure 4.71). A complicated interplay of the effects of siderite, pyrite, organic matter and quartz content appear to determine the measured grain densities. However, the organic horizon in Well B is shallower and whilst it has more significant TOC contents of ~4% it is not associated with low porosities and it is likely to still be immature at Ro=0.6% (Figure 4.73).

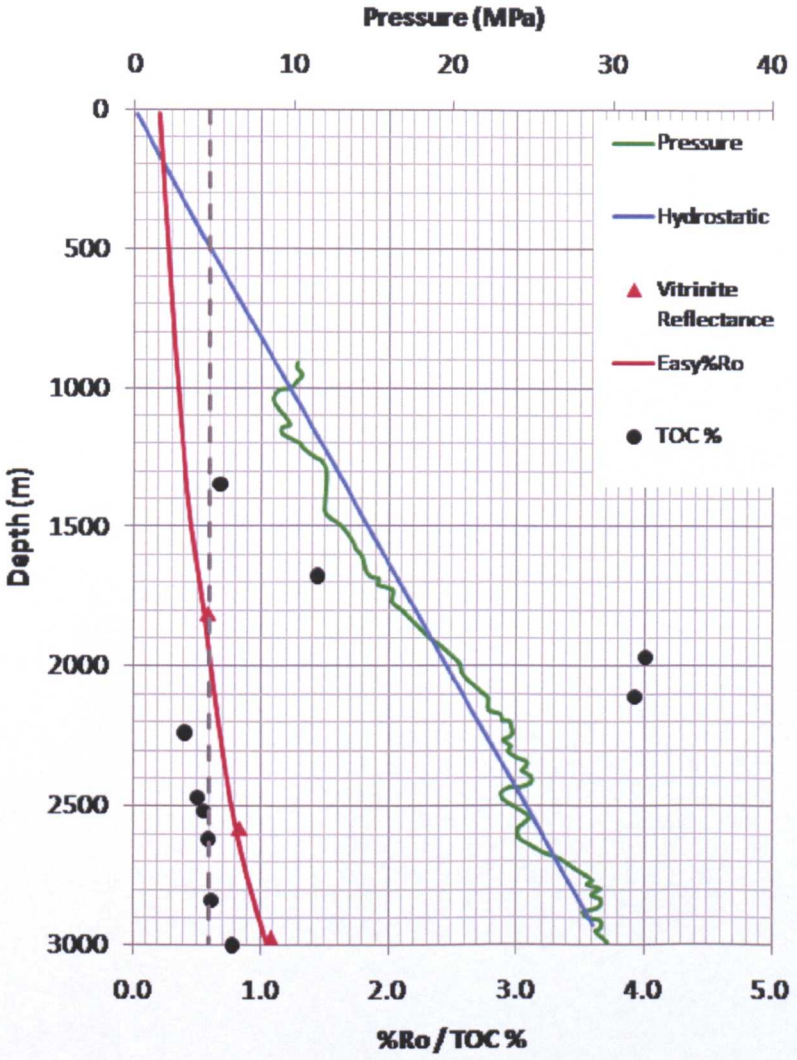

Figure 4.73 Plot of pressure in Well B with depth on primary axes and vitrinite reflectance data (samples – red triangles and modeled – red line – Hoesni, 2004) with TOC (samples measured this study – black circles) both on the secondary horizontal axis. 0.6% cut-off from Ramdhan & Goulty (2010) study displayed also on secondary horizontal axis (grey dashed line).

Calculated permeabiliites reach the μD range and overpressure is not found over much of the well. This could be linked to the an increase in clay recorded in the final sample, with alteration of minerals observed in progress in BSEM images. Relationships are less clear and therefore interpretations less confident.

Chapter 5 of Hoesni (2004) involved the numerical simulation of overpressure evolution in the Malay Basin. 1D and 2D models were built using Temispack software for Wells A and B. The outcome of that modeling was that in Well A the larger observed overpressures could only be matched by disequilibrium compaction with some contribution from volume expansion as a result of gas generation (either directly from kerogen or cracking from oil and chemical compaction enhancing the effect by creating an effective seal in the fluvial-lacustrine facies. Clay diagenesis as a volume expansion mechanism is not invoked as Swarbrick et al. (2002) calculates that it would not generate high overpressures (<~7MPa for a 1nD seal). The gas generation models required a gas-prone source and the study describes how it may be possible that the South Malay Group K, L & M source rocks are more coaly, terriginous compared to the eastern part of the basin where lacustrine facies are developed in these groups. By contrast minimal overpressures in Well B can be matched by disequilirium compaction via mechanical compaction or lateral transfer. Deposition of low permeability shales on 1nD or less is the main requirement.

Whilst the rock property results from this thesis find a number of possibilities for the observed log trends displayed in Figure 4.71, the modelled variables tested in the basin models of Hoesni (2004) are present in the Malay Basin samples (illitization apparently in final stages and lower quality, gas prone source), supporting their modelling conclusions.

4.5 Conclusions

- There are many controls on the observed chemical/mineralogical and physical properties of the samples from Well A and B as is to be expected from the natural, burial environment. These include spatial and group dependant depositional compositions, diagenesis and possibly catagenesis, in addition to stress, temperature and time.
- The mudrocks and shales of Wells A and B are significantly compacted with relatively tight porosity values given their burial depth and exposure to effective stress.
- Well A samples were true clay-rich, fine grained mudstones but their porosities are lower than "mechanical" compaction trends generated from experimental results. They are also lower than calculated porosities based on effective stress relationships such as Yang & Aplin (2004), although these values are closer to the measured values possibly because the equations utilise coefficients based on natural datasets, other non-mechanical mechanisms may be included by proxy. Finally, the Malay dataset falls at lower porosities at shallow depths when compared to natural mudstone compaction trends. As the geothermal gradient of the Malay Basin is known to be anomalously high (~48°C/km at Well A), this seems a likely candidate to be facilitating mechanisms behind the atypical porosity behaviour.
- The Malay Basin porosities that looked anomalous when plotted against depth, plot on trend when plotted with I% in I/S. Similarly, the I% in I/S data appears considerably more mature than those from other locations when plotted against depth. However, when plotted against temperature the data

ties in with several other studies. This would appear to support the hypothesis that elevated geothermal gradient is facilitating more rapid diagenetic change which also appears to correlate with enhanced porosity loss.

- The overall effect of siderite precipitation on porosity reduction over the analysed section is minimal as those intervals where siderite is present are amongst the largest porosities measured. However, the porosity, even in the siderite-bearing section is already tight and siderite precipitation may have some influence on this, chemically shutting down porosity via the precipitation of the new mineral (inferred through BSEM images).
- Illitization in Well A would start above the sampled section, but so does overpressure and the density increase. They all appear roughly coincident at ~1200-1400m. In well B shallower samples do not show evidence of progressive illitization. However, Well B samples are generally less clay-rich with several samples appearing to be quartz siltstones and the well is not generally overpressured over much of the sampled section.
- Making the assumptions of the equivalent depth method, the reduced porosities mean that when, as in Hoesni, (2004), they are used to calculate fluid pressure then it would be assumed that these rocks had been subject to high effective stresses and the fluid pressure would be underpredicted.
- Another chemical factor related to observed compaction, is the reduced porosity observed associated with increased TOC towards the base of Well A. Speculatively gas generation effects could contribute to overpressure, but a link between organic content and the lowest porosities at this level could also point towards either the effects of chemical compaction of organic matter

and/or the additional mechanical compaction that comes with plastic strain of organic matter at high temperature (Johnston, 1987). The permeability is also reduced and through that mechanism, may generate overpressure through disequilibrium compaction. This effect does not appear to take away from the link between I% in I/S and the decreasing R_{mean}.

- In Well A the overall high density is likely linked to the iron mineralogy measured with XRD, but increasing log density and velocity trend may be linked to the final stages of illitization as illite mineralogy is interpreted as denser and associated with higher velocities. The velocity trend may also be linked to compaction in the higher TOC horizon. There is also the possibility that if any gas generation has taken place then the rapid log velocity change could also be viewed as a decrease from the normal compaction curve if read conversely.
- Well B is generally normally pressured until the deepest section >2800m and any deviation from the normal compaction trend on the velocity-density cross-plots appears minimal. A complicated interplay of the effects of effective stress, temperature, depositional and diagenetic mineralogies content appear to determine the properties and pressures measured.
- The modelled variables tested in the basin models of Hoesni (2004) are present in the Malay Basin samples (low permeability horizons, illitization apparently in final stages and lower quality, gas prone source for Well A, low permeability horizons - for disequilibrium compaction only required for Well B), supporting their modelling conclusions.

Chapter 5

Mudstone Compaction: Mechanisms and Causes

5.1 Grain Packing And Rotation As A Result Of Mechanical Stress

5.2 Matrix Collapse As A Consequence Of Thermal Stress

5.3 Chemical Alteration And Alignment Resulting From Mineralogical Change

5.4 Project Conclusions

5.6 Future Work

5. Mudstone Compaction: Mechanisms and Causes

5.1 Grain Packing And Rotation As A Result Of Mechanical Stress

Effective stress and the associated compaction mechanisms of grain packing and rotation were seen in operation most clearly in Chapter 3 during the laboratory compaction tests. One key piece of evidence was that below the preconsolidation stress, the mudstone produced negligible change or actual expansion in post-test dimension measurements due to overconsolidation effects. Surpassing the in-situ stress of a natural mudstone is vital for further compaction to take place even when exposed to increased temperature or potassium. The second is that the mudstone that was cored from a relatively shallow depth and had not undergone natural illitization showed some alignment of the clay particles. This minimal fabric is likely to be generated by mechanical mechanisms such as grain rotation as the sediment compacts initially, in keeping with the findings of Sintubin *et al.* (1995) and Voltolini *et al.* (2009).

However, what was also in evidence during the tests was the limitations of these processes. The compressional effects of surpassing in-situ stress in Test 8 (Mechanical Compaction Test) without the operation of the mechanisms associated with K-exchange or elevated temperature does not significantly, permanently compact the mudstone and a largely elastic response occurs as stress is reduced. The processes that decreased the volume due to stress and temperature in the

North Sea burial environment are more effective than surpassing in-situ stress alone and the compressional mechanism does not appear to be associated with the additional permanent, stable, reorganization of grain contacts. There is also no further increase in grain alignment due to any of the tests.

Established compaction relationships, such as those used in petroleum systems modelling, generally rely on the lithological and effective stress inputs. The effective stress relationship was discussed in Chapter 1, in addition to its link to porosity loss due to mechanical compaction. There is a large volume of literature on the relationship between stress and the compaction behavior of clays and mudstones, including Mondol et al. (2007), Burland (1990), Al-Wardy & Zimmerman (2004) Swan *et al.* (1989) and Vasseur *et al.* (1995). Consolidation is described in the soil mechanics literature as a process where particles pack closer together and reorientate as a stress is applied resulting in a volume reduction as excess water is expelled if the clay/mudstone is saturated.

Figure 5.1 shows the way in which clays consolidate experimentally due to applied effective stress (shown as equivalent depth) depending on clay type compared to natural mudstone porosity loss. This is from earlier work than the similar plot from Mondol (2007) shown in Figure 1.5 (Chapter 1), but is perhaps more useful when analyzing the results of this thesis as it also includes the "mechanical" compaction curve for illite as well as smectite and kaolinite. This is because the North Sea mudstone samples are smectite/ smectitic I/S – rich, but take on some of the characteristics of an illite once processed through the triaxial experiments (reduced expansion upon glycolation/hydration, increased stiffness/mechanical stability). The Malay Basin samples are illite/ mica/ illitic I/S-rich.

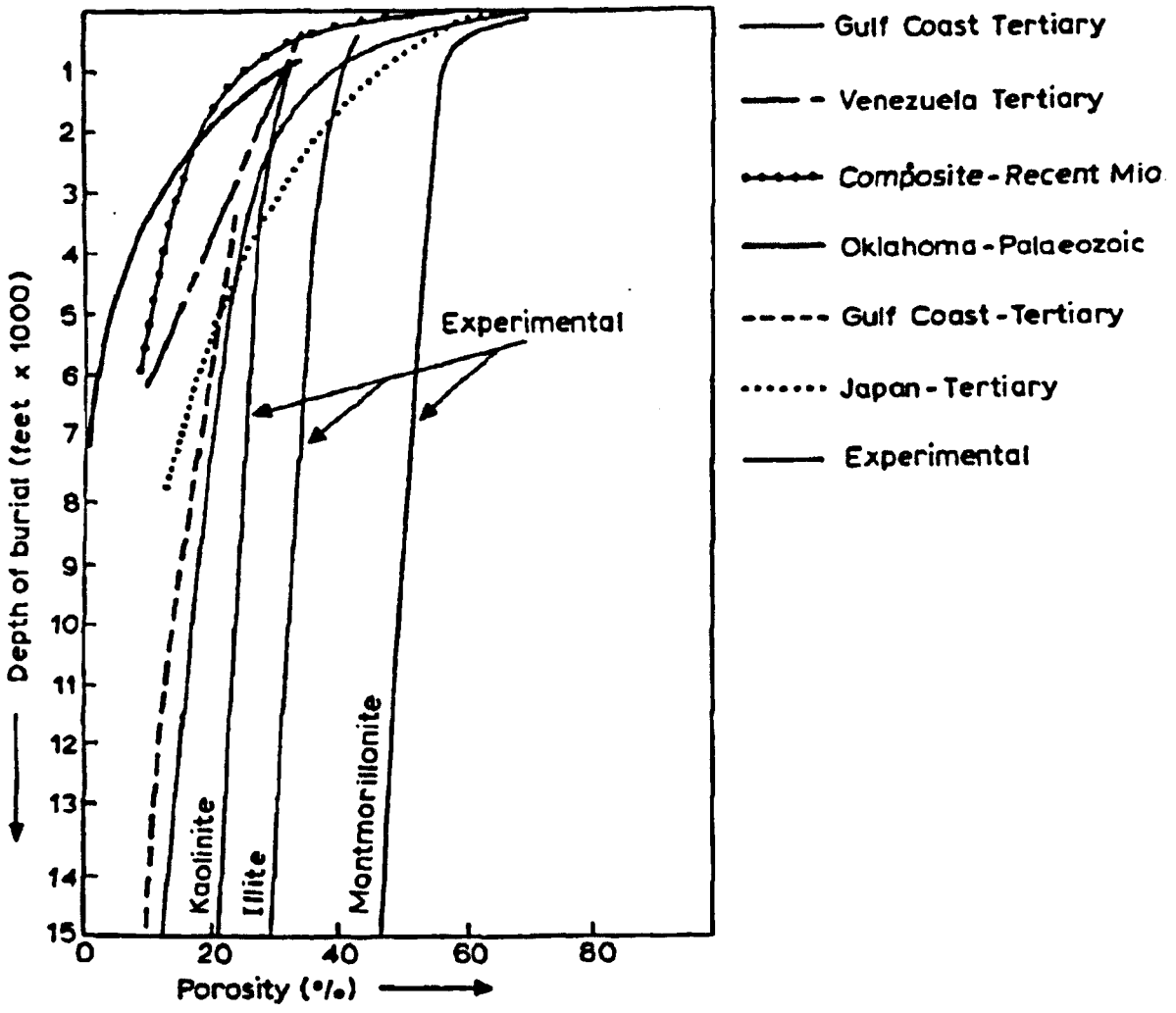

Figure 5.1 Experimental and observed porosity depth trends from Bjorlykke (1998) for clays & mudstones with stress/depth. Experimental data taken from Chilingar & Knight, (1960)

In the early stages of this project, similar "mechanical" approach compaction tests were attempted at much lower stresses upon artificial clay mineral mixtures and were discussed in Chapter 2. Figure 5.2 displays the MICP measured porosity distributions for the pure kaolinite consolidations. Following consoliation to 0.238, 1 and 5MPa the clay compacted to corrected porosities of an average of 54%, 47% and 43% respectively. The distributions show a loss of the larger pores (via a flattening of the larger pore "tail" of the distribution and an increase in the number of smaller pores (via a shift in the mode). This means that the reorganisation of the

matrix during mechanical grain packing and rotation facilitates porosity loss in a similar manner to the mechanism of matrix destabilisation related to temperature already discussed in Chapter 3. This is unsurprising as the destabilisation under normal consolidation at temperature will result in the grains being packed together to increase contacts and so both are actually mechanical mechanisms. The only significant difference with what is traditionally referred to as "mechanical" compaction is that it relates to stress exerted by the overburden and the temperature mechanism relates to the thermal stress upon the system. This is discussed further in the following section.

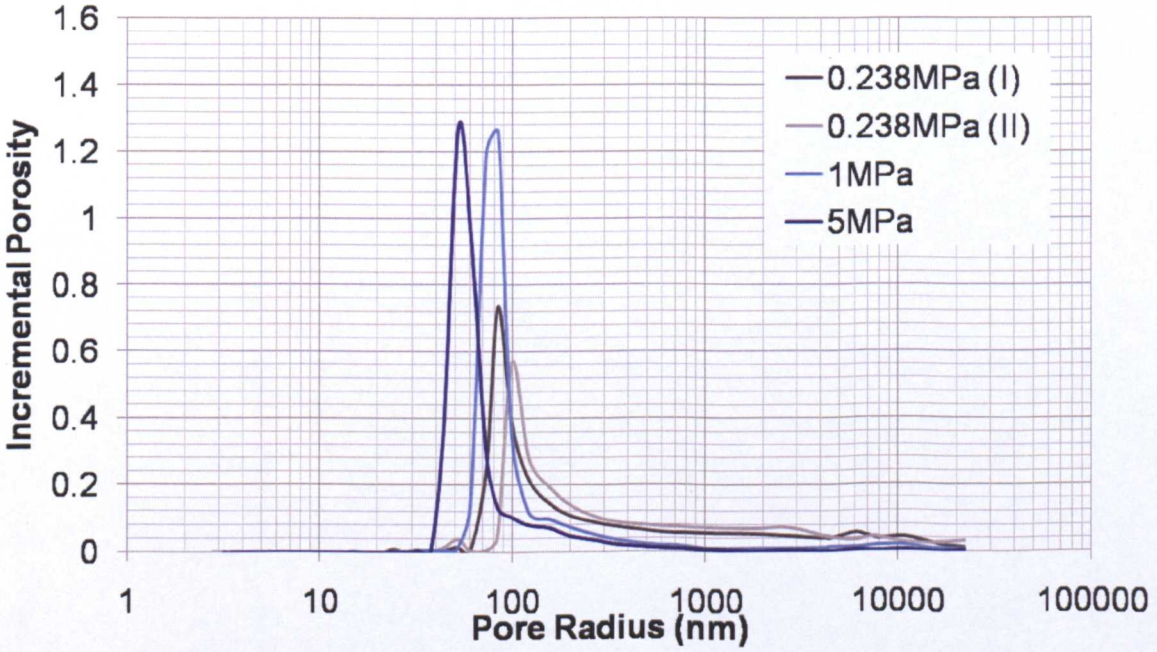

Figure 5.2 MICP measured porosity distributions for experimentally compacted kaolinite, consolidated to 0.238, 1 and 5MPa.

Other models have described the progressive loss of porosity from velocity variations controlled by changes to grain contacts and pore shapes. Holt *et al.*, (1997) detail the idea that thin cracks, possibly representing pore throats close first. At low pressures, velocity shows an increase then levels off at higher stress as cracks are

closed. Their model describes how rocks exhibit stress dependent wave velocities when their constitutive behaviour shows nonlinear elasticity and the main physical mechanism responsible for stress dependency is opening or closure of cracks, where crack formation is also associated with breaking of grain contacts. One of the outcomes of this study, is to provide detail of the actual components of the mudstone matrix that would be broadly classified as a "crack" and would be responsible for stress dependency, whilst reducing porosity via different mechanisms. This would be the clay inter-layer cracks and associated micro-meso porosity that only permanently reduce due to potassium exchange and the larger interparticle pore throats that close with temperature and stress increase once preconsolidation pressure has been surpassed. There are also the actual voids observed in the BSEM images associated with micas and microfossils that may be open in the subsurface as pyrite appears to have been able to develop inside.

The effects of mechanical compaction as result of variation in stress exerted by the overburden and depending upon the properties of the overburden can be seen in Figure 5.3 in the model of lithology/effective stress based mechanical compaction by Fjaer *et al.* (2010), along with Malay Basin samples, analysed in Chapter 4 and the North Sea samples from Chapter 3 for comparison.

The Malay Basin samples are over compacted for their depth according to the model and the samples from deeper sections of Well A (mudstone dominant samples) only just start to tie with the upper limits of the mudstone model (ie. again, if the overburden is particularly sandy). The pre-test North Sea material appears to be

over compacted for its cored depth of 1392m compared with the model results. However, when the moderate uplift estimates on the samples are taken into account, the pre-test porosities are not dissimilar to the mechanical model predictions if the overburden of the original core was particularly sandy. Test 8 (the Mechanical Compaction Test) porosities lie within the pre-test range (and consequently can't actually be seen on the diagram).

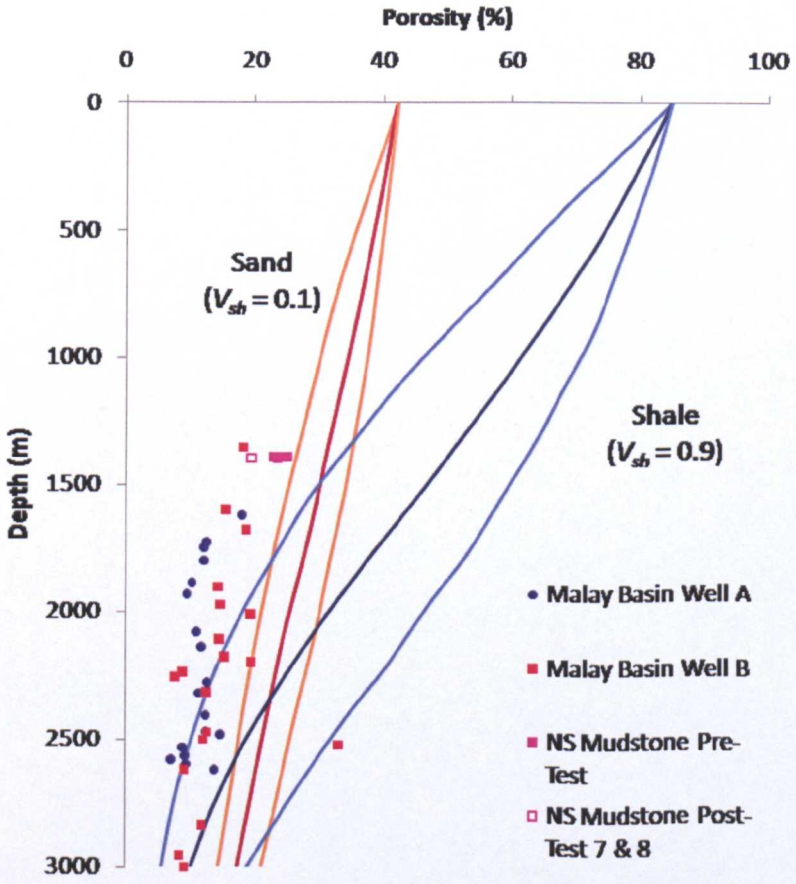

Figure 5.3 Porosity versus depth plot for realively clean sand and nearly pure shale as proposed by the compaction model of Fjaer et al. (2010). The darker red and blue curves show the results if the overburden at any point consists of 70% shale and 30% sand. The lighter orange and blue curves display the results if the overburden consists of pure shale or clean sand. Superimposed on these curves are the data points of samples from the pre and post test North Sea mudstone (Chapter 3) and those from the Malay Basin (Chapter 4).

This is despite being subjected to 50MPa effective stress which should actually take Test 8 (and Test 7 seen further left on Figure 5.3) datapoints off the scale of the Y-axis if plotted according to equivalent depth. Another outcome of the research detailed in Chapter 3 is that despite the mechanisms in operation in the Chemical and Intermediate Compaction Tests, none of the experiments produced "geological" porosities. When plotted at a depth on the graph in Figure 1.5 or 5.1, calculated as equivalent to the stress exerted during the tests, the maximum porosity reduction down to 19.5% in Test 7 (Chemical Compaction Test) still lies with the "experimental" trends above the natural porosities. This is discussed later, however, what is important to note is that the Mechanical Compaction Test (Test 8) did not incur any statistically significant porosity reduction despite being subject to an effective stress of 50MPa.

As stated in Chapter 3, the irrecoverable volume reduction due to temperature depends on the pressure range. The pre-consolidation pressure (previous maximum stress sustained) of natural soft clay depends on temperature, where there is ~1% decrease in pre-consolidation pressure per 1°C increase in the range of 5-40°C and then to a lesser degree at higher temperatures (Leroueil & Hight, 2002). In Test 8, the processes that decreased the volume due to stress and temperature in the North Sea burial environment were more effective than simply significantly increasing stress to 50MPa in the laboratory and surpassing in-situ stress alone does not appear to be associated with the additional permanent reorganization of grain contacts as demonstrated in the cartoon below (Figure 5.4)

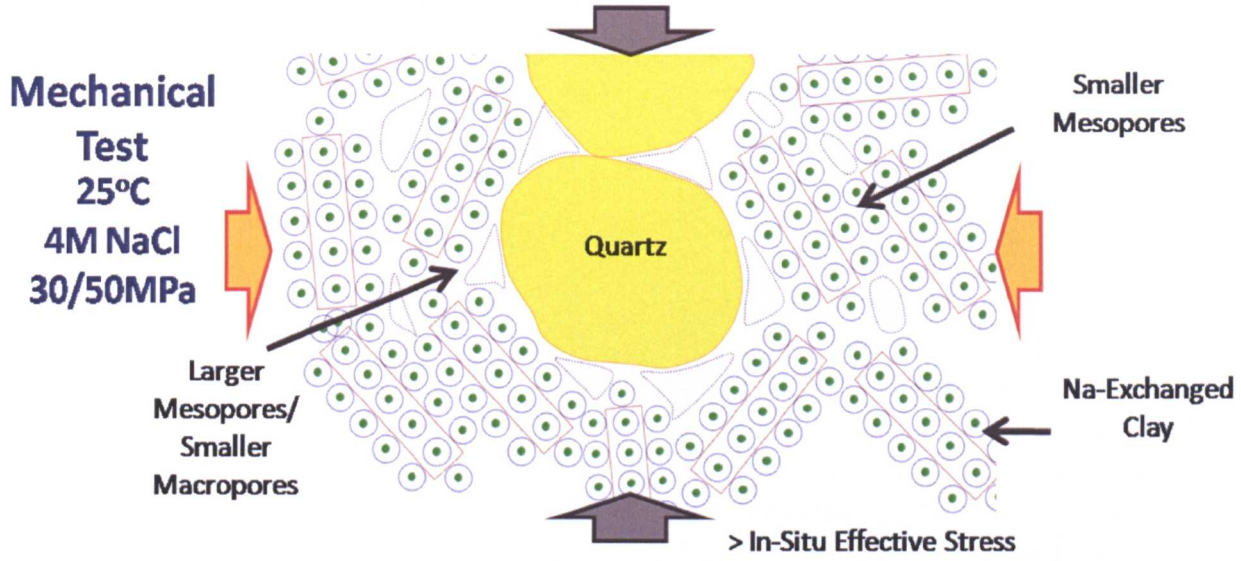

Figure 5.4 Cartoon of suggested grain and pore behaviour during the Mechanical Compaction Test (Test 8). The test was carried out at 25°C, first consolidating to 30MPa effective stress and then 50MPa, whilst flowing an artificial 4M NaCl pore fluid.

However, what is not reproducible in the laboratory is the effect of geological time upon consolidation. Consolidation completes as the sample straining due to the equilibration of pore pressure ceases at t_{100} (the time required to reach 100% consolidation) which forms part of an approximation of the coefficient of consolidation:

$$C_{iso} = \frac{\pi D^2}{\lambda t_{100}}$$

Where D is the samples diameter, λ is a parameter depending on the samples length to diameter ratio and C_{iso} is the consolidation coefficient for isotropic loading (Horsrud *et al.,* 1994). This paper also describes how consolidation dominates the period immediately following increase of load to a saturated rock, but is gradually replaced by the process of creep via a gradual transition.

Creep is a process of long term deformation as a rock is exposed to stress below its yield point. Horsrud *et al.* (2004) published a study on time dependant effects on shale stability based on numerical modeling and experimental work. Their results showed that mechanisms may operate on a timescale of days due to the low permeability of mudstones and shales. Testing the effects of creep, fluid chemistry and temperature on non-smectitic samples in the laboratory (80°C) generated delayed failure within a period of 15 days, whilst altering mechanical properties and weakening both static and dynamic properties.

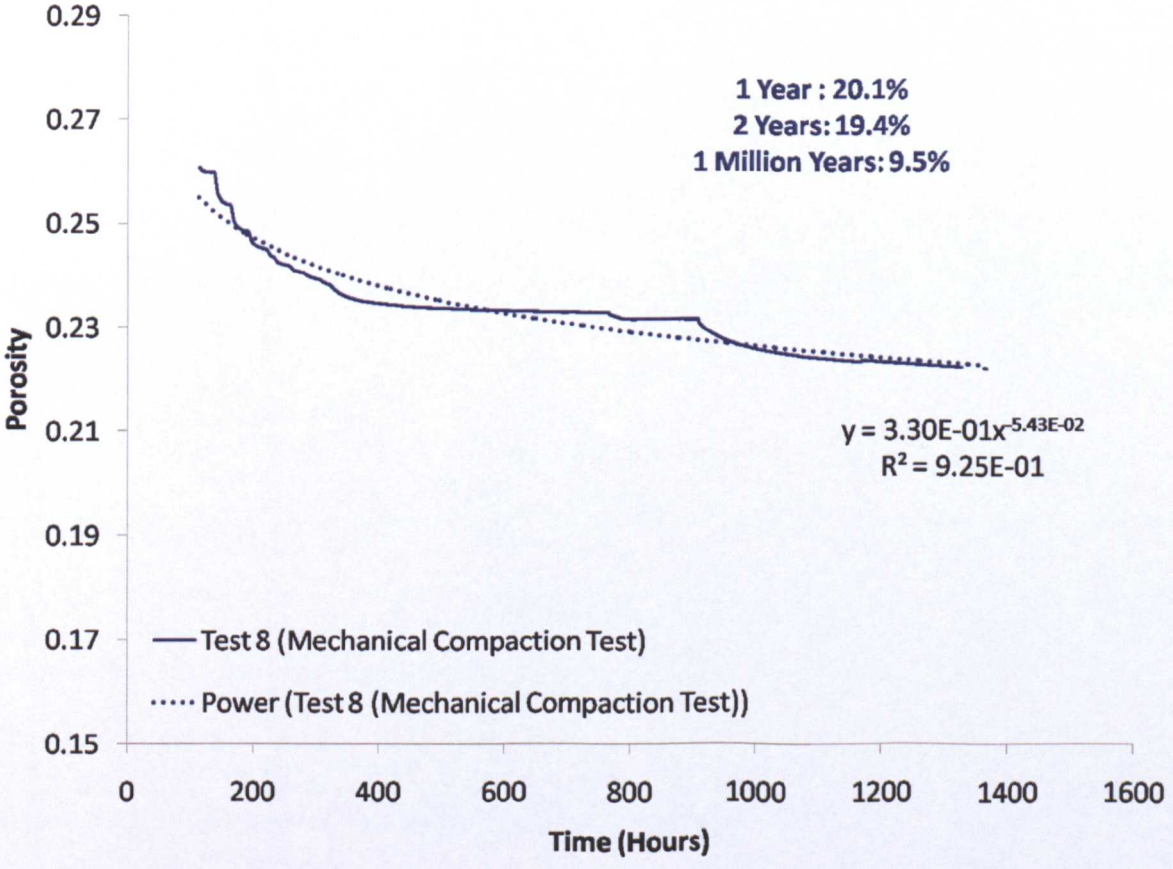

Figure 5.5 Test 8 (Mechanical Compaction Test) mid-test porosity calculations fitted with a power trendline. Using this relationship, some calculated porosities following selected time periods are displayed in blue. The test used 4M NaCl fluid at 25°C whilst it consolidated to 50MPa (final stage).

One of their key conclusions was that the timescale of consolidation is proportional to the permeability and that the longer term process of creep may generate failure at loads significantly below the triaxially determined failure stress. Given that the experiments in this thesis were not designed to measure traditional geomenchanical perameters, calculations such as that to determine the consolidation coefficient for isotropic loading prove difficult in the main compaction simulations. Strain plots and void ratio plots for the extended duration tests indicated that the material was not fully consolidated when the experiments were terminated.

Rough calculations involving fitting a trend through the porosity loss data determined that porosity loss during the Mechanical Test (Test 8), whilst still under 50MPa effective stress could reduce the porosity down to 19.4%, ~ the final MICP measured values of the Chemical Compaction Test (Test 7) after 2 years and down to porosities equivalent to those seen in the more compacted samples of the Malay Basin study in 1 million years just due to compression of the matrix over time (Figure 5.5). Upscaling the results of Test 8 in this way is only used as an indication and has really been included to highlight the fact that Test 7 reached that porosity without the additional time period and that the Malay Basin samples, without 50MPa effective stress (if the deepest Malay samples have been under hydrostatic pressure at some point, at current burial depth, the maximum axial effective stress would be ~36MPa, but given the overpressuring it is actually even less).

5.2 Matrix Collapse As A Consequence Of Thermal Stress

Two temperature related, volume changing mechanisms were identified as operating during the experimental program in Chapter 3. The first involved the lower stress, variable testing triaxial experiments and the second was observed in Test 7, the Chemical Compaction Test.

There was a volume increase generated following a number of the lower stress, variable testing triaxial experiments. The samples compacted whilst under stress inside the cell, but either showed negligible compaction or actual expansion upon removal from the system. In heavily overconsolidated clay (at stresses below in-situ), in the soil mechanics literature, the sample is known to expand upon heating, the rate of which increases with overconsolidation ratio. This is because during the samples consolidation to the maximum stress it has been subjected to, grain contacts will have increased to accommodate the stress. Upon heating, under lower than in-situ stress, expansion of pore fluids will overcome the grain contacts and allow the sample to swell upon removal of stress. The samples in the initial tests were heavily overconsolidated from their burial period in the North Sea compared to test conditions and it is clear from this study that this mechanism proceeds in consolidated mudstones as well as clay soils.

The second mechanism was observed in Tests 4 and 7, the Chemical Compaction Test. Heating the sample and taking it past its in-situ effective stress conditions results in a a process of thermal hardening as described in Mitchell & Soga, (2005) where as temperature increases, the shearing resistance decreases at individual

particle contacts resulting in partial collapse of the of the clay matrix. This is accompanied by a decrease in the void ratio until a sufficient number of additional bonds are formed to allow the mudstone to accommodate the stress at higher temperature. When temperature is decreased there is no secondary volume change as the temperature decrease causes a strengthening of the matrix and no further structural change is required to accommodate the effective stress. This causes an irrecoverable volume reduction due to temperature, but the effect of temperature depends on the pressure range.

Mitchell & Soga (2005) show the derivation of equations describing relationships between pore pressure changes, temperature and porosity under different test conditions. The focus of this thesis was not to establish standard geotechnical perameters for the mudstone and some of the data required to carry out the calculations was not in the required form. The calculations are based on soil mechanics, but the experiments have shown these processes to operate in a consolidated mudstone through the test data and furthermore have provided additional insight by being able to follow-up the tests with reliable MICP due to the consolidated nature of a rock.

As the mudstone is heated, fluid expansion of the pore fluid generates thermal stress upon the matrix, reducing shearing resistance. Larger pores collapse to create a sufficient number of additional contacts to allow the mudstone to accommodate the stress at higher temperature and the mean pore radius reduces. Inter and intra particle pores that were once mesopores or even small macropores are reduced to

form additional, smaller mesoporosity, also reducing permeability of the matrix (Figure 5.6).

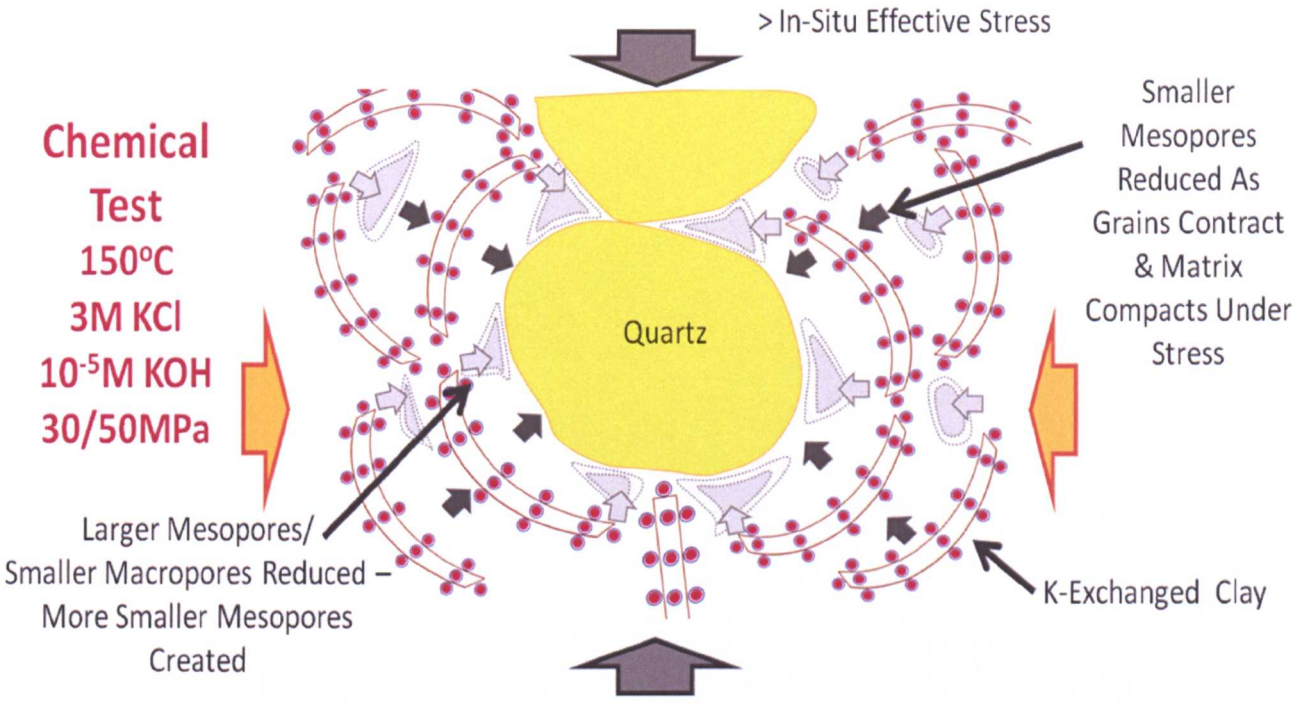

Figure 5.6 Cartoon of suggested grain and pore behaviour during the ChemicalCompaction Test (Test 7). The test was carried out at 150°C, first consolidating to 30MPa effective stress and then 50MPa, whilst flowing an artificial 3M KCl /10^{-5}M KOH solution pore fluid.

Other experiments testing this process in rocks as opposed to soils appear to be limited. An older study by Johnston (1987) describes the deformational properties along with P and S-wave velocities in 3 North Sea Malm shales taken to 80MPa and 100°C. His results infer that deformation in mudstones is dominated by inelastic processes and they show a large change in physical properties with increased temperature. This is demonstrated in Figure 5.7, where the mudstone returns to almost the same dimensions following the 25°C stress cycle, but shows permanent strain following the removal of stress and temperature of 100°C.

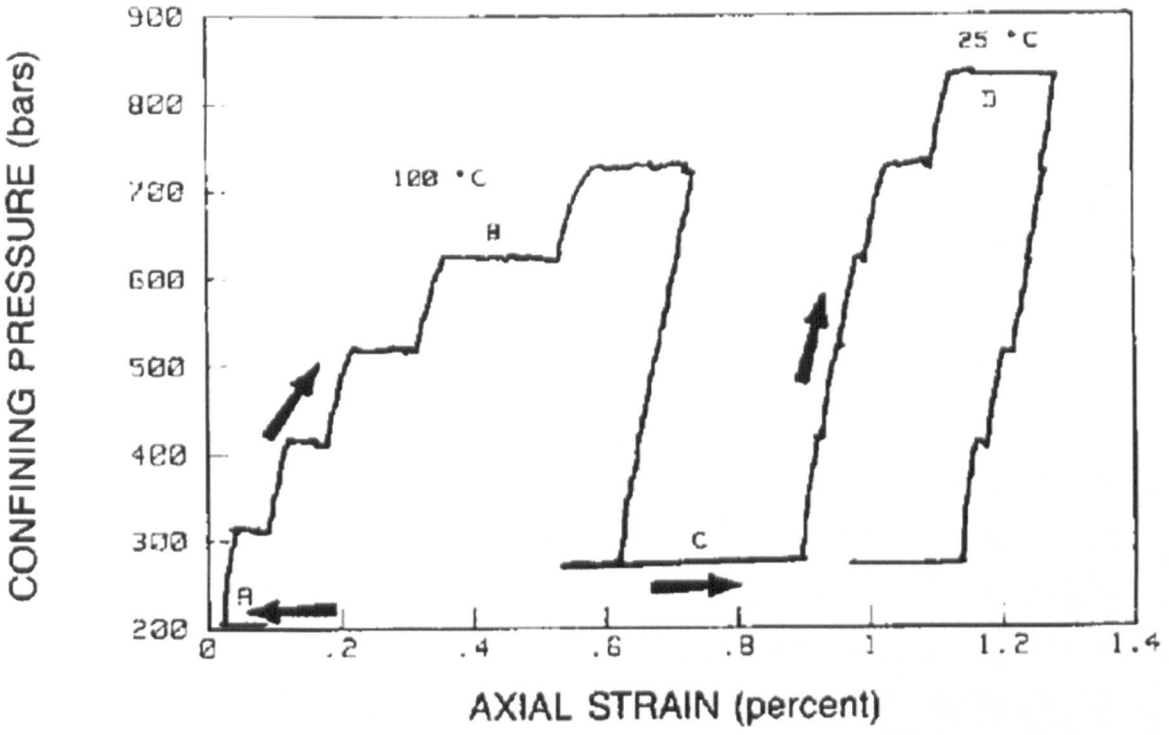

Figure 5.7 Johnston (1987) Hydrostatic loading curve for mudstone sample A. is the initial heating at constant pressure, B is the pressure cycle at 100°C, C. is the cooling at constant pressure and D. is the pressure cycle at 25°C.

There was also a P and S-wave velocity decrease of 10% over the temperature range studied. In the paper the change to velocity is largely attributed to changes to the pore fluid upon heating where the pore fluid will decrease in viscosity and couple with the properties of the solid matrix. There will also be some effect from differential thermal expansion across grain contacts that will influence porosity and thus velocities. This is analogous to the velocity decrease observed in all of the tests coducted at temperature in Chapter 3. The irreversibility of the strain at 100°C is attributed to true plastic flow of the kerogen, which is not recoverable. The paper also states that, at low temperature, this effect is not observed as most of the inelastic strain is taken up by the clays which may recover upon unloading. These are Kimmeridge-type shales with between 5.5 – 12.4% TOC and are different in age and composition to the clay dominated, lower TOC, Maastrichtian North Sea

mudstones used in this study so the hypothesized mechanism of plastic flow of the kerogen is unlikely to be operating and given the results of this study, it is perhaps questionable that it was the only mechanism affecting the Johnston (1987) study. It is likely that if the mudstones were consolidating normally (past in-situ stress), that the clays did not necessarily recover upon unloading and they actually constituted part of the rock undergoing irreversible strain.

In more recent experimental work by Moustafa *et al.* (2008), the increased strain that results from increasing temperature during testing of Tournemire shale was presented. The TOC content of this shale is not discussed in the paper but its mineralogy shows it has low abundance of expandable clays. It offers no real description of mechanism to explain the results.

Some aspects of the theory in Mitchell and Soga are clearly more applicable to lower temperature, civil engineering environments. However, although still on unlithified samples from the IODP, the sediments in Hüpers *et al.* (2010) are geological samples that have been heated to ~110°C offshore Japan. They carried out laboratory measurements and calculations using an adapted Cam Clay model to incorporate thermal hardening by Picard (1994), which has also been used to predict behavior of the Boom clay in Sultan *et al.* (2002). They found that without accounting for thermal hardening of the samples, calculations overpredicted the pre-consolidation stress. This means that tests upon the recovered core appeared to indicate it had seen higher stress than it had and it was more consolidated than expected by unadapted models due to the effects of temperature. Given this information, the temperature adapted Cam Clay model:

$$P_{c\_corr} = P_c \times \exp[-3 \times ((1 + e_0)/(\lambda - k)) \times a_p \times \Delta T]$$

where P_{c_corr} is the corrected pre-consolidation stress for in-situ temperatures, P_c is the pre-consolidation stress measured under standard conditions, e_0 is the initial void ratio, λ is slope of the plastic consolidation curve, k is the slope of the elastic rebound curve, a_p is a positive scalar coefficient and ΔT is the temperature difference between in-situ and test conditions, could quantitatively describe the lack of compaction seen in the Mechanical Compaction Test, Test 8. If the statement that the mudstone in Test 8 did not compact further as it has compacted in the burial environment to an arrangement of grain contacts accommodating overburden and thermal stresses that is greater than the 50MPa laboratory test conditons at 25°C, then the above equation could be used to recalculate what the real stress conditions of the burial environment were. This would require further information that these tests do not give. Standard conditions were not employed in these tests and the hardening coefficient a_p is unknown for this material. Further work and completing more standard geotechnical testing of the North Sea mudstone could take this further.

Where high temperature and high effective stress were applied, burial stress conditions were surpassed and the grain contacts rearranged. This perhaps best observed in porosity distributions (Figure 5.8).

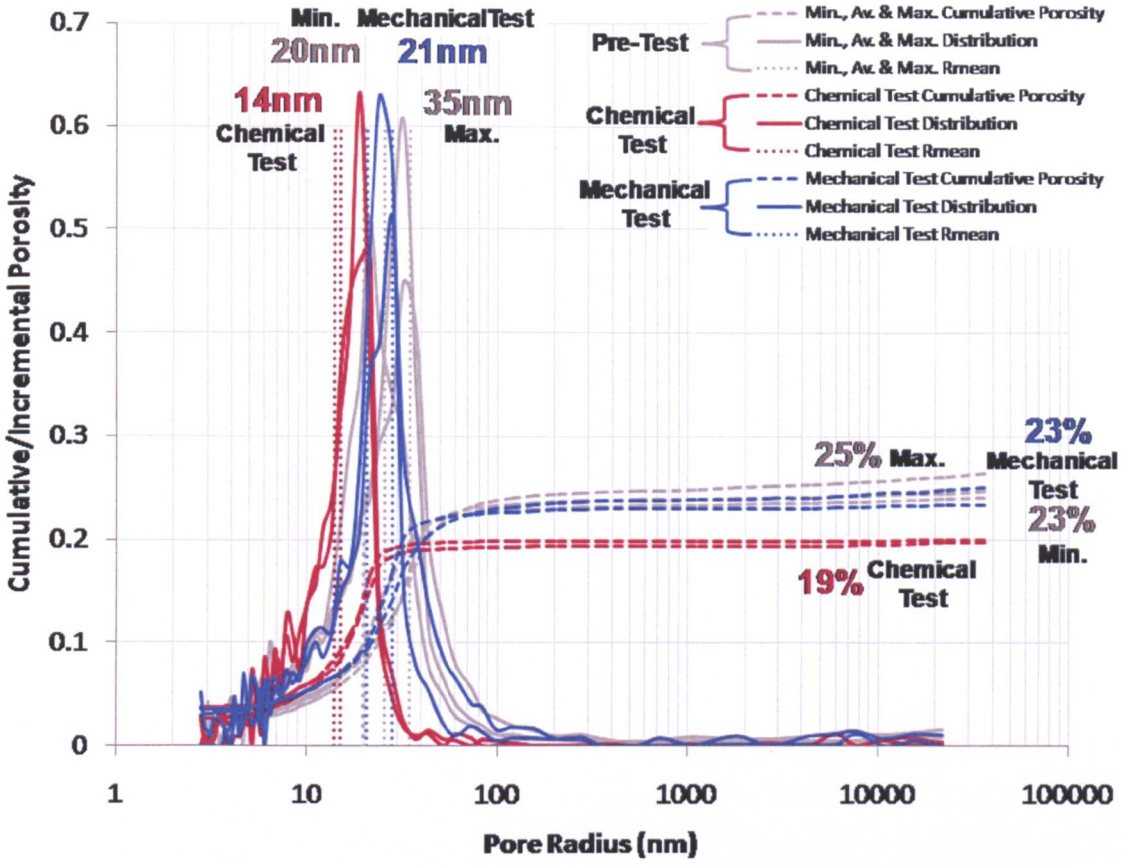

Figure 5.8 Mercury injection porosimetry data for pre-test mudstone (grey) and post-test material from both the "chemical" compaction (red) and "mechanical" compaction (blue) triaxial tests. Whilst the porosity and Rmean values for the mechanical test lie within the range of the pre-test samples, porosity reduces to 19% and Rmean decreases to 14nm following the chemical test.

Yet it is important to remember, given the results of Test 9 (Intermediate Test), that a proportion of the ~5% porosity loss is due to K-exchange. Also, despite restructuring of the grain contacts, no statistically significant alignment is observed and with 19% porosity compacted under an axial effective stress of 50MPa, even the chemical compaction test does not match the natural porosities of mudstones consolidated to 50MPa effective stress in the burial environment. Other processes must be operating in the burial environment that are not matched in the laboratory.

Again, as discussed in the previous section, one unmatchable variable is time. Similar calculations as described in 5.1 were carried out for the Chemical Compaction Test, Test 7 and the results are displayed in Figure 5.9.

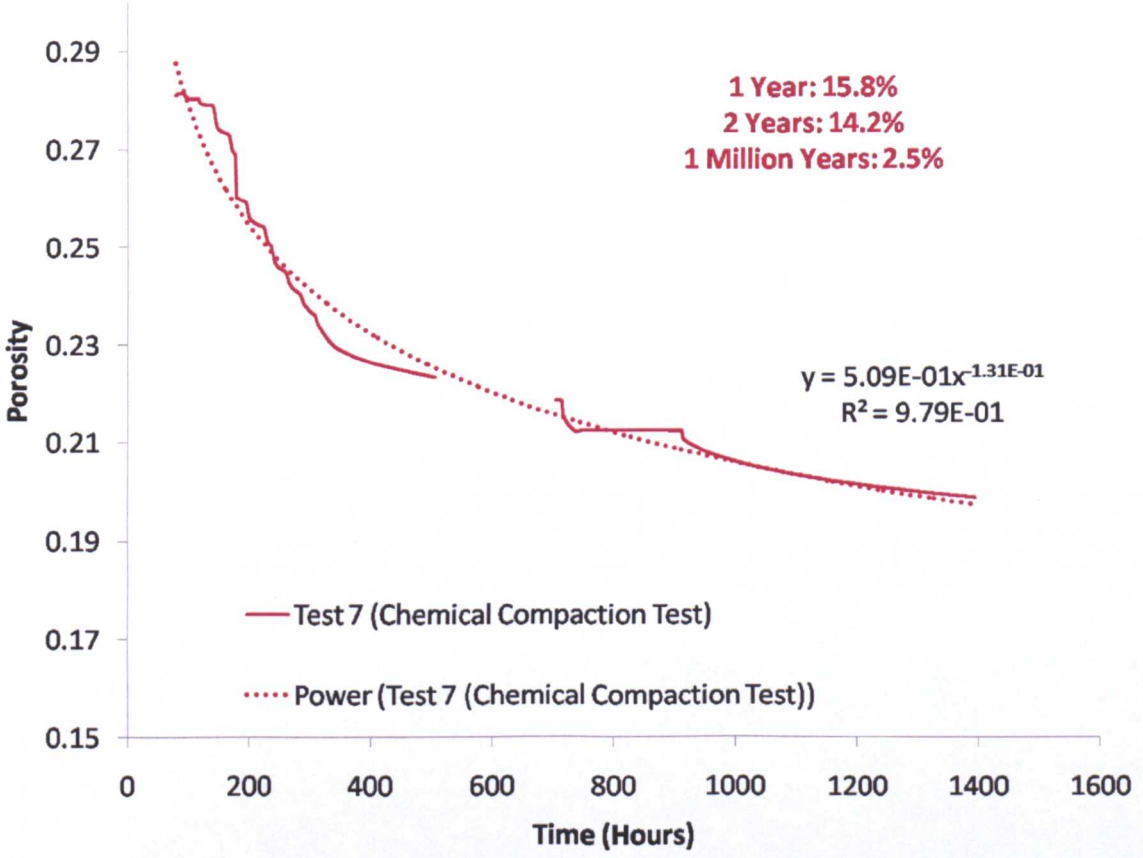

Figure 5.9 Test 7 (Chemical Compaction Test) mid-test porosity calculations fitted with a power trendline. Using this relationship, some calculated porosities following selected time periods are displayed in red. The test used 3M KCl with 10^{-5}M KOH fluid at 150°C whilst it consolidated to 50MPa (final stage).

If consolidation followed the trend calculated through the data over the test period and was extended to keep the sample under 50MPa for a period of 1 year, porosity would start to reach natural values of porosity at depth (15.8%). This is using conditions at 150°C, but also, it should be remembered, providing K-rich pore fluids which allow the expandable clays to take on more illitic characteristics. Again, these calculations are simplistic and should be used as a guide only.

The mechanical effect of temperature could be at work in the Malay Basin samples, reducing the porosities to the tight values measured in the relatively shallow samples. Where more standard geotherms are prevalent and effective stress relationships are utilised employing statistically derived coefficients, the normal effects of thermal stresses exerted under a standard gradient could already be incorporated by proxy, via the coefficients. Once these effects are enhanced in a region of high gradient, such as the Malay Basin, they could be partially or completely behind the enhanced compaction observed in the MICP data. However, given the advanced diagenesis of the sampled section, differentiating between the thermo-mechanical effects and any compaction associated with illitization and/or grain alignment is difficult.

5.3 Chemical Alteration And Alignment Resulting From Mineralogical Change

5.3.1 Effects of Chemical Alteration

The results of Test 7 (Chemical Compaction Test) were discussed in the previous section with the enhanced compaction due to the effects of temperature. However, it did compact along with Tests 4 and 9, in part, because of K-exchange at greater than in-situ stress. The effect of this isolated from the thermo-mechanical meachanisms can only be observed in Test 9. Once in-situ stress has been surpassed, the mechanism for compaction in Test 9B/Intermediate Test is the shrinkage associated with reduction of the interlayer "pores" and exchange on the clay surfaces which reduce the associated portion of the microporosity and smaller mesoporosity in the inter and intra particle network of the clay matrix, perpendicular to bedding (Figure 5.10).

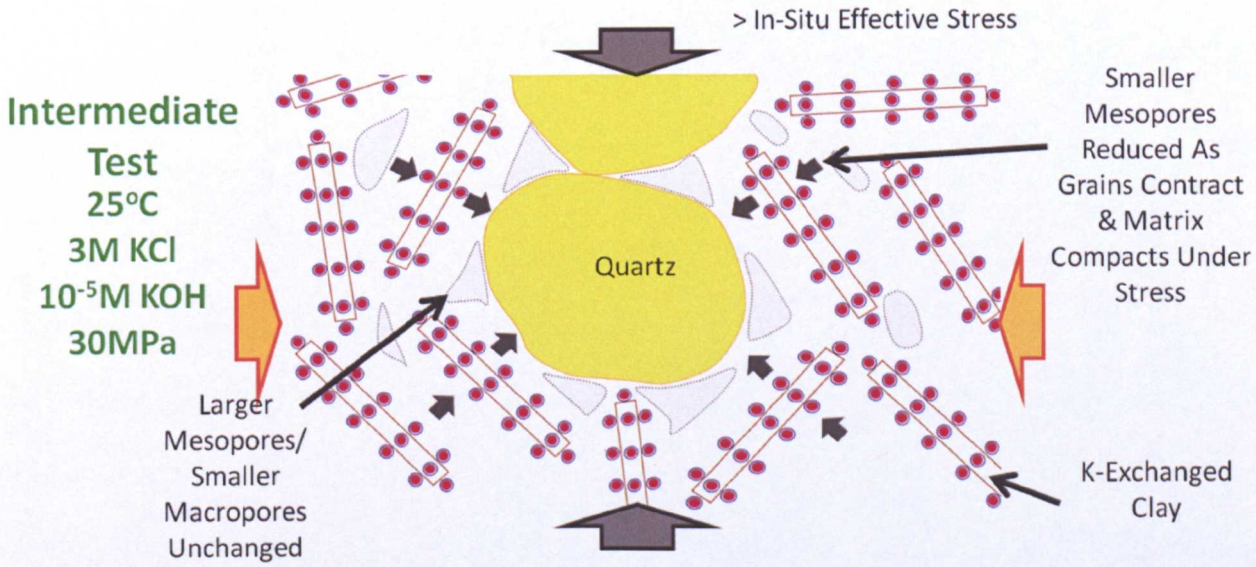

Figure 5.10 Cartoon of suggested grain and pore behaviour during the Intermediate Compaction Tests (Tests 9A & B). The test was carried out at 25°C, with Test 9B consolidating to 30MPa effective stress, whilst flowing an artificial 3M KCl /10^{-5}M KOH solution pore fluid.

Diffusion is efficient enough to alter mechanical properties and KCl effects are persistent. Further stabilisation appeared to be generated by the small pH increase and its effect on the clay minerals. This is despite the prevalence of the finer clay minerals in the North Sea mudstone.

The reasoning behind why the mudstone compacts as other cations are exchanged for K can be found in the literature on wellbore stability (Steiger, 1982; Van Oort, 2003; Yu et al., 2001; Horsrud et al., 1998; Sonstebo & Holt, 2001; Ghassemi & Diek, 2003; Van Gijtenbeek et al., 2006) and also on soil mechanics and slope stability (Di Maio & Fenelli, 1994 and Di Maio, 1996). Mudstone-fluid interaction can result from a number of processes including advection where ions follow Darcy flow of the fluid due to hydraulic pressure, diffusion where ions move in or out of the mudstone due to the chemical potential difference and osmosis/hydration where water is transported in or out of the mudstone via the semipermeable membrane of the mudstone surface due to the chemical potential (Horsrud *et al.*, 2004).

Steiger (1982) discusses the use of potassium in drilling fluids and its uses. The main use of potassium is as a stabilizer, where it exchanges into and onto the clays and reduces their hydration energy, limiting their capacity to swell. The shrinkage of a mudstone associated with stabilization with K^+ creates a strain which is described in Horsrud et al. (1998) and Sonstebo & Holt (2001) as having an effect analgous to thermal stress and described it by adapting the thermoelastic relationship (around a borehole). As with Test 9, plastic deformation described in Horsrud *et al.* (1998) due to potassium exposure is greater in the axial direction than the radial. The permeability increased by 2.6 times due to shrinkage of clay structure opening of

new flow channels or enlarging old ones. Given the high effective stresses involved in the tests of this thesis, any shrinkage associated permeability would not remain open during the experiments and would add to compaction.

In Horsrud *et al.* (1998) when a KCl fluid was used, most of the observed increase in ultrasonic velocity could be explained by changes in the pore fluid compressibility associated with increasing salinity but longer term trends showed reduced velocities associated with alterations in stiffness/strength. The compressibility at temperature would play a part in the velocity increases in Test 7 (Chemical Test), but due to the high effective stresses used the velocity reduction trends were not observed as the material compacted and grain contacts were increased. It is therefore inferred that the velocity trend in Test 7 is not only down to salinity at temperature, but also due to compaction.

As well as the exchange of potassium and its effects on stability, other chemical interactions can also assist with borehole stability, or in the case of this thesis, stability during triaxial testing. Other cations can be used to depress the water activity of a solution and establish an osmotic potential against the semi-permeable membrane of the mudstone surface, drawing water from the formation with stabilizing effects (van Oort, 2003). These cations include Na^+, Ca^{2+} and Mg^{2+}. K^+ generates less effective osmotic pressure (range of 0.1-1.0 MPa compared with 1.0-10 MPa for Ca^{2+} and Mg^{2+}). The paper also discusses the different rates at which the differing fluid interaction processes operate. Pressure transmission, generated from flow of water into or out of the surface of the mudstone, is the most rapid and operates on a scale of decimeters per day. Solute/ion diffusion takes place at

centimeters per day, which is one to two orders of magnitude faster than Darcy flow of mud filtrate/bulk water which proceeds at millimeters per day under down hole conditions.

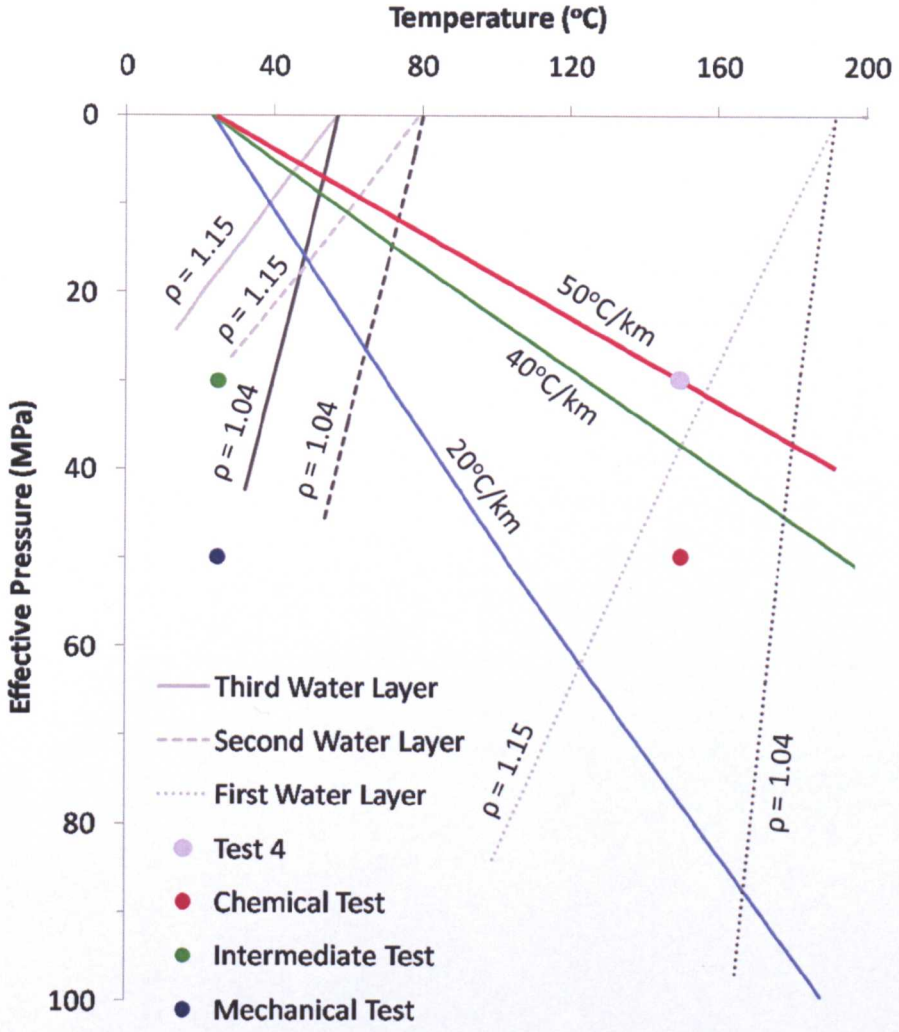

Figure 5.11 Adapted from Colten-Bradley (1987). A comparison of differential pressure system (analogous to mudstone compaction) dehydration curves for interlayer water densities of 1.04 and 1.15g/cm^3 with geothermal-effective pressure gradients. Thermal gradients of 20 and 40°C/km are plotted with the additional 50°C/km gradient which is relevant for the Malay Basin which is discussed in Chapter 4 (though overpressure in that basin would alter the gradient with respect to effective stress). Total effective pressure, $P\sigma = P_L - P_H = 0.535P_L$, where P_L is 0.0226 MPa/m. Test 4, Test 7 (Chemical Test), Test 8 (Mechanical Test) and Test 9B (Intermediate Test) are plotted according to test temperature and axial effective pressure.

This effect is also mentioned in Yu *et al.* (2001) describing how the order reverses in a sandstone, where Darcy flow will be faster than diffusion and will dominate interaction. These rates indicate that potassium exchange was expected on the

timescale of the test and this was confirmed with XRD measurements and EDX. It also indicates that despite the greater hydration energy exerted when Na-fluid was used in Test 8 (the Mechanical Test), the osmotic potential would have been larger than with K-rich fluid and is probably why little stability difference was observed in the pre-test fluid compatability tests between the concentrated Na and K fluids.

The reduction in hydration energy associated with K-exchange is behind the shrinkage of the interlayer in Test 9 and compaction of associated micro-meso porosity. However, this must be balanced with the dehydration associated with stress and temperature increase described in Colten-Bradley (1987) (Figure 5.11).

Once exchanged, Test 9 fluid densities would be expected to approximate the 1.15g/cm^3 conditions, meaning that at maxiumum test conditions it could be expected to have lost its third water layer and be close to losing its second due to P-T constraints. Whereas, Test 7 is dehydrated due to P-T conditions, leaving Test 9, the Intermediate test as the only test to show the compaction effects of potassium exchange clearly.

As potassium was exchanged into the interlayer of the clays in the mudstone during Test 9 (A and B), further dehydration could take place through the removal of other hydrated cations allowing shrinkage down to ~10Å and compaction of the mustone matrix without destabilization of the matrix and loss of the larger pores. This is because the matrix is not rearranging to accommodate greater stress, it is simply shrinking in a particular direction – perpendicular to bedding. Despite taking on more illitic characteristics, the compaction associated with the K-exchanged expandable clays does not match natural porosities over the timescale of the tests in this thesis.

This may be a time factor as described in the previous section or it may be because the actual conversion to illite in the burial environment is associated with further compaction mechanisms.

5.3.2 Effects of Full Mineralogical Change

The effects of full mineralogical transformation were not observed in the experimental program despite best efforts to optimize conditions. This was mainly due to the temperature constraints of the cell.

Osborne & Swarbrick, (1997) describes the smectite to illite reaction as being kinetically controlled but is in agreement with Manning (2003) that there is no conclusively defined kinetic or physical mechanism. Early work on the kinetics of illite formation such as that of Eberl & Hower (1976) described the appearance of illite layers forming mixed-layer I/S using the first-order kinetic equation:

$$\ln\frac{a}{(a-x)} = \mathrm{kt}$$

where a is the initial concentration of smectite, x is the amount of smectite that has reacted to form illite after t days and therefore (a-x) equals the amount of smectite layers in I/S. The rate constant is determined from:

$$\mathrm{E_a} = \frac{\Delta log_{10} k}{\Delta 1/T}\ 2.303\ R$$

Where Ea is the activation energy, R is the gas constant and T is the absolute temperature. Run times of 88-169 days were recorded for the conversion (incomplete – 35-15% S in I/S remaining) of expandable material at temperatures

>152°C using KCl fluid. In nature smectite to illite conversion occurs below 150°C, but in Eberl & Hower (1976) the test at 152°C showed little tendency to convert after 100 days. Calculations based on these kinetics preclude illitization at 150°C. However, lack of a conclusive rate equation and/or model (rate equations have been proposed such as those by Pytte & Reynolds (1989), Altanar (1986), Huang *et al.* (1993) and reaction mechanism and/or kinetic models include Bauer & Berger (1998) Howard & Roy (1985) Cuadros & Linares (1996) Velde & Vasseur (1992)), along with optimisation of other parameters (for example, elevating pH and flushing additional KCl into the system initially), in addition to other information encouraged the tests.

The initial XRD behavior also gave misleading indications on illitization as discussed in Chapter 2. This was also recorded in Mosser-Ruck *et al.* (2001). Attempted illitization of a K-smectite using a 0.5M solution of KCl at 300°C did not succeed. The reason is cited as too short an experimental time period (<6months). Such temperatures and timescales produced significant illitization according to Eberl & Hower (1976). However, Mosser-Ruck *et al.* (2001) also highlighted the issue with potassium exchanged smectite XRD behavior as observed in this project. Material identified as illitized through XRD analysis was shown to be still exchangeable with NH_4^+ prior to infrared spectroscopy.

Work by Bauer & Velde (1999) and Hunnur (2006) indicate that to produce significant illitization under laboratory conditions, very high pH fluids must be utilized which were not compatible with the equipment involved in these tests. However, it should be noted that it would appear that samples in Bauer & Velde (1999) were only

washed with de-ionized water prior to XRD preparation, which given the method development results in Chapter 2 may influence their conclusions. Another lower temperature (50°C), high pH study (using 0.1, 0.5, 1M KOH with seawater) was recorded in Drief et al. (2002) over 30 days. That paper found that XRD analysis of the test materials using seawater and 0.1M solutions did not display any illitization. However, the higher pH and K molarity solutions generated a broadening of the smectite peak and disordered I/S and illite formation. The XRD analyses were confimed by TEM/AEM studies.

Any insight into the compaction mechanisms associated with full mineralogical change must therefore be derived from the Malay Basin sample work program. The relationships displayed in Figure 5.12 below were already described in Chapter 4.

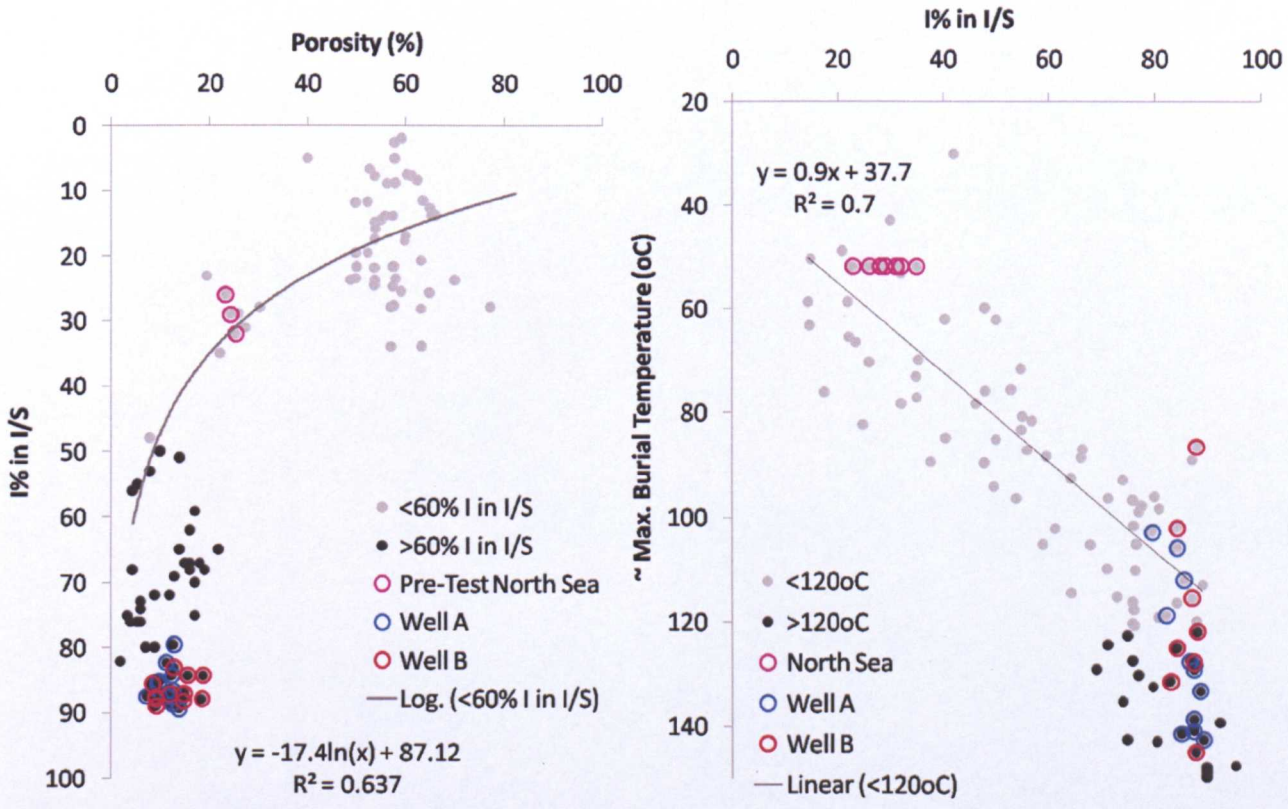

Figure 5.12 I% in I/S with porosity and maximum burial temperature with I% in I/S with data from this study highlighted. *Left:* Composite plot with data from Schoonmaker Tribble (1990),

Day-Stirrat et al. (2008); Aplin et al. (2006) and Day-Stirrat et al. (2010) and this study. Samples are shaded according to illitization. The pre-test North Sea average, minimum and maximum values from Chapter 3 are highlighted in purple and the data from Wells A and B in the Malay Basin are highlighted in blue and red, respectively. *Right:* Composite plot using data from Eberl & Srodon (1984), Day-Stirrat *et al.* (2008), Aplin *et al.* (2006), Day-Stirrat et al. (2010) and Ho et *al.* (1999) and this study. Samples are shaded according to maximum temperature. The North Sea values from Chapter 3 are highlighted in purple and the data from Wells A and B in the Malay Basin are highlighted in blue and red, respectively.

The Malay Basin porosities that looked anomalous when plotted against depth, plot on trend when plotted with I% in I/S. Similarly, the I% in I/S data appears considerably more mature than those from other locations when plotted against depth. However, when plotted against temperature the data ties in with several other studies. This would appear to support the hypothesis that elevated geothermal gradient is facilitating more rapid diagenetic change which also appears to correlate with enhanced porosity loss.

The relationship between temperature increase with depth is stated as the geothermal gradient which for the study wells in Chapter 4 is ~48°C/km. Using the relationship in Figure 5,12 (*right*) maximum burial temperature and illitization can provide an estimate of I% in I/S at a particular temperature. Through the relationship displayed in Figure 5.12 (*left*), once the I% in I/S is determined, porosity can be estimated over the early diagenetic window. Putting these relationships together allows some estimate of porosity to be made as a result of illitization if the depth and geothermal gradient are known as below:

$$\varphi = e^{\frac{(((\mathrm{D\ x\ GG})-37.72)/0.86)-87.12}{-17.40}}$$

Where φ is porosity, D is depth and GG is geothermal gradient. However, as can already be observed visually from the trend on which it is based (Figure 5.12 - *left*)

and its fit through the Malay Basin data, this underpredicts the Malay mudstone porosities. Further work on the porosity-I% in I/S relationship may improve results.

As the previous sections have shown that the effects of expandable clays assuming illitic characteristics does not necessarily generate geologically realistic porosities (at least on the timescales used in these tests), other mechanisms associated with full transformation only were investigated. As statistically significant grain alignment had not been observed in the North Sea mudstone tests and high alignments were measured on the Malay Basin samples this was explored further.

The pre and post-test alignment in the North Sea mudstone was in general agreement with the preferred orientation which one can expect as a result of mechanical compaction (Voltolini *et al.* 2009). This is seen in Figure 5.13.

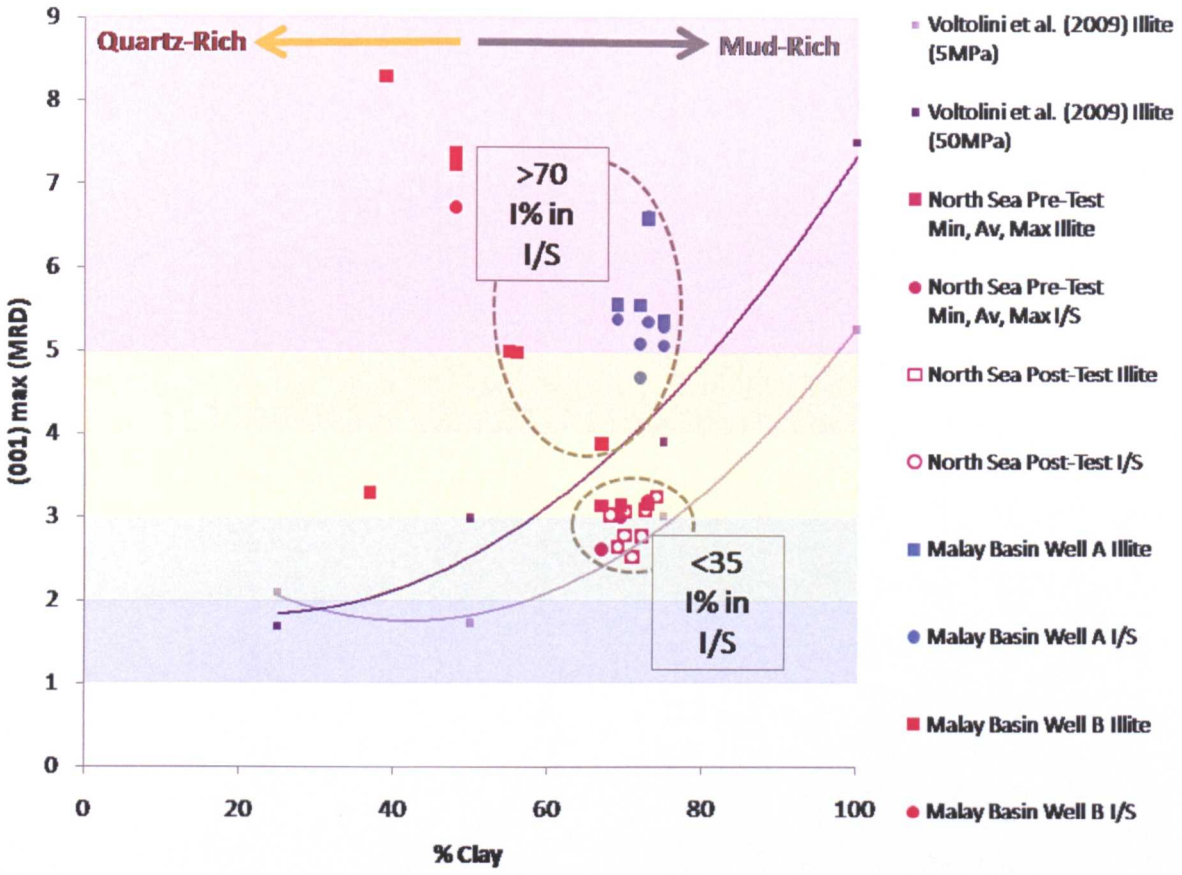

Figure 5.13 Alignment with clay abundance for North Sea samples from Chapter 3 and Malay Basin samples from Chapter 4 in relation to illite alignment trends at 5MPa and 50MPa from Voltolini *et al.* (2009).

The Malay Basin samples display moderate to high alignment that no longer conform to the data set out in Voltolini *et al.* (2010) for samples having undergone mechanical compaction. These natural, high temperature samples show high alignment values with lower stresses and clay contents (65%). Although more quartz-rich sections do show deviation from trends, with larger, non-elongate grains thought to disturb the alignment of clay minerals as the sediment compacts (Day-Stirrat *et al.*, 2010).

One model for alignment related porosity loss is that the formation of an aligned clay fabric, where neoformed clay grains grow perpendicular to the principal effective

stress, increases grain contacts and thereby reducing pore space. Other datasets such as that of Ho *et al.,* (1999) indicate that this may not be a continuous process, but is linked to the restructuring that comes with ordering at an advanced stage of illitization.

This may explain why a broad range of alignments were observed in the mudstone dominant Well A, despite the interpreted advanced illitization even amongst the shallower samples. The shallowest sample that retained its individual, glycolated smectite peak and had associated alignment measurements gave a value only slightly above the North Sea mudstone values. This sample was interpreted as being close to the R1 ordering threshold. The other samples were more mature mineralogically and therefore more advanced in ordering and were also associated with high alignment values.

The dataset is relatively small to make firm conclusions and so compilation plots were constructed using other datasets and can be seen in Figures 5.14 and 5.16. The compilation includes data from basins of low (Gulf of Mexico – Ho *et al.*, 1999), average (North Sea – this study) and high (Malay Basin – this study) geothermal gradients where due to the kinetics of the reaction mean the transformation will be proceeding at different rates with depth. A trend between the datasets emerges where alignment increases with advancing illitization.

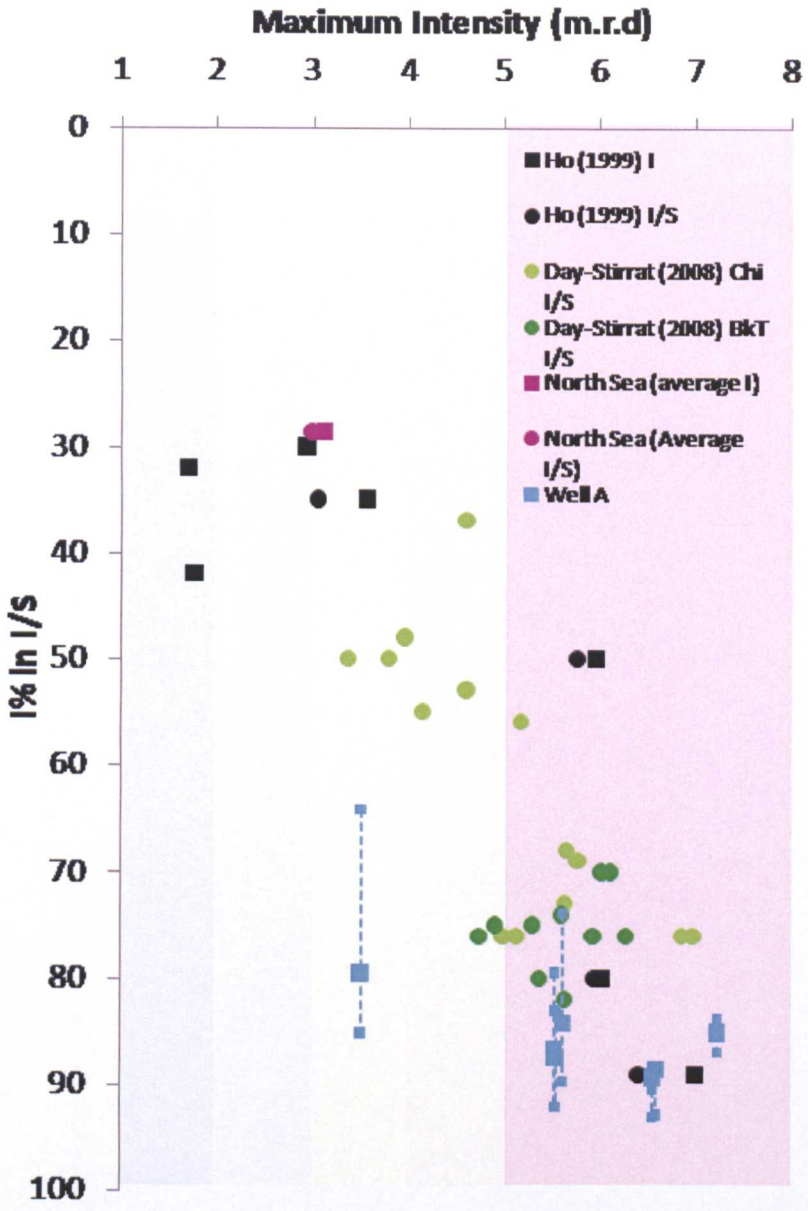

Figure 5.14 Alignment in m.r.d. against illite % in I/S for samples from Well A from Chapter 4 and the North Sea mudstone of Chapter 3 compared to previous published studies.

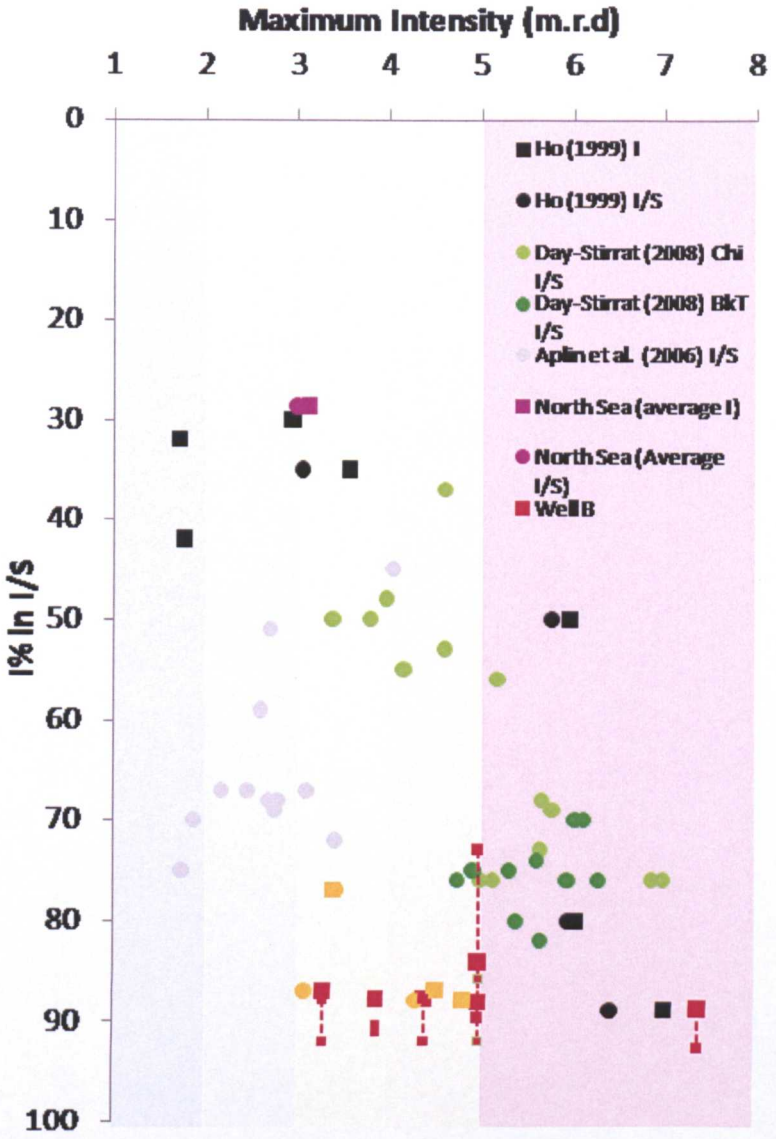

Figure 5.15 Alignment in m.r.d. against illite % in I/S for samples from Well B from Chapter 4 and the North Sea mudstone of Chapter 3 compared to previous published studies.

The abundance of clay minerals and quartz varies greatly between the two Malay Basin wells. Well A is more uniformally mud-rich, where as the shallowest section (tidal-marine facies) of Well A is more mud rich but quartz content increases in the fluvial-lacustrine horizons until the slightly more mud rich horizon sampled at 3000m (despite selective sampling). The quartz content has a relationship with numerous other measured perameters – I% in I/S, grain size distributions, porosity and

permability. Also, it may exert some control on the alignment achieved in the phyllosilicate matrix. Lower quartz content samples in Well A plot roughly with the published trends for I%in I/S with alignment (along with the North Sea mudstone from Chapter 3). However, the more quartz rich samples from Well B plot with the quartz rich samples of Ho *et al.* (1999) in Figure 5.15. The model describing the way in which higher quartz content disrupts the alignment of clay minerals can be seen in Figure 5.16 from Day-Stirrat *et al.* (2010) below.

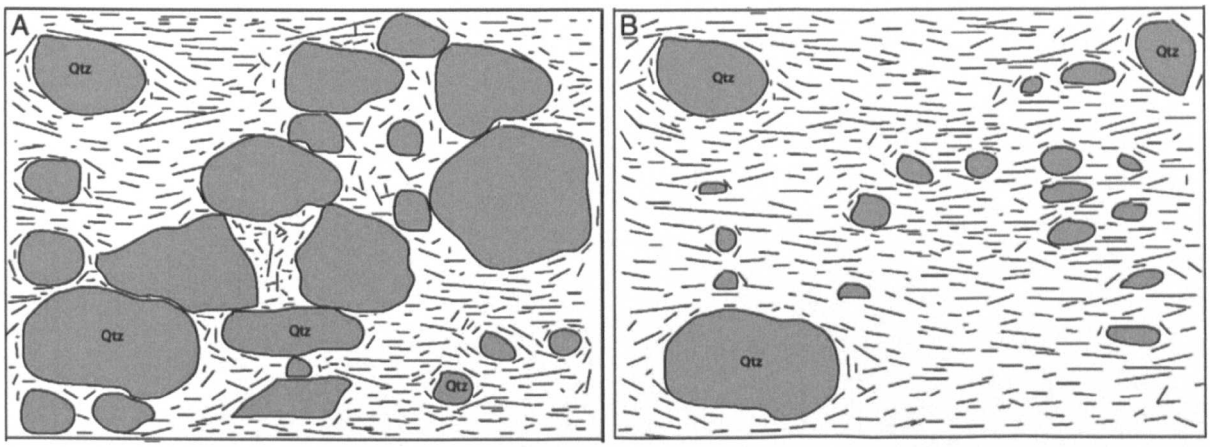

Figure 5.16 Images from Day-Stirrat *et al.* (2010) depicting the effects of higher and lower silt size quartz content in (A) and (B) respectively affects the phyllosilicate alignment.

The Day-Stirrat *et al.* (2010) model infers that silt size quartz grains in contact create pressure shadows, shield the phyllosilicates from the overburden effective stress and thereby do not generate alignment. In a more phyllosilicate-rich system, most clay grains are subject to the vertical component of effective stress and align accordingly. The presence of quartz can be seen to have a negative effect with alignment which can be seen in the BSEM images in this thesis.

Adding additional study data to Figure 5.13, Figure 5.17 displays alignment with clay abundance plotted with the mechanical compaction trends for illite and data classified according to illitization.

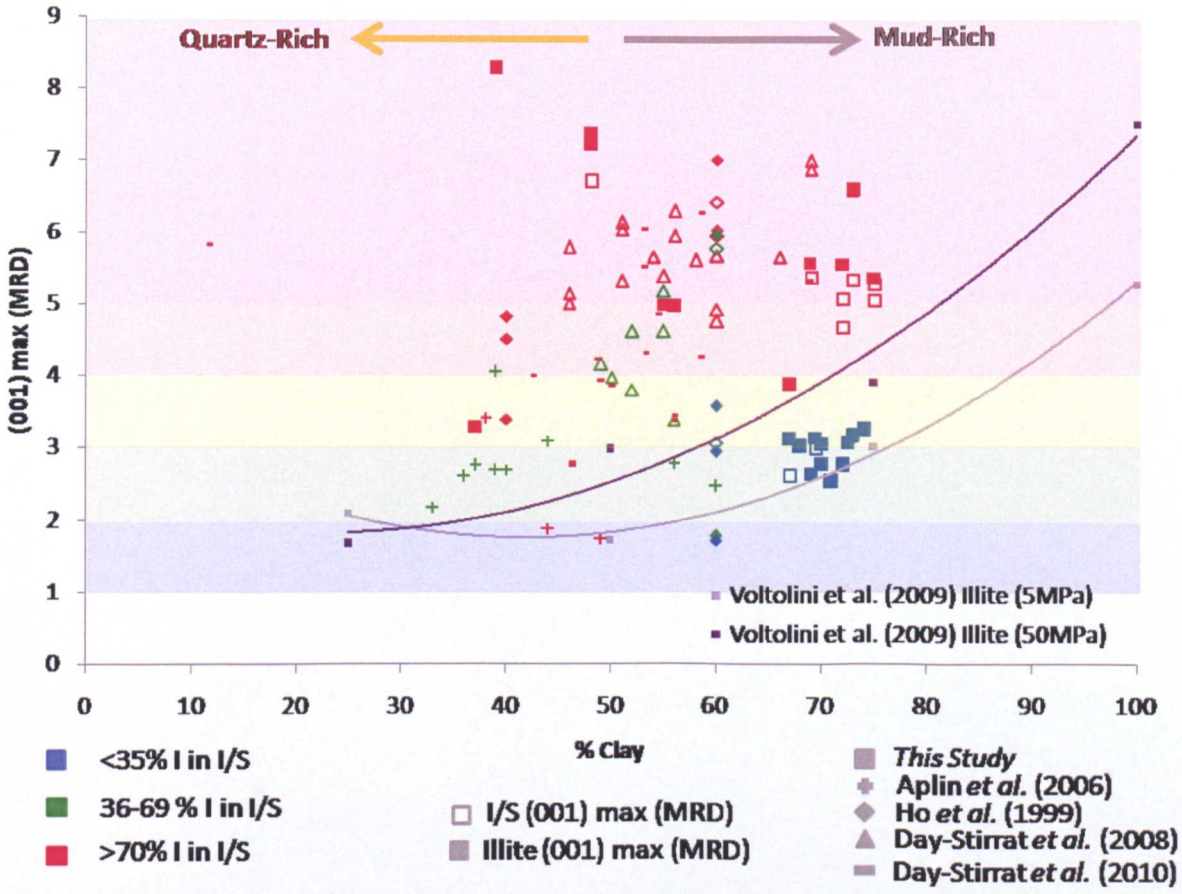

Figure 5.17 Alignment with clay abundance for samples from this study and other published literature in relation to illite alignment trends at 5MPa and 50MPa from Voltolini et al. (2009), classified according to illitization. Nb. Samples of the Ho *et al.* (1999) study are described as clay-rich mudstones, but clay abundance is not detailed. An arbitary value of 60% was allocated to give an indication of how pre and post-transition data would appear.

The scattered data does show that a degree of alignment can be attained mechanically as shown by the Voltolini et al. (2009) dataset and pre-transition mudstones. However, at higher mineralogical maturity, mudstones show greater alignment than predicted by mechanical compaction alone lending support to the

mixed mechanism alignment with depth model displayed in Haines *et al.,* (2009) (Figure 5.18).

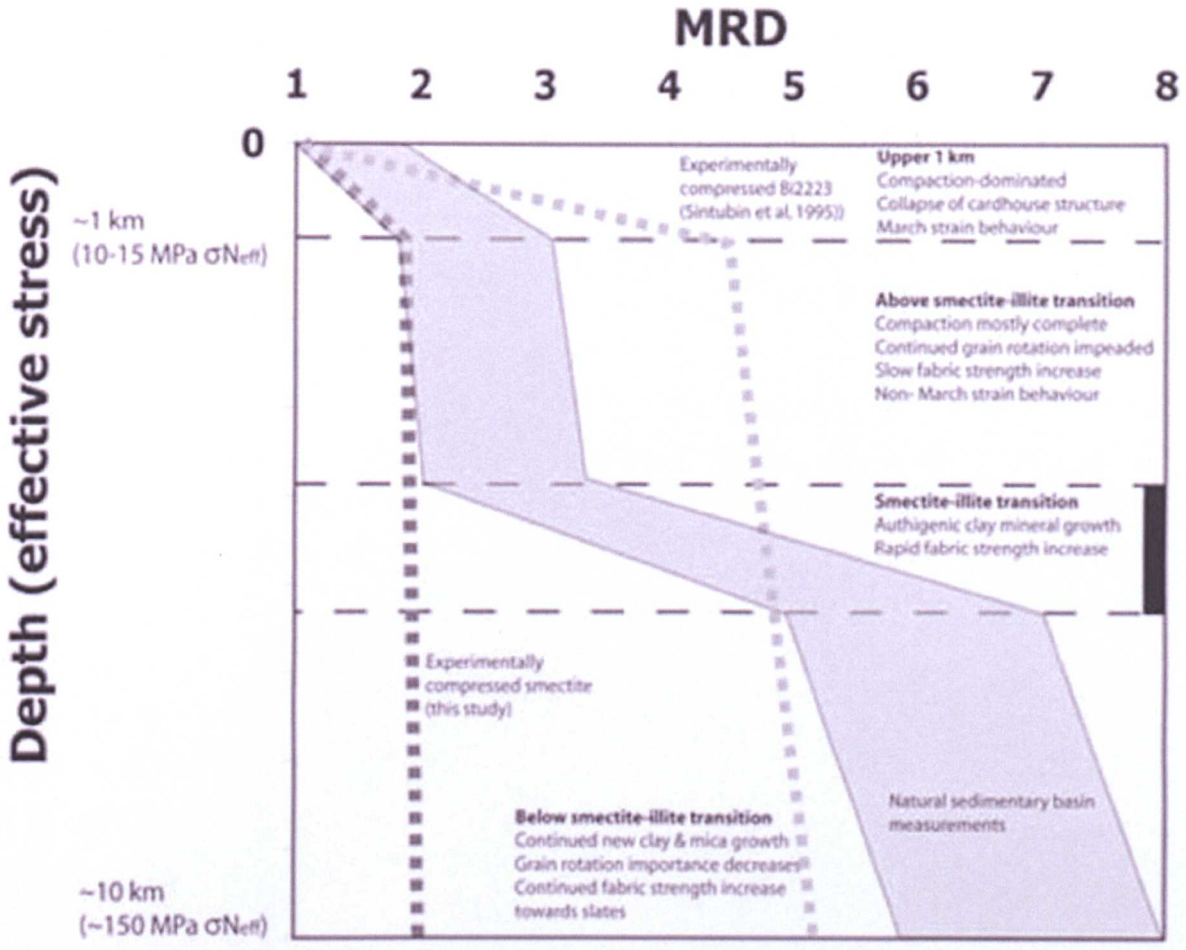

Figure 5.18 Descriptive plot of alignment in MRD with Depth for natural samples or Effective Stress for artificial samples Haines *et al.* (2009).

To understand if this mineralogical transformation and its coincidence with increased alignment are actually related to compaction of a mudrock a further multi-dataset plot was constructed (Figure 5.19). Data from this study, Day-Stirrat *et al.* (2008 and 2010) were classified by I% in I/S and a weakly correlated trend emerged. The R^2 is affected by the highly aligned datpoints at >6MRD.

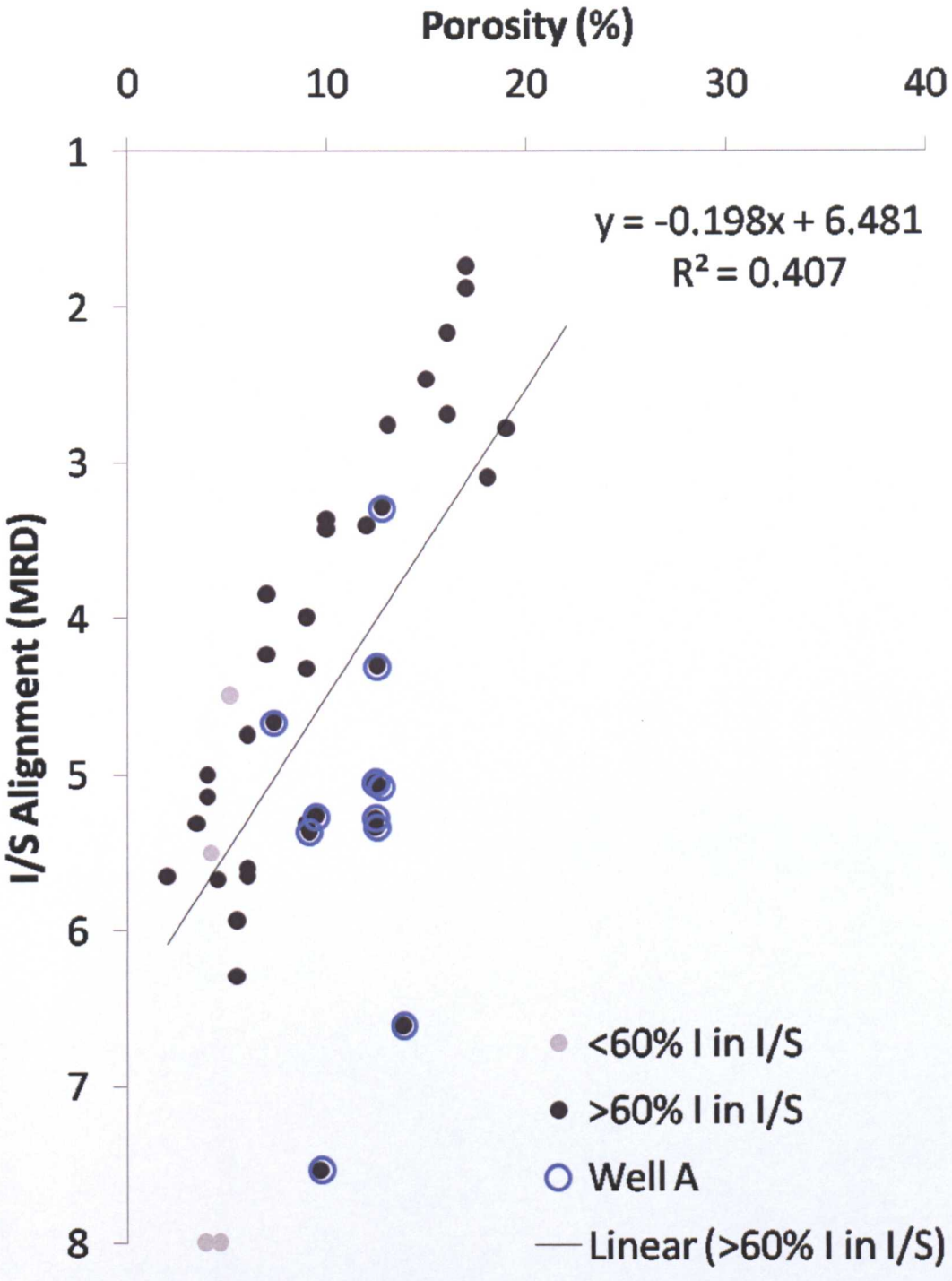

Figure 5.19 Porosity with I/S alignment catorgorized by illitization with data from the clay-rich, Well A samples circled.

Although the correlation shows scatter, what is of interest is the particular porosity range over which alignment takes place. 20% porosity and lower is the range identified on Figure 1.5 in Chapter 1 as the range of porosity loss that mechanical

compaction experiments and indeed, the experiments in Chapter 3 of this thesis are unable to reach. Conversely this is precisely the range that natural mudstones attain in the burial environment at depth.

Although relationships are clearly affected by different variables that reduce correlations, trends do emerge. The ordering effect of illitization and the development of strong, highly aligned clay fabrics appear to coincide with the final, apparently non-mechanical stages of porosity loss.

5.5 Project Conclusions

This thesis details the analysis of experimental results and measurements upon natural samples to quantify the relative roles of mechanical and chemical processes during porosity loss in mudstones and shales, whilst understanding the concepts behind their behaviour at the pore-scale.

The primary controls on the mechanical mechanisms observed are effective stress above the previous maximum, temperature and time. The mechanisms include grain packing/compression and rotation to produce minor fabric development and also thermal hardening.

Packing and rotation due to effective stress, function to increase grain contacts and surpassing the stress conditions that generated the current arrangement of contacts is vital if further compaction is to proceed. Thermal hardening operates where temperature increases and the shearing resistance decreases at individual particle contacts resulting in partial collapse of the of the clay matrix. Porosity decreases as a sufficient number of additional contacts are formed to allow the mudstone to accommodate the stress at higher temperature. MICP illuminates the mechanism at the pore-scale showing the collapse of larger pores to form the additional contacts and the resulting decrease in mean pore radius. Inter and intra particle pores that were once mesopores or even small macropores are reduced to form additional, smaller mesoporosity, also reducing permeability of the matrix.

Calculated porosities during the compaction simulations of Chapter 3 quantified the relative compaction attributed to the varying conditions. Whilst consolidating to 30MPa, stress without the effects of increased temperature or K-exchange reduces the porosity by only 9%. With the effects of thermal hardening and K-exchange this increases to 19% (6% attributed to K-exchange). Increasing effective stress to 50MPa, the same relationship is displayed, but stress is still an important control, compacting the material further to lose 17% porosity compared to 27% with the effects of thermal hardening and K-exchange. This quantifies behavior whilst still under simulated burial conditions, but the permanent magnitude of compaction is only 1.6% volume reduction due to effective stress, without the effects of thermal hardening and K-exchange, but is 8.8% once they are incorporated.

Finally, the effects of time upon mechanical processes which cannot be simulated upon a laboratory timescale were calculated to show that whilst still under simulated burial conditions the grain packing, thermal hardening and K-exchange associated with the Chemical Compaction Test could have reduced porosities down to geologically realistic porosities in the laboratory if left to consolidate for up to 1-2 years. On the same timescale of 1-2 years, without thermal hardening and K-exchange, the stress related packing would only have reduced the calculated porosity to the values achieved by the Chemical Compaction Test in 60 days.

The primary controls on chemical mechanisms are again stress, temperature and time with the addition of fluid chemistry. The mechanisms include the effects of chemical alteration such as potassium exchange and dehydration, but also the

effects of full mineralogical transformation such as the ordering associated with illitization and the proposed link to higher degrees of alignment of phyllosilicates.

The mechanism of dehydration of the expandable clays can occur via loss of the water layers as a result of increased effective stress and temperature. It can also occur as potassium is exchanged for another more hydrated cation. As potassium was exchanged into the interlayer of the clays in the mudstone during the Intermediate Tests, dehydration further to that attributed to P-T conditions could take place through the removal of other hydrated cations allowing shrinkage down to ~10Å and compaction of the mudstone matrix and micro-meso porosity without destabilization and loss of the larger pores. This was because the matrix was not rearranging to accommodate greater stress, it is simply shrinking in a particular direction – perpendicular to bedding whilst under the same effective stress. At an effective stress of 30MPa, this mechanism reduced porosity by 15% by comparison with the 9% lost in the Mechanical Compaction Test at the same stress. However, despite taking on more illitic characteristics, the compaction associated with the K-exchanged expandable clays does not match natural porosities over the timescale of the tests in this thesis.

Mechanisms associated with full mineralogical transformation were not observed in the experimental program and some hypothesised mechanisms, such as sequential pore filling in the Malay Basin samples were not observed in rock property measurements. Some evidence for a proposed alignment mechanism associated with ordering during illitization was found. The Malay Basin porosities that looked anomalous when plotted against depth, plot on trend when plotted with I% in I/S.

Similarly, the I% in I/S data appears considerably more mature than those from other locations when plotted against depth. However, when plotted against temperature the data ties in with several other studies. Elevated geothermal gradient is likely to be facilitating more rapid diagenetic change which also appears to correlate with enhanced porosity loss down to a minimum of ~7% at <2700m.

The Malay Basin samples show a range of phyllosilicate aligned from values similar to the North Sea mudstone to strongly alignment values associated with mineralogically mature samples. Expanding the dataset to include relevant literature showed that, whilst the presence of coarse grains may disguise relationships, alignment associated with mineralogical change and not initial stress related reorganization occurs over a porosity range of <20%. This coincides with the region of porosity loss that is generally seen in natural mudstones at depth, yet mechanical compaction experiments and indeed, the experiments in Chapter 3 of this thesis are unable to reach.

The controls and mechanisms in addition to packing and rotation associated with increased effective stress are not generally incorporated in porosity reduction calculations. However, where more standard geotherms are prevalent and effective stress relationships are utilised employing statistically derived coefficients, the normal effects of other mechanisms exerted under a standard gradient could already by incorporated by proxy, via the coefficients. Once these effects are enhanced in a region of high gradient, such as the Malay Basin, they could be partially or completely behind the enhanced compaction observed in the MICP data. As

mudstone and shale research advances into more challenging areas, full understanding of the interplay of the separate mechanisms may be required.

5.6 Future Work

- This study has utilised a wide variety of compaction equipment and rock property analyses to draw together data from experimental compaction of mudrocks and information from samples compacted in the natural burial environment. Due to the focus on simulation of burial processes, standard geotechnical perameters of the North Sea mudstone were not measured directly and could benefit development of the thermo-mechanical relationships for mudrocks.
- Issues with radial displacement and velocity measurements could be improved by finding components more suitable for the elevated temperatures experienced within the radial oil or finding a method of removing them from it.
- Whilst the experimental program identified several mechanisms separate from grain packing/rotation, the effects of clay mineral diagenesis were not analysed under geologically realistic stress in the laboratory. This could be taken forward by utilizing a cell capable of higher temperatures (~300°C) and/or handling higher pH pore fluids.
- Focussed ion beam techniques could allow better interpretation of microscopic images, clearly identifying features as natural or not. Reflection microscopy could be utilized to better understand the organic-richer sections of the Malay Basin dataset.
- TEM analysis of the shallowest samples of Well A to assess ordering could provide more evidence for a link between ordering and alignmnent.

- Analysis of diagenetic change in the Malay Basin would be improved through further quantitative measurement of the clay fraction, along with physical properties in shallower sections of other mud-rich wells, similar to Well A .

References

6. References

Allen, A.J. (1991) Time-resolved phenomena in cements, clays and porous rocks. Journals of Applied Crystallography 24, 624–634.

Altaner, S. P. & Ylagan, R. F. (1993). Interlayer-by-interlayer dissolution: a new mechanism for smectite illitization. Program with abstracts, 30th Annual Mtg, Clay Minerals Society, San Diego, California, 88.

Altaner, S. P. (1986) Comparison of rates of smectite illitization with rates of K-feldspar disolution. Clays and Clay Minerals, 34, 608-11.

Al-Wardy, W., & Zimmerman, R.W. (2004) Effective stress law for the permeability of clay-rich sandstones, J Geophysical Research – Solid Earth, 109, B04203, doi:10.1029/2003JB002836

Aoyagi, K., Kazama, T., Sekiguchi, K., & Chilingarian, G.V. (1985) Experimental compaction of Na-montmorillonite clay mixed with crude oil and seawater, Water–rock interaction. Elsevier, Amsterdam, Netherlands, 385–392.

Aplin, A.C., Matenaar, I.F., McCarty, D. and van der Pluijm, B.A. (2006) Influence of mechanical compaction and clay mineral diagenesis on the microfabric and pore-scale properties of deep water Gulf of Mexico mudstones. Clays and Clay Minerals, 54, 501-515.

Athy, L.F. (1930) Density, porosity and compaction of sedimentary rocks. AAPG Bulletin 14 (1), 1-24.

Attou, F., Bruand, A. & Le Bissonnais, Y. (1998) Effect of clay content and silt-clay fabric on stability of artificial aggregates. European Journal of Soil Science 49, 569-577

Baker Hughes (2006) Baker Hughes Drilling Fluids Reference Manual.

Baldwin, B., Butler, C.O. (1985) Compaction curves. American Association of Petroleum Geologists Bulletin 69 (4), 622–626.

Bauer, A., Berger, G. (1998) Kaolinite and smectite dissolution rate in high molar KOH solutions at 35 and 80 °C. Appl. Geochem. 13, 905–916.

Bauer, A. and Velde, B. (1999) Smectite transformation in high molar KOH solutions. Clay Minerals, 34, 259–273.

Berger, G., Velde, B. and Aigouy, T. (1999) Potassium sources and illitization in Texas Gulf Coast shale diagenesis Journal of Sedimentary Research 69 (1), 151-157.

Bishop, M.G. (2002) Petroleum systems of the Malay Basin province, Malaysia. United States Geological Survey Open-File Report, 99-50T.

Bjørlykke, K. (1998) Clay mineral diagenesis in sedimentary basins; a key to the prediction of rock properties; examples from the North Sea Basin. Clay Minerals in the Modern Society, 33 (1). Mineralogical Society, London, UK, 15–34.

Bjørlykke, K. (2011) Open-system chemical behaviour of Wilcox Group mudstones. How is large scale mass transfer at great burial depth in sedimentary basins possible? A discussion. Marine and Petroleum Geology , doi:10.1016/j.marpetgeo.2011.01.009.

Bjørlykke, K. (2010) Petroleum Geoscience: From Sedimentary Environments to Rock Physics. Springer, 340.

Bjørlykke, K., Jahren, J., Aagaard, P. & Fisher, Q. (2010) Role of effective permeability distribution in estimating overpressure using basin modelling. Marine and Petroleum Geology 28, 1684–1691.

Boles J. R. & Franks S. G. (1979) Clay diagenesis in Wilcox sandstones of southwest Texas: implications of smectite diagenesis on cementation. J. Sedimentol, Petrol. 49, 55-70.

Boss, B.B. & Fredeen, K.J. (1997) Concepts, instrumentation, and techniques in inductively coupled plasma optical emission spectrometry. The Perkin-Elmer Corporation., Norwalk, CT.

Bowers, G. L., 2001. Determining an appropriate pore-pressure estimation strategy. Offshore Technology Conference, Houston, Texas, OTC 13042.

Brown G. & Brindley G. W. (1980) X-ray diffraction procedures for clay mineral identification: in Brindley, G.W & Brown, G. eds. Crystal Structures of clay minerals and their X-ray idedentifiaction, Monograph 5, Mineralogical Society London, 305-359.

BS 733, Part 2 (1987) Pyknometers. Part 2. Methods for calibration and use of pyknometers. British Standard Institution, London.

BS1377, Parts 2-6 (1990) Determination of moisture content, liquid limit and grain size. British Standard Institution, London.

BS7755, Section 3.8 (1995) ISO 10694, 1995; Soil Quality, Part 3, Chemical Methods, Section 3.8, Determination of organic carbon and total carbon after dry combustion (elementary analysis). British Standard Institution, London.

Buller, A.T. Bjørkum, P.A., Nadeau P. & Walderhaug, O. (2005) Distribution of hydrocarbons in sedimentary basins: The importance of temperature. Statoil Memoir Series No. 7, Netprint.

Burland J.B. (1990) 30th Rankine Lecture - on the compressibility and shear-strength of natural clays. Géotechnique, 40, 329-378.

Chan, K. & Mair, D. (2011) Southeast Asia: Sleeping Giant or Dying Old Man? Petroleum Exploration Society of Great Britain Newsletter (March), 36-43.

Chilingar, G.V. & Knight, L. (1960) Relationship between pressure and moisture content of kaolinite, illite, and montmorillonite clays. American Association of Petroleum Geologists Bulletin, 44 (1), 101–106.

Chipera, S.J. & Bish D.L. (2001) Baseline studies of the clay minerals society source clays: powder x-ray diffraction analyses Clays and clay minerals 49 (5), 398-409.

Claret, F, Bauer. A., Schafer. T, Griflault, L., and Lason, B. (2002) Experimental investigation of the interaction of clays with high-pit solutions: a case study from the callovo-oxfordian fonnation, meuse-haute mame underground laboratory (France). Clays and Clay Minerals. 50,633-646.

Colten-Bradley, V.A. (1987) Role of pressure in smectite dehydration--effects on geopressure and smectite-to-illite transformation. American Association of Petroleum Geologists Bulletin, 71, 1414-1427.

Cornford, C. (1998) Source rocks and hydrocarbons of the North Sea. In: Eds. Glennie, K . Petroleum Geology of the North Sea. Blackwell Sci., Oxford, 376-462.

Cuadros, J. & Linares, J. (1996) Experimental kinetic study of the smectite to illite transformation. Geochimica et Cosmochimica Acta. 60, (3), 439-453.

Day-Stirrat, R. J., Aplin, A. C., Srodon, Jan, and van der Pluijm, B. A., 2008, Diagenetic reorientation of phyllosilicate minerals in Paleogene mudstones of the Podhale Basin, southern Poland: Clays and Clay Minerals, 56 (1), 100–111.

Day-Stirrat, R.J. (2009) High Resolution X-Ray Textural Goniometry Manual (Updated).

Day-Stirrat, R.J., Dutton, S.P., Milliken, K.L., Loucks, R.J., Aplin, A.C., Hillier , S., van der Pluijm, B.A. (2010) Fabric anisotropy induced by primary depositional variations in the silt: clay ratio in two fine-grained slope fan complexes: Texas Gulf Coast and northern North Sea. Sedimentary Geology, 226, 42–53.

Day-Stirrat, R.J. (2011) Discussion in response to Knut Bjørlykke regarding Open-System Chemical Behavior In Deep Wilcox Group Mudstones, Texas Gulf Coast, USA. Marine and Petroleum Geology, doi:10.1016/j.marpetgeo.2011.01.010.

Deer, W.A., Howie, R.A., & Zussman, J. (1966) An introduction to the rock forming minerals. Longman, London.

Delage, P. and Lefebvre, G. (1984) Study of a sensitive Champlain Clay and its evolution during consolidation. Canadian Geotechnical Journal, 21, 21-35.

Deming, D. (1994) Factors necessary to define a pressure seal. AAPG Bulletin, 78, 1005–1009.

Dewhurst, D. N., Aplin, A., Sarda, J. P. and Yang, Y. (1998) Compaction-driven evolution of porosity and permeability in natural mudstones: An experimental Study. Journal of Geophysical Research, 103 (B1), 651-661.

Dickinson, G., 1953. Geological aspects of abnormal reservoir pressures in the Gulf Coast Louisiana. American Association of Petroleum Geologists Bulletin, 37 (2), 410–432.

Di Maio, C. (1996) Exposure of bentonite to salt solution: osmotic and mechanical effects. Géotechnique, 46 (4), 695-707.

Di Maio, C. & Fenelli, G.B. (1994) Residual strength of kaolin and bentonite: the influence of their constituent pore fluid. Géotechnique, 44 (4), 217-226.

Drief, A., Nieto, F. & Sanchez-Navas, A. (2001) Experimental clay-mineral formation from a subvolcanic rock by interaction with 1 M NaOH solution at room temperature. Clays and Clay Minerals, 49 (1), 92–106.

Duffaut, K., and M. Landrø (2007), Vp/Vs ratio versus differential stress and rock consolidation: A comparison between rock models and time-lapse AVO data. Geophysics, 72(5), C81–C94, doi:10.1190/1.2752175.

Dutton, Shirley, P., Loucks, Robert, G., 2010. Diagenetic controls on evolution of porosity and permeability in lower Tertiary Wilcox sandstones from shallow to ultradeep (200–6700 m) burial, Gulf of Mexico Basin U.S.A. Marine and Petroleum Geology, 28, 1775–1787.

Eberl, D. and Hower, J. (1976) The kinetics of illite formation. Bull Geol. Soc. Am. 87, 1326-1330.

Eberl, D. & Hower, J. (1977) The hydrothermal transformation of sodium and potassium smectite into mixed-layer clay. Clays and Clay Minerals, 25, 215-227.

Engelhardt, W.V., Gaida, K.H. (1963) Concentration changes of pore solutions during the compaction of clay sediments. Journal of Sedimentary Petrology, 33 (4), 919–930.

Escoffier S., Homand F., Giraud A., Hoteit N. and Kun Su (2005) Under stress permeability determination of the Meuse/Haute-Marne mudstone. Engineering Geology, 81, 329-340.

Fawad, M., Mondol, N.H., Jahren, J., Bjørlykke, K. (2010). Microfabric quantification of experimentally compressed silt-clay mixtures using image analysis method. Marine and Petroleum Geology, 28, 1698–1712.

Fialips, C.I. (2007) Clay minerals: Physical and chemical properties & Clay minerals: Identification and quantitative analysis. Newcastle University Lecture Notes.

Fies, J.C. & Bruand, A. (1998) Particle packing and organization of the textural porosity in clay-silt-sand mixtures. European Journal of Soil Science, 49, 557-567.

Fjaer, E., Holt, R.M., Horsrud, P., Raaen, A.M. & Risnes, R. (2008) Petroleum Related Rock Mechanics (2nd Edition). Elsevier.

Fjær, E., Lothe, A.E., Sylta Ø. (2010) Effects of Clay Content on Porosity Versus Depth Trends. EAGE Shale Workshop 2010 Abstracts.

Flohr, M.J.K. (1997) X-ray powder diffraction. U.S. Geological Survey Handout.

Freed, R.L. & Peacor, D.R. (1992) Diagenesis and the formation of authigenic illite-rich I/S crystals in Gulf Coast shales: TEM study of clay separates. Journal of Sedimentary Petrology, 62, 220-234.

Garrels, R.M. & Christ, C.L. (1965) Solutions, minerals and equilibria. Harper & Row, New York.

Gautier D.L. (2005) Kimmeridgian Shales Total Petroleum System of the North Sea Graben Province. U.S. Geological Survey Bulletin, 2204-C, 24.

GD SBPS:1 Back Pressured Shearbox (BPS) datasheet.

Ghassemi, A. & Diek, A. (2003) Linear chemo-poroelasticity for swelling shales: theory and application. Journal of Petroleum Science and Engineering, 38, 199–212.

Gluyas J.G. & Swarbrick, R.E. (2004) Petroleum geosciences. Wiley-Blackwell, Oxford.

Goulty, N. R. (2004) Mechanical compaction behaviour of natural clays and implications for pore pressure estimation. Petroleum Geoscience, 10, 73-79.

Goulty, N.R. & Ramdhan, A.M. (2010) Overpressure in the Kutai Basin – A radical reappraisal. Abstract F043, 72nd EAGE Conference & Exhibition incorporating SPE EUROSPEC 2010, Barcelona, Spain.

Gribble, CD. & Hall, A. J. (1992) Optical Mineralogy. Principles & Practice UCL Press, London.

Haines, S. H., van der Pluijm, B. A., Ikari, M. J., Saffer D. M. & Marone C (2009) Clay fabric intensity in natural and artificial fault gouges: Implications for brittle fault zone processes and sedimentary basin clay fabric evolution. J. Geophys. Res., 114, B05406, doi:10.1029/2008JB005866.

Ham, H.H. (1966) New charts help estimate formation pressures. Oil and Gas Journal. 65 (51), 58–63.

Hammer, E., Mørk, M., Britt, E., Næss, A. (2010) Facies controls on the distribution of diagenesis and compaction in fluvial-deltaic deposits. Marine and Petroleum Geology, 28, 1737–1751.

Hansen, S. (1996) A compaction trend for Cretaceous and tertiary shales on the Norwegian shelf based on sonic transit times. Petroleum Geoscience, 2 (2), 159–166.

Hao, F., Zou, H., Gong, Z., Yang, S., Zeng, Z. (2007) Hierarchies of overpressure retardation of organic matter maturation: Case studies from petroleum basins in China. AAPG Bulletin, 91 (10), 1467-1498.

Harrold, T. W. D., Swarbrick, R. E., Goulty, N. R. (1999) Pore pressure estimation from mudrock porosities in Tertiary basins, SE Asia. AAPG Bulletin, 83, 1057-1067.

Hart, B. S., Flemings, P. B. and Deshpande, A. (1995) Porosity and pressure: role of compaction disequilibrium in the development of geopressures in a Gulf Coast Pleistocene basin. Geology, 23 (1), 45-48.

Heng, Y. Y., 1985. Abnormal pressure occurrence in the Malay Basin, Esso Production Malaysia Inc., 165 p, (unpublished report). In: Hoesni, M.J. (2004) Origins of overpressure in the Malay Basin and its influence on petroleum systems. PhD thesis, Durham University, UK.

Hillier, S. (1999) Use of an air brush to spray dry samples for X-ray powder diffraction. Clay Minerals, 34, 127-135.
Hillier, S. (2000) Accurate quantitative analysis of clay and other minerals in sandstones by XRD; comparison of a Rietveld and a reference intensity ratio (RIR) method, and the importance of sample preparation. Clay Minerals, 25, 295-306.

Hillier, S. (2003) Spray drying kit for the preparation of random powder samples for x-ray powder diffraction: Operation and instruction manual.

Ho, N.C., Peacor, D.R., & van der Pluijm, B.A. (1999) Preferred orientation of phyllosilicates in Gulf Coast mudstones and relation to the smectite-illite transition. Clays and Clay Minerals, 47, 495_504.

Ho, N.C., van der Pluijm, B.A., &Peacor, D.R. (2001) Static recrystallization and preferred orientation of phyllosilicates: Michigamme Formation, northern Michigan, USA. Journal of Structural Geology, 23, 887-893.

Hoesni, M.J. (2004) Origins of overpressure in the Malay Basin and its influence on petroleum systems. PhD thesis, Durham University, UK.

Holt, R.M., Furre, A.K., Horsrud, P. (1997) Stress dependent wave velocities in sedimentary rock cores: why and why not? Int. J. Rock Mech. & Min. Sci., 34 (3-4), paper No. 128.

Horsrud, P., Holt, R.M., Sonstebo, E.F., Svano, G. & Bostrom, B. (1994) Time dependant borehole stability: Laboratory studies and numerical simulation of different mechanisms in shale. Eurorock'94 Balkema, Rotterdam.

Horsrud, P., Bostrom, B., Sonstebo, E.F., Holt, R.M. (1998) Interaction between shale and water-based drilling fluids: Laboratory exposure tests give new insight into mechanisms and field consequences of KCl Contents. SPE Paper 48986, Annual Technical Conference and Exhibition, New Orleans.

Howard, J.J. & Roy, D.M. (1985) Development of layer charge and inetics of experimental smectite alteration. Clays and Clay Minerals,33 (2), 81-88.

Hower, J., Eslinger, E.V., Hower, M.E., Perry, E.A. (1976). Mechanism of burial metamorphism of argillaceous sediments. Geol. Soc. Am. Bull., 87, 725–737.

Huang, W-L., Longo, J.D., & Pevear, D.R. (1993) An experimentally derived kinetic model for smectite to illite conversion and its use as a geothermometer. Clays and Clay Minerals,41, 162-77.

Hueckel , T.& Baldi, G. (1990) Thermoplastic behavior of saturated clays: an experimental constitutive study. Journal of geotechnical engineering, ASCE,116, 12, 1778-1796.

Hunnur, A.T. (2006) Smectite to illite transformation: relevence to pore pressure in the subsurface. MSc thesis, University of Oklahoma.

Hüpers, A., Kreiter, S. & Kopf, A.J. (2010) Ramifications of high in-situ temperatures for laboratory testing and inferred stress states of unlithified sediments – a case study from the Nankai margin. Marine and Petroleum Geology, 27, 1565-1571.

Jacob, G., Kisch, H.J., van der Pluijm, B.A. (2000) The relationship of phyllosilicate

orientation, X-ray diffraction intensity ratios, and c/b fissility ratios in metasedimentary rocks of the Helvetic zone of the Swiss Alps and the Caledonides of Jamtland, central western Sweden. Journal of Structural Geology, 22, 245–258.

Jin,L., Gernot, R., Cole, D.R., Mildner, D.F.R., Duffy, C.J., & Brantley, S.L. (2011) Characterization of deep weathering and nanoporosity development in shale—A neutron study American Mineralogist, 96, 498–512.

Johnston, D.H. (1987) Physical properties of shale at temperature and pressure. Geophysics, 52 (10), 1391-1401.

Katsube, J.T. & Collet, L.S. (1975) Electromagnetic propagation characteristics of rocks, in: The Physics and Chemistry of Rocks and Mierals (ed.) Strens, R.G.J., John Wiley & Sons Ltd., London, UK. 279-295.

Katsube (2000) Shale permeablility and pore-structure evolution characteristics. Geological Survey of Canada Current Research 2000-E15.

Kingston, D.R., Dishroon, C.P. & Williams, P.A. (1983) Global basin classification. AAPG Bulletin, 67, 2175-2193.

Kranck, K. and Milligan, T.G. (1985) Origin of grain-size spectra of suspension deposited sediment. Geo-Marine Letters, 5, 61-66.

Kranck, K., Smith, P.C., and Milligan, T.G. (1996) Grain-size characteristics of fine-grained unflocculated sediments. Sedimentology, 43, 589-596.

Krushin, J.T. (2005) Quantifying Shale Porosity—A Thermodynamically Based, Predictive Model which includes the Effects of Mechanical Compaction, Temperature, Mineralogy, and Chemical Diagenesis. GCAGS Transactions, 55, 401 – 414.

Krushin, J.T. (2008) A Compaction-Based Pore Pressure Model for Shales. GCAGS Transactions 58, 575 – 586.

Langford, F. F. and Blanc-Valleron, M.-M. (1990) Interpreting Rock-Eval pyrolysis data using graphs of pyrolizable hydrocarbons vs. total organic carbon. Amer. Assoc. Petrol. Geol. Bull. 74, 799–804.

Lanson, B., Sakharov, B.A., Claret, F., Drits, V.A. (2009) Diagenetic smectite-to-illite transition in clay-rich sediments: A reappraisal of X-ray diffraction results using the multi-specimen method. American Journal of Science 309, 476-516.

Larsen, G. & Chilingar, G.V. (1983) Diagenesis in Sediments and Sedimentary Rocks; 2, Introduction, Developments in Sedimentology 25B. Elsevier Scientific Publishing Co., New York.

Leroueil, S. & Hight,D.W. (2002) Behaviour and properties of natural soils and soft rocks. In Tan, T.S., Phoon, K., Hight,D.W. & Leroueil, S. (Eds.) Characterisation and engineering properties of natural soils, Balkema, Lisse, 29-254

Likos, W.J. & Wayllace, A. (2010) Porosity evolution of free and confined bentonites during interlayer hydration. Clays and Clay Minerals, 58 (3), 399–414.

Liu, G. & Roaldset, E. (1994) A new decompaction model and its application to the northern North Sea. First Break, 12 (2), 81-89.

Loucks, R.G., Reed, R.M., Ruppel, S.C. & Jarvie, D.M. (2009) Morphology, genesis and distribution of nanometer-scale pores in siliceous mudstones of the Mississippian Narnett Shale. Journal of Sedimentary Research 79, 848–861.

Loucks, R.G., Reed, R.M., Ruppel, S.C. & Hammes, U. (2010) Spectrum of Pore Types in Siliceous Mudstones in Shale-Gas Systems. AAPG Search and Discovery Article #90122. AAPG Hedberg Conference, December 5-10, 2010, Austin, Texas.

Lynch, F.L. (1997) Frio shale mineralogy and the stoichiometry of the smectite to illite reaction: the most important reaction in clastic sedimentary diagenesis. Clays and Clay Minerals 45 (5), 618-631.

Lynch, F.L & Reynolds, Jr. R.C. (1985) The stoichemistry of the smectite-illite reaction. Program with abstracts, 21st Ann. Clay Meeting, Clay Minerals Society, Baton Rouge, LA, 84.

Macquaker, J.H.S. & Adams, A.E. (2003) Maximising information from fine-grained sedimentary rocks: an inclusive nomenclature for mudstones. Journal of sedimentary Research, 73 (5), 735-744.

Macquaker, J.H.S., Bentley, S.J. & Bohacs, K.M. (2010) Wave-enhanced sediment-gravity flows and mud dispersal across continental shelves:Reappraising sediment transport processes operating in ancient mudstone successions. Geology, 38 (10) 947-950.

Madon, M. (2007) Overpressure development in rift basins: an example from the Malay Basin, offshore Peninsular Malaysia. Petroleum Geoscience, 13 (2), 169-180.

Magara, K. (1978) Compaction and Fluid Migration: Practical Petroleum Geology. In: Developments in Petroleum Science, 9. Elsevier.

Manning, D.A.C. (2003) Experimental studies of clay mineral occurrence. In: Worden, R.,Morad, S. (Eds.), Clay Mineral Cements in Sandstones. Special Publication of the International Association of Sedimentologists 34. Blackwell Science, Oxford, 177–190.

Marcussen, Ø. Maast, Tom, E. Mondol, N.H., Jahren, J. & Bjørlykke, K. (2010) Changes in physical properties of a reservoir sandstone as a function of burial depth – the Etive Formation, northern North Sea. Marine and Petroleum Geology, 28, 1725–1735.

Mavko, G., Mukerji, T. and Dvorkin, J. (2009) The Rock Physics Handbook (2nd edition). Cambridge University Press, Cambridge.

Meade, R.H. (1966) Factors influencing the early Stages of the compaction of clays and sands: review. Journal of Sedimentary Petrology, 36, 1085–1101.

Meunier, A. & Velde, B. (2004) Illite: origins, evolution and metamorphism. Springer-Verlag, Berlin, Heidelberg.

Minshull, T.A., White, R. (1989) Sediment compaction and fluid migration in the Makran accretionary prism. Journal of Geophysical Research, B, Solid Earth and Planets 94 (6), 7387–7402.

Mitchell, J.K. & Soga, K. (2005) Fundamentals of soil behaviour. 3rd Edition, Wiley & Sons Inc., New Jersey.

Mohd Firdaus Abdul Halim (1994) Geothermics of the Malaysian Sedimentary Basins. Geological Society of Malaysia Bulletin, 36, 163-174.

Mondol, N. H., Bjorlykke, K., Jahren, J., Hoeg, K. (2007) Experimental mechanical compaction of clay mineral aggregates- changes in physical properties of mudstones during burial. Marine and Petroleum Geology, 24, 289-311.

Moore, D. & Reynolds, Jr. R.C. (1997) X-Ray Diffraction and the Identification and Analysis of Clay Minerals, 2nd ed. Oxford University Press, New York.

Mosser-Ruck, R., Pironon, J., Cathelineau, M. and Trouiller, A. (2001) Experimental illitization of smectite in a K-rich solution. European Journal of Mineralogy, 13 (5), 829-840.

Moustafa, M., Malek, S. & Jianfu, S. (2008) Experimental Study of the thermomechanical behavior of the petroleum reservoir. SPE Paper 116953.

Narayanasamy, R., Barr, D. & Milne, A. (2009) Wellbore instability predictions within the Cretaceous mudstones, Clair Field, West of Shetlands. SPE Paper.

Nelson, P.H. (2009) Pore-throat sizes in sandstones, tight sandstones, and shales .AAPG Bulletin, 93 (3), 329-340.

Ngah, K., Madon, M. & Tjia, H. D. (1996) Role of pre-Tertiary fractures in formation and development of the Malay and Penyu basins. In: Hall, R. and Blundell, D. (eds) Tectonic Evolution of Southeast Asia, Geol. Soc. Special Pub. 106, 281-289.

O'Brien, N.R. and Slatt, R.M. (1990) Argillaceous Rock Atlas. Springer-Verlag: New York.

Omi, H., Ueda, T., Miyakubo, K., Eguchi, T. (2005) Dynamics of CO2 molecules confined in the micropores of solids as studied by 13C NMR. Applied Surface Science ,252, 660–667.

Osborne, M. J. and Swarbrick, R. E., (1997) Mechanisms for generating overpressure in sedimentary basins: a reevaluation. AAPG Bulletin, 81 (6), 1023-1041.

Peltonen, C., Marcussen, Ø, Bjørlykke, K. & Jahren, J. (2009) Clay mineral diagenesis and quartz cementation in mudstones: The effects of smectite to illite reaction on rock properties. Marine and Petroleum Geology, 26, 887-898.

Pearson, F.J. (1999) What is the porosity of a mudrock? In: Aplin, A.C., Fleet, A.J. & Macquaker, J.H.S. (eds) Muds and Mudstones: Physical and Fluid Flow Properties. Geological Society, London, Special Publications, 158, 9-21.

Peters, K.E., Moldowan, J.M. , Schoell, M. & Hempkins, W.B. (1986) Petroleum isotopic and biomarker composition related to source rock organic matter and depositional environment. Organic Geochemistry, 10, 17-27.

Post, J.L. (1989) Moisture Content and Density of Smectites. Geotechnical Testing Journal, 12, 217-221.

Potter, P. E., Maynard, J. B. and Depetris, P. J. (2005) Mud and mudstones : introduction and overview. Springer-Verlag: Berlin, Heidelberg, New York.

Pytte, A.M. & Reynolds, Jr. R.C. (1989) The kinetics of the smectite to illite reactionin contact metamorphic shales. In: Naeser, N.D. & McCulloch, T.H. eds. The Thermal History of Sedimentary Basins, Springer-Verlag, New York, 133-140.

Ramdhan, A.M.& Goulty, N.R. (2010) Overpressure and compaction in the Peciko Field, Kutai Basin, Indonesia Abstract F042, 72nd EAGE Conference & Exhibition incorporating SPE EUROSPEC 2010, Barcelona, Spain.

Ramdhan, A.M.& Goulty, N.R. (2010) Overpressure-generating mechanisms in the Peciko Field, Lower Kutai Basin, Indonesia. Petroleum Geoscience, 16, 367-376.

Rieke, H.H., Chilingar, G.V., 1974. Compaction of Argillaceous Sediments. In: Developments in Sedimentology, 16. Elsevier.

Rouquerol, J., Avnir, D., Fairbridge, C.W., Everett, D.H., Haynes, J.H., Pernicone, N., Ramsay, J.D.F., Sing, K.S.W. & Unger, K.K. (1994) International union of pure and applied chemistry recommendations for the characterization of porous solids. Pure & Appl. Chem., 66 (8), 1739-1758.

Rudd, N. & Pandey, G. N. (1973) Threshold pressure profiling by continuous injection. AIME-SPE Paper 4597, 7.

Rule, A.C. & Guggenheim, S. Eds. (2002) CMS Workshop Lectures Vol 11 Teaching clay science CMS.

Schneider, F., Potdevin, J. L., Wolf S., Faille I. (1996) Mechanical and chemical compaction model for sedimentary basin simulators . Tectonophysics, 263, 307-317.

Schoonmaker Tribble, J. (1990) Clay diagenesis in the Barbados accretionary complex: potential impact on hydrology and subduction dynamics. Proceedings of the Ocean Drilling Program, Scientific Results, 110, 97-110.

Schowalter, T. T. (1979) Mechanics of secondary hydrocarbon migration and entrapment. AAPG Bull. 63, 723-760.

Sclater, J.G., Christie, P.A.F. (1980) Continental stretching; an explanation of the post-Mid-Cretaceous subsidence of the central North Sea basin. Journal of Geophysical Research, 85 (B7), 3711–3739.

Singh, I. & Ford, C.H. (1982) The occurrence, causes and detection of abnormal pressure in the Malay Basin. Offshore South East Asia 82 Conference, 9-12th Feb. 1982, Singapore, 11.

Sintubin, M., Wenk, H.R. & Phillips, D. (1995) Texture development in platy materials: Comparison of Bi2223 aggregates with phyllosilicate fabrics. Mater. Sci. Eng. A, 202, 157 – 171, doi:10.1016/0921-5093(95)09811-9.

Sonstebo, E.F., Holt, R.M. (2001) Brine exposure effects on a tertiary North Sea shale. Proc. 38th U.S. Rock Mechanics Symposium. Balkema, The Netherlands, 1375– 1380.

Souque, C., Fisher, Q., Casey, M., Bentham, P. (2010) Structural controls on mechanical compaction within sandstones: an example from the Apsheron Peninsula, Azerbaijan. Marine and Petroleum Geology 28, 1713–1724.

Środoń, J. & Eberl, D. D. (1984) Illite: in Micas, S. W.Bailey, (ed.) Reviews in Mineralogy, Mineralogical Society of America, Washington, D. C., 13, 495-544.

Środoń, J. (1999) Nature of mixed –layer clays and mechanisms of their formation and alteration. Annu. Rev. Earth Planet. Sci., 27, 19-53

Środoń, J., Kotarba, M., Biron˘, A., Suc h, P., Clauer, N., and Wo´ jtowicz, A. (2006) Diagenetic history of the Podhale- Orava Basin and the underlying Tatra sedimentary structural units (Western Carpathians): evidence from XRD and K-Ar of illite-smectite. Clay Minerals, 41, 751-74.

Steiger, R.P. (1982) Fundamentals and use of potassium/polymer drilling fluids to minimize drilling and completion problems associated with hydratable clays. Journal of Petroleum Technology, 34 (8) 1661-1670.

Sultan, N. Delage, P. & Cui, Y.J. (2002) Temperature effects on the volume change behavior of Boom Clay. Engineering Geology, 64, 135-145.

Swan, G., Cook, J., Bruce, S., Meehan, R. (1989) Strain rate effects in Kimmeridge Bay Shale. Int.J. Rock Mech. Min. Sci. & Geomech. Abstr. 26 (2), 135-149.

Swarbrick, R. E., Osborne, M. J. & Yardley, G. S. (2002) Comparison of overpressure magnitude resulting from the main generating mechanisms. In: Huffman, A. R. and Bowers, G. L. (eds), Pressure regimes in sedimentary basins and their prediction. AAPG Memoir, 76, 1-12.

Tan, D.N.K. (2009) Malay and Penyu Basins. In: Geology of Peninsular Malaysia, eds. Hutchinson, C.S. Tan, & D.N.K. Geological Society of Malaysia, Kuala Lumpur, 175-196.

Tan, D.N.K. (2009) Oil and Gas. In: Geology of Peninsular Malaysia, eds. Hutchinson, C.S. Tan, & D.N.K. Geological Society of Malaysia, Kuala Lumpur, 366-405.

Tanner, C.B. & Jackson, M.L. (1947) Nomographs of sedimentation Times for soil particles under gravity or centrifugal acceleration. Soil science society proceedings , 60-65.

Tapponnier, P., Peltzer, G., Le Dain, A.Y., Armijo,R. & Cobbold, P. (1982) Propagating extrusion tectonics in Asia, new insights from simple experiments with plasticene. Geology, 10, 611-616.

Terzaghi, K. (1925) Principles of soil mechanics: I—phenomena of cohesion of clays. IV—settlement and consolidation of clay. Engineering News-Record, 95 (19), 742–746, 874–878.

Thyberg, B., Jahren, J., Winje, T., Bjørlykke, K., Faleide, J.I. (2009) From mud to shale: rock stiffening by micro-quartz cementation. First Break, 27, 27-33.

Thyberg, B., Jahren, J., Winje, T., Faleide, J.I., Marcussen, Ø & Bjørlykke, K. (2010) Quartz cementation in Late Cretaceous mudstones, northern North Sea: Changes in rock properties due to dissolution of smectite and precipitation of micro-quartz crystals. Marine and Petroleum Geology, 28, 1752–1764.

Thyberg, B., Jahren, J. (2011) Quartz cementation in mudstones: sheet-like quartz cement from clay mineral reactions during burial. Petroleum Geoscience, 17, 53-63.

Tullis, T., & Wood D. (1975) Correlation of finite strain from both reduction bodies and preferred orientation of mica in slate from Wales. Geol. Soc. Am. Bull. 86, 632 – 638

Van de Kamp, P.C. (2008) Smectite-Illite-Muscovite transformation, Quartz Dissolution and Silica Release in Shales. Clays and Clay Minerals, 56 (1), 66-81.

Van Gijtenbeek, K., Neyfeld, A. and Prudnikova, A. (2006) One-molar salt solutions used for clay control in water-based frac fluids in Western Siberia. SPE Paper 101203.

Van Oort, E. (2003) On the physical and chemical stability of shales. Journal of Petroleum Science and Engineering, 38, 213– 235.

Vasseur, G., Djeran, M.I., Grunberger, D., Rousset, G., Tessier, D., Velde, B. (1995) Evolution of structural and physical parameters of clays during experimental compaction. Marine and Petroleum Geology, 12 (8), 941–954.

Velde, B., 1996. Compaction trends of clay-rich deep sea sediments. Marine Geology, 133 (3–4), 193–201.

Velde B, Vasseur G. (1992) Estimation of the diagenetic smectite-to-illite transformation in time-temperature space. Am Mineral, 77, 967-976.

Voltolini, M., Wenk, H.R., Mondol, N.H., Bjørlykke, K. & Jahren, J. (2009) Anisotropy of experimentally compressed kaolinite-illite-quartz mixtures. Geophysics , 74(1), D13-D23.

Wang, P. and Li, Q. (2009) The South China Sea: Paleoceanography and Sedimentology Volume 13, Springer Science + Business Media BV. The Netherlands, 139-143.

Waples, D.W., Mahadir R. & Leslie, W. (1995) Implications of vitrinite reflectance suppression for the tectonic and thermal history of the Malay Basin. Geological Society of Malaysia Bulletin, 37, 269-284.

White, J.M., Jr. & Wing, R.S. (1978) Structural development of the South China Sea with particular reference to Indonesia. Proceedings of the 7th Annual Convention of Indonesian Petroleum Association, Jakarta, 159-178.

Worden, R.H. & Burley, S.D. (2003) Sandstone diagenesis: the evolution of sand to stone. In: Worden, R.H. & Burley, S.D. (eds.) Sandstone diagenesis Recent and

Ancient. Blackwell Publishing Ltd., Malden USA, Oxford, UK Melbourne Australia, berlin Germany. 3-44.

Worden, R. H. & Morad, S. (2003) Clay minerals in sandstones: Controls on formation, distribution and evolution. International Association of Sedimentologists Special Publications 34, 3-41.

Yang, Y. L. & Aplin, A. C. (1997) A method for the disaggregation of mudstones. Sedimentology, 44, 559–562.

Yang, Y. L. & Aplin, A. C. (1998) Influence of lithology and effective stress on the pore size distribution and modelled permeability of some mudstones from the Norwegian margin. Mar. Pet. Geol., 15, 163–175.

Yang, Y. & Aplin, A.C. (2004) Definition and practical application of mudstone porosity - effective stress relationships. Petroleum Geoscience, 10, 153-162.

Yang, Y. & Aplin, A.C. (2010) A permeability–porosity relationship for mudstones. Marine and Petroleum Geology, 28, 1692–1697.

Yu, M., Chen G., Chenevert, M. E., and Sharma, M. M. (2001) "Chemical and Thermal Effects on Wellbore Stability of Shale Formations", SPE71366, New Orleans, USA, Sept. 30-Oct. 3, 2001.

Appendices

Appendix A

A.1 Triaxial Test Raw Data

Raw data from the triaxial experiments is considerable in size and is therefore included with this thesis in Excel files on a separate disc , along with other raw data.

Disc 1:

File 1-4 : Triaxial Test Data

File 5: XRD diffractograms & modelling

File 6: CEC raw data

File 7: MICP raw data